SYNTHESIS AND APPLICATIONS OF LARGE SUPRAMOLECULAR NANOCAPSULES: MATRYOSHKA-TYPE MASKS, HIGHER FULLERENE C_{84} PURIFICATION AND STABILIZATION OF METALLIC CLUSTERS AND SUB-NANOPARTICLES

Ernest Ubasart Clarà

Universitat de Girona

Doctoral thesis

SYNTHESIS AND APPLICATIONS OF LARGE SUPRAMOLECULAR NANOCAPSULES: MATRYOSHKA-TYPE MASKS, HIGHER FULLERENE C_{84} PURIFICATION AND STABILIZATION OF METALLIC CLUSTERS AND SUB-NANOPARTICLES

Ernest Ubasart Clarà

Doctoral programme in Chemistry

2022

Supervised by: Dr. Xavi Ribas Salamaña

Tutor: Dr. Xavi Ribas Salamaña

This manuscript has been presented to opt for the doctoral degree from the University of Girona

Universitat de Girona

Dr. Xavi Ribas Salamaña from Universitat de Girona,

I DECLARE:

That the thesis entitled “Synthesis and applications of large supramolecular nanocapsules: Matryoshka-type masks, higher fullerene C_{84} purification and stabilization of metallic clusters and sub-nanoparticles”, presented by Ernest Ubasart Clarà to obtain a doctoral degree, has been completed under my supervision and meets the requirements to opt for a Doctorate.

For all intents and purposes, I hereby sign this document.

Dr. Xavi Ribas Salamaña

Girona, June 3rd, 2022

FULL LIST OF PUBLICATIONS

The thesis is based on a compendium of the following publications:

Chapter III

"Straightforward supramolecular purification of C_{84} from a fullerene extract".

E. Ubasart, C. García-Simón, M. Pujals, K. Asad, N. Chronakis, T. Parella, X. Ribas. *Org. Chem. Front*. **2021**, *8*, *15*, 4101-4105. DOI: 10.1039/D1QO00597A. (Impact factor: 5.281, 1st quartile)

Chapter IV

"Supramolecular nanocapsule as two-fold stabilizer of outer-cavity sub-nanometric Ru NPs and inner-cavity ultra-small Ru clusters".

E. Ubasart, I. Mustieles, J. M. Asensio, G. Mencia, Á. M. López-Vinasco, C. García-Simón, I. del Rosal, R. Poteau, B. Chaudret, X. Ribas. *Nanoscale Horiz*. **2022**, *7*, 607-615. DOI: 10.1039/D1NH00677K (Impact factor: 10.989, 1st quartile)

Publications not included in this thesis:

"A three-shell supramolecular complex enables the symmetry-mismatched chemo- and regioselective bis-functionalization of C_{60}".

E. Ubasart, O. Borodin, C. Fuertes-Espinosa, Y. Xu, C. García-Simón, L. Gómez, J. Juanhuix, F. Gándara, I. Imaz, D. Maspoch, M. von Delius, X. Ribas. *Nat. Chem*. **2021**, *13*, *5*, 420-427. DOI: 10.1038/s41557-021-00658-6. (Impact factor: 24.427, 1st quartile)

"Nanocapsule-Templated Regioselective Synthesis of CPP[2]Catenanes by Regioselective Bingel Bisaddition to C_{60}⊂[10]CPP".

F. M. Steudel, E. Ubasart, X. Ribas, M. von Delius. **2022**. *Manuscript in preparation*.

"Complete dynamic reconstruction of C_{60}, C_{70}, and $(C_{59}N)_2$ encapsulation into an adaptable supramolecular nanocapsule".

C. García-Simón, C. Colomban, Y. A. Çetin, A. Gimeno, M. Pujals, E. Ubasart, C. Fuertes-Espinosa, K. Asad, N. Chronakis, M. Costas, J. Jiménez-Barbero, F. Feixas, X. Ribas. *J. Am. Chem. Soc.* **2020**, *142*, *37*, 16051-16063. DOI: 10.1021/jacs.0c07591. (Impact factor: 15.419, 1st quartile)

LIST OF ABBREVIATIONS

0D	Zero-dimensional
1D	One-dimensional
2D	Bi-dimensional
3D	Three-dimensional
acac	acetylacetonate
biphen	biphenyl
ca.	circa
C6P	calix[6]arene phosphine C6P
CA	Cellulose acetate
CB[n]	Cucurbit[n]uril
$[CBPQT]^{2(+\bullet)}$	cyclobis(paraquat-*p*-phenylene) diradical
CC	Cyclochrysenylene
CD	Cyclodextrins
CNBs	Carbon nanobelts
CNRs	Carbon nanorings
CNTs	Carbon nanotubes
COD	1,5-Cyclooctadiene
COFs	Covalent Organic Frameworks
COT	1,3,5,7-Cyclooctatetraene
CPP	Cycloparaphenylene
CPPA	Cycloparaphenyleneacetylene
CPT	Cyclo-5,15-poprhyrinylene-4,4',4''-terphenyl
CRY	Cryptophane-111
CS_2	Carbon disulfide
CTV	Cyclotriveratrylene
CVE	Cluster valence electron
DETA	Diethylenetriamine
DFT	Density Functional Theory
dppp	1,10-bis(diphenylphosphino)propane
equiv.	Equivalents
ESI-MS	Electrospray Ionization – Mass Spectrometry
EtCy	Ethylcyclohexane

EtBz	Ethylbenzene
exTTF	π-extended tetrathiafulvalene
h	hours
HDO	hydrodeoxygenation
HIV-1	Human immunodeficiency virus 1
HOMO	Highest occupied molecular orbital
HPLC	High-performance liquid chromatography
IPR	Isolated pentagon rule
K_a	Affinity constant
L	Ligand
LUMO	Lowest unoccupied molecular orbital
M	Metal
m/z	Mass-to-charge ratio
MBC	calix[6]arene thiol MBC
MD	Molecular Dynamics
MHz	Megahertz
mL	millilitre
MNPs	Metallic Nanoparticles
MOFs	Metal Organic Frameworks
n.d.	Not detected
NMR	Nuclear Magnetic Resonance
NPs	Nanoparticles
OC	Organic Cage
o-dcb	1,2-Dichlorobenzene
OPV	Organic Photovoltaics
PCC	Porous Coordination Cage
PCE	Power conversion efficiency
PDI	Perylene Diimide
PhH	Benzene
PhMe	Toluene
POC	Porous Organic Cage
POPs	Porous Organic Polymers
porph	Porphyrin
ppp	phenyl-phenyl-phenyl
PSC	Perovskite Solar Cell
PSEP	Polyhedral skeletal electron pair

pTp	Phenyl-Triple bond-Phenyl
PVP	Polyvinylpyrrolidone
pyr-IMes	pyrene-tagged N-heterocyclic-carbene ligands
pyz	pyrazine
r.t.	Room temperature
rac-CRY	Racemic CRY
Ru@rGO	Graphene-supported ruthenium nanoparticles
SEM	scanning transmission electron microscopy
sp	Square pyramid
st-PMMA	syndiotactic poly(methyl methacrylate)
SubPc	Subphtalocyanine
tb	Trigonal bipyramid
TEM	Transmission electron microscopy
THF	Tetrahydrofuran
TLC	Thin-Layer Chromatography
UV-Vis	Ultraviolet-visible spectroscopy
Zn-TCPP	Zinc Tetrakis(4-carboxyphenyl)porphyrin

ACKNOWLEDGEMENTS

This work would not have been possible without the following collaborations:

- Serveis Tècnics de Recerca from Universitat de Girona for technical support, with special remark to Dr. Laura Gómez.
- Dr. Daniel Maspoch, Dr. Inhar Imaz and Dr. Judith Juanhuix from Institut Català de Nanociència i Nanotecnologia (ICN2) and ALBA synchrotron, for the XRD data.
- Dr. Felipe Gándara from Materials Science Institute of Madrid for XRD support.
- Dr. Teodor Parella from Universitat Autònoma de Barcelona for the support with the NMR data.
- Prof. Dr. Max von Delius, Dr. Youzhi Xu, Oleg Borodin and Fabian Steudel from University of Ulm for the collaborative research.
- Dr. Agustí Lledó from Universitat de Girona for .gif support.
- Prof. Dr. Bruno Chaudret, Dr. Juan Manuel Asencio, Dr. Irene Mustieles-Marín, Dr. Ángela M. López-Vinasco and Dr. Gabriel Mencía from Université Toulouse III Paul Sabatier (France) for the collaborative research and hosting during my scientific visits.
- Solène Gentil from Ecole Polytechnique Fédérale de Lausanne (Switzzerland) for the collaborative research and hosting during my scientific visit.
- Dr. Romuald Poteau and Dr. Iker del Rosal from Université Toulouse III Paul Sabatier (France) for the DFT calculations.
- Dr. Karam Asad and Dr. Nikos Chronakis from University of Cyprus for collaborative research and for providing $(C_{59}N)_2$.
- Financial support by:
    - Serveis Tècnics de Recerca from Universitat de Girona (INV218_2017)
    - MINECO-Spain (PID2019-104498GB-I00)
    - Generalitat de Catalunya (2017SGR264)
    - X. Ribas ICREA Academia award 2015 and 2020

TABLE OF CONTENTS

GRAPHICAL ABSTRACT

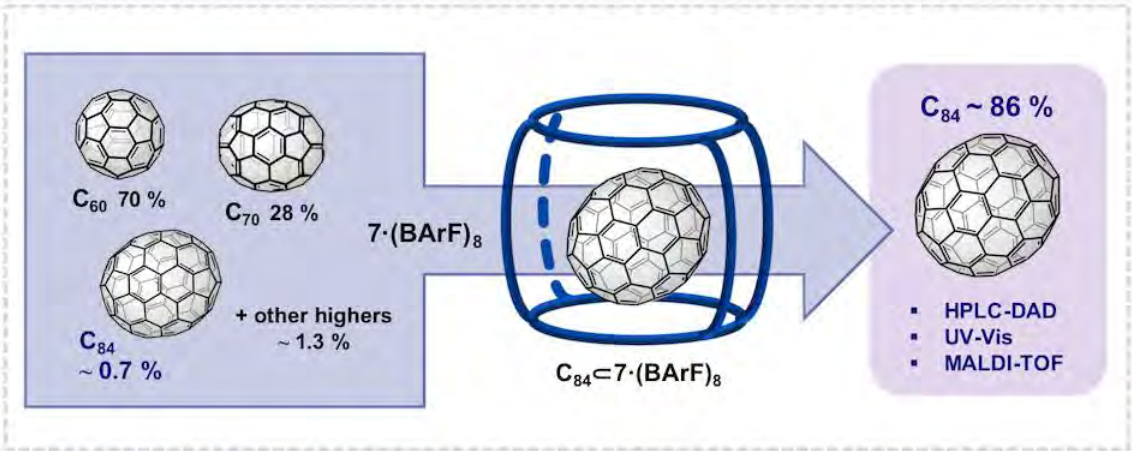

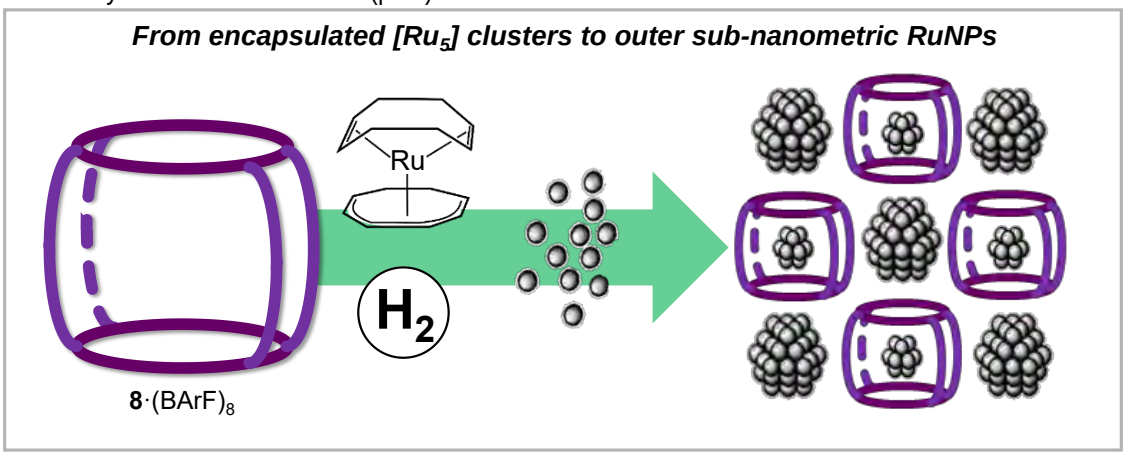

LIST OF FIGURES

LIST OF TABLES

SUMMARY

The development of supramolecular assemblies with big cavities is important to recognize specific guests or infer a chemo- or regioselective chemistry, in analogy to natural enzymes. The objective of this thesis was to design, synthesize and characterize new 3D supramolecular nanocapsules bearing large cavities to use them in different applications. Host-guest studies for each nanocapsule were performed with different guests including fullerene-C_{60}, the **C_{60}⊂[10]CPP** complex, higher fullerenes and the azafullerene-$(C_{59}N)_2$. Furthermore, the synthesis of metallic nanoparticles was investigated in the presence of supramolecular nanocapsules.

In the first part of this thesis, corresponding to the Chapter V.1 and Annex 1, a matryoshka-like assembly was synthesized by encapsulating the **C_{60}⊂[10]CPP** complex in a tetragonal prismatic nanocapsule bearing a pTp-based macrocyclic clip. This new system showed strong host-guest assembly only when the three components were present. The synergistic effect of the tetragonal prismatic nanocapsule and the nanohoop [10]CPP molecule severely limited the exposed surface of the C_{60} entrapped and led to the regioselective formation of ***trans*-3** bis-adduct under Bingel cyclopropanation conditions. The combination of XRD, NMR and void analysis afforded a clear understanding on the specific regioselectivity imposed by the supramolecular mask. The ***trans*-3** bis-adduct products were analyzed and characterized by means of HPLC, UV-Vis and NMR.

In Chapter III and Chapter V.2, the use of large tetragonal prismatic nanocapsules to selective encapsulate higher fullerenes was investigated. Effectiveness on the C_{84} purification directly from fullerene extract soot was demonstrated by using the pTp-based nanocapsule, as ascertained by ESI-MS, HPLC and MALDI-TOF. The affinity of pTp- and ppp-based nanocapsules for other larger fullerenic species such as azafullerene $(C_{59}N)_2$ was studied by UV-Vis titrations. Moreover, competition studies of $(C_{59}N)_2$ and fullerene-C_{84} with a supramolecular nanocapsule served to determine the association constant of pTp-nanocapsule with C_{84} and circumvent the poor solubility of the latter.

Finally, in Chapter IV and Chapter V.3, in the context of developing catalytically-active metallic nanoparticles with large surface/volume ratio, the synthesis of sub-nanometric Ru nanoparticles in the presence of the ppp-based supramolecular nanocapsule was performed. The catalytic properties of this nanoparticles were tested on the hydrogenation of styrene to ethylbenzene, in agreement with the sub-nanometric size of the Ru NPs. Moreover, the encapsulation of clusters of $[Ru_5]$ was observed by ESI-MS monitoring,

suggesting the trapping of the initial stages of the nucleation process towards nanoparticle formation. DFT studies were performed to determine a plausible structure for [Ru_5] clusters and the possible stabilization regions of the nanocapsule.

RESUM

El desenvolupament d'assemblatges supramoleculars amb cavitats grans és important per tal de reconèixer substrats específics o inferir un control en la quimio- o regioselectivitat d'un procés químic, en analogia als enzims naturals. L'objectiu d'aquesta tesi era dissenyar, sintetitzar i caracteritzar noves nanocàpsules supramoleculars 3D amb grans cavitats per utilitzar-les en diferents aplicacions. S'han realitzat estudis d'afinitat per a cada nanocàpsula amb diferents substrats, incloent ful·lerè-C_{60}, el complex C_{60}⊂[10]CPP, ful·lerens d'ordre superior i l'azaful·lerè-$(C_{59}N)_2$. A més, s'ha investigat la síntesi de nanopartícules metàl·liques en presència de nanocàpsules supramoleculars.

A la primera part d'aquesta tesi, corresponent al Capítol V.1 i Annex 1, es va sintetitzar una estructura del tipus matrioixca encapsulant el complex **C_{60}⊂[10]CPP** en una nanocàpsula prismàtica tetragonal basada en clips macrocíclics pTp. Aquest nou sistema presentava una forta interacció entre els diferents components quan els tres hi eren presents. L'efecte sinèrgic de la nanocàpsula prismàtica tetragonal i la molècula circular, [10]CPP, limitava severament la superfície exposada del C_{60} atrapat, provocant així la formació regioselectiva del bis-adducte ***trans*-3** en condicions de ciclopropanació Bingel. La combinació d'experiments de difracció de raigs X, RMN i anàlisi de buits va permetre una comprensió de la regioselectivitat imposada per aquest tipus de màscara supramolecular. Els bis-adductes ***trans*-3** es van analitzar i caracteritzar mitjançant HPLC, UV-Vis i RMN.

Al Capítol III i Capítol V.2, es va investigar l'ús de nanocàpsules prismàtiques tetragonals grans per encapsular selectivament ful·lerens d'ordre superior. Es va demostrar que amb la nanocàpsula supramolecular basada en pTp s'obtenia una eficaç purificació de l'espècie C_{84} directament d'un sutge de ful·lerens, comprovat mitjançant ESI-MS, HPLC i MALDI-TOF. L'afinitat de les nanocàpsules basades en pTp i ppp per a altres espècies de ful·lerens de mida gran com l'azaful·lerè $(C_{59}N)_2$ es va estudiar mitjançant valoracions UV-Vis. A més, es van dur a terme estudis de competició del $(C_{59}N)_2$ i el ful·lerè-C_{84} amb una nanocàpsula supramolecular. D'aquesta manera es va determinar la constant d'associació de la nanocàpsula amb el C_{84}, ja que la poca solubilitat d'aquest ful·lerè feia impossible el càlcul mitjançant valoracions UV-Vis.

Finalment, al Capítol IV i Capítol V.3, per tal de desenvolupar nanopartícules metàl·liques actives en catàlisi amb un valor elevat de superfície/volum es va decidir utilitzar una nanocàpsula supramolecular basada en clips macrocíclics ppp per tal de generar nanopartícules sub-nanomètriques de Ru. Les propietats catalítiques d'aquestes

nanopartícules es van provar en la hidrogenació d'estirè a etilbenzè, d'acord amb la mida sub-nanomètrica de les nanopartícules de Ru. A més, es va observar mitjançant ESI-MS, l'encapsulació de clústers de [Ru_5], suggerint l'encapsulació d'aquests en l'etapa inicial del procés de nucleació seguit de la formació de les nanopartícules. Per últim, es van realitzar estudis DFT per determinar una estructura plausible per als clústers [Ru_5] i les possibles regions d'estabilització de la nanocàpsula.

RESUMEN

El desarrollo de ensamblajes supramoleculares con cavidades grandes es importante para reconocer sustratos específicos o inferir un control en la quimio- o regioselectividad de un proceso químico, de manera análoga a las enzimas naturales. El objetivo de esta tesis era diseñar, sintetizar y caracterizar nuevas nanocápsulas supramoleculares de 3D, cuyas grandes cavidades internas puedan ser utilizadas en distintas aplicaciones. Por tal motivo se han realizado estudios de afinidad de dichas nanocápsulas con diferentes sustratos, incluyendo fullereno-C_{60}, el complejo C_{60}⊂[10]CPP, fullerenos de orden superior y el azafullereno-$(C_{59}N)_2$. Además, se ha investigado la síntesis de nanopartículas metálicas en presencia de nanocápsulas supramoleculares.

En la primera parte de esta tesis, correspondiente al Capítulo V.1 y Annex 1, se sintetizó una estructura del tipo matryoshka encapsulando el complejo **C_{60}⊂[10]CPP** en una nanocápsula prismática tetragonal usando clips macrocíclicos pTp. Este nuevo sistema presentaba una fuerte interacción entre los diferentes componentes cuando los tres estaban presentes. El efecto sinérgico de la nanocápsula prismática tetragonal y la molécula circular, [10]CPP, limitaba severamente la superficie expuesta del C_{60} atrapado, de tal forma que cuando se sometía a las condiciones de ciclopropanación de Bingel se obtenía de forma regioselectiva el bis-aducto ***trans*-3**. Gracias a la combinación de experimentos de difracción de rayos X, RMN y análisis de huecos se obtuvo comprensión adecuada de la regioselectividad impuesta por la máscara supramolecular. Los bis-aductos ***trans*-3** se analizaron y caracterizaron mediante HPLC, UV-Vis y RMN.

En el Capítulo III y Capítulo V.2, se investigó el uso de nanocápsulas prismáticas tetragonales grandes para encapsular selectivamente fulerenos de orden superior. Se demostró que con la nanocápsula supramolecular basada en pTp se obtenía una eficaz extracción de la especie C_{84} directamente de un hollín de fulerenos, tal como se podía comprobar mediante ESI-MS, HPLC y MALDI-TOF. La afinidad de las nanocápsulas basadas en pTp y ppp para otras especies de fulerenos de gran tamaño como el azafullereno $(C_{59}N)_2$ se estudió mediante valoraciones UV-Vis. Además, se llevaron a cabo estudios de competición del $(C_{59}N)_2$ y el fullereno-C_{84} con una nanocápsula supramolecular. De esta forma se determinó la constante de asociación de la nanocápsula con el C_{84}, ya que la baja solubilidad de este fullereno hacía imposible el cálculo mediante valoraciones UV-Vis.

Finalmente, en el Capítulo IV y Capítulo V.3, para desarrollar nanopartículas metálicas activas en catálisis con un valor elevado de superficie/volumen se utilizó una nanocápsula

supramolecular basada en clips macrocíclicos ppp para generar nanopartículas sub-nanométricas de Ru. Las propiedades catalíticas de estas nanopartículas se probaron en la hidrogenación de estireno a etilbenceno, de acuerdo con el tamaño sub-nanométrico de las nanopartículas de Ru. Además, se observó mediante ESI-MS, la encapsulación de clústeres de [Ru_5], sugiriendo la encapsulación de éstos en la etapa inicial del proceso de nucleación seguido de la formación de las nanopartículas. Por último, se realizaron estudios DFT para determinar una estructura plausible para los clústeres [Ru_5] y las posibles regiones de estabilización de la nanocápsula.

Chapter I. General introduction

I.1. Supramolecular chemistry

Supramolecular chemistry was defined in the early 80s by one of the pioneers of the field, Jean-Marie Lehn (Nobel Prize in Chemistry 1987), as "the chemistry of the intermolecular bonding, wrapping the structures and functions of the entities developed by the association of two or more chemical units". In other words, it is the chemistry field that studies the supramolecular interactions beyond molecules.[1]

Oppositely to conventional chemistry, which is focused into the covalent bond, supramolecular chemistry focuses in the weak intermolecular forces such as hydrogen bonding, hydrophobic effects, electrostatic forces, π-π interactions and van der Waals forces as well as metal coordination bonding.[2] These studies are commonly inspired by biological systems to develop complex supramolecular structures and during the past four decades, metallo-supramolecular chemistry have developed a wide range of structures such as helicates, grids, links, knots, spheres and cages.[3] The most common and widely studied unimolecular receptors are cyclodextrins, calixarenes, cyclophanes, cucurbiturils, crown ethers and cryptophanes, while other more complex structures comprise organic capsules, metal-containing cages, proteins, and DNA duplex (Figure I.1).[4] Some important areas of study in supramolecular research include molecular self-assembly and host-guest chemistry.[5-7]

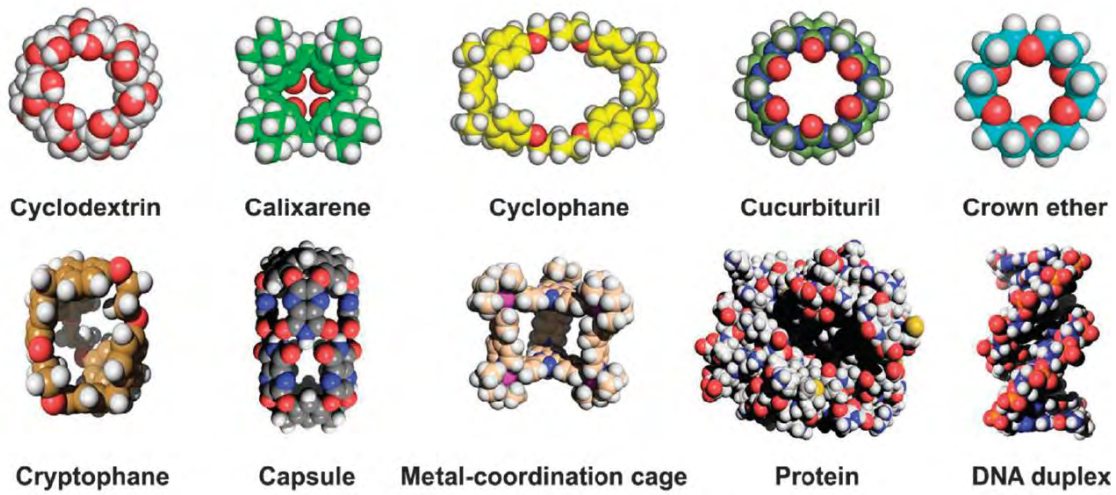

Figure I.1. Families of three-dimensional supramolecular structures. Reprinted with permission of Junqiu Liu (Ref. 4).

Supramolecular self-assembly is based on the arrangement of two or more molecules or ions through reversible intermolecular interactions without the guidance from an external source to develop a new larger aggregates with defined shapes and dimensions (Figure I.2).

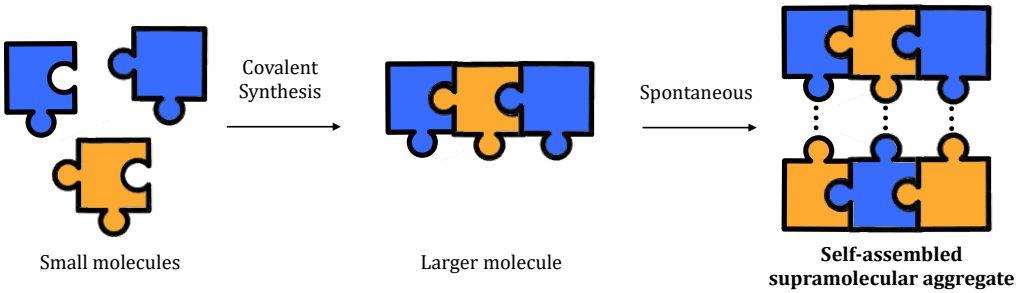

Figure I.2. Representation of the self-assembly process between different building-blocks.

Host-guest chemistry is described as the composition of two or more molecules held together through non-covalent bonds and it is based on the supramolecular recognition which allows a unique structural composition. In general, a supramolecular molecule (host) possesses a cavity in which a smaller molecule (guest) can be accommodated (Figure I.3).

The discovery of crown ethers prompted the study of macrocyclic compounds with the ability to bind atoms or molecules in their cavities. However, host-guest chemistry and molecular recognition were, at that time, challenging topics to study.

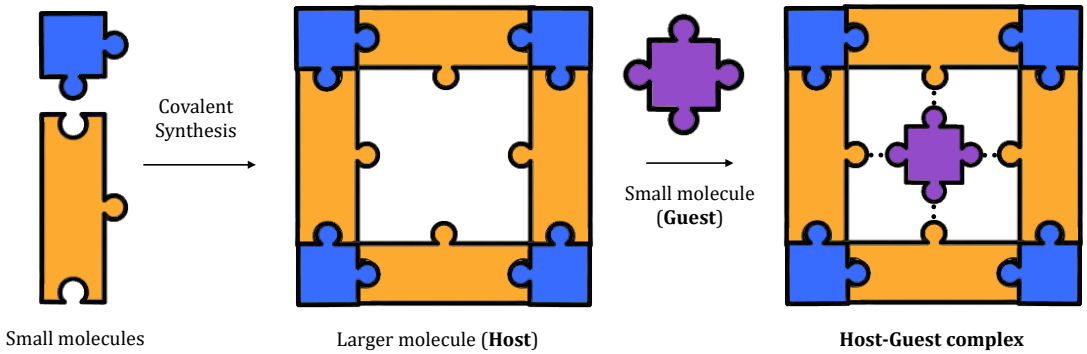

Figure I.3. Representation of the inclusion of a guest into a host molecule forming a host-guest complex.

Supramolecular self-assembled metallocages

The concept of supramolecular 3D self-assembly systems using transition metals was pioneered by Ogura and Fujita in 1995 by developing one of the first supramolecular cage-

complex.[8] However, von Schnering and co-workers some years before, in 1988, developed the first example of tetrahedron shaped chelate complex, Mg_4.[9]

The strategy of metal-mediated self-assembly for the development of new 3D receptor structures has been extensively developed and enabled the preparation of complex nanosized frameworks, which could not be prepared by conventional covalent synthesis.[10-16] More recently, Stang and co-workers reviewed 2D and 3D platinum-based systems which have been broadly studied due to their facile preparation and led up to several applications.[17]

Applications of supramolecular nanoreceptors

The interest in the supramolecular chemistry field evolved in mimicking the biological systems and their cooperative interactions, aiming at controlling the synthesis of structures with well-defined voids. In the past 25 years, the increase in structural and functional complexity of self-assembled coordination cages led to the development of applications such as molecular recognition[18, 19], molecular separation[20], stabilization of reactive species[21], reactivity modulation[22-26], catalysis[27] or biological applications.[28, 29]

With respect to reactivity modulation, many examples have been reported during the last years.[22, 23] Taking advantage of the confinement effect, a different selectivity has been shown in some reactions such as cycloadditions,[24] olefin photodimerization[25] or hydroformylation[26]. Apart from the higher selectivity, these reactions provided higher efficiencies in contrast to the non-hosted reactions.

With regard to molecular sensing, Nitschke and co-workers developed in 2019 a water-soluble tetrahedral capsule capable of binding biologically-relevant species for fluorometric recognition.[18] The cationic metal-organic cage was able to discriminate between neutral and anionic guests in water. For instance, anionic mono- and poly-phosphoric esters, including nucleotides, showed fast-exchange binding.

Finally, there are many examples for biological applications.[28] For instance, a biocompatible octahedral molecular capsule, PCC-1, based on six tetranuclear zinc clusters as vertices assembled by eight ligands as faces, was reported in 2021.[29] This structure was able to encapsulate and deliver a DNA topoisomerase I inhibitor into the nucleus of living cells.

On the other hand, the recognition of spheroidal-shaped molecules such as fullerenes has attracted lots of attention and is highlighted in Chapter I.2.1.

Hosts within a host (Matryoshkas)

A molecular Russian doll or a Matryoshka is defined as a host within a host or a box-in-box complex (Figure I.4), being a very challenging and scarcely explored topic in supramolecular chemistry. Despite this, there are examples in the literature on encapsulation of multiple components in a molecular container to modify their reactivity and properties. Other examples of Russian dolls can act as a template to form a bigger multicomponent structure.[30] However, the use of supramolecular nanocapsules to develop a matryoshka entity and infer a singular regioselectivity in a chemical reaction is so far unexplored.

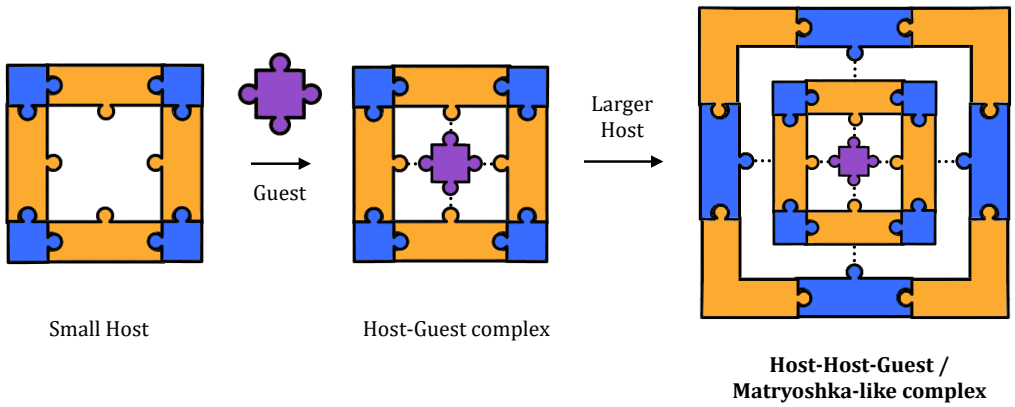

Figure I.4. Representation of a matryoshka upon the inclusion of a host-guest complex into a host molecule bearing a bigger cavity.

Some host-guest systems are defined by the recognition of a cation by a macrocycle. For instance, crown ethers are effective hosts for small cationic guests due to strong intermolecular interactions. On the other hand, supramolecular nanocapsules are ideal candidates to develop Russian doll-like structures due to the confinement effect and the non-covalent interactions. Thereafter, some authors reported the encapsulation of a given host-guest system in a larger self-assembled host.

In 2000 Raymond and co-authors synthesized a host, $[Ga_4L_6]^{12-}$, able to encapsulate crown ethers, which in turn trapped alkaline cations (Figure I.5).[31]

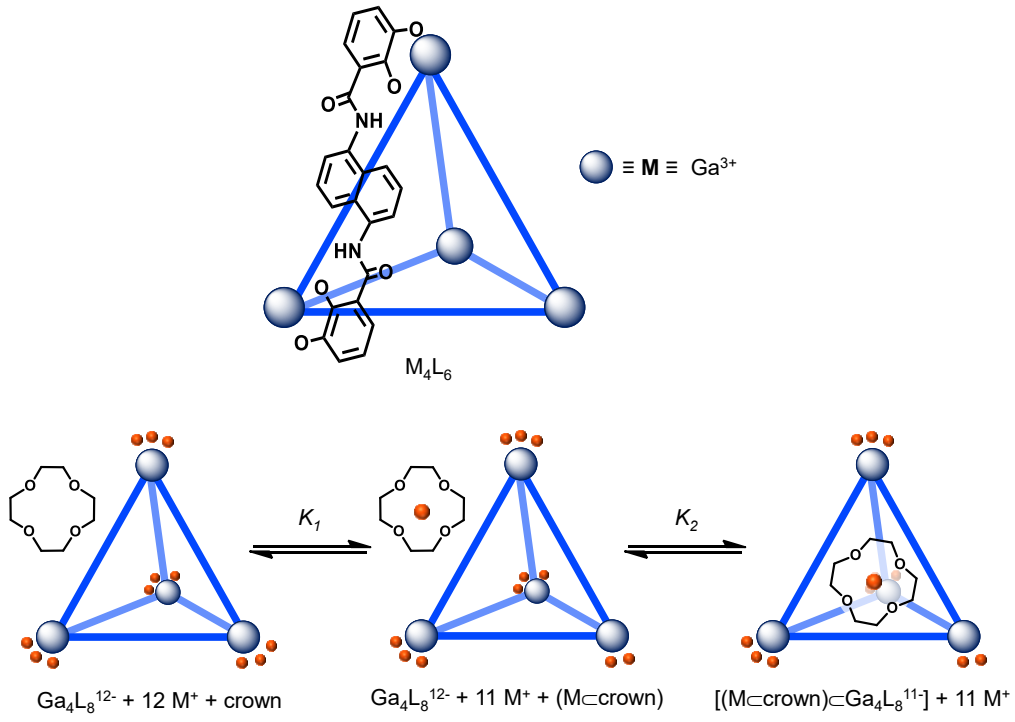

Figure I.5. The encapsulation of an alkali metal cation from $M_{12}[Ga_4L_6]$, (M^+=Li^+, Na^+ or K^+) by a crown ether (equilibrium constant K_1) is followed by encapsulation of the crown ether complex into the cluster cavity (K_2). Reported by Raymond and co-workers in 2000.

In 2002, Dance and co-workers developed a new inclusion complex of cucurbit[5]uril (CB[5]) within cucurbit[10]uril (CB[10]), which are concentric but not coaxial, and with a chloride ion at the centre (Figure I.6).[32]

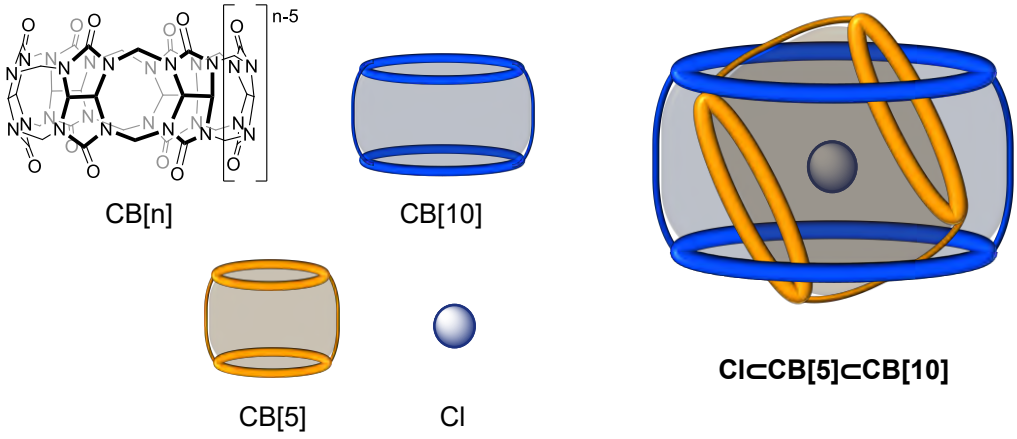

Figure I.6. Inclusion of Cl inside CB[5]⊂CB[10]. The angle between the axis of the inner component CB[5] and the axis of CB[10] is 64º. Reported by Dance and co-workers in 2002.

Another recent example by Nitschke's group reported a self-assembled triazatruxene-based $Fe^{III}_4L_4$ capsule with the ability to host cryptophane-111 (CRY),[33] which at the same time could accommodate a caesium cation or xenon atom (Figure I.7). Apart from the remarkable encapsulation of a cation within an octacationic nanocapsule, the high enantioselectivity of CRY is transferred to the nanocapsule affording an enantiopure nanocapsule, which had two isomers after the encapsulation.

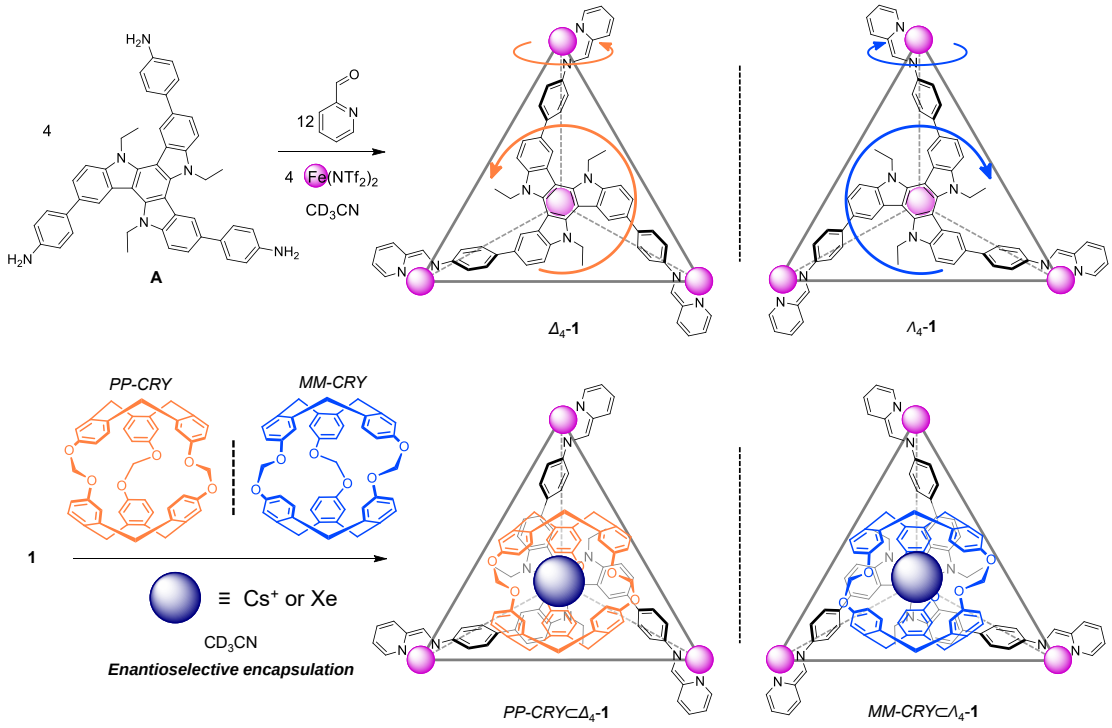

Figure I.7. (a) Subcomponent self-assembly of **1**. (b) Enantioselective encapsulation of Cs/Xe⊂*rac*-CRY by **1**. Reported by Nitschke and co-workers in 2019.

In 2015 Anderson reported a Russian doll formed by two porphyrin-based nanorings coordinated by a bridging ligand resulting in a highly cooperative supramolecular self-assembly (Figure I.8).[30] Some experiments revealed that the Russian doll acted as a single emitter and excitation was transferred outwards. Moreover, the structure was useful as a template to direct the synthesis of amplified covalent nanostructures.

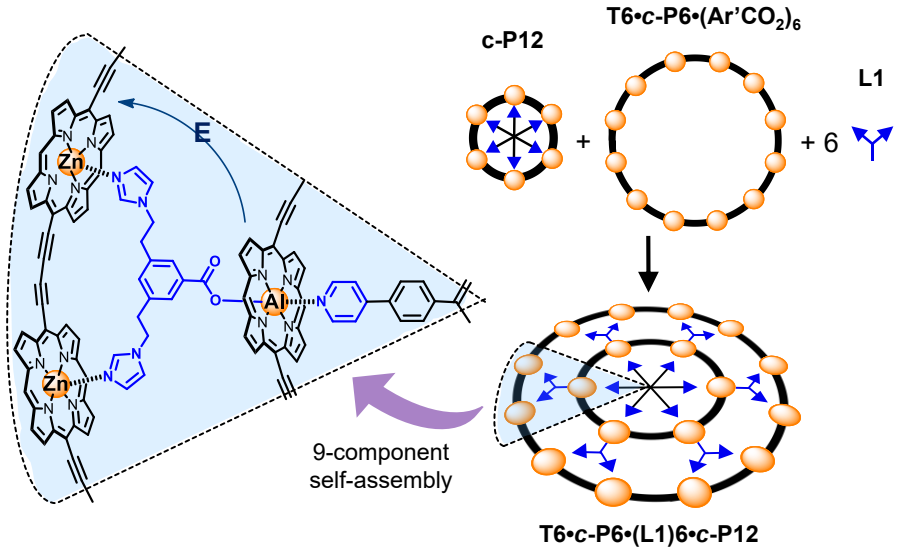

Figure I.8. Self-assembly of the Russian doll complex from a 1:1 mixture of ***c*-P12** and **T6·*c*-P6·(Ar'CO$_2$)$_6$** in the presence of ligand **L1** (in blue). Reported by Anderson in 2015.

In 2016, Liu and co-workers developed a Russian doll using the well-studied Cucurbit[10]uril, CB[10], focusing on the influence on the charge-transfer interactions in the cavity of CB[10] upon encapsulation of bipyridinium molecules and electron-rich compounds (Figure I.9).[34]

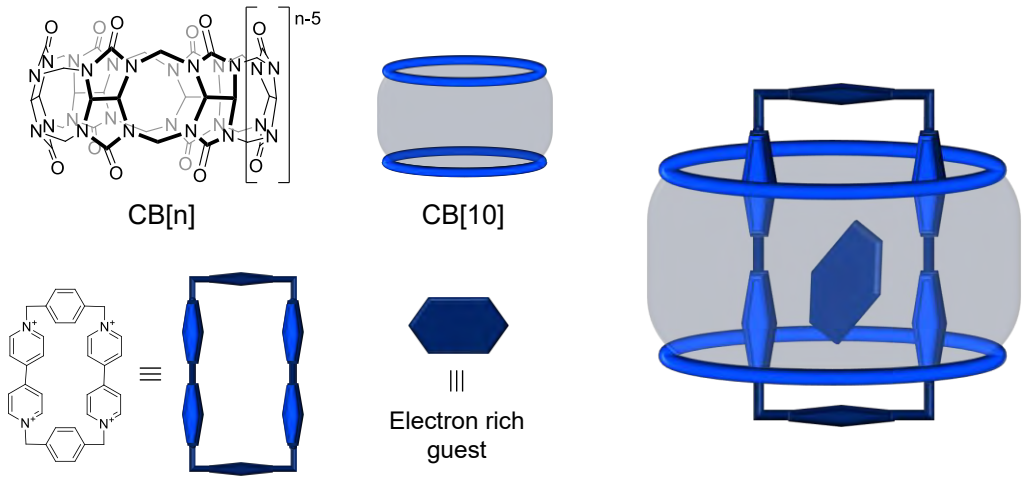

Figure I.9. Schematic illustration of the formation of an inclusion complex between guests and CB[10] reported by Liu and co-workers in 2016.

A similar strategy was published in 2018 by Stoddart and co-workers,[35] who synthesized a rigid tetracationic cyclophane, which, in its diradical dicationic state (**2**$^{2(+\bullet)}$) is ideal for encapsulating cyclobis(paraquat-*p*-phenylene) diradical, [CBPQT]$^{2(+\bullet)}$ (Figure I.10). The strong radical-pairing interactions led to the formation of a unique tetraradical tetracationic, box-in-box complex. This structure indeed, can accommodate small aromatic guests inside such as 1,4-disubstituted benzene derivatives, forming a Russian doll system. The addition of this third component helps to stabilize of the whole structure, which exhibits unusual redox properties.

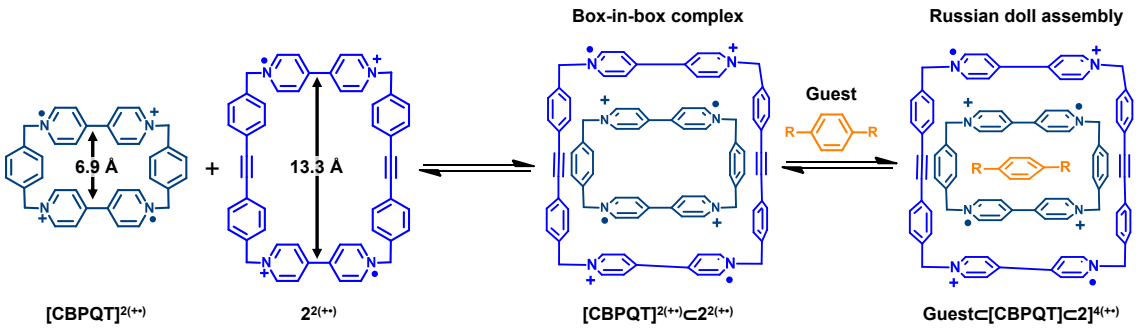

Figure I.10. Proposed superstructures of the tetraradical tetracationic box-in-box complex and Russian doll assemblies reported by Stoddart and co-workers in 2018.

Concerning the encapsulation of fullerenes within Matryoshka assemblies, the example reported by Oda and co-workers in 2004 is highlighted, where they developed a Russian doll system comprised by a fullerene encapsulated in a small nanoring (**1**), which in turn was wrapped in a large nanoring (**4**) (Figure I.11).[36] Carbon nanorings have a curved conjugated surface, which is suitable to encapsulate spheroidal fullerenes.

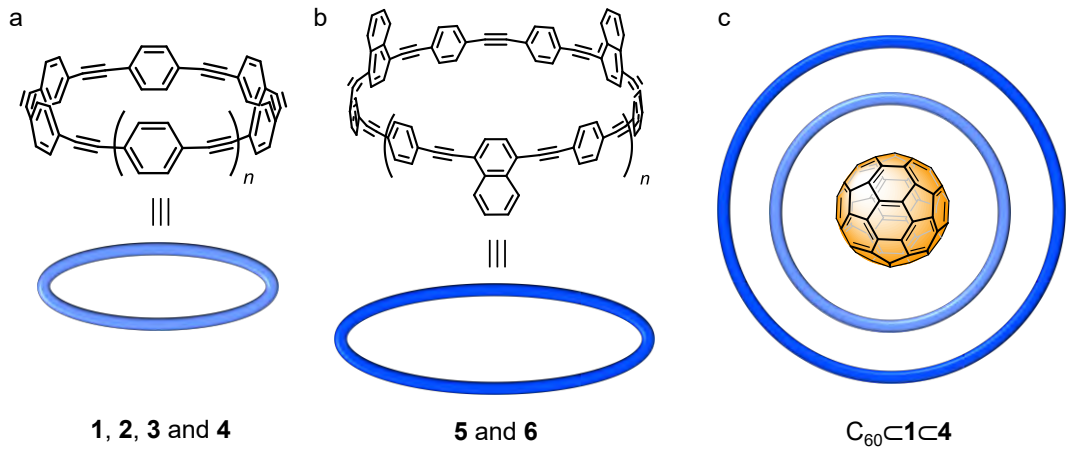

Figure I.11. Molecular structures of (a) CPPAs **1** (n=1), **2** (n=2), **3** (n=3), **4** (n=4), (b) **5** (n=0), **6** (n=1) and (c) C_{60}⊂**1**⊂**4** reported by Oda and co-workers in 2004.

I.2. Fullerenes

Buckminsterfullerene C_{60} was discovered by Kroto, Smalley and Curl in 1985,[37] and it is one of the most renown guests in supramolecular chemistry. It is based on a C_{sp2} cage with a truncated icosahedron structure analogous to a soccer ball, containing 20 hexagons and 12 pentagons. Since its discovery, a huge number of reports have been published concerning new 3D carbon allotropes such as bucky onions, carbon nanotubes or fullerene peapods. Besides, there are the so-called endohedral metallofullerenes (EMF), which contain one or more atoms inside the fullerene carbon cage, highlighting rare earth metals or metallic nitrides and carbides.[38]

Fullerenes are widely used in applications such as organic photovoltaics,[39-43] perovskite solar cells,[44-46] and biomedicine[47-50]. In the field of organic photovoltaics (OPV), the introduction of perovskite compounds as the light-harvesting active layer increased the power conversion efficiency (PCE) from 3.8 to 22% in less than 10 years. However, the main drawback in perovskite solar cells (PSCs) is the low stability due to hysteretic current-voltage behaviour and the high temperatures requirement. To overcome this, new perovskite/fullerene-based hybrid solar cell are being developed to improve their photovoltaic properties.[51, 52] On the other hand, multi-adducts of fullerenes have also been used in biomedical applications. [48, 53-55] Some of these fullerene-based compounds displayed beneficial medical effects such as antioxidant properties and neuroprotective effects.[56] In 2017, Martín and co-workers developed water-soluble hexakis adducts of [60]fullerene with carbohydrate subunits forming nanometric superballs.[48] They were tested in infection assays, being potent inhibitors of cell infection by Ebola virus.

Several studies show that fullerenes under UV light produce singlet oxygen and other reactive oxygen species, so they can be used in photodynamic therapy for cancer treatment.[54] Other studies with rats, revealed the beneficial effects of the fullerene derivatives against diabetes (type 2)[55] and Alzheimer disease[57].

I.2.1. Hosts for fullerene recognition

In this section we will focus on the reported hosts designed to encapsulate fullerene via supramolecular interactions with specific recognition motifs. Importantly, recognition via concave-convex π-π interactions is very relevant, as reviewed by Kurata and co-workers with conjugated C_{sp2}-extended systems.[58] In curved conjugated systems, the electrostatic

interaction plays a fundamental role in addition to the dispersion force, being this important for the development of new materials or supramolecular structures.

I.2.1.1. Organic macrocycles and molecular tweezers (1D and 2D structures)

In 1992, the group of Weinstein reported the first host for fullerenes based on a macrocyclic azacrown ether with long side chains (Figure I.12).[59]

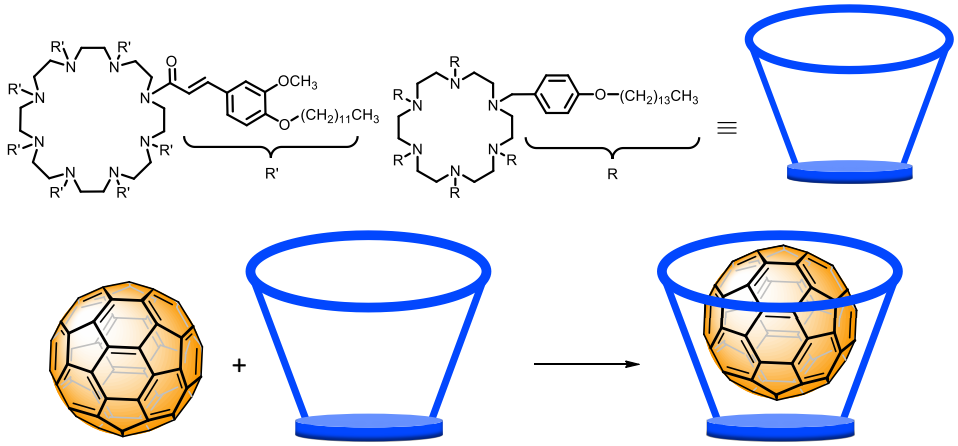

Figure I.12. First host for fullerenes C_{60} and C_{70} based on amphiphilic molecules containing a lipophilic cavity, reported by Weinstein and co-workers in 1992.

Other hydrophobic organic macrocycles such as cyclodextrins[60-62] and calixarenes[63-65] were studied to host and stabilize fullerene species in the early 90s. These structures have been widely used in supramolecular chemistry for diverse applications due to their synthetic accessibility and their tuneable cavities. In 1996, Burkhalter reported the formation of "ball and socket" complexes of cyclotriveratrylene (CTV) binding with C_{60}.[65] In 2004, Zhang and co-workers reported a new type of fullerene assembly by using dimeric cyclodextrins coordinated through metal centres (Figure I.13).[62] This kind of polymer showed interesting properties for application in biomedicine.

In 2010, Chen and co-workers synthesized a triptycene-derived oxacalixarene (**7**) capable to bind fullerenes C_{60} and C_{70} (Figure I.14a).[66] As shown in Figure I.14b, the fluorescence intensity of the macrocycle at λ = 394 nm in toluene decreased constantly with increasing amount of C_{70}. This represented a first example of the complexation of an oxacalixarene with fullerenes.

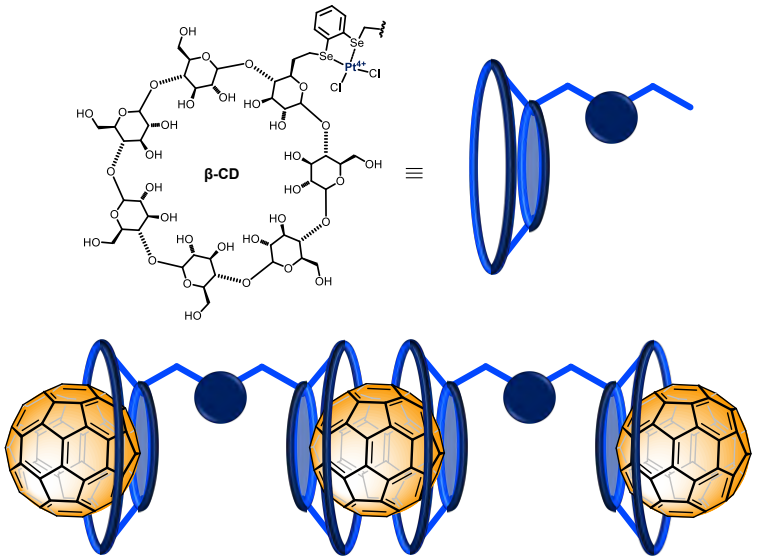

Figure I.13. 1:1 intermolecular C_{60} inclusion mode between metallobridged bis(β-CD) and fullerene reported by Zhang and co-workers in 2004.

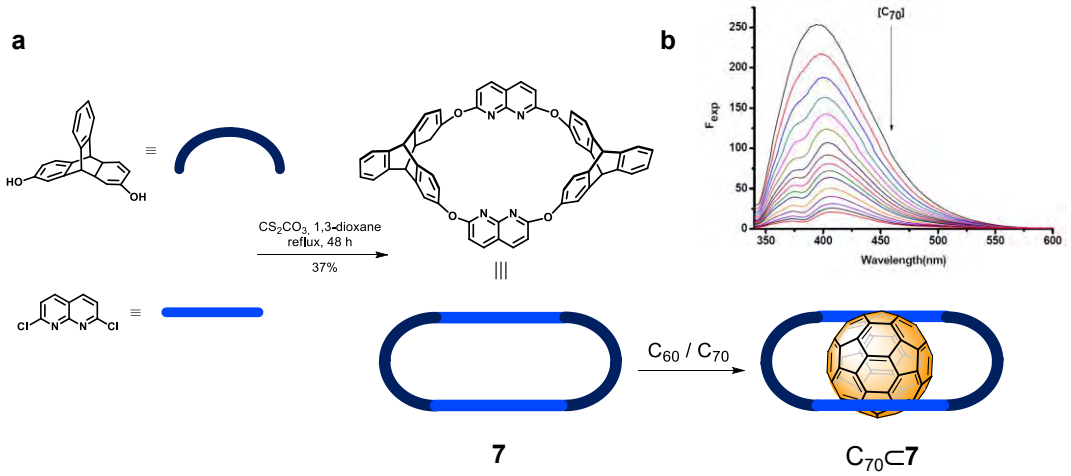

Figure I.14. (a) Synthesis of the triptycene-derived oxacalixarene **7** reported by Chen and co-workers in 2010. (b) Emission spectra (λ_{exc} = 394 nm) of **7** (2 x 10^{-5} mol dm^{-3}) in the presence of C_{70} (0 - 2.5 equiv.) in toluene.

On the other hand, de Mendoza and co-workers developed also in 2010 a new tripodal receptor for fullerenes, exTTF-CTV (Figure I.15).[67] It was based on three π-extended tetrathiafulvalene (exTTF) subunits linked to the CTV scaffold through ether linkages. The concave surface of these aromatic motifs made it a suitable host for the recognition of fullerenes with high binding affinities for C_{60} and also for C_{70}. Later, the same authors optimized the receptors by using bis-exTTF units and the binding constants were increased by 3 orders of magnitude, being the highest values reported by then.[68] Electronic interactions between the exTTF and fullerenes had a crucial role on the stabilization of the complex.

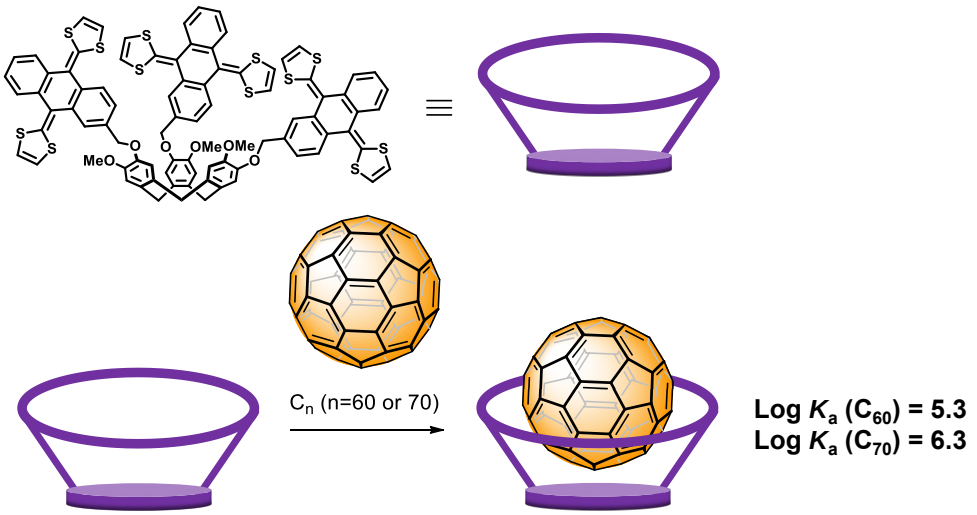

Figure I.15. Schematic representation of the exTTF-CTV that bind C_{60} or C_{70} reported by De Mendoza in 2010.

In the recent years new strategies have appeared such as the use of corannulene[69, 70] or coronene[71] moieties as recognition motives for fullerenes. In 2017, a new molecular tweezer, **8**, with two corannulene subunits linked by a tetrahydro[5]helicene imide was synthesized (Figure I.16).[69] It showed high selectivity for C_{60} and C_{70} due to concave-convex π-π interactions. Moreover, the association constant for C_{70} was found to be 230 times higher than for C_{60}. Later, in 2019, a similar strategy was reported but using a tetracorannulene-perylenediimide that was able to bind two C_{60} units with preference over C_{70}.[70]

Another recent strategy for the recognition of fullerenes was reported by Beer's group in 2020.[72] A novel large, macrocyclic receptor composed of two covalently strapped electron-rich Perylene diimide (PDIs) panels, can trap one molecule of C_{60} or C_{70}. Low polarity solvents showed to be partial charge transfer in the host-guest complex. However, depending on the polarity of the solvent, full electron transfer from the box to the encapsulated fullerene was achieved.

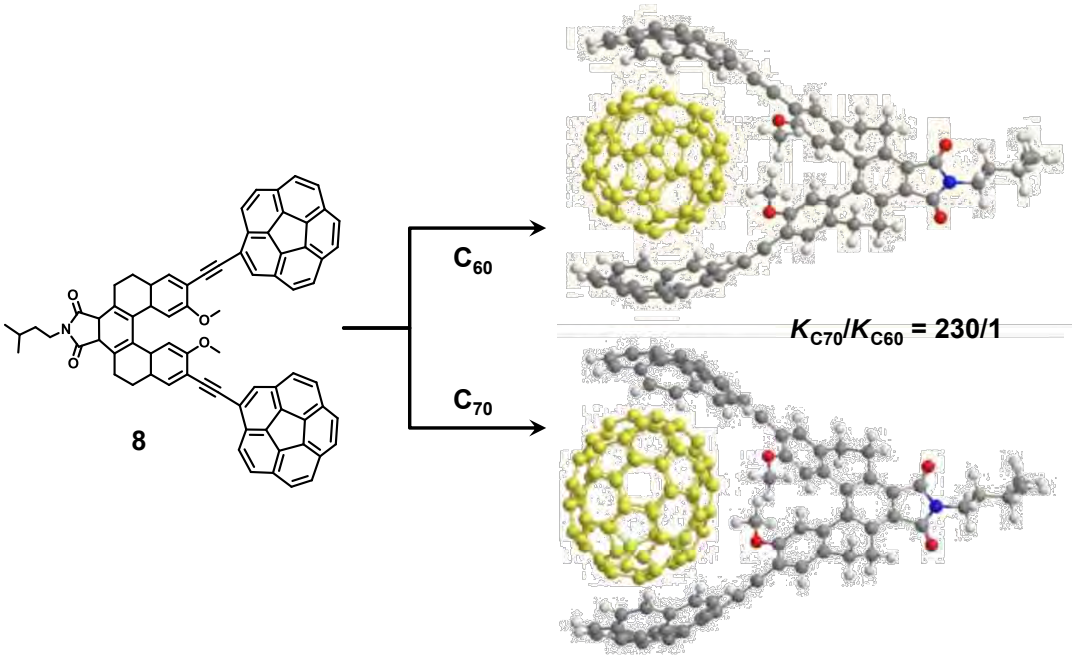

Figure I.16. Bis-corannulene-based molecular tweezer, **8**, that acts as receptor for C_{60} and C_{70}. Reported by Chen and co-workers in 2017.

I.2.1.1.a. All-carbon hosts

Other relevant examples of macrocyclic hosts are the arene-based receptors which can complexate fullerene and assemble in a variety of peapod-like structures. There are bowl-shaped carbon nanobelts (CNBs),[73] single-wall carbon nanotubes (SWCNTs)[74] and the carbon nanorings (CNRs),[75-77] which are based in a cyclic array of phenylene rings that present a ring-shaped π-system with a that adapts perfectly to the fullerenes affording high binding affinities (Figure I.17).

Since 2003, examples of host-guest complexes of fullerenes with CNRs, π-conjugated hydrocarbon macrocycles such as **[6]CPPA**[78] and **[10]CPP**,[79] have been reported (Figure I.17a). Another example was reported by Iizuka and co-workers and represented the shortest possible nanotube, [4]cyclochrysenylene (**[4]CC**) (Figure I.17b).[74]

In 2020, Wu and co-workers reported the synthesis and characterization two carbon nanobelts, **CNB1** and **CNB2**, bearing six/eight cyclopentane-rings with a macrocycle containing three/four alternately linked 2,7-pyrenyl and 2,7-phenanthryl units (Figure I.17c).[73] The small bowl-shaped **CNB1** affords the selective encapsulation of fullerene C_{70} over C_{60}, with large association constant (K_a = 8 x 10^5 M^{-1}).

In 2019, von Delius and co-workers synthesized a new type of strained macrocycles based on π-conjugated porphyrinylene/phenylene nanohoops (Figure I.17d).[80] For instance, the strain energy of the host is 54 kcal/mol, which means a narrowed HOMO-LUMO gap and a red shift in the visible absorption spectrum. Moreover, **[2]CPT** have a diameter of 13 Å, similar to [10]CPP, making it an ideal host to accommodate the C_{60} ($K_a \sim 10^8$ M^{-1}).

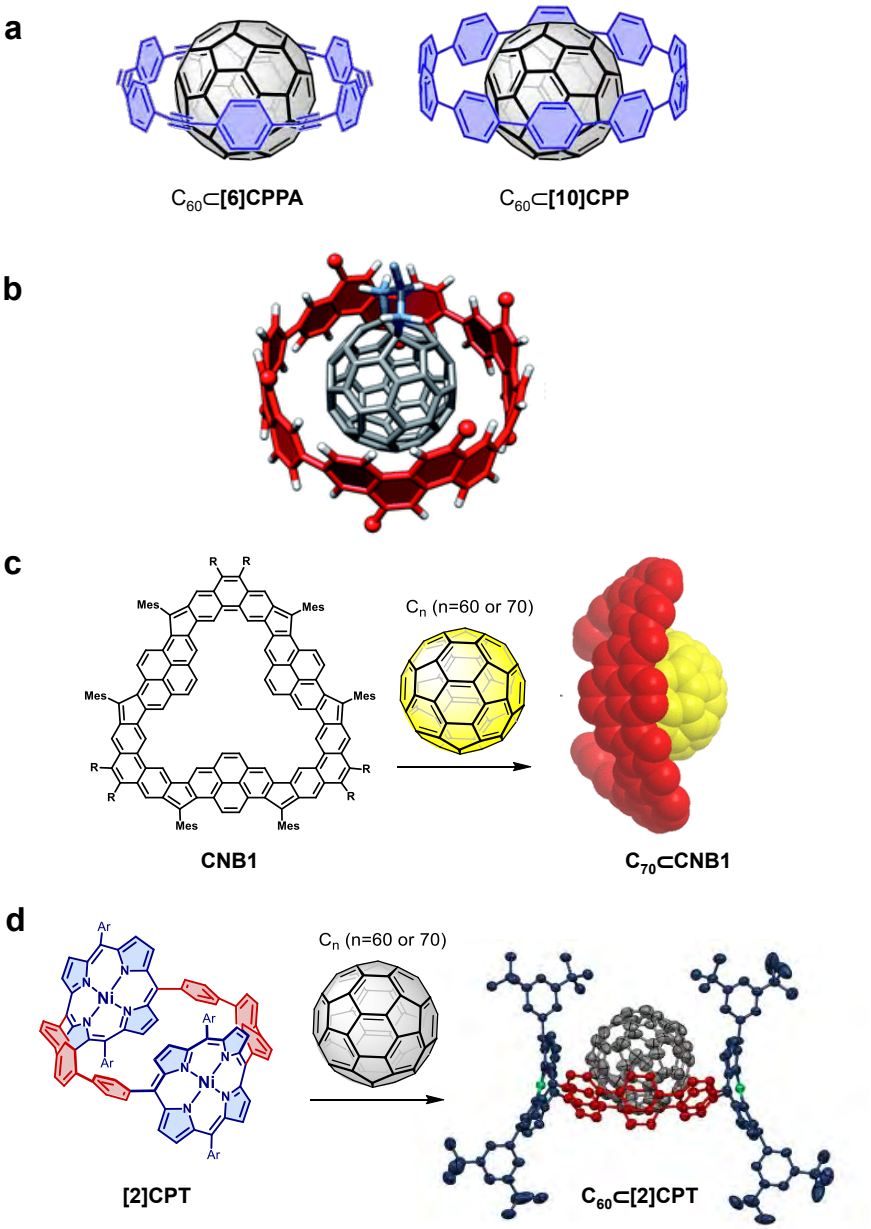

Figure I.17. (a) 1:1 complexes of π-conjugated CNRs and fullerenes. **[6]CPPA** reported by Oda and co-workers. **[10]CPP** reported by Yamago and co-workers. (b) [4]cyclochrysenylene, **[4]CC**, belt based on cycloarylene molecules reported by Iizuka and co-workers. (c) Carbon nanobelt (**CNB1**) which selectively encapsulate fullerene-C_{70} over C_{60} reported by Wu and co-workers. (d) Encapsulation of C_{60} into a π-conjugated porphyrinylene/phenylene nanohoop, C_{60}⊂**[2]CPT**, reported by von Delius and co-workers.

I.2.1.1.b. Porphyrin- and phthalocyanine-based hosts

The quest for hosts showing very high association constants drove the development of molecular systems including metalloporphyrin units. These metallporphyrins present a π-conjugated system which act as π-donor moieties and interact strongly with π-acceptor fullerenes.[81, 82 83-87] One of the first examples of a porphyrin-based receptor was reported by Yamaguchi and co-workers in 1999, where π-interactions allowed the inclusion of C_{60}.[88, 89] In 2010, Anderson and co-workers designed a cyclic Zn^{II}-porphyrin trimer, **9**, as a receptor for fullerenes which present high affinity constant values (2 x 10^6 M^{-1} for C_{60} and 2 x 10^8 M^{-1} for C_{70}) (Figure I.19a).[90] Another kind of hosts for fullerene are the ones based on porphyrin nanobarrels.[91-93] In 2010, Osuka and co-workers reported the synthesis of a porphyrin nanobarrel via consecutive Suzuki-Miyaura cross-coupling reactions at multiple sites starting from a simple monomer. On the other hand, C_{60} was used as a template to develop a tetrameric porphyrin barrel via Zn-mediated self-assembly, utilizing labile capping ligands like TsO^- anions.

Other concave electron rich π-extended systems such as phthalocyanines were used to develop metallocages. For instance, Torres and co-workers reported a Pd^{II}-based C_3 symmetric cage that can encapsulate the C_{60}, C_{60}-PCBM (K_a = 4.6·10^4 M^{-1}) and C_{70}-PCBM (K_a = 1.5·10^5 M^{-1}) (Figure I.18).[94, 95] In 2020 the same authors developed a well-defined tweezer formed by two SubPc-monomers, **10**, rigidly attached to the surface of an electron-poor SubPc-dimer, which resulted in a cavity ideal for C_{60} and C_{70} complexation (K_a ~ 10^5 M^{-1}) (Figure I.19b).[96]

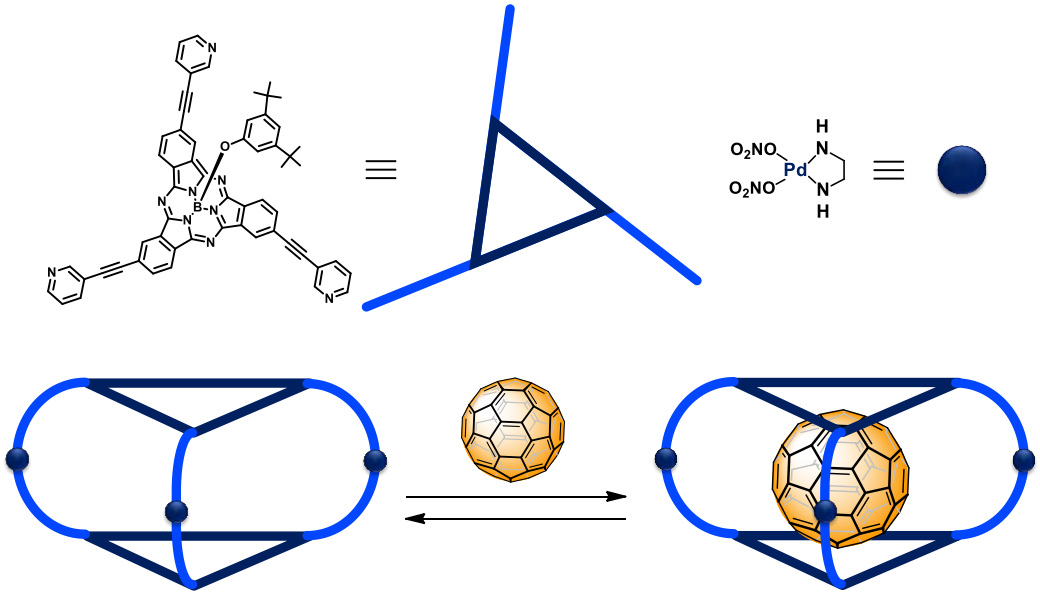

Figure I.18. C_3 symmetric subphtalocyanine (SubPc) M_3L_2 cage which encapsulates C_{60} reported by Torres and co-workers.

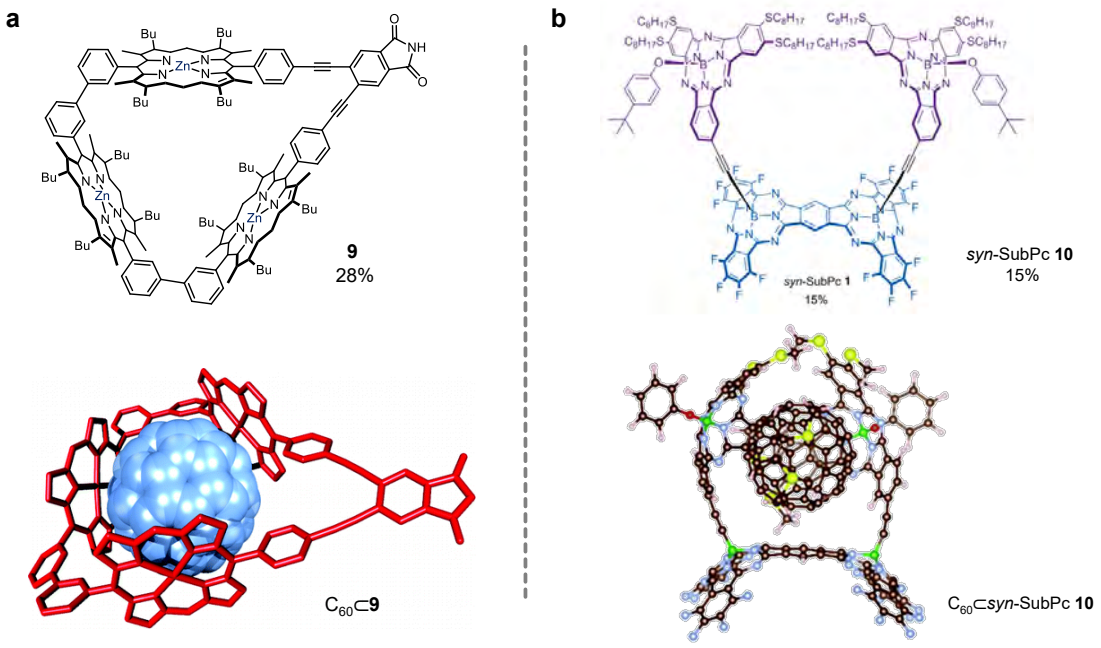

Figure I.19. (a) Cyclic porphyrin trimer (**9**) with high affinities for C_{60} and C_{70} reported by Anderson and co-workers. (b) Subphtalocyanine-based multicomponent ensemble (**10**) consisting of two electron-rich SubPc-monomers rigidly attached to the convex surface of an electron-poor SubPc-dimer reported by Torres and co-workers.

I.2.1.2. Nanocapsules, cages and boxes (0D)

The design of a supramolecular nanocapsule suitable for the selective encapsulation of fullerene species requires some features: 1) large cavity sizes to host large guests, 2) small window-pore sizes to isolate guests from the environment, 3) flexibility and lability to allow the capture (but also the release) of the guests, and 4) π-electron rich building blocks to provide tight interactions with π-acceptor fullerene guests.

I.2.1.2.a. Organic nanocapsules

Most cage compounds are based on the coordination of metal ions, and only a few are charge neutral. Pure organic cages are usually charge neutral since they are formed by covalent bonds.[97, 98] One of the first examples was reported in 2007 when de Mendoza and co-workers synthesized a supramolecular receptor specially designed for fullerene binding (Figure I.20).[99] The nanocapsule synthesized was based in two self-assembled CTV units. This nanocapsule presented a good affinity for C_{60} (K_a = 1.82 x 10^3 M^{-1}) and C_{70} (K_a = 3.89 x

10^4 M^{-1}). The higher affinity observed for C_{70} was rationalized by the higher hydrogen-bond interactions between the host and the guest.

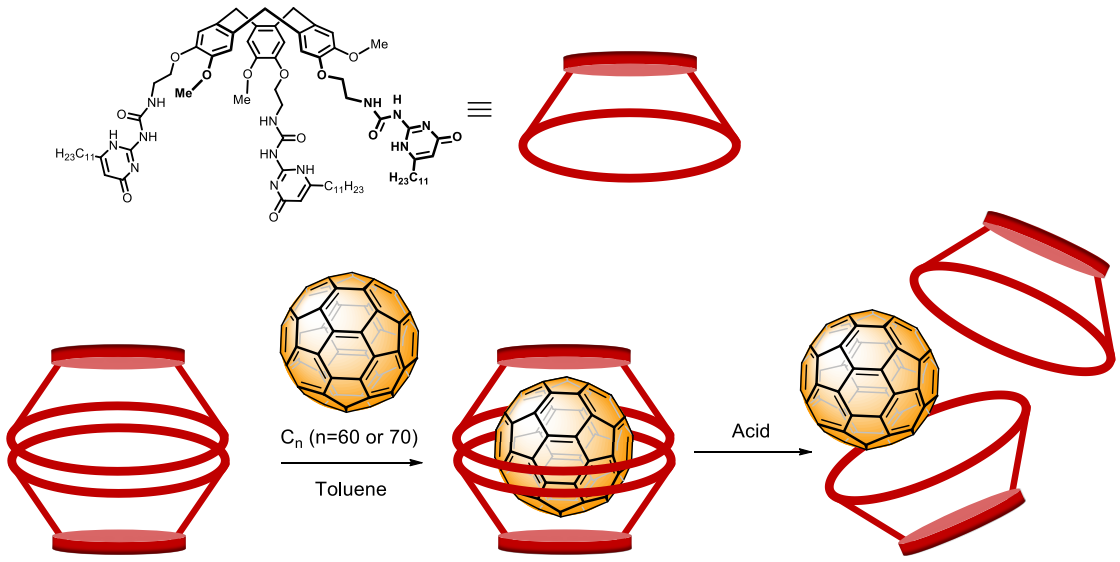

Figure I.20. CTV-based host capable of complexing fullerenes reported by De Mendoza and co-workers.

In 2011, Zhang and co-workers reported another example of fully organic, rectangular prismatic cage highly selective for fullerenes.[100] The synthesis was through a one-step alkyne metathesis from a porphyrin-based precursor. Association constants of 1.4 x 10^5 M^{-1} for C_{60} and 1.5 x 10^8 M^{-1} for C_{70} were found, being the highest values reported at that time. Moreover, the association of fullerenes was found to be a reversible process regulated by pH, being an effective way to selectively separate C_{70} from a fullerene mixture. On the other hand, Chiu and co-workers developed in 2012 a CTV-based hemicarceplex cage selective for C_{70} suitable for purification from a fullerene mixture without the use of HPLC (Figure I.21).[101]

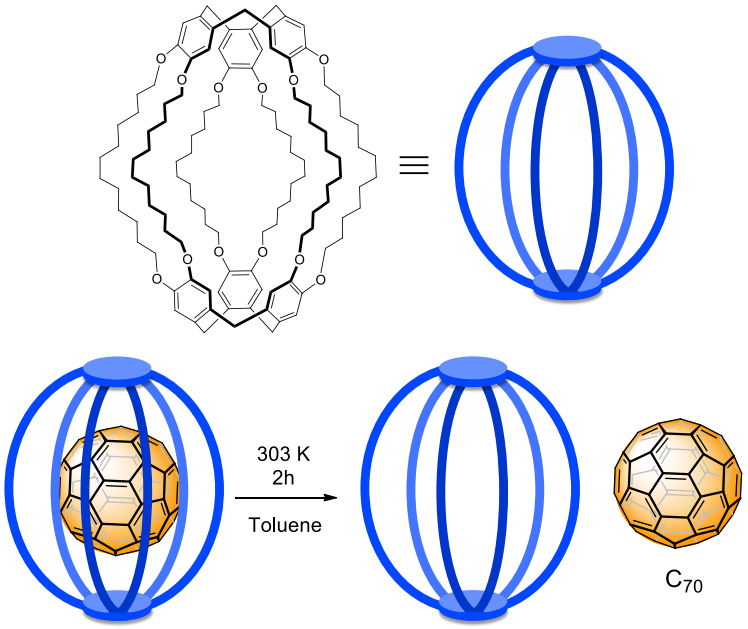

Figure I.21. CTV-based hemicarceplex capable to isolate fullerene-C_{70} reported by Chiu and co-workers.

I.2.1.2.b. Metal-containing nanocapsules

The formation of metal-coordination bonds is a commonly used strategy to develop a wide range of supramolecular structures.[10, 102-105] Metal-containing nanocapsules (or metallocages) are self-assembled from simple building blocks, metal ions and organic ligands.[10] One of the first examples of coordination nanocapsules for the encapsulation of fullerenes was reported by Shinkai and co-workers in 1999.[106] They used two homooxocalix[3]arenes to design a dimeric capsule by self-assembly. Later, the same authors reported the increase of the affinity constant for C_{60} when Li^+ cations were bound to the lower rims of the assembled host.[107] In 2006, Dalcanale and co-workers developed a self-assembled coordination cage, **11**, constituted of two tetrapyridyl-substituted resorcin[4]arene cavitands coupled through four square-planar palladium complexes (Figure I.22).[108] Its internal cavity had a suitable geometry capable to accommodate spherical guests such as methano[60]fullerene derivatives. This association is achieved by π-stacking interactions between the host and the guest.

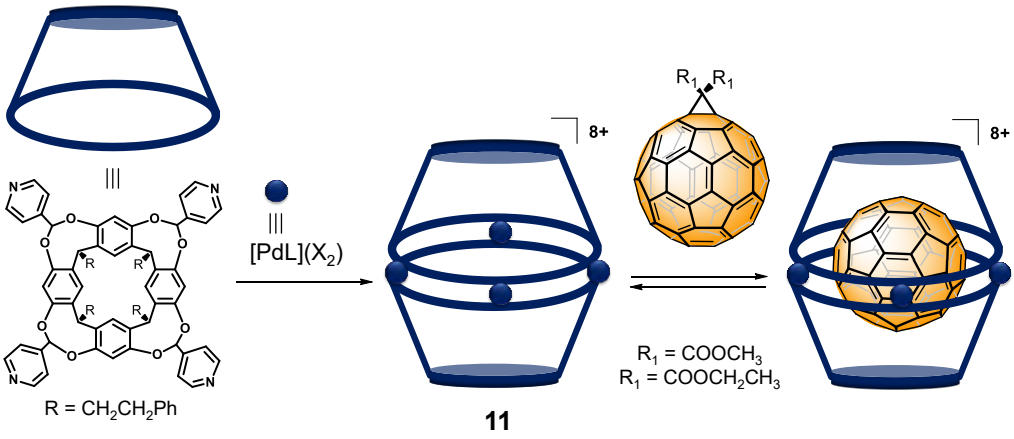

Figure I.22. Schematic representation of the coordination cage reported by Dalcanale and co-workers and complexation of **11** with methano[60]fullerene derivatives. [PdL](X$_2$) = [Pd(dppp)]·(CF$_3$SO$_3$)$_2$

As mentioned in the section I.2.1.1.b. , metalloporphyrins are very useful building blocks to develop hosts for fullerenes recognition, and in the past decade, several examples of metalloporphyrin-based supramolecular cages have been reported.[109-112] Ribas and co-workers reported in 2014 a self-assembled supramolecular tetragonal nanocapsule bearing two metalloporphyrin units that allowed the encapsulation of C_{60} and C_{70} with association constants higher than 10^7 and 10^8 M^{-1}, respectively (Figure I.23).[112] Moreover, the authors designed a solvent-washing strategy to extract solely the pure C_{60} from the nanocapsule, owing to the stronger binding with C_{70}.

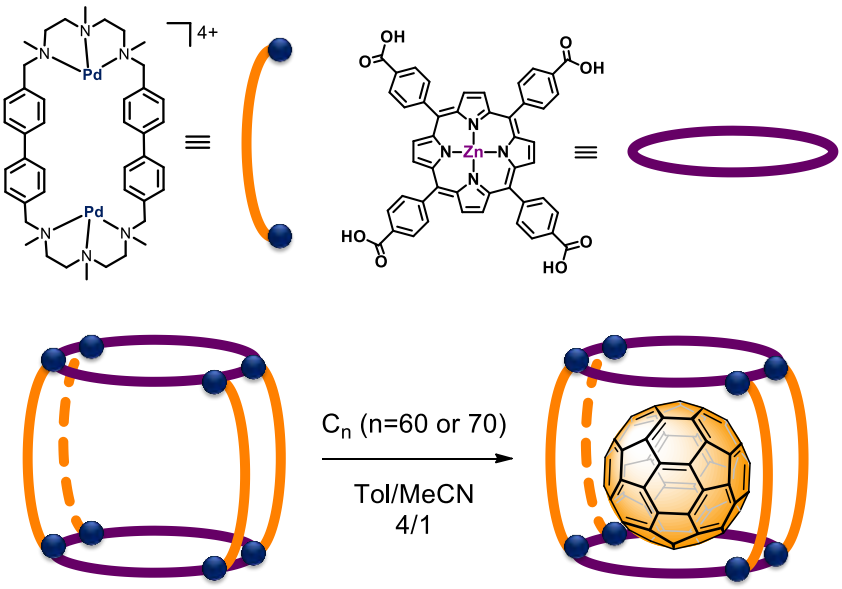

Figure I.23. Self-assembled tetragonal prismatic nanocapsule reported by Ribas and co-workers.

Würthner and co-workers designed a self-assembled host composed of photo- and redox-active perylene bisimide (PBI) edges and $[Fe(bpy)_3]^{2+}$ corners,[113] being one of the largest M_4L_6 tetrahedra reported. They proved the effective encapsulation of C_{60} and moreover, they revealed by CV a reversible 34 electron cycling between a +18 and a -16 charged species, suggesting that this supramolecular host was able to accommodate photo- and electrocatalytic processes in its cavity.

Another class of metallocages are the ones responsive to a non-invasive stimulus as light, temperature, or addition of new metals, leading to a new structure and therefore, changing their affinity for different guests. In this context, Yoshizawa group reported several examples.[114-117] They designed an M_2L_4 nanocapsule using two Pd^{II} ions and four bis anthracene ligands that was able to encapsulate C_{60} in quantitative yields.[114] In 2013, the same authors reported a new M_2L_2 metallocycle which was able to entrap C_{60} in a reversible way by using a light-irradiation stimulus (Figure I.24).[115] Remarkably, this was one of the first examples of functional hosts possessing bimodal photoresponsive units.

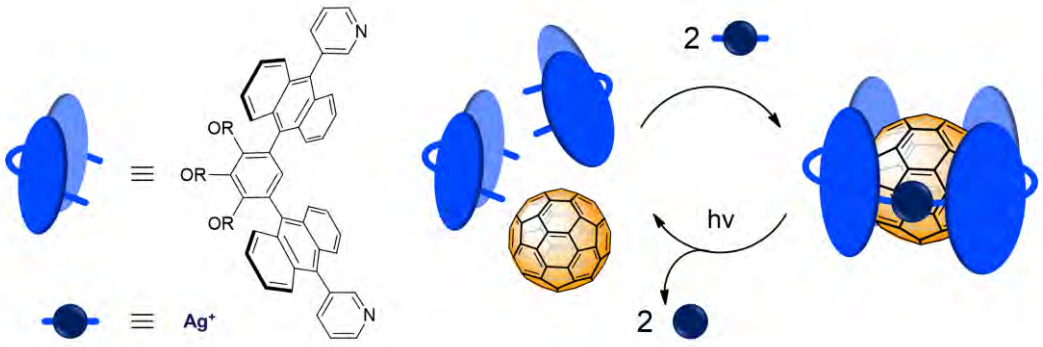

Figure I.24. M_2L_2 molecular capsule prepared using two Pd(II) ions and four bis-anthracene ligands reported by Yoshizawa and co-workers.

Another example was reported by Clever's group by developing a photochromic coordination cage self-assembled from ligands based on a dithienylethene photoswitch.[118] This capsule could be reversibly interconverted from a flexible form (o-C) to a rigid form (c-C) by irradiation with UV or white light, respectively.

In 2019, Peris group reported a palladium-based molecular square synthesized by a self-assembly of pyrene-bis-imidazolylidene ligand with $[Pd(ally)Cl]_2$.[119] This host showed some flexibility to adapt the shape depending on the fullerene size.

I.2.1.3. MOFs (3D)

Metal-organic frameworks (MOFs) are a family of crystalline porous polymeric materials constituted by metal clusters and organic ligands.[120] There is a huge number of possible combinations of metal sources and organic ligands, thus a wide range of geometries can be developed with different pore size distributions and functionalities. However, few examples in the use of MOFs for fullerene recognition have been reported.[121-132]

Most of the examples of cages that selectively bind guests are performed in solution. However, in 2010, Fujita's group achieved an heterogeneous solid-state host-guest chemistry by synthesizing an MOF-like infinite arrays of octahedral coordination cages, M_6L_4.[133] The interstitial void spaces between this octahedral structure afforded the generation of two $M_{12}L_8$ and $M_{12}L_{24}$ cavities, thus creating a 3D network of different nanocages capable to accommodate C_{60} in a 35 wt%.

For instance, Berna and co-workers recently published the preparation of robust copper(II)- and zinc(II)-based metal-organic frameworks with flexible benzylic amide macrocyclic units functionalized with two carboxylic acid groups (Figure I.25).[132] They studied the incorporation of fullerene C_{60} inside the cavities generated between two macrocycles connected to the same dinuclear clusters, occupying a remarkable 98% of the cavities inside the network.

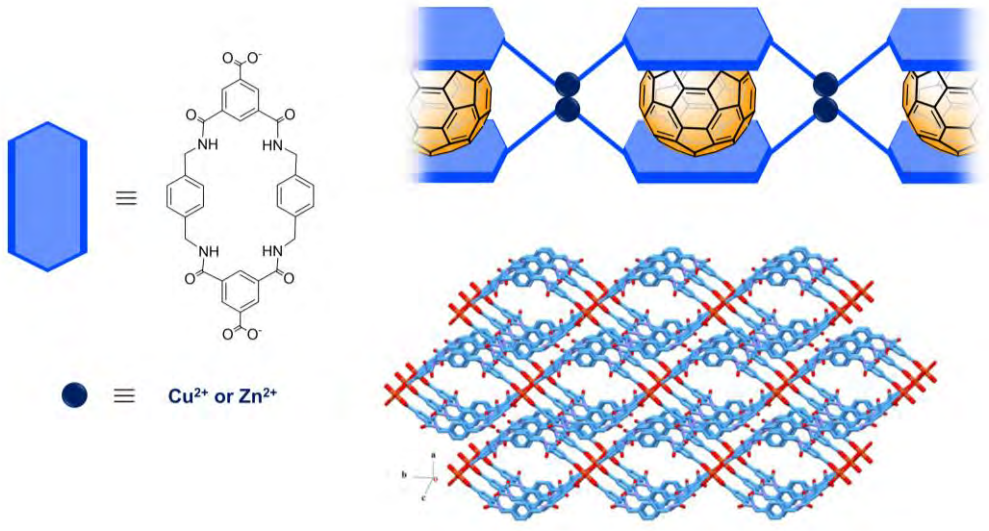

Figure I.25. Linked frameworks forming channels along the c-axis (hydrogen atoms are omitted for clarity) reported by Berna and co-workers.

I.2.2. Strategies for fullerene regioselective functionalization

Fullerene-C_{60} present thirty equivalent double bonds [6,6] with very similar reactivity, which makes the chemo- and regioselective poly-functionalization of fullerene a long-standing problem in organic synthesis. The selective synthesis of C_{60} mono- and hexakis-adducts can be considered a solved problem, because an excess of C_{60} or the reagent for functionalization can be used to guarantee predominant mono- or hexakis-functionalization and minor side products can be removed via chromatographic separation.[134] However, obtaining isomerically pure bis-, tris-, tetra- or penta-adducts of C_{60} by chromatographic separation is very challenging because the lack of efficient stoichiometric control leads to a mixture of oligo-adducts (bis-, tris-adducts and so on), while each oligo-adduct may exist in the form of more than a dozen distinct regioisomers. When considering the synthesis of fullerene bis-adducts, the addition of a second identical and symmetric addend to a fullerene mono-adduct leads to eight potential different regioisomers as depicted in Figure I.26a (ordered by increasing distance between the substituents: *cis*-1, *cis*-2, *cis*-3, *e*, *trans*-4, *trans*-3, *trans*-2, *trans*-1)[135]. The experimental mixture of bis-regioisomers obtained in the Bingel cyclopropanation reaction of C_{60} with diethyl bromomalonate is shown in Figure I.26b. If addends are non-symmetric, as is the case in bis-$PC_{60}BM$[136], 18 bis-adduct regioisomers are obtained in the crude reaction mixture, and their HPLC separation is extremely challenging.[137, 138] Different studies demonstrated that isomerically pure bis-adducts can exceed the typically isomer mixtures in these applications.[139, 140] So, there is a need to generate pure multiple-adducts of C_{60} not just to solve a technical problem, i.e. increasing the yield, but also to obtain compounds in a pure form and avoid tedious chromatographic separations. In this section, we disclose the different approaches for achieving chemo- and regioselective syntheses of multiply functionalized derivatives of C_{60}.[141] Much of this research is motivated by the need to enhance the solubility of fullerene derivatives and therefore enable the preparation of organic electronic devices by solution processing.[142] Diels–Alder or Prato cycloadditions,[143] the Bingel,[144] Bingel–Hirsch[138] as well as related cyclopropanation reactions[145] represent the most commonly used transformations, whose feasibility under mild conditions is mainly due to the unique reactivity of the fullerene double bonds.[146]

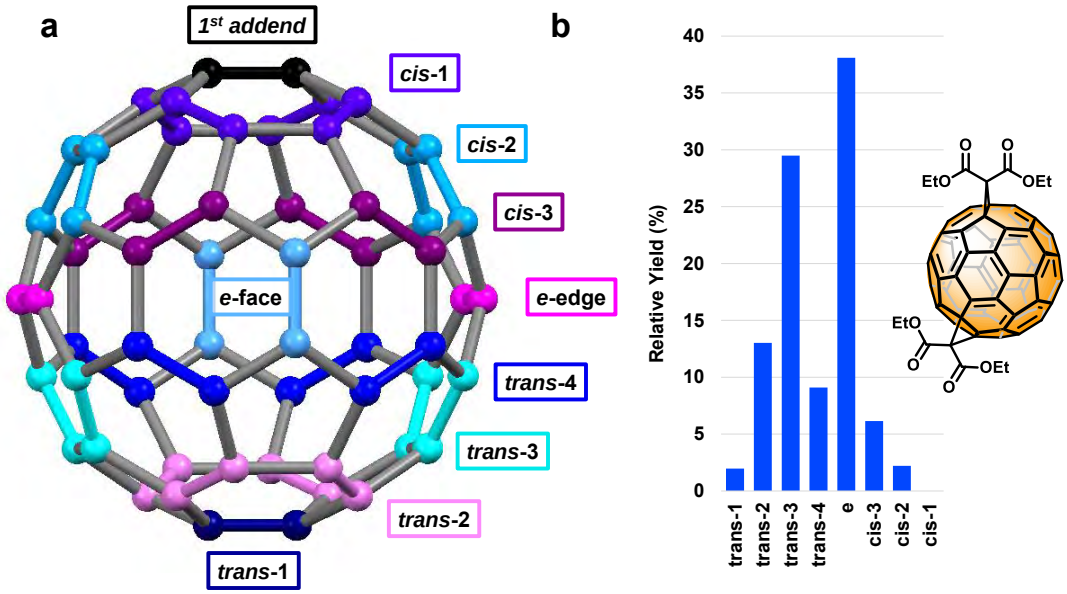

Figure I.26. (a) C_{60} structure and possible bis-adduct regioisomers upon the addition of a second symmetric addend. (b) Relative yield (%) for each isomer in the Bingel cyclopropanation reaction of C_{60} with diethyl bromomalonate, NaH and PhMe as solvent.[138]

I.2.2.1. Tethered remote functionalization

One of the first strategies, pioneered by Diederich in the mid-90s, was the tether-directed remote functionalization for the Bingel cyclopropanation reaction or Diels-Alder reaction (Figure I.27).[147] In this approach one single bis-adduct (equatorial isomer) isomer is formed predominantly because the length of a tether bridge in a ditopic malonate reagent dictates the maximum distance between the two addends. The main drawback of this system is that the bridge is not removable, which compromises the applicability of the functionalized products.

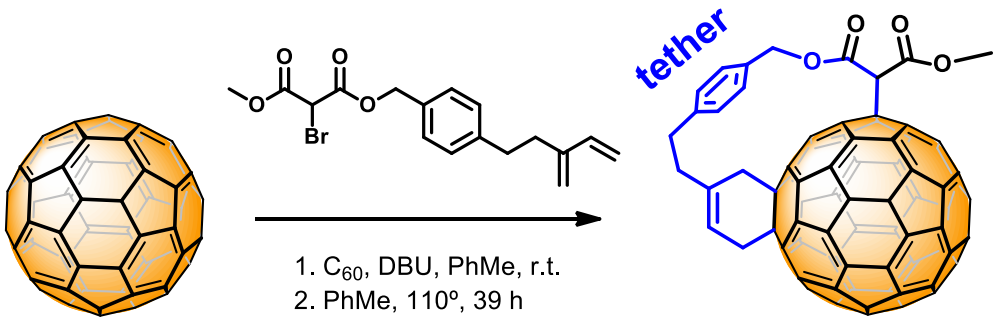

Figure I.27. Synthesis of equatorial bis-adduct by a tether-directed strategy reported by Haldimann and co-workers.

Very recently, Nierengarten reported a removable tether family bearing di-*tert*-butylsilylene or tetra-iso-propyldisiloxane subunits, which can be cleaved after the formation of the bis- or tris-adducts of C_{60} (Figure I.28).[148] By changing the length and rigidity of the silyl-based spacers, different fullerene bis- (mainly *e* and *trans*-3) or tris-adducts (*e,e,e*) can be obtained. With the same strategy, a [3:3]-hexa-adduct is obtained.[149]

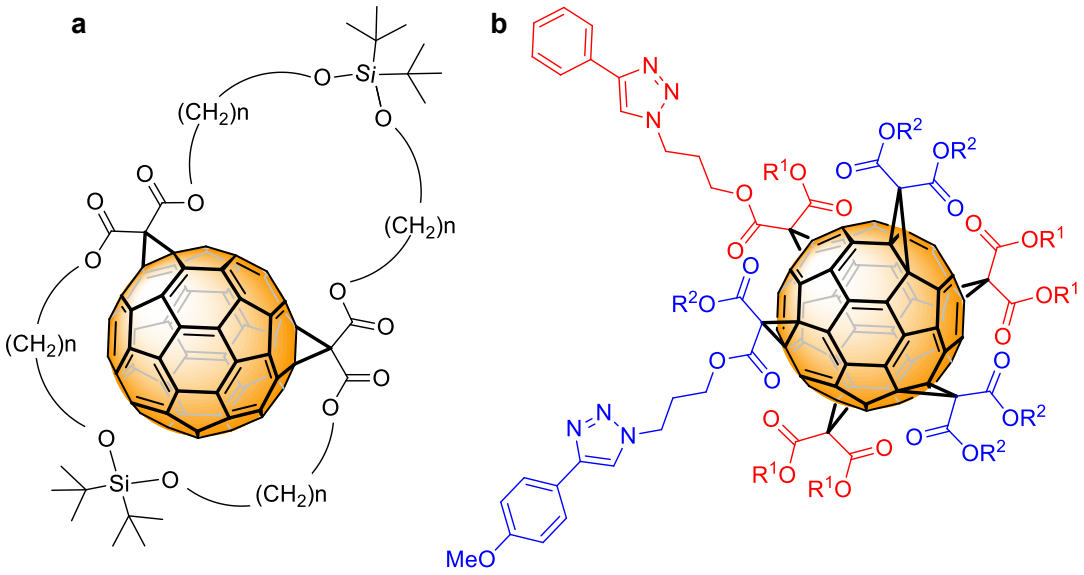

Figure I.28. (a) di-tert-butylsilylene tether affords a *trans*-3 bis-adduct (54%) reported by Nierengarten and co-workers. (b) C_3 symmetrical fullerene [3:3]-hexa-adduct prepared by cleavable di-tert-butylsilylene protecting groups that afford *e,e,e* addition pattern.

I.2.2.2. Removable template addends

In 1997, Kräutler and co-workers reported the synthesis of a tetra-adduct of C_{60} following the so-called orthogonal transposition strategy (Figure I.29).[150] This protocol used *trans*-1-bis-anthracene-C_{60} (independently synthesized through a solid-state high-temperature synthesis), to direct the synthesis of the fully-equatorial Bingel cyclopropanation to form a hexakis-adduct. Subsequent thermal retro-Diels Alder elimination of the two *trans*-1 anthracene moieties afforded the fully equatorial tetrakis-adduct single isomer as the final product.

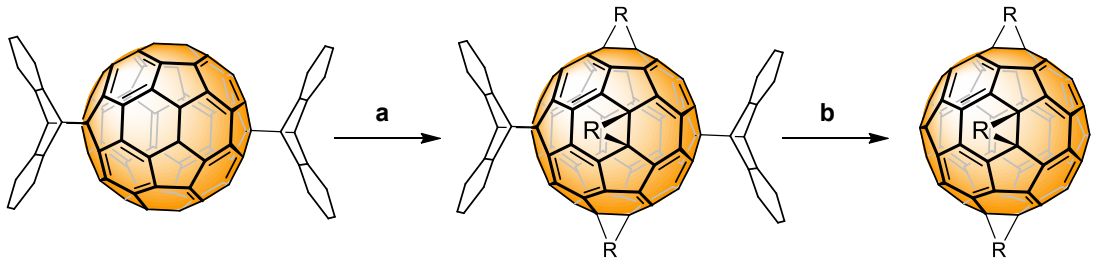

Figure I.29. Synthetic scheme for equatorial tetrakis-adduct synthesis by orthogonal transposition reported by Kräutler and co-workers. (a) $BrHC(CO_2Et)_2$/DBU in CH_2Cl_2/room temperature. (b) 195 ºC, 5 min. R = $C(CO_2CH_2CH_3)_2$.

I.2.2.3. Supramolecular-directed functionalization

Scarce number of non-tethered strategies have been reported. In 2016, Torres and co-workers developed a supramolecular-directed functionalization based on non-covalent π-interactions between the addends (Figure I.30).[151] The residues bearing π-extended surfaces promoted a *cis*-1 C_{60} addition pattern.

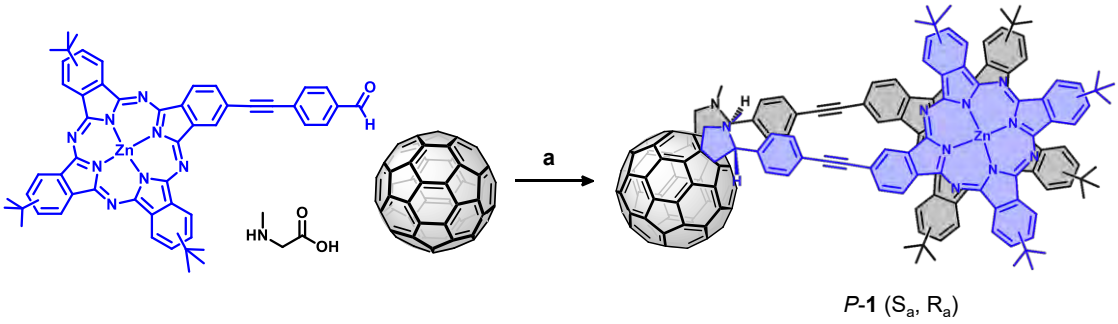

Figure I.30. Synthetic scheme for the supramolecular-directed functionalization reported by Torres and co-workers. (a) Reflux in toluene.

The modulation of the regioselectivity of multiple addition reactions by confinement of C_{60} in supramolecular receptors has emerged as an alternative approach. For instance, von Delius and co-workers reported on the ability of the nanoring [10]CPP to form a supramolecular complex **C_{60}⊂[10]CPP** and infer a significant regiocontrol on the formation of Bingel bis-adducts (Figure I.31).[152] Specifically, the *trans*-2 and *trans*-3 regioisomers were obtained as major products in almost equimolar amounts, along with traces of *trans*-1, excluding the rest of possible isomers (see Figure I.26b).

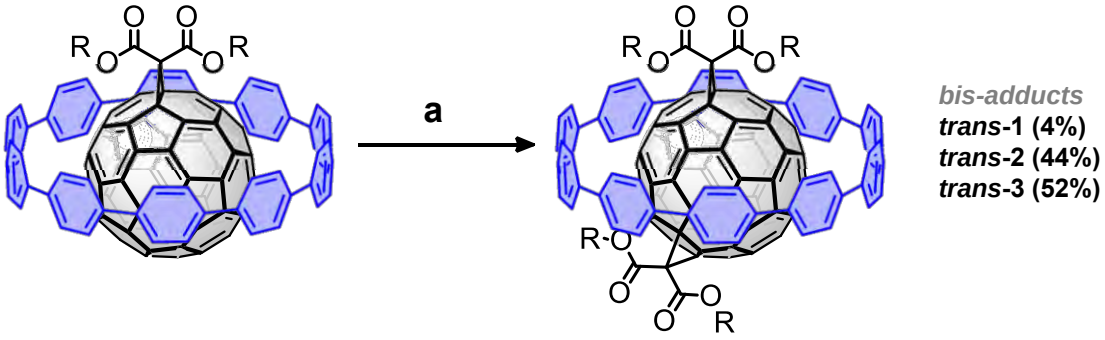

Figure I.31. Nanohoop template, **C_{60}⊂[10]CPP**, that restricts the accessibility of the reagents and imposes selectivity on the formation of Bingel bis-adducts reported by Delius and co-workers. (a) diethyl malonate, CBr_4, DBU, toluene, room temperature.

In 2020, Ribas and co-workers reported a supramolecular mask strategy for the equatorial regiofunctionalization of C_{60} (Figure I.32).[153] By using a tetragonal prismatic nanocapsule, **1a**, the authors obtained a full control on the regioselectivity for obtaining sequentially equatorial bis-, tris- and tetrakis- Bingel-adducts of C_{60}.

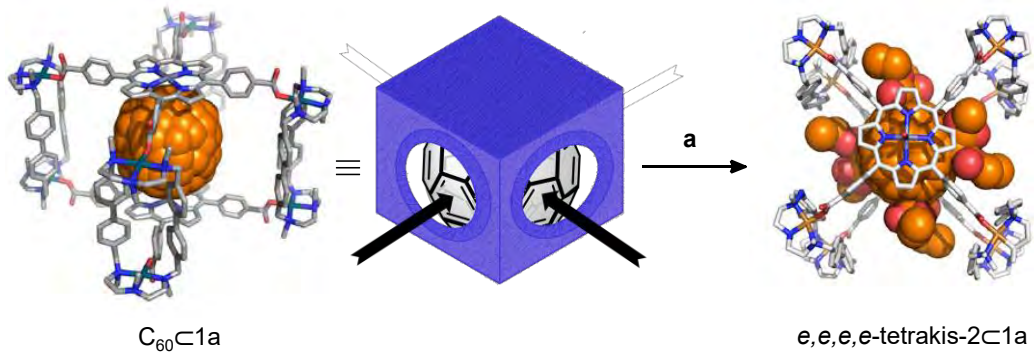

Figure I.32. Supramolecular mask strategy for regioselective equatorial Bingel functionalization through the four cross-shaped gates of a tetragonal prismatic nanocapsule reported by Ribas and co-workers. (a) diethyl bromomalonate, NaH, CH_3CN, r.t.

I.3. Higher fullerenes

Higher fullerenes (>C_{70}) were first discovered in 1991 and their low abundance, poor solubility and difficult separation converted them in a challenging topic to investigate.[154, 155] Among higher fullerenes, C_{84} is the most abundant one. A total of 24 isomers of C_{84} are predicted by calculations obeying the isolated pentagon rule (IPR). There have been reported many publications regarding to the characterization of different isomers of C_{84},[156-

[161] their properties[162, 163] and applications.[164-169] In this section we are going to focus on the few examples that have been reported concerning the purification of higher fullerenes from raw soot. [110, 170-174]

I.3.1. Hosts with large voids for higher fullerenes

In the recent years, a wide range of supramolecular nanocapsules have been developed for a variety of applications, such as catalysis in a confined space, purification of fullerene species from soot, among others. However, supramolecular nanocapsules showing large accessible cavities are not that common. Focusing on hosts capable to encapsulate one or more than one guests with a volume higher than fullerene-C_{70}, multi-porphyrinic-based hosts are the main examples of expansion of cavities size by self-assembly.[175-178] Aida and co-workers developed rectangular-shaped supramolecular nanobox by self-assembly of ethynylene-bridged zinc porphyrin dimers (**Z2**).[176] As depicted in Figure I.33, the nanobox adopt a planar conformation with a syn-parallel geometry as for the pyridyl groups.

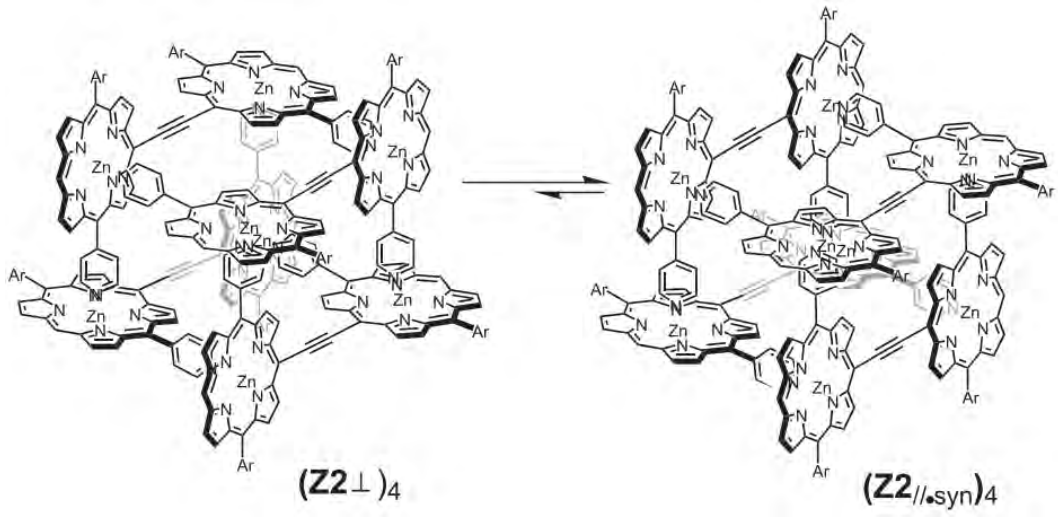

Figure I.33. Schematic representations of two possible conformers of **Z2** reported by Aida and co-workers.

In 2020, Kim and co-workers designed a one-pot template-free strategy to form a porphyrin-based gigantic cage, $P_{12}L_{24}$ (**12**) (Figure I.34).[178] Single crystal X-ray analysis revealed a cuboctahedron structure with a diameter of ~ 5.3 nm.

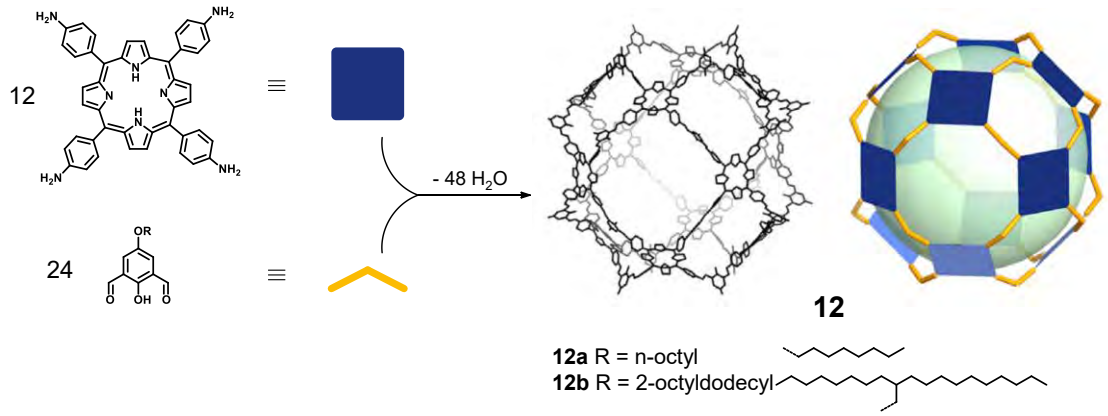

Figure I.34. Design and synthesis of the gigantic porphyrinic cages $P_{12}L_{24}$ (**12a** and **12b**) reported by Kim and co-workers.

In the early 90s, several strategies for fullerene purification were reported. First, the controlled sublimation of carbon soot was reported.[179] Another method consisted in extractions with organic solvents and a third method was the purification by crystallization.

Nowadays, chromatographic techniques are the mostly used for the purification of fullerenes. Some common stationary phases are alumina, graphite, activated carbon, polystyrene gel, γ-cyclodextrins or pyrenyl-grafted silica (Cosmosil Buckyprep). HPLC is indeed the most useful method to obtain pure quantities of higher fullerenes.[180, 181] However, this technique, if successful, requires large amounts of solvent, it is time-consuming and expensive to obtain pure higher fullerenes. So, a challenging objective of the scientific community has been the quest for cheap and facile alternative methods. The best way to selectively entrap fullerenes is by using supramolecular hosts classified in section I.2.1., which are prone to stabilize the fullerene species by hydrogen bonding or π-π-interactions.

Nevertheless, selective extraction of higher fullerenes via selective encapsulation in host molecules is very challenging. Remarkably in 2004, Aida's group designed a cyclic dimer of zinc porphyrins with different-sized alkylene spacers featuring different distances between the two porphyrins (Figure I.35).[170] The selectivity toward higher fullerenes depended on the size of the host cavity and the cycles of extraction. For instance, three cycles of extraction with the $\mathbf{7}_{C6}$ dimer allowed the remarkable enrichment of C_{102}-C_{110} fullerenes from 0.1 % to 82 % of total fullerenes.

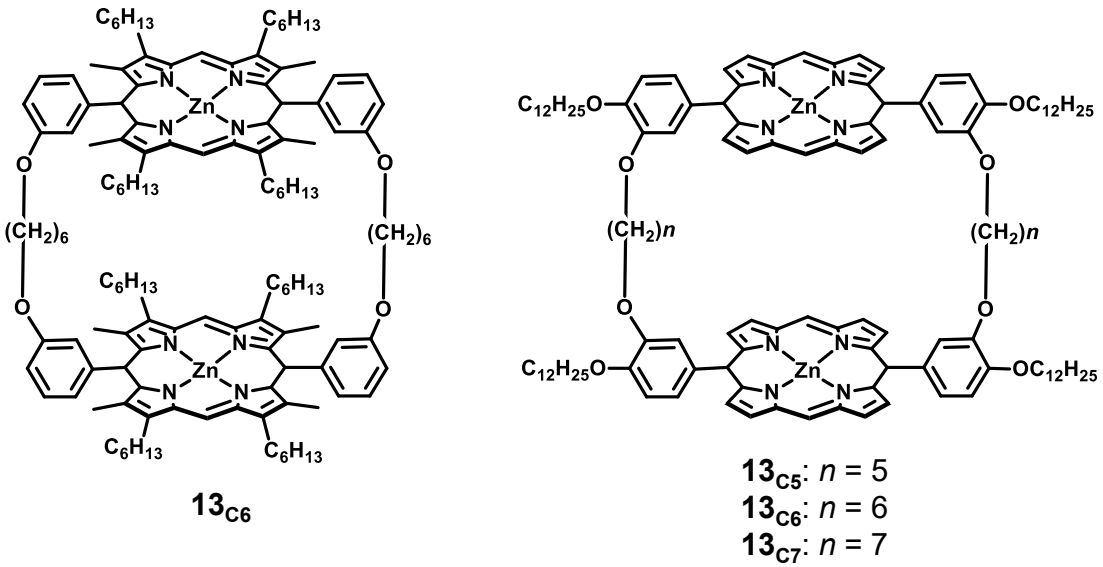

Figure I.35. Cyclic dimers of metalloporphyrins $\mathbf{13}_{C6}$, $\mathbf{13}_{C5}$, $\mathbf{13}_{C6}$ and $\mathbf{13}_{C7}$ reported by Aida and co-workers.

Also, as mentioned in section I.2.1.1, calixarenes are ideal candidates to act as a receptor for fullerenes. In 2006, Fukazawa and co-workers developed a new calix[5]arene-based host (**14**) that could adopt two conformations (*syn* and *anti*).[171] Upon the exposure to a mixture of fullerenes (C_{60}, C_{70} and 10 % of higher fullerenes), the *syn* conformer showed high binding affinities for the higher fullerenes. The wrapped fullerenes were released by heating affording an enriched sample with higher fullerenes (excluding the C_{60}) and the host in the *anti* conformation (Figure I.36).

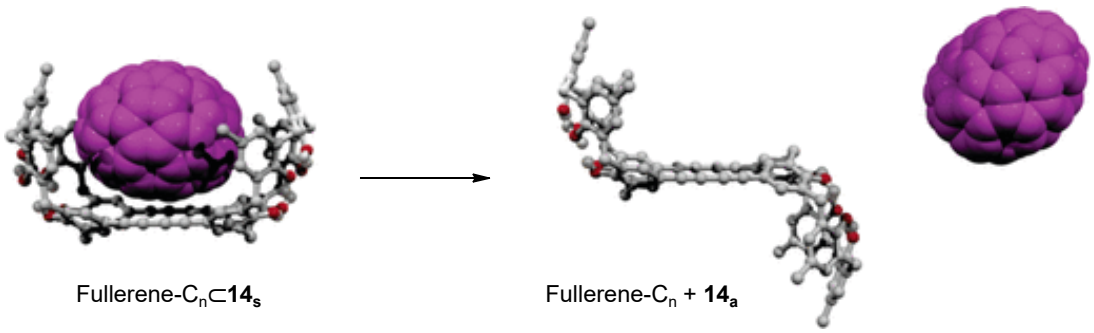

Figure I.36. Calix[5]arene-based host (**14**) reported by Fukazawa and co-workers that adopt a syn conformation to extract higher fullerenes (n > 70) from a fullerene extract.

On the other hand, de Mendoza reported in 2007 a host (**15**) based on a CTV derivative,[172] and they reported the encapsulation properties with a sample composed of 65 % C_{60}, 22% C_{70}, 5% C_{84} and 8% of other fullerenes. Considering that a low concentration afforded a lower solubility for C_{60}, they observed an enrichment of C_{84} up to 76% with a single extraction (Figure I.37).

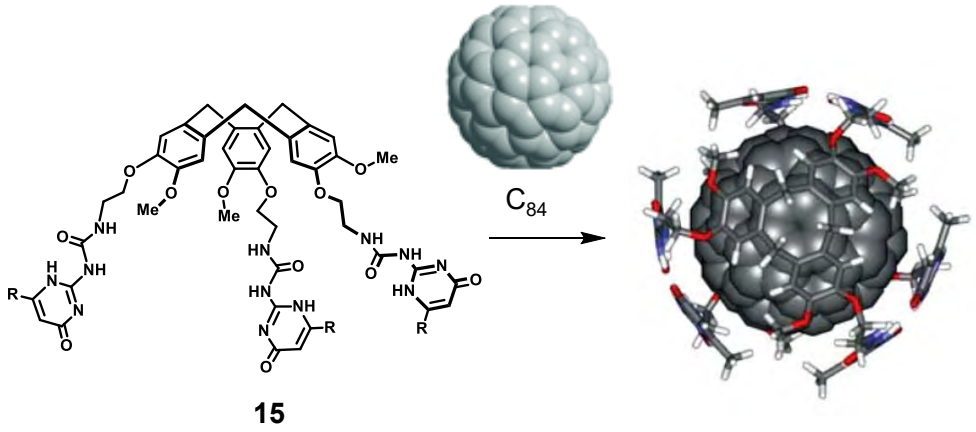

Figure I.37. CTV-based host (**15**) reported by de Mendoza that affords an enrichment of C_{84} up to 76% from a soot mixture. Optimized model of 1_2:C_{84} complex. R = $C_{11}H_{23}$.

A different strategy was published by Yashima and co-workers in 2010.[173] It was based on a one-handed helical polymer which could recognize the size and chirality of higher fullerenes through an induced-fit mechanism, and could selectively extract enantiomers of the higher fullerenes (Figure I.38). Remarkably, the higher fullerene content significantly increased from 8.8% to 95.4% in the carbon soot by single extraction with st-PMMA. At room temperature, C_{70} is selectively encapsulated over C_{60}. When the mixture is exposed to 110 ºC, followed by cooling to room temperature it results a st-PMMA gel complexed with higher fullerenes.

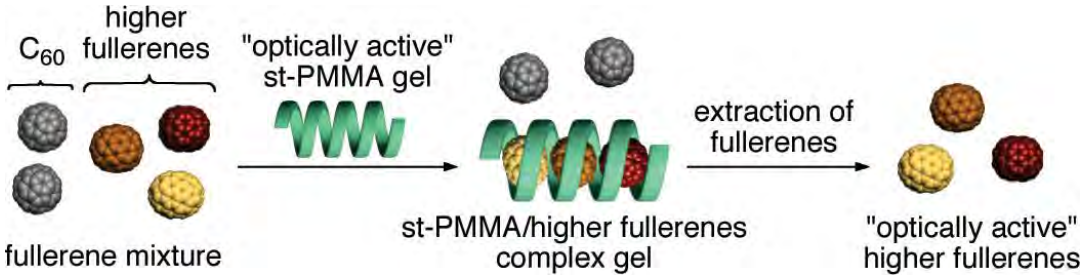

Figure I.38. Induced-fit mechanism reported by Yashima and co-workers that can selectively extract enantiomers of the higher fullerenes, such as C_{76}, C_{80}, C_{84}, C_{86}, C_{88}, C_{90}, C_{92}, C_{94} and C_{96}. st-PMMA = syndiotactic poly(methyl methacrylate).

As described in section I.2.1.4, the use of self-assembled nanocapsules has been widely used for the encapsulation of C_{60} and C_{70}. Nonetheless, the use of that supramolecular systems for the complexation of higher fullerene species has been less explored. For instance, Nitschke and co-workers in 2011, reported a cubic structure, M_8L_6, formed with porphyrin moieties that allow the interaction with fullerenes (Figure I.39).[110] The Ni-based cage, **Ni-1**, showed a stronger binding affinity for C_{70} and coronene over C_{60}. The authors wanted to explore further and the nanocapsule was mixed with a fullerene soot containing 53 % of C_{60}, 1.54 % of C_{70} and 0.14 % of higher fullerenes. C_{60} encapsulation was detected by ESI-MS but there was as well C_{70}, C_{76}, C_{82} and C_{84}, indicating the nanocapsule had a high affinity towards higher fullerenes.

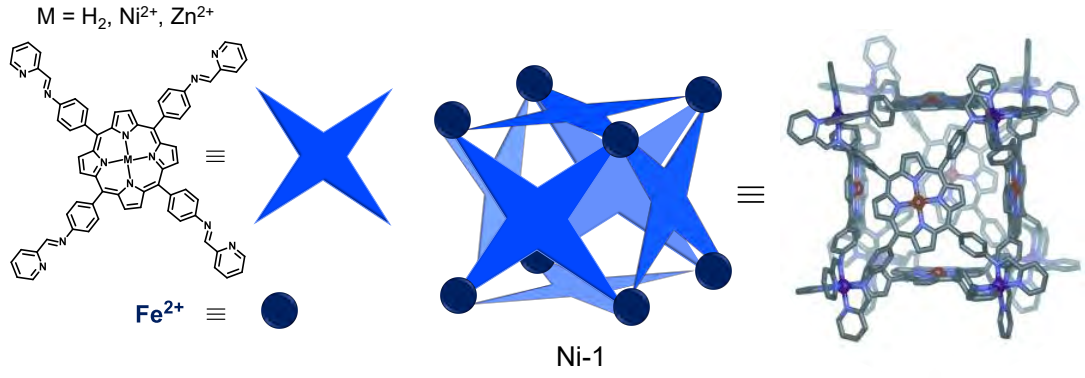

Figure I.39. Nitschke and co-workers reported the combination of C_4 symmetric tetrakis-bidentate ligands with C_3-symmetric iron(II) tris(pyridylimine) centers resulted in the formation of a cubic cage. X-ray structure of **Ni-1**·16 OTf·26 Et_2O·28 DMF·30 H_2O.

In 2014, Ribas and co-workers, developed a tetragonal prismatic coordination nanocapsule, **16**, which showed a high affinity towards C_{60} ($K_a = 3 \times 10^7$ M^{-1}) and C_{70} ($K_a = 4 \times 10^8$ M^{-1}) (see Figure I.23).[112] Crystallographic data evidenced different distances between the two Zn^{II}-porphyrins of the nanocapsule depending on the presence or absence of guest, indicating the ability of the capsule to adapt upon the guest size. The authors investigated further this breathing ability using a fullerene extract (C_{60} 70%, C_{70} 28% and higher fullerenes 2%) and a fullerene soot (C_{60} 5.3%, C_{70} 1.54% and higher fullerenes 0.14%). A major part of encapsulated species was C_{60} and C_{70} but they also observed higher fullerenes in both experiments (C_{76}, C_{78} and C_{84}), confirmed by ESI-MS. DFT calculations reinforced the possibility of C_{84} encapsulation (Figure I.40).

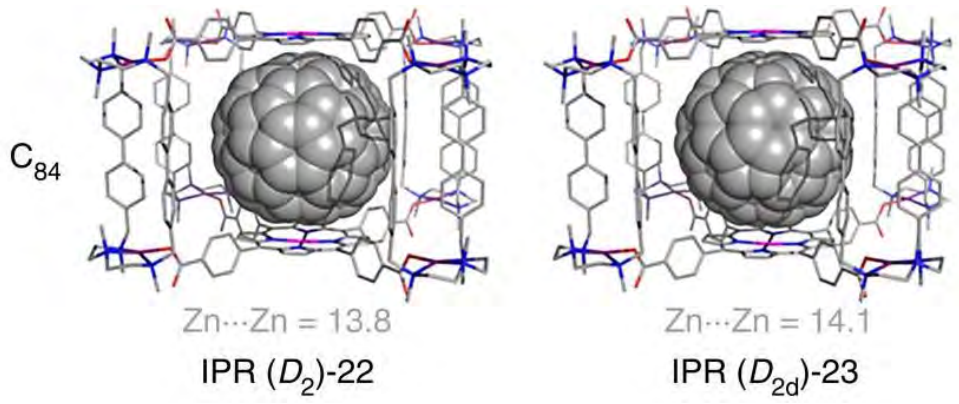

Figure I.40. DFT calculation for $C_{84}\subset\mathbf{16}^{8+}$ isomers IPR (D_2)-22 and IPR (D_{2d})-23 (Zn···Zn distances in Å) reported by Ribas and co-workers.

In 2010, Fujita and co-workers synthesized a MOF featuring infinite arrays of octahedral coordination cages, capable to encapsulate C_{60} and C_{70} were encapsulated in a 35 wt%.[133] This nanocapsules were also tested with fullerene soot and they detect also the encapsulation of higher fullerenes, C_n (n = 76, 78, 82 and 84).

In 2016, Chiu and co-workers studied the encapsulation and release of higher-order fullerenes in a CTV-based host (Figure I.41).[174] In particular, C_{76}/C_{78} and C_{84} were isolated with remarkable purities (up to 95% and 88%, respectively) from a mixture of higher fullerenes.

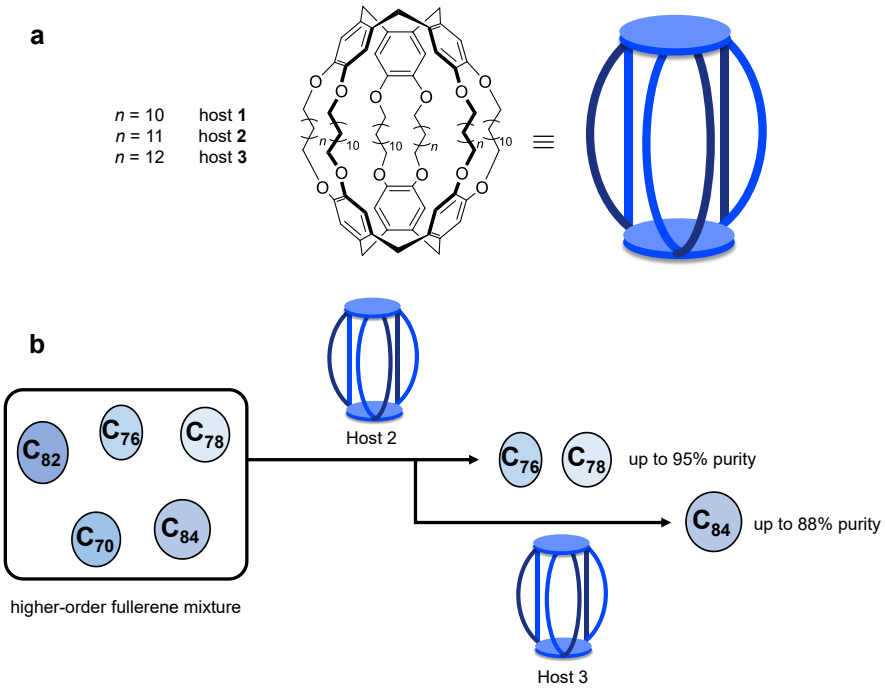

Figure I.41. (a) CTV-based host reported by Chiu and co-workers. (b) Procedure that allows the selective isolation of C_{76}, C_{78}, and C_{84} from a mixture of fullerenes.

I.3.2. Non-encapsulation strategies for higher fullerene purification

Recently, Stevenson and co-workers reported a chemical separation method to isolate fullertubes (structure that merges subunits of nanotube and fullerene caps).[182] Fullertubes had been predicted theoretically and herein they reported their experimental evidence and isolation. The high reactivity of amines with spheroidal fullerene cages and not with fullertubes enabled their removal and allowed a facile isolation of C_{96}-D_{3d}(3), C_{90}-D_{5h}(1) and C_{100}-D_{5d}(1) fullertubes. A non-chromatographic step (stage 1) consisted of a selective reaction of carbon cages with aminopropanol to permit the isolation of a highly enriched sample of fullertubes (Figure I.42). Subsequently, spheroidal fullerenes are reacted and removed by attaching water-soluble groups onto their cage surfaces. With this enriched (100-1000 times) fullertube mixture, stage 2 becomes a simple HPLC collection with a single column. This two-stage separation approach permitted fullertubes in scalable quantities.

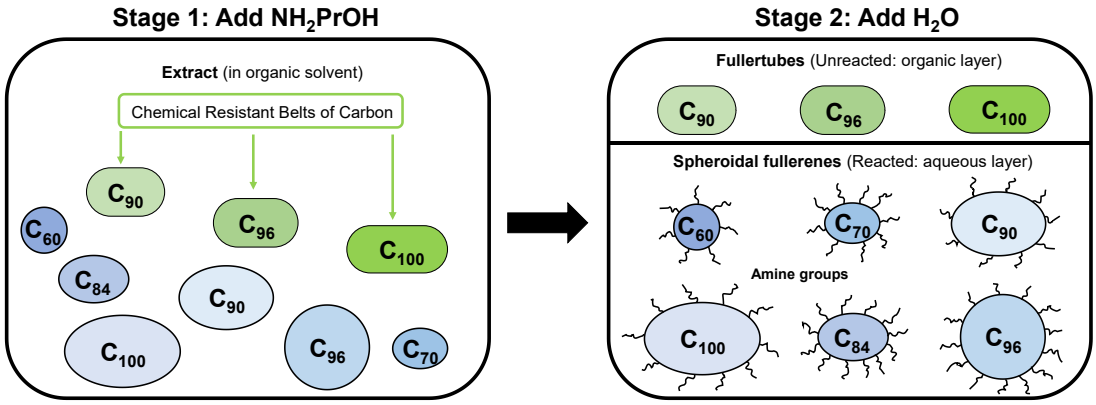

Figure I.42. Strategy to chemically separate fullertubes from spheroidal fullerenes reported by Stevenson and co-workers.

I.4. Metallic nanoparticles

The development and study of new metallic nanoparticles (MNPs) has promising applications, for example, in the fields of catalysis and biomedicine. The metal nature but also the size, shape and accessibility to their surface determine the activity of these MNPs and their implementation in applications.

The control of size and shape of metallic nanoparticles (MNPs) is a challenging topic aiming at comprehending the implications of these parameters in their catalytic performance. In

general terms, the quest for sub-nanometric MNPs in a reproducible form is appealing, owing the fact that enhanced catalytic activity is expected for MNPs with larger surface/volume ratio, *i.e.* of the smaller size possible.[183, 184]

I.4.1. MNPs stabilized by ligands

In order to stabilize MNPs and to avoid aggregations, organic molecules are employed as ligands attached to the surface of the nanoparticles, affording a wide range of stabilization modes.[185] In 2003, Chaudret's group reported the synthesis of Ru NPs,[186, 187] by using Ru(COD)(COT) as precursor (Figure I.43). They found that this precursor decomposes under very mild reducing conditions without leaving residues on the resulting nanoparticles. The nanoparticles are in situ stabilized by polymers (such as PVP or CA) or ligands (phosphines designed by van Leeuwen[188], amines, thiols, polydentate ligands, etc.). MNPs have been widely used as catalysts because of their synthetic accessibility and catalytic efficiency.

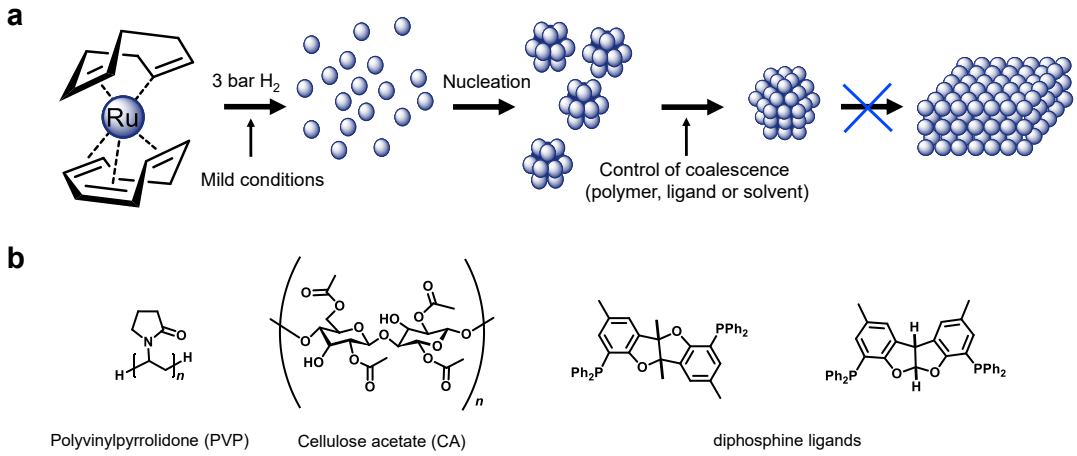

Figure I.43. (a) Formation of ruthenium nanoparticles (RuNPs) using Ru(COD)(COT) as precursor and polymers, ligands or solvents as stabilizers. (b) Polymers (PVP and CA) and specific diphosphine ligands used to stabilize RuNPs.

In 2013, Katz and co-workers reported the mechanism of the reduction of 4-nitrophenol to 4-aminophenol using gold nanoparticle catalysts.[189] Comparing different organic ligand-bound nanoparticles, the nature of the active site was investigated. It was determined that the rate and induction time for catalysis depended on the nature of the organic ligand (C6P or MBC, Figure I.44). This is consistent with the surface restructuring in the gold nanoparticle during catalysis. The environment created by the ligands plays a crucial role

because they alter the NPs both sterically and electronically. Flexibility of the ligand allows controlling the accessibility to the active surface, while bulkiness prevents aggregation and stabilizes the NP.

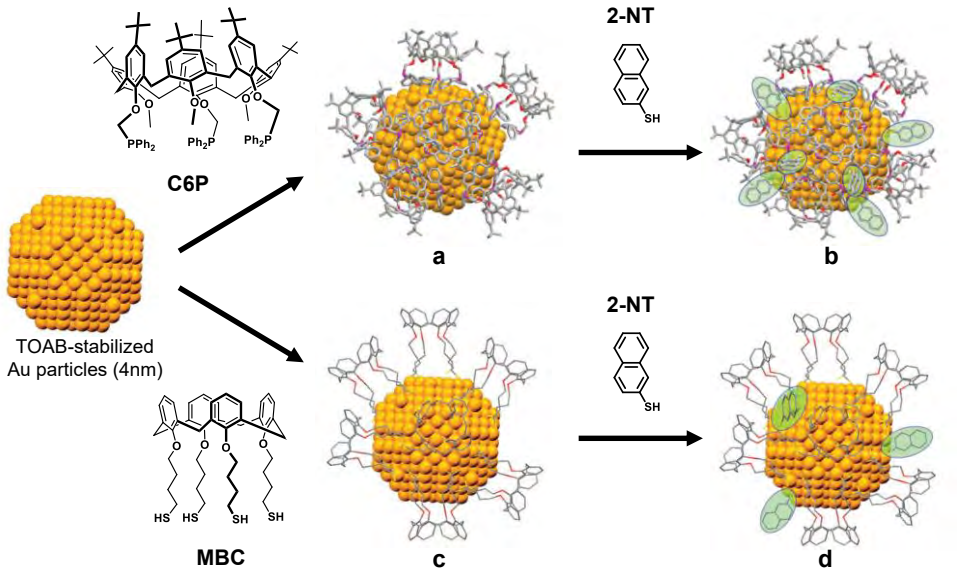

Figure I.44. Schematic representation of calixarene-bound Au NPs used by Katz and co-workers. (a) C6P-bound NPs. (b) C6P-bound nanoparticles + 2-NT. (c) MBC-bound nanoparticles. (d) MBC-bound nanoparticles + 2-NT.

Very recently, in 2022, Martínez-Prieto and co-workers reported an enhancement in the catalytic properties of graphene-supported ruthenium nanoparticles (Ru@rGO) by modifying their metal surface with pyrene-tagged N-heterocyclic-carbene ligands (pyr-IMes) (Figure I.45).[190]

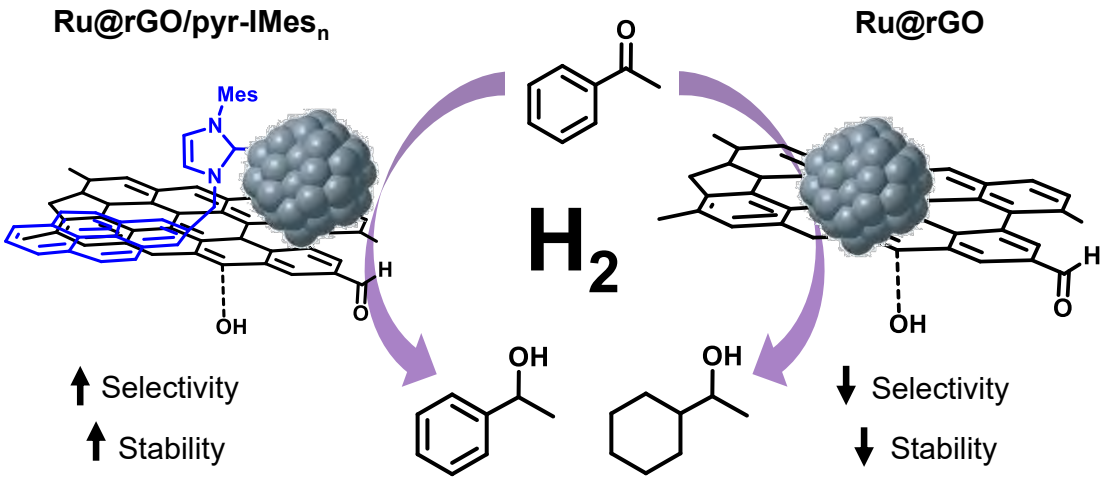

Figure I.45. Comparison of the acetophenone hydrogenation by using modified or non-modified graphene-supported NPs, reported by Martínez-Prieto and co-workers.

I.4.2. Hosts for stabilization of MNPs

The encapsulation of MNPs inside cavities of MOFs, COFs, POPs, organic cages, and ionic liquids has attracted attention of scientific community during the recent years with the goal of isolating and stabilizing them.[191, 192] In this context, different synthetic strategies and catalytic applications have been developed.[193-195]

I.4.2.1. MOFs or zeolites

As described in section I.2.1.3, MOFs form porous 3D matrices that can be constituted of many transition metals and different ligands. Therefore, owing to their predictable crystallinity, large surface area and porosity, they are good candidates to embed nanoparticles in their cavities. Trapping NPs (including Au, Pt, $NiCl_2$, $PdCl_2$ and $PtCl_2$)[196-198] in the channels of MOFs has been demonstrated to be a successful strategy[191, 199] to enhance the selectivity of selected transformations.[184, 200] Stabilization of the NPs dimensions can be achieved by encapsulation of the MNPs inside a porous host such as MOF to prevent aggregation. In general, two different approaches exist for the synthesis of MNPs inside MOFs. The first and most widely used method is to use MOFs as stabilizing host material providing a confined space that limits particle growth and impedes agglomeration. The procedure consists of the stepwise precursor infiltration, followed by decomposition or reduction. In this way, the dimension and shape of the NPs directly synthesized in the pores of the framework should be controlled by the pore size, shape and channel structure of the host material (Figure I.46). Also, it has been reported that simple grinding of MOFs with organometallic complexes could also lead to formation of NPs inside MOFs. In 2011, Cao and co-workers obtained highly dispersed Pd NPs (~ 2.6 nm) encapsulated in the mesoporous cages of the MOF MIL-101(Cr).[201] The encapsulation was achieved by a wetness impregnation method and the resulting Pd/MIL-101(Cr) catalyst exhibited extremely high catalytic activities in the direct C2 arylation of substituted indoles by using only 0.1 mol % of catalytic load.

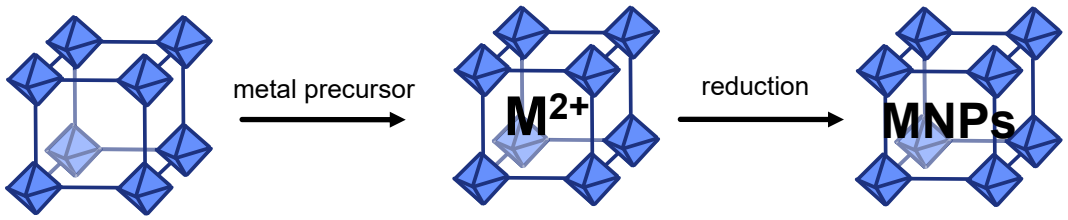

Figure I.46. General strategy employed for loading of MNPs inside a MOF.

A more recent example was reported by Wu and co-workers that developed a high-aluminium zeolite (**ZSM-5**) to encapsulate ultrafine Ru NPs and enhance catalytic transformations (Figure I.47).[202] Small Ru clusters with an average size of ~1 nm were identified by scanning transmission electron microscopy (SEM). The resulting Ru@**ZSM-5** showed an enhanced activity and stability for the crucial hydrodeoxygenation (HDO) of phenol to cyclohexane.

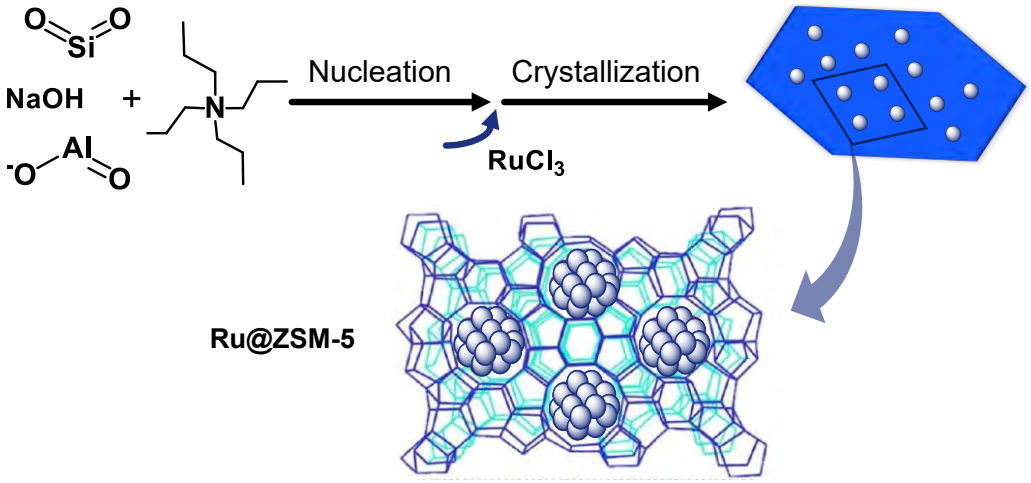

Figure I.47. Schematic procedure for the encapsulation of Ru NPs within a zeolite host reported by Hu and co-workers.

I.4.2.2. Metallosupramolecular cages and organic cages

The development of metallosupramolecular cages and organic cages represents a step forward in the controlled-preparation and stabilization of MNPs due to the putative affinity of the nanoparticles to the hollow cavity of the host. Examples of Pd NPs mainly, but also Au, Ag, ferrihydrite, TiO_2 and Ru NPs, have been reported. For instance, Fujita and co-workers developed a self-assembled spherical nanocapsule, $M_{12}L_{24}$, which was used as a template to prepare silica nanoparticles smaller than 5 nm in diameter.[203] In 2013, the same authors used this spherical coordination template for the preparation of TiO_2 nanoparticles with strict control of size, mass, and density.[204] Those were prepared by hydrolysing the precursor, $Ti(acac)_2(biphen)$, and the template was easily removed by reducing the Pd^{II} ions. Calcination gave crystalline TiO_2 NPs of 2 nm in diameter, which showed photocatalytic activity. NP/support composites are widely used for catalysis because the space confinement effect of these supports (hosts or templates) increase substrate selectivity.[205, 206] Moreover, it improves the catalytic activity because of enhanced exposure of active centres.

Another example, in 2014, Zhang and co-workers designed a 3D, shape-persistent organic molecular cage to act as a template for the growth of Au NPs with a small size (1.9 ± 0.4 nm),[207] being one of the first examples of Au NPs synthesized in a confined space.

However, most of the studies rely on the stabilization of Pd NPs since their catalytic activity is of great interest. In 2018, Xu and co-workers reported another example of porous organic cage, **RCC3**, able to encapsulate active nanoparticles.[208] The Pd NPs were synthesized in a controlled sub-nanometric size (0.72 nm) and due to the confinement effect showed high stability and durability (Figure I.48). They were found to be catalytically active in the hydrogenation of nitroarenes and reduction of organic dyes.

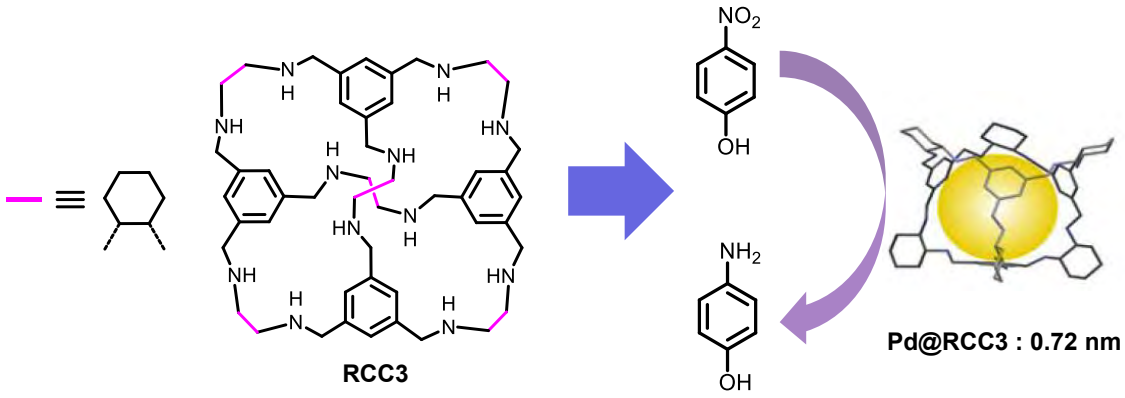

Figure I.48. Pd-NPs encapsulated in a imine linked POC for hydrogenation of nitroarenes reported by Xu and co-workers.

In 2018, Li and co-workers developed a new porous organic nanocapsule that was used as an efficient heterogeneous catalyst for the carbonylation of aryl halides.[209] The group of Zhang followed the same strategy and used a nanocapsule to act as a template for synthesizing Pd NPs with small size (1.8 ± 0.2 nm).[210] They successfully tested this active species in the Suzuki-Miyaura coupling (Figure I.49).

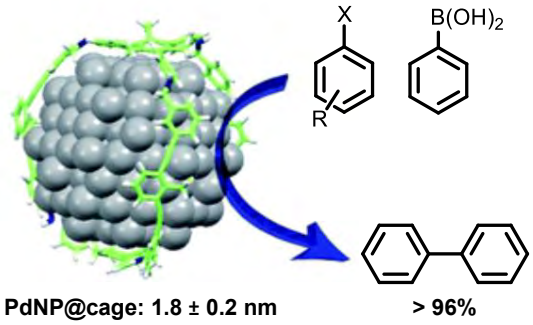

Figure I.49. Pd-NPs encapsulated in porous organic cage for Suzuki-Miyaura catalysis reported by Zhang and co-workers.

Later, in 2019, Jiang's group developed Pd NPs (1.9 ± 0.4 nm) stabilized by an organic nanocapsule.[211] In this work, the authors demonstrated the ability of a water soluble nanocapsule to sensing, controlling nanoparticle growth, and developing a catalytic active platform. By light-induction, they could demonstrate the effectiveness in hydroxylation of 4-nitrophenylboronic acid to 4-nitrophenol along with hydride reduction.

One of the most recent examples published was reported by Beaumont and co-workers.[212] They demonstrated with the synthesis of small Pd NPs (1.6 nm) with a POC known as **RCC3** (Figure I.50). Their catalytic efficiency was tested by using the carbon monoxide oxidation reaction. Pd NPs⊂**RCC3** exhibited similar catalytic activity to other Pd catalysts, even though the other catalysts are not manageable in solution.

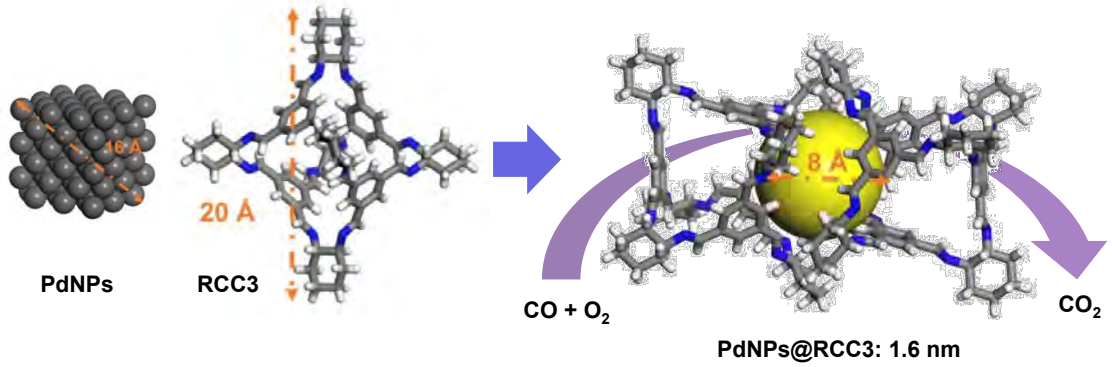

Figure I.50. Pd-NPs encapsulated in porous organic (**RCC3**) cage for CO oxidation reported by Beaumont and co-workers.

In 2020, Bharadwaj reported a series of three positional isomers of organic cages (***o*-OC**, ***m*-OC** and ***p*-OC**) that gave Pd NPs with a 1-2 nm of diameter.[213] Theoretical studies indicated that the driving force for the specific orientational preference is ascribed to variations on the π-π interactions which control the growth of Pd NPs. This NPs showed excellent catalysis of Tsuji-Trost allylation at room temperature (Figure I.51).

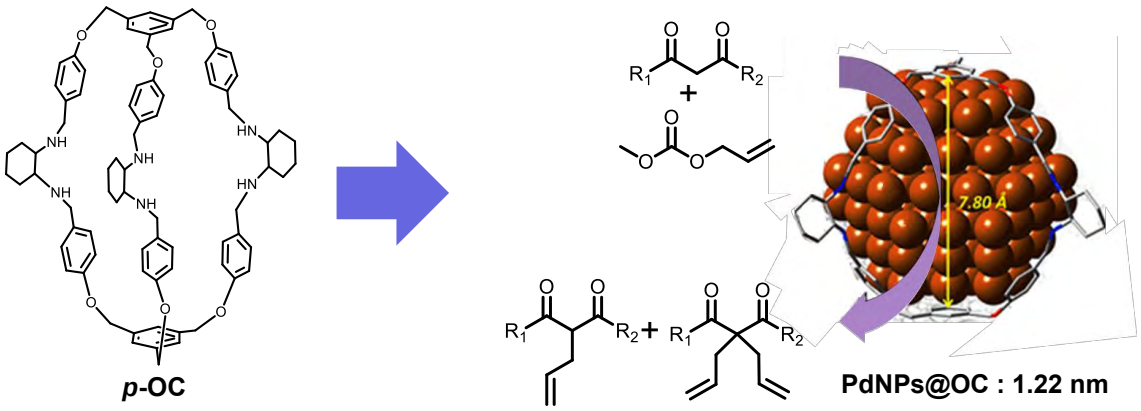

Figure I.51. Pd-NPs encapsulated in porous organic cage for Tsuji-Trost allylation reported by Bharadwaj and co-workers.

A sole example of the stabilization of Ru NPs in cages was reported by Zhou and co-workers in 2018. They developed an anionic porous coordination cage (**PCC-2**) to encapsulate Ru^{3+} ions through electrostatic interactions and the cavity confinement effect.[214] Then, Ru NPs (~2 nm) were formed upon mild reduction with $NaBH_4$. Encapsulated NPs were uniform in size with a face-centred-cubic crystal structure and Ru NPs@**PCC-2** composite exhibited high catalytic activity in methanolysis of ammonia borane, which is important in chemical hydrogen storage (Figure I.52).

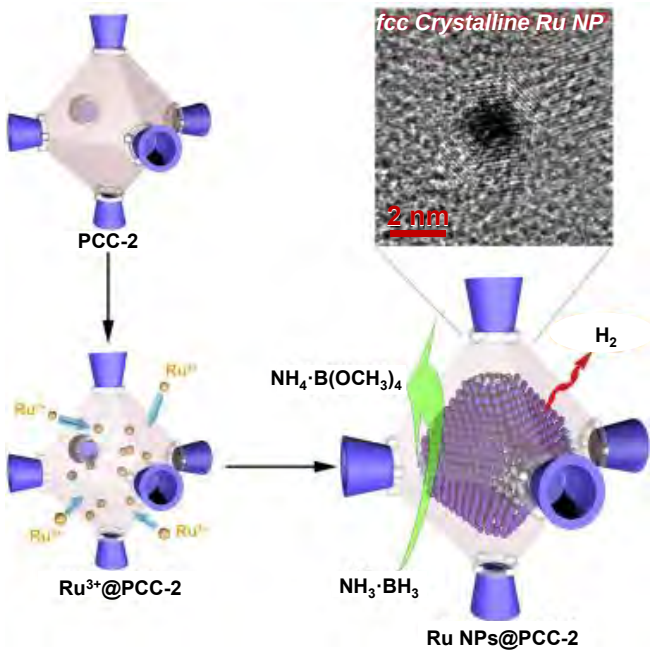

Figure I.52. Ru-NPs encapsulated in porous coordination cage for dehydrogenation reported by Zhou and co-workers.

I.5. References

1. Lehn, J. M., Supramolecular chemistry. *Science* **1993,** *260* (5115), 1762-1763.

2. Schneider, H. J., Binding mechanisms in supramolecular complexes. *Angew. Chem. Int. Ed.* **2009,** *48* (22), 3924-3977.

3. Pullen, S.; Tessarolo, J.; Clever, G. H., Increasing structural and functional complexity in self-assembled coordination cages. *Chem. Sci.* **2021,** *12* (21), 7269-7293.

4. Dong, Z.; Luo, Q.; Liu, J., Artificial enzymes based on supramolecular scaffolds. *Chem. Soc. Rev.* **2012,** *41* (23), 7890-7908.

5. Steed, J.; Turner, D.; Wallace, K., Core Concepts in Supramolecular Chemistry and Nanochemistry. Wiley, 2007.

6. Steed, J. W.; Atwood, J. L., *Supramolecular Chemistry*. Wiley, 2013.

7. Piskorz, T. K.; Martí-Centelles, V.; Young, T. A.; Lusby, P. J.; Duarte, F., Computational Modeling of Supramolecular Metallo-organic Cages–Challenges and Opportunities. *ACS Catal.* **2022**, 5806-5826.

8. Fujita, M.; Nagao, S.; Ogura, K., Guest-Induced Organization of a Three-Dimensional Palladium(II) Cagelike Complex. A Prototype for "Induced-Fit" Molecular Recognition. *J. Am. Chem. Soc.* **1995,** *117* (5), 1649-1650.

9. Saalfrank, R. W.; Stark, A.; Peters, K.; von Schnering H. G., The First “Adamantoid” Alkaline Earth Metal Chelate Complex: Synthesis, Structure, and Reactivity. *Angew. Chem. Int. Ed. Engl.* **1988,** *27* (6), 851-853.

10. McConnell, A. J., Metallosupramolecular cages: from design principles and characterisation techniques to applications. *Chem. Soc. Rev.* **2022**, 51, 2957-2971.

11. Rota Martir, D.; Zysman-Colman, E., Photoactive supramolecular cages incorporating Ru(ii) and Ir(iii) metal complexes. *ChemComm* **2019,** *55* (2), 139-158.

12. Lisboa, L. S.; Findlay, J. A.; Wright, L. J.; Hartinger, C. G.; Crowley, J. D., A Reduced-Symmetry Heterobimetallic [PdPtL4]4+ Cage: Assembly, Guest Binding, and Stimulus-Induced Switching. *Angew. Chem. Int. Ed.* **2020,** *59* (27), 11101-11107.

13. Ogata, D.; Yuasa, J., Dynamic Open Coordination Cage from Nonsymmetrical Imidazole–Pyridine Ditopic Ligands for Turn-On/Off Anion Binding. *Angew. Chem. Int. Ed.* **2019,** *58* (51), 18424-18428.

14. Lewis, J. E. M.; Crowley, J. D., Metallo-Supramolecular Self-Assembly with Reduced-Symmetry Ligands. *ChemPlusChem* **2020,** *85* (5), 815-827.

15. Sudan, S.; Li, R.-J.; Jansze, S. M.; Platzek, A.; Rudolf, R.; Clever, G. H.; Fadaei-Tirani, F.; Scopelliti, R.; Severin, K., Identification of a Heteroleptic Pd6L6L′6 Coordination Cage by Screening of a Virtual Combinatorial Library. *J. Am. Chem. Soc.* **2021,** *143* (4), 1773-1778.

16. Domoto, Y.; Abe, M.; Fujita, M., A Highly Entangled (M3L2)8 Truncated Cube from the Anion-Controlled Oligomerization of a π-Coordinated M3L2 Subunit. *J. Am. Chem. Soc.* **2021,** *143* (23), 8578-8582.

17. Sun, Y.; Chen, C.; Liu, J.; Stang, P. J., Recent developments in the construction and applications of platinum-based metallacycles and metallacages via coordination. *Chem. Soc. Rev.* **2020,** *49* (12), 3889-3919.

18. Plajer, A. J.; Percástegui, E. G.; Santella, M.; Rizzuto, F. J.; Gan, Q.; Laursen, B. W.; Nitschke, J. R., Fluorometric Recognition of Nucleotides within a Water-Soluble Tetrahedral Capsule. *Angew. Chem. Int. Ed.* **2019,** *58* (13), 4200-4204.

19. Dong, J.; Zhou, Y.; Zhang, F.; Cui, Y., A Highly Fluorescent Metallosalalen-Based Chiral Cage for Enantioselective Recognition and Sensing. *Eur. J. Chem.* **2014,** *20* (21), 6455-6461.

20. Zhang, D.; Ronson, T.; Zou, Y.-Q.; Nitschke, J., Metal–organic cages for molecular separations. *Nat. Rev. Chem.* **2021,** *5* (3), 168-182.

21. Mal, P.; Breiner, B.; Rissanen, K.; Nitschke, J. R., White phosphorus is air-stable within a self-assembled tetrahedral capsule. *Science* **2009,** *324* (5935), 1697-1699.

22. Gonell, S.; Caumes, X.; Orth, N.; Ivanović-Burmazović, I.; Reek, J. N. H., Self-assembled M12L24 nanospheres as a reaction vessel to facilitate a dinuclear Cu(i) catalyzed cyclization reaction. *Chem. Sci.* **2019,** *10* (5), 1316-1321.

23. Grommet, A. B.; Feller, M.; Klajn, R., Chemical reactivity under nanoconfinement. *Nat. Nanotechnol.* **2020,** *15* (4), 256-271.

24. Chen, J.; Rebek, J., Selectivity in an Encapsulated Cycloaddition Reaction. *Org. Lett.* **2002,** *4* (3), 327-329.

25. Yoshizawa, M.; Takeyama, Y.; Kusukawa, T.; Fujita, M., Cavity-directed, highly stereoselective [2+2] photodimerization of olefins within self-assembled coordination cages. *Angew. Chem. Int. Ed.* **2002,** *41* (8), 1347-9.

26. García-Simón, C.; Gramage-Doria, R.; Raoufmoghaddam, S.; Parella, T.; Costas, M.; Ribas, X.; Reek, J. N. H., Enantioselective Hydroformylation by a Rh-Catalyst Entrapped in a Supramolecular Metallocage. *J. Am. Chem. Soc.* **2015,** *137* (7), 2680-2687.

27. Fang, Y.; Powell, J. A.; Li, E.; Wang, Q.; Perry, Z.; Kirchon, A.; Yang, X.; Xiao, Z.; Zhu, C.; Zhang, L.; Huang, F.; Zhou, H.-C., Catalytic reactions within the cavity of coordination cages. *Chem. Soc. Rev.* **2019,** *48* (17), 4707-4730.

28. Pöthig, A.; Casini, A., Recent Developments of Supramolecular Metal-based Structures for Applications in Cancer Therapy and Imaging. *Theranostics* **2019,** *9* (11), 3150-3169.

29. Liang, Y.; Fang, Y.; Cui, Y.; Zhou, H., A stable biocompatible porous coordination cage promotes in vivo liver tumor inhibition. *Nano Res.* **2021,** *14* (10), 3407-3415.

30. Rousseaux, S. A. L.; Gong, J. Q.; Haver, R.; Odell, B.; Claridge, T. D. W.; Herz, L. M.; Anderson, H. L., Self-Assembly of Russian Doll Concentric Porphyrin Nanorings. *J. Am. Chem. Soc.* **2015,** *137* (39), 12713-12718.

31. Parac, T. N.; Scherer, M.; Raymond, K. N., Host within a Host: Encapsulation of Alkali Ion – Crown Ether Complexes into a [Ga4L6]12− Supramolecular Cluster. *Angew. Chem. Int. Ed.* **2000,** *39* (7), 1239-1242.

32. Day, A. I.; Blanch, R. J.; Arnold, A. P.; Lorenzo, S.; Lewis, G. R.; Dance, I., A Cucurbituril-Based Gyroscane: A New Supramolecular Form. *Angew. Chem. Int. Ed.* **2002,** *41* (2), 275-277.

33. Zhang, D.; Ronson, T. K.; Greenfield, J. L.; Brotin, T.; Berthault, P.; Léonce, E.; Zhu, J.-L.; Xu, L.; Nitschke, J. R., Enantiopure [Cs+/Xe⊂Cryptophane]⊂FeII4L4 Hierarchical Superstructures. *J. Am. Chem. Soc.* **2019,** *141* (20), 8339-8345.

34. Gong, W.; Yang, X.; Zavalij, P. Y.; Isaacs, L.; Zhao, Z.; Liu, S., From Packed "Sandwich" to "Russian Doll": Assembly by Charge-Transfer Interactions in Cucurbit[10]uril. *Eur. J. Chem.* **2016,** *22* (49), 17612-17618.

35. Cai, K.; Lipke, M. C.; Liu, Z.; Nelson, J.; Cheng, T.; Shi, Y.; Cheng, C.; Shen, D.; Han, J.-M.; Vemuri, S.; Feng, Y.; Stern, C. L.; Goddard, W. A.; Wasielewski, M. R.; Stoddart, J. F., Molecular Russian dolls. *Nat. Commun.* **2018,** *9* (1), 5275.

36. Kawase, T.; Tanaka, K.; Shiono, N.; Seirai, Y.; Oda, M., Onion-Type Complexation Based on Carbon Nanorings and a Buckminsterfullerene. *Angew. Chem. Int. Ed.* **2004,** *43* (13), 1722-1724.

37. Kroto, H. W.; Heath, J. R.; O'Brien, S. C.; Curl, R. F.; Smalley, R. E., C60: Buckminsterfullerene. *Nature* **1985,** *318* (6042), 162-163.

38. Fuertes-Espinosa, C.; Pujals, M.; Ribas, X., Supramolecular Purification and Regioselective Functionalization of Fullerenes and Endohedral Metallofullerenes. *Chem* **2020,** *6* (12), 3219-3262.

39. He, Y.; Li, Y., Fullerene derivative acceptors for high performance polymer solar cells. *Phys. Chem. Chem. Phys.* **2011,** *13* (6), 1970-1983.

40. Mishra, A.; Bäuerle, P., Small Molecule Organic Semiconductors on the Move: Promises for Future Solar Energy Technology. *Angew. Chem. Int. Ed.* **2012,** *51* (9), 2020-2067.

41. Mazzio, K. A.; Luscombe, C. K., The future of organic photovoltaics. *Chem. Soc. Rev.* **2015,** *44* (1), 78-90.

42. Ragoussi, M.-E.; Torres, T., New generation solar cells: concepts, trends and perspectives. *ChemComm* **2015,** *51* (19), 3957-3972.

43. Inganäs, O., Organic Photovoltaics over Three Decades. *Adv. Mater. Lett.* **2018,** *30* (35), 1800388.

44. Deng, L.-L.; Xie, S.-Y.; Gao, F., Fullerene-Based Materials for Photovoltaic Applications: Toward Efficient, Hysteresis-Free, and Stable Perovskite Solar Cells. *Adv. Electron. Mater.* **2018,** *4* (10), 1700435.

45. Kumari, M.; Swetha, T.; Singh, S., Fullerene derivatives: A review on perovskite solar cells. *Mater. Express* **2018,** *8*, 389-406.

46. Fernandez-Delgado, O.; Chandrasekhar, P. S.; Cano-Sampaio, N.; Simon, Z. C.; Puente-Santiago, A. R.; Liu, F.; Castro, E.; Echegoyen, L., The role of fullerene derivatives in

perovskite solar cells: electron transporting or electron extraction layers? *J. Mater. Chem.* **2021,** *9* (33), 10759-10767.

47. Castro, E.; Garcia, A. H.; Zavala, G.; Echegoyen, L., Fullerenes in biology and medicine. *J. Mater. Chem.* **2017,** *5* (32), 6523-6535.

48. Muñoz, A.; Sigwalt, D.; Illescas, B. M.; Luczkowiak, J.; Rodríguez-Pérez, L.; Nierengarten, I.; Holler, M.; Remy, J. S.; Buffet, K.; Vincent, S. P.; Rojo, J.; Delgado, R.; Nierengarten, J. F.; Martín, N., Synthesis of giant globular multivalent glycofullerenes as potent inhibitors in a model of Ebola virus infection. *Nat. Chem.* **2016,** *8* (1), 50-57.

49. Nierengarten, J.-F.; Schneider, J. P.; Trinh, T. M. N.; Joosten, A.; Holler, M.; Lepage, M. L.; Bodlenner, A.; García-Moreno, M. I.; Ortiz Mellet, C.; Compain, P., Giant Glycosidase Inhibitors: First- and Second-Generation Fullerodendrimers with a Dense Iminosugar Shell. *Eur. J. Chem.* **2018,** *24* (10), 2483-2492.

50. Skipa, T.; Koltover, V., Fullerene Trend in Biomedicine: Expectations and Reality Crimson Publishers Opinion. *RMES* **2019,** *8* (3), 877-879.

51. Jia, L.; Chen, M.; Yang, S., Functionalization of fullerene materials toward applications in perovskite solar cells. *Mater. Chem. Front.* **2020,** *4* (8), 2256-2282.

52. Liu, J.; Qiu, L.; Shao, S., Emerging electronic applications of fullerene derivatives: an era beyond OPV. *J. Mater. Chem.* **2021,** *9* (45), 16143-16163.

53. Sijbesma, R.; Srdanov, G.; Wudl, F.; Castoro, J. A.; Wilkins, C.; Friedman, S. H.; DeCamp, D. L.; Kenyon, G. L., Synthesis of a fullerene derivative for the inhibition of HIV enzymes. *J. Am. Chem. Soc.* **1993,** *115* (15), 6510-6512.

54. Sharma, S. K.; Chiang, L. Y.; Hamblin, M. R., Photodynamic therapy with fullerenes in vivo: reality or a dream? *Nanomedicine* **2011,** *6* (10), 1813-1825.

55. Soldatova, Y. V.; Kotelnikova, R. A.; Zhilenkov, A. V.; Faingold, I. I.; Troshin, P. A.; Kozlova, M. A.; Areshidze, D. A.; Aldoshin, S. M., Potassium Salt of Fullerenylpenta-N-Dihydroxytyrosine Effects on Type 2 Diabetes Mellitus Therapeutic Targets. *Dokl. Biochem. Biophys.* **2019,** *488* (1), 320-323.

56. Kazemzadeh, H.; Mozafari, M., Fullerene-based delivery systems. *Drug Discov. Today* **2019,** *24* (3), 898-905.

57. Bobylev, A. G.; Kraevaya, O. A.; Bobyleva, L. G.; Khakina, E. A.; Fadeev, R. S.; Zhilenkov, A. V.; Mishchenko, D. V.; Penkov, N. V.; Teplov, I. Y.; Yakupova, E. I.; Vikhlyantsev, I. M.; Troshin, P. A., Anti-amyloid activities of three different types of water-soluble fullerene derivatives. *Colloids Surf. B.* **2019,** *183*, 110426.

58. Kawase, T.; Kurata, H., Ball-, Bowl-, and Belt-Shaped Conjugated Systems and Their Complexing Abilities: Exploration of the Concave−Convex π−π Interaction. *Chem. Rev.* **2006,** *106* (12), 5250-5273.

59. Effing, J.; Jonas, U.; Jullien, L.; Plesnivy, T.; Ringsdorf, H.; Diederich, F.; Thilgen, C.; Weinstein, D., C60 and C70 in a Basket? – Investigations of Mono- and Multilayers from Azacrown Compounds and Fullerenes. *Angew. Chem. Int. Ed. Engl.* **1992,** *31* (12), 1599-1602.

60. Andersson, T.; Nilsson, K.; Sundahl, M.; Westman, G.; Wennerström, O., C60 embedded in γ-cyclodextrin: a water-soluble fullerene. *J. Chem. Soc., Chem.* **1992,** (8), 604-606.

61. Yoshida, Z.-i.; Takekuma, H.; Takekuma, S.-i.; Matsubara, Y., Molecular Recognition of C60 with γ-Cyclodextrin. *Angew. Chem. Int. Ed. Engl.* **1994,** *33* (15-16), 1597-1599.

62. Liu, Y.; Wang, H.; Liang, P.; Zhang, H.-Y., Water-Soluble Supramolecular Fullerene Assembly Mediated by Metallobridged β-Cyclodextrins. *Angew. Chem. Int. Ed.* **2004,** *43* (20), 2690-2694.

63. Tsuyoshi, S.; Kazuaki, N.; Seiji, S., Very Convenient and Efficient Purification Method for Fullerene (C60) with 5,11,17,23,29,35,41,47-Octa-tert-butylcalix[8]arene-49,50,51,52,53,54,55,56-octol. *Chem. Lett.* **1994,** *23* (4), 699-702.

64. Atwood, J. L.; Koutsantonis, G. A.; Raston, C. L., Purification of C60 and C70 by selective complexation with calixarenes. *Nature* **1994,** *368* (6468), 229-231.

65. Steed, J. W.; Junk, P. C.; Atwood, J. L.; Barnes, M. J.; Raston, C. L.; Burkhalter, R. S., Ball and Socket Nanostructures: New Supramolecular Chemistry Based on Cyclotriveratrylene. *J. Am. Chem. Soc.* **1994,** *116* (22), 10346-10347.

66. Hu, S.-Z.; Chen, C.-F., Triptycene-derived oxacalixarene with expanded cavity: synthesis, structure and its complexation with fullerenes C60 and C70. *ChemComm* **2010,** *46* (23), 4199-4201.

67. Huerta, E.; Isla, H.; Pérez, E. M.; Bo, C.; Martín, N.; Mendoza, J. d., Tripodal exTTF-CTV Hosts for Fullerenes. *J. Am. Chem. Soc.* **2010,** *132* (15), 5351-5353.

68. Canevet, D.; Gallego, M.; Isla, H.; de Juan, A.; Pérez, E. M.; Martín, N., Macrocyclic Hosts for Fullerenes: Extreme Changes in Binding Abilities with Small Structural Variations. *J. Am. Chem. Soc.* **2011,** *133* (9), 3184-3190.

69. Yang, D.-C.; Li, M.; Chen, C.-F., A bis-corannulene based molecular tweezer with highly sensitive and selective complexation of C70 over C60. *ChemComm* **2017,** *53* (67), 9336-9339.

70. García-Calvo, V.; Cuevas, J. V.; Barbero, H.; Ferrero, S.; Álvarez, C. M.; González, J. A.; Díaz de Greñu, B.; García-Calvo, J.; Torroba, T., Synthesis of a Tetracorannulene-perylenediimide That Acts as a Selective Receptor for C60 over C70. *Org. Lett.* **2019,** *21* (15), 5803-5807.

71. Jiménez, V. G.; David, A. H. G.; Cuerva, J. M.; Blanco, V.; Campaña, A. G., A Macrocycle Based on a Heptagon-Containing Hexa-peri-hexabenzocoronene. *Angew. Chem. Int. Ed.* **2020,** *59* (35), 15124-15128.

72. Barendt, T.; Myers, W.; Cornes, S.; Lebedeva, M.; Porfyrakis, K.; Marques, I.; Félix, V.; Beer, P., The Green Box: An Electronically Versatile Perylene Diimide Macrocyclic Host for Fullerenes. *J. Am. Chem. Soc.* **2019,** *142* (1), 349–364.

73. Lu, X.; Gopalakrishna, T. Y.; Han, Y.; Ni, Y.; Zou, Y.; Wu, J., Bowl-Shaped Carbon Nanobelts Showing Size-Dependent Properties and Selective Encapsulation of C(70). *J. Am. Chem. Soc.* **2019,** *141* (14), 5934-5941.

74. Isobe, H.; Hitosugi, S.; Yamasaki, T.; Iizuka, R., Molecular bearings of finite carbon nanotubes and fullerenes in ensemble rolling motion. *Chem. Sci.* **2013,** *4* (3), 1293-1297.

75. Miki, K.; Matsushita, T.; Inoue, Y.; Senda, Y.; Kowada, T.; Ohe, K., Electron-rich carbon nanorings as macrocyclic hosts for fullerenes. *ChemComm* **2013,** *49* (80), 9092-9094.

76. Nakanishi, Y.; Omachi, H.; Matsuura, S.; Miyata, Y.; Kitaura, R.; Segawa, Y.; Itami, K.; Shinohara, H., Size-Selective Complexation and Extraction of Endohedral Metallofullerenes with Cycloparaphenylene. *Angew. Chem. Int. Ed.* **2014,** *53* (12), 3102-3106.

77. Minameyer, M. B.; Xu, Y.; Frühwald, S.; Görling, A.; von Delius, M.; Drewello, T., Investigation of Cycloparaphenylenes (CPPs) and their Noncovalent Ring-in-Ring and Fullerene-in-Ring Complexes by (Matrix-Assisted) Laser Desorption/Ionization and Density Functional Theory. *Eur. J. Chem.* **2020,** *26* (40), 8729-8741.

78. Kawase, T.; Tanaka, K.; Fujiwara, N.; Darabi, H. R.; Oda, M., Complexation of a Carbon Nanoring with Fullerenes. *Angew. Chem. Int. Ed.* **2003,** *42* (14), 1624-1628.

79. Iwamoto, T.; Watanabe, Y.; Sadahiro, T.; Haino, T.; Yamago, S., Size-Selective Encapsulation of C60 by [10]Cycloparaphenylene: Formation of the Shortest Fullerene-Peapod. *Angew. Chem. Int. Ed.* **2011,** *50* (36), 8342-8344.

80. Xu, Y.; Gsänger, S.; Minameyer, M. B.; Imaz, I.; Maspoch, D.; Shyshov, O.; Schwer, F.; Ribas, X.; Drewello, T.; Meyer, B.; von Delius, M., Highly Strained, Radially π-Conjugated Porphyrinylene Nanohoops. *J. Am. Chem. Soc.* **2019,** *141* (46), 18500-18507.

81. von Delius, M.; Xu, Y.; Wang, B.; Kaur, R.; Minameyer, M.; Bothe, M.; drewello, t.; Guldi, D., A Supramolecular [10]CPP Junction Enables Efficient Electron Transfer in Modular Porphyrin-[10]CPP-Fullerene Complexes. *Angew. Chem. Int. Ed.* **2018,** *57* (36), 11549-11553.

82. Tashiro, K.; Aida, T., Metalloporphyrin hosts for supramolecular chemistry of fullerenes. *Chem. Soc. Rev.* **2007,** *36* (2), 189-197.

83. Gil-Ramírez, G.; Karlen, S. D.; Shundo, A.; Porfyrakis, K.; Ito, Y.; Briggs, G. A. D.; Morton, J. J. L.; Anderson, H. L., A Cyclic Porphyrin Trimer as a Receptor for Fullerenes. *Org. Lett.* **2010,** *12* (15), 3544-3547.

84. Wu, Z.-Q.; Shao, X.-B.; Li, C.; Hou, J.-L.; Wang, K.; Jiang, X.-K.; Li, Z.-T., Hydrogen-Bonding-Driven Preorganized Zinc Porphyrin Receptors for Efficient Complexation of C60, C70, and C60 Derivatives. *J. Am. Chem. Soc.* **2005,** *127* (49), 17460-17468.

85. Kieran, A. L.; Pascu, S. I.; Jarrosson, T.; Sanders, J. K. M., Inclusion of C60 into an adjustable porphyrin dimer generated by dynamic disulfide chemistry. *ChemComm* **2005,** (10), 1276-1278.

86. Hernández-Eguía, L. P.; Escudero-Adán, E. C.; Pintre, I.; Ventura, B.; Flamigni, L.; Ballester, P., Supramolecular inclusion complexes of two cyclic zinc bisporphyrins with C60 and C70: structural, thermodynamic, and photophysical characterization. *Eur. J. Chem.* **2011,** *17 (51)*, 14564-14577.

87. Mulholland, A. R.; Woodward, C. P.; Langford, S. J., Fullerene-templated synthesis of a cyclic porphyrin trimer using olefin metathesis. *ChemComm* **2011,** *47* (5), 1494-1496.

88. Tashiro, K.; Aida, T.; Zheng, J.-Y.; Kinbara, K.; Saigo, K.; Sakamoto, S.; Yamaguchi, K., A Cyclic Dimer of Metalloporphyrin Forms a Highly Stable Inclusion Complex with C60. *J. Am. Chem. Soc.* **1999,** *121* (40), 9477-9478.

89. Zheng, J.-Y.; Tashiro, K.; Hirabayashi, Y.; Kinbara, K.; Saigo, K.; Aida, T.; Sakamoto, S.; Yamaguchi, K., Cyclic Dimers of Metalloporphyrins as Tunable Hosts for Fullerenes: A Remarkable Effect of Rhodium(III). *Angew. Chem. Int. Ed.* **2001,** *40* (10), 1857-1861.

90. Tashiro, K.; Aida, T., Metalloporphyrin Hosts for Supramolecular Chemistry of Fullerenes. *Chem. Soc. Rev.* **2007,** *36*, 189-197.

91. Nakamura, T.; Ube, H.; Miyake, R.; Shionoya, M., A C60-Templated Tetrameric Porphyrin Barrel Complex via Zinc-Mediated Self-Assembly Utilizing Labile Capping Ligands. *J. Am. Chem. Soc.* **2013,** *135* (50), 18790-18793.

92. Nobukuni, H.; Shimazaki, Y.; Tani, F.; Naruta, Y., A Nanotube of Cyclic Porphyrin Dimers Connected by Nonclassical Hydrogen Bonds and Its Inclusion of C60 in a Linear Arrangement. *Angew. Chem. Int. Ed.* **2007,** *46* (47), 8975-8978.

93. Song, J.; Aratani, N.; Shinokubo, H.; Osuka, A., A Porphyrin Nanobarrel That Encapsulates C60. *J. Am. Chem. Soc.* **2010,** *132* (46), 16356-16357.

94. Claessens, C. G.; Torres, T., Inclusion of C60 fullerene in a M3L2 subphthalocyanine cage. *ChemComm* **2004,** (11), 1298-1299.

95. Sánchez-Molina, I.; Grimm, B.; Krick Calderon, R. M.; Claessens, C. G.; Guldi, D. M.; Torres, T., Self-Assembly, Host–Guest Chemistry, and Photophysical Properties of Subphthalocyanine-Based Metallosupramolecular Capsules. *J. Am. Chem. Soc.* **2013,** *135* (28), 10503-10511.

96. Zango, G.; Krug, M.; Krishna, S.; Mariñas, V.; Clark, T.; Martinez-Diaz, M. V.; Guldi, D. M.; Torres, T., Photoactive preorganized subphthalocyanine-based molecular tweezers for selective complexation of fullerenes. *Chem. Sci.* **2020,** *11* (13), 3448-3459.

97. Zhang, G.; Mastalerz, M., Organic cage compounds – from shape-persistency to function. *Chem. Soc. Rev.* **2014,** *43* (6), 1934-1947.

98. Mastalerz, M., Porous Shape-Persistent Organic Cage Compounds of Different Size, Geometry, and Function. *Acc. Chem. Res.* **2018,** *51* (10), 2411-2422.

99. Huerta, E.; Metselaar, G. A.; Fragoso, A.; Santos, E.; Bo, C.; de Mendoza, J., Selective Binding and Easy Separation of C70 by Nanoscale Self-Assembled Capsules. *Angew. Chem. Int. Ed.* **2007,** *46* (1-2), 202-205.

100. Zhang, C.; Wang, Q.; Long, H.; Zhang, W., A Highly C70 Selective Shape-Persistent Rectangular Prism Constructed through One-Step Alkyne Metathesis. *J. Am. Chem. Soc.* **2011,** *133* (51), 20995-21001.

101. Li, M.-J.; Huang, C.-H.; Lai, C.-C.; Chiu, S.-H., Hemicarceplex Formation With a Cyclotriveratrylene-Based Molecular Cage Allows Isolation of High-Purity (≥99.0%) C70 Directly from Fullerene Extracts. *Org. Lett.* **2012,** *14* (24), 6146-6149.

102. Seidel, S. R.; Stang, P. J., High-Symmetry Coordination Cages via Self-Assembly. *Acc. Chem. Res.* **2002,** *35* (11), 972-983.

103. Kuehl, C. J.; Kryschenko, Y. K.; Radhakrishnan, U.; Seidel, S. R.; Huang, S. D.; Stang, P. J., Self-assembly of nanoscopic coordination cages of D(3h) symmetry. *Proc. Natl. Acad. Sci. U.S.A.* **2002,** *99* (8), 4932-4936.

104. Cook, T. R.; Stang, P. J., Recent Developments in the Preparation and Chemistry of Metallacycles and Metallacages via Coordination. *Chem. Rev.* **2015,** *115* (15), 7001-7045.

105. García-Simón, C.; Costas, M.; Ribas, X., Metallosupramolecular receptors for fullerene binding and release. *Chem. Soc. Rev.* **2016,** *45* (1), 40-62.

106. Ikeda, A.; Yoshimura, M.; Udzu, H.; Fukuhara, C.; Shinkai, S., Inclusion of [60]Fullerene in a Homooxacalix[3]arene-Based Dimeric Capsule Cross-Linked by a PdII−Pyridine Interaction. *J. Am. Chem. Soc.* **1999,** *121* (17), 4296-4297.

107. Ikeda, A.; Udzu, H.; Yoshimura, M.; Shinkai, S., Inclusion of [60]Fullerene in a Self-assembled Homooxacalix[3]arene-based Dimeric Capsule Constructed by a PdII–pyridine Interaction. The Li+-binding to the Lower Rims can Improve the Inclusion Ability. *Tetrahedron Lett.* **2000,** *56* (13), 1825-1832.

108. Pirondini, L.; Bonifazi, D.; Cantadori, B.; Braiuca, P.; Campagnolo, M.; Zorzi, R. D.; Geremia, S.; Diederich, F.; Dalcanale, E., Inclusion of methano[60]fullerene derivatives in cavitand-based coordination cages. *Tetrahedron Lett.* **2006,** *62*, 2008-2015.

109. Schmittel, M.; He, B.; Mal, P., Supramolecular Multicomponent Self-Assembly of Shape-Adaptive Nanoprisms: Wrapping up C60 with Three Porphyrin Units. *Org. Lett.* **2008,** *10* (12), 2513-2516.

110. Meng, W.; Breiner, B.; Rissanen, K.; Thoburn, J. D.; Clegg, J. K.; Nitschke, J. R., A Self-Assembled M8L6 Cubic Cage that Selectively Encapsulates Large Aromatic Guests. *Angew. Chem. Int. Ed.* **2011,** *50* (15), 3479-3483.

111. Zhang, J.; Zheng, X.; Jiang, R.; Yu, Y.; Li, Y.; Liu, H.; Li, Q.; Shuai, Z.; Li, Y., A "clicked" porphyrin cage with high binding affinity towards fullerenes. *RSC Adv.* **2014,** *4* (52), 27389-27392.

112. García-Simón, C.; Garcia-Borràs, M.; Gómez, L.; Parella, T.; Osuna, S.; Juanhuix, J.; Imaz, I.; Maspoch, D.; Costas, M.; Ribas, X., Sponge-like molecular cage for purification of fullerenes. *Nat. Commun.* **2014,** *5*, 5557.

113. Mahata, K.; Frischmann, P. D.; Würthner, F., Giant Electroactive M4L6 Tetrahedral Host Self-Assembled with Fe(II) Vertices and Perylene Bisimide Dye Edges. *J. Am. Chem. Soc.* **2013,** *135* (41), 15656-15661.

114. Kishi, N.; Li, Z.; Yoza, K.; Akita, M.; Yoshizawa, M., An M2L4 Molecular Capsule with an Anthracene Shell: Encapsulation of Large Guests up to 1 nm. *J. Am. Chem. Soc.* **2011,** *133* (30), 11438-11441.

115. Kishi, N.; Akita, M.; Kamiya, M.; Hayashi, S.; Hsu, H.-F.; Yoshizawa, M., Facile Catch and Release of Fullerenes Using a Photoresponsive Molecular Tube. *J. Am. Chem. Soc.* **2013,** *135* (35), 12976-12979.

116. Kishi, N.; Akita, M.; Yoshizawa, M., Selective Host–Guest Interactions of a Transformable Coordination Capsule/Tube with Fullerenes. *Angew. Chem. Int. Ed.* **2014,** *53* (14), 3604-3607.

117. Yamashina, M.; Yuki, T.; Sei, Y.; Akita, M.; Yoshizawa, M., Anisotropic Expansion of an M2L4 Coordination Capsule: Host Capability and Frame Rearrangement. *Eur. J. Chem.* **2015,** *21* (11), 4200-4204.

118. Han, M.; Michel, R.; He, B.; Chen, Y.-S.; Stalke, D.; John, M.; Clever, G. H., Light-Triggered Guest Uptake and Release by a Photochromic Coordination Cage. *Angew. Chem. Int. Ed.* **2013,** *52* (4), 1319-1323.

119. Martínez-Agramunt, V.; Eder, T.; Darmandeh, H.; Guisado-Barrios, G.; Peris, E., A Size-Flexible Organometallic Box for the Encapsulation of Fullerenes. *Angew. Chem. Int. Ed.* **2019,** *58* (17), 5682-5686.

120. Wuttke, S., Introduction to Reticular Chemistry. Metal–Organic Frameworks and Covalent Organic Frameworks By Omar M. Yaghi, Markus J. Kalmutzki, and Christian S. Diercks. *Angew. Chem. Int. Ed.* **2019,** *58* (40), 14024-14024.

121. Chae, H. K.; Siberio-Pérez, D. Y.; Kim, J.; Go, Y.; Eddaoudi, M.; Matzger, A. J.; O'Keeffe, M.; Yaghi, O. M.; Materials, D.; Discovery, G., A route to high surface area, porosity and inclusion of large molecules in crystals. *Nature* **2004,** *427* (6974), 523-527.

122. Yang, C.-X.; Yan, X.-P., Selective adsorption and extraction of C70 and higher fullerenes on a reusable metal–organic framework MIL-101(Cr). *J. Mater. Chem.* **2012,** *22* (34), 17833-17841.

123. Cook, T. R.; Zheng, Y.-R.; Stang, P. J., Metal–Organic Frameworks and Self-Assembled Supramolecular Coordination Complexes: Comparing and Contrasting the Design, Synthesis, and Functionality of Metal–Organic Materials. *Chem. Rev.* **2013,** *113* (1), 734-777.

124. Foster, M. E.; Azoulay, J. D.; Wong, B. M.; Allendorf, M. D., Novel metal–organic framework linkers for light harvesting applications. *Chem. Sci.* **2014,** *5* (5), 2081-2090.

125. Matsuzaki, S.; Arai, T.; Ikemoto, K.; Inokuma, Y.; Fujita, M., Networked-Cage Microcrystals for Evaluation of Host–Guest Interactions. *J. Am. Chem. Soc.* **2014,** *136* (52), 17899-17901.

126. Feng, Y.; Wang, T.; Li, Y.; Li, J.; Wu, J.; Wu, B.; Jiang, L.; Wang, C., Steering Metallofullerene Electron Spin in Porous Metal–Organic Framework. *J. Am. Chem. Soc.* **2015,** *137* (47), 15055-15060.

127. Escudero-Adán, E. C.; Bauzá, A.; Hernández-Eguía, L. P.; Würthner, F.; Ballester, P.; Frontera, A., Solid-state inclusion of C60 and C70 in a co-polymer induced by metal–ligand coordination of a Zn–porphyrin cage with a bis-pyridyl perylene derivative. *CrystEngComm* **2017,** *19* (33), 4911-4919.

128. Souto, M.; Calbo, J.; Mañas-Valero, S.; Walsh, A.; Mínguez Espallargas, G., Charge-transfer interactions between fullerenes and a mesoporous tetrathiafulvalene-based metal-organic framework. *Beilstein J. Nanotechnol.* **2019,** *10*, 1883-1893.

129. Meng, H.; Zhao, C.; Nie, M.; Wang, C.; Wang, T., Changing the Hydrophobic MOF Pores through Encapsulating Fullerene C60 and Metallofullerene Sc3C2@C80. *J. Phys. Chem.* **2019,** *123* (10), 6265-6269.

130. Martinez, V.; Karadeniz, B.; Biliškov, N.; Lončarić, I.; Muratović, S.; Žilić, D.; Avdoshenko, S. M.; Roslova, M.; Popov, A. A.; Užarević, K., Tunable Fulleretic Sodalite MOFs: Highly Efficient and Controllable Entrapment of C60 Fullerene via Mechanochemistry. *Chem. Mater.* **2020,** *32* (24), 10628-10640.

131. Pratik, S. M.; Gagliardi, L.; Cramer, C. J., Boosting Photoelectric Conductivity in Porphyrin-Based MOFs Incorporating C60. *J. Phys. Chem.* **2020,** *124* (3), 1878-1887.

132. Saura-Sanmartin, A.; Martinez-Cuezva, A.; Marin-Luna, M.; Bautista, D.; Berna, J., Effective Encapsulation of C60 by Metal–Organic Frameworks with Polyamide Macrocyclic Linkers. *Angew. Chem. Int. Ed.* **2021,** *60* (19), 10814-10819.

133. Inokuma, Y.; Arai, T.; Fujita, M., Networked molecular cages as crystalline sponges for fullerenes and other guests. *Nat. Chem.* **2010,** *2* (9), 780-783.

134. Yan, W.; Seifermann, S. M.; Pierrat, P.; Bräse, S., Synthesis of highly functionalized C60 fullerene derivatives and their applications in material and life sciences. *Org. Biomol. Chem.* **2015,** *13* (1), 25-54.

135. Djojo, F.; Herzog, A.; Lamparth, I.; Hampel, F.; Hirsch, A., Regiochemistry of Twofold Additions to [6,6] Bonds in C60: Influence of the Addend-Independent Cage Distortion in 1,2-Monoadducts. *Eur. J. Chem.* **1996,** *2* (12), 1537-1547.

136. Lenes, M.; Wetzelaer, G.-J. A. H.; Kooistra, F. B.; Veenstra, S. C.; Hummelen, J. C.; Blom, P. W. M., Fullerene Bisadducts for Enhanced Open-Circuit Voltages and Efficiencies in Polymer Solar Cells. *Adv. Mater. Lett.* **2008,** *20* (11), 2116-2119.

137. Shi, W.; Hou, X.; Liu, T.; Zhao, X.; Sieval, A. B.; Hummelen, J. C.; Dennis, T. J. S., Purification and electronic characterisation of 18 isomers of the OPV acceptor material bis-[60]PCBM. *ChemComm* **2017,** *53* (5), 975-978.

138. Hirsch, A.; Lamparth, I.; Karfunkel, H. R., Fullerene Chemistry in Three Dimensions: Isolation of Seven Regioisomeric Bisadducts and Chiral Trisadducts of C60 and Di(ethoxycarbonyl)methylene. *Angew. Chem. Int. Ed. Engl.* **1994,** *33* (4), 437-438.

139. Cao, T.; Chen, N.; Liu, G.; Wan, Y.; Perea, J. D.; Xia, Y.; Wang, Z.; Song, B.; Li, N.; Li, X.; Zhou, Y.; Brabec, C. J.; Li, Y., Towards a full understanding of regioisomer effects of indene-C60 bisadduct acceptors in bulk heterojunction polymer solar cells. *J. Mater. Chem.* **2017,** *5* (21), 10206-10219.

140. Zhang, F.; Shi, W.; Luo, J.; Pellet, N.; Yi, C.; Li, X.; Zhao, X.; Dennis, T. J. S.; Li, X.; Wang, S.; Xiao, Y.; Zakeeruddin, S. M.; Bi, D.; Grätzel, M., Isomer-Pure Bis-PCBM-Assisted Crystal Engineering of Perovskite Solar Cells Showing Excellent Efficiency and Stability. *Adv. Mater. Lett.* **2017,** *29* (17), 1606806.

141. Beil, S.; von Delius, M., Supramolecular Approaches for Taming the Chemo- and Regiochemistry of C60 Addition Reactions. *Org. Mat.* **2021,** *3 (2)*, 146-154.

142. Puente Santiago, A. R.; Fernandez-Delgado, O.; Gomez, A.; Ahsan, M. A.; Echegoyen, L., Fullerenes as Key Components for Low-Dimensional (Photo)electrocatalytic Nanohybrid Materials. *Angew. Chem. Int. Ed.* **2021,** *60* (1), 122-141.

143. Guldi, D. M.; Maggini, M.; Scorrano, G.; Prato, M., Intramolecular Electron Transfer in Fullerene/Ferrocene Based Donor−Bridge−Acceptor Dyads. *J. Am. Chem. Soc.* **1997,** *119* (5), 974-980.

144. Bingel, C., Cyclopropanierung von Fullerenen. *Chem. Ber.* **1993,** *126* (8), 1957-1959.

145. Hummelen, J. C.; Knight, B. W.; LePeq, F.; Wudl, F.; Yao, J.; Wilkins, C. L., Preparation and Characterization of Fulleroid and Methanofullerene Derivatives. *J. Org. Chem. Res.* **1995,** *60* (3), 532-538.

146. Hirsch, A.; Brettreich, M.; Wudl, F., *Fullerenes: Chemistry and Reactions*. Wiley, 2006.

147. Isaacs, L.; Diederich, F.; Haldimann, R. F., Multiple Adducts of C60 by Tether-Directed Remote Functionalization and synthesis of soluble derivatives of new carbon allotropes Cn(60+5). *Helv. Chim. Acta* **1997**, 80, 317-342.

148. Trinh, T. M. N.; Schillinger, F.; Guerra, S.; Meichsner, E.; Nierengarten, I.; Hahn, U.; Holler, M.; Nierengarten, J.-F., Regioselective Preparation of Fullerene Bis-adducts from Cleavable Macrocyclic Bis-malonates. *Eur. J. Org. Chem.* **2021,** *2021* (27), 3770-3786.

149. Meichsner, E.; Schillinger, F.; Trinh, T. M. N.; Guerra, S.; Hahn, U.; Nierengarten, I.; Holler, M.; Nierengarten, J.-F., Regioselective Synthesis of Fullerene Tris-adducts for the Preparation of Clickable Fullerene [3:3]-Hexa-adduct Scaffolds. *Eur. J. Org. Chem.* **2021,** *2021* (27), 3787-3797.

150. Schwenninger, R.; Müller, T.; Kräutler, B., Concise Route to Symmetric Multiadducts of [60]Fullerene: Preparation of an Equatorial Tetraadduct by Orthogonal Transposition. *J. Am. Chem. Soc.* **1997,** *119* (39), 9317-9318.

151. Bottari, G.; Trukhina, O.; Kahnt, A.; Frunzi, M.; Murata, Y.; Rodríguez-Fortea, A.; Poblet, J. M.; Guldi, D. M.; Torres, T., Regio-, Stereo-, and Atropselective Synthesis of C60 Fullerene Bisadducts by Supramolecular-Directed Functionalization. *Angew. Chem. Int. Ed.* **2016,** *55* (37), 11020-11025.

152. Xu, Y.; Kaur, R.; Wang, B.; Minameyer, M. B.; Gsänger, S.; Meyer, B.; Drewello, T.; Guldi, D. M.; von Delius, M., Concave–Convex π–π Template Approach Enables the Synthesis of [10]Cycloparaphenylene–Fullerene [2]Rotaxanes. *J. Am. Chem. Soc.* **2018,** *140* (41), 13413-13420.

153. Fuertes, C.; García-Simón, C.; Pujals, M.; Garcia-Borràs, M.; Gomez, L.; Parella, T.; Juanhuix, J.; Imaz, I.; Maspoch, D.; Costas, M.; Ribas, X., Supramolecular Fullerene Sponges as Catalytic Masks for Regioselective Functionalization of C60. *Chem* **2019,** *6* (1), 169-186.

154. Diederich, F.; Ettl, R.; Rubin, Y.; Whetten, R.; Beck, R.; Alvarez, M.; Anz, S.; Sensharma, D.; Wudl, F.; Khemani, K.; Koch, A., The Higher Fullerenes: Isolation and Characterization of C76, C84, C90, C94, and C70O, and Oxide of D5h-C70. *Science* **1991,** *252* (5005), 548-551.

155. Diederich, F.; Whetten, R. L., Beyond C60: the higher fullerenes. *Acc. Chem. Res.* **1992,** *25* (3), 119-126.

156. Crassous, J.; Rivera, J.; Fender, N.; Shu, L.; Echegoyen, L.; Thilgen, C.; Herrmann, A.; Diederich, F., Chemistry of C84 : Separation of Three Constitutional Isomers and

Optical Resolution of D2 -C84 by Using the "Bingel-Retro-Bingel" Strategy. *Angew. Chem. Int. Ed.* **1999,** *38 11*, 1613-1617.

157. Wang, G.-W.; Saunders, M.; Khong, A.; Cross, R. J., A New Method for Separating the Isomeric C84 Fullerenes. *J. Am. Chem. Soc.* **2000,** *122* (13), 3216-3217.

158. Azamar-Barrios, J. A.; Dennis, T. J. S.; Sadhukan, S.; Shinohara, H.; Scuseria, G. E.; Pénicaud, A., Characterization of Six Isomers of [84]Fullerene C84 by Electrochemistry, Electron Spin Resonance Spectroscopy, and Molecular Energy Levels Calculations. *J. Phys. Chem.* **2001,** *105* (19), 4627-4632.

159. Zalibera, M.; Rapta, P.; Dunsch, L., The power of in situ ESR spectroelectrochemistry in the analysis of a C84 fullerene isomer. *Electrochem. Commun.* **2008,** *10* (6), 943-946.

160. Khamatgalimov, A.; Kovalenko, V., 24 IPR isomers of fullerene C84: Cage deformation as geometrical characteristic of local strains. *Int. J. Quantum Chem.* **2012,** *112*, 1055-1065.

161. Waite, S. L.; Chan, B.; Karton, A.; Page, A. J., Accurate Thermochemical and Kinetic Stabilities of C84 Isomers. *J. Phys. Chem.* **2018,** *122* (20), 4768-4777.

162. Shinohara, H.; Yamaguchi, H.; Hayashi, N.; Sato, H.; Ohkohchi, M.; Ando, Y.; Saito, Y., Isolation and spectroscopic properties of scandium fullerenes (Sc2@C74, Sc2@C82, and Sc2@C84). *J. Phys. Chem.* **1993,** *97* (17), 4259-4261.

163. Hawkins, J. M.; Nambu, M.; Meyer, A., Resolution and Configurational Stability of the Chiral Fullerenes C76, C78, and C84: A Limit for the Activation Energy of the Stone-Wales Transformation. *J. Am. Chem. Soc.* **1994,** *116* (17), 7642-7645.

164. Shibata, K.; Kubozono, Y.; Kanbara, T.; Hosokawa, T.; Fujiwara, A.; Ito, Y.; Shinohara, H., Fabrication and characteristics of C84 fullerene field-effect transistors. *Appl. Phys. Lett.* **2004,** *84* (14), 2572-2574.

165. Harigaya, K., Nonlinear optical response from excitons in C60,C70, and higher fullerenes. *J. Lumin.* **1998,** *76-77*, 652-654.

166. Denning, M. S.; Dennis, T. J. S.; Rosseinsky, M. J.; Shinohara, H., K3+δC84. Higher Fullerene Analogues of the A3C60 Superconductors. *Chem. Mater.* **2001,** *13* (12), 4753-4759.

167. Koudoumas, E.; Konstantaki, M.; Mavromanolakis, A.; Michaut, X.; Couris, S.; Leach, S., Transient and instantaneous third-order nonlinear optical response of C60 and the higher fullerenes C70, C76 and C84. *J. Phys. B: At. Mol. Opt. Phys.* **2001,** *34* (24) 4983-4996.

168. Kooistra, F. B.; Mihailetchi, V. D.; Popescu, L. M.; Kronholm, D.; Blom, P. W. M.; Hummelen, J. C., New C84 Derivative and Its Application in a Bulk Heterojunction Solar Cell. *Chem. Mater.* **2006,** *18* (13), 3068-3073.

169. Anthopoulos, T. D.; Kooistra, F. B.; Wondergem, H. J.; Kronholm, D.; Hummelen, J. C.; de Leeuw, D. M., Air-Stable n-Channel Organic Transistors Based on a Soluble C84 Fullerene Derivative. *Adv. Mater. Lett.* **2006,** *18* (13), 1679-1684.

170. Shoji, Y.; Tashiro, K.; Aida, T., Selective Extraction of Higher Fullerenes Using Cyclic Dimers of Zinc Porphyrins. *J. Am. Chem. Soc.* **2004,** *126* (21), 6570-6571.

171. Haino, T.; Fukunaga, C.; Fukazawa, Y., A New Calix[5]arene-Based Container: Selective Extraction of Higher Fullerenes. *Org. Lett.* **2006,** *8* (16), 3545-3548.

172. Huerta, E.; Cequier, E.; Mendoza, J. d., Preferential separation of fullerene[84] from fullerene mixtures by encapsulation. *ChemComm* **2007,** (47), 5016-5018.

173. Kawauchi, T.; Kitaura, A.; Kawauchi, M.; Takeichi, T.; Kumaki, J.; Iida, H.; Yashima, E., Separation of C70 over C60 and selective extraction and resolution of higher fullerenes by syndiotactic helical poly(methyl methacrylate). *J. Am. Chem. Soc.* **2010,** *132* (35), 12191-12193.

174. Liu, K. S.; Li, M. J.; Lai, C. C.; Chiu, S. H., Incarceration of Higher-Order Fullerenes within Cyclotriveratrylene-Based Hemicarcerands Allows Selective Isolation of C(76) , C(78) , and C(84) from a Commercial Fullerene Mixture. *Eur. J. Chem.* **2016,** *22* (48), 17468-17476.

175. Tsuda, A.; Nakamura, T.; Sakamoto, S.; Yamaguchi, K.; Osuka, A., A Self-Assembled Porphyrin Box from meso–meso-Linked Bis{5-p-pyridyl-15-(3,5-di-octyloxyphenyl)porphyrinato zinc(II)}. *Angew. Chem. Int. Ed.* **2002,** *41* (15), 2817-2821.

176. Tsuda, A.; Hu, H.; Watanabe, R.; Aida, T., π-Conjugated multiporphyrin box via self-assembly of an ethynylene-bridged zinc porphyrin dimer. *J. Porphyr. Phthalocyanines* **2003,** *07* (05), 388-393.

177. Johnston, M.; Latter, M., Capsules, Cages and Three-dimensional Hosts: Self-Assembly of Complementary Monomers. *Supramol. Chem.* **2005,** *17*, 595-607.

178. Koo, J.; Kim, I.; Kim, Y.; Cho, D.; Hwang, I.-C.; Mukhopadhyay, R. D.; Song, H.; Ko, Y. H.; Dhamija, A.; Lee, H.; Hwang, W.; Kim, S.; Baik, M.-H.; Kim, K., Gigantic Porphyrinic Cages. *Chem* **2020,** *6* (12), 3374-3384.

179. Yeretzian, C.; Wiley, J. B.; Holczer, K.; Su, T.; Nguyen, S.; Kaner, R. B.; Whetten, R. L., Partial separation of fullerenes by gradient sublimation. *J. Phys. Chem.* **1993,** *97* (39), 10097-10101.

180. Wakahara, T.; Han, A.; Niino, Y.; Maeda, Y.; Akasaka, T.; Suzuki, T.; Yamamoto, K.; Kako, M.; Nakadaira, Y.; Kobayashi, K.; Nagase, S., Silylation of higher fullerenes. *J. Mater. Chem.* **2002,** *12* (7), 2061-2064.

181. Darwish, A. D.; Martsinovich, N.; Taylor, R., Methylation of [76]fullerene and [84]fullerenes; the first oxahomo derivatives of a higher fullerene. *Org. Biomol. Chem.* **2004,** *2* (9), 1364-1367.

182. Koenig, R. M.; Tian, H.-R.; Seeler, T. L.; Tepper, K. R.; Franklin, H. M.; Chen, Z.-C.; Xie, S.-Y.; Stevenson, S., Fullertubes: Cylindrical Carbon with Half-Fullerene End-Caps and Tubular Graphene Belts, Their Chemical Enrichment, Crystallography of Pristine C90-D5h(1) and C100-D5d(1) Fullertubes, and Isolation of C108, C120, C132, and C156 Cages of Unknown Structures. *J. Am. Chem. Soc.* **2020,** *142* (36), 15614-15623.

183. Du, Y.; Sheng, H.; Astruc, D.; Zhu, M., Atomically Precise Noble Metal Nanoclusters as Efficient Catalysts: A Bridge between Structure and Properties. *Chem. Rev.* **2020,** *120* (2), 526-622.

184. Gao, C.; Lyu, F.; Yin, Y., Encapsulated Metal Nanoparticles for Catalysis. *Chem. Rev.* **2021,** *121* (2), 834-881.

185. Heuer-Jungemann, A.; Feliu, N.; Bakaimi, I.; Hamaly, M.; Alkilany, A.; Chakraborty, I.; Masood, A.; Casula, M. F.; Kostopoulou, A.; Oh, E.; Susumu, K.; Stewart, M. H.; Medintz, I. L.; Stratakis, E.; Parak, W. J.; Kanaras, A. G., The Role of Ligands in the Chemical Synthesis and Applications of Inorganic Nanoparticles. *Chem. Rev.* **2019,** *119* (8), 4819-4880.

186. Philippot, K.; Chaudret, B., Organometallic approach to the synthesis and surface reactivity of noble metal nanoparticles. *C. R. Chim.* **2003,** *6* (8), 1019-1034.

187. Martínez-Prieto, L. M.; Chaudret, B., Organometallic Ruthenium Nanoparticles: Synthesis, Surface Chemistry, and Insights into Ligand Coordination. *Acc. Chem. Res.* **2018,** *51* (2), 376-384.

188. González-Gálvez, D.; Nolis, P.; Philippot, K.; Chaudret, B.; van Leeuwen, P. W. N. M., Phosphine-Stabilized Ruthenium Nanoparticles: The Effect of the Nature of the Ligand in Catalysis. *ACS Catal.* **2012,** *2* (3), 317-321.

189. Nigra, M. M.; Ha, J.-M.; Katz, A., Identification of site requirements for reduction of 4-nitrophenol using gold nanoparticle catalysts. *Catal. Sci. Technol.* **2013,** *3* (11), 2976-2983.

190. García-Zaragoza, A.; Cerezo-Navarrete, C.; Mollar-Cuni, A.; Oña-Burgos, P.; Mata, J. A.; Corma, A.; Martínez-Prieto, L. M., Tailoring graphene-supported Ru nanoparticles by functionalization with pyrene-tagged N-heterocyclic carbenes. *Catal. Sci. Technol.* **2022**, 12, 1257-1270.

191. Yang, X.; Xu, Q., Encapsulating Metal Nanocatalysts within Porous Organic Hosts. *Trends Chem.* **2020,** *2* (3), 214-226.

192. Yang, X.; Xu, Q., Ru Nanoparticles Confined within a Coordination Cage. *Chem* **2018,** *4* (3), 403-404.

193. Kunz, S., Supported, Ligand-Functionalized Nanoparticles: An Attempt to Rationalize the Application and Potential of Ligands in Heterogeneous Catalysis. *Top. Catal.* **2016,** *59* (19), 1671-1685.

194. Schrader, I.; Neumann, S.; Himstedt, R.; Zana, A.; Warneke, J.; Kunz, S., The effect of particle size and ligand configuration on the asymmetric catalytic properties of proline-functionalized Pt-nanoparticles. *ChemComm* **2015,** *51* (90), 16221-16224.

195. Wang, S.; Wang, Z.; Zha, Z., Metal nanoparticles or metal oxide nanoparticles, an efficient and promising family of novel heterogeneous catalysts in organic synthesis. *Dalton Trans.* **2009,** *43*, 9363-9373.

196. Gutterød, E. S.; Lazzarini, A.; Fjermestad, T.; Kaur, G.; Manzoli, M.; Bordiga, S.; Svelle, S.; Lillerud, K. P.; Skúlason, E.; Øien-Ødegaard, S.; Nova, A.; Olsbye, U., Hydrogenation of CO2 to Methanol by Pt Nanoparticles Encapsulated in UiO-67: Deciphering the Role of the Metal–Organic Framework. *J. Am. Chem. Soc.* **2020,** *142* (2), 999-1009.

197. Liu, Y.; Shen, Y.; Zhang, W.; Weng, J.; Zhao, M.; Zhu, T.; Chi, Y. R.; Yang, Y.; Zhang, H.; Huo, F., Engineering channels of metal–organic frameworks to enhance catalytic selectivity. *ChemComm* **2019,** *55* (78), 11770-11773.

198. Gonzalez, M. I.; Turkiewicz, A. B.; Darago, L. E.; Oktawiec, J.; Bustillo, K.; Grandjean, F.; Long, G. J.; Long, J. R., Confinement of atomically defined metal halide sheets in a metal–organic framework. *Nature* **2020,** *577* (7788), 64-68.

199. Dhakshinamoorthy, A.; Garcia, H., Catalysis by metal nanoparticles embedded on metal–organic frameworks. *Chem. Soc. Rev.* **2012,** *41* (15), 5262-5284.

200. Olaechea, L. M.; Montero de Espinosa, L.; Oveisi, E.; Balog, S.; Sutton, P.; Schrettl, S.; Weder, C., Spatially Resolved Production of Platinum Nanoparticles in Metallosupramolecular Polymers. *J. Am. Chem. Soc.* **2020,** *142* (1), 342-348.

201. Huang, Y.; Lin, Z.; Cao, R., Palladium Nanoparticles Encapsulated in a Metal–Organic Framework as Efficient Heterogeneous Catalysts for Direct C2 Arylation of Indoles. *Eur. J. Chem.* **2011,** *17* (45), 12706-12712.

202. Yang, J.; He, Y.; He, J.; Liu, Y.; Geng, H.; Chen, S.; Lin, L.; Liu, M.; Chen, T.; Jiang, Q.; Weckhuysen, B. M.; Luo, W.; Wu, Z., Enhanced Catalytic Performance through In Situ Encapsulation of Ultrafine Ru Clusters within a High-Aluminum Zeolite. *ACS Catal.* **2022**, 1847-1856.

203. Suzuki, K.; Sato, S.; Fujita, M., Template synthesis of precisely monodisperse silica nanoparticles within self-assembled organometallic spheres. *Nat. Chem.* **2010,** *2* (1), 25-29.

204. Ichijo, T.; Sato, S.; Fujita, M., Size-, Mass-, and Density-Controlled Preparation of TiO2 Nanoparticles in a Spherical Coordination Template. *J. Am. Chem. Soc.* **2013,** *135* (18), 6786-6789.

205. Guo, M.; Jayakumar, S.; Luo, M.; Kong, X.; Li, C.; Li, H.; Chen, J.; Yang, Q., The promotion effect of π-π interactions in Pd NPs catalysed selective hydrogenation. *Nat. Commun.* **2022,** *13* (1), 1770-1778.

206. Li, C.; Ren, X.; Guo, M.; Li, W.; Li, H.; Yang, Q., Highly active ultrafine Pd NPs confined in imine-linked COFs for nitrobenzene hydrogenation. *Catal. Sci. Technol.* **2021,** *11* (11), 3873-3879.

207. McCaffrey, R.; Long, H.; Jin, Y.; Sanders, A.; Park, W.; Zhang, W., Template Synthesis of Gold Nanoparticles with an Organic Molecular Cage. *J. Am. Chem. Soc.* **2014,** *136* (5), 1782-1785.

208. Yang, X.; Sun, J.-K.; Kitta, M.; Pang, H.; Xu, Q., Encapsulating highly catalytically active metal nanoclusters inside porous organic cages. *Nat. Catal.* **2018,** *1* (3), 214-220.

209. Zhang, Y.; Xiong, Y.; Ge, J.; Lin, R.; Chen, C.; Peng, Q.; Wang, D.; Li, Y., Porous organic cage stabilised palladium nanoparticles: efficient heterogeneous catalysts for carbonylation reaction of aryl halides. *ChemComm* **2018,** *54* (22), 2796-2799.

210. Qiu, L.; McCaffrey, R.; Jin, Y.; Gong, Y.; Hu, Y.; Sun, H.; Park, W.; Zhang, W., Cage-templated synthesis of highly stable palladium nanoparticles and their catalytic activities in Suzuki–Miyaura coupling. *Chem. Sci.* **2018,** *9* (3), 676-680.

211. Sun, N.; Wang, C.; Wang, H.; Yang, L.; Jin, P.; Zhang, W.; Jiang, J., Multifunctional Tubular Organic Cage-Supported Ultrafine Palladium Nanoparticles for Sequential Catalysis. *Angew. Chem. Int. Ed.* **2019,** *58* (50), 18011-18016.

212. Jiang, S.; Cox, H. J.; Papaioannou, E. I.; Tang, C.; Liu, H.; Murdoch, B. J.; Gibson, E. K.; Metcalfe, I. S.; Evans, J. S. O.; Beaumont, S. K., Shape-persistent porous organic cage supported palladium nanoparticles as heterogeneous catalytic materials. *Nanoscale* **2019,** *11* (31), 14929-14936.

213. Sharma, V.; De, D.; Saha, R.; Chattaraj, P. K.; Bharadwaj, P. K., Flexibility Induced Encapsulation of Ultrafine Palladium Nanoparticles into Organic Cages for Tsuji–Trost Allylation. *ACS Appl. Mater. Interfaces.* **2020,** *12* (7), 8539-8546.

214. Fang, Y.; Li, J.; Togo, T.; Jin, F.; Xiao, Z.; Liu, L.; Drake, H.; Lian, X.; Zhou, H.-C., Ultra-Small Face-Centered-Cubic Ru Nanoparticles Confined within a Porous Coordination Cage for Dehydrogenation. *Chem* **2018,** *4* (3), 555-563.

Chapter II. Objectives

Supramolecular nanocapsules have become useful tools to host different guests in a selective manner and infer them distinct reactivity due to the confinement effect. Following the coordination-driven self-assembly strategy, this thesis will focus on the synthesis of new and enlarged versions of the already reported biphenyl-macrocycle based tetragonal prismatic nanocapsule by our research group. The objective is to host larger fullerene species such as the C_{60}⊂[[10]CPP adduct, the azafullerene $(C_{59}N)_2$, or higher fullerenes like C_{84}, which properties and reactivity have been scarcely studied upon confinement. In this context, two different nanocapsules will be prepared aiming the self-assembly of two porphyrin units and four Pd(II)- or Cu(II)-based macrocyclic clips. These nanocapsules will be characterized by NMR, ESI-MS and XRD, and subsequently explored as supramolecular masks for regioselective functionalization of C_{60}, and as hosts for higher fullerenes.

Development of a new structure: the Matryoshka-like three-shell system (Chapter V.1 and Annex 1)

Several strategies to obtain pure isomers from mixtures of fullerene adducts have been reported. However, few of them rely on selective supramolecular encapsulation.

A newly designed tetragonal prismatic nanocapsule, **6**·$(BArF)_8$, featuring a 1,2-diphenylethyne-macrocycle-based clip, will be used to attempt the encapsulation of the **C_{60}⊂[10]CPP** adduct. The exposure of the tightly associated three-shell adduct, **C_{60}⊂[10]CPP⊂6**·$(BArF)_8$, to Bingel cyclopropanation reaction conditions, might restrict the exposed surface of the fullerene, aiming at avoiding the over-functionalization and affording a unique isomer species.

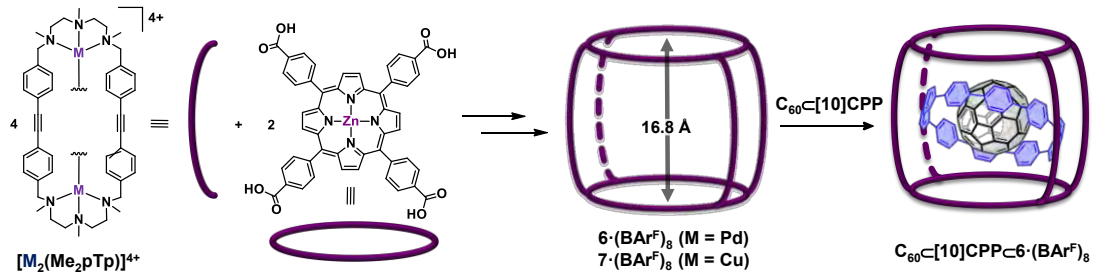

Purification of higher fullerenes and design of an enlarged nanocapsule (Chapter III and Chapter V.2)

Higher fullerenes are produced in very tiny quantities using the known arc-discharge methodology. Besides C_{60} and C_{70}, the third more abundant fullerene in a fullerene soot is C_{84}, albeit below 0.7%. For this reason, finding a strategy to purify higher fullerenes is highly desirable. The second objective of this thesis is to use of the nanocapsule already reported

in the previous chapter to study the ability to host higher fullerenes. On the other hand, a larger terphenyl-macrocycle based nanocapsule will be designed to study the host-guest chemistry with large fullerenes of variable sizes and shapes, including azafullerene $(C_{59}N)_2$.

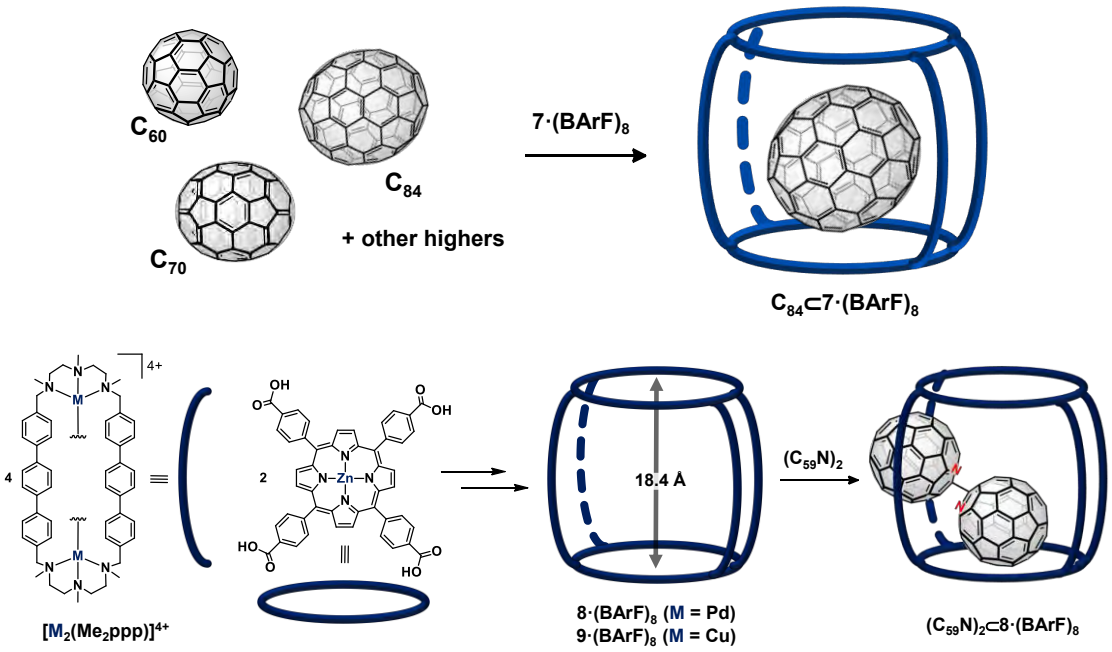

Synthesis of Ru nanoparticles applying a nanocapsule as a template (Chapter IV and Chapter V.3)

Some reports have been postulated the formation of NPs within cages, even though their size is too big to be hosted inside the cavity of the cage. The third objective of the thesis will be the use of the largest tetragonal prismatic nanocapsules reported in the previous chapter to target the formation of small Ru NPs *via* mild decomposition of the precursor Ru(cyclooctadiene)(cyclooctatriene). The Ru NPs will be characterized by TEM and ESI-MS. The catalytic performance of the Ru NPs obtained will be tested in the alkene hydrogenations.

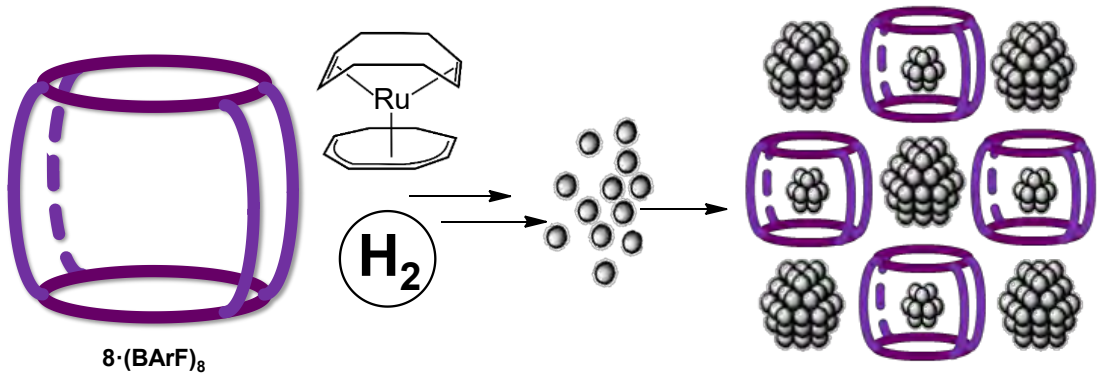

Chapter III.

Straightforward supramolecular purification of C_{84} from a fullerene extract

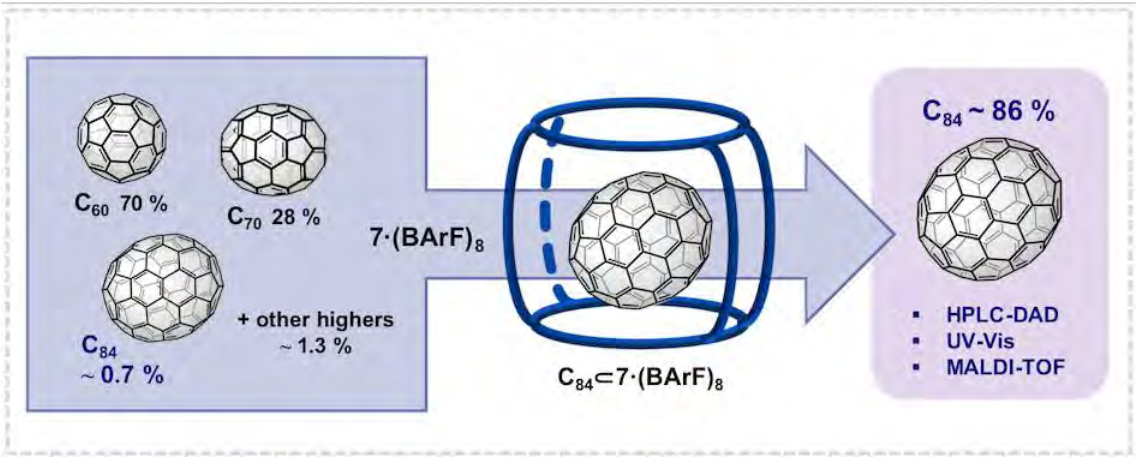

This chapter corresponds to the following publication:

E. Ubasart, C. García-Simón, M. Pujals, K. Asad, N. Chronakis, T. Parella, X. Ribas*

Org. Chem. Front. **2021**, *8*, *15*, 4101-4105. DOI: 10.1039/D1QO00597A

For this publication E.U. performed all the experimental data: synthesis of the clips, metalation of TCPP, synthesis of the nanocapsules and characterization of products. E.U. performed all the encapsulation and purification of fullerene soot, and all the UV-Vis titration experiments. Besides, E.U. contributed in writing the manuscript and was involved in argumentations and discussions.

Reprinted with permission from:

E. Ubasart, C. García-Simón, M. Pujals, K. Asad, N. Chronakis, T. Parella, X. Ribas*. "Straightforward supramolecular purification of C_{84} from a fullerene extract"

Organic Chemistry Frontiers **2021**, *8*, *15*, 4101-4105.

DOI: 10.1039/D1QO00597A

ORGANIC CHEMISTRY FRONTIERS

RESEARCH ARTICLE

Cite this: *Org. Chem. Front.*, 2021, **8**, 4101

Straightforward supramolecular purification of C_{84} from a fullerene extract†

Ernest Ubasart, [a] Cristina García-Simón, [a] Míriam Pujals, [a] Karam Asad, [b] Nikos Chronakis, [b] Teodor Parella [c] and Xavi Ribas *[a]

Received 20th April 2021,
Accepted 27th May 2021

DOI: 10.1039/d1qo00597a

rsc.li/frontiers-organic

Selective purification of fullerene mixtures *via* supramolecular encapsulation is an appealing strategy to circumvent the tedious HPLC chromatographic purification protocols. In this work, we utilize tetragonal prismatic nanocapsules of different cavity sizes and shapes to selectively encapsulate C_{84} from a mixture containing fullerenes ranging from C_{60} to C_{96} (fullerene extract), allowing the enrichment of the C_{84} content from 0.7% to 86%. Moreover, terphenyl-based extra-large nanocapsules were prepared for the first time that can strongly bind the dumbbell-shaped azafullerene dimer $(C_{59}N)_2$ as a guest. Competition experiments between $(C_{59}N)_2$ and C_{84} allowed the deduction of $K_a > 1.0 \times 10^7$ M^{-1} for C_{84} in nanocapsule **6**·$(BArF)_8$. The preference of nanocapsule **7**·$(BArF)_8$ to bind C_{84}-D_2(22) among all IPR-isomers is also discussed.

Introduction

Higher fullerenes are stable compounds that are produced in very tiny quantities using the known arc-discharge methodology.[1] Besides the available C_{60} and C_{70}, the third more abundant fullerene found in soot is C_{84}, although its content is below 0.7%.[2] Moreover, the isolation of C_{84} is very challenging mainly due to the tedious HPLC purification required.[3,4] In addition, it has 24 possible IPR-isomers, the C_{84}-D_2(22) and C_{84}-D_{2d}(23) isomers being the most abundant (as empty fullerenes in a 2 : 1 ratio), which further handicaps the availability of pure samples.[5–8] Recently, even higher fullerenes such as C_{90}-D_{5h}(1) and C_{100}-D_{5d}(1), featuring a tubular shape and named fullertubes, were isolated and crystallized from a soot extract by Stevenson following combined aminopropanol selective discrimination and intensive HPLC purification.[9]

As a consequence, finding a straightforward methodology for the purification of higher fullerenes is highly appealing, since it would bring the opportunity to extensively investigate the mostly unknown electronic properties and reactivity of higher fullerenes.[10] In this sense, supramolecular nanocages capable of encapsulating large guests such as fullerenes have been explored, mainly focusing on the most readily available fullerenes C_{60} and C_{70}.[11,12] Modest attempts to encapsulate higher fullerenes were described by Nitschke in 2011 and Ribas in 2014.[13,14] In the former, a self-assembled cubic cage bearing six Ni-porphyrin units trapped a mixture of higher fullerenes (C_{70}, C_{76}, C_{78}, C_{82} and C_{84}) from a fullerene extract in a non-selective manner.[13] On the other hand, our group designed and synthesized a tetragonal prismatic nanocapsule capable of encapsulating fullerenes ranging from C_{60} to C_{84} by squeezing the guests through the gates of the capsule (Fig. 1a).[14,15]

Supramolecular purification requires the facile release of guests and this has been achieved in a few selected cases, *i.e.* for C_{60},[14] C_{78}- and C_{80}-based uranium endohedral metallofullerenes (EMFs) (Fig. 1b),[16,17] and C_{84} utilizing cyclotriveratrylene-based capsules.[18]

Despite the difficulty in disposing of milligram-scale amounts of C_{84}, an additional drawback is its occurrence as an IPR isomeric mixture (mainly D_2 and D_{2d}). The different reactivity of the double bonds depending on each isomer has been used as a successful strategy to crystallize the $(\eta^2\text{-}C_{84})Ir(CO)Cl(PPh_3)_2$ complex corresponding to the D_{2d} isomer.[19] Also, the kinetic resolution of the chiral D_2 isomer was reported *via* asymmetric osmylation triggering a Stone–Wales transformation.[20] Later in 1998, Shinohara reported the tedious multiple-step HPLC purification of D_2(22) and D_{2d}(23).[3] On the other hand, Echegoyen used a Bingel-retro-Bingel strategy to isolate the two enantiomers of C_{84}-D_2 and also C_{84}-D_{2d} as a pure isomer.[21]

In this work, we envisioned that modular tetragonal prismatic nanocapsules with larger cavities could be designed to selectively host C_{84} and higher fullerenes. Based on (a) the

[a]*QBIS-CAT group, Institut de Química Computacional i Catàlisi (IQCC) and Departament de Química, Universitat de Girona, Girona E-17003, Catalonia, Spain. E-mail: xavi.ribas@udg.edu*

[b]*Department of Chemistry, University of Cyprus, University str. 1, Building No. 13, 2109 Aglantzia, Nicosia, Cyprus*

[c]*Servei de RMN and Departament de Química, Facultat de Ciències, Universitat Autònoma de Barcelona (UAB), Campus UAB, 08193 Bellaterra, Catalonia, Spain*

†Electronic supplementary information (ESI) available. See DOI: 10.1039/d1qo00597a

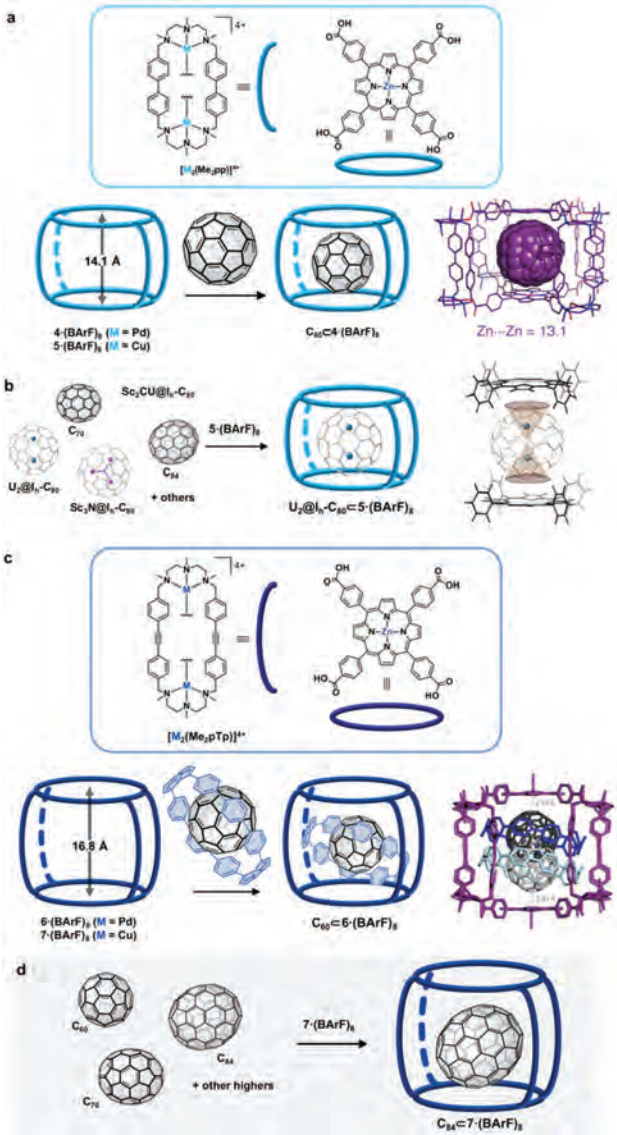

Fig. 1 Supramolecular encapsulation of fullerenes and EMFs for (a) the purification of C_{60}[14] and (b) the purification of U-based C_{80}-EMFs.[16] (c) Three-shell matryoshka-like assembly featuring encapsulated C_{60}⊂[10]CPP.[22] (d) Selective encapsulation of C_{84} in nanocapsule **7**·$(BArF)_8$ (this work).

poor affinity of C_{84} previously observed for the biphenyl-macrocycle-based nanocapsule and (b) the affinity of the large guest C_{60}⊂[10]CPP for a 1,2-diphenylethyne-macrocycle-based nanocapsule (Fig. 1c),[22] we reasoned that the latter could serve as an ideal host for C_{84}. Moreover, a larger terphenyl-macrocycle-based nanocapsule is reported for the first time and the host–guest chemistry with fullerenes of variable sizes and shapes is explored.

Results and discussion

Pd-Based nanocapsule **6**·$(BArF)_8$ and Cu-based nanocapsule **7**·$(BArF)_8$ were prepared following the literature procedures (Fig. 1c).[22] These nanocapsules, featuring a cavity height of 16.8 Å, were dissolved in toluene : CH_3CN (9 : 1) and exposed to 100 eq. of fullerene extract (70% C_{60}, 28% C_{70} and 2% higher fullerenes – from C_{76} to C_{96}, of which C_{84} was the most abundant and accounts for 0.7%) at room temperature (Fig. 2a). It was rapidly observed by HRMS monitoring that the nanocapsules remained empty after short periods of time and therefore, longer periods of time were tested. Despite the low content of higher fullerenes in the extract, after 7 days, selective encapsulation of C_{84} occurred and C_{84}⊂**7**·$(BArF)_8$ was detected as the major thermodynamic product by HRMS (Fig. 2b and 3), indicating very good size and shape complementarity between the capsule and C_{84}.

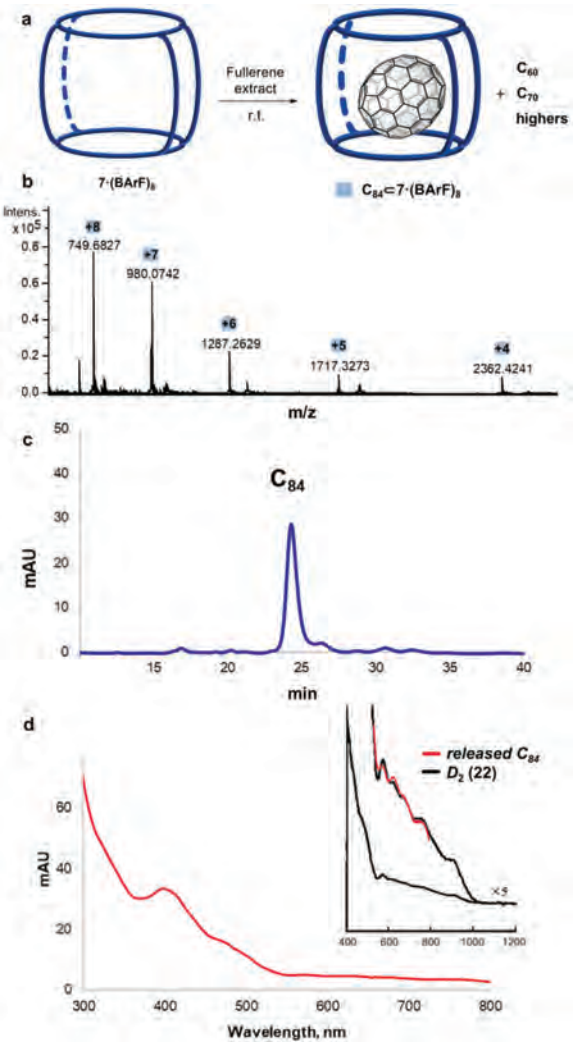

Fig. 2 (a) Schematic representation of the selective encapsulation of C_{84} in nanocapsule **7**·$(BArF)_8$ from a fullerene extract. (b) HRMS (ESI^+) monitoring for **7**·$(BArF)_8$ upon the addition of 100 eq. of fullerene extract and stirring at room temperature for 7 days in toluene. (c) HPLC-DAD chromatogram recorded after the disassembly of the nanocapsule. (d) UV-vis spectra of the peak at 24.3 min corresponding to the C_{84} fullerene [inset showing the amplification of the 500–800 nm range and matching with the reported spectrum for isomer D_2 (22)].

Indeed, upon removal of the solvent, redissolution in CH_3CN and treatment with acid (HOTf) to disassemble the nanocapsule, the guests were released and the fullerene C_{84} was predominantly detected by HPLC (Buckyprep M column, toluene eluent, Fig. 2c) and characterized by UV-vis spectroscopy (Fig. 2d) and by MALDI mass spectrometry (m/z = 1008.24, Fig. S16†). However, with a careful examination of the HRMS spectra (Fig. 3a), weak m/z ions corresponding to the C_{70}⊂**7**·$(BArF)_8$ complex were also observed, indicating that the nanocapsule encapsulated small quantities of the abundant C_{70} (28%). Moreover, other weak m/z ions were present, attributed to other encapsulated higher fullerenes (C_{76}, C_{78}, C_{82}, C_{86}, C_{88}, C_{90}, C_{92}, C_{94} and C_{96}), despite their very low content.

To this end, we reasoned that encapsulation might be even more selective by performing a solid/liquid experiment with the nanocapsule suspended as a solid in a toluene solution of the fullerene extract. This strategy was previously successfully applied in the purification of U-based EMFs owing to the restricted flexibility of the nanocapsule.[15–17] Upon suspending **7**·$(BArF)_8$ in a toluene solution of 100 eq. of fullerene extract, at room temperature for 12 hours, no improvement of the selectivity was observed (Fig. 3b). However, on extending the time to 7 days, the C_{70} and C_{76} m/z ions disappeared, all m/z ions of higher fullerenes were diminished, and the one corresponding to C_{84} was enhanced (Fig. 3c). The comparison was performed considering the relative intensity of the m/z peaks with respect to the C_{84} m/z ion peak in the HRMS spectra. The peak intensity corresponding to C_{78} was decreased from 6.4% to 1.7%, that for C_{82} decreased from 10.7% to 3.4%, that for C_{86} decreased from 14.3% to 13.3%, that for C_{88} decreased from 4.8% to 3.3%, that for C_{90} decreased from 10.7% to 5.0%, that for C_{92} decreased from 6.2% to 3.3% and finally, the m/z peak intensities for C_{94} and C_{96} were both decreased from 3.5 to 3.3%. The latter revealed that C_{84} was the most thermodynamically favored guest among all fullerenes present in the extract. The quantification of the C_{84} enrichment was performed by first disassembling the capsule upon acid treatment, followed by HPLC analysis. Integration of the peaks in the HPLC chromatogram indicated a ~125-fold enrichment of C_{84} (from 0.7% in the initial soot to 86% in the encapsulated mixture). By selective collection of the peak corresponding to C_{84}, 2.2 mg of pure C_{84} were isolated and ^{13}C NMR spectroscopic characterization was attempted to decipher whether the nanocapsule was able to select among different C_{84} isomers. Despite recording the spectrum on a 500 MHz NMR system (equipped with a cryoprobe) for 3 days (1.6×10^5 scans, CS_2 : acetone-d^6, 40 mM $Cr(acac)_3$ as the relaxing agent and d1 = 2s),[4] weak peaks were detected probably due to the low concentration of C_{84} (Fig. S17 and S18†). However, careful inspection of the UV-vis spectrum of C_{84} liberated from the nanocapsule (HPLC-DAD) pointed towards the accumulation of C_{84}-D_2(22) (Fig. 2d) which is one of the main isomers of C_{84} present in the fullerene extract. The latter might indicate a slight preference of nanocapsule **7**·$(BArF)_8$ to bind C_{84}-D_2(22) among all IPR-isomers contained in the starting fullerene extract (see Fig. 2d and S15†).

In an effort to improve the selective binding of higher fullerenes, we designed a nanocapsule with a larger cavity, by introducing a terphenyl-macrocycle-based clip with a calculated cavity height of 18.4 Å (Fig. 4a). The Pd-based **8**·$(BArF)_8$ and Cu-based **9**·$(BArF)_8$ nanocapsules were synthesized following an analogous procedure. The encapsulation of fullerenes

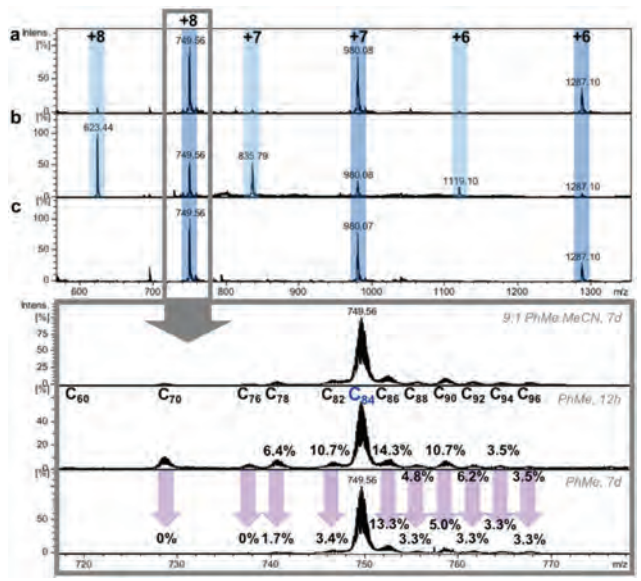

Fig. 3 Study of the binding affinity in solution/solid phase. HRMS (ESI+) monitoring for encapsulation of the C_{84} fullerene. (a) **7**·$(BArF)_8$ in solution (toluene : CH_3CN = 9 : 1), 100 eq. of fullerene extract, r.t., 7 days (liquid/liquid). (b) **7**·$(BArF)_8$ in the solid state (suspension in toluene), 100 eq. of fullerene extract, r.t., 12 hours. (c) **7**·$(BArF)_8$ in the solid state (suspension in toluene), 100 eq. of fullerene extract, r.t., 7 days.

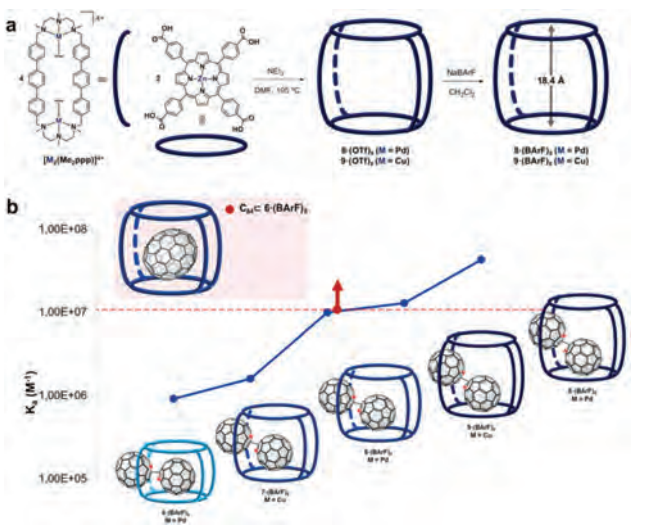

Fig. 4 (a) Synthesis of terphenyl-based tetragonal prismatic nanocapsules **8**·$(BArF)_8$ (Pd-based) and **9**·$(BArF)_8$ (Cu-based). (b) Comparative association constants (K_a) of $(C_{59}N)_2$ with different sized nanocapsules and estimation of the K_a value for C_{84}⊂**6**·$(BArF)_8$ (see Fig. 5).

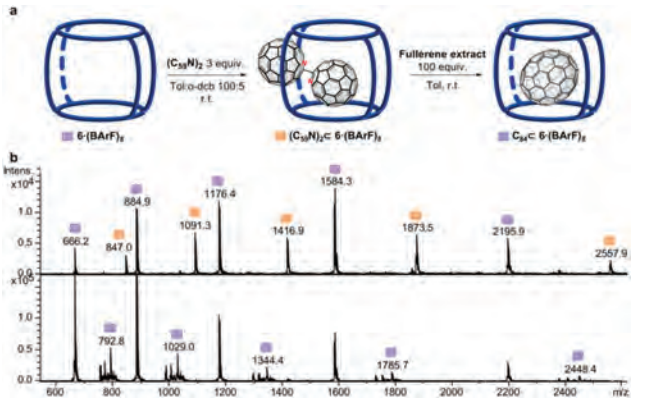

Fig. 5 (a) Competitive host–guest binding studies of the azafullerene dimer $(C_{59}N)_2$ and the fullerene extract with nanocapsule **6**·$(BArF)_8$. (b) HRMS spectra of $(C_{59}N)_2$⊂**6**·$(BArF)_8$ and HRMS spectra upon exposure to the fullerene extract showing complete replacement of $(C_{59}N)_2$ to form C_{84}⊂**6**·$(BArF)_8$.

present in the extract was not successful and HRMS spectrometric investigation of the reaction mixture revealed the major *m*/*z* ions corresponding to empty nanocapsules. This clearly indicated that the cavities of **8** and **9** were too large to stabilize any of the higher fullerenes present in the extract.

With this in mind, we reasoned that the dumbbell-shaped azafullerene dimer $(C_{59}N)_2$ might show an enhanced affinity for nanocapsules **8** and **9** due to its large size. The association constant of the $(C_{59}N)_2$ guest in the **8**·$(BArF)_8$ host was calculated by UV-vis titration, with K_a = 4.3 (±1.0) × 10^7 M^{-1}. This value is comparable to the association constant measured for the encapsulation of C_{60} in the Pd-based biphenyl nanocapsule, reported in 2014.[14] A similar value was calculated for the Cu-analogue **9**·$(BArF)_8$ (K_a = 1.3 (±0.6) × 10^7 M^{-1}). As expected, the association constant decreased upon shrinking the cavity size, leading to K_a = 1.0 (±1.1) × 10^7 M^{-1} for **6**·$(BArF)_8$, 1.6 (±0.1) × 10^6 M^{-1} for **7**·$(BArF)_8$ and 9.4 (±0.5) × 10^5 M^{-1} for the smaller biphenyl-based nanocapsule **4**·$(BArF)_8$,[15] featuring a cavity height of 14.1 Å (see Fig. 4b).

Since the insolubility of pure C_{84} precluded the calculation of the association constant with **6**·$(BArF)_8$, we circumvented this problem by performing a competition experiment exposing $(C_{59}N)_2$⊂**6**·$(BArF)_8$ to the fullerene extract in toluene solvent. After 4 days, a full exchange of the encapsulated azafullerene dimer by fullerene C_{84} was observed by HRMS (Fig. 5), thus indicating a K_a value higher than 1.0 × 10^7 M^{-1} for C_{84}⊂**6**·$(BArF)_8$ (Fig. 4b).

Conclusions

In summary, we have successfully developed an efficient, one-step protocol for the enrichment of C_{84} (up to 86%) directly from a fullerene extract, utilizing nanocapsule **7**·$(BArF)_8$ which features a large cavity (16.8 Å height). Enlargement of the cavity height to 18.4 Å was accomplished by employing a terphenyl-based molecular clip for the construction of nanocapsules **8**·$(BArF)_8$ and **9**·$(BArF)_8$. However, in this case, the cavity was proven to be too large to host even the higher fullerenes (>C_{90}). In contrast, the extra-large terphenyl-based nanocapsules were perfectly sized to host the dumbbell-shaped azafullerene dimer $(C_{59}N)_2$.[15] Comparison of the association constants of $(C_{59}N)_2$ with nanocapsules **4**, **6**, **7**, **8** and **9**, differing in their size, together with the results derived from a competition experiment between $(C_{59}N)_2$ and the fullerene extract, allowed us to conclude that the association constant of C_{84} with nanocapsule **6** must be greater than 1.0 × 10^7 M^{-1}. Moreover, nanocapsule **7**·$(BArF)_8$ shows a slight preference to bind C_{84}-D_2(22) among all IPR-isomers contained in the starting fullerene extract. This study shows that supramolecular design is a key tool for the selective encapsulation of fullerenes featuring different sizes and that fine-tuning of these tetragonal prismatic nanocapsules is a successful strategy to improve the selectivity for a targeted fullerene. In future work, further efforts will be guided towards fine-tuning the capsule architecture in order to be able to more precisely separate the different isomers of C_{84} following our well-established purification strategy.

Conflicts of interest

There are no conflicts to declare.

Acknowledgements

This work was supported by grants from MINECO-Spain (CTQ2016-77989-P, PID2019-104498GB-I00 and EQC2018-004422-P) and Generalitat de Catalunya (2017SGR264) to X. R. N. C. thanks the Research Committee of the University of Cyprus for financial support (Project code: 8037P-24037). X. R. also thanks ICREA-Acadèmia awards. E. U. thanks UdG for a PhD grant. We thank Dr Carles Fuertes for fruitful discussions and STR-UdG for technical support.

References

1 F. Diederich, R. Ettl, Y. Rubin, R. L. Whetten, R. Beck, M. Alvarez, S. Anz, D. Sensharma, F. Wudl, K. C. Khemani and A. Koch, The Higher Fullerenes: Isolation and Characterization of C76, C84, C90, C94, and C70O, an Oxide of D5h-C70, *Science*, 1991, **252**, 548–551.

2 F. Diederich and R. L. Whetten, Beyond C60: the higher fullerenes, *Acc. Chem. Res.*, 1992, **25**, 119–126.

3 T. John, S. Dennis and H. Shinohara, Isolation and characterisation of the two major isomers of [84]fullerene (C84), *Chem. Commun.*, 1998, **1998**, 619–620.

4 T. J. S. Dennis, T. Kai, K. Asato, T. Tomiyama, H. Shinohara, T. Yoshida, Y. Kobayashi, H. Ishiwatari, Y. Miyake, K. Kikuchi and Y. Achiba, Isolation and

Characterization by ^{13}C NMR Spectroscopy of [84]Fullerene Minor Isomers, *J. Phys. Chem. A*, 1999, **103**, 8747–8752.

5 S. L. Waite, B. Chan, A. Karton and A. J. Page, Accurate Thermochemical and Kinetic Stabilities of C84 Isomers, *J. Phys. Chem. A*, 2018, **122**, 4768–4777.

6 A. R. Khamatgalimov and V. I. Kovalenko, 24 IPR isomers of fullerene C84: Cage deformation as geometrical characteristic of local strains, *Int. J. Quantum Chem.*, 2012, **112**, 1055–1065.

7 D. E. Manolopoulos, P. W. Fowler, R. Taylor, H. W. Kroto and D. R. M. Walton, Faraday communications. An end to the search for the ground state of C84?, *J. Chem. Soc., Faraday Trans.*, 1992, **88**, 3117–3118.

8 Y. Achiba, K. Kikuchi, Y. Aihara, T. Wakabayashi, Y. Miyake and M. Kainosho, Higher Fullerenes: Structure and Properties, *MRS Online Proc. Libr.*, 1994, **359**, 3–9.

9 R. M. Koenig, H.-R. Tian, T. L. Seeler, K. R. Tepper, H. M. Franklin, Z.-C. Chen, S.-Y. Xie and S. Stevenson, Fullertubes: Cylindrical Carbon with Half-Fullerene End-Caps and Tubular Graphene Belts, Their Chemical Enrichment, Crystallography of Pristine C90-D5 h(1) and C100-D5d(1) Fullertubes, and Isolation of C108, C120, C132, and C156 Cages of Unknown Structures, *J. Am. Chem. Soc.*, 2020, **142**, 15614–15623.

10 T. D. Anthopoulos, F. B. Kooistra, H. J. Wondergem, D. Kronholm, J. C. Hummelen and D. M. de Leeuw, Air-Stable n-Channel Organic Transistors Based on a Soluble C84 Fullerene Derivative, *Adv. Mater.*, 2006, **18**, 1679–1684.

11 C. García-Simón, M. Costas and X. Ribas, Metallosupramolecular receptors for fullerene binding and release, *Chem. Soc. Rev.*, 2016, **45**, 40–62.

12 C. Fuertes-Espinosa, M. Pujals and X. Ribas, Supramolecular Purification and Regioselective Functionalization of Fullerenes and Endohedral Metallofullerenes, *Chem*, 2020, **6**, 3219–3262.

13 W. Meng, B. Breiner, K. Rissanen, J. D. Thoburn, J. K. Clegg and J. R. Nitschke, A Self-Assembled M8L6 Cubic Cage that Selectively Encapsulates Large Aromatic Guests, *Angew. Chem., Int. Ed.*, 2011, **50**, 3479–3483.

14 C. García-Simón, M. Garcia-Borràs, L. Gómez, T. Parella, S. Osuna, J. Juanhuix, I. Imaz, D. Maspoch, M. Costas and X. Ribas, Sponge-like molecular cage for purification of fullerenes, *Nat. Commun.*, 2014, **5**, 5557.

15 C. García-Simón, C. Colomban, Y. A. Çetin, A. Gimeno, M. Pujals, E. Ubasart, C. Fuertes-Espinosa, K. Asad, N. Chronakis, M. Costas, J. Jiménez-Barbero, F. Feixas and X. Ribas, Complete Dynamic Reconstruction of C60, C70, and (C59N)2 Encapsulation into an Adaptable Supramolecular Nanocapsule, *J. Am. Chem. Soc.*, 2020, **142**, 16051–16063.

16 C. Fuertes-Espinosa, A. Gómez-Torres, R. Morales-Martínez, A. Rodríguez-Fortea, C. García-Simón, F. Gándara, I. Imaz, J. Juanhuix, D. Maspoch, J. M. Poblet, L. Echegoyen and X. Ribas, Purification of Uranium-based Endohedral Metallofullerenes (EMFs) by Selective Supramolecular Encapsulation and Release, *Angew. Chem., Int. Ed.*, 2018, **57**, 11294–11299.

17 C. Fuertes-Espinosa, J. Murillo, M. E. Soto, M. R. Ceron, R. Morales-Martínez, A. Rodríguez-Fortea, J. M. Poblet, L. Echegoyen and X. Ribas, Highly selective encapsulation and purification of U-based C78-EMFs within a supramolecular nanocapsule, *Nanoscale*, 2019, **11**, 23035–23041.

18 E. Huerta, E. Cequier and J. d. Mendoza, Preferential separation of fullerene[84] from fullerene mixtures by encapsulation, *Chem. Commun.*, 2007, **2007**, 5016–5018.

19 A. L. Balch, A. S. Ginwalla, J. W. Lee, B. C. Noll and M. M. Olmstead, Partial Separation and Structural Characterization of C84 Isomers by Crystallization of (. eta.2-C84)Ir(CO)Cl(P(C6H5)3)2, *J. Am. Chem. Soc.*, 1994, **116**, 2227–2228.

20 J. M. Hawkins, M. Nambu and A. Meyer, Resolution and Configurational Stability of the Chiral Fullerenes C76, C78, and C84: A Limit for the Activation Energy of the Stone-Wales Transformation, *J. Am. Chem. Soc.*, 1994, **116**, 7642–7645.

21 J. Crassous, J. Rivera, N. S. Fender, L. Shu, L. Echegoyen, C. Thilgen, A. Herrmann and F. Diederich, Chemistry of C84: Separation of Three Constitutional Isomers and Optical Resolution of D2-C84 by Using the "Bingel–Retro-Bingel" Strategy, *Angew. Chem., Int. Ed.*, 1999, **38**, 1613–1617.

22 E. Ubasart, O. Borodin, C. Fuertes-Espinosa, Y. Xu, C. García-Simón, L. Gómez, J. Juanhuix, F. Gándara, I. Imaz, D. Maspoch, M. von Delius and X. Ribas, A three-shell supramolecular complex enables the symmetry-mismatched chemo- and regioselective bis-functionalization of C60, *Nat. Chem.*, 2021, **13**, 420–427.

Chapter IV.

Supramolecular nanocapsule as two-fold stabilizer of outer-cavity sub-nanometric Ru NPs and inner-cavity ultra-small Ru clusters

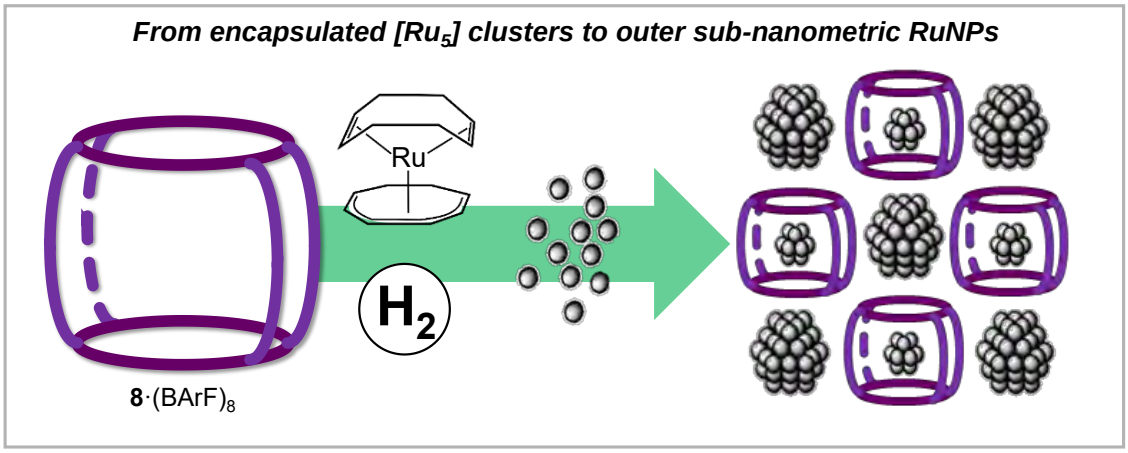

This chapter corresponds to the following publication:

E. Ubasart,‡ I. Mustieles,‡ J. M. Asensio, G. Mencia, Á. M. López-Vinasco, C. García-Simón, I. del Rosal, R. Poteau,* B. Chaudret,* X. Ribas*

Nanoscale Horiz. **2022**, *7*, 607-615. DOI: 10.1039/d1nh00677k

‡both authors contributed equally to this work

For this publication E.U. performed the experimental data: synthesis of the nanocapsules and characterization of products. E.U. performed the NPs synthesis and characterization. I.M. contributed in the additional NPs synthesis and TEM characterization. Besides, E.U. contributed in writing the manuscript and was involved in argumentations and discussions.

Reprinted with permission from:

E. Ubasart,‡ I. Mustieles,‡ J. M. Asensio, G. Mencia, Á. M. López-Vinasco, C. García-Simón, I. del Rosal, R. Poteau,* B. Chaudret,* X. Ribas*. "Supramolecular nanocapsule as two-fold stabilizer of outer-cavity sub-nanometric Ru NPs and inner-cavity ultra-small Ru clusters".

*Nanoscale Horiz*ons **2022**, *7*, 607-615.

DOI: 10.1039/d1nh00677k

Volume 7
Number 6
June 2022
Pages 565–656

Nanoscale Horizons

The home for rapid reports of exceptional significance in nanoscience and nanotechnology

rsc.li/nanoscale-horizons

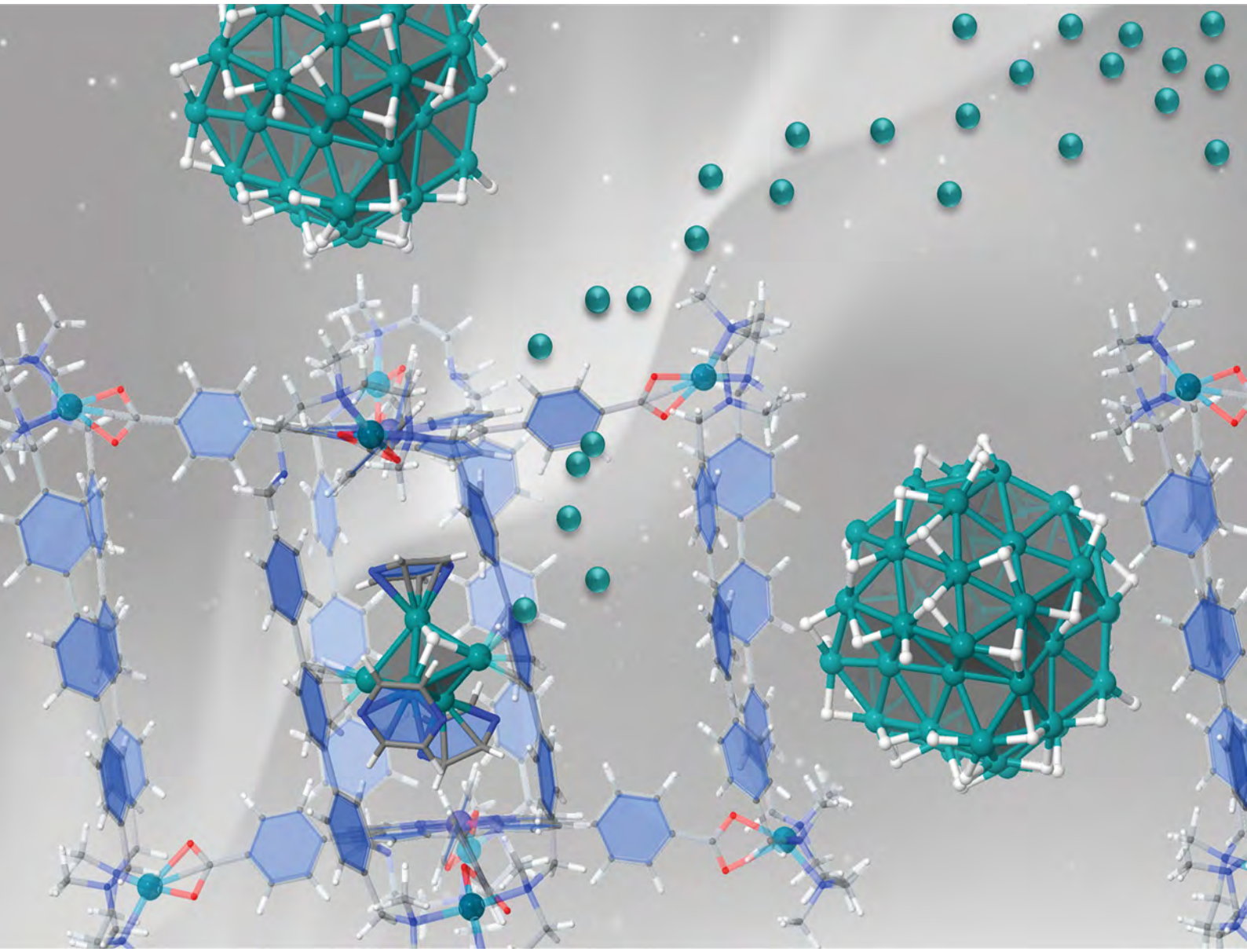

ISSN 2055-6756

ROYAL SOCIETY OF CHEMISTRY

COMMUNICATION

Romuald Poteau, Bruno Chaudret, Xavi Ribas *et al.*
Supramolecular nanocapsules as two-fold stabilizers of outer-cavity sub-nanometric Ru NPs and inner-cavity ultra-small Ru clusters

NCNST

Nanoscale Horizons

ROYAL SOCIETY OF CHEMISTRY

COMMUNICATION

Cite this: *Nanoscale Horiz.*, 2022, 7, 607

Received 26th December 2021,
Accepted 1st April 2022

DOI: 10.1039/d1nh00677k

rsc.li/nanoscale-horizons

Supramolecular nanocapsules as two-fold stabilizers of outer-cavity sub-nanometric Ru NPs and inner-cavity ultra-small Ru clusters†

Ernest Ubasart, ‡[a] Irene Mustieles Marin, ‡[b] Juan Manuel Asensio, [b] Gabriel Mencia, [b] Ángela M. López-Vinasco, [b] Cristina García-Simón, [a] Iker del Rosal, [b] Romuald Poteau, *[b] Bruno Chaudret *[b] and Xavi Ribas *[a]

The synthesis of metallic nanoparticles (MNP) with high surface area and controlled shape is of paramount importance to increase their catalytic performance. The detailed growing process of NP is mostly unknown and understanding the specific steps would pave the way for a rational synthesis of the desired MNP. Here we take advantage of the stabilization properties exerted by the tetragonal prismatic supramolecular nanocapsule 8·(BArF)$_8$ to develop a synthetic methodology for sub-nanometric RuNP (0.6–0.7 nm). The catalytic properties of these sub-nanometric nanoparticles were tested on the hydrogenation of styrene, obtaining excellent selectivity for the hydrogenation of the alkene moiety. In addition, the encapsulation of [Ru$_5$] clusters inside the nanocapsule is strikingly observed in most of the experimental conditions, as ascertained by HR-MS. Moreover, a thorough DFT study enlightens the nature of the [Ru$_5$] clusters as tb-Ru$_5$H$_2$(η^6-PhH)$_2$(η^6-pyz)$_3$ (2) trapped by two arene moieties of the clip, or as tb-Ru$_5$H$_2$(η^1-pyz)$_6$(η^6-pyz)$_3$ (3) trapped between the two Zn–porphyrin units of the nanocapsule. Both options fulfill the Wade-Mingos counting rules, *i.e.* 72 CVEs for the *closo* tb. The trapped [Ru$_5$] metallic clusters are proposed to be the first-grown seeds of subsequent formation of the subnanometric RuNP. Moreover, the double role of the nanocapsule in stabilising ~0.7 nm NPs and also in hosting ultra-small Ru clusters, is unprecedented and may pave the way towards the synthesis of ultra-small metallic clusters for catalytic purposes.

New concepts

Designing new methodologies to control the size and shape of metallic nanoparticles is highly desirable. The stabilization of sub-nanometric NP or even metallic clusters will allow the access to ultra-small metallic species very active in catalysis. In order to do that, it is mandatory to gain control on the nucleation of the metallic atoms towards the formation of metallic clusters, which sequentially aggregate in the form of NPs, and there is an evident lack of detailed understanding of the NPs growth process. We introduce here a new supramolecular-controlled methodology for the direct observation of both sub-nanometric Ru NPs and [Ru$_5$] metallic clusters. Our study combines experimental evidences with a thorough computational study for comprehending the formation of the small metallic clusters en-route to sub-nanometric aggregates, thanks to the stabilization effect in the supramolecular cavity, which is constituted by multiple arene rings and porphyrin units. The direct observation of the metallic cluster seeds for the formation of NP sheds light into this fundamental process, where the double role of the nanocapsule in stabilising 0.6–0.7 nm NPs in the outer-cavity and also host ultra-small Ru$_5$ clusters inside the cavity is unprecedented. Moreover, the modularity of the supramolecular hosts and the use of other metal precursors renders a versatile strategy towards the synthesis of ultra-small metallic clusters for catalytic purposes.

Introduction

The control of size and shape of metallic nanoparticles (MNPs) is mandatory to comprehend the implications of these parameters in their catalytic performance. In general terms, the quest for sub-nanometric MNPs in a reproducible form is appealing, owing to the fact that enhanced catalytic activity is expected for MNPs with larger surface/volume ratio, *i.e.* of the smaller size possible.[1,2] In order to stabilize MNPs, organic molecules acting as ligands attached to the surface of the nanoparticles can be employed leading to a large variety of possibilities.[3] In addition, trapping NPs (including Au, Pt, and $NiCl_2$, $PdCl_2$ and $PtCl_2$)[4–6] in the channels of MOFs has been demonstrated to be a successful strategy[7,8] to enhance the selectivity of selected reactions.[2,9] However, the stabilization of ultra-small MNPs is far more challenging. In this regard, some examples of organic or supramolecular cages capable of stabilizing MNPs have been reported, taking advantage of their putative affinity to the hollow cavity of the host. Examples of Pd NPs mainly, but also of Au NPs,[10,11] Ag NPs,[12] ferrihydrite NPs[13] and Ru NPs[14] have been reported. For instance, in 2014,

[a] *Institut de Química Computacional i Catàlisi and Departament de Química, Universitat de Girona, Campus Montilivi, E-17003 Girona, Catalonia, Spain. E-mail: xavi.ribas@udg.edu*

[b] *Laboratoire de Physique et Chimie des Nano-objets (LPCNO), INSA-CNRS, Université de Toulouse, 135 Ave. de Rangueil, 31077 Toulouse, France*

† Electronic supplementary information (ESI) available. CCDC 2127407. For ESI and crystallographic data in CIF or other electronic format see https://doi.org/10.1039/d1nh00677k

‡ Both authors contributed equally to this work.

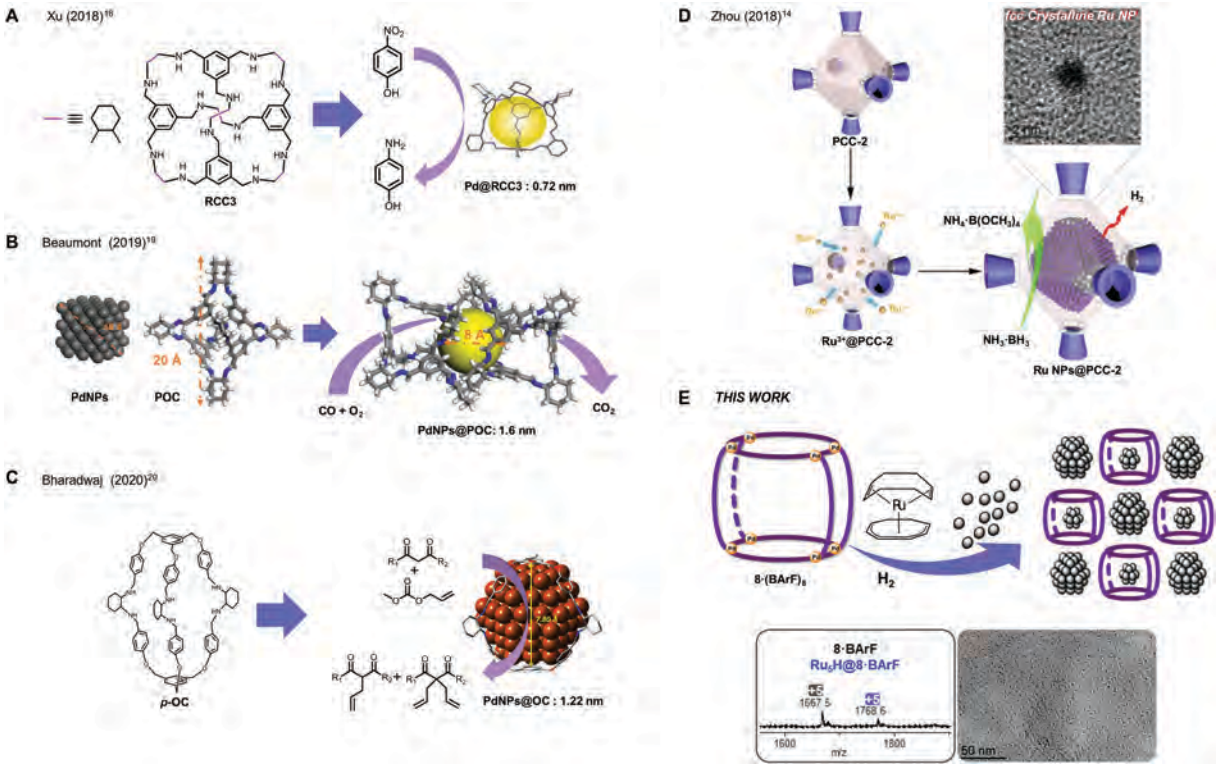

Fig. 1 Pd-NPs encapsulated in porous organic cages for (A) catalytic hydrogenation of nitroarenes, (B) for CO oxidation and (C) for Tsuji–Trost allylation; (D) Ru NPs encapsulated in a porous coordination cage for dehydrogenation; (E) supramolecular nanocapsule **8**·$(BArF)_8$ for stabilization of outer-cavity sub-nanometric Ru NPs and inner-cavity ultra-small Ru clusters (this work).

Zhang and co-workers designed a 3D, shape-persistent organic molecular cage to act as a template for the growth of Au NPs with a small size (1.9 ± 0.4 nm),[15] standing as one of the first examples of Au NPs synthesized in a confined space. However, most of the studies rely on the stabilization of Pd NPs, since their catalytic activity is of paramount interest. In 2018, Xu and co-workers reported a porous organic cage, RCC3, able to encapsulate active Pd NPs (Fig. 1a).[16] The sub-nanometric NPs (0.72 nm) showed high stability and durability and demonstrated to be catalytically active in the hydrogenation of nitroarenes and reduction of organic dyes. On the other hand, Li and co-workers developed a porous organic nanocapsule that was used as an efficient heterogeneous catalyst for the carbonylation of aryl halides.[17] Later, in 2019, Jiang's group developed Pd NPs (1.9 ± 0.4 nm) stabilized by an organic nanocapsule.[18] The authors demonstrated the ability of a water soluble nanocapsule of sensing, controlling nanoparticle growth and developing a catalytic active platform for the hydroxylation of 4-nitrophenylboronic acid to 4-nitrophenol. Also in 2019, Beaumont and co-workers designed a porous organic cage that could incorporate very small Pd NPs (1.6 nm),[19] being an effective system for the CO oxidation (Fig. 1b). More recently, Bharadwaj reported in 2020 a series of three positional isomers of organic cages (*o*-OC, *m*-OC and *p*-OC) capable to stabilize Pd NPs with a 1–2 nm of diameter (Fig. 1c).[20] These NPs showed excellent catalysis of Tsuji–Trost allylation at room temperature.

A sole example of the stabilization of Ru NPs in cages was reported by Zhou in 2018, by taking advantage of the accumulation of Ru^{3+} ions in an anionic porous coordination cage (PCC-2), in which Ru NPs ($\sim$2 nm) were formed upon mild reduction with $NaBH_4$ (Fig. 1d).[14] The resulting Ru NPs@PCC-2 composite exhibited high catalytic activity in methanolysis of ammonia borane, which is relevant in chemical hydrogen storage.

Many of the above mentioned reports have argued or postulated that the NPs form within the cages, but this has been questioned since the 1.3–1.9 nm relative size range is far too big for the small cavity size (diameter < 1 nm), and an inter-pore arrangement among different cages is a more realistic scenario in many cases.[19] The role of the cages is thus unclear and doubts are cast whether they promote external stabilization of NPs or incipient encapsulation of metallic cluster seeds.

On the other hand, we developed supramolecular tetragonal prismatic nanocapsules as hosts for large guests, as for example higher fullerenes and dumbbell-shaped azafullerene $(C_{59}N)_2$.[21,22] In the present work, we targeted the formation of small Ru NPs stabilized by a tetragonal prismatic nanocapsule, *via* mild decomposition of the precursor Ru(cyclooctadiene)(cyclooctatriene). Remarkably, we have succeeded in obtaining sub-nanometric Ru NPs stabilized by nanocapsule **8**·$(BArF)_8$ throughout the outer-cavity surface. The small size is in agreement with the outcome of styrene hydrogenation catalysis. Surprisingly, in addition to acting as outer-surface NP-stabilizer, this nanocapsule can trap ultra-small ruthenium clusters ($[Ru_5]$, $[Ru_{10}]$ and $[Ru_{15}]$) in the

inner-cavity, as unequivocally indicated by HRMS studies. Moreover, the clusters' nature has been revealed by a thorough DFT computational study, focusing on the evaluation of the relative thermodynamic stability of [Ru_5] models. Within the framework of Wade–Mingos rules, possible [Ru_5] clusters coated with hydrides and different ligands have been evaluated, including ligands from the solution or from possible adsorption or growth sites of the nanocapsule. The remarkable occurrence of the [Ru_5] cluster in the mass spectrum is explained both in terms of electronic effects and of cavities' size of the nanocapsule. The two-fold stabilization of sub-nanometric NPs and clusters is reported for the first time (Fig. 1e), and might pave the way towards the selective preparation and stabilization of metallic clusters for catalysis.

Results and discussion

The formation of Ru NPs was studied employing different nanocapsules displaying different cavity sizes. The supramolecular structures **6**·$(BArF)_8$ and **8**·$(BArF)_8$ (see Fig. 2) were synthesized by self-assembly of a Zn-porphyrin with a macrocyclic Pd-based complex that led to different cavity size from 16.8 to 18.4 Å. In Fig. 2 there is a schematic representation of the synthons of the nanocapsules. The synthesis of the nanoparticles was studied by decomposing Ru(COD)(COT) under 1 bar of H_2 at room temperature, which have demonstrated to be successful conditions to synthesize Ru NPs.[23] THF was chosen as solvent since both the nanocapsules and Ru(COD)(COT) complex are soluble. Different parameters such as the addition of an auxiliary ligand (pyrazine), reaction time and number of equivalents of the Ru precursor were studied. In addition, the Ru NP synthesis was also performed in the presence of the different nanocapsule fragments in order to study the influence of the different moieties in the NPs stabilization. The different conditions used are summarized in Table 1. The resulting Ru NPs were analysed by TEM and HR-ESI-MS (see details in the ESI†).

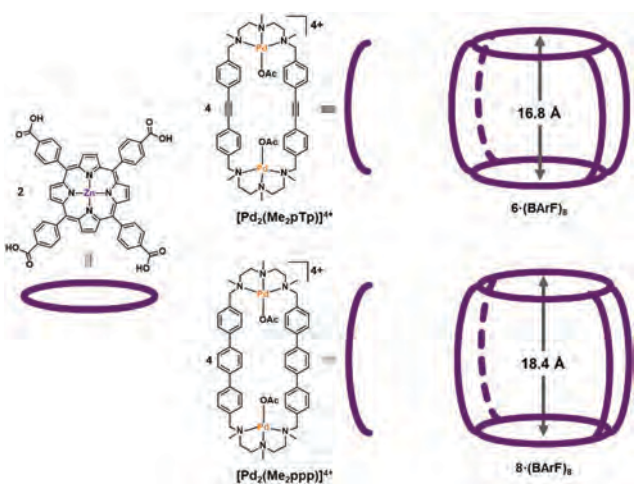

Fig. 2 Tetragonal prismatic nanocapsules **6**·$(BArF)_8$ and **8**·$(BArF)_8$ used in this work, bearing the $[Pd_2(Me_2pTp)]^{4+}$ and $[Pd_2(Me_2ppp)]^{4+}$ clips, respectively.

Table 1 Experiment conditions studied for the Ru NPs formation. All reactions were performed at room temperature and under 1 bar of H_2 in a total volume of 3–3.5 mL of THF. Ru(COD)(COT) was employed as precursor

Exp.	*N*·$(BArF)_8$ *N* = 6 or 8	Ru equiv.	Pyz equiv.	Time (min)	Size Ru NP (nm)
E1	**6**	130	0	10	1.28 ± 0.17
E2	**6**	130	0.2	10	0.68 ± 0.22
E3	**8**	130	0	10	1.33 ± 0.24
E4	**8**	130	0.2	10	0.65 ± 0.15
E5	**8**	40	0.2	10	0.67 ± 0.19
E6	**8**	20	0.2	10	0.74 ± 0.19
E7	**8**	200	0.2	2	0.74 ± 0.18
E8	**8**	130	0.2	2	0.72 ± 0.20
E9	**8**	80	0.2	2	0.69 ± 0.18
E10	**8**	60	0.2	2	0.71 ± 0.20
E11	**8**	40	0.2	2	0.70 ± 0.21
E12	**8**	130	1	2	0.60 ± 0.12
E13	$[Pd_2(Me_2ppp)]$ clip	32	0.2	10	0.96 ± 0.24
E14	ZnTCPP	65	0.2	10	>100

The synthesis of the Ru NPs was first studied in presence of the nanocapsules **6**·$(BArF)_8$ and **8**·$(BArF)_8$ in order to determine the influence of the cavity size (see Table 1, experiments E1 and E3, respectively). For these experiments 130 eq. of Ru precursor respect to the nanocapsule load and, after introduction of H_2, a color change occurred almost immediately. The solution containing both nanocapsules changed from a pink solution to a dull dark solution. TEM images of the final solutions are present in Fig. 3a and c. In both cases amorphous NPs of a mean size of 1.3 nm were obtained (see Fig. S1, S3 and S16, ESI†), indicating that the cavity size had no influence, and furthermore, that the NPs were not encapsulated since the size obtained was bigger to that of the nanocapsules.

To favour the formation of the small NPs an ancillary ligand was added to the reaction mixture. The addition of pyrazine to the solution was intended to help in the stabilization of the Ru nuclei during the decomposition. A small amount, only 0.2 eq.

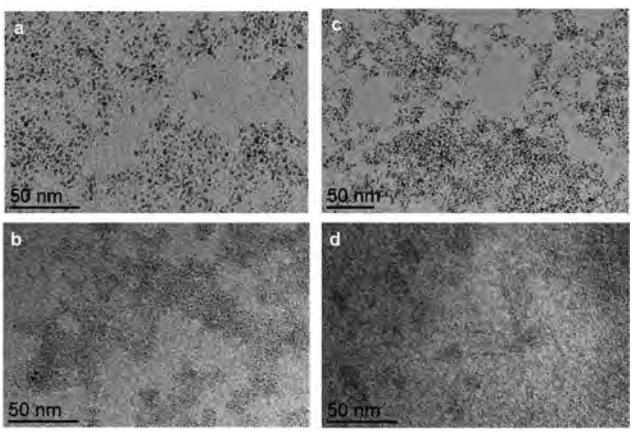

Fig. 3 TEM images of (a) E1, NPs synthesized with the **6**·$(BArF)_8$ nanocapsule, 130 eq. Ru(COD)(COT) and 0 eq. pyrazine; (b) E2 NPs synthesized with **6**·$(BArF)_8$ nanocapsule, 130 eq. Ru(COD)(COT) and 0.2 eq. pyrazine; (c) E3, NPs synthesized with **8**·$(BArF)_8$ nanocapsule, 130 eq. Ru(COD)(COT) and 0 eq. pyrazine; (d) E4, NPs synthesized with **8**·$(BArF)_8$ with 130 eq. Ru(COD)(COT) and 0.2 eq. pyrazine.

with respect to Ru, was employed to avoid the ligand saturation at the formed NPs surface. Thus, experiments E1 and E3 were repeated in presence of pyrazine (E2 and E4). TEM images are present in Fig. 3b and d. The NPs formed possess a mean size of 0.65 nm in the case of E4. Thus, the presence of pyrazine has a relevant role in the stabilization outside the nanocapsule, decreasing the nanoparticle size by half (Table 1). At this point, in order to determine the influence of the Ru concentration in the medium, we lowered the equivalents of Ru(COD)(COT) to 40 and 20 (experiments E5 and E6, respectively), instead of 130 equiv. TEM images showed the formation of NPs with a mean size of 0.67 and 0.74 nm, respectively (see Fig. S14, ESI†).

By keeping this amount of pyrazine (0.2 eq. respect to Ru), the time of reaction was decreased from 10 to 2 min and a larger range of Ru equivalents employed was screened: 200, 130, 80, 60 and 40 equiv., corresponding to experiments E7 to E11. The diminution of the reaction time hadn't an impact in the size distribution of the NPs, which ranged between 0.65 and 0.74 nm, indicating that these sub-nanometric NPs formed at the first stage of the reaction. For instance, Ru NP size obtained for E4 (10 min, 130 eq. Ru) is 0.65 nm, very close to 0.72 nm for E8 (2 min, 130 eq. Ru). Likewise, E5 (10 min, 40 eq. Ru) afforded a mean size of 0.67 nm, also close to 0.74 for E11 (2 min, 40 eq. Ru). Further increasing the pyrazine concentration (1 eq. respect to Ru, E12 in Table 1) led within 2 minutes to the formation of uniform Ru NPs of even smaller size (0.6 ± 0.1 nm).

To obtain more information about the role of the nanocapsule moieties we performed blank experiments using the $[Pd_2(Me_2ppp)]^{4+}$ clip or the ZnTCPP building blocks instead of the whole nanocapsule (see Fig. 2). By using the Pd-clip (experiment E13), sub-nanometric nanoparticles were obtained, while with the Zn-porphyrin (experiment E14) only aggregates were observed, confirming that the clip moiety has a prominent role if the synthesis and stabilization of this sub-nanometric Ru NPs (Fig. 4).

In order to get a more precise value of the size of the NPs formed, HR-TEM analysis was conducted for E4 (Fig. 5), confirming the subnanometric size (diameter of 0.65 nm average) for the nanoparticles, which showed a non-defined shape. The catalytic properties of these sub-nanometric nanoparticles were tested on the hydrogenation of styrene. Different volumes from the solutions E8 to E12 were taken to set a catalytic loading of 0.25 mol% and the reactions were performed under 3 bar of H_2 at 50 °C (see Table S1, ESI†). As shown in Fig. 6, hydrogenation of the double bond occurs with high conversion and excellent selectivity for RuNPs in the range of 0.7 to 1.3 nm (experiments E3, E8–E10 and E13, and in moderate conversion and good selectivity in E11 (Fig. 6)). Catalytic reactions were also performed using the smallest RNPs obtained, *i.e.* 0.6 nm for E12, observing a conversion drop to 16.5% while keeping a 100% selectivity for ethylbenzene. The latter is rationalized by the hampered accessibility to the active surface of the nanoparticle due to the large amount of pyrazine molecules covering the nanoparticle. No hydrogenation of the aromatic ring was observed, which is a clear indication that nanoparticles are small enough, since larger size NPs favour surface interaction with the aromatic ring and full hydrogenation.[23,24]

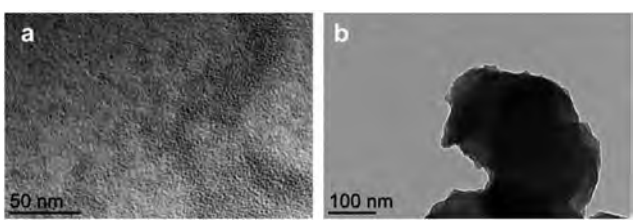

Fig. 4 TEM images of (a) experiment E13, with $[Pd_2(Me_2ppp)]^{4+}$ clip, and (b) experiment E14, with Zn-TCPP.

Fig. 5 STEM and HR-TEM images for experiment E4.

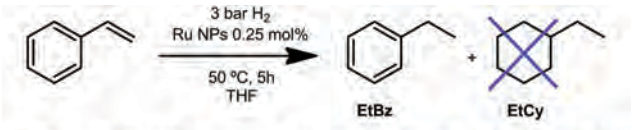

Solution	Conversion (%)	Yield EtBz (%)	Yield EtCy (%)
E3	100	100	n.d.
E8	95	94	n.d.
E9	95	94	n.d.
E10	95	94	n.d.
E11	68	56	n.d.
E12	16.5	100	n.d.
E13*	100	89	n.d.

Fig. 6 Hydrogenation of styrene catalysed by Ru NPs from experiments E8–E12. Conditions: 1 mmol of substrate, 0.25 mol% Ru, 5 h, 50 °C and 5.5 mL of THF. EtBz = ethylbenzene. EtCy = ethylcyclohexane *total volume 3 mL. See more details in the ESI.†

At this point, we analysed the integrity of the nanocapsules at the end of the reaction by HRMS. The peak of the empty nanocapsule was detected at the end of the experiment in most of the cases, which indicates the stability of the cage throughout the reaction conditions. However, other peaks with higher molecular weight representing a 10% of the capsule content (comparing peak intensity) were found in samples E5, E6, E8, E9, E10, E11 and were assigned to $(Ru_5H_2) \subset \mathbf{8}\cdot(BArF)_8$ (Fig. 7 and Fig. S17, ESI†). Nanocapsule recovery was high in most of the samples (40% for E5, 95% for E6, >98% for E8, 76% for E9, 82% for E10 and 40% for E11). Furthermore, peaks corresponding to $(Ru_{10}H_2) \subset \mathbf{8}\cdot(BArF)_8$ and $(Ru_{15}H_2) \subset \mathbf{8}\cdot(BArF)_8$ were also detected in experiment E4 (see Fig. S18, ESI†).

This intriguing result prompted us to investigate theoretically the formation of ultrasmall Ru clusters. Computational studies were performed to gain insight into the putative structure of the ultra-small Ru clusters and the possibility to stabilize these nanoclusters with hydride anions and different ligands. The present

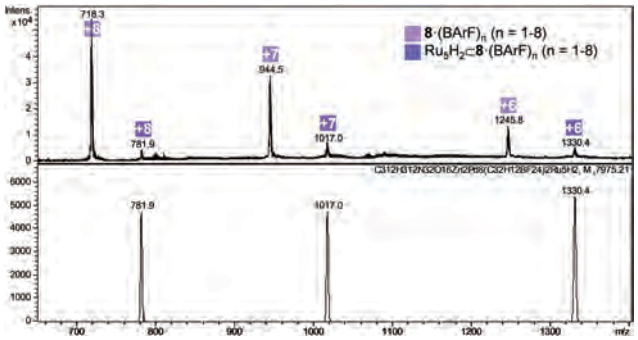

Fig. 7 HRMS analysis of experiment E5 (addition of 40 eq. Ru(COD)(COT) and 0.2 eq. pyrazine in the presence of 2 mg of **8**·$(BArF)_8$). Calculated (bottom) and found (top) *m*/*z* peaks.

observation of stable clusters made of 5, 10 and 15 Ruthenium atoms is reminiscent of magic numbers. Clusters of 3, 4, 5, 6, 9, 10 ruthenium atoms have been found in the past,[25–31] most of them following the Wade–Mingos rules.[32–35] According to the Wade–Mingos polyhedral skeletal electron pair (PSEP) theory, the total cluster valence electron (CVE) number of TM *closo*, *nido* and *arachno* deltahedral clusters is expected to be 14 m + 2, 14 m + 4 and 14 m + 6, respectively. It is both with the electron-counting rules in mind, and by using the *ab initio* thermodynamic methodology, that DFT calculations have been achieved to shed light on the present experimental results. They first aim at evaluating the relative thermodynamic stability of $[Ru_5]$ models coated with hydrides and ligands available either from the solution (pyrazine) or from possible adsorption or growth sites of a nanocapsule.

The most stable geometry of bare $[Ru_5]$ clusters was found to be a square pyramid (**sp**).[36,37] The same result is found in the present study, with the trigonal bipyramid (**tb**) that lies at 26.4 kcal mol^{-1} above **sp**, in good agreement with the results reported in the literature.[36] Given its occurrence in MS experiments, Ru_5H has also been studied. All structures, magnetic moments and relative energies are reported in Fig. S20 and S21 (ESI†). The most stable one is an **sp** with a terminal H. According to the Wade-Mingos rules, $[Ru_5]$ clusters in solution are expected to have 74 CVEs for the *nido* **sp** and 72 CVEs for the *closo* **tb**. The 24 and 22 additional CVEs to the 40 CVEs of the $[Ru_5]$ metal core can be brought by some hydrides, and mainly by the available ligands: either thanks to a π donation from the aromatic rings of the nanocapsule pillars or from the pyrazine solvent molecules, or either through the σ-donating ability of pyrazine. In the latter case, Ru atoms lying at an apex can be coordinated in a trigonal-pyramidal fashion to three η^1-donating pyrazine ligands, that bring 6 CVEs. Some possible $[Ru_5]$ models that fulfill the ideal CVE count are reported in Fig. 8: **sp**-$Ru_5H_4(\eta^6\text{-PhH})_2(\eta^6\text{-pyz})_3$, **1**, **tb**-$Ru_5H_2(\eta^6\text{-PhH})_2(\eta^6\text{-pyz})_3$, **2**, **tb**-$Ru_5H_2(\eta^1\text{-pyz})_6(\eta^6\text{-pyz})_3$, **3**, and **tb**-$Ru_5H_4(\eta^6\text{-PhH})_2(\eta^6\text{-pyz})_2(\eta^4\text{-pyz})$, **4**, where benzene molecules in compounds **1**, **3** and **4** model phenylene groups of the Pd clip. Some energy clues can be obtained from these clusters, completed with all those considered in this work and reported in the ESI:† (i) the 74 CVEs **sp** cluster **1** is slightly more stable than the 72 CVEs **tb** cluster **4** by less than 2 kcal mol^{-1}. Given the energies

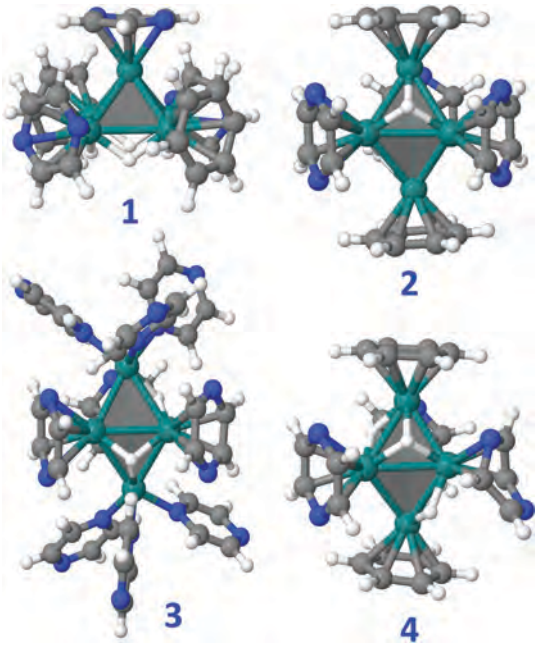

Fig. 8 $[Ru_5]$ clusters stabilized by hydrides, benzene (PhH) and pyrazine (pyz) ligands. (1) **sp**-$Ru_5H_4(\eta^6\text{-PhH})_2(\eta^6\text{-pyz})_3$, (2) **tb**-$Ru_5H_2(\eta^6\text{-PhH})_2(\eta^6\text{-pyz})_3$, (3) **tb**-$Ru_5H_2(\eta^1\text{-pyz})_6(\eta^6\text{-pyz})_3$, and (4) **tb**-$Ru_5H_4(\eta^6\text{-PhH})_2(\eta^6\text{-pyz})_2(\eta^4\text{-pyz})$. They all fulfill the Wade-Mingos counting rules, *i.e.* 74 CVEs for the *nido* **sp** and 72 CVEs for the *closo* **tb**. While **4** has the same composition as **1**, with one η^4-pyrazine it is a 72 CVE cluster, thus having the optimal electron counting number of a closo structure.

of the bare clusters, it means that the **tb** metal core is more strongly stabilized by the surface species than the **sp** core; (ii) the optimization of the 72 CVEs **sp**-$Ru_5H_2(\eta^6\text{-PhH})_2(\eta^6\text{-pyz})_3$ directly converges toward its **tb** counterpart, **2**. Besides, it is shown in the (ESI†) that **sp**-$Ru_5H_2(\eta^6\text{-PhH})_2(\eta^6\text{-pyz})_3$, noted $\mathbf{TS_{2-2'}}$ in Fig. S22 (ESI†), is a transition state that allows an easy structural isomerization between **2** and a **tb** cluster, **2′**, where the two η^6-benzene ligands lie perpendicular to the vertical axis and not to the equatorial plane as in **2**; (iii) the gas-phase substitution reaction **2** + 2 pyz → **tb**-$Ru_5H_2(\eta^6\text{-pyz})_5$ + 2 PhH is endothermic by 11.1 kcal mol^{-1} per ligand as expected, given that benzene is a stronger π ligand than pyrazine. This value could be higher with ppp, that exhibits an extended conjugation; (iv) each benzene could be replaced in **2** by three σ-donating pyrazine ligands, given that the reaction **2** + 6 pyz → **3** + 2 PhH is exothermic by −26.8 cal mol^{-1} per Ru site. Of course, there must be no steric conflict that prevents the metal core from being stabilized by this bulky environment; (v) the π adsorption energy of pyrazine on Ru_5H_2, evaluated from the reaction Ru_5H_2 + 5 pyz → **tb**-$Ru_5H_2(\eta^6\text{-pyz})_5$, is found to be −37.0 kcal mol^{-1} per ligand, indicating a fairly strong adsorption.

In order to identify the available growth/stabilizing zones of the nanocapsule **8**·$(BArF)_8$, it has been fully optimized at the DFT level of theory (see computational details in the ESI†). With a 1.2 nm height × 1.7 nm wide inner cavity (I site in Fig. 9), the resulting geometry is more compact than that found with Molecular Dynamics (MD) simulations using force

fields.[38] These MD simulations actually suggest an important flexibility involved by the palladium coordination geometry, that gives the possibility that the height of the inner cavity increases up to the *ca.* 18 Å value reported in Fig. 2. Other sites can also contribute to the stabilization of Ruthenium clusters or NPs (see Fig. 9). They can lie outside a ZnTCPP building block, with a *ca.* 1.2 nm width available space (Zn site). The pillars, which can provide through the phenylene groups six π electrons stabilizers to metal cores, are not equally separated. Small clusters can be trapped in either ~0.6 or ~0.8 nm coordination sites (P1 and P2 sites). Finally, pillars can also rotate around their main axis of inertia, thus favouring the binding of larger nanoclusters outside the cage (P3 site). With a ~1.6–2.0 Å radius, [Ru_5] clusters fit the P1 site, whereas ~1 nm RuNPs could fit the larger coordination sites Zn, I and P3. We will see in the following that small clusters coated with η^1-pyrazine ligands, such as in **3**, can also be remarkably stabilized in site I.

We then focused on identifying the number of hydrides that could lie on the $Ru_5H_n(PhH)_2(pyz)_3$ clusters. Their energies as well as the Ru–H vibrational properties and the μ_{H2} chemical potential (see computational details in the ESI†) have been used to establish the stability diagram plotted in Fig. 10. Its purpose is to assess if the optimal number of hydrides that could lie on a [Ru_5] core stabilized by the P1 site is consistent with the optimal 72 or 74 CVE numbers, with the reasonable assumption that in experimental conditions the actual number of valence electrons is likely to be reached first of all thanks to the π-coordination of five aromatic rings. **2** is remarkably stable over a wide pressure and temperature range, in agreement with the 72 CVEs of the *closo* metal core. All stable structures exhibit a **tb** metal core, with the exception of the most stable 74 CVE **sp**-$Ru_5H_6(\eta^6\text{-PhH})_2(\eta^6\text{-pyz})_2(\eta^4\text{-pyz})$ cluster found in the very low temperature range. Interestingly, these remarkably stable structures are consistent with the second order energy differences plotted in Fig. S23 (ESI†), with the exception of the **tb**-$Ru_5H(\eta^6\text{-PhH})_2(\eta^6\text{-pyz})_3$. This odd hydride-number cluster appears stable in a narrow domain, whereas such spin-doublet cluster is expected to be very reactive upon hydrogenation.

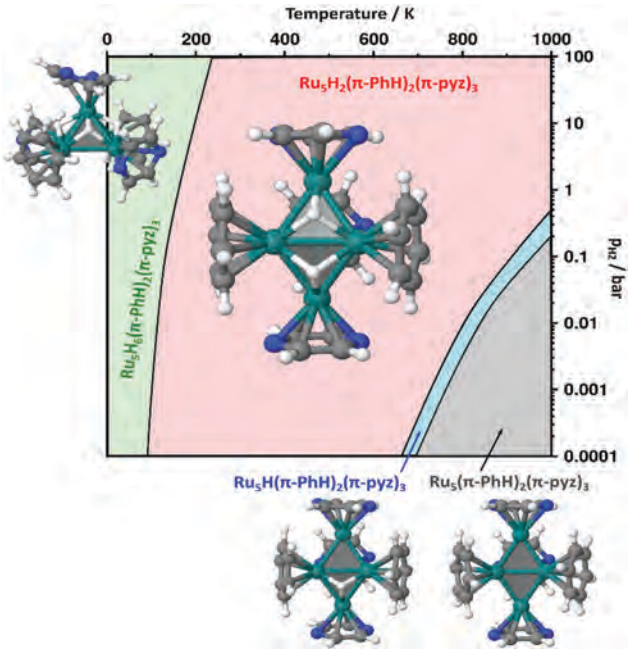

Fig. 10 Stability diagram established for **sp**- or **tb**-$Ru_5H_n(PhH)_2(pyz)_3$ (see text and computational details in the ESI†). The temperature range is set up to 1000 K, just to check the consistency of the model, *i.e.* that there is a gradual increase in the number of surface hydrides as the pressure increases and the temperature decreases.

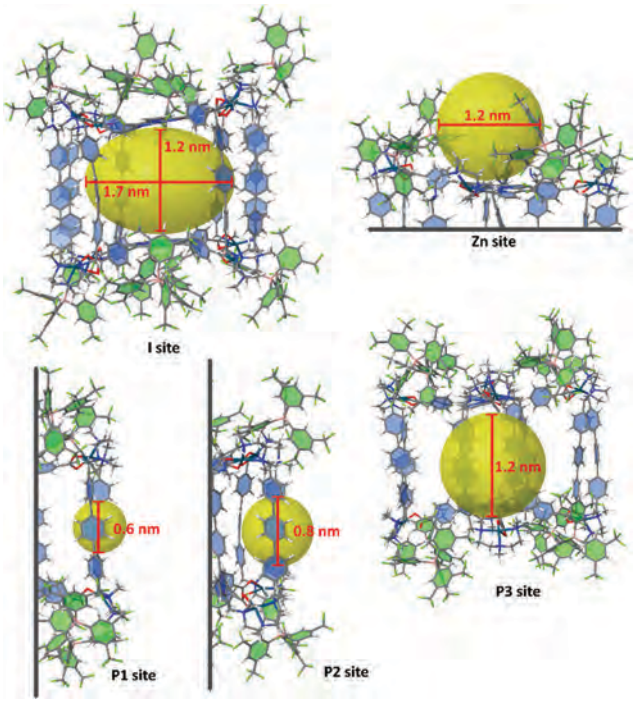

Fig. 9 Possible Ru_n clusters or RuNPs coordination sites in the **8**·$(BArF)_8$ nanocapsule. Given the overall plasticity of the cage, cavity sizes, shown as yellow spheres (sites Zn, P1–P3) or ellipsoids (site I), are only indicative. They are based on the optimization of a host-free cage. For the sake of clarity, aromatic rings of BArFs and of the ppp part of Pd-clips are highlighted in green and blue, respectively.

The adsorption energies of Ru_5 and Ru_{57} clusters on the coordination sites I, Zn, P1 and P3 were also evaluated and schematized in Fig. 9. The adsorption of $Ru_5H_2(\eta^6\text{-pyz})_3$ in the P1 site of a Pd clip has been first evaluated (Fig. 11a). It follows the Wade–Mingos rules, thanks to the coordination with two phenylene groups. The resulting cluster does correspond to cluster **2′**, slightly less stable than **2**, but which structure is better coordinated with both phenylene groups. Overall, Ru_5H_2 is stabilized by the two phenylene groups and the three pyrazine ligands by −209 kcal mol^{-1}, *i.e.* −41.8 kcal mol^{-1} per ligand (to be compared to −202.9 kcal mol^{-1} in **2′**). The resulting 0.7 nm wide geometry involves a very small spacing of the ppp pillars. Compound **3** could also be formed inside the cage (site I) and further stabilized thanks to the σ-donation of nitrogen atoms of pyrazine at the apex of the cluster toward zinc atoms of the zinc-porphyrin building blocks (Fig. 11b). The stabilization of the Ru_5H_2 moiety in site I is −38.1 kcal mol^{-1} per pyrazine ligand, with a moderate −18.6 kcal mol^{-1} energy

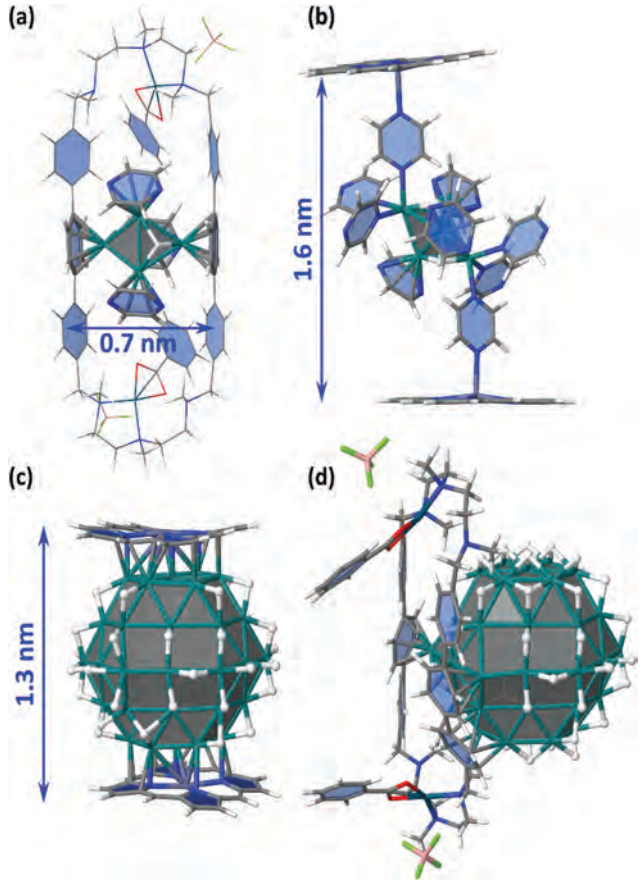

Fig. 11 Study of the possible trapping of ligand-coated Ru_5H_2 clusters and $Ru_{57}H_{44}$ NPs in the nanocapsule (see also Fig. 9). (a) adsorption of $Ru_5H_2(\eta^6\text{-pyz})_3$ in the P1 site of a Pd clip (with BF_4 instead of BArF); (b) coordination of compound **3** between two Zn-porphyrin building blocks (model for site I); (c) coordination of a $Ru_{57}H_{44}$ NP between two Zn-porphyrin building blocks (model for site I); (d) stabilization of a $Ru_{57}H_{44}$ NP in the P3 site of a Pd-ppp clip.

per pyrazine-Zn coordination. With a final 1.6 nm inter-porphyrin width and given the adaptability of the whole cage, it appears feasible. Such coordination could also occur outside the nanocapsule, *i.e.* in the Zn site of Fig. 9.

It is not obvious that the 0.8 nm spacing between the farthest ppp allows the diffusion of several precursors and seeds within the cage. Nevertheless, the possible growth of RuNPs inside the nanocapsule (Fig. 11c) cannot be discarded. Moreover, hydrides are very mobile and could move in order to favour the simultaneous stabilization of an NP by the Zn–porphyrin parts of the nanocage, as shown in Fig. 11c. Such encapsulation would be stabilized by -97.6 kcal mol^{-1} per interaction, with respect to the cage and to a free $Ru_{57}H_{44}$ with hydrides randomly scattered on all facets of this NP. NPs could also be stabilized outside the cage, in the Zn site, probably with additional pyrazine on the surface. The possible growth of RuNPs outside the cage, but stabilized in the P3 site, has also been considered (Fig. 11d). Phenylene groups can slightly rotate around the vertical ppp axis in order to maximize their coordination on the RuNP surface. On the contrary to the previous case, it does involve a concerted shift of several hydrides to favour this grafting. In this example, two facets of the $Ru_{57}H_{44}$ NP are firmly grafted to the ppp clip by a (η^6-phenylene)(η^6,μ_3-phenylene)-(η^6,μ_4-phenylene) motif. The resulting strong adsorption energy, -162.3 kcal mol^{-1}, *i.e. ca.* -54 kcal mol^{-1} per phenylene, might be lower with the **8**·$(BArF)_8$ nanocapsule, as the pillars could be slightly less adaptive, and as the number of surface hydrides could be slightly higher. Even in this case, this external grafting is very likely to be significantly stable.

All the above DFT study shows the ability of the nanocapsule to stabilize both small $[Ru]_5$ clusters at different trapping sites, but most likely, as (a) Ru_5H_2 stabilized at P1 site by the two phenylene groups and the three pyrazine ligands (*i.e.* compound **2**, Fig. 8 and Fig. 11a or Fig. 11b) as compound **3** formed inside the cage (site I) and further stabilized thanks to the σ-donation of nitrogen atoms of pyrazine at the apex of the cluster toward zinc atoms of the zinc-porphyrin building blocks (Fig. 11b), with similar stabilization energies for both options. The remarkable occurrence of the $[Ru_5]$ cluster in the mass spectrum is thus explained both in terms of electronic effects and of cavities' size of the nanocapsule. Moreover, the outer or inner-cavity stabilization of a *ca.* 1 nm RuNP model have also been considered. Given the combined experimental observations and computational insights, we propose that the trapped $[Ru_5]$ metallic clusters are the first-grown seeds of subsequent formation of the subnanometric RuNP, which are also stabilized by outer-nanocapsule interactions.

In conclusion, sub-nanometric Ru NPs were successfully synthesized and stabilized using the Pd-based tetragonal prismatic nanocapsule **8**·$(BArF)_8$ along with pyrazine as stabilizing agent. The data registered indicate that nanocapsule remains intact and the Ru NPs are stabilized through the outer-cavity of the nanocapsule, being the macrocyclic-based molecular clip moieties the ones mostly responsible for the stabilization of the ultra-small Ru NPs. Simultaneously, the same nanocapsule is able to trap in its inner-cavity ruthenium clusters $[Ru_5]$ as ascertained by HRMS, which is fully diagnostic for the mass identity of the encapsulated guests.[21,39–41] Computational data point towards two main isoenergetic adsorption modes of the $[Ru_5]$ cluster: (a) adsorption of $Ru_5H_2(\eta^6\text{-pyz})_3$ in the P1 site of a Pd clip (*ca.* **tb**-$Ru_5H_2(\eta^6\text{-PhH})_2(\eta^6\text{-pyz})_3$ (**2**)) or (b) coordination of **tb**-$Ru_5H_2(\eta^1\text{-pyz})_6(\eta^6\text{-pyz})_3$ (**3**) between two Zn–porphyrin building blocks (model for site I), both options fulfilling the Wade-Mingos counting rules, *i.e.* 72 CVEs for the *closo* **tb**.

The direct observation of the metallic cluster seeds for the formation of NP sheds light into this fundamental process. Moreover, the double role of the nanocapsules in stabilising ~0.7 nm NPs and also host ultra-small Ru clusters, is unprecedented and may pave the way towards the synthesis of ultra-small metallic clusters for catalytic purposes.

Methods

The synthesis of the different nanocapsules was performed following the reported procedure (see Fig. 1).[22] The synthesis

of the Ru NPs was performed in a Fisher–Porter bottle by decomposition of Ru(cyclooctadiene)(cyclooctatriene) in presence of the molecular cage and small amount of pyrazine.[23,24] For this, in the glove box, 2 mg of nanocapsule were dissolved in 2 mL of THF, then the corresponding Ru equivalents (130, 80, 60, 40 or 20) were added from a 0.06 M solution of the complex, followed (in some cases) by 0.2 equivalents of pyrazine with respect to Ru from a 0.024 M solution. The final volume is 3.0–3.5 mL. Out of the glove box, the solution was then charged with 1 bar of H_2 and stirred at room temperature for 2 min. At this time, the pressure was released and the Fisher–Porter opened to air quenching the decomposition. The NPs were characterized by Transmission Electron Microscopy (TEM) and High-Resolution Transmission Electron Microscopy (HRTEM). The solutions were also analysed by High Resolution Electrospray Ionization Mass Spectrometry (HR-ESI-MS).

The catalytic tests were performed also in a Fisher-Porter bottle and were prepared at the air. To the solution of Ru NPs 135 μL (1 mmol) of styrene and 227 μL of dodecane (1 mmol, internal standard) were added. The volume of the Ru NPs solution utilised was different depending on the Ru equivalents employed in the initial solutions, and are specified in Table S1 (ESI†). In all the cases the Ru present in the solution constituted a 0.25 mol% with respect to the substrate.

All DFT calculations were performed with the VASP software,[42,43] with the exchange–correlation potential approximated by the generalized gradient approach proposed by Perdew, Burke, and Ernzerhof (PBE),[44,45] and using the projector-augmented wave (PAW) scheme to treat core electrons.[46,47] Other computational details are given in the ESI.†

Conflicts of interest

There are no conflicts to declare.

Acknowledgements

This work was supported by grants from MINECO-Spain (PID2019-104498GB-I00 and EQC2018-004422-P) and Generalitat de Catalunya (2017SGR264) to X. R. E. U. thanks UdG for a PhD grant. CNRS, INSAT and UT3-UPS are also acknowledged for financial support. I. d. R. and R. P. thank the HPC CALcul en MIdi-Pyrénées (CALMIP, OLYMPE machine, grant P0611) for a very generous allocation of computer time on this project. IMM, JMA and BC thank ERC Advanced Grant (MONACAT 2015-694159) for financial support. X. R. also thanks ICREA-Acadèmia awards. We thank STR-UdG for technical support.

References

1 Y. Du, H. Sheng, D. Astruc and M. Zhu, *Chem. Rev.*, 2020, **120**, 526–622.
2 C. Gao, F. Lyu and Y. Yin, *Chem. Rev.*, 2021, **121**, 834–881.
3 A. Heuer-Jungemann, N. Feliu, I. Bakaimi, M. Hamaly, A. Alkilany, I. Chakraborty, A. Masood, M. F. Casula, A. Kostopoulou, E. Oh, K. Susumu, M. H. Stewart, I. L. Medintz, E. Stratakis, W. J. Parak and A. G. Kanaras, *Chem. Rev.*, 2019, **119**, 4819–4880.
4 E. S. Gutterød, A. Lazzarini, T. Fjermestad, G. Kaur, M. Manzoli, S. Bordiga, S. Svelle, K. P. Lillerud, E. Skúlason, S. Øien-Ødegaard, A. Nova and U. Olsbye, *J. Am. Chem. Soc.*, 2020, **142**, 999–1009.
5 Y. Liu, Y. Shen, W. Zhang, J. Weng, M. Zhao, T. Zhu, Y. R. Chi, Y. Yang, H. Zhang and F. Huo, *Chem. Commun.*, 2019, **55**, 11770–11773.
6 M. I. Gonzalez, A. B. Turkiewicz, L. E. Darago, J. Oktawiec, K. Bustillo, F. Grandjean, G. J. Long and J. R. Long, *Nature*, 2020, **577**, 64–68.
7 A. Dhakshinamoorthy and H. Garcia, *Chem. Soc. Rev.*, 2012, **41**, 5262–5284.
8 X. Yang and Q. Xu, *Trends Chem.*, 2020, **2**, 214–226.
9 L. M. Olaechea, L. Montero de Espinosa, E. Oveisi, S. Balog, P. Sutton, S. Schrettl and C. Weder, *J. Am. Chem. Soc.*, 2020, **142**, 342–348.
10 Q.-T. Fu, X. Yan, X.-Y. Zhang, Y. He, W.-D. Zhang, Y. Liu, Y. Li and Z.-G. Gu, *Dalton Trans.*, 2020, **49**, 12145–12149.
11 B. Mondal and P. S. Mukherjee, *J. Am. Chem. Soc.*, 2018, **140**, 12592–12601.
12 G.-J. Chen, W.-L. Xin, J.-S. Wang, J.-Y. Cheng and Y.-B. Dong, *Chem. Commun.*, 2019, **55**, 3586–3589.
13 M. Nihei, H. Ida, T. Nibe, A. M. P. Moeljadi, Q. T. Trinh, H. Hirao, M. Ishizaki, M. Kurihara, T. Shiga and H. Oshio, *J. Am. Chem. Soc.*, 2018, **140**, 17753–17759.
14 Y. Fang, J. Li, T. Togo, F. Jin, Z. Xiao, L. Liu, H. Drake, X. Lian and H.-C. Zhou, *Chem*, 2018, **4**, 555–563.
15 R. McCaffrey, H. Long, Y. Jin, A. Sanders, W. Park and W. Zhang, *J. Am. Chem. Soc.*, 2014, **136**, 1782–1785.
16 X. Yang, J.-K. Sun, M. Kitta, H. Pang and Q. Xu, *Nat. Catal.*, 2018, **1**, 214–220.
17 Y. Zhang, Y. Xiong, J. Ge, R. Lin, C. Chen, Q. Peng, D. Wang and Y. Li, *Chem. Commun.*, 2018, **54**, 2796–2799.
18 N. Sun, C. Wang, H. Wang, L. Yang, P. Jin, W. Zhang and J. Jiang, *Angew. Chem., Int. Ed.*, 2019, **58**, 18011–18016.
19 S. Jiang, H. J. Cox, E. I. Papaioannou, C. Tang, H. Liu, B. J. Murdoch, E. K. Gibson, I. S. Metcalfe, J. S. O. Evans and S. K. Beaumont, *Nanoscale*, 2019, **11**, 14929–14936.
20 V. Sharma, D. De, R. Saha, P. K. Chattaraj and P. K. Bharadwaj, *ACS Appl. Mater. Interfaces*, 2020, **12**, 8539–8546.
21 E. Ubasart, O. Borodin, C. Fuertes-Espinosa, Y. Xu, C. García-Simón, L. Gómez, J. Juanhuix, F. Gándara, I. Imaz, D. Maspoch, M. von Delius and X. Ribas, *Nat. Chem.*, 2021, **13**, 420–427.
22 E. Ubasart, C. García-Simón, M. Pujals, K. Asad, N. Chronakis, T. Parella and X. Ribas, *Org. Chem. Front.*, 2021, **8**, 4101–4105.
23 L. M. Martínez-Prieto and B. Chaudret, *Acc. Chem. Res.*, 2018, **51**, 376–384.
24 L. M. Martínez-Prieto, C. Urbaneja, P. Palma, J. Cámpora, K. Philippot and B. Chaudret, *Chem. Commun.*, 2015, **51**, 4647–4650.
25 M. I. Bruce, *J. Organomet. Chem.*, 1990, **394**, 365–384.

26 P. J. Bailey, M. J. Duer, B. F. G. Johnson, J. Lewis, G. Conole, M. McPartlin, H. R. Powell and C. E. Anson, *J. Organomet. Chem.*, 1990, **383**, 441–461.

27 J. W. Benson, T. Ishida, K. Lee, S. R. Wilson and J. R. Shapley, *Organometallics*, 1997, **16**, 4929–4932.

28 J. A. Cabeza, I. del Río, P. García-Álvarez and D. Miguel, *Inorg. Chem.*, 2006, **45**, 6020–6027.

29 I. del Rosal, F. Jolibois, L. Maron, K. Philippot, B. Chaudret and R. Poteau, *Dalton Trans.*, 2009, 2142–2156, DOI: **10.1039/B817055J**.

30 G. Meister, G. Rheinwald, H. Stoeckli-Evans and G. Süss-Fink, *J. Chem. Soc., Dalton Trans.*, 1994, 3215–3223, DOI: **10.1039/DT9940003215**.

31 R. Gautier, F. Chérioux, G. Süss-Fink and J.-Y. Saillard, *Inorg. Chem.*, 2003, **42**, 8278–8282.

32 D. M. P. Mingos, *J. Chem. Soc., Chem. Commun.*, 1985, 1352–1354, DOI: **10.1039/C39850001352**.

33 M. A. Fox and K. Wade, *Pure Appl. Chem.*, 2003, **75**, 1315–1323.

34 J.-Y. Saillard and J.-F. Halet, in *The Chemical Bond I: 100 Years Old and Getting Stronger*, ed. D. M. P. Mingos, Springer International Publishing, Cham, 2016, pp. 157–179, DOI: **10.1007/430_2015_210**.

35 D. M. P. Mingos and D. J. Wales, *Introduction to Cluster Chemistry*, Prentice Hall, 1990.

36 W. Zhang, H. Zhao and L. Wang, *J. Phys. Chem. B*, 2004, **108**, 2140–2147.

37 F. Aguilera-Granja, L. C. Balbás and A. Vega, *J. Phys. Chem. A*, 2009, **113**, 13483–13491.

38 C. García-Simón, C. Colomban, Y. A. Çetin, A. Gimeno, M. Pujals, E. Ubasart, C. Fuertes-Espinosa, K. Asad, N. Chronakis, M. Costas, J. Jiménez-Barbero, F. Feixas and X. Ribas, *J. Am. Chem. Soc.*, 2020, **142**, 16051–16063.

39 C. Fuertes-Espinosa, C. García-Simón, M. Pujals, M. Garcia-Borràs, L. Gómez, T. Parella, J. Juanhuix, I. Imaz, D. Maspoch, M. Costas and X. Ribas, *Chem*, 2020, **6**, 169–186.

40 C. Fuertes-Espinosa, A. Gómez-Torres, R. Morales-Martínez, A. Rodríguez-Fortea, C. García-Simón, F. Gándara, I. Imaz, J. Juanhuix, D. Maspoch, J. M. Poblet, L. Echegoyen and X. Ribas, *Angew. Chem., Int. Ed.*, 2018, **57**, 11294–11299.

41 C. García-Simón, M. Garcia-Borràs, L. Gómez, T. Parella, S. Osuna, J. Juanhuix, I. Imaz, D. Maspoch, M. Costas and X. Ribas, *Nat. Commun.*, 2014, **5**, 5557.

42 G. Kresse and J. Furthmüller, *Phys. Rev. B: Condens. Matter Mater. Phys.*, 1996, **54**, 11169–11186.

43 G. Kresse and J. Furthmüller, *Comput. Mater. Sci.*, 1996, **6**, 15–50.

44 J. P. Perdew, K. Burke and M. Ernzerhof, *Phys. Rev. Lett.*, 1996, **77**, 3865–3868.

45 J. P. Perdew, K. Burke and M. Ernzerhof, *Phys. Rev. Lett.*, 1997, **78**, 1396.

46 P. E. Blöchl, *Phys. Rev. B: Condens. Matter Mater. Phys.*, 1994, **50**, 17953–17979.

47 G. Kresse and D. Joubert, *Phys. Rev. B: Condens. Matter Mater. Phys.*, 1999, **59**, 1758–1775.

Chapter V. Results and discussion

Coordination-driven self-assembly is a strategy based on the use of metal-ligand coordination bonds to allow a controlled synthesis of supramolecular entities due to the directionality degree of the M-L bonds. It has been a useful strategy to design a wide range of hosts, featuring different shapes and sizes, capable to interact with a variety of guests. In this context, the QBIS-CAT group has developed several tetragonal prismatic nanocapsules based on the self-assembly of tetra-carboxylated metalloporphyrins with different macrocyclic clips, resulting in different cavities size (Figure V.1). The first 3D nanocapsule developed in the group was reported in 2013, named as **3**·$(OTf)_8$. The macrocyclic clip featuring a phenyl unit produced a nanocapsule with a cavity size of 7.5 Å.[1] The nanocapsule showed high affinity for different anionic planar π-guests molecules ($K_a \sim 10^9$ M^{-1}), whereas aromatic neutral or cationic substrates were non-interacting. Later, in 2014, a biphenyl-based nanocapsule named **4**·$(BArF)_8$ was reported, bearing an expanded distance between porphyrins of 14.1 Å.[2] The nanocapsule showed the ability to recognize fullerenes of different sizes, such as C_{60}, C_{70}, C_{76}, C_{78} and C_{84} with a clear preference for C_{60} and C_{70}. What's more, the selective purification of C_{60} by a solvent washing strategy was achieved. In 2017, the Cu-based analogue of the biphenyl-based nanocapsule, named **5**·$(OTf)_8$, showed high affinity for endohedral metallofullerenes such as $Sc_3N@C_{80}$ from a metallofullerene soot. In 2019, the cavity size of the very first nanocapsule **3**·$(OTf)_8$ was slightly increased to 8.5 Å utilizing a naphthalene-based nanocapsule, named **3b**·$(BArF)_8$, capable to host C_{60} selectively from a fullerene soot mixture.[3] Moreover, this nanocapsule could encapsulate C_{60}-derivatives such as C_{60}-PCBM and N-methylpyrrolidine-C_{60}.

The applications of these nanocapsules at the start of this thesis included a) the use of the host as a second coordination sphere to perform enantioselective catalysis,[4] b) the selective purification of fullerenes[2, 3, 5] or endohedral fullerenes,[6, 7] and c) the regioselective Bingel functionalization of C_{60} up to fully equatorial tetrakis-adducts.[8] In addition, DFT studies were performed to understand the flexibility and adaptability of the nanocapsule depending on the guest size or shape.[9] Figure V.1 summarizes the nanocapsules synthesized during the last ten years in the QBIS-CAT group, including the ones developed in this thesis. Here we have developed new tetragonal prismatic nanocapsules following the coordination-driven self-assembly strategy. We have tuned with the host-guest properties for each nanoreceptor, making them useful supramolecular structures for a) the regiofunctionalization of C_{60} restricted to bis-adducts, b) hosting new species such as higher fullerene or azafullerene, and c) mediating the synthesis of sub-nanometric metallic nanoparticles and clusters.

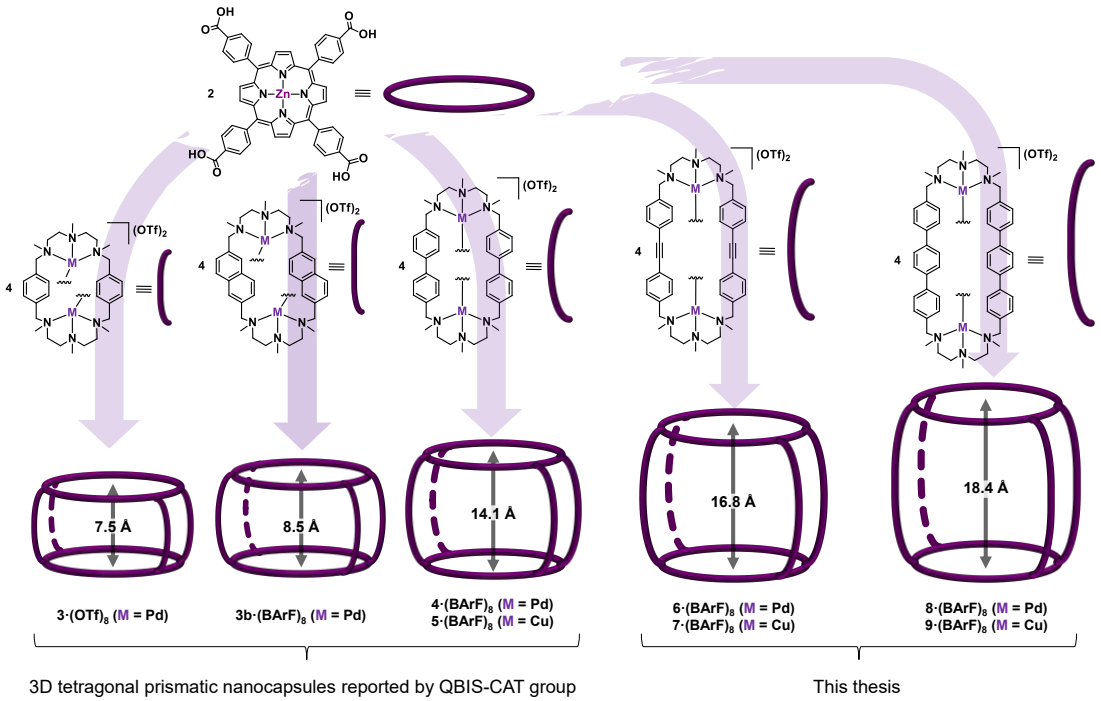

2013	Synthesis of **3·(OTf)8** to selectively encapsulate anionic π-guests (*Chem. Eur. J.*)[1]
2014	Synthesis of **4·(BArF)8**. Recognition of fullerenes and purification of C_{60} (*Nat. Comm.*)[2]
2015	Enantioselective hydroformylation by a confined Rh catalyst in **4**·(BArF)8 (*J. Am. Chem. Soc.*)[4]
2017	Synthesis of **5·(BArF)8** and purification of $Sc_3N@C_{80}$ from EMF soot (*Chem. Eur. J.*)[6]
	Reversible C_{60} ejection from **4**·(BArF)8 through redox-dependent binding of a competitive guest (*Chem. Eur. J.*)[10]
2018	Design of Zn-, Cu- and Fe-coordination complexes confined in **4**·(BArF)8 (*Inorg. Chem.*)[11]
	Cofacial Zn-porph as tuneable 1O2 photosensitizers (*Chem. Eur. J.*)[12]
	Purification of $U_2@C_{80}$ and $Sc_2CU@C_{80}$ from EMF soot (*Angew. Chem. Int. Ed.*)[7]
2019	Selectively encapsulation of U-based C_{78}-EMFs over C_{80}-based EMFs (*Nanoscale*)[13]
	Synthesis of **3b·(BArF)8** to selectively encapsulate C_{60} and C_{60}-derivatives (*Chem. Commun.*)[3]
	Regioselective tetra-functionalization of C_{60} using the supramolecular mask strategy (*Chem*)[8]
2020	Fullerene recognition and binding processes studied by 2D-EXSY, MD and aMD simulations (*J. Am. Chem. Soc.*)[9]
2021	Synthesis of **6·(BArF)8** and **7·(BArF)8**. Development of the Matryoshka-like three-shell complex for the bis-functionalization of C_{60} (*Nat. Chem.*)[14] - **Chapter VI.1**
	Synthesis of **8·(BArF)8** and **9·(BArF)8** and purification of C_{84} (*Org. Chem. Front.*)[15] - **Chapter VI.2**
2022	Synthesis of Ru NPs using **8**·(BArF)8 as stabilizer (*Nanoscale Horiz.*)[16] **- Chapter VI.3**

Figure V.1. Different-sized 3D tetragonal prismatic nanocapsules reported by QBIS-CAT group and new nanocapsules developed in this thesis (in purple). Their uses or applications are included.

V.1. A three-shell supramolecular complex enables the symmetry-mismatched chemo- and regioselective bis-functionalization of C_{60}

In this chapter we disclose the design and synthesis of a new self-assembled system, designated as Matryoshka or Russian dolls, comprised by three units: a supramolecular nanocapsule, a cycloparaphenylene ([10]CPP) and a fullerene-C_{60}. This three-shell supramolecular complex will be fully characterized by HRMS, NMR and XRD. Then, Bingel conditions will be applied to the Matryoshka assembly affording a unique bis-regioselectivity, which cannot be obtained without the Matryoshka acting as a supramolecular mask. In particular, the ***trans*-3** bis-adduct will be characterized by HPLC-DAD and NMR. X-Ray diffraction (XRD) studies will help us to understand this characteristic regioselectivity. Moreover, bromomalonates that differ in volume will be tested for the Bingel reactivity and void analysis studies will rationalise the variation in yield of the ***trans*-3** bis-adduct (see Annex 1).

V.1.1. Synthesis and characterization of the extended nanocapsule 6·$(BArF)_8$ and 7·$(BArF)_8$

To design a nanocapsule large enough to accommodate the host-guest complex C_{60}⊂[10] CPP, the previously reported self-assembled tetragonal prismatic nanocapsules **3**, **4** and **5** were modified.[1, 2, 6] The synthesis of the Pd-based and Cu-based nanocapsules, **6**·$(BArF)_8$ and **7**·$(BArF)_8$ respectively, consisted of seven reaction steps (Figure V.2 and V.4). The first reaction step consists in a decarboxylative coupling of 4-bromobenzaldehyde with propiolic acid, which was catalysed by Pd as reported in the literature.[17] With this, a larger linker for the subsequent synthesis of the macrocyclic molecular clip is afforded, the 4,4'-(ethyne-1,2-diyl)dibenzaldehyde (pTp). Once purified by column chromatography, a 2+2 cyclization is achieved with diethylenetriamine (DETA), obtaining the imine-containing macrocycle S_2pTp. In the same reaction flask, excess of $NaBH_4$ was added to reduce the imine groups, obtaining the hydrogenated macrocycle (H_2pTp) after work-up (extractions with $CHCl_3$ in a basic pH). The last step to obtain the Me_2pTp ligand was the methylation of the amines with formic acid, formaldehyde and water. The product was recrystallized in hot acetone and precipitated at -20 ºC. Once the ligand was obtained, it can be metalated with either $Cu(OTf)_2$ or $Pd(OAc)_2$; for the latter, a counteranion exchange with $Na(OTf)_2$ after the metalation reaction is required. Both molecular clips were recrystallized with slow diffusion of diethyl

ether obtaining the molecular clips $[Cu_2(Me_2pTp)]\cdot(OTf)_4$ and $[Pd_2(Me_2pTp)(OAc)_2]\cdot(OTf)_2$ which were analysed by HRMS (see Figure S39 and S41 in Annex 1). For the copper-based clip, suitable crystals for single X-ray diffraction were obtained in acetonitrile/diethyl ether mixtures (Figure V.3).

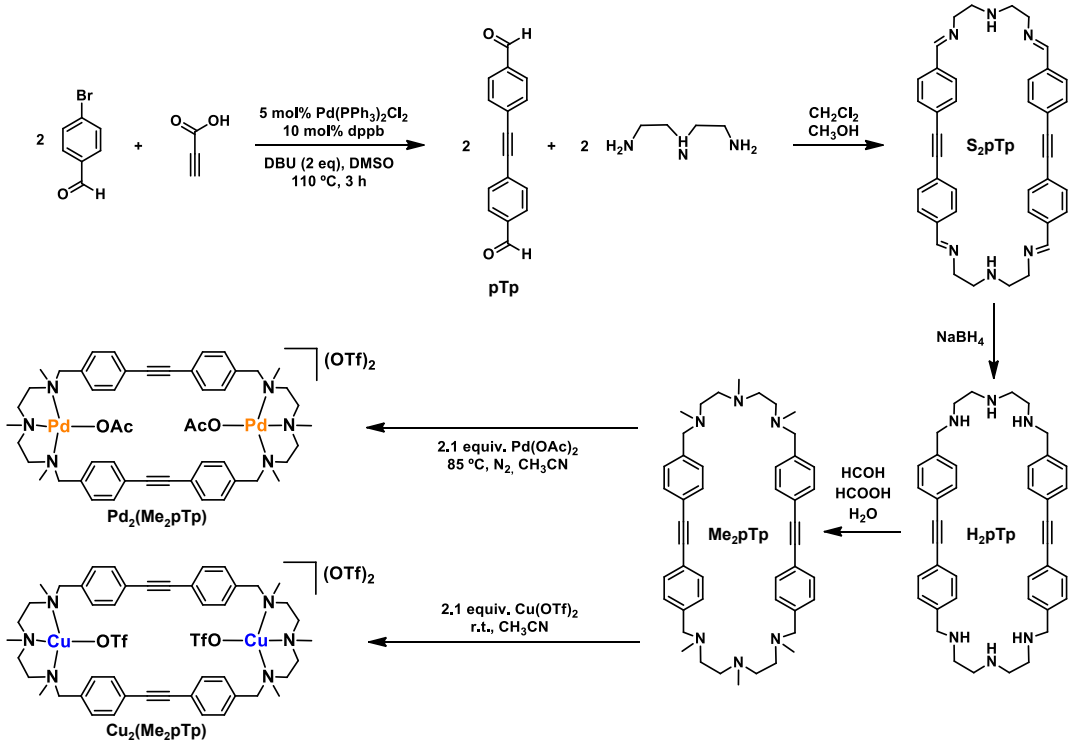

Figure V.2. Reaction steps required to obtain the $[Cu_2(Me_2pTp)]\cdot(OTf)_4$ and $[Pd_2(Me_2pTp)(OAc)_2]\cdot(OTf)_2$ molecular clips from the dialdehyde (pTp).

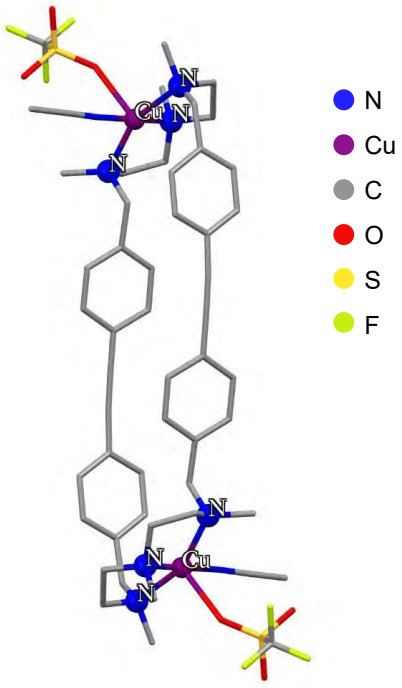

Figure V.3. XRD of $[Cu_2(Me_2pTp)]\cdot(OTf)_4$ clip.

The palladium-based nanocapsule, **6**·$(OTf)_8$, was obtained after self-assembly of molecular clip $[Pd_2(Me_2pTp)(OAc)_2]$·$(OTf)_2$ and Zn(II)-based 5,10,15,20-(tetra-4-carboxyphenyl)porphyrin in a 2:1 ratio, in refluxing DMF and NEt_3 as base (Figure V.4). The last step consisted in the counteranion exchange with sodium (3,5-bis(trifluoromethyl)phenyl)borate (NaBArF) and recrystallization with slow diffusion of diethyl ether (75% yield). On the other hand, the synthesis of the copper-based nanocapsule, **7**·$(BArF)_8$, followed the same steps but in this case using the $[Cu_2(Me_2pTp)]$·$(OTf)_4$ clip, and the reaction was carried out at room temperature (77% yield). The diamagnetic Pd(II)-based nanocapsule **6**·$(OTf)_8$, was characterized by NMR spectroscopy (see Figure S44 in Annex 1) and high-resolution mass spectrometry (HRMS) (Figure V.5), whereas the paramagnetic Cu(II)-based nanocapsule **7**·$(BArF)_8$ was characterized by HRMS (Figure V.6) and XRD (Figure V.7).

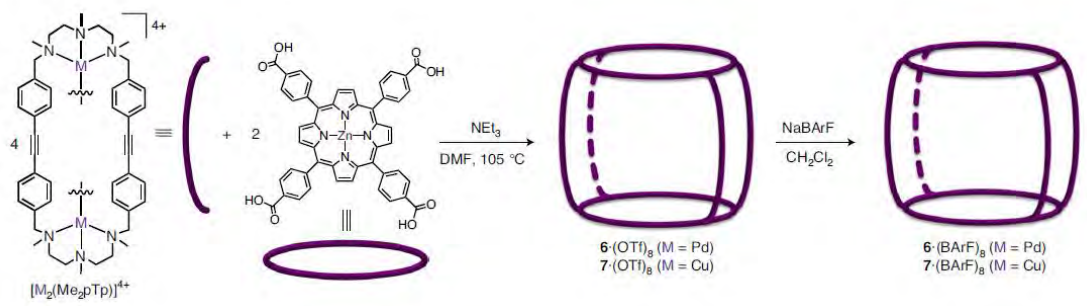

Figure V.4. Synthesis of Pd- and Cu-based nanocapsules **6**·$(BArF)_8$ and **7**·$(BArF)_8$.

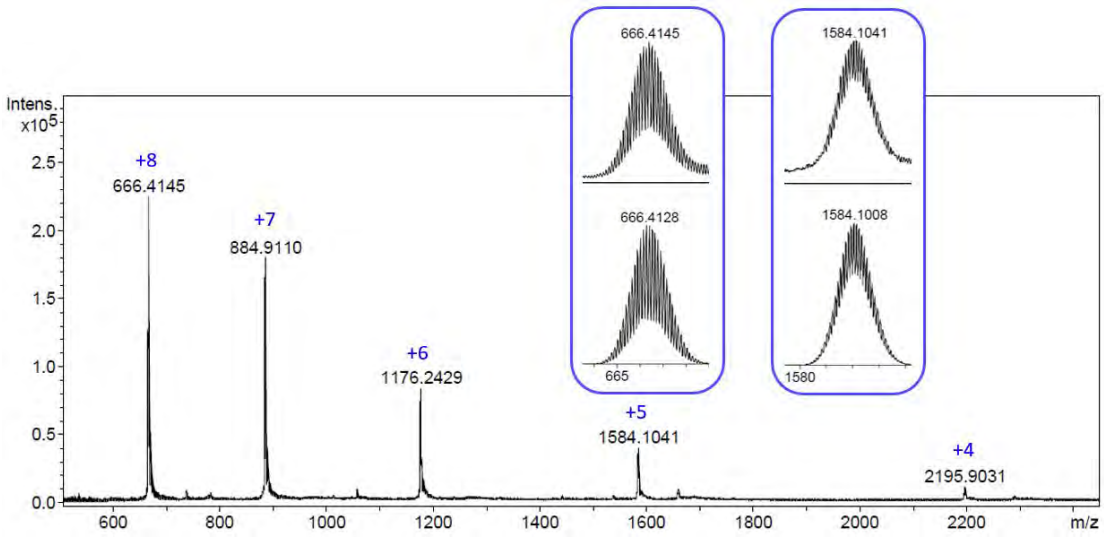

Figure V.5. ESI-MS spectra for Pd-based nanocapsule **6**·$(BArF)_8$. Experimental (top) and calculated (bottom) for +8 and +5 charged m/z peaks.

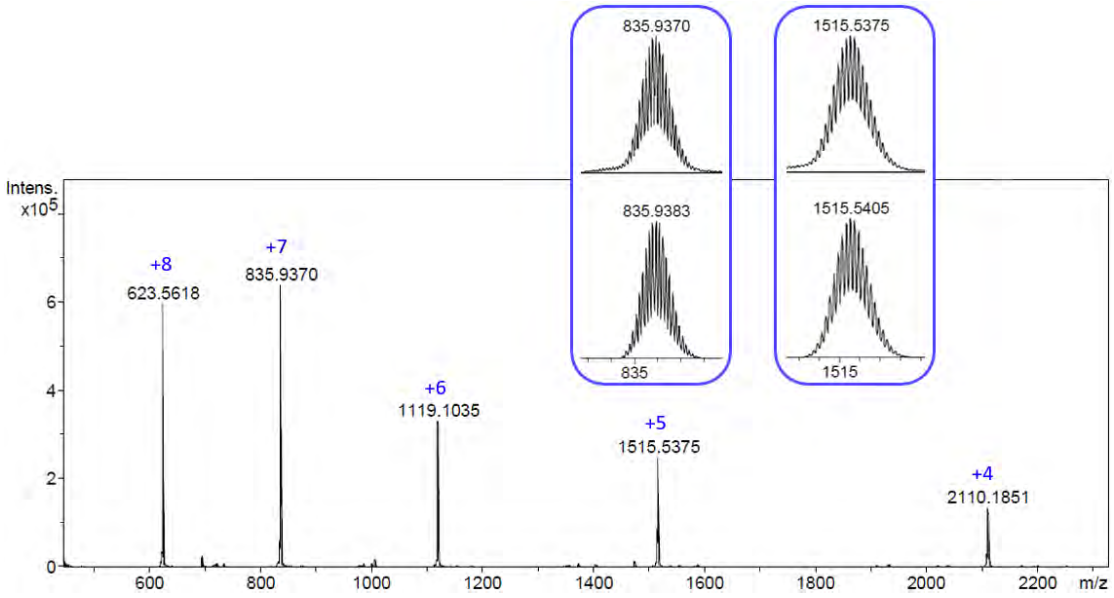

Figure V.6. ESI-MS spectra for Cu-based nanocapsule **7**·(BArF)$_8$. Experimental (top) and calculated (bottom) for +7 and +5 charged m/z peaks.

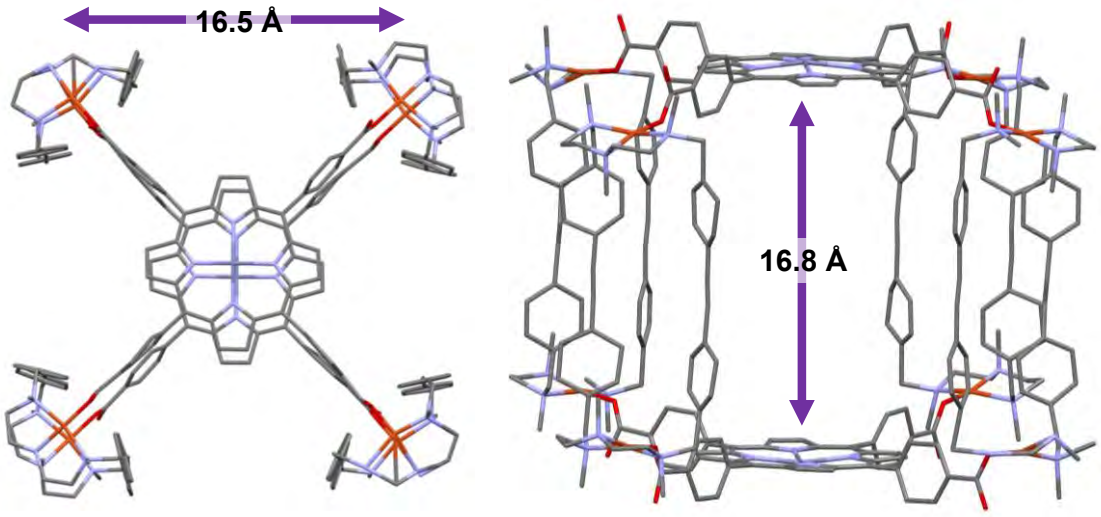

Figure V.7. XRD of Cu-based nanocapsule **7**·(BArF)$_8$.

V.1.2. Host-Guest experiments

The association of [10]CPP molecule with C_{60} was performed following reported procedures, showing a high affinity.[18, 19] Then, the reported nanocapsule **4**·(BArF)$_8$ (Zn–porph···Zn–porph distance, 14.1 Å) was tested as host for C_{60}⊂[10]CPP, but this nanocapsule has high affinity for C_{60}, therefore, the [10]CPP was expelled, obtaining the host-guest system C_{60}⊂**4**·(BArF)$_8$ as confirmed by HRMS (Figure V.8).

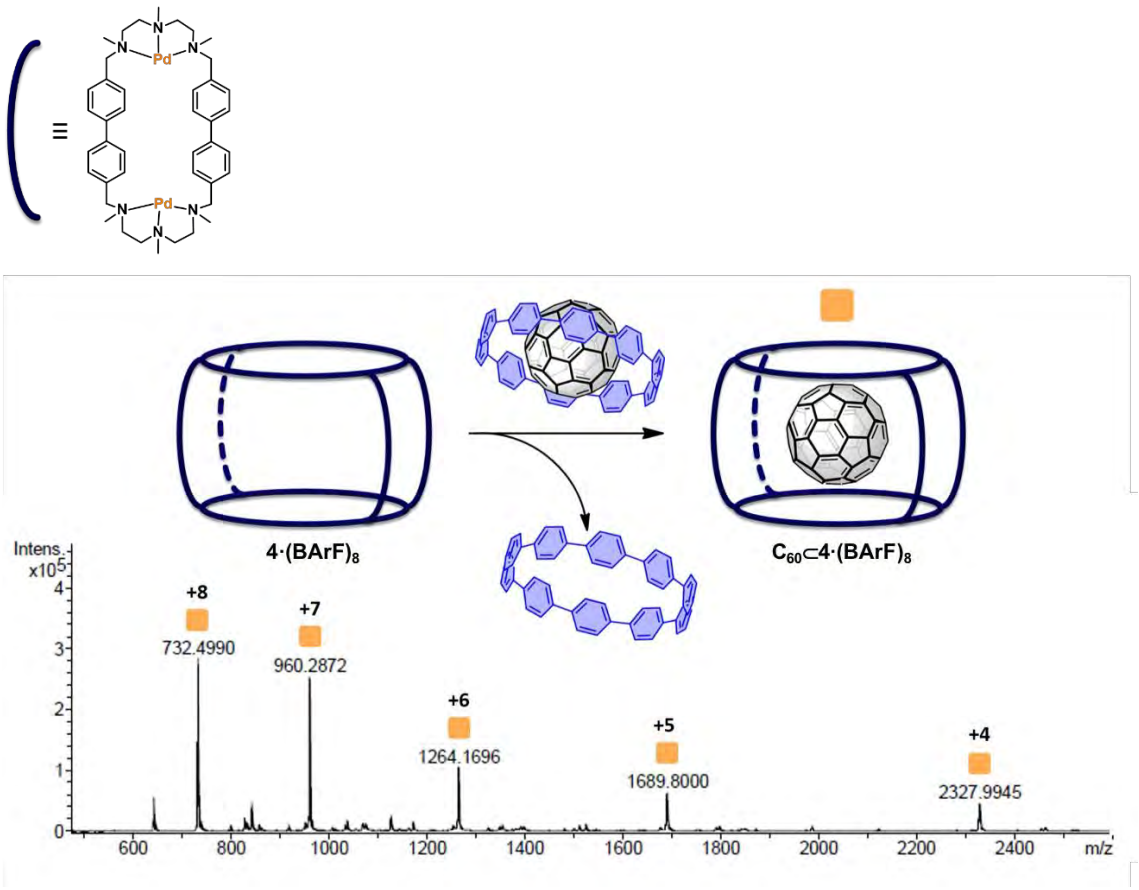

Figure V.8. Schematic representation for the encapsulation of C_{60} and ESI-MS spectra for C_{60}⊂**4**·$(BArF)_8$.

After that, we focused our attention on the host-guest properties of **6**·$(BArF)_8$, featuring a larger cavity (Zn–porph···Zn–porph distance, 16.8 Å). First, bare C_{60} was tested as guest and HRMS experiments revealed a very weak affinity, which was confirmed by UV-Vis titration (K_a = 5.4 ± 0.9 × 10^3 M^{-1}) in toluene/acetonitrile 9:1 solvent. This value confirmed the weak interaction of C_{60} with **6**·$(BArF)_8$ observed by ^{1}H-NMR and HRMS (Figure V.9). It could be demonstrated that C_{60} binds approximately four orders of magnitude less strongly to the extended nanocapsule **6**·$(BArF)_8$ (K_a = 5.4 ± 0.9 × 10^3 M^{-1}) than to the nanocapsule **4**·$(BArF)_8$ (K_a of 2.8 ± 0.6 × 10^7 M^{-1}), which was reported previously in the same solvent mixture.[2]

Then, other binary equilibria studies were performed. The association constant of the nanohoop [10]CPP to nanocapsule **6**·$(BArF)_8$ was determined as K_a of 1.1 ± 0.1 × 10^5 M^{-1} by fluorescence titration (see Figure S90 in Annex 1). It was also determined the affinity constant between C_{60} and [10]CPP, (K_a = 5.7 ± 0.4 × 10^6 M^{-1}) (see Figure S89 in Annex 1). Strikingly, experimental observations clearly indicated a neat formation of a three-shell complex in a quantitative manner upon the addition of 1 equiv. of [10]CPP to the previously

prepared mixture of C_{60} and **6**·$(BArF)_8$, as shown by ^{1}H-NMR (see Figure S55 in Annex 1) and HRMS analyses (Figure V.9 and Figure S54 in Annex 1).

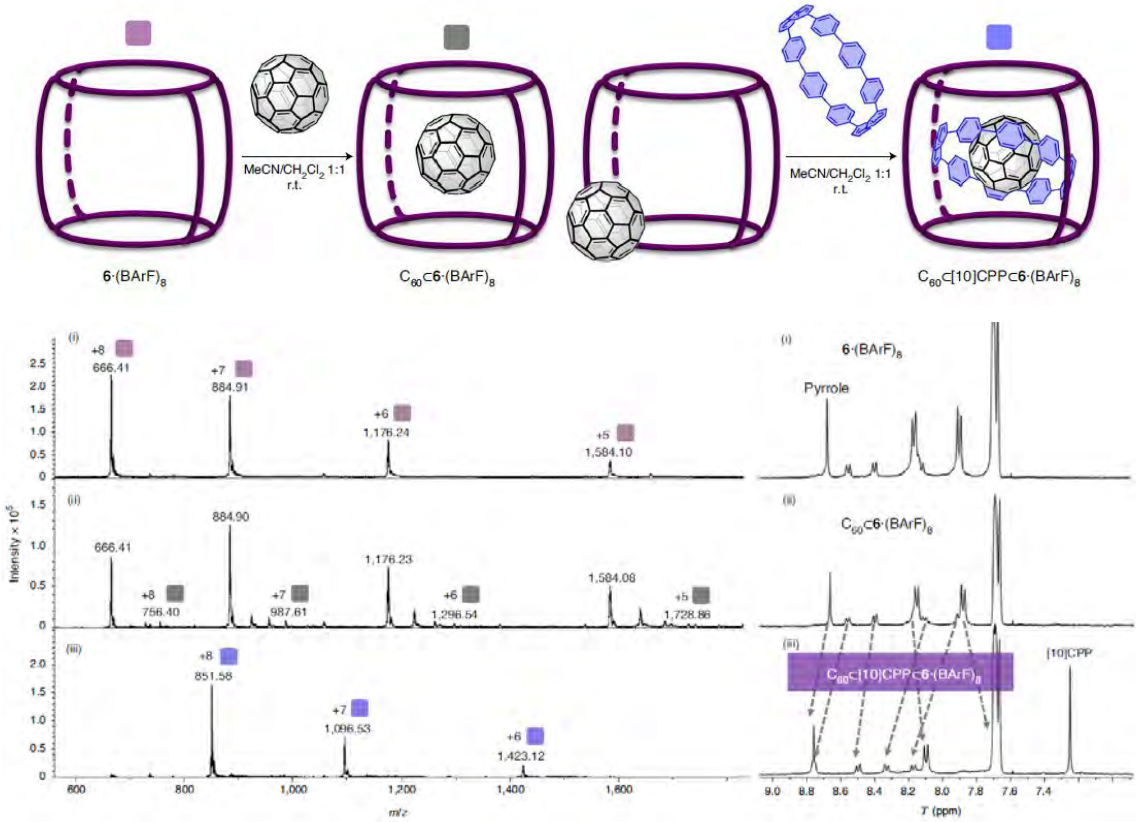

Figure V.9. (top) Schematic representation of the encapsulation of C_{60} in the nanocapsule **6**·$(BArF)_8$ and subsequent addition of [10]CPP (in MeCN/CH_2Cl_2 1:1 solvent mixture). (bottom left) HRMS (positive-ion electrospray ionization) and (bottom right) ^{1}H-NMR (in CD_3CN after solvent switch) for (i) **6**·$(BArF)_8$, (ii) **6**·$(BArF)_8$ with the addition of C_{60} and (iii) C_{60}⊂[10]CPP⊂**6**·$(BArF)_8$.

To delve into the study of the matryoshka-like complex we performed spectroscopic titration in toluene/acetonitrile 9:1, using the Thordarson and Stoddart approximation for three-component systems.[20, 21] Taking into account the previously determined strong affinity constant for the binary system C_{60}⊂[10]CPP, the latter was treated as a single guest for nanocapsule **6**·$(BArF)_8$, giving a binding isotherm that could be fitted with a 1:1 model and affording a K_a of 9.3 ± 0.4 × 10^6 M^{-1} (Figure V.10 and Tables S10 and S11 in Annex 1). With all these results in hand we concluded that the different bindings in the three-shell complex are relatively independent from one another and that any cooperativity, if present, would be moderate and positive.

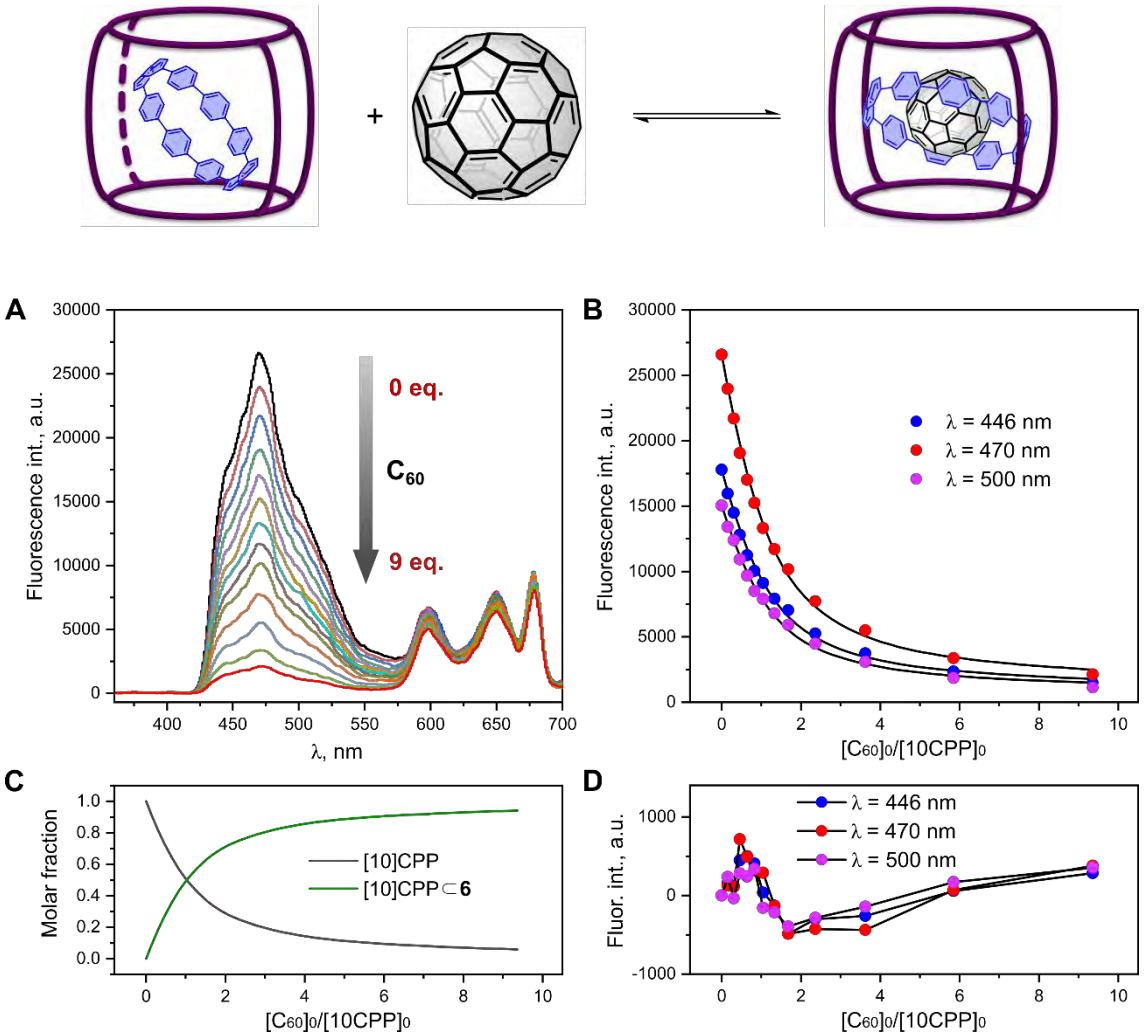

Figure V.10. Representative titration data for C_{60}⊂[10]CPP⊂**6**·$(BArF)_8$ host-guest system. Solvent: PhMe/MeCN. (A) Changes in emission spectra of [10]CPP (2.0×10^{-7} M, λ_{exc} = 340 nm) upon addition of C_{60} (0 - 1.9×10^{-6} M) in the presence of nanocapsule **6**·$(BArF)_8$ (6.1×10^{-6} M, 30 equiv. with respect to [10]CPP). (B) Fit of the titration data according to 1:1 binding model. (C) Dependence of molar fractions of [10]CPP and **C_{60}⊂[10]CPP** on relative amount of C_{60}. (D) Residual plots.

V.1.3. Crystal structure of C_{60}⊂[10]CPP⊂7·$(BArF)_8$

We succeeded in obtaining high-quality single crystals for the three-shell assembly of the Cu(II)-based nanocapsule, **7**·$(BArF)_8$ (Figure V.11 and Figure S95 in Annex 1). After many efforts, by using X-ray diffraction in a synchrotron facility, we could obtain the crystal structure of **C_{60}⊂[10]CPP**⊂**7**·$(BArF)_8$, showing the Saturn-like **C_{60}⊂[10]CPP** species inside the nanocapsule in a slightly tilted orientation with respect to the porphyrin planes (~15º). The vertical alignment is precluded due to the large diameter of [10]CPP (14 Å), whereas the nanocapsule features a Zn-porph···Zn-porph distance of 16.8 Å. Moreover, the guest was found in two equal positions (50% occupation), interacting the fullerene with the pyrroles

of the porphyrin, indicating an up and down motion. By NMR experiments we could confirm that this is a rapid equilibrium because we observe a singlet for the [10]CPP signal at 7.25 ppm, and another singlet as well for the pyrrole protons at 8.75 ppm (Figure V.9).

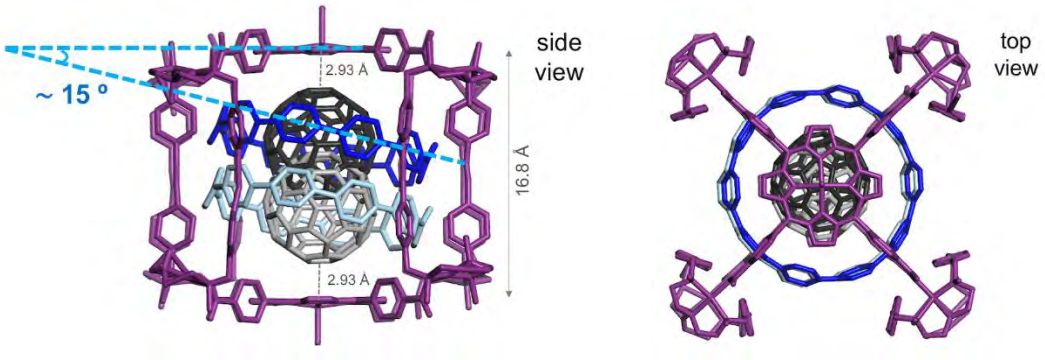

Figure V.11. Crystal structure of **C_{60}⊂[10]CPP⊂7**·$(BArF)_8$, showing 50% occupancy of **C_{60}⊂[10]CPP** in two positions inside the cavity of **7**·$(BArF)_8$ and featuring an up and down movement (side and top views).

V.1.4. Single-isomer *trans*-3 bis-adduct synthesis

The crystal structure of **C_{60}⊂[10]CPP⊂7**·$(BArF)_8$ proved that the combination of [10]CPP and the nanocapsule act as a steric mask that limits the exposed surface of the C_{60} fullerene, *i.e*. restricts the exposure of the [6,6] double bounds of the fullerene susceptible to be functionalized. Therefore, we then exposed the three-shell complex to Bingel cyclopropanation conditions, consisting in an excess of bromomalonate (5 equiv.) and NaH as base (5 equiv.) in acetonitrile (Figure V.12a). After 2.5 h stirring at room temperature, the full formation of the C_{60} bis-adduct was determined by HRMS (Figure V.12b). Despite the reaction time was increased, over-functionalization was not observed and this system afforded bis-adducts exclusively. In order to characterize the inner fullerene species, we added excess of C_{60} to the matryoshka, allowing the exchange of the bis-adduct by bare C_{60}. The latter is in agreement with the fact that encapsulation of (bis-adduct)⊂[10]CPP is significantly lower (K_a = 3.6 ± 0.5 × 10^5 M^{-1}) than for the **C_{60}⊂[10]CPP** (K_a = 9.3 ± 0.4 × 10^6 M^{-1}), as ascertained by UV-Vis titrations. After that, the released bis-C_{60} adduct species was characterized by HPLC obtaining a chromatogram with a major peak corresponding to the obtained bis-adduct, matching the UV-Vis spectrum for a Bingel cyclopropanation at a *trans*-3 substitution pattern.[22] Further purification through preparative TLC afforded pure ***trans*-3** bis-adduct in a high yield (76% for the diethyl bromomalonate, ***trans*-3-(1-C_{60})**). As it is depicted in Figure V.12a, once the functionalization reaction finished, a washing with $CHCl_3$ liberated a small amount of ***trans*-3-(1-C_{60})⊂[10]CPP** adduct. By adding excess of C_{60} we

obtained the bis-adduct in a 14% yield, as confirmed by UV-Vis (Figure V.12d) and HPLC (Figure V.13). Altogether, ***trans*-3** isomer was solely formed, with an excellent total yield of 90% for ***trans*-3-(1-C_{60})**.

Remarkably, the exclusive ***trans*-3** bis-adduct formation using the three-shell strategy contrasts with the mixture of multiple-addition products with uncontrolled regioselectivity (with no trace of bis-adducts) obtained for the non-templated functionalization of C_{60} (Figure V.13).

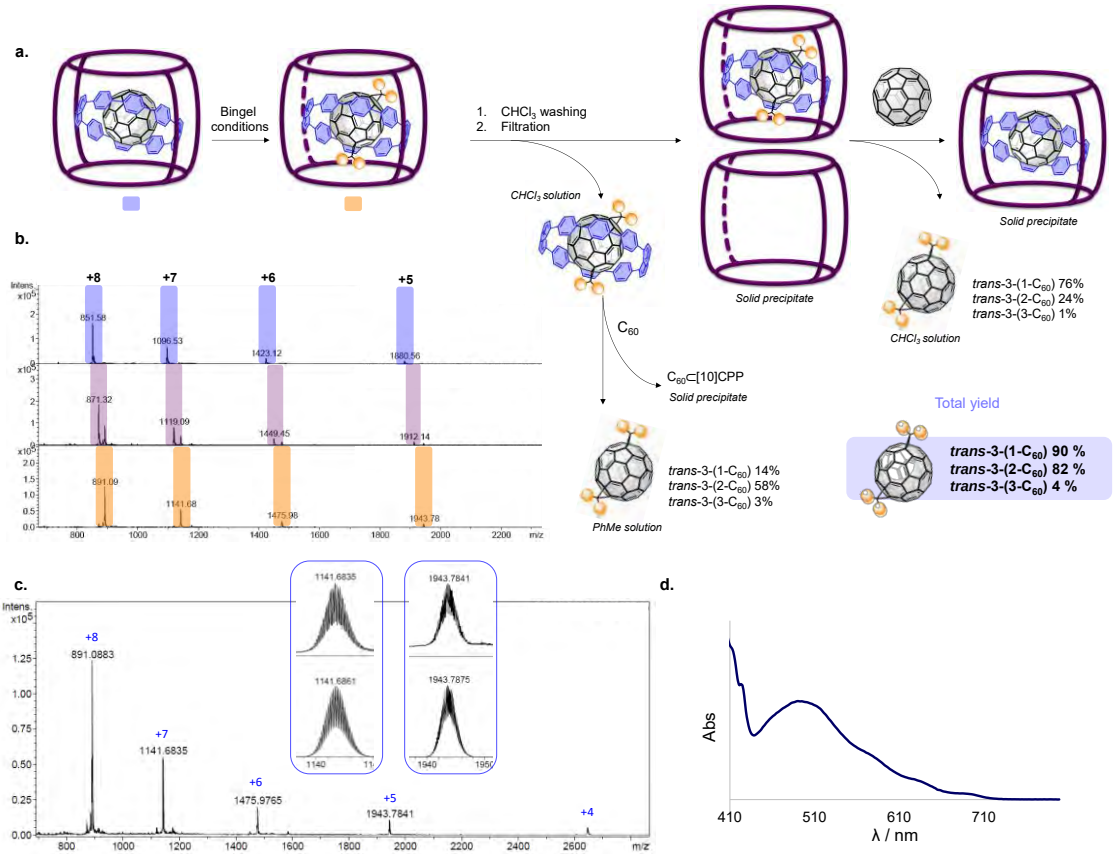

Figure V.12. (a) Schematic representation of Bingel cyclopropanation reaction and work-up procedure. (b) HRMS monitoring of the ***trans*-3-(1-C_{60})** bis-adduct formation. (c) HRMS spectra of ***trans*-3-(1-C_{60})⊂[10]CPP⊂6·$(BArF)_8$**. Experimental (top) and calculated (bottom) for +7 and +5 charged m/z peaks. (d) UV-Vis of the ***trans*-3-(1-C_{60})**.

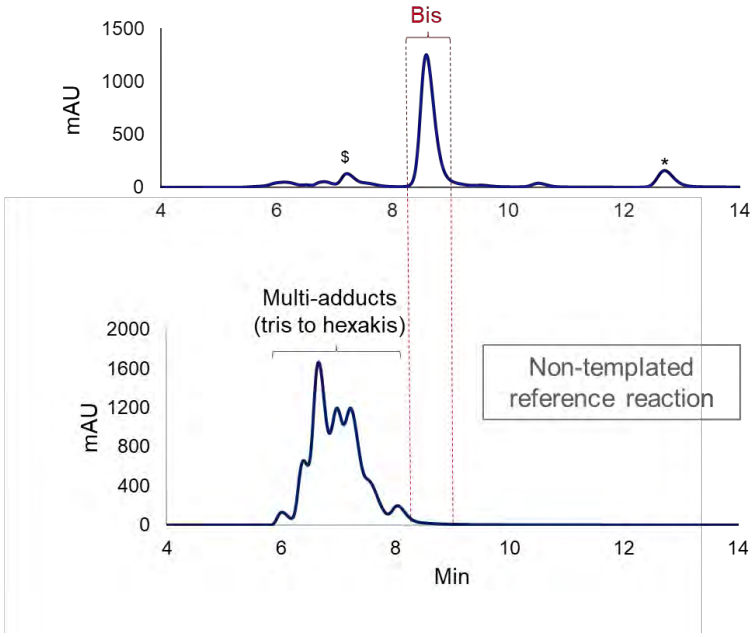

Figure V.13. HPLC analysis of (top) the extracted ***trans*-3-(1-C_{60})** bis-adduct compared to (bottom) the mixture of polyadducts obtained with bare C_{60} (performed using 5 equiv. NaH in MeCN/1,2-dichlorobenzene 1:4 to achieve solubility of pristine C_{60}, 3h, r.t.) (λ=320 nm; *C_{60}; $non-fullerene impurities).

Remarkably, single crystals of ***trans*-3-(1-C_{60})⊂[10]CPP⊂7**·$(BArF)_8$ were also obtained analyzed by XRD at the synchrotron facility. Although the complexity of the structure and the fragility of the crystals lead to a low-resolution crystal structure, we could determine a similar arrangement of the initial matryoshka-like structure, but with a considerable change in the tilted angle of the [10]CPP ring, which was ~26º (Figure V.14 and Figure S96 in Annex 1) compared to the previous 15º (Figure V.11). This torsion suggested that the presence of the functionalized fullerene species induced a steric crowding within the three-shell complex. The location of the two functional groups, which was identified from analysis of the difference Fourier maps, imposed the steric effect that explained the selectivity to give the ***trans*-3** isomer. Since the latter features a 120º angle between the two functional groups but the nanocapsules gates feature a 90º angle, a symmetry mismatched functionalization is achieved. Given the [10]CPP titled arrangement within the nanocapsule, basically a single possibility to locate the malonate groups exists, which is by accessing through contiguous windows of the nanocapsule. The strained environment of the bis-adduct was further confirmed with ^{1}H-NMR spectrum of the ***trans*-3-(1-C_{60})⊂[10]CPP⊂6**·$(BArF)_8$ (see Figure S79 in Annex 1). The signal for the pyrrole, which appeared as a singlet in the initial structure, evolved into a multiplet once the fullerene is functionalized, indicating the loss of the symmetry in the structure (Figure V.15).

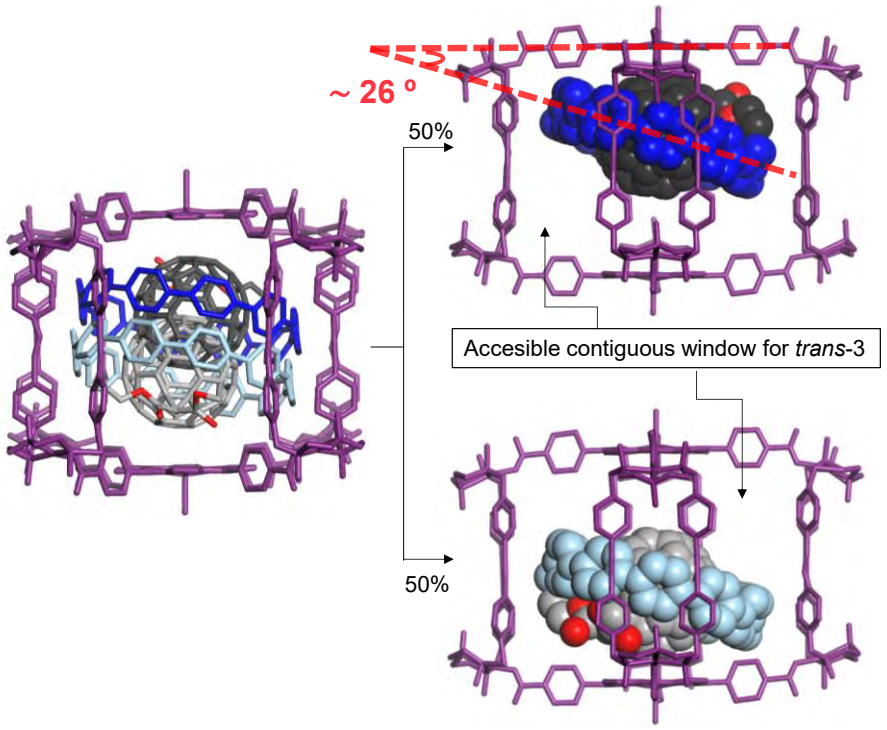

Figure V.14. View of three-component assembly as determined by single-crystal XRD refinement of ***trans*-3-(1-C$_{60}$)⊂[10]CPP⊂7**·(BArF)$_8$.

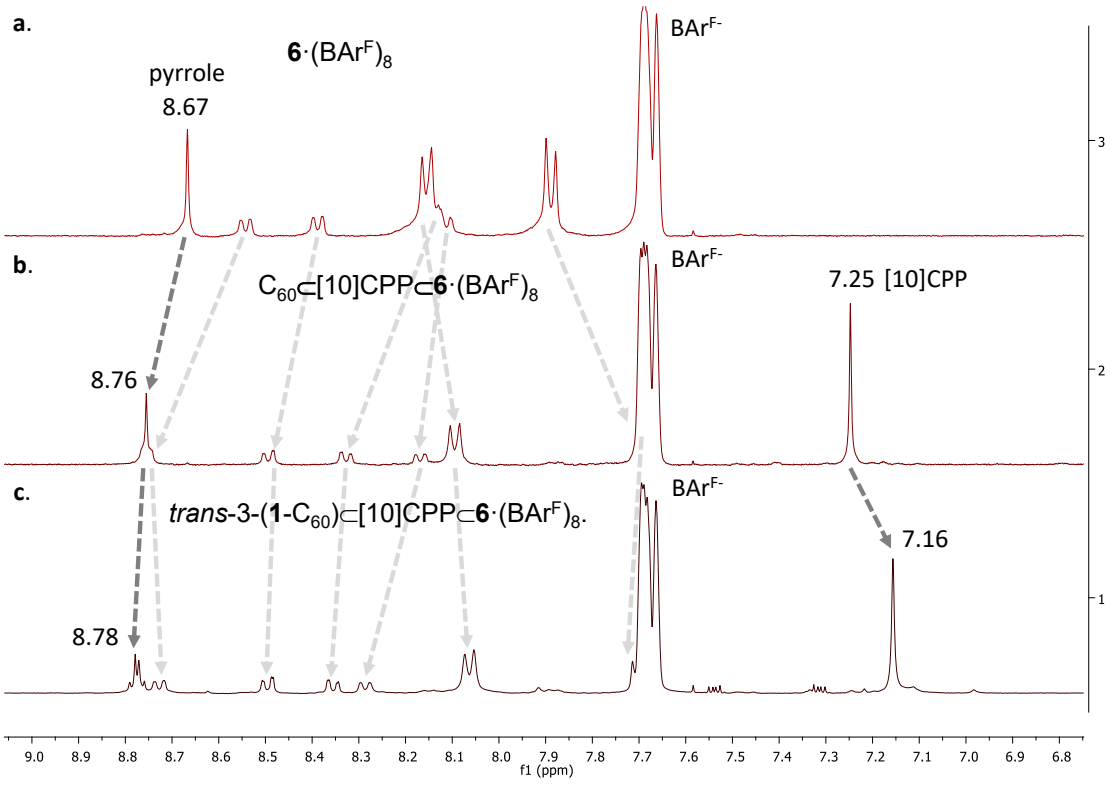

Figure V.15. Comparative ^{1}H-NMR spectrum (CD_3CN, 400 MHz, 298 K) of (a) **6**·(BArF)$_8$, (b) **C$_{60}$⊂[10]CPP⊂6**·(BArF)$_8$ and (c) ***trans*-3-(1-C$_{60}$)⊂[10]CPP⊂6**·(BArF)$_8$.

At this point, we decided to test the generality of the observed ideal chemoselectivity (bis-adduct) and the symmetry-mismatched *trans*-3 regioselectivity. To that end, bromomalonates with different bulkiness, *i.e.* di-isopropyl (**2**) and dibenzyl (**3**) bromomalonates (Figure V.16 and Figures S68 and S69 in Annex 1) were tested under identical reaction Bingel cyclopropanation conditions. For both **2** and **3** bromomalonates, the ***trans*-3** bis-adducts were obtained exclusively, even though the yield depends a lot on the steric bulk of the malonate substituents (Figure V.17). For isopropyl bromomalonate (**2**) the total yield slightly decreased to 82%, with respect to the 90% obtained for diethyl bromomalonate (**1**). On the other hand, the partial yields were opposed to **1**, since $CHCl_3$ washing afforded a 58% yield of ***trans*-3**-(**2**-$\mathbf{C_{60}}$), whereas C_{60}-exchange with the functionalized three-shell Matryoshka only afforded 24% yield. Finally, talking about the dibenzyl bromomalonate (**3**), the total yield was 4%, indicating the high steric hindrance and the narrow space available to reach the fullerene surface. To study in depth these results we performed void space analysis, confirming that there is a trend in agreement with the Rebek's rule (Figure V.18). The volume occupancy for ***trans*-3**-(**1**-$\mathbf{C_{60}}$)⊂**[10]CPP** inside the nanocapsule is 53% that is below 55% Rebek's rule,[23] for that reason there is a low amount of guest expelled (14%) during the $CHCl_3$ washing. The volume occupancy for ***trans*-3**-(**2**-$\mathbf{C_{60}}$)⊂**[10]CPP** is 56% (slightly above 55% Rebek's rule), which leads to more quantity of guest release (58%) by $CHCl_3$ washing. Finally, for ***trans*-3**-(**3**-$\mathbf{C_{60}}$)⊂**[10]CPP**, the volume occupancy is 61%, far beyond 55% Rebek's rule, confirming first the low total yield (4%) obtained for this reaction and second, that the majority of the product expelled was by solvent washing (Figure V.18). Substrates with higher steric bulk (for example, di-tert-butyl bromomalonate, **4**) represent the steric limitation of the three-shell system, since no reaction was observed. In conclusion, there is a perfect selectivity in all substrate scope, however the steric bulk represents a limitation in terms of reaction rates and yields. For substrates with low to moderate bulk (for example diethyl and di-isopropyl) selectivity is perfect and the reaction rate and yields are very high, while for substrates with moderate to high steric bulk (for example, dibenzyl) selectivity remains perfect but yields decrease abruptly.

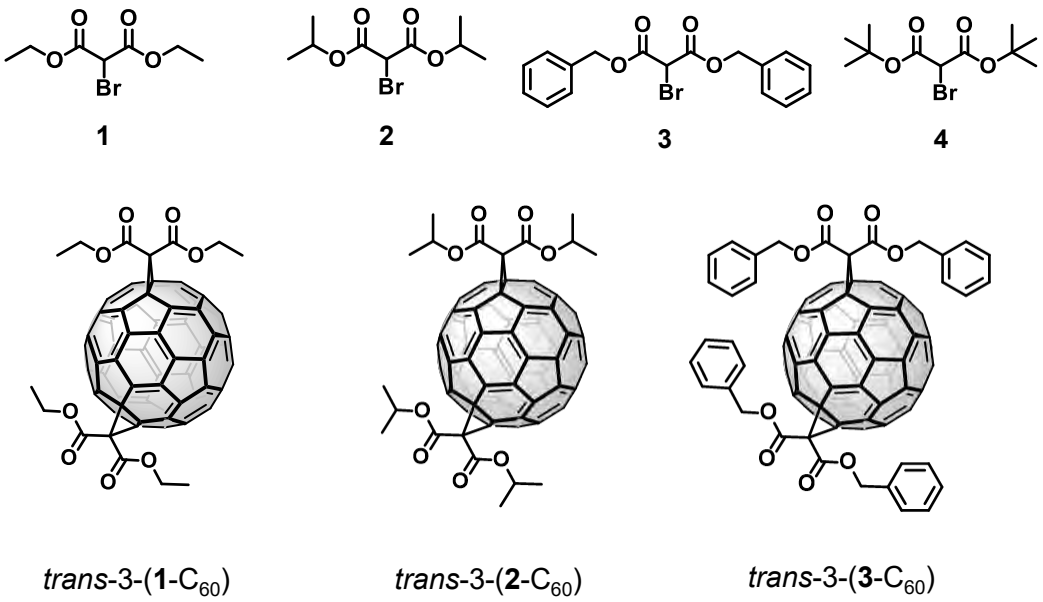

Figure V.16. Scope of bromomalonates (top): diethyl bromomalonate (**1**), di-isopropyl bromomalonate (**2**), dibenzyl bromomalonate (**3**) and di-tert-butyl bromomalonate (**4**) and bis-functionalized ***trans*-3** products (bottom).

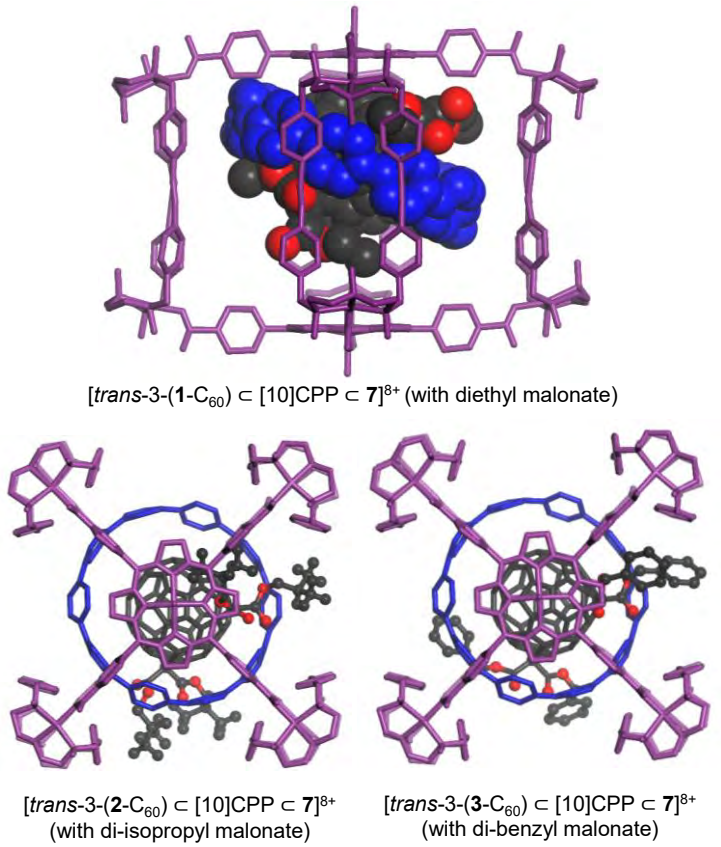

Figure V.17. Different representations of the ***trans*-3-(1-C60)⊂[10]CPP**, ***trans*-3-(2-C60)⊂[10]CPP** and ***trans*-3-(3-C60)⊂[10]CPP** models inside the nanocapsule featuring the 120° bis-functionalization at contiguous windows of the tetragonal prismatic host. The orientation of the malonate substituent groups (ethyl, isopropyl or benzyl) was geometrically optimized with a universal-forcefield-based minimization process, as implemented in the Forcite module of Materials Studio software (2019 version, BIOVIA).

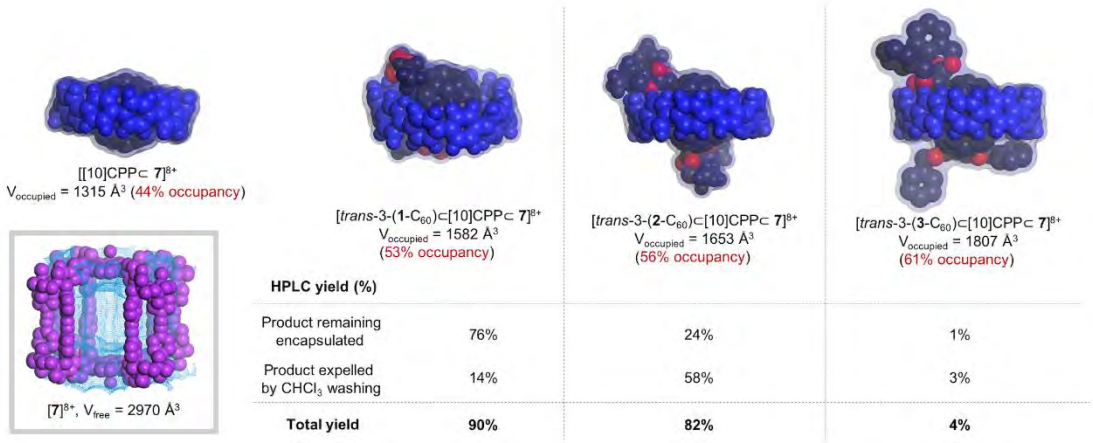

Figure V.18. Void analysis study of the free accessible volume of the nanocapsule and volume occupancies of the different guests correlated with the yields of the ***trans*-3** adducts obtained from the workflow described in Figure V.12a.

In summary, it has been developed an unprecedented three-shell heteroleptic Matryoshka-like assembly, **C_{60}⊂[10]CPP⊂X**·$(BArF)_8$ (X = **6**-**7**). Spectroscopic titrations and crystallographic data have given us an understanding of the thermodynamic stability of the overall assembly. Bingel cyclopropanation conditions afforded 100% regioselectivity in the bis-functionalization of C_{60} obtaining the ***trans*-3** bis-adduct with different bromomalonates. High yields have been obtained for those bromomalonates with low steric bulkiness whereas bromomalonates like dibenzyl-bromomalonate have shown low yields due to the steric hindrance.

V.2. Straightforward supramolecular purification of C_{84} from a fullerene extract

In this chapter we will focus on the ability of supramolecular nanocapsules with large cavity sizes to host higher fullerenes and azafullerene $(C_{59}N)_2$. Since the biphenyl-based nanocapsule (**4**·$BArF)_8$ showed high affinity for C_{60} we envisioned the putative ability of the new pTp-based nanocapsule, (**7**·$BArF)_8$, to encapsulate higher fullerene species such as the C_{84}. Moreover, new large terphenyl-based nanocapsules, **X**·$(BArF)_8$ (X = 8-9), will be developed and tested as host for bulky fullerenes as azafullerene $(C_{59}N)_2$.

V.2.1. Selective encapsulation of C_{84} in **7**·$(BArF)_8$ from fullerene extract

In order to expand the applications for our Pd-based **6**·$(BArF)_8$ and Cu-based **7**·$(BArF)_8$ nanocapsules we tested them for selective encapsulation of a soot mixture of higher fullerenes, envisioning their large cavity would be a host for higher fullerenes. These nanocapsules comprise a distance between porphyrins of 16.8 Å and previous results showed a low affinity for fullerenes like C_{60}. Thus, **7**·$(BArF)_8$ was exposed to 100 equiv. of fullerene extract (70% C_{60}, 28% C_{70} and 2% higher fullerenes) at r.t and using toluene:CH_3CN 9:1 as a solvent. By adding 100 equiv. of fullerene extract we envisioned that at least 2 equiv. of higher fullerenes were exposed to the nanocapsule. After 12 hours, it was observed by HRMS monitoring that the nanocapsule remained empty, for this reason larger times were tested. Despite the low content of higher fullerenes, after 7 days, m/z ions corresponding to C_{84}⊂**7**·$(BArF)_8$ were detected as the major thermodynamic product by HRMS (Figure V.19). The selectivity in the encapsulation of C_{84} indicated an ideal size and shape complementarity between the fullerene and the host. The inner product was released after the addition of triflic acid to disassemble the nanocapsule, consisting of C_{84} as shown by MALDI mass spectrometry (m/z = 1008.24, Figure V.20).

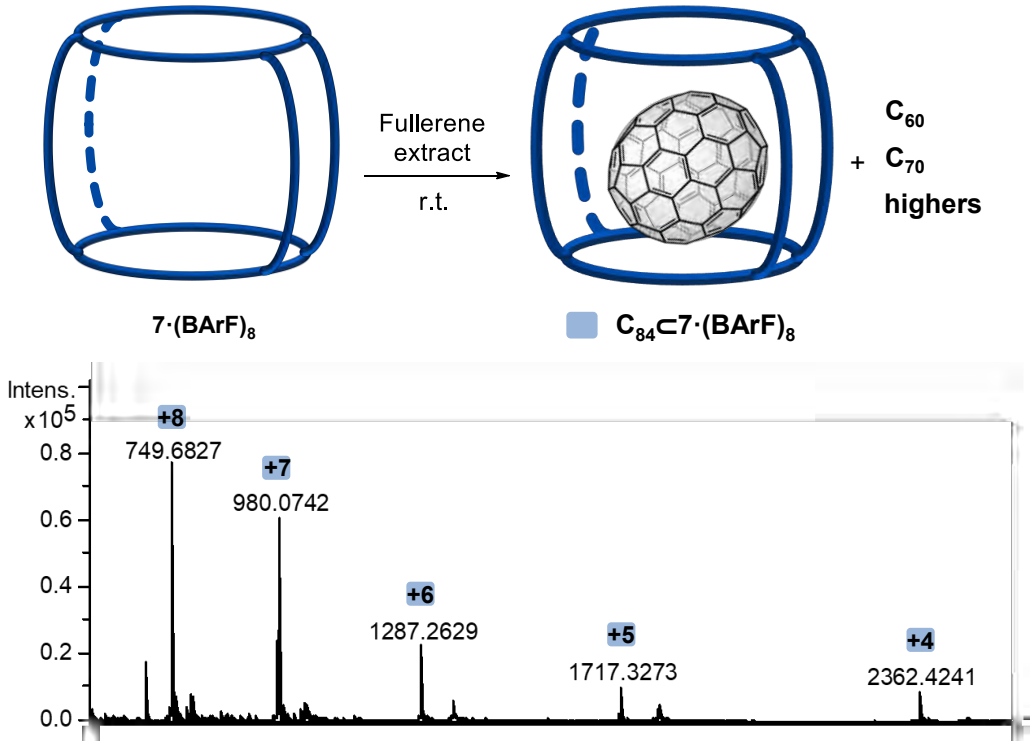

Figure V.19. Schematic representation of the selective encapsulation of C_{84} in nanocapsule **7**·$(BArF)_8$ from a fullerene extract and HRMS (ESI^+) monitoring for **7**·$(BArF)_8$ upon the addition of 100 equiv. of fullerene extract and stirring at room temperature for 7 days in toluene.

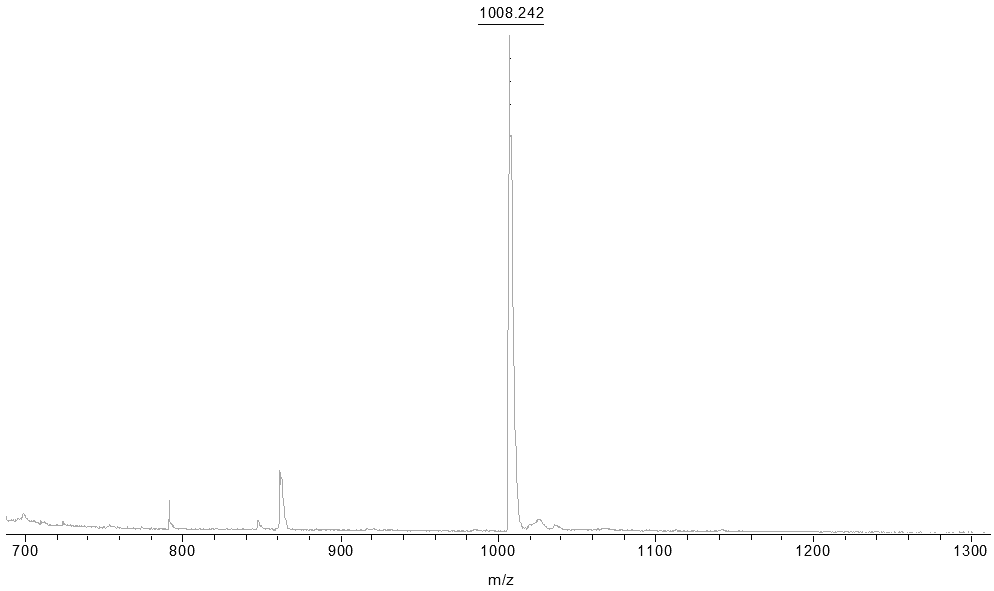

Figure V.20. MALDI-TOF spectra of purified C_{84} released from the nanocapsule.

However, with an accurate examination of HRMS spectra other m/z ions were found, suggesting the encapsulation of fullerenes C_{70}, C_{76}, C_{78}, C_{82}, C_{86}, C_{88}, C_{90}, C_{92}, C_{94} and C_{96}, despite their low amount in the initial mixture (Figure V.21a). To enhance the selectivity for the C_{84} species we performed solid/liquid biphasic experiments (nanocapsule as a solid suspension and fullerene extract dissolved in toluene). At 12 hours, as observed by ESI-MS, the nanocapsule was remaining partially empty but the spectra already showed $C_{84}\subset$**7**$\cdot(BArF)_8$ m/z ions (Figure V.21b). After 7 days significant improvements were observed: the $C_{70}\subset$**7**$\cdot(BArF)_8$ and $C_{76}\subset$**7**$\cdot(BArF)_8$ m/z ions disappeared and the ones corresponding to other encapsulated higher fullerenes decreased with respect to the $C_{84}\subset$**7**$\cdot(BArF)_8$ m/z ions (Figure V.21c). The comparison was performed considering the relative intensity of the m/z peaks with respect to the C_{84} m/z peak in the HRMS spectra. The peak intensity corresponding to C_{78} was decreased from 6.4% to 1.7%, that for C_{82} decreased from 10.7% to 3.4%, that for C_{86} decreased from 14.3% to 13.3%, that for C_{88} decreased from 4.8% to 3.3%, that for C_{90} decreased from 10.7% to 5.0%, that for C_{92} decreased from 6.2% to 3.3%, and finally, the m/z peak intensities for C_{94} and C_{96} slightly decreased from 3.5% to 3.3%. Thus, the C_{84} was the most thermodynamically favored guest among all fullerenes present in the extract.

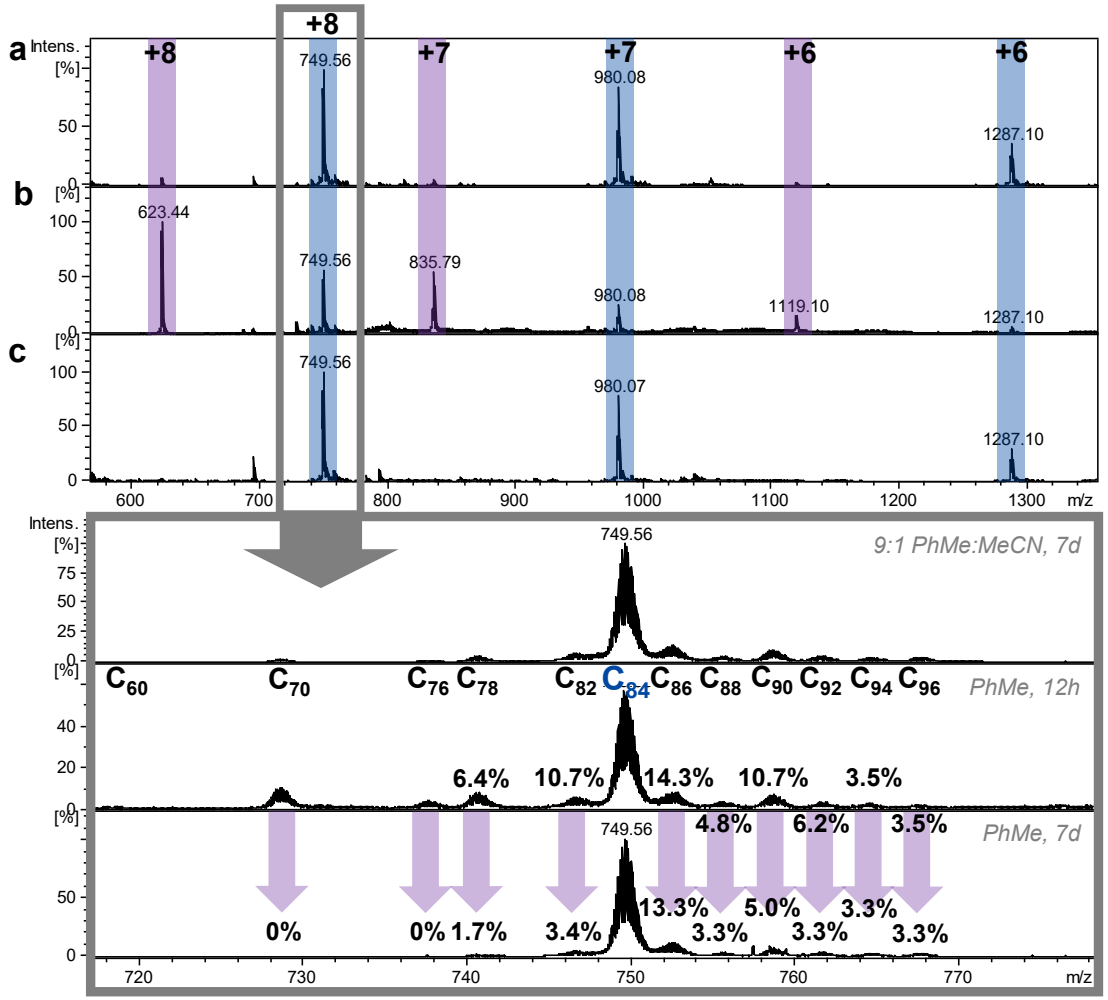

Figure V.21. Study of the binding affinity in solution/solid phase. HRMS (ESI⁺) monitoring for encapsulation of the C_{84} fullerene. (a) **7**·$(BArF)_8$ in solution (toluene:CH_3CN, 9:1), 100 equiv. of fullerene extract, r.t., 7 days (liquid/liquid). (b) **7**·$(BArF)_8$ in the solid state (suspension in toluene), 100 equiv. of fullerene extract, r.t., 12 hours. (c) **7**·$(BArF)_8$ in the solid state (suspension in toluene), 100 equiv. of fullerene extract, r.t., 7 days.

The quantification was performed after disassembling the nanocapsule upon acid treatment and injecting the released products to HPLC (Figure V.22a and Table S1 in Annex 2). Integration of the peaks in the HPLC indicated a remarkable ~125-fold enrichment of C_{84} (from 0.7 % in the initial fullerene extract to 86% in the encapsulated mixture). By selective collection of the peak corresponding to C_{84} (see Figure S13 in Annex 2), 2.2 mg of pure C_{84} were isolated and ^{13}C-NMR spectroscopy was attempted to characterize it among different C_{84} isomers (see Figure S17 in Annex 2). However, very weak peaks were obtained, so we moved to careful inspection of the UV-Vis spectrum of C_{84} released from the nanocapsule (HPLC-DAD), pointing towards the accumulation of C_{84}-D_2(22) isomer (Figure V.22b). The latter is in agreement with the fact that C_{84}-D_2(22) and C_{84}-D_{2d}(23) are the two main isomers

of C_{84} present in the fullerene extract, thus indicating a slight preference of nanocapsule **7**·$(BArF)_8$ to bind C_{84}-D_2(22) among all IPR-isomers contained in the starting fullerene extract. Once characterized, the C_{84}-D_2(22) isomer was again encapsulated obtaining a clean HRMS-ESI to demonstrate the selectivity towards this species and avoiding the trace signals for other higher fullerenes (Figure V.23).

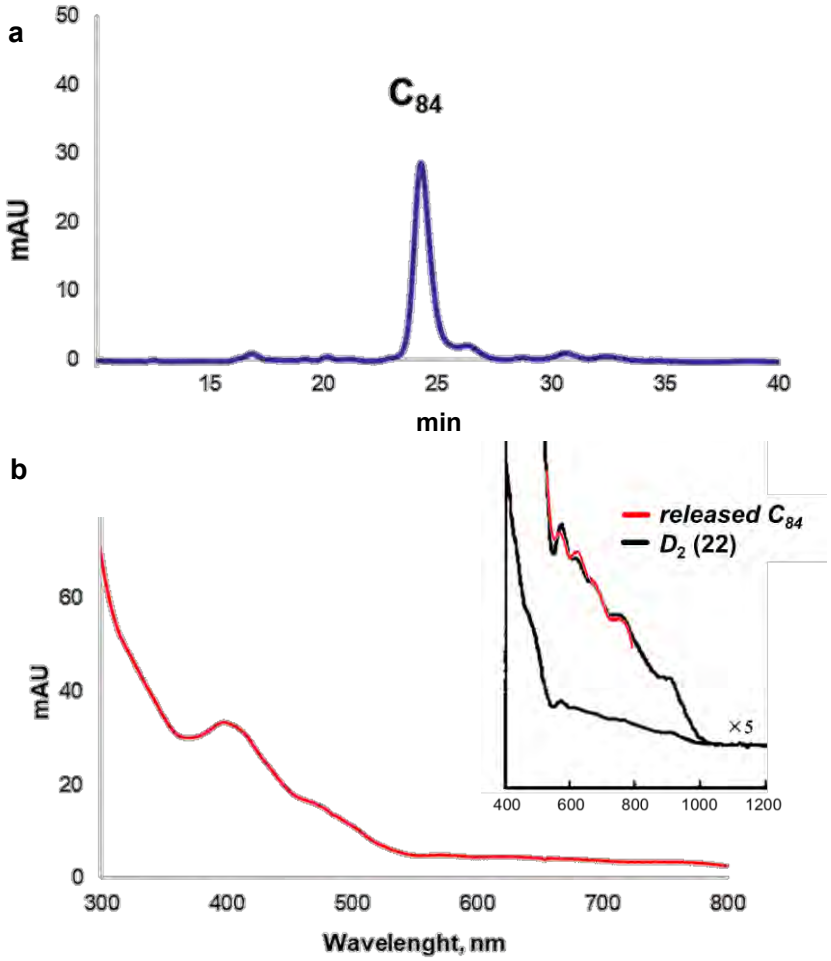

Figure V.22. (a) HPLC-DAD chromatogram recorded after the disassembly of the nanocapsule. (b) UV-Vis spectra of the peak at 24.3 min corresponding to the C_{84} fullerene [inset showing the amplification of the 500-800 nm range and matching with the reported spectrum for isomer C_{84}-D_2(22).

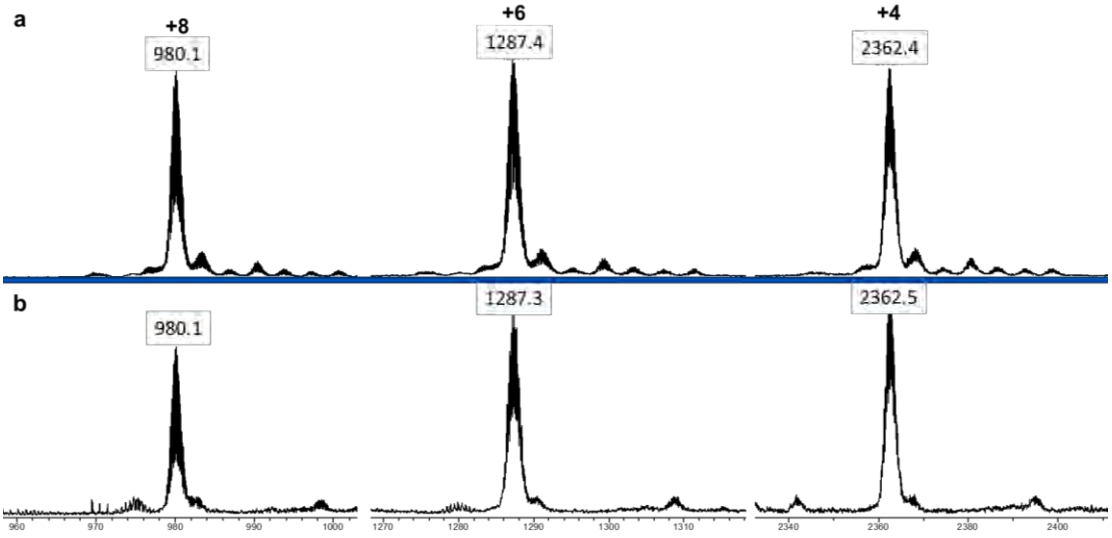

Figure V.23. HR-MS-ESI spectrum (a) after encapsulation of fullerene extract to **7**·(BArF)$_8$ and (b) after encapsulation of the purified C_{84} to **7**·(BArF)$_8$. The most intense m/z peaks correspond to C_{84}⊂**7**·(BArF)$_8$.

V.2.2. Synthesis and characterization of the extended nanocapsules 8·(BArF)$_8$ and 9·(BArF)$_8$

Two new nanocapsules, **8**·(BArF)$_8$ and **9**·(BArF)$_8$, with an enlarged cavity of 18.4 Å were synthesized aiming at binding larger fullerenes species (Figure V.24). We used the self-assembly strategy with two porphyrin units and four molecular clips. The first step, consisting in synthesizing the terphenyl-based dialdehyde (ppp), was developed following a reported procedure.[24] The synthesis is based on a Suzuki-Miyaura coupling reaction of 1 equiv. 1,4-phenylenediboronic acid with 2 equiv. of 4-bromobenzaldehyde, thus obtaining the desired ppp dialdehyde. After the addition of DETA, the macrocycle S_2ppp was obtained which was then submitted to hydrogenation (H_2ppp), methylation (Me2ppp), and metalation steps. We synthesized in a quantitative manner both Pd- and Cu-based macrocyclic clips and they were characterized by means of NMR and HRMS. In the case of the Cu analogue [Cu_2(Me_2ppp)]·$(OTf)_4$, we obtained single crystals to perform XRD analysis (Figure V.25). Finally, the self-assembly with Zn-porphyrin and counteranion exchange proceeded the same way as for the previous reported nanocapsules as depicted in Figure V.26.[14] The Pd-based nanocapsule, **8**·(BArF)$_8$, was characterized by 1D and 2D-NMR experiments (see Figures S62-S69 in Annex 2) and HRMS (Figure V.27) while the paramagnetic Cu-based nanocapsule, **9**·(BArF)$_8$, was characterized by HRMS (Figure V.28).

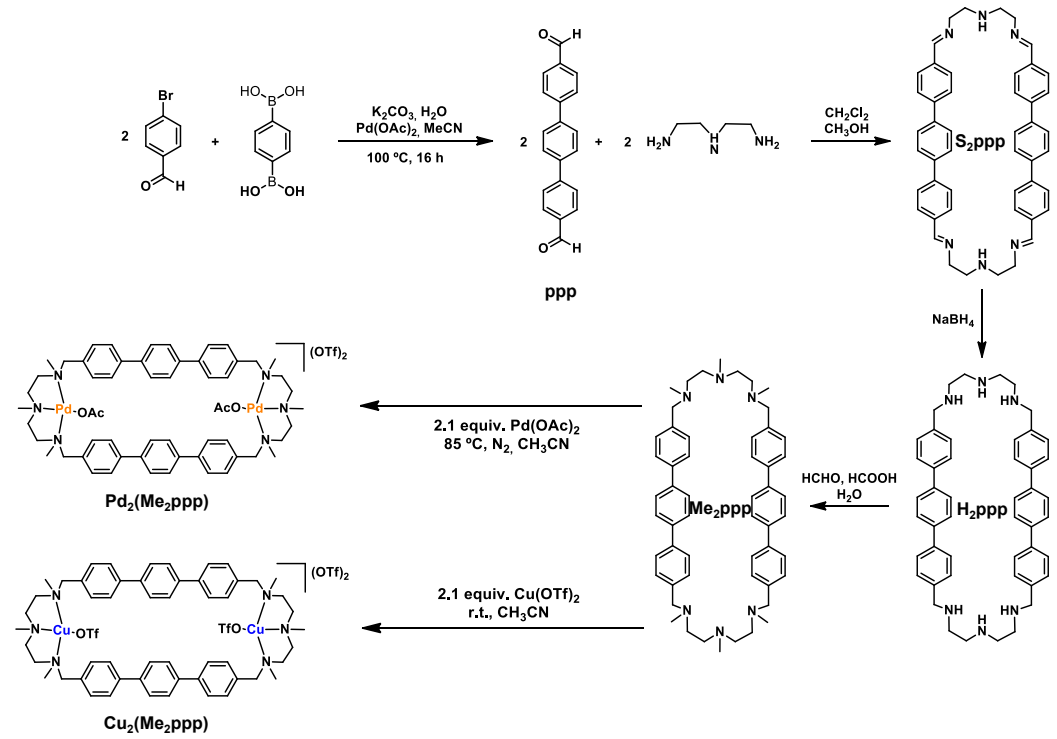

Figure V.24. Reaction steps required to obtain the $[Cu_2(Me_2ppp)]\cdot(OTf)_4$ and $[Pd_2(Me_2ppp)(OAc)_2]\cdot(OTf)_2$ molecular clips from the dibenzaldehyde (ppp).

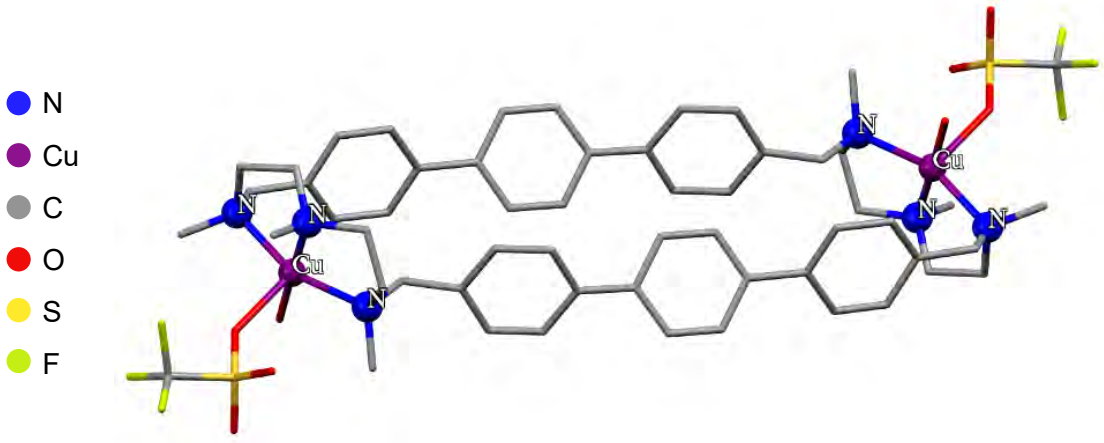

Figure V.25. XRD for $[Cu_2(Me_2ppp)]\cdot(OTf)_4$ clip.

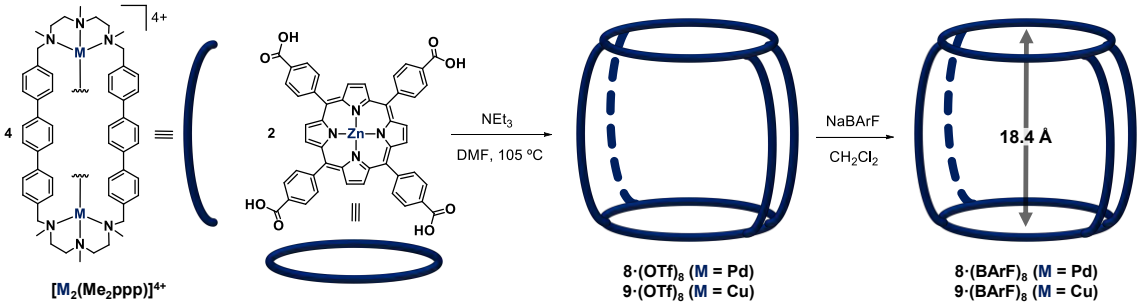

Figure V.26. Synthesis of terphenyl-based tetragonal prismatic nanocapsules **8**·$(BArF)_8$ (Pd-based) and **9**·$(BArF)_8$ (Cu-based).

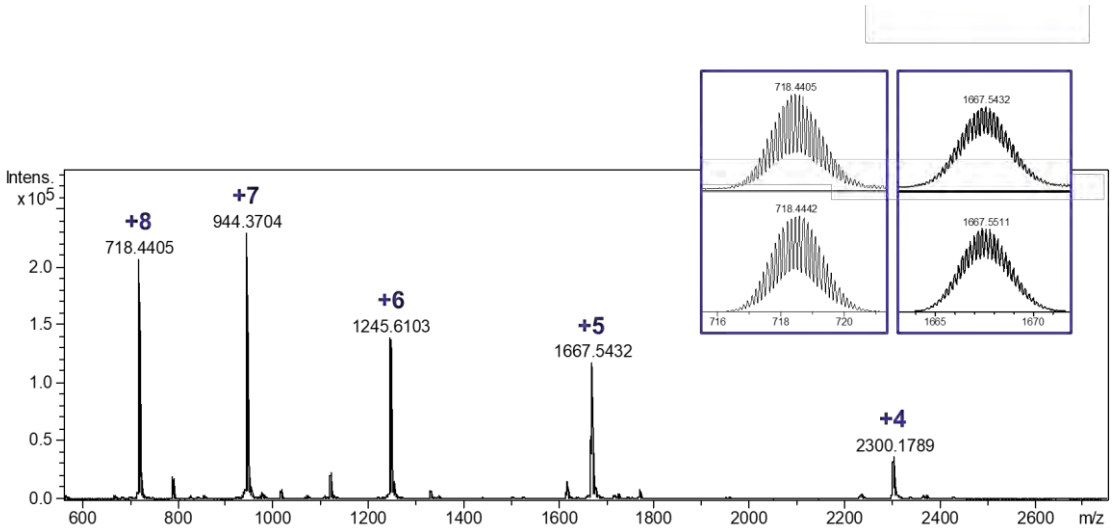

Figure V.27. HRMS spectrum of the Pd-based nanocapsule **8**·$(BArF)_8$. Experimental (top) and theoretical (bottom) isotopic pattern for selected peaks is shown.

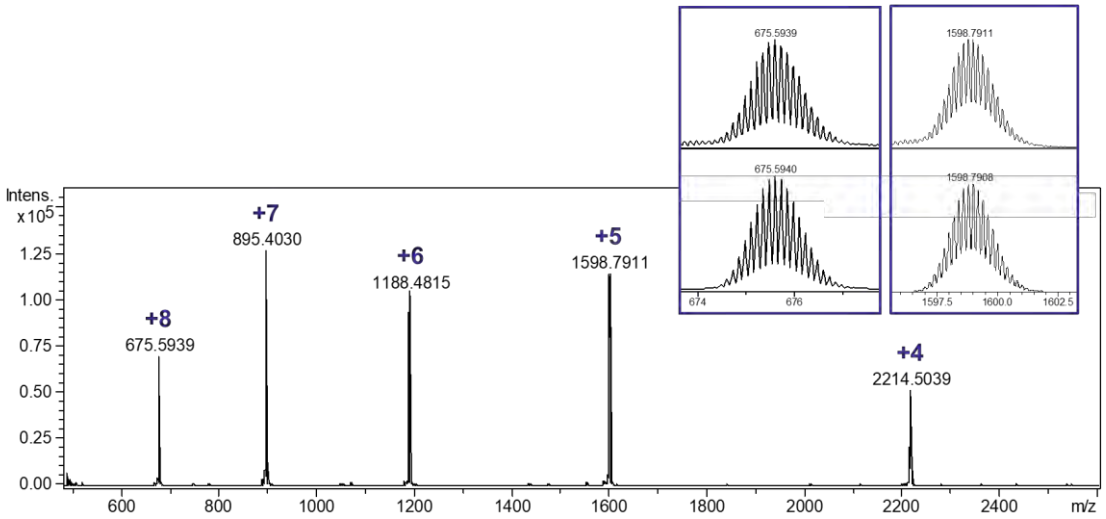

Figure V.28. HRMS spectrum of the Cu-based nanocapsule **9**·$(BArF)_8$. Experimental (top) and theoretical (bottom) isotopic pattern for selected peaks is shown.

V.2.3. Encapsulation of $(C_{59}N)_2$ in different sized nanocapsules, association constant calculations and competitive experiments

Both nanocapsules were exposed to a fullerene extract (70% C_{60}, 28% C_{70} and 2% higher fullerenes), however none of the higher fullerenes were encapsulated and the HRMS monitoring showed mainly m/z ions corresponding to empty nanocapsule, even at large time scale (Figure V.29). This clearly indicated that the cavities of nanocapsules **8** and **9** were too large to stabilize any of the higher fullerenes present in the extract.

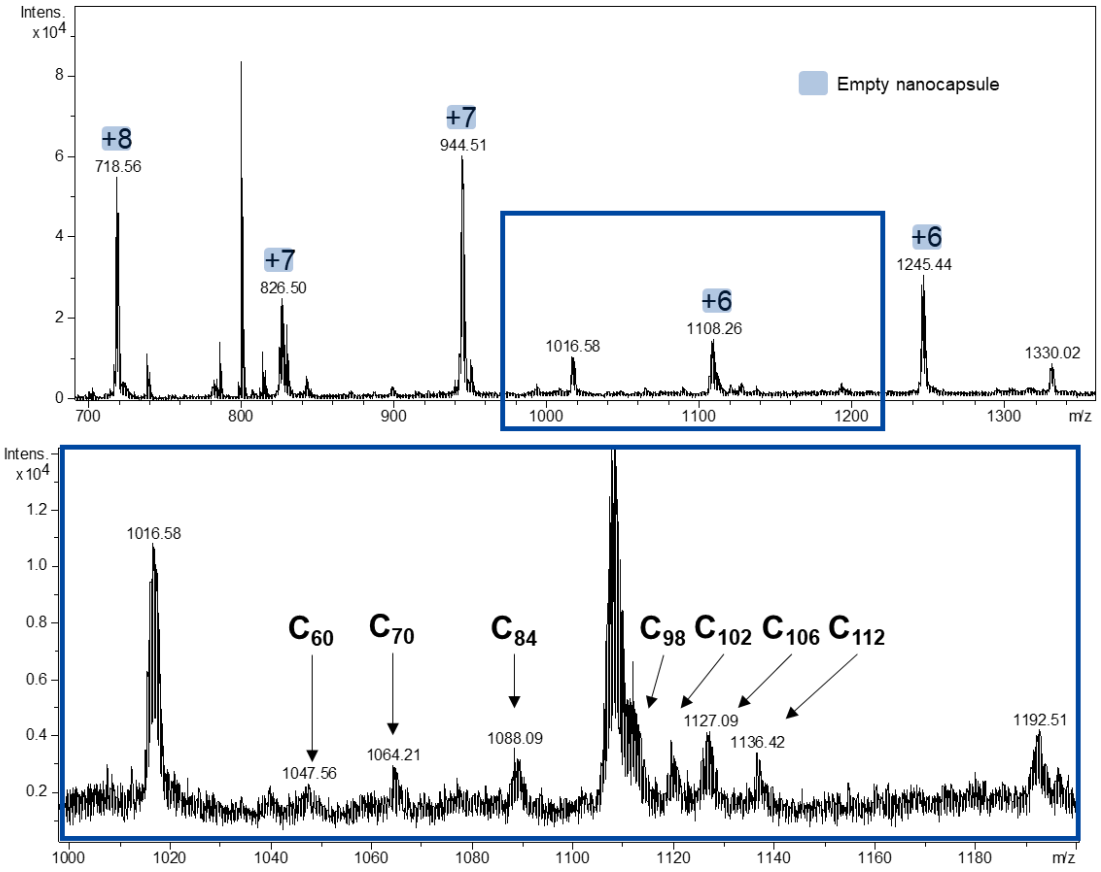

Figure V.29. HR-MS-ESI after the addition of 100 equiv. of fullerene extract to **8**·$(BArF)_8$ at r.t. for 7 days in the solid state (suspension in toluene). Identified fullerene⊂**8** m/z peaks correspond to 7+ charged. m/z 1016.58 corresponds to $\mathbf{8}^{7+}$ and m/z 1108.26 corresponds to $\mathbf{8}^{6+}$·2Cl^-.

At this point, we decided to study the affinity of the terphenyl-based nanocapsules **8**·$(BArF)_8$ and **9**·$(BArF)_8$ over a new guest: the dumbbell-shaped azafullerene $(C_{59}N)_2$. The binding of the $(C_{59}N)_2$ guest to **8**·$(BArF)_8$ and **9**·$(BArF)_8$ hosts were both quite strong, showing association constants of 4.3 ± 1.0 × 10^7 M^{-1} for the Pd-based nanocapsule and 1.3 ± 0.6 × 10^7 M^{-1} for the Cu-analogue, calculated by UV-Vis titration experiments (see Table V.1 and Figures S24-S25 in Annex 2). Then, the affinity constant was calculated for the smaller (ethyne-1,2-diyl)-based nanocapsules, showing a decrease in the binding ability with respect the terphenyl-based ones: K_a = 1.0 ± 1.1 × 10^7 M^{-1} for **6**·$(BArF)_8$ (Figure V.30) and K_a = 1.6 ± 0.1 × 10^6 M^{-1} for **7**·$(BArF)_8$ (Figure S23 in Annex 2). The same procedure with the smallest biphenyl-based nanocapsule **4**·$(BArF)_8$ featuring a cavity height of 14.1 Å was performed and reported by our group in 2020.[9] That one showed the lowest of the affinity constant series (K_a = 9.4 ± 0.5 × 10^5 M^{-1}). These findings showed a clear trend, indicating that the smaller the cavity, the lower is the affinity. The latter is in agreement with the hypothesis that the guest would fit horizontally to the host for the smallest nanocapsule, with one fullerene interacting with the two porphyrins and the other one located at an

entrance gate. A similar binding can be hypothesized for **6**·$(BArF)_8$ and **7**·$(BArF)_8$, presenting in this case with a tilted orientation, allowing the interaction of the one fullerenic sphere with one Zn-porphyrin. Finally, the biggest nanocapsule **8**·$(BArF)_8$ features a porph-porph distance of 18.4 Å, which suggest that a guest of ~15 Å along the long axis would fit in the cavity, and $(C_{59}N)_2$ meets the shape-requirements to the placed in a vertical orientation, in line with the high affinity constant found.

Table VI.1. Comparison of different binding constants. Solvent: PhMe/MeCN/o-DCB (9:1:0.09). *K_a previously reported in ref [9]

Nanocapsule	K_a (M^{-1})
4*	9.2 (± 0.5) x 10^5
7	1.6 (± 0.1) x 10^6
6	1.0 (± 1.1) x 10^7
9	1.3 (± 0.6) x 10^7
8	4.3 (± 1.0) x 10^7

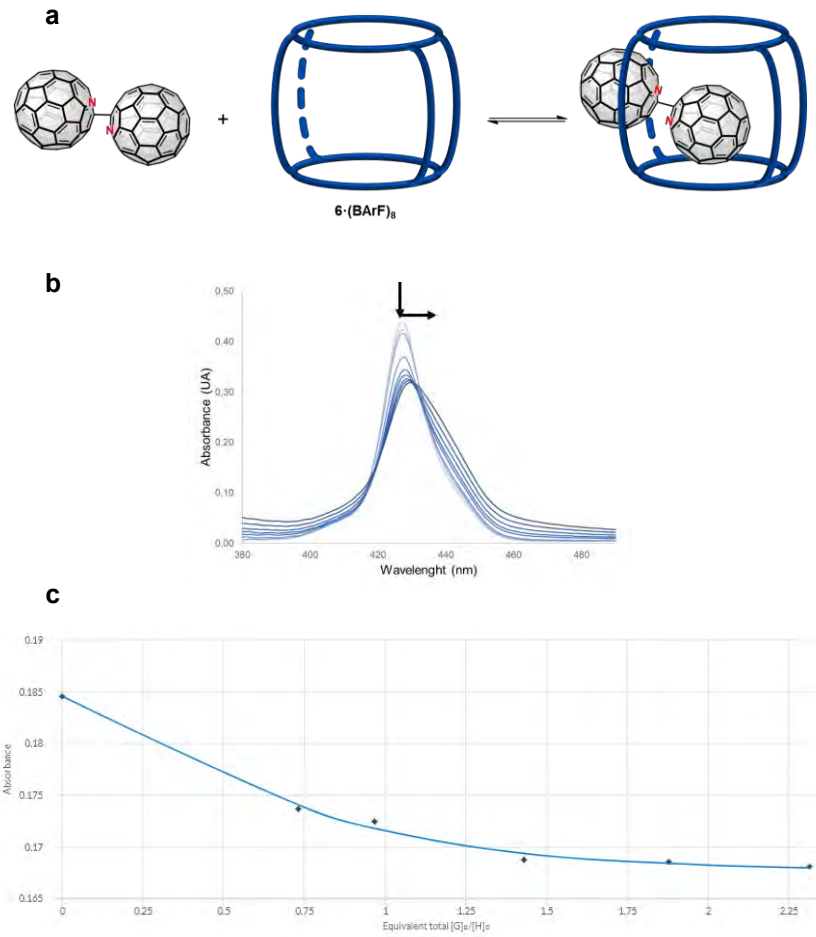

Figure V.30. Representative titration data for **6**/$(C_{59}N)_2$ host-guest system. Solvent: PhMe/MeCN/o-DCB (9:1:0.09). (a) Changes in absorption spectra of **6** ($8.3x10^{-7}$ M, λ_{exc} = 420 nm) upon addition of azafullerene

$(C_{59}N)_2$ (0 – 3.4x10^{-5} M). (b) UV-Vis spectrum for the titration. (c) Fit of the titration data according to 1:1 binding model (K_a = 1.0 ± 1.1 × 10^7 M^{-1} for **6**·$(BArF)_8$).

The poor solubility of bare as-purchased C_{84} precluded the proper calculation of the affinity constant. This prompted us to develop a competition experiment exposing the $(C_{59}N)_2$⊂**6**·$(BArF)_8$ to the soluble extract of fullerenes containing C_{84}. The encapsulation of $(C_{59}N)_2$ within **6**·$(BArF)_8$ was performed and checked by HRMS, showing a 1:1 ratio for $(C_{59}N)_2$-filled and empty nanocapsule. At this point, 100 equiv. of fullerene extract was added to the toluene solution and after 4 days the $(C_{59}N)_2$ guest was completely exchanged for the C_{84} species. This unequivocally indicated that the affinity constant for C_{84}⊂**6**·$(BArF)_8$ should be a value higher than 1.0 × 10^7 M^{-1} (Figures V.31 and V.32).

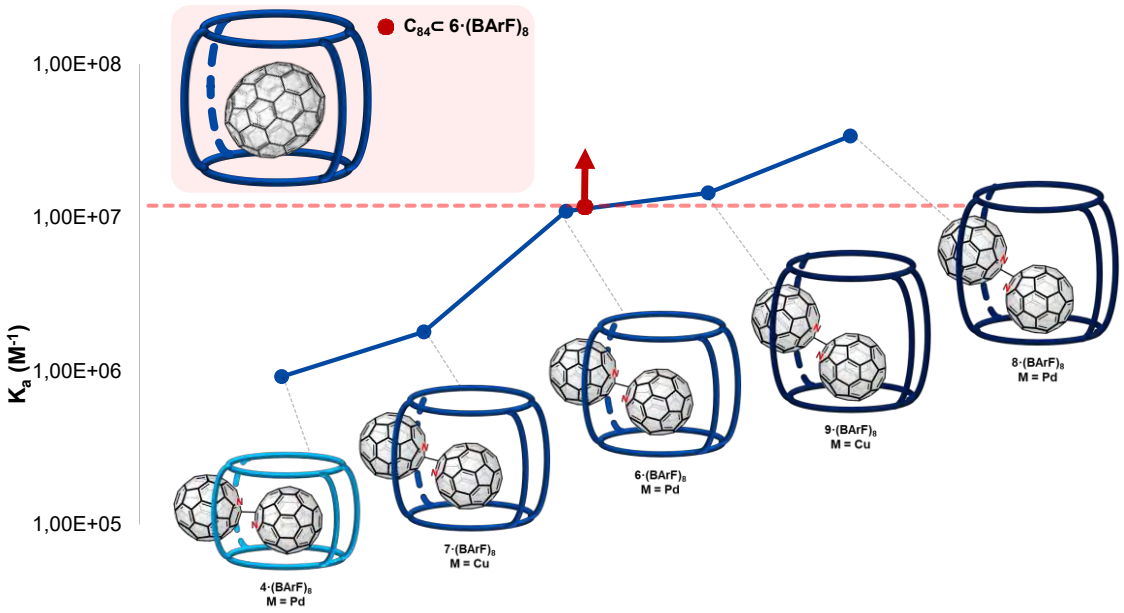

Figure V.31. Comparative association constants (K_a) of $(C_{59}N)_2$ with different sized nanocapsules and estimation of the K_a value for C_{84}⊂**6**·$(BArF)_8$.

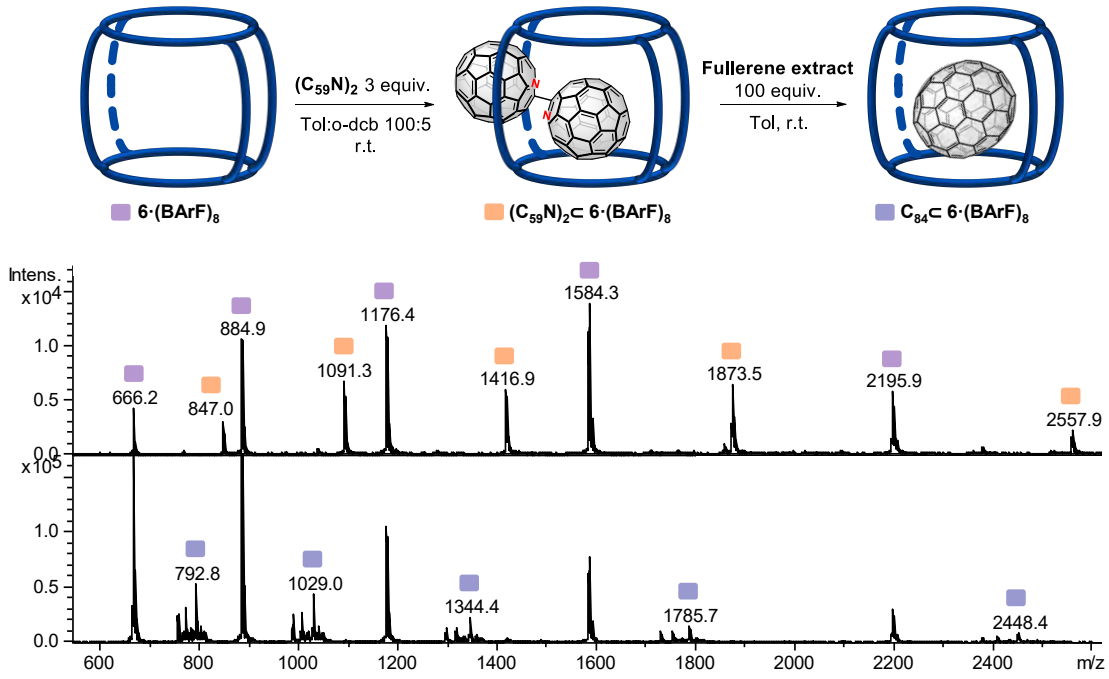

Figure V.32. Competitive host-guest binding studies of the azafullerene dimer $(C_{59}N)_2$ and the fullerene extract with nanocapsule **6**·$(BArF)_8$. HRMS spectra of $(C_{59}N)_2$⊂**6**·$(BArF)_8$ (top) and HRMS spectra upon exposure to the fullerene extract showing complete replacement of $(C_{59}N)_2$ to form C_{84}⊂**6**·$(BArF)_8$ (bottom).

In summary, it has been developed an efficient one-step protocol for the enrichment of C_{84} (from 0.7% in the initial mixture up to 86% in the final encapsulation) using a the **7**·$(BArF)_8$ supramolecular nanocapsule. New terphenyl-based nanocapsules, **X**·$(BArF)_8$ (X = **8**-**9**), have been developed increasing the cavity size to a distance of 18.4 Å between porphyrin center. The differently-sized nanocapsules (biphenyl-, diarylalkyne- and terphenyl-based nanocapsules) have been explored as hosts for the dumbbell-shaped azafullerene $(C_{59}N)_2$, showing an increase in the association constants while enlarging the cavity size. The association constant of C_{84} was determined by a competition experiment with $(C_{59}N)_2$ in the **7**·$(BArF)_8$ nanocapsule, obtaining a value higher than 1.0×10^7 M^{-1}.

V.3. Supramolecular nanocapsule as a two-fold stabilizer of outer-cavity sub-nanometric Ru NPs and inner-cavity ultra-small Ru clusters

In this chapter a new methodology to synthesize sub-nanometric (0.5 – 1 nm) Ru NPs will be developed by using a supramolecular nanocapsule as a stabilizer. The catalytic properties of these nanoparticles will be tested on the hydrogenation of styrene, obtaining excellent selectivity for the hydrogenation of the alkene moiety. Moreover, the encapsulation of small [Ru_5] clusters (< 0.5 nm) will be analysed by HR-MS, and DFT studies will afford an understanding on the nature of those Ru_5 clusters.

V.3.1. Ru NPs synthesis (outside stabilization vs. inner encapsulation)

Due to their confined cavity, it was envisioned that supramolecular nanocapsules could be used as a template for the growth and stabilization of metallic Ru NPs. In a collaborative project with the group of Prof. B. Chaudret (Univ. Paul Sabatier, Toulouse), the synthesis of Ru NPs was performed by using the two nanocapsules reported previously, **6** and **8**·$(BArF)_8$ bearing a different cavity size 16.8 Å for **6**·$(BArF)_8$ and 18.4 Å for **8**·$(BArF)_8$ to study the influence of the nanocapsule and its cavity dimensions in the NPs growth. The experimental conditions consisted in a NPs synthesis by using the Ru(COD)(COT) as a precursor (130 equiv.) and in situ addition of 1 equiv. of nanocapsule dissolved in THF (Figure V.33). That mixture was exposed to 1 bar of H_2, at room temperature, which was demonstrated to be effective for the synthesis of Ru NPs.[25] However, TEM analysis indicated that the mean NPs size was above 1 nm (~ 1.3 nm), which was not particularly relevant compared to other reported methodologies.[26-33] On the contrary, by adding such a small amount of pyrazine (0.2 equiv.) as ancillary ligand, we could observe a remarkable change, showing an average sub-nanometric NPs size of 0.7 nm. As depicted in Figure V.34, the cavity size of the nanocapsule does not take a crucial role in the NPs size, being for both **6** and **8**·$(BArF)_8$ nanocapsules practically the same, 1.3 nm without pyrazine and 0.7 nm with pyrazine. Therefore, we focused the study on the use of nanocapsule **8**·$(BArF)_8$.

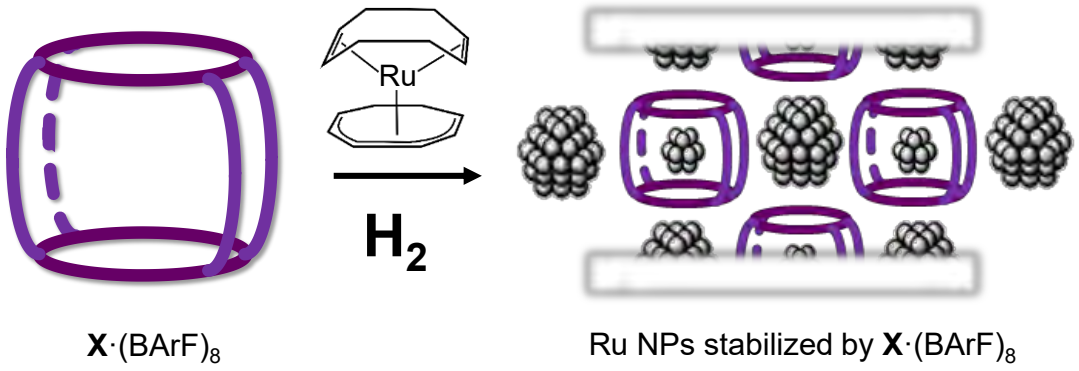

Figure V.33. Schematic representation of the hydrogenation of Ru(COD)(COT) to obtain sub-nanometric Ru NPs stabilized by **X**·(BArF)$_8$. X = **6** or **8**.

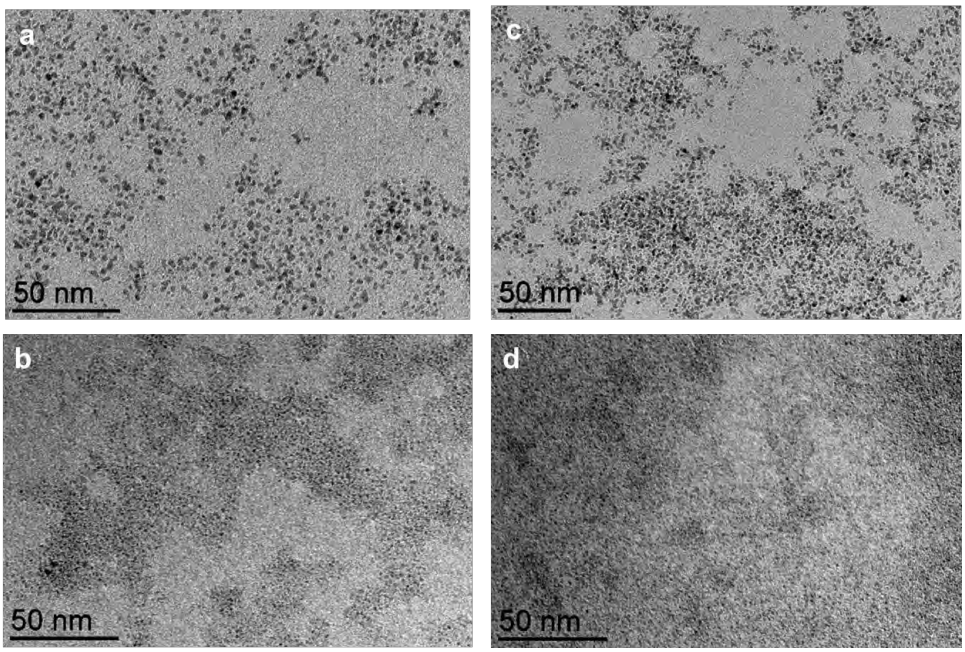

Figure V.34. TEM images of a) E1, NPs synthesized with the **6**·(BArF)$_8$ nanocapsule, 130 equiv. Ru(COD)(COT) and 0 equiv. pyrazine; b) E2, NPs synthesized with **6**·(BArF)$_8$ nanocapsule, 130 equiv. Ru(COD)(COT) and 0.2 equiv. pyrazine; c) E3, NPs synthesized with **8**·(BArF)$_8$ nanocapsule, 130 equiv. Ru(COD)(COT) and 0 equiv. pyrazine; d) E4, NPs synthesized with **8**·(BArF)$_8$ with 130 equiv. Ru(COD)(COT) and 0.2 equiv. pyrazine.

At this point, to determine the influence on the Ru concentration, we decreased the amount of Ru(COD)(COT) added to **8**·(BArF)$_8$. Experiments bearing 20, 40, 60 and 80 equiv. of Ru (E5, E6, E9-E11 in Table V.2) were performed and NPs with a mean size of 0.7 nm were obtained, as determined by TEM distribution of particle analysis (Figure V.35). Then, we wondered how much we could increase the amount of Ru precursor by adding 200 equiv., (E7 in Table V.2) obtaining similar results (see Figure S7 in Annex 3). With the aim to observe a change in size, the pyrazine concentration with respect the Ru was increased, from 0.2 to 1 equiv. (E12 in Table V.2). This leaded to the formation of uniform ultra-small

Ru NPs of 0.6 ± 0.1 nm. Therefore, a trend was observed, and by increasing the amount of pyrazine, the Ru NPs mean size decreased.

Table V.2. Experiment conditions studied for the Ru NPs formation. All reactions were performed at room temperature and under 1 bar of H_2 in a total volume of 3-3.5 ml of THF. Ru(COD)(COT) was used as precursor.

Exp.	**N·(BArF)$_8$ N = 6 or 8**	Ru equiv.	Pyz equiv.	Time (min)	**Size Ru NP (nm)**
E1	**6**	130	0	10	1.28 ± 0.17
E2	**6**	130	0.2	10	0.68 ± 0.22
E3	**8**	130	0	10	1.33 ± 0.24
E4	**8**	130	0.2	10	0.65 ± 0.15
E5	**8**	40	0.2	10	0.67 ± 0.19
E6	**8**	20	0.2	10	0.74 ± 0.19
E7	**8**	200	0.2	2	0.74 ± 0.18
E8	**8**	130	0.2	2	0.72 ± 0.20
E9	**8**	80	0.2	2	0.69 ± 0.18
E10	**8**	60	0.2	2	0.71 ± 0.20
E11	**8**	40	0.2	2	0.70 ± 0.21
E12	**8**	130	1	2	0.60 ± 0.24
E13	[$Pd_2(Me_2ppp)$]	32	0.2	10	0.96 ± 0.24
E14	Zn-TCPP	65	0.2	10	>100

To obtain more information about the stabilization of the NPs by the nanocapsule, we performed blank experiments by using one of the building blocks of the nanocapsule. Both Pd-based clip (E13 in Table V.2) and Zn-TCPP (E14 in Table V.2) were exposed to NPs synthesis conditions obtaining different results. While for the Zn-TCPP an aggregate was formed, when Pd-clip was tested, the same 0.7 nm sub-nanometric Ru NPs were obtained, indicating that the Pd-clip plays a crucial role in the stabilization of the sub-nanometric Ru NPs by the nanocapsule (Figure V.36 and Figure S13 in Annex 3).

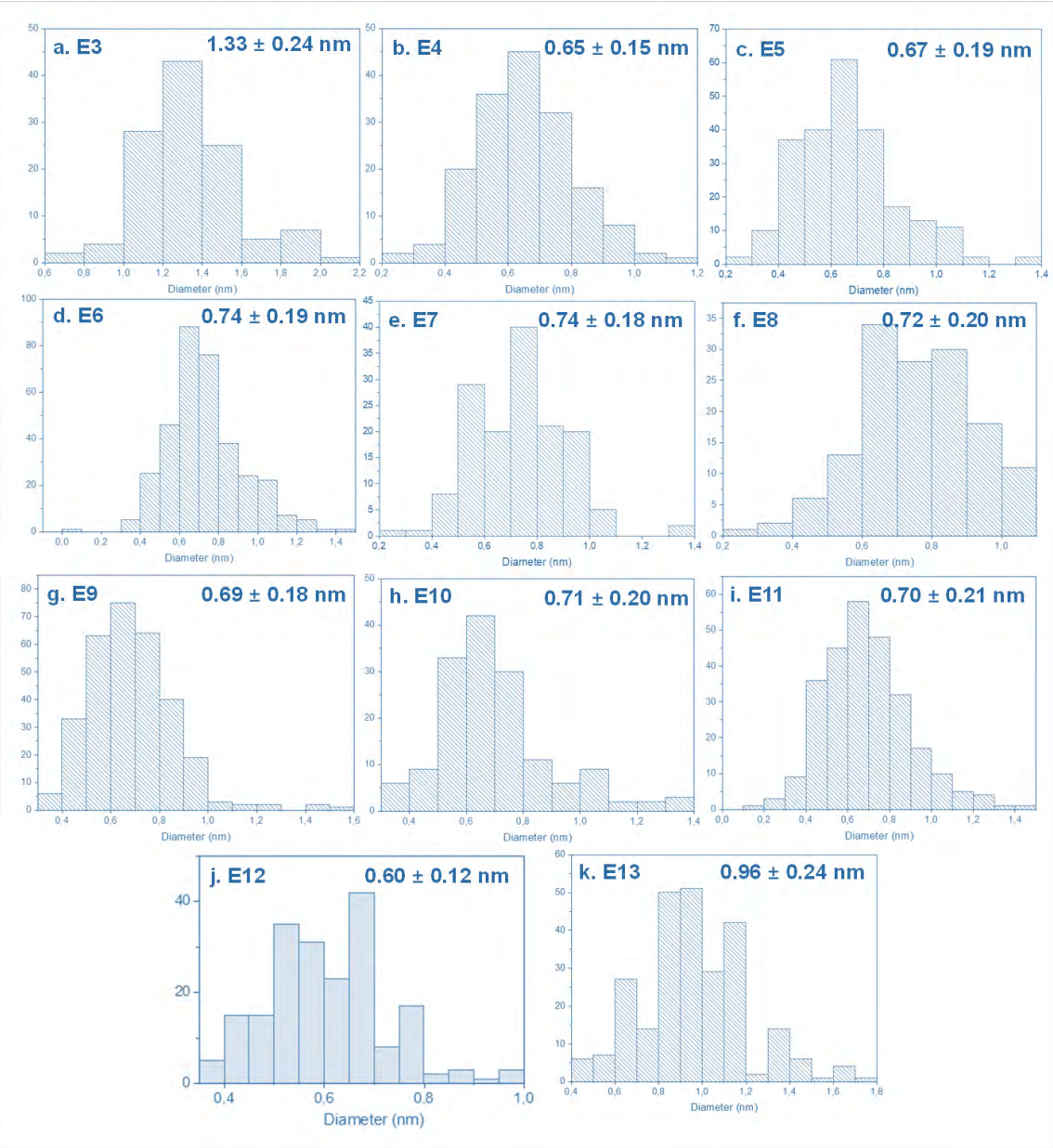

Figure V.35. Ru NPs size distribution for E3 (a), E4 (b), E5 (c), E6 (d), E7 (e), E8 (f), E9 (g). E10 (h), E11 (i), E12 (j) and E13 (k).

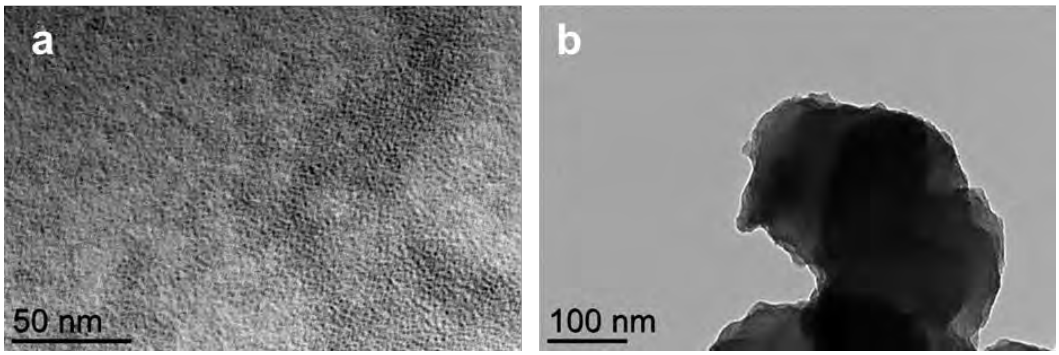

Figure V.36. TEM images of a) E13, NPs synthesized with $[Pd_2(Me_2ppp)]^{4+}$ clip, and b) E14, with Zn-TCPP.

To further study the properties of these sub-nanometric nanoparticles, we evaluated their catalytic performance in the hydrogenation of styrene (Table V.3). Catalytic loading of 0.25 mol% of different Ru NPs solutions, 3 bar of H_2 and 50 ºC were used for the hydrogenation catalysis and the exclusive hydrogenation of the alkene moiety was observed. On the contrary, the arene moiety remained unreacted, which is in agreement with a subnanometric size of the Ru NPs in all samples, since only NPs size above 1 nm allow the hydrogenation of the arene ring.[34] High conversion and excellent selectivity (experiments E3, E8-E10 and E13) and moderate conversion and good selectivity (experiment E11) were observed for Ru NPs in the range of 0.7-1.3 nm. On the other hand, catalytic experiments performed using the smallest Ru NPs (0.6 nm for E12) showed a drastic decrease on the conversion to 16.5% while keeping a 100% selectivity for EtBz. This can be justified because of the hampered accessibility to the active surface of the NP due to the large amount of pyrazine molecules covering the NP.

Table V.3. Hydrogenation of styrene catalyzed by Ru NPs from experiments E3 and E8-E12. Conditions: 1 mmol of substrate, 0.25 mol% Ru, 5h, 50 °C and 5.5 mL of THF. EtBz = ethylbenzene. EtCy = ethylcyclohexane. n.d. = not detected. *Total volume 3 mL.

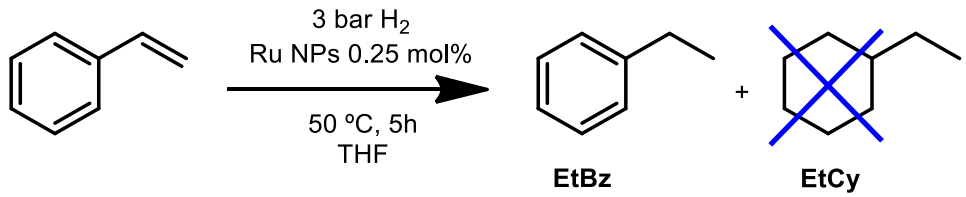

Solution	Conversion (%)	Yield EtBz (%)	Yield EtCy (%)
E3	100	100	n.d.
E8	95	94	n.d.
E9	95	94	n.d.
E10	95	94	n.d.
E11	68	56	n.d.
E12	17	17	n.d.
E13*	100	89	n.d.

Then, we decided to analyze the Ru NPs solutions by HRMS to detect if any species remained encapsulated. In the 10 min experiments, no nanocapsule could be recovered indicating a partial or total decomposition, which would indicate a stabilization by some building block of the nanocapsule. Thus, we decided to reduce the reaction time from 10 to 2 min (see E7-E12 in Table V.2). While Ru NPs were obtained with a same size (~ 0.7 nm), the nanocapsules were recovered in a 40-90% by CH_3CN washing. Recovered nanocapsules were analyzed by HRMS showing m/z ions mainly attributed to empty nanocapsule.

However, in all the experiments it was observed a ~10% of a m/z ion corresponding to Ru_5H_2⊂**8**·$(BArF)_8$ (Figure V.37 and Figure S17 in Annex 3). And, when using 130 equiv. of precursor, apart from the Ru_5H_2⊂**8**·$(BArF)_8$, we could identify m/z ions corresponding to $Ru_{10}H_2$⊂**8**·$(BArF)_8$ and $Ru_{15}H_2$⊂**8**·$(BArF)_8$ (see Figure S18 in Annex 3). These findings determined that during the NPs synthesis two processes were occurring at the same time. On one hand and majorly, the stabilization of the sub-nanometric NPs at the outer cavity; and on the other hand, the encapsulation of very small Ru clusters, mainly [Ru_5] clusters.

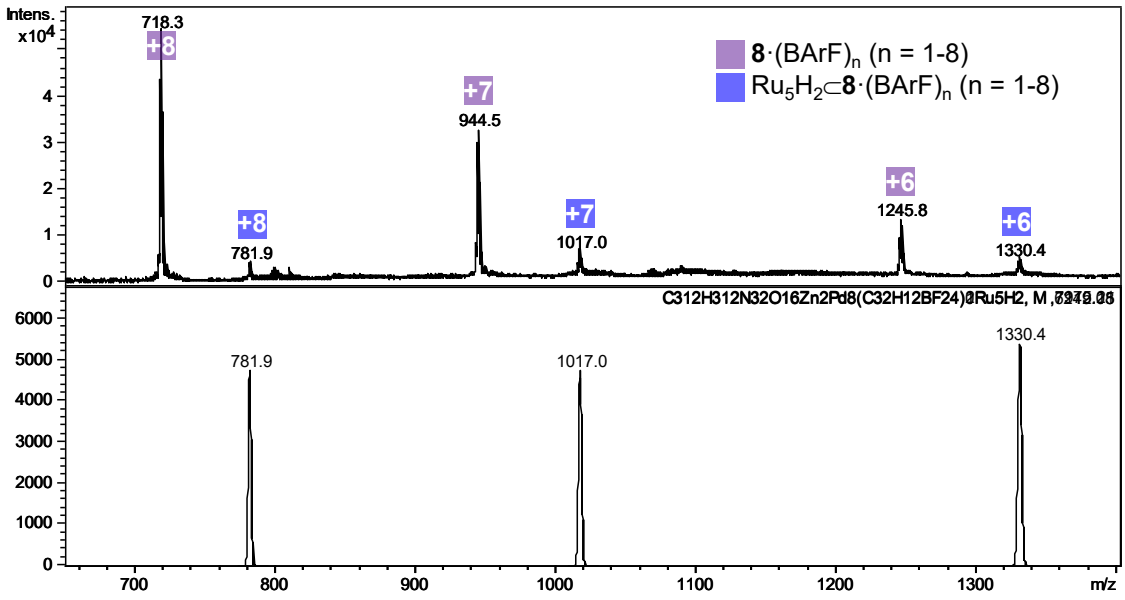

Figure V.37. HRMS analysis of nanocapsule recovered from experiment E5 final mixture (experimental conditions: addition of 40 equiv. Ru(COD)(COT) and 0.2 equiv. pyrazine in the presence of 2 mg of **8**·$(BArF)_8$). Calculated (bottom) and found (top) m/z peaks.

V.3.2. DFT studies: stabilization factors of small [Ru_5] clusters

DFT studies were performed to further investigate the nature of the encapsulated ultra-small [Ru_5] clusters, in collaboration with Prof. R. Poteau (Univ. Paul Sabatier, Toulouse). First, their stability was evaluated considering the possibility to interact with some hydrides or different ligands. According to the Wade-Mingos polyhedral skeletal electron pair (PSEP) theory, the total cluster valence electron (CVE) number of TM *closo*, *nido* and *arachno* deltahedral clusters is mandatory to be 14*m*+2, 14*m*+4 and 14*m*+6, respectively. For a [Ru_5] cluster, the most stable geometries are a square pyramid (**sp**) and a trigonal bipyramid (**tb**), being the latter 26.4 kcal·mol^{-1} above **sp** (Figure V.38).

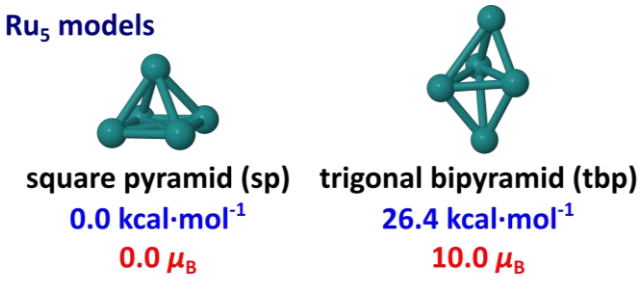

Figure V.38. Square pyramid (**sp**) and trigonal bipyramid (**tb**) [Ru_5] models. Their relative energy (blue) and magnetic moment (red) are reported below.

Following the Wade-Mingos PSEP theory, [Ru_5] clusters should have 74 CVEs for the *nido* **sp** and 72 CVEs for the *closo* **tb** and these additional CVEs can be taken by hydrides, by the σ-donating pyrazines or by the π-donating aromatic rings from the terphenyl-based nanocapsule. From that point, several possible [Ru_5] models exist that fulfill the required CVEs (Figure V.39): **sp**-$Ru_5H_4(\eta^6\text{-PhH})_2(\eta^6\text{-pyz})_3$ (**1**), **tb**-$Ru_5H_2(\eta^6\text{-PhH})_2(\eta^6\text{-pyz})_3$ (**2**), **tb**-$Ru_5H_2(\eta^1\text{-pyz})_6(\eta^6\text{-pyz})_3$ (**3**) and **tb**-$Ru_5H_4(\eta^6\text{-PhH})_2(\eta^6\text{-pyz})_2(\eta^4\text{-pyz})$ (**4**), where arene moieties belong to the Pd terphenyl-based clip moiety.

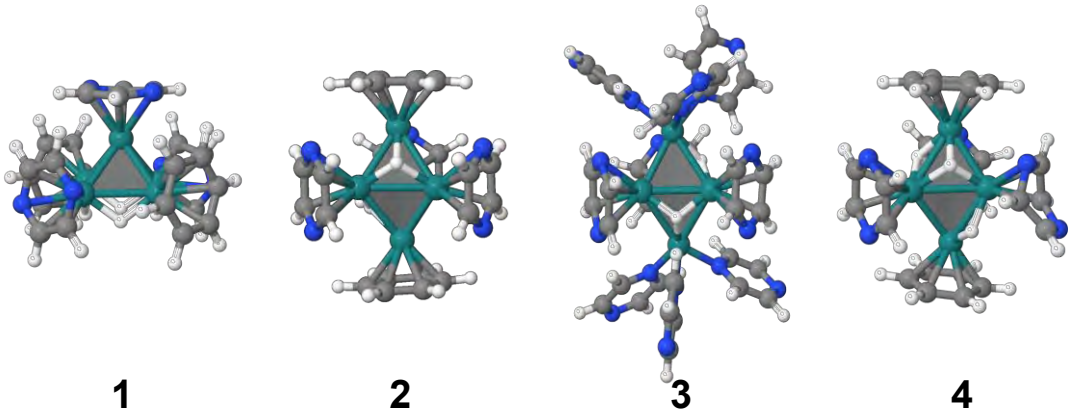

Figure V.39. [Ru_5] clusters stabilized by hydrides, benzene (PhH) and pyrazine (pyz) ligands. (**1**) **sp**-$Ru_5H_4(\eta^6\text{-PhH})_2(\eta^6\text{-pyz})_3$, (**2**) **tb**-$Ru_5H_2(\eta^6\text{-PhH})_2(\eta^6\text{-pyz})_3$, (**3**) **tb**-$Ru_5H_2(\eta^1\text{-pyz})_6(\eta^6\text{-pyz})_3$ and (**4**) **tb**-$Ru_5H_4(\eta^6\text{-PhH})_2(\eta^6\text{-pyz})_2(\eta^4\text{-pyz})$.

Based on the energy values for each bare cluster, it could be explained that **tb** metal core is more strongly stabilized by the surface species than the **sp** core (Figure V.40a).

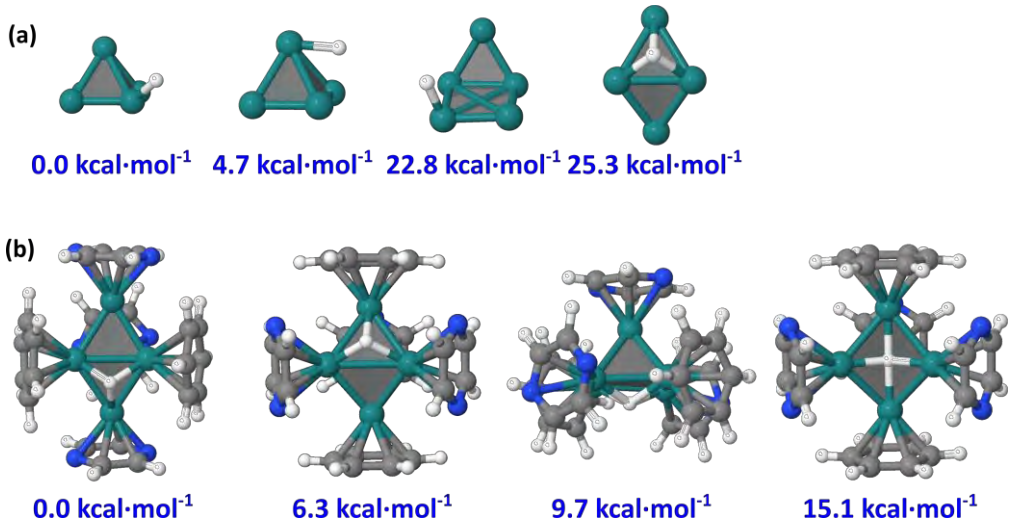

Figure V.40. (a) Bare Ru_5H isomers; (b) $Ru_5H(\eta_6\text{-PhH})_2(\eta_6\text{-pyz})_3$ isomers. Relative energies in blue.

On the other hand, nanocapsule [**8**]$^{8+}$ was fully optimized by DFT studies revealing an inner cavity fitting an ellipsoid with 1.2 x 1.7 nm diameter size. This represents a more constrained geometry compared to the MD simulations using force field, which showed a cavity size (Porph⋯Porph distance) up to 18 Å.[9] This discrepancy indicated the high flexibility displayed by the nanocapsule, specially due to the palladium-OOCR bond rotation. Studying the nanocapsule effect, different zones were identified as possible stabilization sites of the [Ru_5] clusters, as depicted in Figure V.41. The clip pillars were considered, which can provide electrons to the metal core through the phenylene rings. This possibility would afford ~ 0.6-0.8 nm coordination sites (P1 and P2 sites). Finally, as the phenylene groups are capable to rotate, the [Ru_5] cluster can be accommodated outside the cavity of the nanocapsule (P3 site). Taking into account the small size of the [Ru_5] cluster (1.6-2.0 Å radius), preferential coordination site is located at P1 and P2, whereas for larger ~0.7 nm Ru NPs, I and P3 sites are preferred. The interaction of clusters or NP with the Zn-TCPP group was discarded based on the experimental results (Table V.2).

The calculated energies, Ru-H vibrational properties and the μ_{H2} chemical potential have been used to plot a stability diagram (Figure V.42), with the aim to find the optimal number of hydrides that could lie on the [Ru_5] core stabilized by P1 site. In this diagram, **tb**-$Ru_5H_2(\eta^6\text{-PhH})_2(\eta^6\text{-pyz})_3$ (**2**) is found to be stable over a wide temperature and pressure range, in agreement with the 72 CVEs of the *closo* metal core.

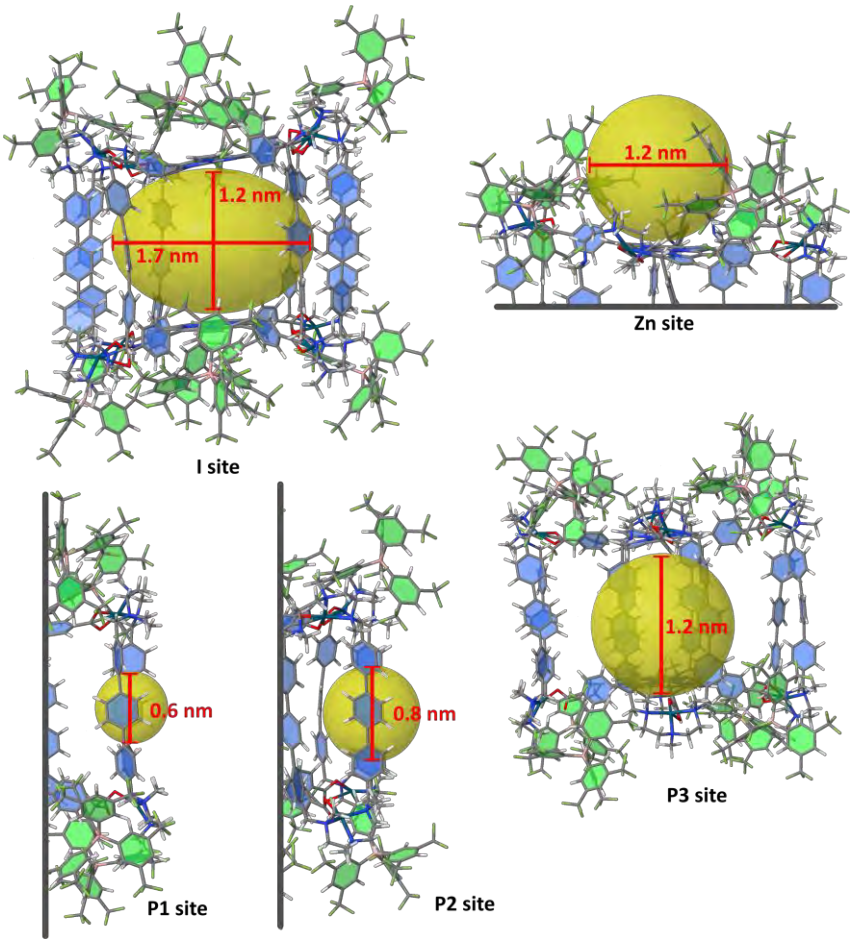

Figure V.41. Possible Ru clusters or RuNPs coordination sites in the **8**·$(BArF)_8$ nanocapsule. Given the overall plasticity of the cage, cavity sizes, shown as yellow spheres (sites Zn, P1-P3) or ellipsoids (site I), are only indicative. They are based on the optimization of a host-free cage. For the sake of clarity, BArF anions and the ppp part of Pd-clips are highlighted in green and blue, respectively.

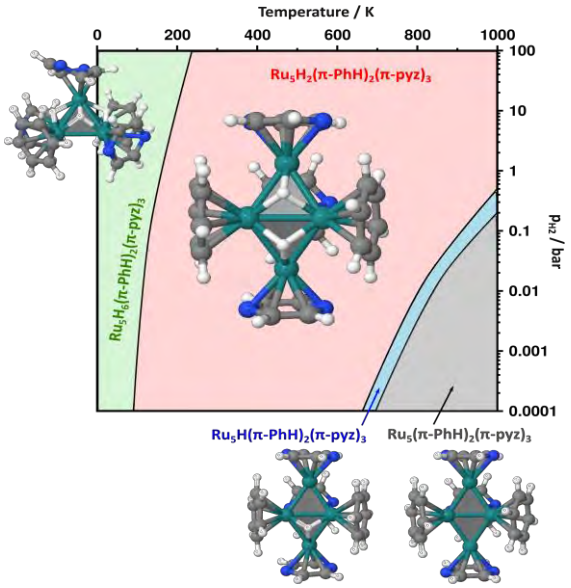

Figure V.42. Stability diagram established for **sp**- or **tb**-$Ru_5H_n(PhH)_2(pyz)_3$. The temperature range is set up to 1000K, just to check the consistency of the model, i.e. that there is a gradual increase in the number of surface hydrides as the pressure increases and the temperature decreases.

The last part of the DFT calculations comprised the study the coordination of Ru_5H_2 cluster and *ca*. 1 nm RuNPs (optimized as Ru_{57}) at some possible stabilizing zones of the nanocapsule **8**·$(BArF)_8$. First, the absorption of $Ru_5H_2(\eta^6\text{-pyz})_3$ at P1 site was evaluated (Figure V.43a). It follows the Wade-Mingos rules, thanks to the coordination with two phenylene groups from the ppp clip and this new structure is named **2'**, slightly less stable than **2**.

Another Ru_5H_2 cluster stabilized inside the cage (site I) is the compound **3** which can be further stabilized thanks to σ-donating of nitrogen atoms from the pyrazine ligands coordinated to the Zn-TCPP (Figure V.43b). This site I could also afford the stabilization of *ca*. 1 nm RuNPs due to the 0.8 nm spacing between the ppp clips (Figure V.43c). Such encapsulation was found to be energetically favourable, as $Ru_{57}H_{44}$ stabilized by the Zn-TCPP with hydrides randomly scattered on all facets of the NP. The latter option was not favoured according to experimental data (E14, Table V.2).

Finally, the possible growth of *ca*. 1 nm RuNPs outside the cage, but stabilized in the P3 site, was also considered (Figure V.43d). Phenylene groups can slightly rotate around the vertical ppp axis in order to maximize their coordination on the RuNP surface. In this example, two facets of the $Ru_{57}H_{44}$ NP are firmly grafted to the ppp clip by a (η_6-phenylene)(η_6, μ_3-phenylene)(η_6, μ_4-phenylene) motif. This process resulted in a strong absorption energy as the pillars could be slightly less adaptive, and the number of surface hydrides could be slightly higher. Even in this case, this external grafting is very likely to be significantly stable.

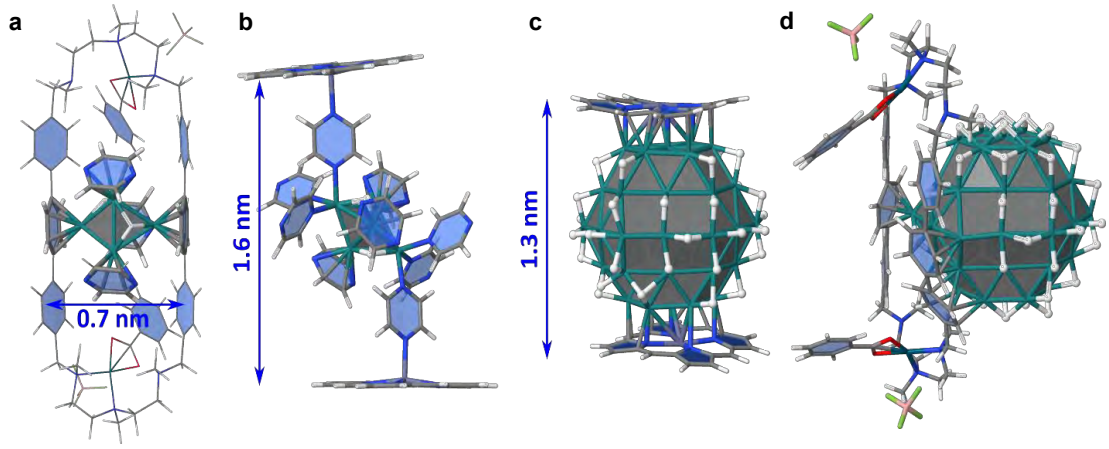

Figure V.43. Study of the possible trapping of ligand-coated Ru_5H_2 clusters and $Ru_{57}H_{44}$ NPs in the nanocapsule. (a) adsorption of $Ru_5H_2(\eta_6\text{-pyz})_3$ in the P1 site of a Pd clip (with BF_4 instead of BArF); (b) coordination of compound **3** between two Zn-porphyrin building blocks (model for site I); (c) coordination of a $Ru_{57}H_{44}$ NP between two Zn porphyrin building blocks (model for site I); (d) stabilization of a $Ru_{57}H_{44}$ NP in the P3 site of a Pd-ppp clip.

All the DFT studies show the ability to stabilize [Ru_5] clusters at different trapping sites, but most likely as a) Ru_5H_2 (**2**) stabilized at P1 site by the two phenylene groups from the Pd-based clip and three pyrazine units or b) Ru_5H_2 (**3**) coordinated between two Zn-porph (I site) and stabilized by σ-donating pyrazines. The remarkable occurrence of [Ru_5] cluster observed by HRMS is explained both in terms of electronic effects and of cavity size of the nanocapsule. Given the combined experimental and computational insights, two steps can be distinguished in the Ru NPs formation. First, the generation of [Ru_5] clusters, subsequently followed by the smooth growth to sub-nanometric Ru NPs, which are stabilized by outer-nanocapsule interactions, mainly thanks to the Pd ppp-based clip.

In summary, sub-nanometric Ru NPs have been successfully synthesized and stabilized using a supramolecular nanocapsule, **8**·$(BArF)_8$, along with pyrazine as ancillary ligand. The data obtained by TEM and HR-MS determined that these nanoparticles are stabilized through the outer-cavity of the nanocapsule specifically by the terphenyl-based clips. Catalytic properties of the sub-nanometric NPs showed excellent selectivity for the hydrogenation of the alkene moiety of the styrene. Small clusters trapped within the nanocapsule were studied by DFT which determined the stability of [Ru_5] and the most probable coordination sites of the nanocapsule.

V.4. References

1. García-Simón, C.; Garcia-Borràs, M.; Gómez, L.; Garcia-Bosch, I.; Osuna, S.; Swart, M.; Luis, J. M.; Rovira, C.; Almeida, M.; Imaz, I.; Maspoch, D.; Costas, M.; Ribas, X., Self-Assembled Tetragonal Prismatic Molecular Cage Highly Selective for Anionic π Guests. *Eur. J. Chem.* **2013,** *19* (4), 1445-1456.

2. García-Simón, C.; Garcia-Borràs, M.; Gómez, L.; Parella, T.; Osuna, S.; Juanhuix, J.; Imaz, I.; Maspoch, D.; Costas, M.; Ribas, X., Sponge-like molecular cage for purification of fullerenes. *Nat. Comm.* **2014,** *5* (1), 5557-5565.

3. García-Simón, C.; Monferrer, A.; Garcia-Borràs, M.; Imaz, I.; Maspoch, D.; Costas, M.; Ribas, X., Size-selective encapsulation of C60 and C60-derivatives within an adaptable naphthalene-based tetragonal prismatic supramolecular nanocapsule. *Chem. Comm.* **2019,** *55* (6), 798-801.

4. García-Simón, C.; Gramage-Doria, R.; Raoufmoghaddam, S.; Parella, T.; Costas, M.; Ribas, X.; Reek, J. N. H., Enantioselective Hydroformylation by a Rh-Catalyst Entrapped in a Supramolecular Metallocage. *J. Am. Chem. Soc.* **2015,** *137* (7), 2680-2687.

5. García-Simón, C.; Costas, M.; Ribas, X., Metallosupramolecular receptors for fullerene binding and release. *Chem. Soc. Rev.* **2016,** *45* (1), 40-62.

6. Fuertes-Espinosa, C.; García-Simón, C.; Castro, E.; Costas, M.; Echegoyen, L.; Ribas, X., A Copper-based Supramolecular Nanocapsule that Enables Straightforward Purification of Sc3N-based Endohedral Metallofullerene Soots. *Eur. J. Chem.* **2017,** *23* (15), 3553-3557.

7. Fuertes-Espinosa, C.; Gómez-Torres, A.; Morales-Martínez, R.; Rodríguez-Fortea, A.; García-Simón, C.; Gándara, F.; Imaz, I.; Juanhuix, J.; Maspoch, D.; Poblet, J. M.; Echegoyen, L.; Ribas, X., Purification of Uranium-based Endohedral Metallofullerenes (EMFs) by Selective Supramolecular Encapsulation and Release. *Angew. Chem. Int. Ed.* **2018,** *57* (35), 11294-11299.

8. Fuertes, C.; García-Simón, C.; Pujals, M.; Garcia-Borràs, M.; Gomez, L.; Parella, T.; Juanhuix, J.; Imaz, I.; Maspoch, D.; Costas, M.; Ribas, X., Supramolecular Fullerene Sponges as Catalytic Masks for Regioselective Functionalization of C60. *Chem* **2019,** *6* (12), 3219-3262.

9. García-Simón, C.; Colomban, C.; Çetin, Y. A.; Gimeno, A.; Pujals, M.; Ubasart, E.; Fuertes-Espinosa, C.; Asad, K.; Chronakis, N.; Costas, M.; Jiménez-Barbero, J.; Feixas, F.; Ribas, X., Complete Dynamic Reconstruction of C60, C70, and (C59N)2 Encapsulation into an Adaptable Supramolecular Nanocapsule. *J. Am. Chem. Soc.* **2020,** *142* (37), 16051-16063.

10. Colomban, C.; Szalóki, G.; Allain, M.; Gómez, L.; Goeb, S.; Sallé, M.; Costas, M.; Ribas, X., Reversible C(60) Ejection from a Metallocage through the Redox-Dependent Binding of a Competitive Guest. *Eur. J. Chem.* **2017,** *23* (13), 3016-3022.

11. Colomban, C.; Martin-Diaconescu, V.; Parella, T.; Goeb, S.; García-Simón, C.; Lloret-Fillol, J.; Costas, M.; Ribas, X., Design of Zn-, Cu-, and Fe-Coordination Complexes Confined in a Self-Assembled Nanocage. *Inorg. Chem.* **2018,** *57* (7), 3529-3539.

12. Colomban, C.; Fuertes-Espinosa, C.; Goeb, S.; Sallé, M.; Costas, M.; Blancafort, L.; Ribas, X., Self-Assembled Cofacial Zinc–Porphyrin Supramolecular Nanocapsules as Tuneable 1O2 Photosensitizers. *Eur. J. Chem.* **2018,** *24* (17), 4371-4381.

13. Fuertes-Espinosa, C.; Murillo, J.; Soto, M. E.; Ceron, M. R.; Morales-Martínez, R.; Rodríguez-Fortea, A.; Poblet, J. M.; Echegoyen, L.; Ribas, X., Highly selective encapsulation and purification of U-based C78-EMFs within a supramolecular nanocapsule. *Nanoscale* **2019,** *11* (47), 23035-23041.

14. Ubasart, E.; Borodin, O.; Fuertes-Espinosa, C.; Xu, Y.; García-Simón, C.; Gómez, L.; Juanhuix, J.; Gándara, F.; Imaz, I.; Maspoch, D.; von Delius, M.; Ribas, X., A three-shell supramolecular complex enables the symmetry-mismatched chemo- and regioselective bis-functionalization of C60. *Nat. Chem.* **2021,** *13* (5), 420-427.

15. Ubasart, E.; García-Simón, C.; Pujals, M.; Asad, K.; Chronakis, N.; Parella, T.; Ribas, X., Straightforward supramolecular purification of C84 from a fullerene extract. *Org. Chem. Front.* **2021,** *8* (15), 4101-4105.

16. Ubasart, E.; Mustieles, I.; Asensio, J. M.; Mencia, G.; López-Vinasco, Á. M.; García-Simón, C.; del Rosal, I.; Poteau, R.; Chaudret, B.; Ribas, X., Supramolecular nanocapsules as two-fold stabilizers of outer-cavity sub-nanometric Ru NPs and inner-cavity ultra-small Ru clusters. *Nanoscale Horiz.* **2022**, 7, 607-615.

17. Park, K.; Bae, G.; Moon, J.; Choe, J.; Song, K. H.; Lee, S., Synthesis of Symmetrical and Unsymmetrical Diarylalkynes from Propiolic Acid Using Palladium-Catalyzed Decarboxylative Coupling. *J. Org. Chem. Res.* **2010,** *75* (18), 6244-6251.

18. Iwamoto, T.; Watanabe, Y.; Sadahiro, T.; Haino, T.; Yamago, S., Size-Selective Encapsulation of C60 by [10]Cycloparaphenylene: Formation of the Shortest Fullerene-Peapod. *Angew. Chem. Int. Ed.* **2011,** *50* (36), 8342-8344.

19. Xu, Y.; Kaur, R.; Wang, B.; Minameyer, M. B.; Gsänger, S.; Meyer, B.; Drewello, T.; Guldi, D. M.; von Delius, M., Concave–Convex π–π Template Approach Enables the Synthesis of [10]Cycloparaphenylene–Fullerene [2]Rotaxanes. *J. Am. Chem. Soc.* **2018,** *140* (41), 13413-13420.

20. Cai, K.; Lipke, M. C.; Liu, Z.; Nelson, J.; Cheng, T.; Shi, Y.; Cheng, C.; Shen, D.; Han, J.-M.; Vemuri, S.; Feng, Y.; Stern, C. L.; Goddard, W. A.; Wasielewski, M. R.; Stoddart, J. F., Molecular Russian dolls. *Nat. Comm.* **2018,** *9* (1), 5275-5282.

21. Thordarson, P.; Coumans, R. G. E.; Elemans, J. A. A. W.; Thomassen, P. J.; Visser, J.; Rowan, A. E.; Nolte, R. J. M., Allosterically Driven Multicomponent Assembly. *Angew. Chem. Int. Ed.* **2004,** *43* (36), 4755-4759.

22. Djojo, F.; Herzog, A.; Lamparth, I.; Hampel, F.; Hirsch, A., Regiochemistry of Twofold Additions to [6,6] Bonds in C60: Influence of the Addend-Independent Cage Distortion in 1,2-Monoadducts. *Eur. J. Chem.* **1996,** *2* (12), 1537-1547.

23. Mecozzi, S.; Rebek, J., The 55 % Solution: A Formula for Molecular Recognition in the Liquid State. *Eur. J. Chem.* **1998,** *4*, 1016-1022.

24. Prakash, O.; Joshi, H.; Sharma, K. N.; Sharma, A. K.; Singh, A. K., Catalytic Synthesis of Bi- and Teraryls in Aqueous Medium with Palladium(II) Complexes of 2-(Pyridine-2-ylmethylsulfanyl)benzoic Acid. *Eur. J. Inorg. Chem.* **2015,** *2015* (3), 520-526.

25. Martínez-Prieto, L. M.; Chaudret, B., Organometallic Ruthenium Nanoparticles: Synthesis, Surface Chemistry, and Insights into Ligand Coordination. *Acc. Chem. Res.* **2018,** *51* (2), 376-384.

26. Yang, J.; He, Y.; He, J.; Liu, Y.; Geng, H.; Chen, S.; Lin, L.; Liu, M.; Chen, T.; Jiang, Q.; Weckhuysen, B. M.; Luo, W.; Wu, Z., Enhanced Catalytic Performance through In Situ Encapsulation of Ultrafine Ru Clusters within a High-Aluminum Zeolite. *ACS Catal.* **2022**, 1847-1856.

27. Ichijo, T.; Sato, S.; Fujita, M., Size-, Mass-, and Density-Controlled Preparation of TiO2 Nanoparticles in a Spherical Coordination Template. *J. Am. Chem. Soc.* **2013,** *135* (18), 6786-6789.

28. McCaffrey, R.; Long, H.; Jin, Y.; Sanders, A.; Park, W.; Zhang, W., Template Synthesis of Gold Nanoparticles with an Organic Molecular Cage. *J. Am. Chem. Soc.* **2014,** *136* (5), 1782-1785.

29. Qiu, L.; McCaffrey, R.; Jin, Y.; Gong, Y.; Hu, Y.; Sun, H.; Park, W.; Zhang, W., Cage-templated synthesis of highly stable palladium nanoparticles and their catalytic activities in Suzuki–Miyaura coupling. *Chem. Sci.* **2018,** *9* (3), 676-680.

30. Sun, N.; Wang, C.; Wang, H.; Yang, L.; Jin, P.; Zhang, W.; Jiang, J., Multifunctional Tubular Organic Cage-Supported Ultrafine Palladium Nanoparticles for Sequential Catalysis. *Angew. Chem. Int. Ed.* **2019,** *58* (50), 18011-18016.

31. Jiang, S.; Cox, H. J.; Papaioannou, E. I.; Tang, C.; Liu, H.; Murdoch, B. J.; Gibson, E. K.; Metcalfe, I. S.; Evans, J. S. O.; Beaumont, S. K., Shape-persistent porous organic cage supported palladium nanoparticles as heterogeneous catalytic materials. *Nanoscale* **2019,** *11* (31), 14929-14936.

32. Sharma, V.; De, D.; Saha, R.; Chattaraj, P. K.; Bharadwaj, P. K., Flexibility Induced Encapsulation of Ultrafine Palladium Nanoparticles into Organic Cages for Tsuji–Trost Allylation. *ACS Appl. Mater. Interfaces* **2020,** *12* (7), 8539-8546.

33. Fang, Y.; Li, J.; Togo, T.; Jin, F.; Xiao, Z.; Liu, L.; Drake, H.; Lian, X.; Zhou, H.-C., Ultra-Small Face-Centered-Cubic Ru Nanoparticles Confined within a Porous Coordination Cage for Dehydrogenation. *Chem* **2018,** *4* (3), 555-563.

34. Martínez-Prieto, L. M.; Urbaneja, C.; Palma, P.; Cámpora, J.; Philippot, K.; Chaudret, B., A betaine adduct of N-heterocyclic carbene and carbodiimide, an efficient ligand to produce ultra-small ruthenium nanoparticles. *Chem. Comm.* **2015,** *51* (22), 4647-4650.

Chapter VI. General conclusions

Two palladium(II)- and copper(II)-based tetragonal prismatic supramolecular nanocapsules bearing a diarylalkyne-based macrocyclic clip have been developed, **6**·$(BArF)_8$ and **7**·$(BArF)_8$, respectively. The self-assembly of Zn-TCPP and the pTp-based clip led to the formation of a nanocapsule featuring a cavity size of 16.8 Å. Following the same strategy, two larger palladium(II)- and copper(II)-based supramolecular nanocapsules bearing a terphenyl(ppp)-based macrocyclic clip have been developed, **8**·$(BArF)_8$ and **9**·$(BArF)_8$, respectively, featuring an increased cavity size up to 18.4 Å. All new 3D tetragonal prismatic supramolecular nanocapsules have been fully characterized by NMR, ESI-MS and XRD.

In **Chapter V.1** and **Annex 1**, an unprecedented example of three-shell heteroleptic matryoshka-like assembly was developed due to the high affinity of **C_{60}⊂[10]CPP** complex for **6**·$(BArF)_8$. Spectroscopic titrations and crystallographic data allowed an understanding of the high thermodynamic stability of the matryoshka-like assembly, being the affinity constant of the **C_{60}⊂[10]CPP** for the nanocapsule $K_a = 9.3 \pm 0.4 \times 10^6$ M^{-1}. The matryoshka assembly was used as a supramolecular mask for C_{60}, since upon Bingel cyclopropanation reaction conditions, a chemo- and regioselective bis-functionalization of C_{60} was afforded obtaining exclusively the ***trans*-3** bis-adduct. This species has been characterized by HPLC, UV-Vis and NMR. Crystallographic evidence for the bis-functionalized fullerene within the nanocapsule have demonstrated the ability of this structure to restrict a symmetry-mismatched functionalization of C_{60} to form the ***trans*-3** bis-adduct, since the latter presents a 120° angle between their two groups being the two available regions most exposed in contiguous windows of the nanocapsule, despite the nanocapsule features a 90° symmetry. When exploring substrates with different bulkiness, the ***trans*-3** regioselectivity is exclusively maintained but the yield changed according to the Rebek's rule. The use of matryoshka-like assemblies might become a useful strategy to synthesize highly challenging, regioisomerically pure fullerene bis-adducts, which in turn may lead to further advances in organic electronics and solar cells. This regiocontrolled bis-functionalization could also open the door to the templated oligomerization of fullerenes or to design mechanically interlocked materials such as catenanes.

In **Chapter III** and **Chapter V.2**, the supramolecular nanocapsule **7**·$(BArF)_8$ have proven to be effective in the purification of C_{84} from fullerene extract (70% C_{60}, 28% C_{70} and 2% higher fullerenes). The encapsulation and release procedure resulted in a ~125-fold enrichment of C_{84} (from 0.7 % in the initial fullerene extract to 86% in the encapsulated mixture). The affinity of other higher fullerenes has been studied with the nanocapsule **9**·$(BArF)_8$, showing poor affinity due to its too large cavity. In contrast, the terphenyl-based nanocapsule have

been a suitable host to bind the azafullerene $(C_{59}N)_2$, showing high affinity constants for both Pd- and Cu-based nanocapsules. By shrinking the inner cavity (**6**, **7** and **4** nanocapsules), a gradual decrease in the binding affinity for $(C_{59}N)_2$ is observed. In order to find an approximate value for the C_{84} affinity constant for **6**·$(BArF)_8$, competitive experiments have been performed showing an exchange of $(C_{59}N)_2$ for C_{84}, indicating the affinity constant for C_{84}⊂**6**·$(BArF)_8$ must be higher than 1.0×10^7 M^{-1}. This study has proven that supramolecular design is a key tool for the selective encapsulation of fullerenes featuring different sizes and the ability of tuning these tetragonal prismatic nanocapsule is a successful strategy to improve the selectivity for a targeted fullerene.

In **Chapter IV** and **Chapter V.3**, a new strategy to synthesize sub-nanometric Ru NPs in the presence of supramolecular nanocapsules has been developed. The experimental protocol comprised the use of Ru(COD)(COT) as NP precursor, pyrazine as auxiliar stabilizer and the presence of the supramolecular nanocapsule **8**·$(BArF)_8$, under hydrogenation conditions (1 bar H_2). TEM analysis has shown reproducible ~0.7 nm NPs by using different experimental conditions (time, Ru concentration, pyrazine concentration…). Blank experiments have evidenced that the ppp-based clip is the main responsible for the outer NPs stabilization. The catalytic properties of these sub-nanometric NPs have been tested on the hydrogenation of styrene, obtaining excellent selectivity for the hydrogenation of the alkene moiety, in agreement with the sub-nanometric sized Ru NPs. By HRMS, encapsulated ruthenium clusters [Ru_5] have been detected in most of the experiments and DFT studies have afforded a reasonable explanation of their nature. According to the Wade-Mingos rule, there have been determined two main isoenergetic adsorption modes of the [Ru_5] cluster: a) **tb**-$Ru_5H_2(\eta_6\text{-PhH})_2(\eta_6\text{-pyz})_3$ (**2**) in the P1 site (with the involvement of two phenylene rings of the clip) or b) coordination of **tb**-$Ru_5H_2(\eta_1\text{-pyz})_6(\eta_6\text{-pyz})_3$ (**3**) in I site (coordination of η_1-pyz moieties to the two Zn-porph). The double role of the nanocapsule in stabilizing sub-nanometric NPs and at the same time hosting ultra-small Ru clusters, is an unprecedented phenomenon and may be useful to synthesize other metallic clusters for catalytic purposes. The direct observation of the metallic cluster seeds en-route to the formation of NP sheds light into this fundamental process.

Annex. Supporting information

Annex 1. A three-shell supramolecular complex enables the symmetry-mismatched chemo- and regioselective bis-functionalization of C_{60}

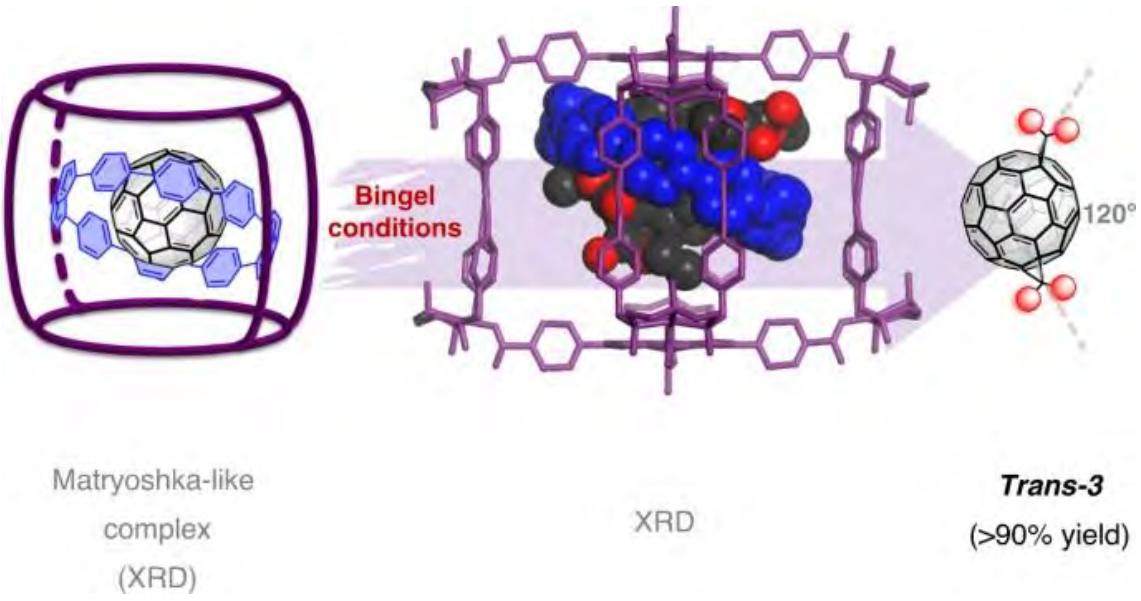

This annex corresponds to the following publication:

E. Ubasart, O. Borodin, C. Fuertes-Espinosa, Y. Xu, C. García-Simón, L. Gómez, J. Juanhuix, F. Gándara, I. Imaz, D. Maspoch, M. von Delius,* X. Ribas*

Nat. Chem. **2021**, *13*, *5*, 420-427. DOI: 10.1038/s41557-021-00658-6

For this publication E.U. performed all the experimental data: synthesis of the molecular clips, metalation of TCPP, synthesis of the nanocapsules and characterization of products, including the single crystals for XRD. E.U. performed all the fullerene functionalization experiments. Besides, E.U. contributed in writing the manuscript and was involved in argumentations and discussions.

Reprinted with permission from:

E. Ubasart, O. Borodin, C. Fuertes-Espinosa, Y. Xu, C. García-Simón, L. Gómez, J. Juanhuix, F. Gándara, I. Imaz, D. Maspoch, M. von Delius,* X. Ribas*. "Annex 1. A three-shell supramolecular complex enables the symmetry-mismatched chemo- and regioselective bis-functionalization of C_{60}".

Nature Chemistry **2021**, *13*, *5*, 420-427.

DOI: 10.1038/s41557-021-00658-6

ARTICLES
https://doi.org/10.1038/s41557-021-00658-6

nature chemistry

A three-shell supramolecular complex enables the symmetry-mismatched chemo- and regioselective bis-functionalization of C_{60}

Ernest Ubasart[1], Oleg Borodin[2], Carles Fuertes-Espinosa[1], Youzhi Xu[2], Cristina García-Simón[1], Laura Gómez[3], Judith Juanhuix[4], Felipe Gándara[5], Inhar Imaz[6], Daniel Maspoch[6,7], Max von Delius[2]✉ and Xavi Ribas[1]✉

Molecular Russian dolls (matryoshkas) have proven useful for testing the limits of preparative supramolecular chemistry but applications of these architectures to problems in other fields are elusive. Here we report a three-shell, matryoshka-like complex—in which C_{60} sits inside a cycloparaphenylene nanohoop, which in turn is encapsulated inside a self-assembled nanocapsule—that can be used to address a long-standing challenge in fullerene chemistry, namely the selective formation of a particular fullerene bis-adduct. Spectroscopic evidence indicates that the ternary complex is sufficiently stable in solution for the two outer shells to affect the addition chemistry of the fullerene guest. When the complex is subjected to Bingel cyclopropanation conditions, the exclusive formation of a single *trans*-3 fullerene bis-adduct was observed in a reaction that typically yields more than a dozen products. The selectivity facilitated by this matryoshka-like approach appears to be a general phenomenon and could be useful for applications where regioisomerically pure C_{60} bis-adducts have been shown to have superior properties compared with isomer mixtures.

The regioselective multiple functionalization of C_{60} is a long-standing problem in fullerene chemistry, with implications for applied research fields such as organic photovoltaics[1–5], perovskite solar cells[6] or biomedicine[7,8]. The selective synthesis of C_{60} mono- and hexakis-adducts can be considered a solved problem, because an excess of C_{60} or the reagent for functionalization can be used to guarantee predominant mono- or hexakis-functionalization and minor side products can be removed via chromatographic separation[9]. However, obtaining isomerically pure bis-, tris-, tetra- or penta-adducts of C_{60} by chromatographic separation is very challenging because the lack of efficient stoichiometric control leads to a mixture of oligo-adducts (bis-, tris-adducts and so on), while each oligo-adduct may exist in the form of more than a dozen distinct regioisomers. Generating isomerically pure multiple adducts of C_{60} would therefore not only solve a technical problem (increased yield), but in many cases would represent the only feasible way to obtain these compounds in pure form[10].

When considering the synthesis of fullerene bis-adducts, the addition of a second identical and symmetric addend to a fullerene mono-adduct leads to eight potential different regioisomers (in order of increasing distance between the substituents: *cis*-1, *cis*-2, *cis*-3, *e*, *trans*-4, *trans*-3, *trans*-2, *trans*-1)[11,12]. If addends are non-symmetric, as is the case in bis-$PC_{60}BM$ (ref. [13]), 18 bis-adduct regioisomers are obtained in the crude reaction mixture, and their HPLC separation is extremely challenging[14]. Furthermore, recent studies by Li and co-workers[15] and Grätzel and co-workers[16] have demonstrated that isomerically pure bis-adducts of C_{60} can outperform the commonly employed isomer mixtures in bulk heterojunction and perovskite solar cells, indicating that there is a need to develop a methodology for accessing pure fullerene regioisomers[17].

Several strategies have been reported to effectively control the regioselective bis-adduct functionalization of C_{60}, the most common being the 'tether-directed remote functionalization' approach pioneered by Diederich and co-workers in the mid-1990s for the Bingel cyclopropanation reaction[18–20]. In this approach one single bis-adduct isomer is formed predominantly, because the length of the tether bridge in a ditopic malonate reagent dictates the maximum distance between the two addends (Fig. 1a)[21–23]. The obvious drawback is that the tether bridge is not removable and remains in the bis-adduct product, which compromises the applicability of the functionalized products. Beyond the tether approach, elegant strategies have been developed for the synthesis of *trans*-1 Diels–Alder[24], *e*,*e*,*e*,*e*-tetrakis[25,26] and pentakis[27] Bingel cyclopropanated adducts.

The modulation of the regioselectivity of multiple addition reactions by confinement of C_{60} in supramolecular receptors has recently emerged as an alternative approach[28]. For instance, a cubic[29] coordination cage and a metal–organic framework[30] have been demonstrated to selectively bind to Diels–Alder bis-adducts of C_{60} and preliminary studies on using these hosts to direct the fullerene functionalization towards C_{60}-anthracene bis-adducts have been carried out (the regioisomer issue was not investigated). Further recent advances include a supramolecular bowl to furnish a selective Diels–Alder monofunctionalization of C_{60} despite a 10-fold excess of the reagent anthracene[31], a boronate ester cage giving rise to a symmetry-matched Prato tris-adduct as major reaction product[32] and a supramolecular tether approach that afforded the isolation of a rare *cis*-1 C_{60} bis-adduct in 14% yield[33]. Von Delius and

[1]Institut de Química Computacional i Catàlisi and Departament de Química, Universitat de Girona, Girona, Spain. [2]Institute of Organic Chemistry, Ulm University, Ulm, Germany. [3]Serveis Tècnics de Recerca, Universitat de Girona, Girona, Spain. [4]ALBA Synchrotron, Cerdanyola del Vallès, Spain. [5]Materials Science Institute of Madrid, Spanish National Research Council, Madrid, Spain. [6]Catalan Institute of Nanoscience and Nanotechnology, CSIC and The Barcelona Institute of Science and Technology, Barcelona, Spain. [7]ICREA, Barcelona, Spain. ✉e-mail: max.vondelius@uni-ulm.de; xavi.ribas@udg.edu

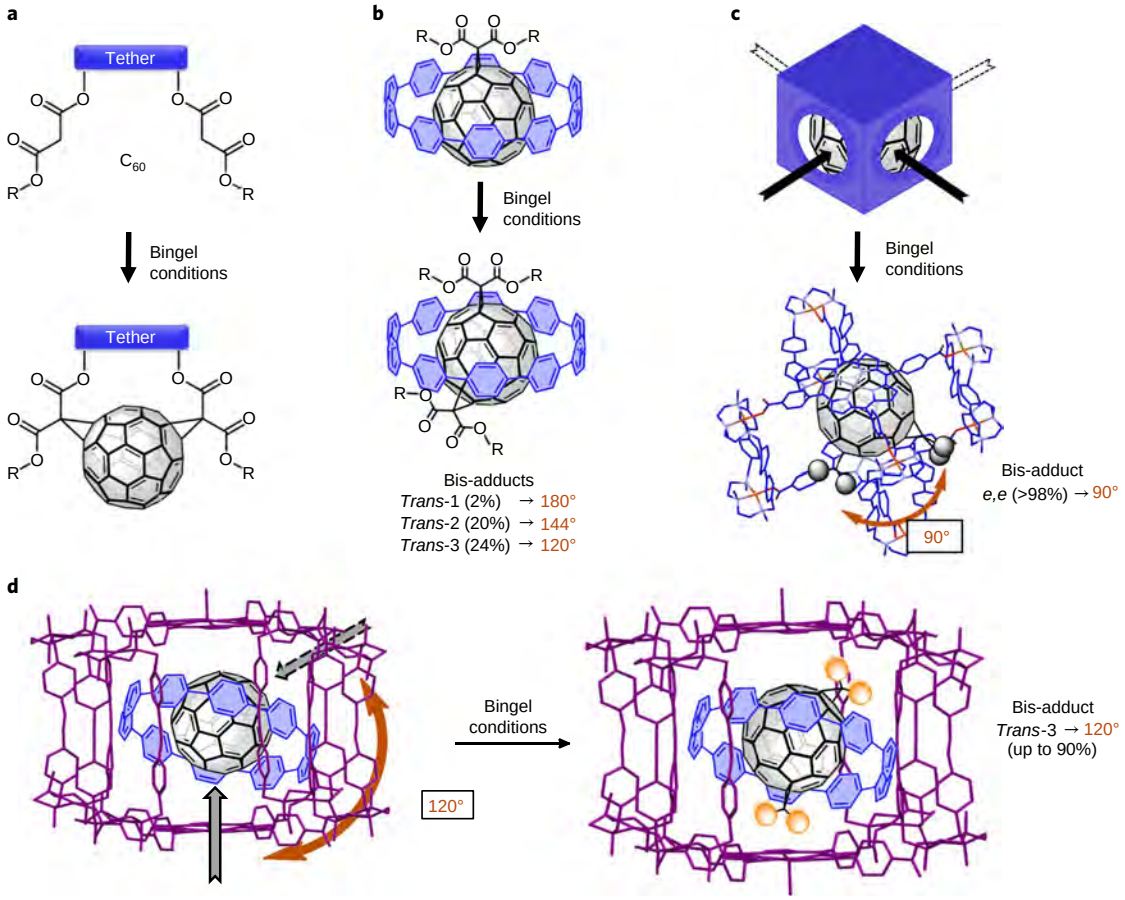

Fig. 1 | Strategies reported for the regioselective synthesis of C_{60} adducts. a, Tether approach, where a length-modifiable tether is installed in a bidentate adduct to obtain preferential Bingel bis-adduct isomers (conditions: $\mathbf{C_{60}}$, I_2, 1,8-diazabicyclo[5.4.0]undec-7-ene (DBU), toluene, r.t.). **b**, Nanohoop template, that is, C_{60}⊂[10]CPP, where the nanohoop restricts the accessibility of the reagents and imposes selectivity on the formation of Bingel bis-adducts (conditions: diethyl malonate, CBr_4, DBU, toluene, r.t.). **c**, Supramolecular mask strategy for regioselective equatorial Bingel functionalization (symmetry match) through the four cross-shaped gates of the tetragonal prismatic (biphenyl-based) nanocapsule (conditions: diethyl bromomalonate, NaH, CH_3CN, r.t.). Orange arrows and orange numerals represent angles between cyclopropane addends or angles of attack. Grey and orange spheroids represent malonate substituents. **d**, Matryoshka-like strategy for regioselective *trans*-3 bis-functionalization (symmetry mismatch, this work) using an enlarged tetragonal prismatic nanocapsule (conditions: diethyl bromomalonate, NaH, CH_3CN, r.t.).

co-workers reported on the ability of the nanohoop [10]cycloparaphenylene (**[10]CPP**), which forms the supramolecular complex C_{60}⊂[10]CPP ($K_a \approx 10^6\,M^{-1}$ in toluene)[34–38], to infer a substantial degree of regiocontrol on the formation of Bingel bis-adducts (Fig. 1b)[39]. Specifically, the *trans*-2 and *trans*-3 regioisomers were obtained as major products in almost equimolar amounts, along with a small amount of *trans*-1, whereas the *e*, *cis*-1, *cis*-2, *cis*-3 and *trans*-4 regioisomers were avoided.

On the other hand, Ribas and co-workers have successfully developed a supramolecular mask strategy using tetragonal prismatic nanocapsules to gain full control on the regioselectivity for Bingel *e*-isomer bis-adducts (Fig. 1c)[40]. Thus, in the present work we have combined the latter two strategies by encapsulating the C_{60}⊂[10]CPP adduct in a newly designed tetragonal prismatic nanocapsule **6**·$(BArF)_8$, featuring an enlarged cavity with macrocyclic **Me_2pTp**-based clips, capable of the strong encapsulation of the Saturn-like C_{60}⊂[10]CPP guest (Fig. 1d). Upon exposure of the tightly associated three-shell supramolecular complex[41–44] to Bingel cyclopropanation reaction conditions, the functionalization of the inner $\mathbf{C_{60}}$ was directed to form exclusively the *trans*-3 bis-isomer. The combination of the **[10]CPP** and supramolecular mask encapsulation into the matryoshka-like three-shell system not only leads to perfect regioselectivity, which has no precedents, but also prevents any overfunctionalization due to the confined environment. Crystallographic analysis of pre- and postfunctionalized C_{60}⊂[10]CPP⊂**7**·$(BArF)_8$ matryoshka-like complexes affords a compelling explanation for the counterintuitive, symmetry-mismatched *trans*-3 regioselectivity.

Results and discussion

Synthesis and characterization of the extended nanocapsule 6·$(BArF)_8$. To prepare a nanocapsule large enough to accommodate the host–guest complex C_{60}⊂[10]CPP, we modified the previously reported strategy for the self-assembly of tetragonal prismatic nanocapsules **3**, **4** and **5**·$(BArF)_8$ (refs. [40,45,46]) by designing a larger linker for the macrocyclic molecular clip (Extended Data Fig. 1). To this end, we initially synthesized a phenyl-acetylene-phenyl *para*-dialdehyde[47] that underwent a 2+2 cyclization to form the imine-containing **S_2pTp** macrocycle, which was hydrogenated, methylated and finally complexated with Pd(ii) or Cu(ii) salts to obtain the corresponding molecular clip synthons, respectively ($[Pd_2(Me_2pTp)(AcO)_2](OTf)_2$ and $[Cu_2(Me_2pTp)(OTf)_2](OTf)_2$, see crystal structure in Supplementary Fig. 42). The molecular clips were self-assembled with Zn(ii)-based 5,10,15,20-(tetra-4-carboxyphenyl)porphyrin in a 2:1 ratio in refluxing DMF and NEt_3 as base to finally obtain the tetragonal prismatic nanocapsules **6**·$(OTf)_8$

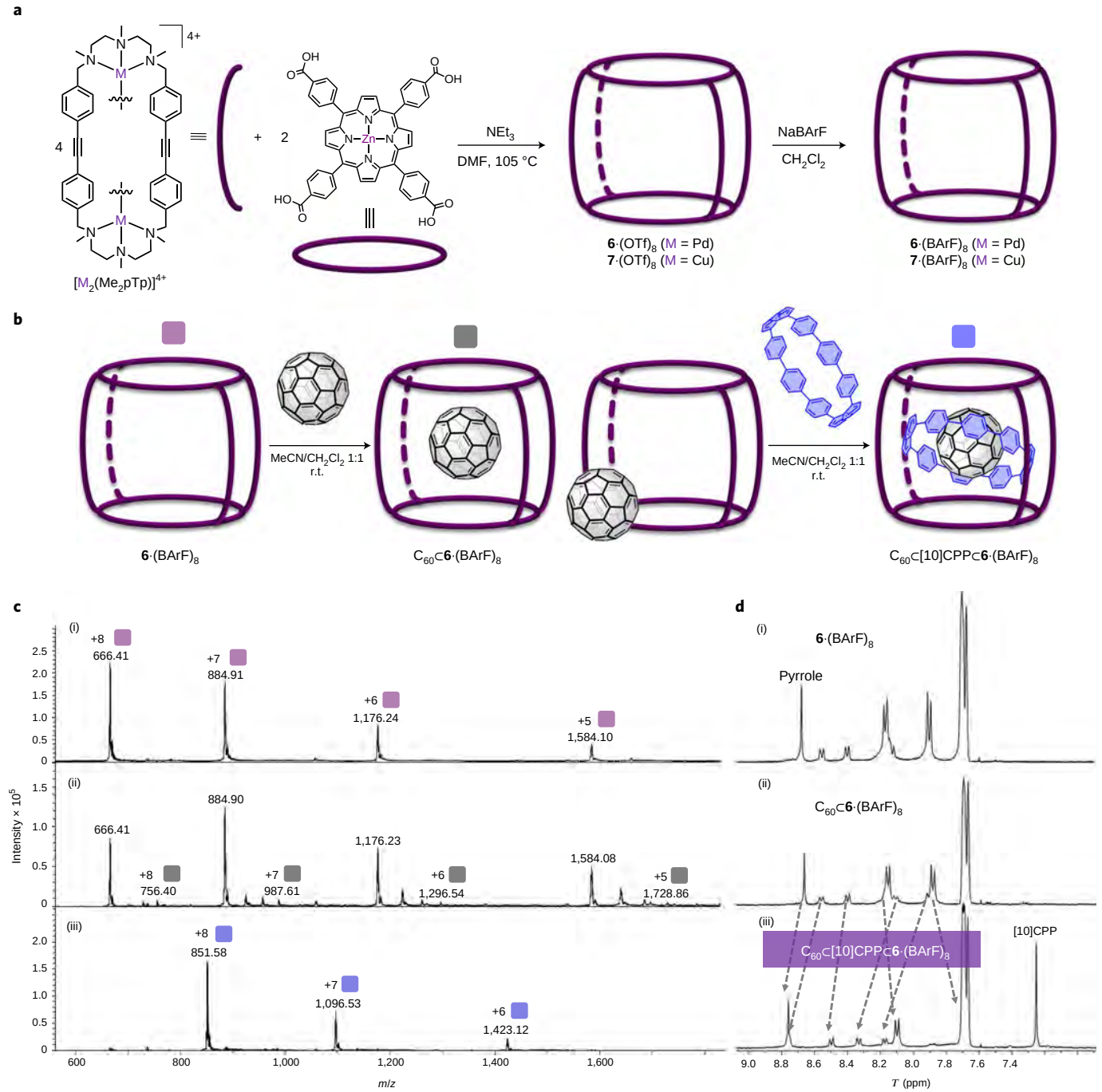

Fig. 2 | Synthesis of the tetragonal prismatic nanocapsules used and encapsulation of C_{60}⊂[10]CPP. a, Synthesis of Pd- and Cu-based nanocapsules **6**·$(X)_8$ and **7**·$(X)_8$ (X = OTf, BArF). **b**, Schematic representation of the encapsulation of $\mathbf{C_{60}}$ in the nanocapsule **6**·$(BArF)_8$ and subsequent addition of **[10]CPP** (in $MeCN/CH_2Cl_2$ 1:1 solvent mixture). **c**, HRMS (positive-ion electrospray ionization) for (i) **6**·$(BArF)_8$, (ii) **6**·$(BArF)_8$ with the addition of $\mathbf{C_{60}}$ and (iii) C_{60}⊂[10]CPP⊂**6**·$(BArF)_8$ (spectrum recorded after 10 min of mixing). **d**, ^{1}H NMR (in CD_3CN after solvent switch) for (i) **6**·$(BArF)_8$, (ii) C_{60}⊂**6**·$(BArF)_8$ and (iii) C_{60}⊂[10]CPP⊂**6**·$(BArF)_8$.

(Pd(ii) analogue, 81% yield) and **7**·$(OTf)_8$ (Cu(ii) analogue, 83% yield). Anion metathesis with NaBArF in CH_2Cl_2 afforded the target nanocapsules **6**·$(BArF)_8$ (75% yield) and **7**·$(BArF)_8$ (77% yield) (Fig. 2). The diamagnetic Pd(ii)-based nanocapsule **6**·$(BArF)_8$ was characterized by ^{1}H NMR spectroscopy and high-resolution mass spectrometry (HRMS) (Fig. 2c and Supplementary Fig. 50), whereas the paramagnetic Cu(ii)-based **7**·$(BArF)_8$ was characterized by HRMS (Supplementary Fig. 53) and X-ray diffraction (XRD) (see below).

Encapsulation of C_{60}⊂[10]CPP in nanocapsule 6·$(BArF)_8$. Having obtained the nanocapsule **6**·$(BArF)_8$, we focused our attention on its host–guest properties. Given its larger cavity (Zn–porph···Zn–porph distance, 16.8 Å) compared with that of the previously reported nanocapsule **4**·$(BArF)_8$ (Zn–porph···Zn–porph distance, 14.1 Å)[40,45], we speculated whether encapsulation of $\mathbf{C_{60}}$ could be achieved. HRMS experiments indicated that the affinity was very weak and an ultraviolet–visible titration allowed us to determine

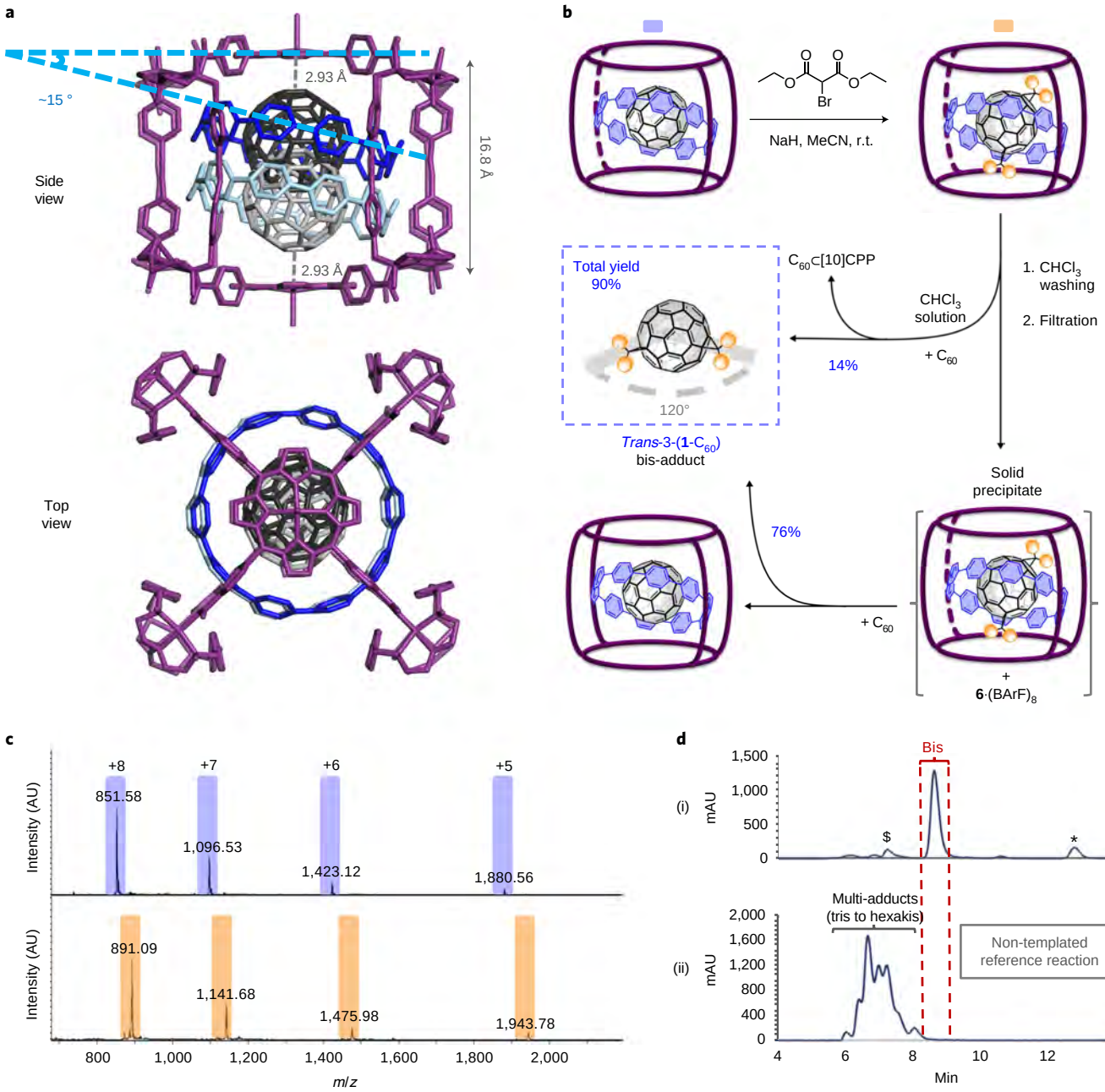

Fig. 3 | Structural characterization of the matryoshka-like ensemble and its reactivity towards selective formation of Bingel *trans*-3 bis-adducts. a, Crystal structure of C_{60}⊂[10]CPP⊂**7**·$(BArF)_8$, showing 50% occupancy of C_{60}⊂[10]CPP in two positions inside the cavity of **7**·$(BArF)_8$ and featuring an up and down piston-stroke-like movement (side and top views). **b**, Exposure of C_{60}⊂[10]CPP⊂**6**·$(BArF)_8$ to Bingel cyclopropanation conditions with diethyl bromomalonate leads to the chemoselective and regioselective formation of the *trans*-3 bis-adduct; solvent washing with $CHCl_3$ and exchange with pristine $\mathbf{C_{60}}$ liberates the product (detailed work-up flow in Supplementary Fig. 65). **c**, HRMS monitoring of the bis-adduct formation upon addition of 5 equiv. of bromomalonate (two sequential additions of 2.5 equiv.). **d**, HPLC analysis of (i) the extracted bis-adduct product compared to (ii) the mixture of polyadducts obtained with bare $\mathbf{C_{60}}$ (performed using 5 equiv. NaH in MeCN/1,2-dichlorobenzene 1:4 to achieve solubility of pristine $\mathbf{C_{60}}$, 3 h, r.t.) ($\lambda = 320$ nm; *C_{60}; $non-fullerene impurities, more details are given in Supplementary Information, section 1.13).

a K_a of $5.4 \pm 0.9 \times 10^3\ M^{-1}$ (Supplementary Fig. 91, Supplementary Tables 7–9 and http://supramolecular.org/)[48,49] in toluene/acetonitrile 9:1 solvent, which was used throughout this study for spectroscopic titrations. $\mathbf{C_{60}}$ therefore binds approximately four orders of magnitude less strongly to the extended nanocapsule **6**·$(BArF)_8$ than to the original nanocapsule **4**·$(BArF)_8$, for which a K_a of $2.8 \pm 0.6 \times 10^7\ M^{-1}$ was reported previously in the same solvent mixture[45]. When only **[10]CPP** was added to nanocapsule **6**·$(BArF)_8$, we were able to determine a K_a of $1.1 \pm 0.1 \times 10^5\ M^{-1}$ by fluorescence titration (Supplementary Fig. 90 and Supplementary Tables 4–6). To complete the picture on binary host–guest equilibria, we determined a K_a of $5.7 \pm 0.4 \times 10^6\ M^{-1}$ for the known complex C_{60}⊂[10]CPP in toluene/acetonitrile 9:1 (Supplementary Fig. 89 and Supplementary Tables 1–3). The equilibrium between nanohoop and fullerene is therefore the strongest of the three relevant host–guest association events, while the binding of $\mathbf{C_{60}}$ to the nanocapsule is the weakest.

In accordance with these data on the three binary equilibria, we were able to assemble the matryoshka-like complex C_{60}⊂[10]

CPP⊂**6**·$(BArF)_8$ (Fig. 2b) by adding 1 equiv. of **[10]CPP** to the previously prepared mixture of **6**·$(BArF)_8$ and $\mathbf{C_{60}}$ in a suitable solvent mixture. The fact that a solvent switch to pure acetonitrile (HRMS in Fig. 2c and ^{1}H NMR in Fig. 2d) was possible despite the lack of solubility of $\mathbf{C_{60}}$ and **[10]CPP** in this pure solvent is a qualitative indication of the stability of the three-shell complex under these conditions. To study the matryoshka-like complex by spectroscopic titration in toluene/acetonitrile 9:1, we adopted an approximation previously used by Thordarson and Stoddart for related three-component systems[43,50]. Having previously confirmed that C_{60}⊂[10]CPP represents the strongest binary association event, we sought to answer the question whether the presence of the nanocapsule (in excess and at constant concentration) would substantially affect the stability of the C_{60}⊂[10]CPP complex. The resulting binding isotherm could be fitted relatively well with a 1:1 model, giving an apparent K_a of $9.3 \pm 0.4 \times 10^6\ M^{-1}$ (Supplementary Fig. 92 and Supplementary Tables 10–12). We deduce from the feasibility of this approximation and from the small difference to the K_a observed for pristine C_{60}⊂[10]CPP ($5.7 \pm 0.4 \times 10^6\ M^{-1}$) that all binding events in the three-shell complex are relatively independent from one another and that any cooperativity[51], if present, would be moderate and positive. Finally, we corroborated the high preference for the encapsulation of the C_{60}⊂[10]CPP complex within **6**·$(BArF)_8$ in an experiment aimed at encapsulating C_{60}⊂[10]CPP in the smaller nanocapsule **4**·$(BArF)_8$ (refs. [45,52]). Upon mixing, the only observed supramolecular adduct in the HRMS spectrum was C_{60}⊂**4**·$(BArF)_8$, which indicated that the C_{60}⊂[10]CPP was fully dissociated in this competition experiment (Supplementary Fig. 64).

Crystal structure of C_{60}⊂[10]CPP⊂7·$(BArF)_8$. The high thermodynamic stability of the Pd(ii)-based three-shell complex C_{60}⊂[10]CPP⊂**6**·$(BArF)_8$ prompted us to try to obtain high-quality single crystals, without success. However, by using the Cu(ii)-based analogous nanocapsule **7**·$(BArF)_8$, suitable crystals for XRD under synchrotron light were obtained, featuring the Saturn-like complex C_{60}⊂[10]CPP inside the cavity in slightly tilted orientation with respect to the porphyrin planes (~15°) (Fig. 3a). The guest complex is found in two positions (50% occupation), thus prioritizing the interaction between the zinc porphyrin and the fullerene[53] over other possible geometric arrangements. This preference for two fullerene positions, which in solution are connected by rapid equilibria (one singlet observed by ^{1}H NMR spectroscopy for both **[10]CPP** protons and pyrrol protons from Zn–porphyrin units, respectively, see Fig. 2d; one singlet observed by ^{13}C NMR spectroscopy for $\mathbf{C_{60}}$ guest, see Supplementary Fig. 56)[54], has the important consequence that the **[10]CPP** nanohoops are preferentially in slightly tilted orientation (~15°) to the two Zn–porphyrins (vertical alignment precluded due to large diameter of [10]CPP, that is, ~14 Å for a nanocapsule featuring a Zn–porph···Zn–porph distance of 16.8 Å). The latter finding severely limits possible angles of 'attack' for bromomalonate reagents that need to enter through the four windows of the nanocapsule and subsequently avoid any steric clash with **[10]CPP** before adding to a fullerene [6,6] double bond.

Single-isomer *trans*-3 bis-adduct synthesis. Given the successful use of tetragonal prismatic nanocapsules, that is, **4**·$(BArF)_8$, as supramolecular masks for the regioselective equatorial Bingel cyclopropanation of $\mathbf{C_{60}}$ (ref. [40]), we hypothesized that the matryoshka-like assembly C_{60}⊂[10]CPP⊂**6**·$(BArF)_8$ might induce a different regioselectivity for the cyclopropanation of $\mathbf{C_{60}}$. Upon exposure of the matryoshka-like compound to an excess of diethyl bromomalonate (5 equiv.) and NaH (5 equiv.) in CH_3CN at room temperature for 2.5 h, a complex containing a bis-adduct C_{60} was obtained chemoselectively (Fig. 3b), with no signs of multiple additions or nanocapsule decomposition, as clearly shown by HRMS (Fig. 3c). The removal of the bis-adduct $\mathbf{C_{60}}$ from the inner shell of the matryoshka-like assembly was achieved by a two-step work-up routine, including an initial $CHCl_3$ washing step and displacement from **[10]CPP** by addition of excess $\mathbf{C_{60}}$ (detailed work-up flowchart in Supplementary Fig. 65). In this manner, a solution of the bis-adduct in $CHCl_3$ was obtained, allowing us to directly quantify the product by HPLC analysis, and then further fully characterize the sample by ultraviolet–visible and NMR spectroscopy. These analyses unequivocally showed that a single bis-adduct regioisomer, ***trans*-3-(1-$\mathbf{C_{60}}$)**, had been formed in a total yield of 90% (Fig. 3b). Having obtained this isolated sample, we were able to determine the association constant for the formation of the *trans*-3-(**1**-C_{60})⊂[10]CPP inclusion complex by fluorescence titration (Supplementary Fig. 93 and Supplementary Tables 13–15), affording a K_a of $3.6 \pm 0.5 \times 10^5\ M^{-1}$, which is about 20-fold lower than the K_a observed for the starting material C_{60}⊂[10]CPP in the same solvent mixture (toluene/acetonitrile 9:1). This difference in binding constants explains why the release protocol shown in Fig. 3b is effective[39].

The identity and purity of the ***trans*-3-(1-$\mathbf{C_{60}}$)** bis-adduct was verified by an independent, unselective synthesis starting from $\mathbf{C_{60}}$, followed by time-consuming chromatographic purification of the *trans*-3 regioisomer. As expected, the diffusion coefficents (D) and solvodynamic radii (r_S) of nanocapsule **6**·$(BArF)_8$, matryoshka-like C_{60}⊂[10]CPP⊂**6**·$(BArF)_8$ and *trans*-3-(**1**-C_{60})⊂[10]CPP⊂**6**·$(BArF)_8$ are fundamentally the same, irrespective of which guest is encapsulated, thus confirming that the size of the capsule is the major factor defining D values (Supplementary Table 17). Remarkably, the product distribution observed by HPLC analysis showed exclusive *trans*-3 bis-adduct formation using the three-shell strategy (Fig. 3d), whereas a mixture of multiple-addition products with uncontrolled regioselectivity (with no trace of bis-adducts) was obtained for the non-templated functionalization of $\mathbf{C_{60}}$ (Fig. 3d).

Fortunately, single crystals of *trans*-3-(**1**-C_{60})⊂[10]CPP⊂**7**·$(BArF)_8$ could be grown and were subjected to XRD at the synchrotron facility. However, due to the complexity of the structure and the fragility of the crystals, only preliminary crystal data up to 1.30 Å resolution can be reported here. Several attempts were made to achieve higher resolutions. However, no observable reflections were detected beyond this resolution, even after increasing the X-ray exposure time. This limitation must be imposed by the large number of disordered groups in the crystals. Nevertheless, these data show on a qualitative level a similar arrangement of the matryoshka-like assembly with $\mathbf{C_{60}}$ (Fig. 4a), but with a substantial change in the tilted angle of the **[10]CPP** arrangement with respect to the porphyrin planes (~26° compared with the previous 15°). This substantial change in the tilted angle of the **[10]CPP** suggests that the presence of a bis-adduct $\mathbf{C_{60}}$ increased the steric crowding within the matryoshka-like assembly. Due to the limited resolution and the statistical positional disorder of the $\mathbf{C_{60}}$ inside the nanocapsule, the position of the *trans*-3 bis-cyclopropanated adducts could not be located by XRD refinement. Nonetheless, the position of one of the malonate groups could be identified from analysis of the difference Fourier maps, and added as a rigid-body group for subsequent refinements. The location of this group, along with the tilted angle of the **[10]CPP**, imposes steric constraints that explain the *trans*-3 selectivity.

At first hand, this selectivity is highly counterintuitive, because the ***trans*-3-(1-$\mathbf{C_{60}}$)** bis-adduct features a 120° angle between the two addends, whereas the nanocapsule exhibits four-fold symmetry and thus a 90° angle between the windows (which in the case of capsule **4**·$(BArF)_8$ leads to the formation of *e*-bis-adducts). However, in the present case there is only one possibility to locate all components within the matryoshka-like assembly, which is by accessing through contiguous windows of the nanocapsule as depicted in Fig. 4b. The position of the second *trans*-3 malonate group could not be included in the final crystallographic refinement because the atomic positions were superimposed with those of the alternative, symmetrically generated $\mathbf{C_{60}}$ derivative inside

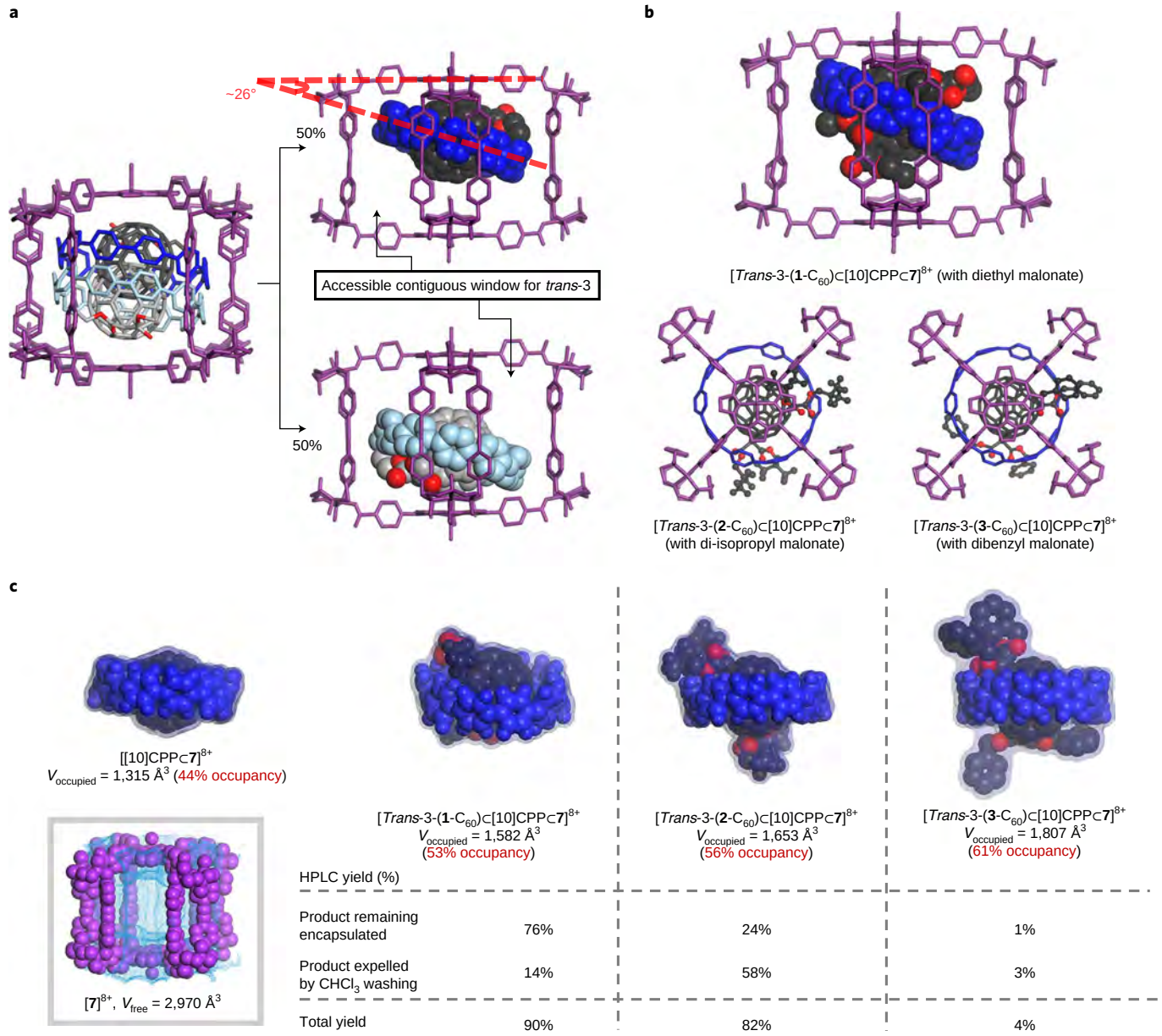

Fig. 4 | Crystal structure of the encapsulated *trans*-3 bis-adducts and void analysis study on the impact of the different bis-adduct sterics. a, View of three-component assembly as determined by single-crystal XRD refinement of *trans*-3-(**1**-C_{60})⊂[10]CPP⊂**7**·$(BArF)_8$. **b**, Different representations of the *trans*-3-(**1**-C_{60})⊂[10]CPP, *trans*-3-(**2**-C_{60})⊂[10]CPP and *trans*-3-(**3**-C_{60})⊂[10]CPP models inside the nanocapsule featuring the 120° bis-functionalization at contiguous windows of the tetragonal prismatic host. The orientation of the malonate substituent groups (ethyl, isopropyl or benzyl) was geometrically optimized with a universal-forcefield-based minimization process, as implemented in the Forcite module of Materials Studio software (2019 version, BIOVIA). **c**, Void analysis study of the free accessible volume of the nanocapsule and volume occupancies of the different guests (Materials Studio) correlated with the yields of the *trans*-3 adducts obtained from the workflow described in Fig. 3b.

the nanocapsule. Nevertheless, based on the crystallographic data, a model was created confirming the feasibility of this geometric arrangement of the *trans*-3 bis-adduct for ***trans*-3-(1-C_{60})** within the capsule. Further evidence for the constrained nature of the *trans*-3-(**1**-C_{60})⊂[10]CPP⊂**7**·$(BArF)_8$ complex can be derived from the ^{1}H NMR spectrum in CD_3CN, which shows a lowering of capsule symmetry, that is, splitting of the pyrrole singlet into a multiplet (Supplementary Fig. 87).

At this point we decided to test the generality of the observed ideal chemoselectivity (bis-adduct) and the symmetry-mismatched *trans*-3 regioselectivity. We therefore synthesized di-isopropyl, di-*tert*-butyl and dibenzyl bromomalonates and tested these substrates under identical reaction conditions. For both the di-isopropyl and dibenzyl bromomalonates, the *trans*-3 bis-adducts were obtained exclusively (Supplementary Figs. 68 and 69), although differing in the total yield (HPLC quantification): 82% for ***trans*-3-(2-C_{60})** and 4% for ***trans*-3-(3-C_{60})** (Fig. 4b,c). Furthermore, following the workflow detailed in Fig. 3b, the first washing of the three-shell product complex with $CHCl_3$ removed some of the encapsulated *trans*-3-C_{60}⊂[10]CPP product complex from the nanocapsule. Moreover, the amount of this first release was very much dependent on the steric bulk of the malonate substituents (Et, ^{i}Pr, Bn). Thus, for each product we have essentially obtained two types of yields for *trans*-3-C_{60} products (one after $CHCl_3$

release of *trans*-3-C_{60}⊂[10]CPP plus $\mathbf{C_{60}}$ exchange, and one after $\mathbf{C_{60}}$ exchange directly on the *trans*-3-(**1**-C_{60})⊂[10]CPP⊂**6**·$(BArF)_8$ complex. The amount of product release correlates well with the void space analysis (although increasing solubility of the product in $CHCl_3$ might also be a factor): the volume occupancy is 53% (that is, below 55% Rebek's rule)[55] for *trans*-3-(**1**-C_{60})⊂[10]CPP, which leads to a low amount of guest release by $CHCl_3$ washing (14%). The volume occupancy is 56% for *trans*-3-(**2**-C_{60})⊂[10]CPP (that is, slightly above 55% Rebek's rule), which leads to 58% of guest release by solvent washing (~2-fold with respect to the guest remaining encapsulated). For *trans*-3-(**3**-C_{60})⊂[10]CPP the volume occupancy is 61%, far beyond Rebek's rule of 55%, which, on the one hand, explains the low yield observed for this reaction, and, on the other hand, explains why we observed a higher fraction (~3-fold) of guest released by solvent washing than guest remaining encapsulated (see yields and void analysis in Fig. 4c).

The exclusive *trans*-3 regioselectivity of our matryoshka-like approach therefore seems to be a general finding, but the scope of substrates is somewhat limited due to the necessity for the reagents to reach the encapsulated fullerene. For substrates with low to moderate steric bulk (for example, diethyl and di-isopropyl) selectivity is perfect and the reaction rate and yields are optimal, while for substrates with moderate to high steric bulk (for example, dibenzyl, Fig. 4b) selectivity remains perfect but the rate and yields decrease abruptly. Substrates with higher steric bulk (for example, di-*tert*-butyl bromomalonate) represent the steric limitation of the three-shell system, since no reaction was observed.

All accessible *trans*-3 bis-adducts (using the diethyl, di-isopropyl and dibenzyl bromomalonates) were independently synthesized using uncontrolled syntheses and purified by preparative chromatography to confirm their identity. All spectroscopic and spectrometric analyses matched the *trans*-3 isomers obtained using the matryoshka-like assembly C_{60}⊂[10]CPP⊂**6**·$(BArF)_8$ (Supplementary Figs. 70–78).

Conclusions

We have developed an unprecedented example of a three-shell heteroleptic matryoshka-like assembly, C_{60}⊂[10]CPP⊂**6**·$(BArF)_8$, by using an extended tetragonal prismatic nanocapsule **6**·$(BArF)_8$ to host the previously reported nanohoop–fullerene complex. Spectroscopic titrations and crystallographic evidence for the matryoshka-like assembly allowed an understanding of the high thermodynamic stability of the overall assembly. Upon submission of C_{60}⊂[10]CPP⊂**6**·$(BArF)_8$ to Bingel cyclopropanation reaction conditions, only the *trans*-3 fullerene bis-adduct was obtained for the bromomalonates tested (excluding the di-*tert*-butyl derivative for steric reasons). Crystallographic evidence for the bis-functionalized three-shell matryoshka-like assembly demonstrated the unique ability of this architecture to restrict the complex functionalization chemistry of $\mathbf{C_{60}}$ exclusively to 120° angles in contiguous windows of the nanocapsule. These results contrast with the mixture of *trans*-1, *trans*-2 and *trans*-3 obtained by functionalizing C_{60}⊂[10]CPP, and also with the *e*-bis-isomer obtained applying only the nanocapsule supramolecular mask strategy. Thus by combining the two previous approaches, we enabled a regioisomeric outcome which could not have been predicted and which represents a unique case of symmetry mismatch between supramolecular nanocontainer and reaction product.

The use of three-shell, heteroleptic matryoshka-like assemblies can become a strategy of choice to synthesize highly challenging, regioisomerically pure fullerene bis-adducts, which in turn may lead to further advances in organic electronics and solar cells. This regiocontrolled bis-functionalization could also open the door to the templated oligomerization of fullerenes, such that novel conductive channels or mechanically interwoven materials could be designed.

Online content

Any methods, additional references, Nature Research reporting summaries, source data, extended data, supplementary information, acknowledgements, peer review information; details of author contributions and competing interests; and statements of data and code availability are available at https://doi.org/10.1038/s41557-021-00658-6.

Received: 15 March 2020; Accepted: 5 February 2021;
Published online: 15 April 2021

References

1. He, Y. & Li, Y. Fullerene derivative acceptors for high performance polymer solar cells. *Phys. Chem. Chem. Phys.* **13**, 1970–1983 (2011).
2. Mishra, A. & Bäuerle, P. Small molecule organic semiconductors on the move: promises for future solar energy technology. *Angew. Chem. Int. Ed.* **51**, 2020–2067 (2012).
3. Mazzio, K. A. & Luscombe, C. K. The future of organic photovoltaics. *Chem. Soc. Rev.* **44**, 78–90 (2015).
4. Ragoussi, M.-E. & Torres, T. New generation solar cells: concepts, trends and perspectives. *Chem. Commun.* **51**, 3957–3972 (2015).
5. Inganäs, O. Organic photovoltaics over three decades. *Adv. Mater.* **30**, 1800388 (2018).
6. Deng, L.-L., Xie, S.-Y. & Gao, F. Fullerene-based materials for photovoltaic applications: toward efficient, hysteresis-free, and stable perovskite solar cells. *Adv. Electron. Mater.* **4**, 1700435 (2018).
7. Muñoz, A. et al. Synthesis of giant globular multivalent glycofullerenes as potent inhibitors in a model of Ebola virus infection. *Nat. Chem.* **8**, 50–57 (2015).
8. Nierengarten, J.-F. et al. Giant glycosidase inhibitors: first- and second-generation fullerodendrimers with a dense iminosugar shell. *Chem. Eur. J.* **24**, 2483–2492 (2018).
9. Hirsch, A. & Brettreich, M. *Fullerenes, Chemistry and Reactions* (Wiley-VCH, 2005).
10. Fuertes-Espinosa, C., Pujals, M. & Ribas, X. Supramolecular purification and regioselective functionalization of fullerenes and endohedral metallofullerenes. *Chem* **6**, 3219–3262 (2020).
11. Djojo, F., Herzog, A., Lamparth, I., Hampel, F. & Hirsch, A. Regiochemistry of twofold additions to [6,6] bonds in C_{60}: influence of the addend-independent cage distortion in 1,2-monoadducts. *Chem. Eur. J.* **2**, 1537–1547 (1996).
12. Hirsch, A., Lamparth, I. & Karfunkel, H. R. Fullerene chemistry in three dimensions: isolation of seven regioisomeric bisadducts and chiral trisadducts of C_{60} and di(ethoxycarbonyl)methylene. *Angew. Chem. Int. Ed.* **33**, 437–438 (1994).
13. Lenes, M. et al. Fullerene bisadducts for enhanced open-circuit voltages and efficiencies in polymer solar cells. *Adv. Mater.* **20**, 2116–2119 (2008).
14. Shi, W. et al. Purification and electronic characterisation of 18 isomers of the OPV acceptor material bis-[60]PCBM. *Chem. Commun.* **53**, 975–978 (2017).
15. Cao, T. et al. Towards a full understanding of regioisomer effects of indene-C_{60} bisadduct acceptors in bulk heterojunction polymer solar cells. *J. Mater. Chem. A* **5**, 10206–10219 (2017).
16. Zhang, F. et al. Isomer-pure bis-PCBM-assisted crystal engineering of perovskite solar cells showing excellent efficiency and stability. *Adv. Mater.* **29**, 1606806 (2017).
17. Umeyama, T. & Imahori, H. Isomer effects of fullerene derivatives on organic photovoltaics and perovskite solar cells. *Acc. Chem. Res.* **52**, 2046–2055 (2019).
18. Isaacs, L., Diederich, F. & Haldimann, R. F. Multiple adducts of C_{60} by tether-directed remote functionalization and synthesis of soluble derivatives of new carbon allotropes Cn(60+5). *Helv. Chim. Acta* **80**, 317–342 (1997).
19. Isaacs, L., Haldimann, R. F. & Diederich, F. Tether-directed remote functionalization of buckminsterfullerene: regiospecific hexaadduct formation. *Angew. Chem. Int. Ed.* **33**, 2339–2342 (1994).
20. Đorđević, L. et al. Light-controlled regioselective synthesis of fullerene bis-adducts. *Angew. Chem. Int. Ed.* **60**, 313–320 (2021).
21. Qian, W. & Rubin, Y. Complete control over addend permutation at all six pseudooctahedral positions of fullerene C_{60}. *J. Am. Chem. Soc.* **122**, 9564–9565 (2000).
22. Beuerle, F. & Hirsch, A. Synthesis and orthogonal functionalization of [60] fullerene *e,e,e*-trisadducts with two spherically defined addend zones. *Chem. Eur. J.* **15**, 7434–7446 (2009).
23. Beuerle, F., Chronakis, N. & Hirsch, A. Regioselective synthesis and zone selective deprotection of [60]fullerene tris-adducts with an *e,e,e* addition pattern. *Chem. Commun.* 3676–3678 (2005).
24. Kräutler, B. et al. A topochemically controlled, regiospecific fullerene bisfunctionalization. *Angew. Chem. Int. Ed.* **35**, 1204–1206 (1996).

25. Schwenninger, R., Müller, T. & Kräutler, B. Concise route to symmetric multiadducts of [60]fullerene: preparation of an equatorial tetraadduct by orthogonal transposition. *J. Am. Chem. Soc.* **119**, 9317–9318 (1997).
26. Ortiz, A. L. & Echegoyen, L. Unexpected and selective formation of an (*e*,*e*,*e*,*e*)-tetrakis-[60]fullerene derivative via electrolytic retro-cyclopropanation of a D_{2h}-hexakis-[60]fullerene adduct. *J. Mater. Chem.* **21**, 1362–1364 (2011).
27. Hörmann, F., Donaubauer, W., Hampel, F. & Hirsch, A. Efficient synthesis of C_{2v}-symmetrical pentakisadducts of C_{60} as versatile building blocks for fullerene architectures that involve a mixed octahedral addition pattern. *Chem. Eur. J.* **18**, 3329–3337 (2012).
28. Yoshizawa, M., Klosterman, J. K. & Fujita, M. Functional molecular flasks: new properties and reactions within discrete, self-assembled hosts. *Angew. Chem. Int. Ed.* **48**, 3418–3438 (2009).
29. Brenner, W., Ronson, T. K. & Nitschke, J. R. Separation and selective formation of fullerene adducts within an $M^{II}_8L_6$ cage. *J. Am. Chem. Soc.* **139**, 75–78 (2017).
30. Huang, N. et al. Tailor-made pyrazolide-based metal–organic frameworks for selective catalysis. *J. Am. Chem. Soc.* **140**, 6383–6390 (2018).
31. Chen, B., Holstein, J. J., Horiuchi, S., Hiller, W. G. & Clever, G. H. Pd(ii) coordination sphere engineering: pyridine cages, quinoline bowls, and heteroleptic pills binding one or two fullerenes. *J. Am. Chem. Soc.* **141**, 8907–8913 (2019).
32. Leonhardt, V., Fimmel, S., Krause, A.-M. & Beuerle, F. A covalent organic cage compound acting as a supramolecular shadow mask for the regioselective functionalization of C_{60}. *Chem. Sci.* **11**, 8409–8415 (2020).
33. Bottari, G. et al. Regio-, stereo-, and atropselective synthesis of C_{60} fullerene bisadducts by supramolecular-directed functionalization. *Angew. Chem. Int. Ed.* **55**, 11020–11025 (2016).
34. Iwamoto, T., Watanabe, Y., Sadahiro, T., Haino, T. & Yamago, S. Size-selective encapsulation of C_{60} by [10]cycloparaphenylene: formation of the shortest fullerene-peapod. *Angew. Chem. Int. Ed.* **50**, 8342–8344 (2011).
35. Xia, J., Bacon, J. W. & Jasti, R. Gram-scale synthesis and crystal structures of [8]- and [10]CPP, and the solid-state structure of C_{60}@[10]CPP. *Chem. Sci.* **3**, 3018–3021 (2012).
36. Xu, Y. et al. A supramolecular [10]CPP junction enables efficient electron transfer in modular porphyrin–[10]CPP⊃fullerene complexes. *Angew. Chem. Int. Ed.* **57**, 11549–11553 (2018).
37. Rio, J. et al. Electronic communication between two [10]cycloparaphenylenes and bis(azafullerene) $(C_{59}N)_2$ induced by cooperative complexation. *Angew. Chem. Int. Ed.* **57**, 6930–6934 (2018).
38. Xu, Y. & von Delius, M. The supramolecular chemistry of strained carbon nanohoops. *Angew. Chem. Int. Ed.* **59**, 559–573 (2020).
39. Xu, Y. et al. Concave–convex π–π template approach enables the synthesis of [10]cycloparaphenylene–fullerene [2]rotaxanes. *J. Am. Chem. Soc.* **140**, 13413–13420 (2018).
40. Fuertes-Espinosa, C. et al. Supramolecular fullerene sponges as catalytic masks for regioselective functionalization of C_{60}. *Chem* **6**, 169–186 (2020).
41. Kawase, T., Tanaka, K., Shiono, N., Seirai, Y. & Oda, M. Onion-type complexation based on carbon nanorings and a buckminsterfullerene. *Angew. Chem. Int. Ed.* **43**, 1722–1724 (2004).
42. Rousseaux, S. A. L. et al. Self-assembly of Russian doll concentric porphyrin nanorings. *J. Am. Chem. Soc.* **137**, 12713–12718 (2015).
43. Cai, K. et al. Molecular Russian dolls. *Nat. Commun.* **9**, 5275 (2018).
44. Zhang, D. et al. Enantiopure $[Cs^+/Xe⊂$cryptophane$]⊂Fe^{II}_4L_4$ hierarchical superstructures. *J. Am. Chem. Soc.* **141**, 8339–8345 (2019).
45. García-Simón, C. et al. Sponge-like molecular cage for purification of fullerenes. *Nat. Commun.* **5**, 5557 (2014).
46. Fuertes-Espinosa, C. et al. Purification of uranium-based endohedral metallofullerenes (EMFs) by selective supramolecular encapsulation and release. *Angew. Chem. Int. Ed.* **57**, 11294–11299 (2018).
47. Park, K. et al. Synthesis of symmetrical and unsymmetrical diarylalkynes from propiolic acid using palladium-catalyzed decarboxylative coupling. *J. Org. Chem.* **75**, 6244–6251 (2010).
48. Brynn Hibbert, D. & Thordarson, P. The death of the Job plot, transparency, open science and online tools, uncertainty estimation methods and other developments in supramolecular chemistry data analysis. *Chem. Commun.* **52**, 12792–12805 (2016).
49. Thordarson, P. Determining association constants from titration experiments in supramolecular chemistry. *Chem. Soc. Rev.* **40**, 1305–1323 (2011).
50. Thordarson, P. et al. Allosterically driven multicomponent assembly. *Angew. Chem. Int. Ed.* **43**, 4755–4759 (2004).
51. Rizzuto, F. J. & Nitschke, J. R. Stereochemical plasticity modulates cooperative binding in a CoII12L6 cuboctahedron. *Nat. Chem.* **9**, 903–908 (2017).
52. García-Simón, C. et al. Complete dynamic reconstruction of C_{60}, C_{70}, and $(C_{59}N)_2$ encapsulation into an adaptable supramolecular nanocapsule. *J. Am. Chem. Soc.* **142**, 16051–16063 (2020).
53. Dannhäuser, J. et al. σ-donor and π-acceptor stacking interactions in a trans-2-linked C_{60}–cobalt(ii) tetraphenylporphyrin diad. *Angew. Chem. Int. Ed.* **45**, 3368–3372 (2006).
54. Matsuno, T., Nakai, Y., Sato, S., Maniwa, Y. & Isobe, H. Ratchet-free solid-state inertial rotation of a guest ball in a tight tubular host. *Nat. Commun.* **9**, 1907 (2018).
55. Mecozzi, S. & Rebek, J. J. The 55% solution: a formula for molecular recognition in the liquid state. *Chem. Eur. J.* **4**, 1016–1022 (1998).

Methods

Synthesis of *trans*-3-(1-C_{60})⊂[10]CPP⊂6·$(BArF)_8$. First, 15 mg of C_{60}⊂[10]CPP⊂(**6**·$BArF)_8$ was dissolved in CH_3CN. Then, 5 equiv. of the corresponding bromomalonate (diethyl (**1**), di-isopropyl (**2**), dibenzyl (**3**)) and 5 equiv. of NaH as a base were added sequentially and the reaction was stirred for 16 h under nitrogen. Once the bis-adduct was formed, the reaction was stopped by filtration and removal of the solvent under reduced pressure.

^{1}H NMR (400 MHz, CD_3CN) δ ppm: 8.78 (m, 16H, pyrrole ring), 8.73 (d, J = 8.2 Hz, 8H, aromatic (arom)–porphyrin (porph)), 8.50 (d, J = 8.2 Hz, 8H, arom–porph), 8.35 (d, 8H, arom–porph), 8.29 (d, 8H, arom–porph), 8.06 (d, J = 8.2 Hz, 32H, arom–clip), 7.70 (d, 32H, arom–clip), 7.69–7.66 (m, 96H, $BArF^-$), 7.16 (s, 40H, [10]CPP), 4.05 (d, J = 13 Hz, 16H, $-CH_2-$), 3.64 (m, 16H, $-CH_2-$), 3.58 (s, 48H, N–CH_3), 3.23 (m, 16H, $-CH_2-$), 3.13 (d, J = 13 Hz, 16H, $-CH_2-$), 2.44 (dd, J = 13.5 Hz, 16H, $-CH_2-$), 2.33 (dd, J = 13.5 Hz, 16H, $-CH_2-$), 1.41 (s, 24H, N–CH_3). ^{13}C NMR (100 MHz, CD_3CN, signals and assignment based on heteronuclear single quantum coherence and heteronuclear multiple quantum coherence spectra) δ ppm: 165.4 (arom–porph), 161.9 (BArF), 155.4 (pyrrole ring), 137.0 ([10]CPP), 134.9 (BArF), 133.4 (arom–porph), 132.8 (arom–clip), 132.5 (arom–clip), 131.4 (pyrrole ring), 127.0 ([10]CPP), 122.7 (arom–clip), 117.7 (BArF), 64.4 ($-CH_2-$), 59.9 ($-CH_2-$), 57.9 ($-CH_2-$), 51.3 ($-CH_3$), 42.9 ($-CH_3$).

HRMS (*m*/*z*): calculated 891.0920 and found, 891.0883 (*trans*-3-(**1**-C_{60})⊂[10]CPP⊂[**6**·$(BArF)_0]^{+8}$); calculated, 1141.6861 and found, 1141.6835 (*trans*-3-(**1**-C_{60})⊂[10]CPP⊂[**6**·$(BArF)_1]^{+7}$); calculated, 1475.9784 and found, 1475.9765 (*trans*-3-(**1**-C_{60})⊂[10]CPP⊂[**6**·$(BArF)_2]^{+6}$); calculated, 1943.7875 and found, 1943.7841 (*trans*-3-(**1**-C_{60})⊂[10]CPP⊂[**6**·$(BArF)_3]^{+5}$).

Isolation of *trans*-3-(1-C_{60}). The crude *trans*-3-(**1**-C_{60})⊂[10]CPP⊂**6**·$(BArF)_8$ reaction mixture was washed with $CHCl_3$ affording a precipitate. Then the precipitate was dissolved in CH_3CN and C_{60} (4 equiv.) was added as a suspension in $CHCl_3$ ($CH_3CN/CHCl_3$ 1:1) and stirred at room temperature for 3 h. Then, the solution was dried with a nitrogen gas flow and the ***trans*-3-(1-C_{60})** was obtained after toluene (or $CHCl_3$) addition and filtration of the solid C_{60}⊂[10]CPP complex. Alternatively, **C_{60}** (4 equiv.) was added to the $CHCl_3$ supernatant from the washing step and stirred at room temperature for 3 h. After this time, the solution was dried with a nitrogen gas flow and the ***trans*-3-(1-C_{60})** was obtained after toluene addition and filtration of the solid C_{60}⊂[10]CPP complex. Both fractions were characterized by HPLC and ultraviolet–visible spectroscopy to confirm the *trans*-3 isomer identity, which was also cross-matched with an independently synthesized sample of *trans*-3 bis-adduct. The 90% total yield of the reaction was calculated involving the two fractions of ***trans*-3-(1-C_{60})**. See Supplementary Fig. 65 for a detailed work-up flow.

^{1}H NMR (600 MHz, $CDCl_3$) δ ppm: 1.51 (doublet of quartets, J = 7.1, 3.9 Hz, 4H, $-CH_2-$), 1.48 (doublet of quartets, J = 7.1, 2.1 Hz, 4H, $-CH_2-$), 1.51 (t, J = 7.1 Hz, 6H, $-CH_3$), 1.42 (t, J = 7.1 Hz, 6H, $-CH_3$). ^{13}C NMR (150 MHz, $CDCl_3$) δ ppm: 163.89 (C=O), 163.87 (C=O), 147.60 (C_{60}, sp^2), 147.32 (C_{60}, sp^2), 146.92 (C_{60}, sp^2), 146.88 (C_{60}, sp^2), 146.85 (C_{60}, sp^2), 146.81 (C_{60}, sp^2), 146.77 (C_{60}, sp^2), 146.47 (C_{60}, sp^2), 146.39 (C_{60}, sp^2), 146.02 (C_{60}, sp^2), 145.85 (C_{60}, sp^2), 145.67 (C_{60}, sp^2), 145.00 (C_{60}, sp^2), 144.76 (C_{60}, sp^2), 144.51 (C_{60}, sp^2), 144.22 (C_{60}, sp^2), 143.94 (C_{60}, sp^2), 143.88 (C_{60}, sp^2), 143.73 (C_{60}, sp^2), 143.41 (C_{60}, sp^2), 142.88 (C_{60}, sp^2), 142.59 (C_{60}, sp^2), 142.52 (C_{60}, sp^2), 142.25 (C_{60}, sp^2), 142.01 (C_{60}, sp^2), 140.72 (C_{60}, sp^2), 139.53 (C_{60}, sp^2), 138.90 (C_{60}, sp^2), 72.11 (C_{60} sp^3), 71.62 (C_{60} sp^3), 51.80 (OCCCO), 63.74 ($-CH_2-$), 63.64 ($-CH_2-$), 14.53 ($-CH_3$), 14.51 ($-CH_3$).

The full experimental details and characterization of the new compounds can be found in the Supplementary Information.

Data availability

All data generated or analysed during this study are included in this published article (and its supplementary information files). Crystallographic data for the structures reported in this article have been deposited at the Cambridge Crystallographic Data Centre, under deposition numbers CCDC 1984575 (C_{60}⊂[10]CPP⊂**7**·$(BArF)_8$), 1984576 (*trans*-3-(**1**-C_{60})⊂[10]CPP⊂**6**·$(BArF)_8$) and 1984937 ($[Cu_2(Me_2pTp)(OTf)_2](OTf)_2$). Copies of the data can be obtained free of charge via https://www.ccdc.cam.ac.uk/structures/.

Acknowledgements

This work was supported by grants from MINECO-Spain (CTQ2016-77989-P and PID2019-104498GB-I00 to X.R., RTI2018-095622-B-100 to D.M. and I.I., and EUR2019-103824 to F.G.), Generalitat de Catalunya (2017SGR264 and a PhD grant to C.F.-E.) and the Severo Ochoa Center of Excellence Program (Catalan Institute of Nanoscience and Nanotechnology, grant SEV-2017-0706). X.R. is also grateful for ICREA-Acadèmia awards. M.v.D. is grateful for financial support from the Deutsche Forschungsgemeinschaft (project number 182849149-SFB953 'Synthetic Carbon Allotropes'), the Fonds der Chemischen Industrie (FCI), the University of Ulm and the Deutscher Akademischer Austauschdienst (PhD fellowship to O.B.). E.U. thanks Universitat de Girona for a PhD grant and we thank Serveis Tècnics de Recerca, Universitat de Girona for technical support. We thank A. Lledó for artwork assistance and H. Maid (Friedrich-Alexander-Universität Erlangen-Nürnberg, Germany) for assistance with cryoprobe NMR spectroscopy.

Author contributions

E.U., C.F.-E. and C.G.-S. performed all self-assembly as well as fullerene functionalization experiments and isolated all products. O.B. performed all spectroscopic host–guest titrations and analysed the results with M.v.D. Y.X. synthesized a batch of **[10]CPP** and the bromomalonate Bingel reagents. L.G. provided technical assistance on HRMS studies. J.J., I.I., F.G. and D.M. technically assisted, performed and solved the XRD structure of C_{60}⊂[10]CPP⊂**7**·$(BArF)_8$ and *trans*-3-(**1**-C_{60})⊂[10]CPP⊂**7**·$(BArF)_8$ at the ALBA synchrotron. M.v.D., C.F. and X.R. conceived the project idea. M.v.D and X.R. wrote the manuscript. X.R. directed the project.

Competing interests

The authors declare no competing interests.

Additional information

Extended data are available for this paper at https://doi.org/10.1038/s41557-021-00658-6.

Supplementary information The online version contains supplementary material available at https://doi.org/10.1038/s41557-021-00658-6.

Correspondence and requests for materials should be addressed to M.v.D. or X.R.

Peer review information *Nature Chemistry* thanks T. Barendt, E. Peris and the other, anonymous reviewer(s), for their contribution to the peer review of this work.

Reprints and permissions information is available at www.nature.com/reprints.

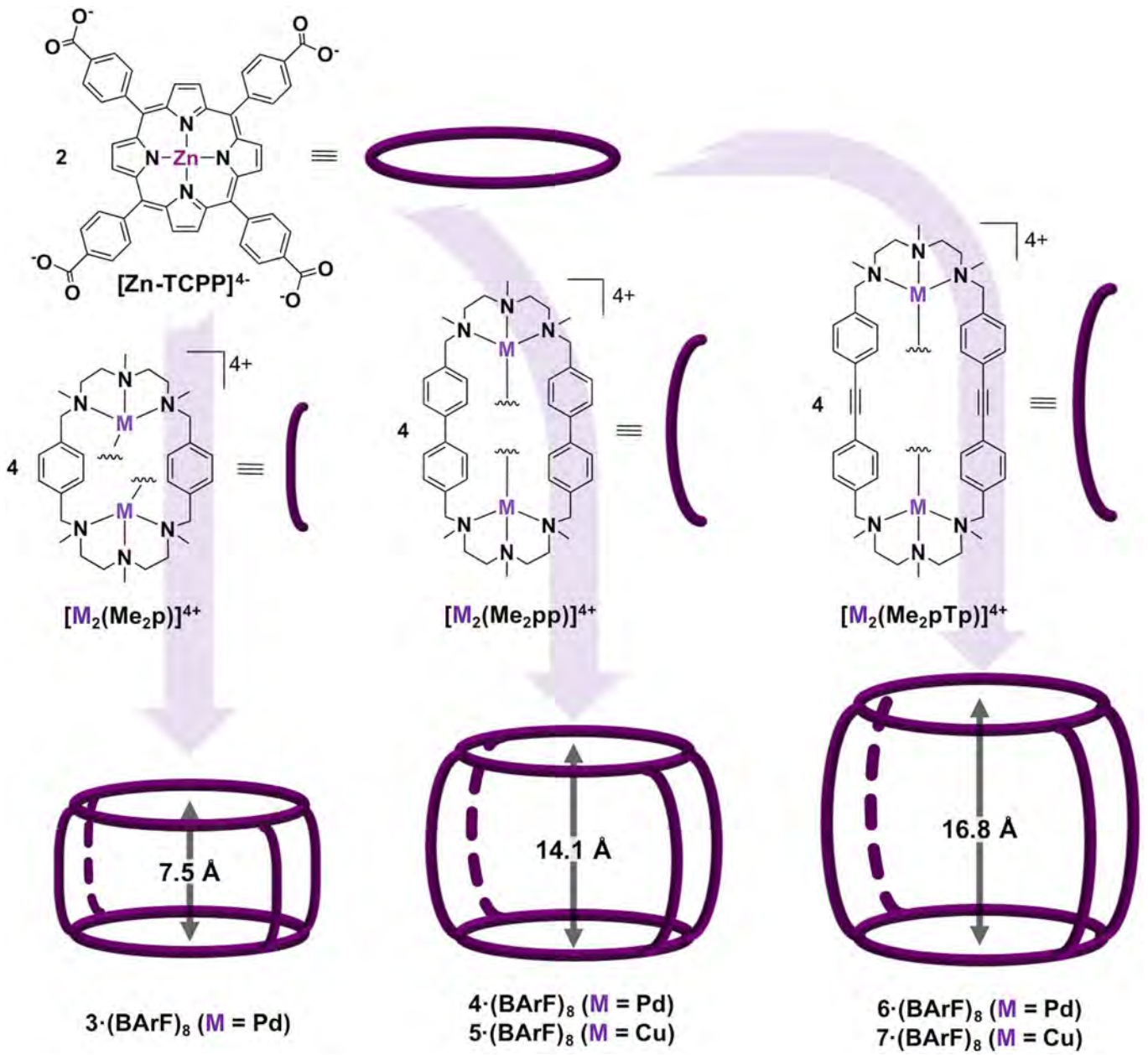

Extended Data Fig. 1 | Self-assembled tetragonal prismatic nanocapsules. Self-assembly of the Zn-TCPP and the bimetallic macrocyclic clips $[M_2(Me_2p)]^{4+}$, $[M_2(Me_2pp)]^{4+}$ and $[M_2(Me_2pTp)]^{4+}$, to afford the corresponding tetragonal prismatic nanocapsules with increasing cavity-size, that is, **3**·$(BArF)_8$, **4**·$(BArF)_8$, **5**·$(BArF)_8$, **6**·$(BArF)_8$, **7**·$(BArF)_8$.

Supporting information for

A three-shell supramolecular complex enables the symmetry-mismatched chemo- and regioselective bis-functionalization of C_{60}

Ernest Ubasart, Oleg Borodin, Carles Fuertes-Espinosa, Youzhi Xu, Cristina García-Simón, Laura Gómez, Judit Juanhuix, Felipe Gándara, Inhar Imaz, Daniel Maspoch, Max von Delius,* Xavi Ribas*

TABLE OF CONTENTS

1. Supplementary methods

1.1. Materials and instrumentation

Reagents and solvents used were commercially available reagent quality unless indicated otherwise. [10]CPP and the **C_{60}⊂[10]CPP** complex were prepared following a published procedure.[1,2] NMR data concerning product characterization were collected on Bruker 400 MHz AVANCE spectrometers in $CDCl_3$ or CD_3CN, and calibrated relative to the residual protons of the solvent. ESI-MS experiments were collected and analysed on Bruker MicroTOF-Q-II using $CDCl_3$ or CH_3CN as a mobile phase. HPLC data concerning fullerene adducts identity were collected on Agilent series 1200 chromatograph equipped with Cosmosil Buckyprep-M column, or LC-9130 NEXT apparatus (Japan Analytical Industry Co.Ltd.) monitored using a UV detector at 320 nm and using toluene as solvent (0.5 ml/min flow). UV-Vis spectroscopy was performed on an Agilent 8452 UV-vis spectrophotometer with 1 cm quartz cell, using CH_3CN as solvent. X-ray diffraction data were collected on both Bruker D8 QUEST ECO and ALBA synchrotron.

1.2. Synthesis and characterization of 4,4'-(Ethyne-1,2-diyl)dibenzaldehyde (pTp)

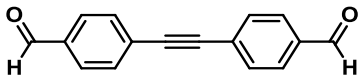

4,4'-(Ethyne-1,2-diyl)dibenzaldehyde (pTp) was synthetized following reported procedures.[3] 4-bromobenzaldehyde (1100 mg, 6 mmol), propiolic acid (186 µl, 6 mmol), 1,4-bis(diphenylphosphino)butane (128 mg, 0.30 mmol), $Pd(PPh_3)_2Cl_2$ (110 mg, 0.15 mmol) and DBU (900 µl, 6 mmol) were combined in a 50 ml round-bottom flask. DMSO (16 ml) was added and the flask sealed with a septum was placed in an oil bath at 80 ºC for 4 hours. Then, the reaction crude was filtered and purified by flash chromatography on silica gel. The product was eluted with hexane:ethyl acetate (1:1). (Yield 70 %)

^{1}H-NMR (400 MHz, $CDCl_3$) δ p.p.m.: 10.04 (s, 2H, -CHO), 7.90 (d, J=8.4 Hz, 4H, arom), 7.71 (d, J=8.2 Hz, 4H, arom).

^{13}C-NMR (100 MHz, $CDCl_3$) δ p.p.m.: 191.7 (C=O), 136.3 (C arom), 132.7 (CH arom), 130.0 (CH arom), 129.0 (C arom), 92.5 (C sp).

1.3.Synthesis and characterization of S_2pTp

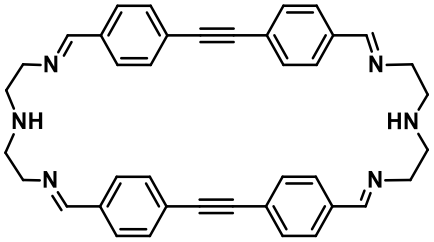

Dialdehyde (0.46 g, 1 mmol) was dissolved in 150 ml of DCM and were charged in a 100 ml addition funnel. Then, diethylenetriamine (210 µl, 1 mmol) was added in a 500 ml round-bottom flask with 200 ml of MeOH. The dialdehyde solution was added dropwise into the amine solution for 6 h and stirred for 16 h. After this time, a white solid was obtained.

^{1}H-NMR (400 MHz, $CDCl_3$) δ p.p.m.: 8.27 (s, 4H, CH imine), 7.45 (d, J=8.3 Hz, 8H, arom), 7.39 (d, J=8.3 Hz, 8H, arom), 3.81-3.79 (m, 8H, CH_2), 3.01-2.98 (m, 8H, CH_2).

^{13}C-NMR (100 MHz, $CDCl_3$) δ p.p.m.: 162.0 (C sp2 imine), 135.9 (C arom), 132.2 (CH arom), 128.2 (CH arom), 125.6 (C arom), 91.2 (C sp), 60.3 (-CH_2-), 48.7 (-CH_2-).

HRMS (m/z): calculated 302.1649 and found 302.1652 ($\{S_2pTp + 2H^+\}^{+2}$); calculated 603.3231 and found 603.3237 ($\{S_2pTp + H^+\}^{+1}$); calculated 625.3050 and found 625.3062 ($\{S_2pTp + Na^+\}^{+1}$).

1.4.Synthesis and characterization of H_2pTp

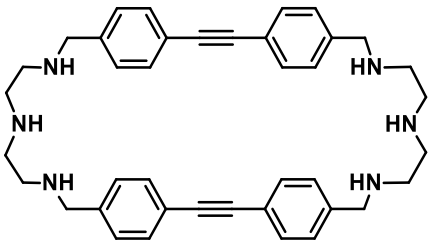

To a solution of S_2pTp, $NaBH_4$ (0.22 g, 6 mmols) was added and the mixture was stirred for 16 h. After this time, 7 ml of an acid solution (HCl:H_2O 1:10) were added and the reaction crude stirred for 45 minutes. Then, the solution was evaporated under reduced pressure until a constant volume and 125 ml of H_2O were added. The product was extracted with $CHCl_3$ (3 x 50 ml). Organic phases were combined, dried with anhydrous $MgSO_4$ and filtered. The remaining solution was dried under vacuum, and a white solid of H_2pTp was obtained. (Yield: 82%).

^{1}H-NMR (400 MHz, $CDCl_3$) δ p.p.m.: 7.43 (d, J=8.2 Hz, 8H, arom), 7.24 (d, J=8.2 Hz, 8H, arom), 3.77 (s, 8H, CH_2), 2.84-2.77 (m, 16H, CH_2).

^{13}C-NMR (100 MHz, $CDCl_3$) δ p.p.m.: 141.0 (C arom), 132.0 (CH arom), 128.3 (CH arom), 122.2 (C arom), 89.5 (C sp), 54.0 (-CH_2-), 49.2 (-CH_2-), 48.8 (-CH_2-).

HRMS (m/z): calculated 306.1965 and found 306.1969 ({H_2pTp + 2H^+}$^{+2}$); calculated 611.3857 and found 611.3874 ({H_2pTp + H^+}$^{+1}$).

1.5. Synthesis and characterization of Me_2pTp

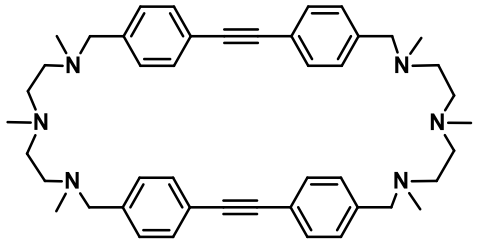

H_2pTp (0.45 g, 1 mmol) were added to a 50 ml round-bottom flask and mixed with: 7 ml of formaldehyde, 6 ml of formic acid and 10 ml of water. The resulting mixture was heated to reflux during 16 h. After this time, the reaction mixture was cooled to room temperature and the solvent was removed under reduced pressure. Then, 50 ml of NaOH 1M were added. The product was extracted with $CHCl_3$ (3 x 25 ml). Organic phases were combined, dried with anhydrous $MgSO_4$ and filtered. The remaining solution was dried under vacuum, and the obtained product purified by recrystallization with acetone. (Yield: 92%).

^{1}H-NMR (400 MHz, $CDCl_3$) δ p.p.m.: 7.40 (d, J=8.2 Hz, 8H, arom), 7.25 (d, J=8.2 Hz, 8H, arom), 3.44 (s, 8H, CH_2), 2.50-2.41 (m, 16H, CH_2), 2.25 (s, 6H, CH_3), 2.21 (s, 12H, CH_3).

^{13}C-NMR (100 MHz, $CDCl_3$) δ p.p.m.: 139.5 (C arom), 131.6 (CH arom), 129.2 (CH arom), 122.1 (C arom), 89.4 (C sp), 62.6 (-CH_2-), 54.9 (-CH_2-), 54.4 (-CH_2-), 43.8 (-CH_3), 43.1 (-CH_3).

HRMS (m/z): calculated 348.2434 and found 348.2435 ({Me_2pTp + 2H^+}$^{+2}$); calculated 695.4796 and found 695.4809 ({Me_2pTp + H^+}$^{+1}$).

1.6. Synthesis and characterization of dinuclear Pd^{II} molecular clip, $[Pd_2(Me_2pTp)(AcO)_2](OTf)_2$

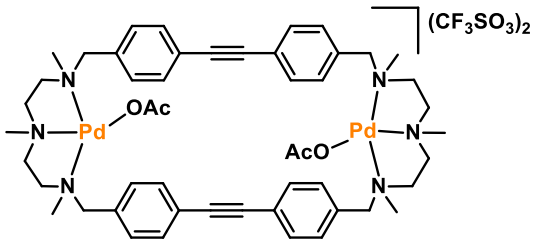

In a 50 ml round-bottom flask, Me_2pTp (0.065 g, 1 mmol), $Pd(AcO)_2$ (0.044 g, 2.1 mmols) and 30 ml of anhydrous CH_3CN were mixed. The mixture was heated to reflux temperature, under nitrogen atmosphere for 16h. After this time, the reaction mixture was cooled to room temperature. Subsequently, an excess of $NaCF_3SO_3$ salt was added (4.2 mmols) and the mixture was stirred vigorously for 8h. The mixture was concentrated to a volume of 2-3 ml under reduced pressure, filtered through Celite and recrystallized under slow diethyl ether diffusion. Yellow crystalline solid was obtained. (Yield: 90%).

^{1}H-NMR (400 MHz, CD_3CN) δ p.p.m.: 8.27 (d, J=8.2 Hz, 8H, arom), 8.15 (d, J=8.2 Hz, 8H, arom), 7.90 (d, J=8.2 Hz, 8H, arom), 7.79 (d, J=8.2 Hz, 8H, arom), 4.01 (dd, 8H, CH_2), 3.63-3.54 (m, 8H, CH_2), 3.29 (s, 12H, CH_3), 3.27 (s, 12H, CH_3), 3.24-3.15 (m, 8H, CH_2), 3.07 (dd, 8H, CH_2), 2.40-2.33 (m, 8H, CH_2), 2.31-2.25 (m, 8H, CH_2), 2.06 (s, 6H, AcO), 2.04 (s, 6H, AcO), 1.35 (s, 6H, CH_3), 1.35 (s, 6H, CH_3) (equimolar amounts of two conformational forms of the same complex are present).

^{13}C-NMR (100 MHz, $CDCl_3$) δ p.p.m.: 178.0 (C=O, AcO), 177.9 (C=O, AcO), 135.1 (arom), 134.9 (arom), 134.0 (arom), 133.9 (arom), 133.1 (arom), 133.1 (arom), 124.7 (CF_3SO_3), 124.6 (CF_3SO_3), 90.9 (-CH-), 90.6 (-CH-), 65.8 (-CH_2-), 65.7 (-CH_2-), 61.3 (-CH_2-), 61.2 (-CH_2-), 59.5 (-CH_2-), 59.3 (-CH_2-), 51.5 (-CH_3), 51.2 (-CH_3), 44.1 (-CH_3), 44.0 (-CH_3), 24.7(-CH_3, AcO), 24.6 (-CH_3, AcO).

HRMS (m/z): calculated 513.1536 and found 513.1509 ($\{Pd_2(Me_2pTp)(AcO)_2\}^{+2}$).

1.7. Synthesis and characterization of dinuclear Cu^{II} molecular clip, $[Cu_2(Me_2pTp)(OTf)_2](OTf)_2$

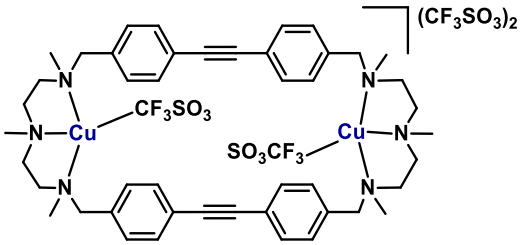

In a 20 ml glass vial, Me_2pTp (0.018 g, 1 mmol) and $Cu(CF_3SO_3)_2$ (0.019 g, 2 mmols) were dissolved in 2.5 ml of CH_3CN. The mixture was stirred at room temperature for 16 h. After this time, the reaction crude was filtered through Celite and recrystallized by slow diethyl ether diffusion. A blue crystalline solid was obtained. (Yield: 95%). XRD of this complex was registered (see Supplementary Figure 42).

HRMS (m/z): calculated 560.1164 and found 560.1173 ($\{Cu_2(Me_2pTp)(CF_3SO_3)_2\}^{+2}$); calculated 1269.1854 and found 1269.1832 ($\{Cu_2(Me_2pTp)(CF_3SO_3)_3\}^{+1}$).

1.8. Synthesis and characterization of Pd^{II}-based tetragonal prismatic nanocapsule $6\cdot(BArF)_8$

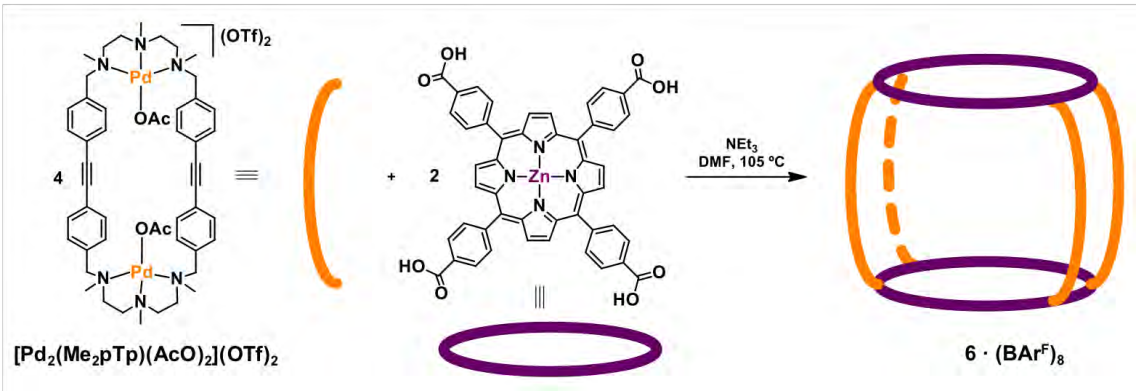

5,10,15,20-tetrakis(4-carboxyphenyl)porphyrin-Zn^{II} (9.1 mg, 2 mmols) was weighted in a 10 ml round-bottom flask and solved in 1 ml of DMF. Then, 7.4 µl of triethylamine mixed in 0.5 ml of DMF were added to the porphyrin solution. Finally, $[Pd_2(Me_2pTp)(AcO)_2](CF_3SO_3)_2$ (24.5 mg, 4 mmols) molecular clip was dissolved in 2.5 ml of DMF were added to the mixture. The solution was heated to 105 °C under reflux for 16 h. After the reaction time, the reaction crude was cooled to room temperature, filtered through Celite and recrystallized by diethyl ether diffusion. The **6**$\cdot(CF_3SO_3)_8$ crystalline solid obtained was suspended in 12 ml of DCM, an excess of NaBArF salt was added (6 to 10 mmols) and the

mixture was stirred vigorously for 16 h. The mixture was filtered through Celite and the product was obtained by precipitation with slow diffusion of diethyl ether. (Yield: 75%).

^{1}H-NMR (400 MHz, CD_3CN) δ p.p.m.: 8.67 (s, 16H, pyrrole ring), 8.54 (d, J=8.2 Hz, 8H, arom-porph), 8.39 (d, J=8.2 Hz, 8H, arom-porph), 8.15 (d, J=8.2 Hz, 32H, arom-clip), 8.13 (m, 16H, arom-porph), 7.89 (d, J=8.2 Hz, 32H, arom-clip), 7.69-7.66 (m, 96H, $BArF^-$), 4.02 (d, J=13 Hz, 16H, $-CH_2-$), 3.66 (m, 16H, $-CH_2-$), 3.57 (s, 48H, $N-CH_3$), 3.28 (m, 16H, $-CH_2-$), 3.13 (d, J=13 Hz, 16H, $-CH_2-$), 2.46 (dd, J=13.5 Hz, 16H, $-CH_2-$), 2.37 (dd, J=13.5 Hz, 16H, $-CH_2-$), 1.50 (s, 24H, $N-CH_3$).

^{13}C-NMR (100 MHz, $CDCl_3$) δ p.p.m.: 162.0 (BArF), 149.8 (pyrrole ring), 134.7 (BArF), 133.5 (arom-porph), 133.0 (arom-clip), 132.5 (arom-clip), 131.5 (pyrrole ring), 127.5 (arom-porph), 124.0 (arom-porph), 123.3 (arom-clip), 117.9 (BArF), 64.4 ($-CH_2-$), 60.0 ($-CH_2-$), 58.6 ($-CH_2-$), 51.4 ($-CH_3$), 43.6 ($-CH_3$).

HRMS (m/z): calculated 666.4128 and found 666.4145 ([**6**·$(BArF)_0$]$^{+8}$); calculated 884.9099 and found 884.9110 ([**6**·$(BArF)_1$]$^{+7}$); calculated 1176.2394 and found 1176.2429 ([**6**·$(BArF)_2$]$^{+6}$); calculated 1584.1008 and found 1584.1041 ([**6**·$(BArF)_3$]$^{+5}$); calculated 2195.8928 and found 2195.9031 ([**6**·$(BArF)_4$]$^{+4}$).

1.9. Synthesis and characterization of Cu^{II}-based tetragonal prismatic nanocapsule 7·$(BArF)_8$

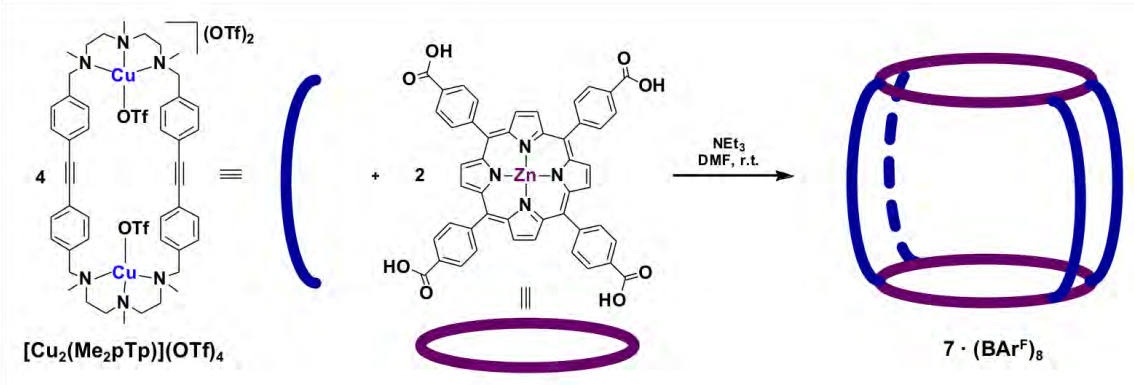

5,10,15,20-tetrakis(4-carboxyphenyl)porphyrin-Zn^{II} (15.9 mg, 2 mmols) was weighted in a 20 ml glass vial and solved in 1.5 ml of DMF. Then, 13 µl of triethylamine mixed in 0.5 ml of DMF were added to the porphyrin solution. Finally, $[Cu_2(Me_2pTp)(OTf)_2](OTf)_2$ (43.4 mg, 4 mmols) molecular clip was dissolved in 3.5 ml of DMF were added to the mixture. The solution was stirred at room temperature for 16 h. After the reaction time, the reaction crude was filtered through Celite and recrystallized by diethyl ether diffusion. The **7**·$(CF_3SO_3)_8$ crystalline solid obtained was suspended in 12 ml of DCM, an excess of NaBArF

salt was added (6 to 10 mmols) and the mixture was stirred vigorously for 16 h. The mixture was filtered through Celite and the product was obtained by precipitation with slow diffusion of diethyl ether. (Yield: 77%).

HRMS (m/z): calculated 623.5626 and found 623.5618 ([**7**·$(BArF)_0$]$^{+8}$); calculated 835.9383 and found 835.9370 ([**7**·$(BArF)_1$]$^{+7}$); calculated 1119.1059 and found 1119.1035 ([**7**·$(BArF)_2$]$^{+6}$); calculated 1515.5405 and found 1515.5375 ([**7**·$(BArF)_3$]$^{+5}$); calculated 2110.1925 and found 2110.1851 ([**7**·$(BArF)_4$]$^{+4}$).

1.10. Preparation of C_{60}⊂[10]CPP, C_{60}⊂[10]CPP⊂6·$(BArF)_8$ and C_{60}⊂[10]CPP⊂7·$(BArF)_8$

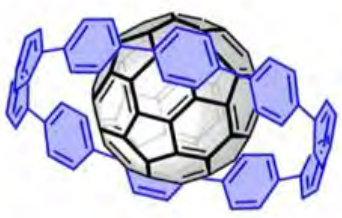

Preparation of C_{60}⊂[10]CPP.[4] A 20 ml glass vial was charged with C_{60} (1.2 mmols), [10]CPP (1 mmol) and 20 ml of $CHCl_3$. The reaction mixture was stirred at room temperature for 1 hour. After this time, solvent was removed under reduced pressure and toluene was added and the excess of C_{60} was removed by centrifugation. This procedure was repeated several times until the toluene was not coloured anymore.

^{1}H-NMR (400 MHz, $CDCl_3$) δ p.p.m.: 7.62 (s, 40H, arom).

^{13}C-NMR (100 MHz, $CDCl_3$) δ p.p.m.: 138.0 ([10]CPP), 127.6 ([10]CPP), 141.7 (C_{60}).

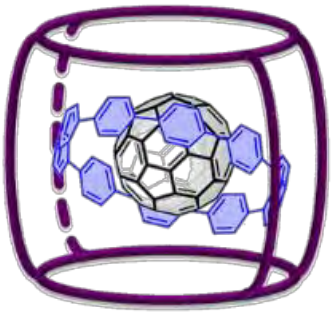

Preparation of C_{60}⊂[10]CPP⊂6·$(BArF)_8$. **6**·$(BArF)_8$ nanocapsule (15 mg, 1 mmol) was dissolved in the minimum amount of CH_3CN. Then 1.2 mmols of **C_{60}⊂[10]CPP** dissolved in DCM were added to the nanocapsule solution and stirred at room temperature for 16 h.

^{1}H-NMR (400 MHz, CD_3CN) δ p.p.m.: 8.76 (s, 16H, pyrrole ring), 8.74 (d, 8H, arom-porph), 8.50 (d, J=8.2 Hz, 8H, arom-porph), 8.33 (d, J=8.2 Hz, 8H, arom-porph), 8.17 (d, 8H, arom-porph), 8.09 (d, J=8.2 Hz, 32H, arom-clip), 7.69 (d, 32H, arom-clip), 7.69-7.66 (m, 96H, BArF-), 4.07 (d, J=13 Hz, 16H, -CH_2-), 3.64 (m, 16H, -CH_2-), 3.59 (s, 48H, N-CH_3), 3.24 (m, 16H, -CH_2-), 3.14 (d, J=13 Hz, 16H, -CH_2-), 2.45 (dd, J=13.5 Hz, 16H, -CH_2-), 2.34 (dd, J=13.5 Hz, 16H, -CH_2-), 1.43 (s, 24H, N-CH_3).

^{13}C-NMR (151 MHz, CD_3CN) δ 172.46 (C carboxylic), 162.6 (q, $^{1}J_{B-C}$ = 49.8 Hz, C_{Ar} *BArF*), 150.6 (C_α, pyrrole), 147.4 (C, phenylene@porphyrin, *para* to CO_2^-), 140.4 (C_{60}), 138.1 (C, [10]CPP), 135.7 (C_{Ar} *BArF* + C, phenylene@porphyrin, *ipso* to CO_2^-*)*, 135.0 (CH, phenylene@porphyrin, *meta* to CO_2^-), 134.6 (C, phenylene@clip, *para* to alkyne), 134.0 (CH, phenylene@porphyrin, *meta* to CO_2^-), 133.5 (CH, phenylene@clip, *meta* to alkyne), 133.3 (CH, phenylene@clip, *ortho* to alkyne), 132.2 (C_β pyrrole), 129.9 (qd, $^{2}J_{C-F}$ = 31.6 Hz, $^{3}J_{B-C}$ = 2.9 Hz C_{Ar} *BArF)*, 128.5 (CH, phenylene@porphyrin, *ortho* to CO_2^-), 128.3 (CH, phenylene@porphyrin, *ortho* to CO_2^-), 127.7 (CH, [10]CPP), 125.5 (q, $^{1}J_{C-F}$ = 272 Hz, CF_3 *BArF*), 124.6 (C, phenylene@clip, *ipso* to alkyne), 121.1 (C porphyrin), 118.7 (m, C_{Ar} *BArF*), 90.8 (C alkyne), 65.4 (CH_2 benzylic, clip), 60.9 (CH_2 clip), 59.4 (CH_2 clip), 52.5 (CH_3 clip), 44.1 (CH_3 clip).

HRMS (m/z): calculated 851.5774 and found 851.5753 (**C_{60}⊂[10]CPP**⊂[**6**·$(BArF)_0$]$^{+8}$); calculated 1096.5266 and found 1096.5264 (**C_{60}⊂[10]CPP**⊂[**6**·$(BArF)_1$]$^{+7}$); calculated 1423.1256 and found 1423.1248 (**C_{60}⊂[10]CPP**⊂[**6**·$(BArF)_2$]$^{+6}$); calculated 1880.5643 and found 1880.5646 (**C_{60}⊂[10]CPP**⊂[**6**·$(BArF)_3$]$^{+5}$); calculated 2566.4721 and found 2566.4703 (**C_{60}⊂[10]CPP**⊂[**6**·$(BArF)_4$]$^{+4}$).

Preparation of C_{60}⊂[10]CPP⊂7·$(BArF)_8$. Analogous synthesis has been carried out to obtain the Cu^{II}-based **C_{60}⊂[10]CPP**⊂[**7**·$(BArF)_8$].

HRMS (m/z): calculated 808.7273 and found 808.7202 (**C_{60}⊂[10]CPP**⊂[**7**·$(BArF)_0$]$^{+8}$); calculated 1047.5550 and found 1047.5482 (**C_{60}⊂[10]CPP**⊂[**7**·$(BArF)_1$]$^{+7}$); calculated 1365.9921 and found 1365.9842 (**C_{60}⊂[10]CPP**⊂[**7**·$(BArF)_2$]$^{+6}$); calculated 1811.8040 and found 1811.7939 (**C_{60}⊂[10]CPP**⊂[**7**·$(BArF)_3$]$^{+5}$); calculated 2480.7718 and found 2480.7637 (**C_{60}⊂[10]CPP**⊂[**7**·$(BArF^F)_4$]$^{+4}$).

1.11. General procedure for the synthesis of bromomalonates

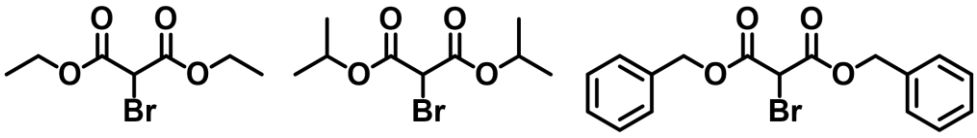

Bromomalonates were prepared according to a published procedure.[5] Under Argon atmosphere, a 100 mL oven-dried Schlenk flask was charged with malonate (5.0 mmol), anhydrous THF (50 mL) and DBU (5.0 mmol) at 0 °C. The mixture was stirred at room temperature for 1 h and then cooled to -78 °C. CBr_4 (8.5 mmol) was added, the mixture was stirred at -78 °C for 2 h and quenched with saturated aqueous NH_4Cl. The aqueous layer was extracted with DCM and the solvent was removed under reduced pressure. The residue was purified by column chromatography to afford the bromomalonates as colourless oil. Characterization data was consistent with the previous report.

1.12. General procedure for Bingel reaction (Matryoshka system)

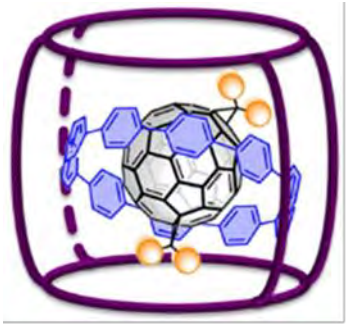

15 mg of **C_{60}⊂[10]CPP⊂(6**·BArF)$_8$ were totally dissolved in 0.5 ml of CH_3CN. Then, 5 equiv. of the corresponding bromomalonate (diethyl (**1**); diisopropyl (**2**); dibenzyl (**3**)) and 5 equiv. of NaH as a base were added sequentially and the reaction was stirred 16 h under N_2 at room temperature. Once the bis-adduct was formed, the reaction was stopped by filtering and removing the solvent under reduced pressure.

Characterization of *trans*-3-(1-C_{60})⊂[10]CPP⊂6·(BArF)$_8$

^{1}H-NMR (400 MHz, CD_3CN) δ p.p.m.: 8.78 (m, 16H, pyrrole ring), 8.73 (d, J=8.2 Hz, 8H, arom-porph), 8.50 (d, J=8.2 Hz, 8H, arom-porph), 8.35 (d, 8H, arom-porph), 8.29 (d, 8H, arom-porph), 8.06 (d, J=8.2 Hz, 32H, arom-clip), 7.70 (d, 32H, arom-clip), 7.69-7.66 (m, 96H, BArF$^-$), 7.16 (s, 40H, [10]CPP), 4.05 (d, J=13 Hz, 16H, -CH_2-), 3.64 (m, 16H, -CH_2-), 3.58 (s, 48H, N-

CH_3), 3.23 (m, 16H, -CH_2-), 3.13 (d, J=13 Hz, 16H, -CH_2-), 2.44 (dd, J=13.5 Hz, 16H, -CH_2-), 2.33 (dd, J=13.5 Hz, 16H, -CH_2-), 1.41 (s, 24H, N-CH_3).

^{13}C-NMR (100 MHz, CD_3CN, assignment based on HSQC/HMBC) δ p.p.m.: 165.4 (arom-porph), 161.9 (BArF), 155.4 (pyrrole ring), 137.0 ([10]CPP), 134.9 (BArF), 133.4 (arom-porph), 132.8 (arom-clip), 132.5 (arom-clip), 131.4 (pyrrole ring), 127.0 ([10]CPP), 122.7 (arom-clip), 117.7 (BArF), 64.4 (-CH_2-), 59.9 (-CH_2-), 57.9 (-CH_2-), 51.3 (-CH_3), 42.9 (-CH_3).

HRMS (m/z): calculated 891.0920 and found 891.0883 (***trans*-3**-(**1**-$\mathbf{C_{60}}$)⊂**[10]CPP**⊂[**6**·$(BArF)_0]^{+8}$); calculated 1141.6861 and found 1141.6835 (***trans*-3**-(**1**-$\mathbf{C_{60}}$)⊂**[10]CPP**⊂[**6**·$(BArF)_1]^{+7}$); calculated 1475.9784 and found 1475.9765 (***trans*-3**-(**1**-$\mathbf{C_{60}}$)⊂**[10]CPP**⊂[**6**·$(BArF)_2]^{+6}$); calculated 1943.7875 and found 1943.7841 (***trans*-3**-(**1**-$\mathbf{C_{60}}$)⊂**[10]CPP**⊂[**6**·$(BArF)_3]^{+5}$).

Characterization of *trans*-3-(2-C_{60})⊂[10]CPP⊂6·$(BArF)_8$

HRMS (m/z): calculated 898.0998 and found 898.1032 (***trans*-3**-(**2**-$\mathbf{C_{60}}$)⊂**[10]CPP**⊂[**6**·$(BArF)_0]^{+8}$); calculated 1149.8380 and found 1141.8409 (***trans*-3**-(**2**-$\mathbf{C_{60}}$)⊂**[10]CPP**⊂[**6**·$(BArF)_1]^{+7}$); calculated 1485.3222 and found 1475.3287 (***trans*-3**-(**2**-$\mathbf{C_{60}}$)⊂**[10]CPP**⊂[**6**·$(BArF)_2]^{+6}$); calculated 1955.0001 and found 1954.0051 (***trans*-3**-(**2**-$\mathbf{C_{60}}$)⊂**[10]CPP**⊂[**6**·$(BArF)_3]^{+5}$).

Characterization of *trans*-3-(3-C_{60})⊂[10]CPP⊂6·$(BArF)_8$

HRMS (m/z): calculated 922.2249 and found 922.2215 (***trans*-3**-(**3**-$\mathbf{C_{60}}$)⊂**[10]CPP**⊂[**6**·$(BArF)_0]^{+8}$); calculated 1177.2666 and found 1177.2609 (***trans*-3**-(**3**-$\mathbf{C_{60}}$)⊂**[10]CPP**⊂[**6**·$(BArF)_1]^{+7}$); calculated 1517.3223 and found 1517.3148 (***trans*-3**-(**3**-$\mathbf{C_{60}}$)⊂**[10]CPP**⊂[**6**·$(BArF)_2]^{+6}$); calculated 1993.4002 and found 1993.3938 (***trans*-3**-(**3**-$\mathbf{C_{60}}$)⊂**[10]CPP**⊂[**6**·$(BArF)_3]^{+5}$).

Isolation of *trans*-3-(X-C_{60}) (where X = 1, 2, 3).

The crude ***trans*-3**-(**X**-$\mathbf{C_{60}}$)⊂**[10]CPP**⊂**6**·$(BArF)_8$ reaction mixture was washed with $CHCl_3$ affording a precipitate. In one hand, the precipitate was dissolved in CH_3CN and C_{60} (4.0 equiv.) was added as a suspension in $CHCl_3$ (CH_3CN:$CHCl_3$ 1:1) and stirred at room temperature during 3h. Then, the solution was dried with N_2 gas flow and the ***trans*-3**-(**1**-$\mathbf{C_{60}}$) was obtained after toluene (or $CHCl_3$) addition and filtration of the solid $\mathbf{C_{60}}$⊂**[10]CPP** complex. On the other hand, C_{60} (4.0 equiv.) was added to the $CHCl_3$ supernatant from the washing step and stirred at room temperature during 3h. After this time, the solution was dried with N_2 gas flow and the ***trans*-3**-(**X**-$\mathbf{C_{60}}$) was obtained after toluene addition and

filtration of the solid **C_{60}⊂[10]CPP** complex. Both fractions were characterized by HPLC and UV-Vis to confirm the ***trans*-3** isomer identity, which was also cross-matched with an independently synthesized sample of ***trans*-3** bis-adduct. The yield of the reaction was calculated involving the two fractions of ***trans*-3**-(**1-C_{60}**). See Supplementary Figure 65 for a detailed work-up flow.

1.13. General procedure for statistical Bingel reaction (bare C_{60})

Preparation of ***trans*-3**-(**X-C_{60}**) (X = **1** (diethyl), **2** (diisopropyl), **3** (dibenzyl)): C_{60} (6.8 mg, 1.0 mmol) was solved in 500 µl of *o*-DCB, then bromomalonate (1.5 µl, 0.75 mmols) was added. At the same time, Na_2CO_3 (4.8 mg, 4.0 mmols) was dissolved in 250 µl of DMSO and added to the first solution. The DMSO:*o*-DCB ratio 1:2 was used. The reaction took place in a few minutes leading to a mixture of multiple adducts of C_{60} which were isolated by preparative TLC (SiO_2, Toluene:Et_2O, 20:1) after filtering. In some cases, semi-preparative HPLC was required to obtain a pure single species. ***trans*-3**-(**1-C_{60}**) ***trans*-3**-(**2-C_{60}**) ***trans*-3**-(**3-C_{60}**) were characterized by means of HPLC, UV-Vis, ^{1}H-NMR and ^{13}C-NMR.

For the reaction depicted in Figure 3d.2 (main text), and for a proper comparison with the reaction obtained using the Matryoshka-like assembly, the reaction was performed using 5 eq. NaH in MeCN:1,2-DCB 1:4 to achieve solubility of pristine C_{60}, during 3h at R.T.

trans-3-(1-C_{60}) bis-adduct (with diethyl bromomalonate)[6]

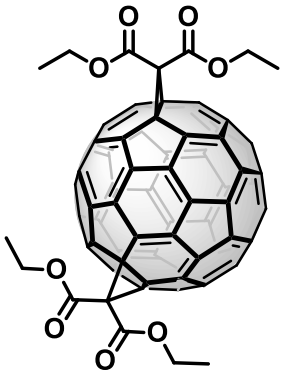

^{1}H-NMR (600 MHz, $CDCl_3$) δ p.p.m.: 4.58 (dq, J = 7.1, 3.9 Hz, 4H, -CH_2-), 4.48 (dq, J = 7.1, 2.1 Hz, 4H, -CH_2-), 1.51 (t, J = 7.1 Hz, 6H, -CH_3), 1.42 (t, J = 7.1 Hz, 6H, -CH_3).

^{13}C-NMR (600 MHz, $CDCl_3$) δ p.p.m.: 163.9 (*C=O*), 163.9 (*C=O*), 147.6 (C_{60}, sp^2), 147.3 (C_{60}, sp^2), 146.9 (C_{60}, sp^2), 146.9 (C_{60}, sp^2), 146.9 (C_{60}, sp^2), 146.8 (C_{60}, sp^2), 146.8 (C_{60}, sp^2), 146.5 (C_{60}, sp^2), 146.4 (C_{60}, sp^2), 146.0 (C_{60}, sp^2), 145.9 (C_{60}, sp^2), 145.7 (C_{60}, sp^2), 145.0 (C_{60}, sp^2),

144.8 (C_{60}, sp^2), 144.5 (C_{60}, sp^2), 144.2 (C_{60}, sp^2), 143.9 (C_{60}, sp^2), 143.9 (C_{60}, sp^2), 143.7 (C_{60}, sp^2), 143.4 (C_{60}, sp^2), 142.9 (C_{60}, sp^2), 142.6 (C_{60}, sp^2), 142.5 (C_{60}, sp^2), 142.3 (C_{60}, sp^2), 142.0 (C_{60}, sp^2), 140.7 (C_{60}, sp^2), 139.5 (C_{60}, sp^2), 138.9 (C_{60}, sp^2), 72.1 (C_{60} sp^3), 71.6 (C_{60} sp^3), 51.8 (OCCCO), 63.7 (-CH_2-), 63.6 (-CH_2-), 14.5 (-CH_3), 14.5 (-CH_3).

trans-3-(2-C_{60}) bis-adduct (with diisopropyl bromomalonate)[7]

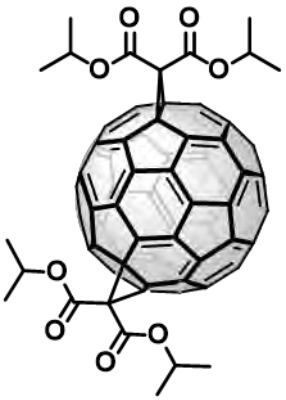

^{1}H-NMR (600 MHz, $CDCl_3$) δ p.p.m.: 5.43 (sept., J= 5.9 Hz, 2H, -CH-), 5.31 (sept., J= 5.8 Hz, 2H, -CH-), 1.51 (d, J = 6.3 Hz, 3H, -CH_3), 1.48 (d, J = 6.3 Hz, 3H, -CH_3), 1.42 (d, J = 6.2 Hz, 3H, -CH_3), 1.39 (d, J = 6.2 Hz, 3H, -CH_3).

^{13}C-NMR (600 MHz, $CDCl_3$) δ p.p.m.: 163.4 (*C=O*), 163.4 (*C=O*), 147.6 (C_{60}, sp^2), 147.3 (C_{60}, sp^2), 146.9 (C_{60}, sp^2), 146.9 (C_{60}, sp^2), 146.9 (C_{60}, sp^2), 146.9 (C_{60}, sp^2), 146.8 (C_{60}, sp^2), 146.6 (C_{60}, sp^2), 146.5 (C_{60}, sp^2), 146.0 (C_{60}, sp^2), 146.0 (C_{60}, sp^2), 145.6 (C_{60}, sp^2), 145.0 (C_{60}, sp^2), 144.8 (C_{60}, sp^2), 144.5 (C_{60}, sp^2), 144.2 (C_{60}, sp^2), 144.0 (C_{60}, sp^2), 143.9 (C_{60}, sp^2), 143.7 (C_{60}, sp^2), 143.4 (C_{60}, sp^2), 142.8 (C_{60}, sp^2), 142.5 (C_{60}, sp^2), 142.5 (C_{60}, sp^2), 142.2 (C_{60}, sp^2), 142.0 (C_{60}, sp^2), 140.7 (C_{60}, sp^2), 139.5 (C_{60}, sp^2), 138.9 (C_{60}, sp^2), 72.3 (C_{60}, sp^3), 71.8 (C_{60}, sp^3), 71.8 (*CH*), 71.7 (*CH*), 52.3 (*OCCCO*), 22.2 (-CH_3), 22.2 (-CH_3), 22.1 (-CH_3), 22.1 (-CH_3).

trans-3-(3-C_{60}) bis-adduct (with dibenzyl bromomalonate)[7,8]

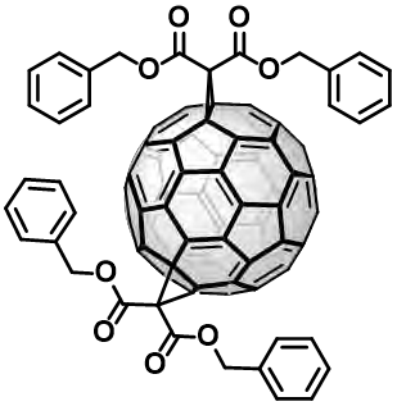

^{1}H-NMR (600 MHz, $CDCl_3$) δ p.p.m.: 7.45-7.44 (m, 8H, arom), 7.39-7.38 (m, 8H, arom), 7.33-7.32 (m, 4H, arom), 5.36 (s, 8H, -CH_2-).

^{13}C-NMR (600 MHz, $CDCl_3$) δ p.p.m.: 163.5 (*C=O*), 163.4 (*C=O*), 147.3 (C_{60}, sp^2), 147.1 (C_{60}, sp^2), 146.7 (C_{60}, sp^2), 146.6 (C_{60}, sp^2), 146.6 (C_{60}, sp^2), 146.5 (C_{60}, sp^2), 146.3 (C_{60}, sp^2), 145.9 (C_{60}, sp^2), 145.8 (C_{60}, sp^2), 145.7 (C_{60}, sp^2), 145.5 (C_{60}, sp^2), 145.3 (C_{60}, sp^2), 144.8 (C_{60}, sp^2), 144.5 (C_{60}, sp^2), 144.3 (C_{60}, sp^2), 144.0 (C_{60}, sp^2), 143.6 (C_{60}, sp^2), 143.6 (C_{60}, sp^2), 143.5 (C_{60}, sp^2), 143.1 (C_{60}, sp^2), 142.6 (C_{60}, sp^2), 142.5 (C_{60}, sp^2), 142.4 (C_{60}, sp^2), 142.0 (C_{60}, sp^2), 141.7 (C_{60}, sp^2), 140.4 (C_{60}, sp^2), 139.3 (C_{60}, sp^2), 138.7 (C_{60}, sp^2), 134.7 (C arom.), 134.6 (C arom.), 129.1 (CH arom.), 129.0 (CH arom.), 128.9 (CH arom.), 128.8 (CH arom.), 71.7 (C_{60}, sp^3), 71.2 (C_{60}, sp^3), 69.1 (*CH_2*), 69.0 (*CH_2*), 51.4 (*OCCCO*).

2. Supplementary Figures

2.1. Synthesis and characterization of 4,4'-(Ethyne-1,2-diyl)dibenzaldehyde (pTp)

Supplementary Figure 1. Synthesis of 4,4'-(Ethyne-1,2-diyl)dibenzaldehyde (pTp).

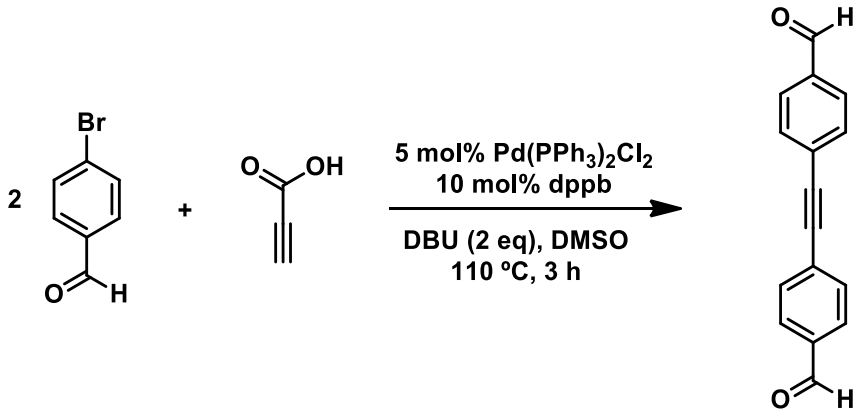

Supplementary Figure 2. ^{1}H-NMR of 4,4'-(Ethyne-1,2-diyl)dibenzaldehyde (pTp). Experiment performed in $CDCl_3$ at 298 K (400 MHz). (ϕ) $CHCl_3$, (*) ethyl acetate, (#) H_2O, (γ) TMS.

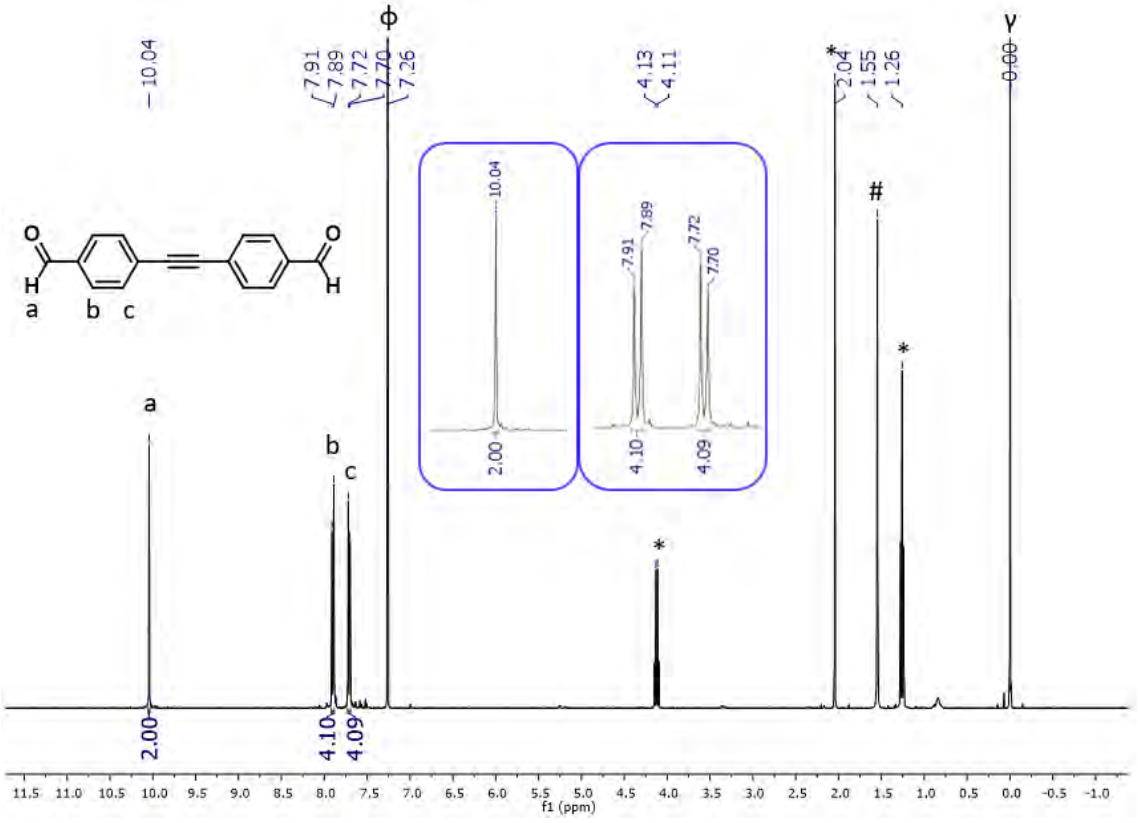

Supplementary Figure 3. ^{13}C-NMR of 4,4'-(Ethyne-1,2-diyl)dibenzaldehyde (pTp). Experiment performed in $CDCl_3$ at 298 K (400 MHz). (ϕ) $CHCl_3$, (*) ethyl acetate, (γ) TMS.

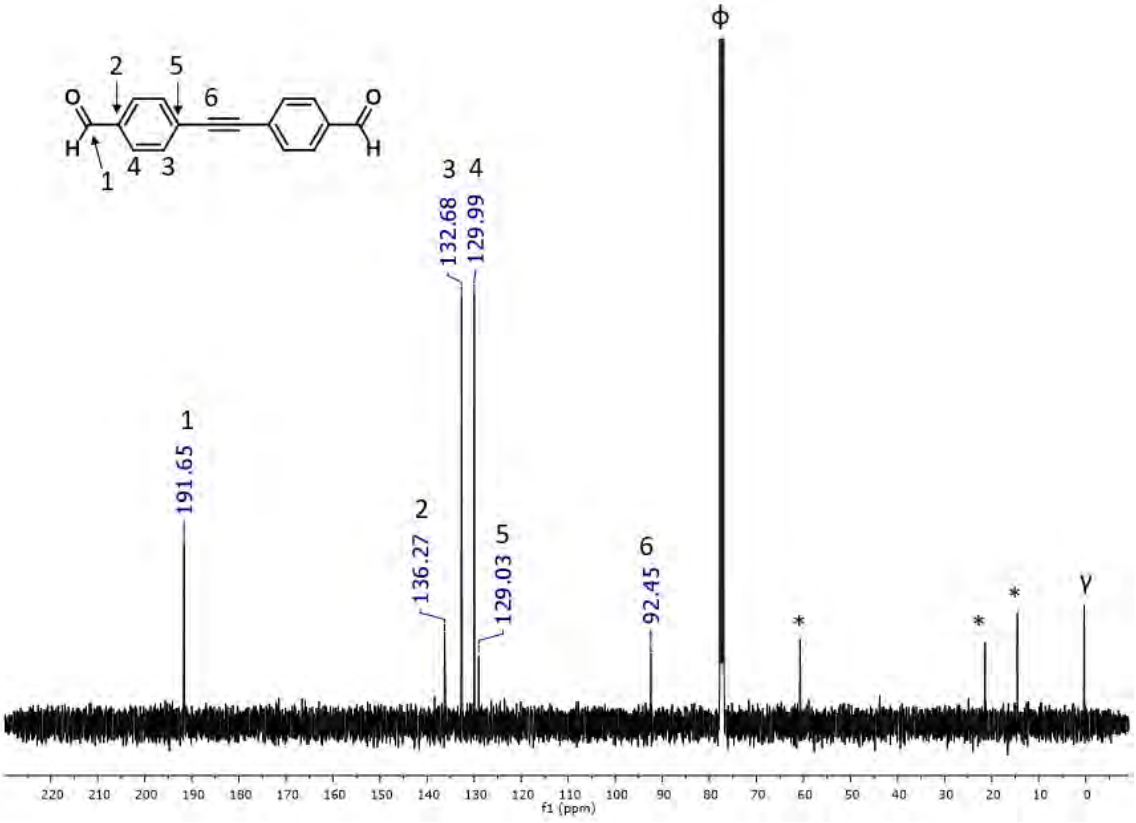

2.2.Synthesis and characterization of S_2pTp

Supplementary Figure 4. Synthesis of the S_2pTp macrocycle.

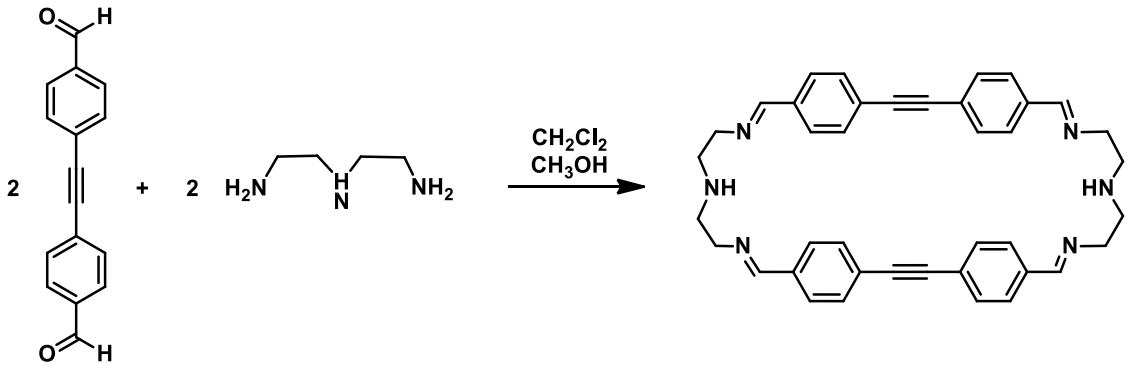

Supplementary Figure 5. ^{1}H-NMR of S_2pTp macrocycle. Experiment performed in $CDCl_3$ at 298 K (400 MHz). (ϕ) $CHCl_3$, (*) acetone, (γ) TMS.

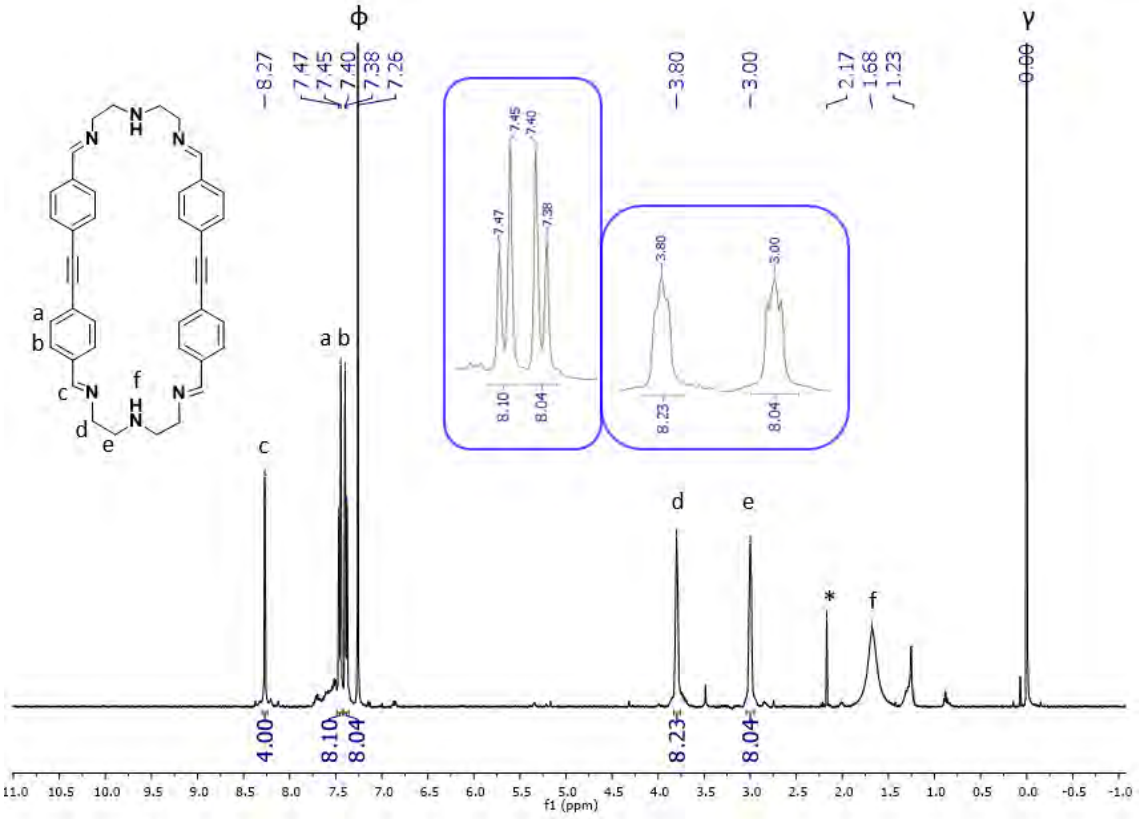

Supplementary Figure 6. ^{13}C-NMR of S_2pTp macrocycle. Experiment performed in $CDCl_3$ at 298 K (100 MHz). (ϕ) $CHCl_3$, (γ) TMS.

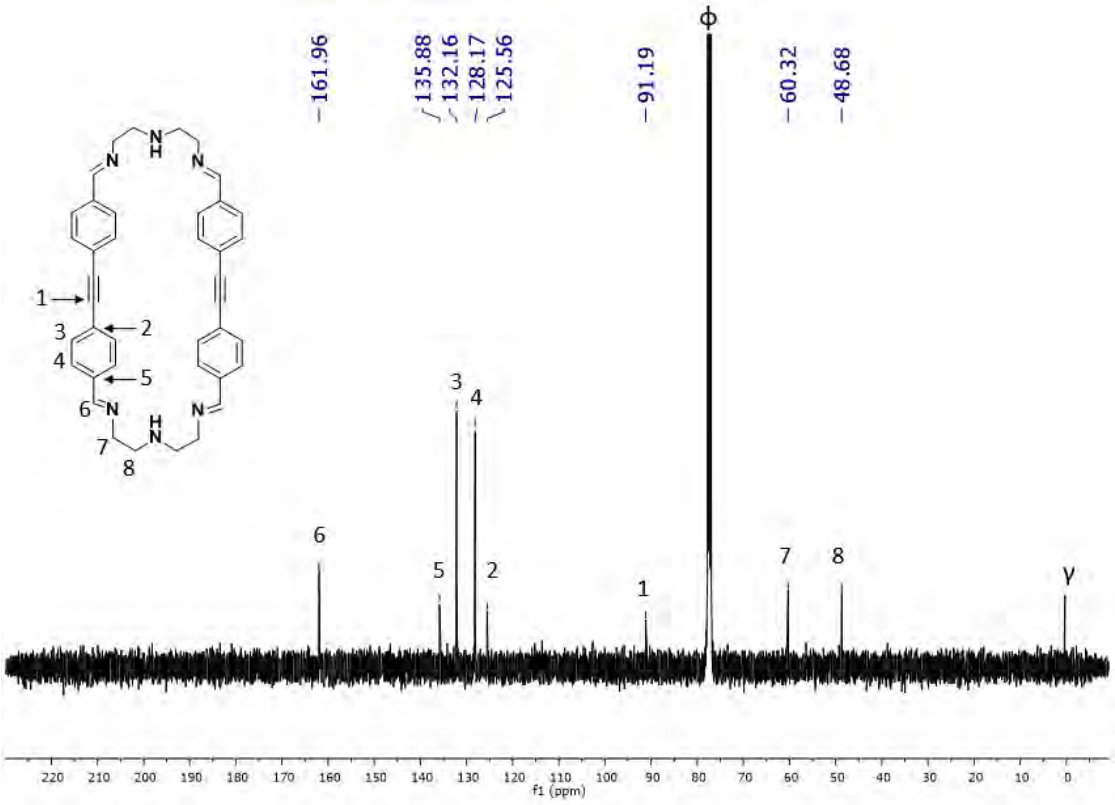

Supplementary Figure 7. HMBC of S_2pTp macrocycle. Experiment performed in $CDCl_3$ at 298 K (400 MHz).

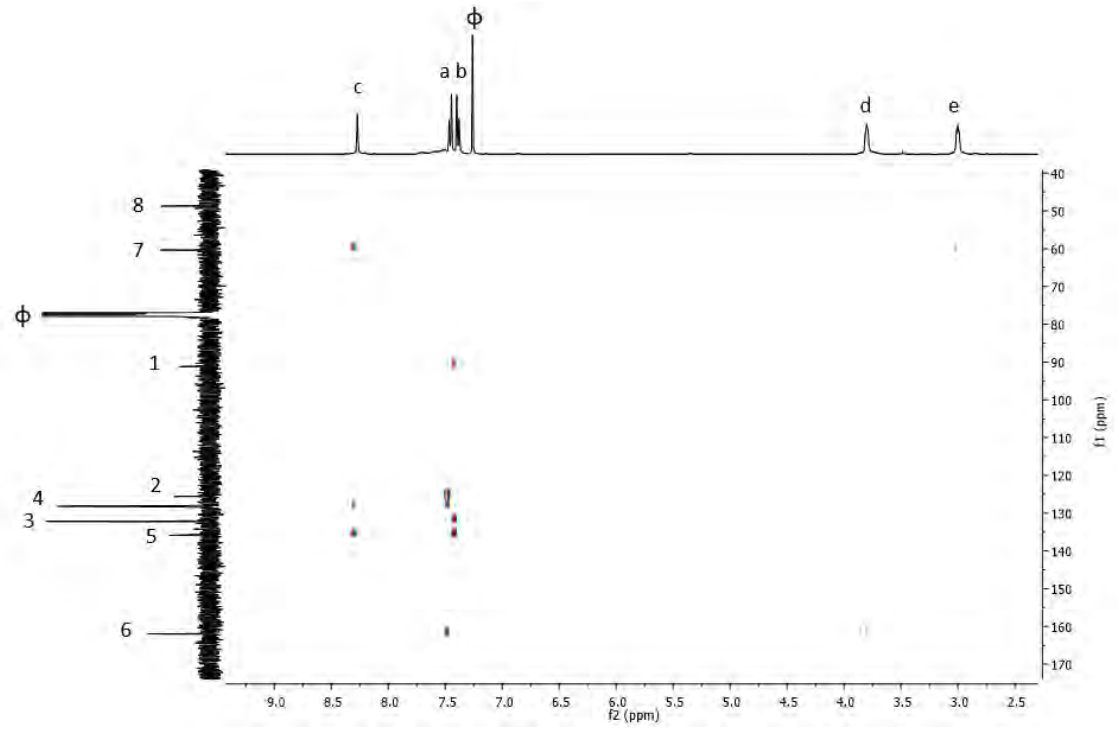

Supplementary Figure 8. HSQC of S_2pTp macrocycle. Experiment performed in $CDCl_3$ at 298 K (400 MHz).

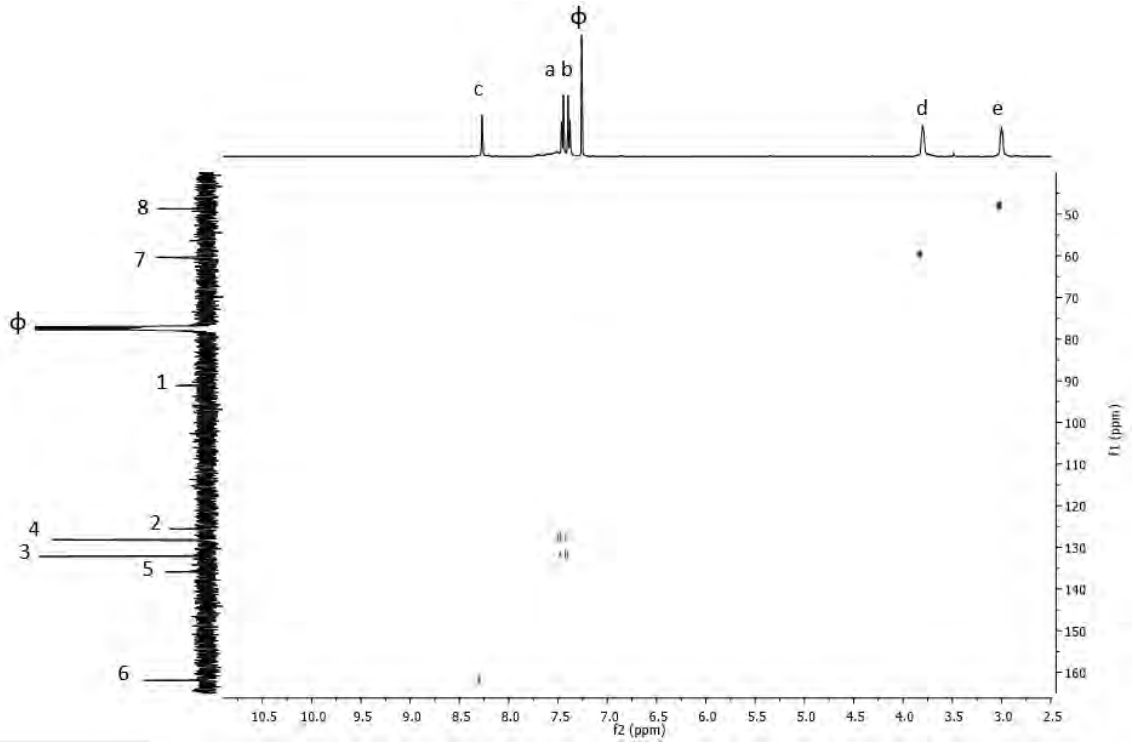

Supplementary Figure 9. COSY of S_2pTp macrocycle. Experiment performed in $CDCl_3$ at 298 K (400 MHz).

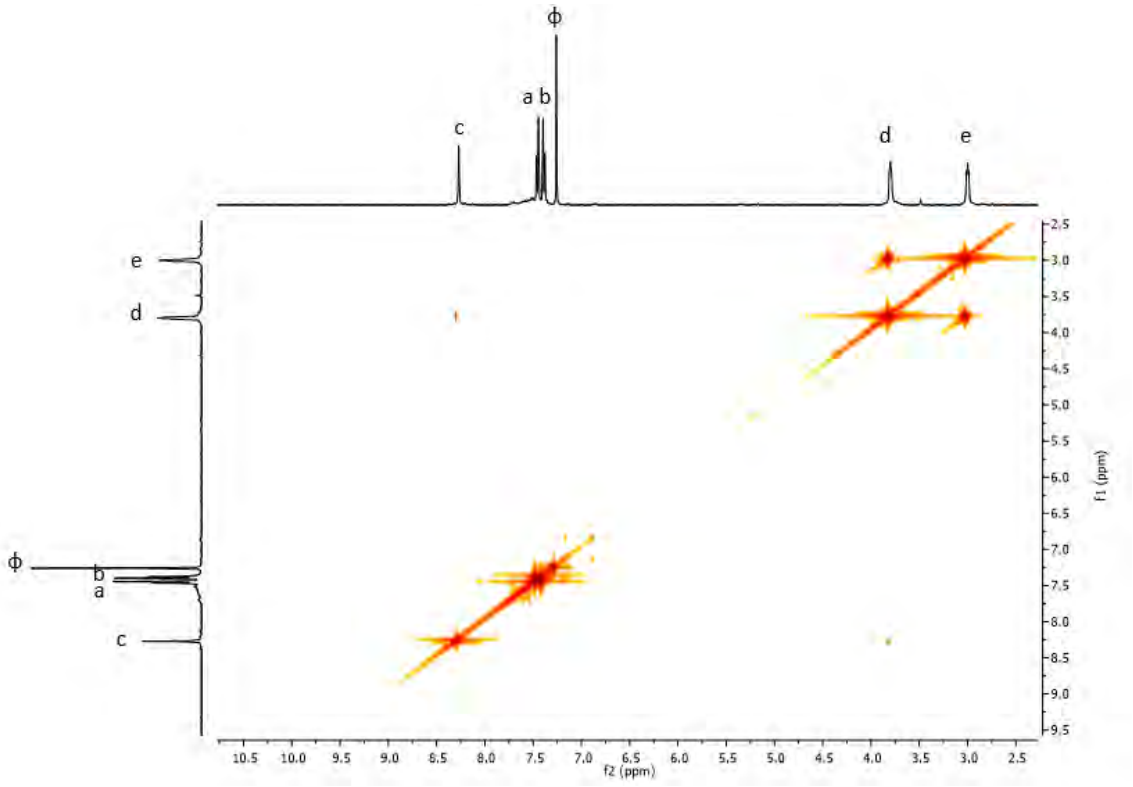

Supplementary Figure 10. TOCSY of S_2pTp macrocycle. Experiment performed in $CDCl_3$ at 298 K (400 MHz).

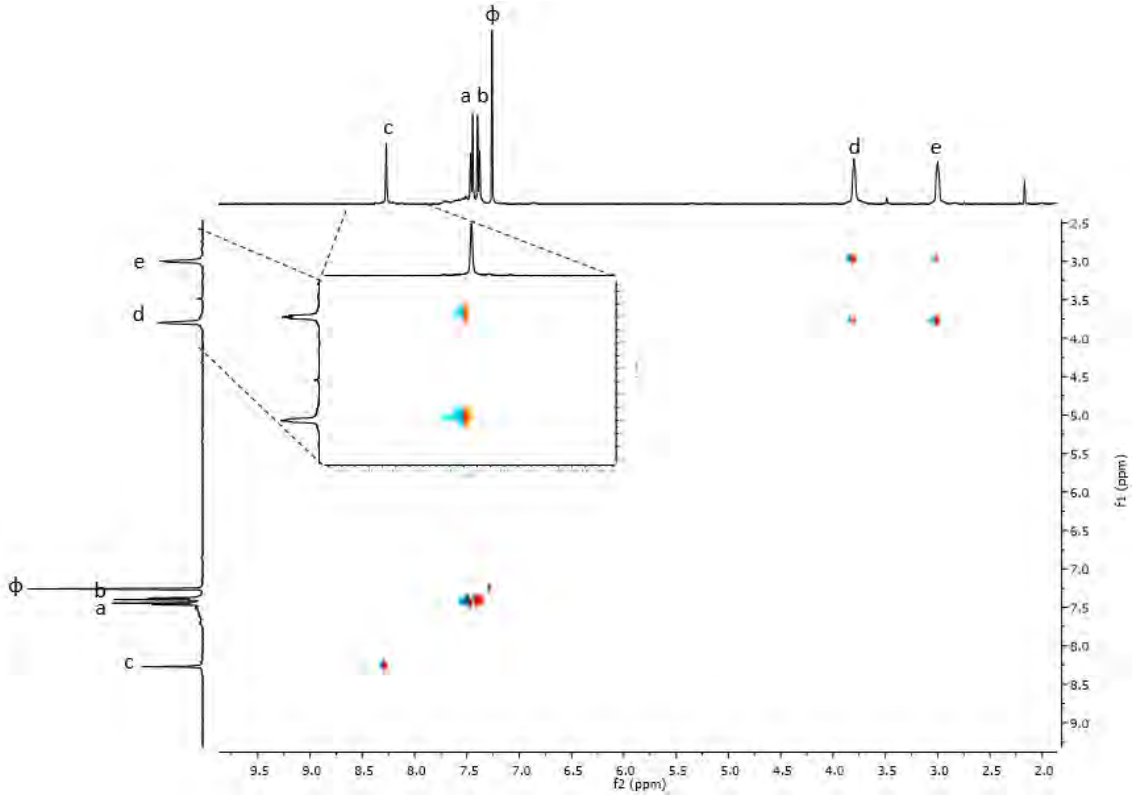

Supplementary Figure 11. NOESY of S_2pTp macrocycle. Experiment performed in $CDCl_3$ at 298 K (400 MHz).

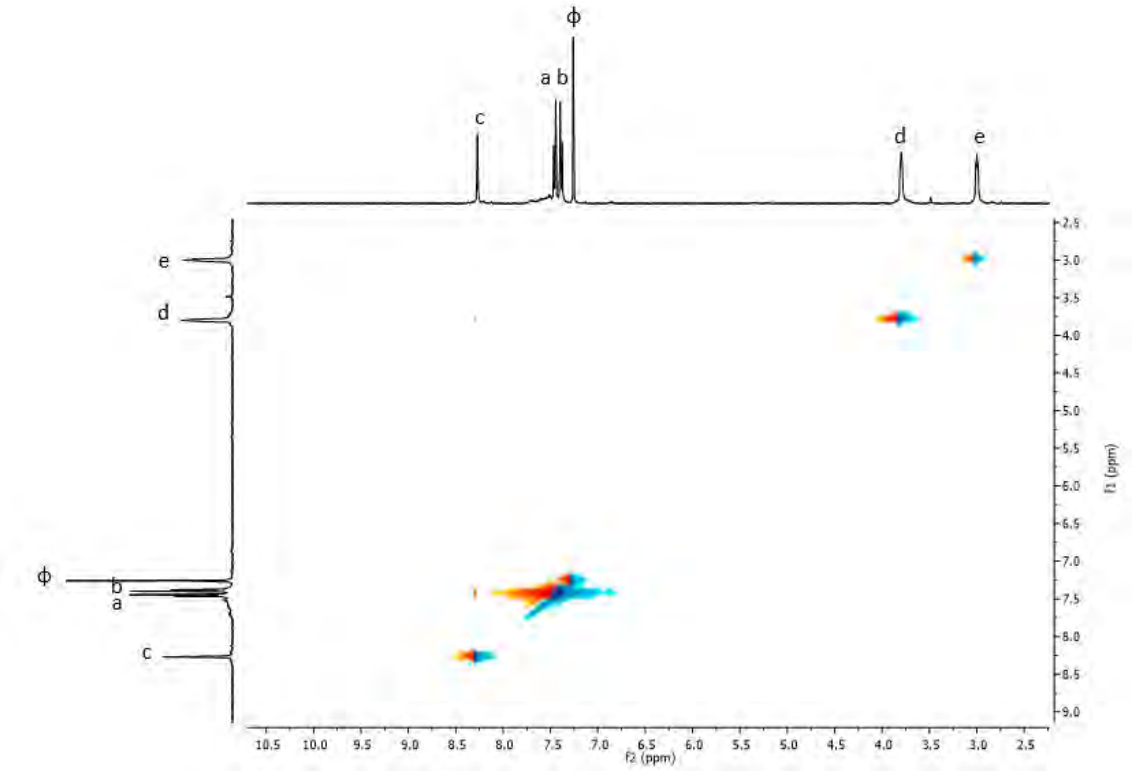

Supplementary Figure 12. HRMS spectrum of S_2pTp macrocycle. Experimental (top) and theoretical (bottom) isotopic pattern for selected peak is shown. Sample solved in chloroform and registered with a Bruker Micro TOF-Q-II exact mass spectrometer.

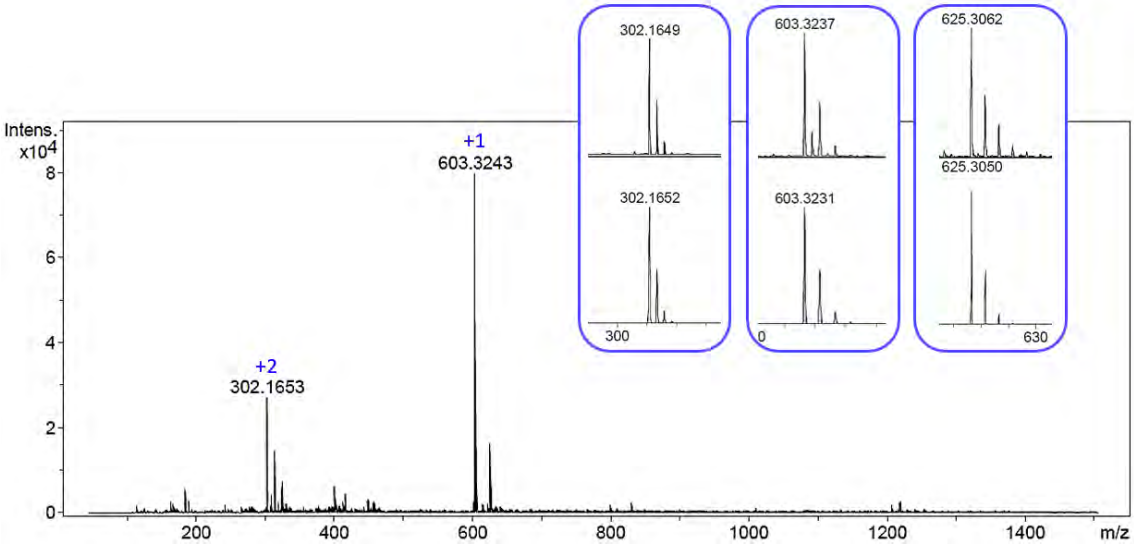

2.3. Synthesis and characterization of H_2pTp

Supplementary Figure 13. Synthesis of the H_2pTp macrocycle.

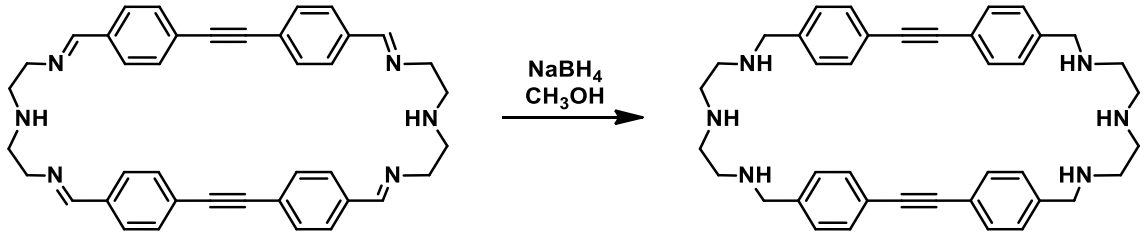

Supplementary Figure 14. ^{1}H-NMR of H_2pTp macrocycle. Experiment performed in $CDCl_3$ at 298 K (400 MHz). (ϕ) $CHCl_3$, (*) acetone, (γ) TMS.

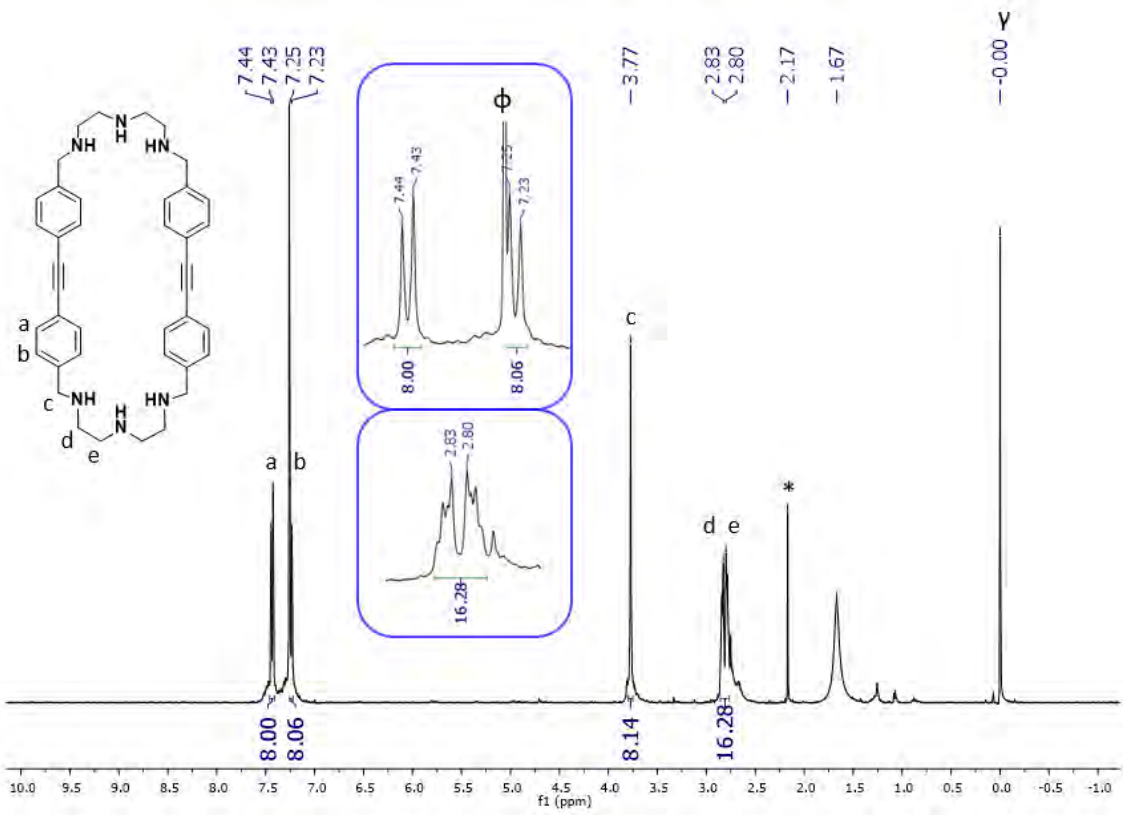

Supplementary Figure 15. ^{13}C-NMR of H_2pTp macrocycle. Experiment performed in $CDCl_3$ at 298 K (100 MHz). (ϕ) $CHCl_3$, (γ) TMS.

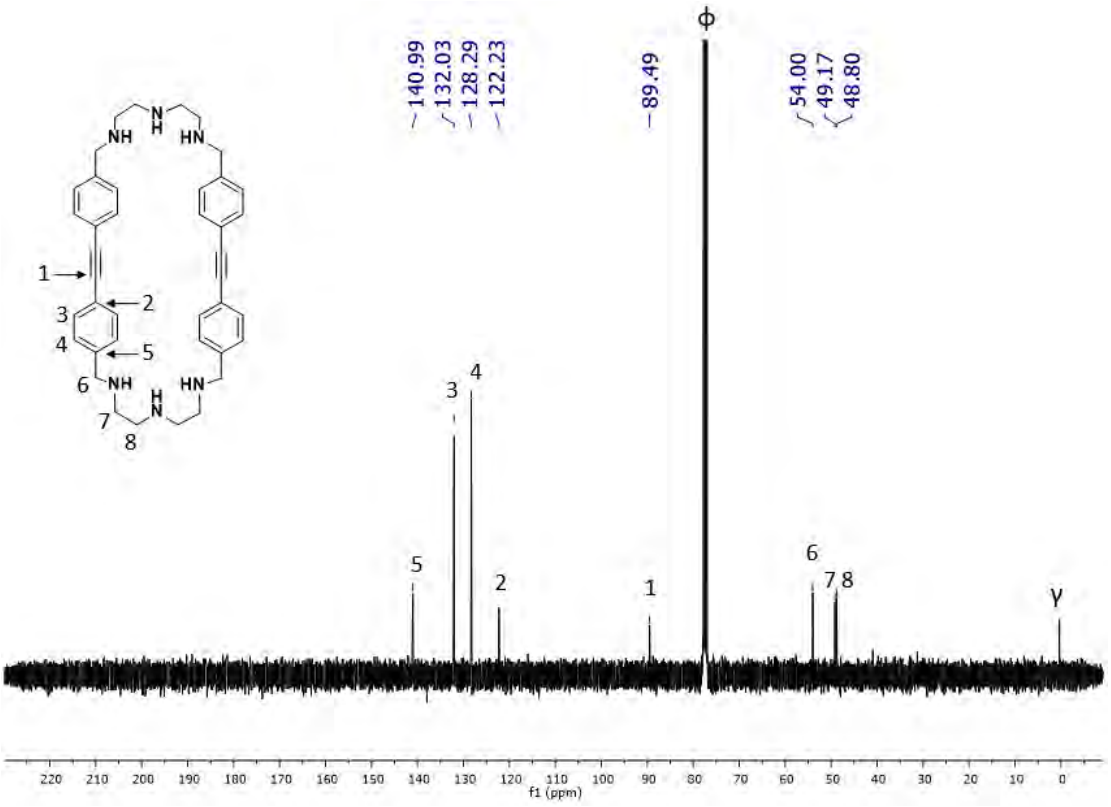

Supplementary Figure 16. HMBC of H_2pTp macrocycle. Experiment performed in $CDCl_3$ at 298 K (400 MHz).

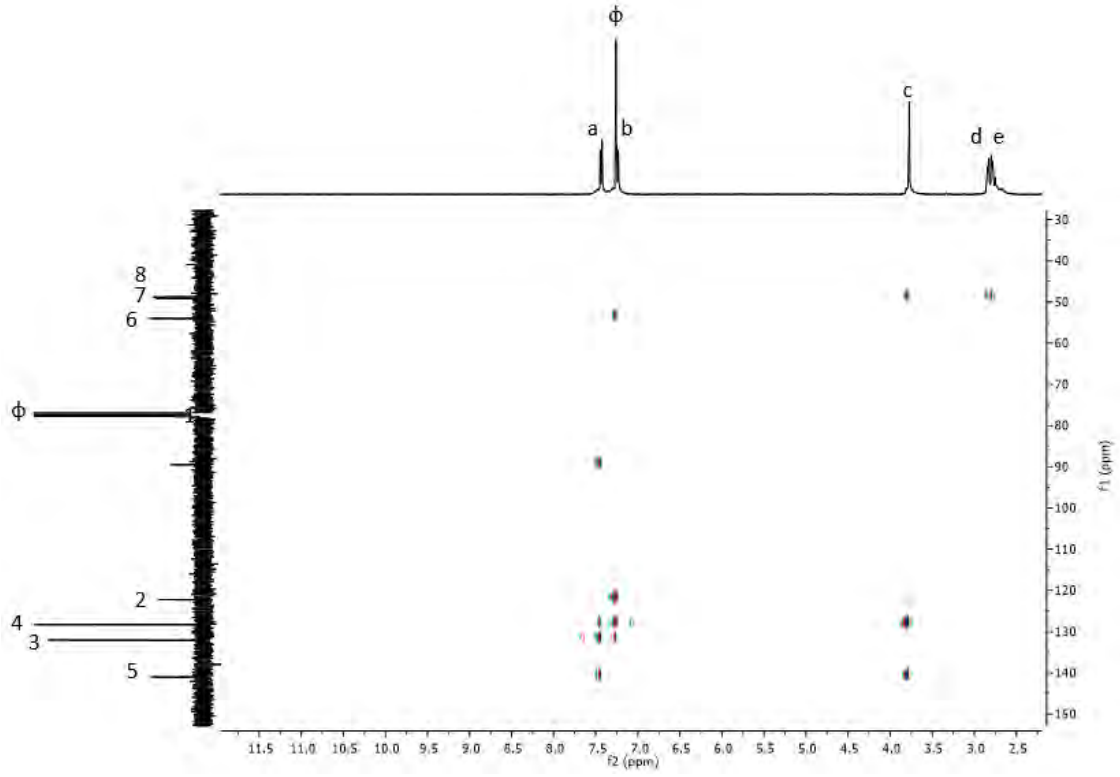

Supplementary Figure 17. HSQC of H_2pTp macrocycle. Experiment performed in $CDCl_3$ at 298 K (400 MHz).

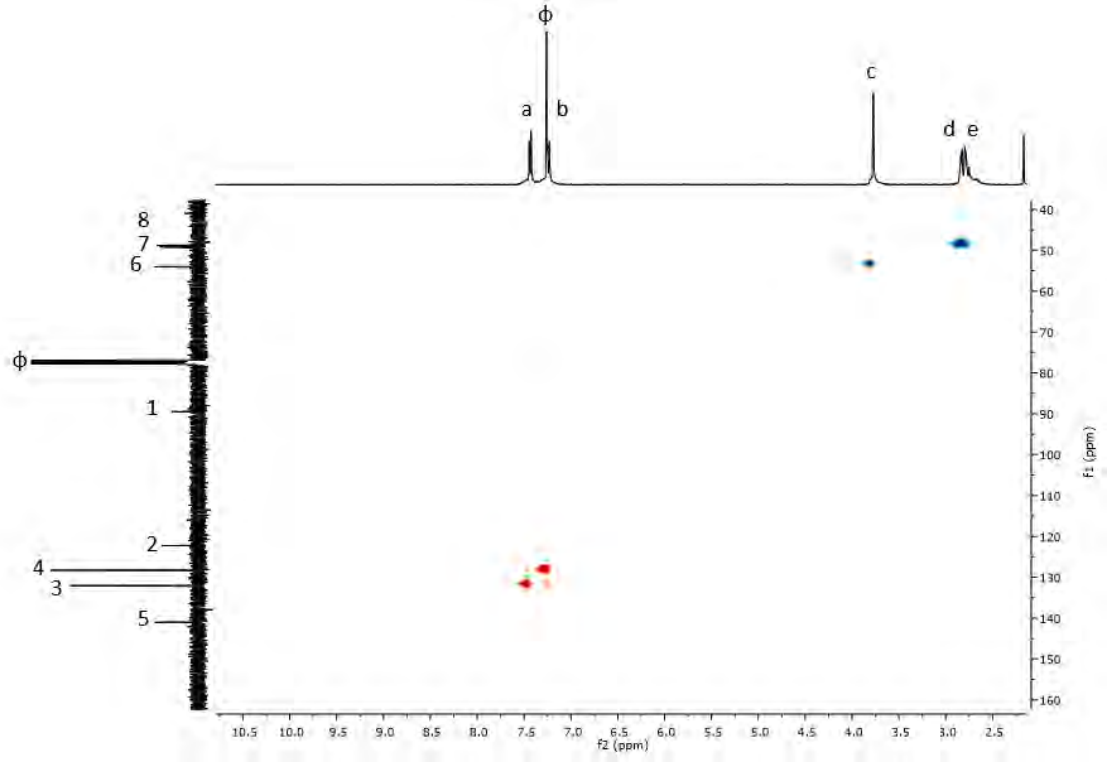

Supplementary Figure 18. COSY of H_2pTp macrocycle. Experiment performed in $CDCl_3$ at 298 K (400 MHz).

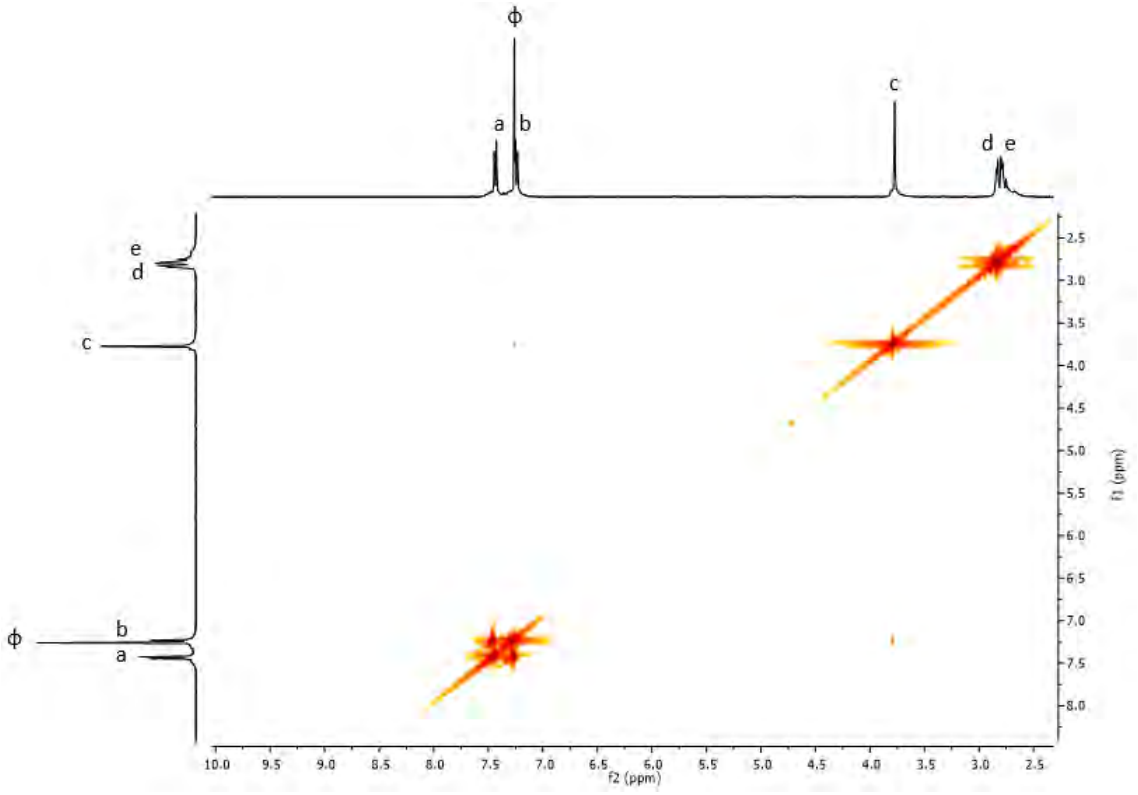

Supplementary Figure 19. TOCSY of H_2pTp macrocycle. Experiment performed in $CDCl_3$ at 298 K (400 MHz).

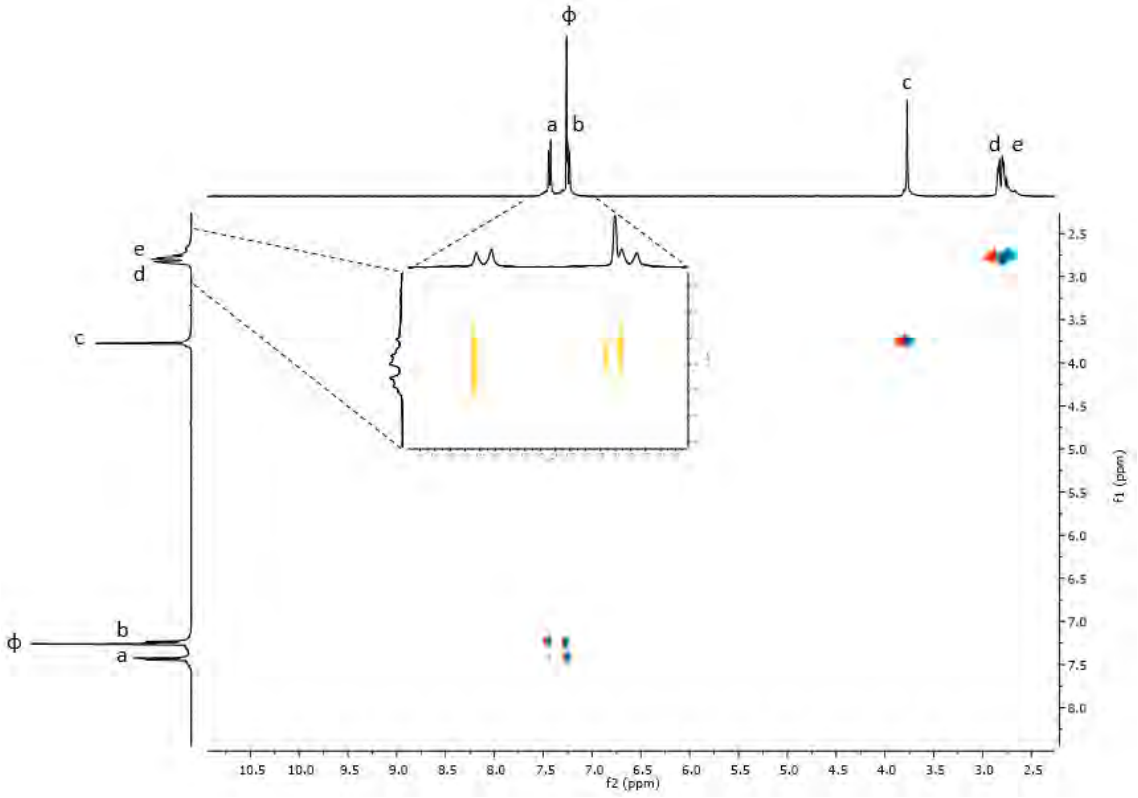

Supplementary Figure 20. NOESY of H_2pTp macrocycle. Experiment performed in $CDCl_3$ at 298 K (400 MHz).

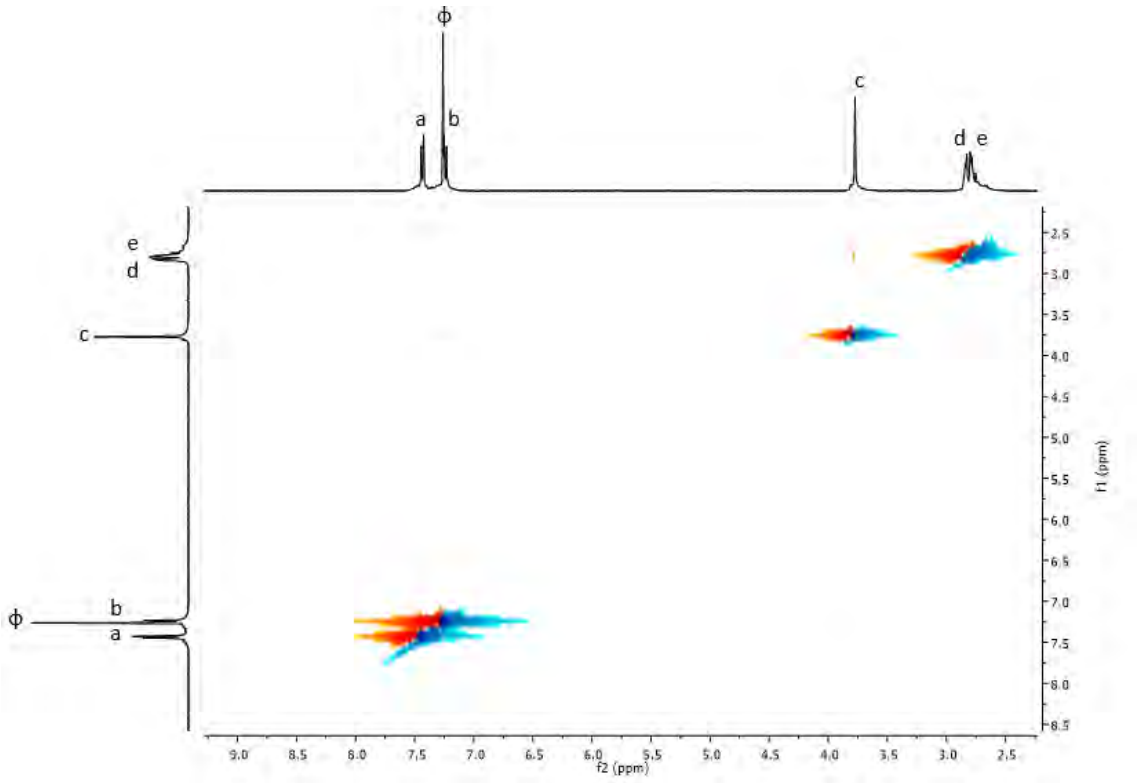

Supplementary Figure 21. HRMS spectrum of H_2pTp macrocycle. Sample solved in chloroform and registered with a Bruker MicrOTOF-Q-II mass spectrometer.

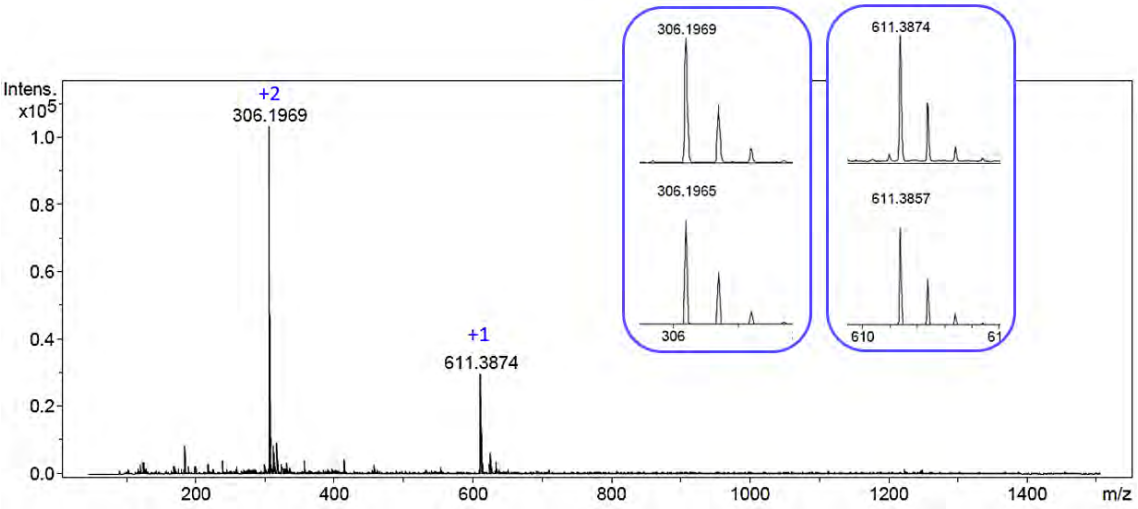

2.4.Synthesis and characterization of the macrocyclic ligand, Me_2pTp

Supplementary Figure 22. Synthesis of the macrocyclic ligand, Me_2pTp.

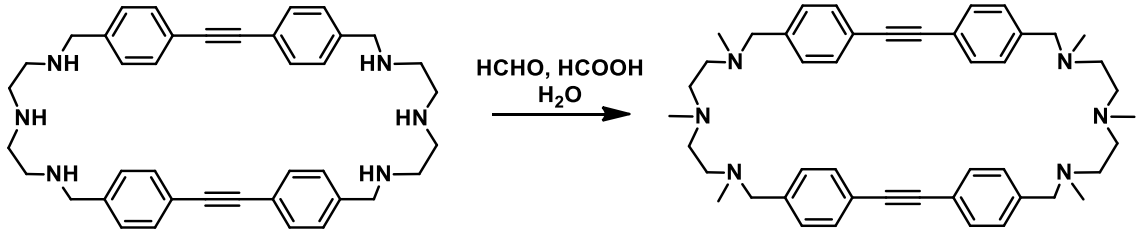

Supplementary Figure 23. ^{1}H-NMR of Me_2pTp macrocycle. Experiment performed in $CDCl_3$ at 298 K (400 MHz). (*) acetone, (γ) TMS.

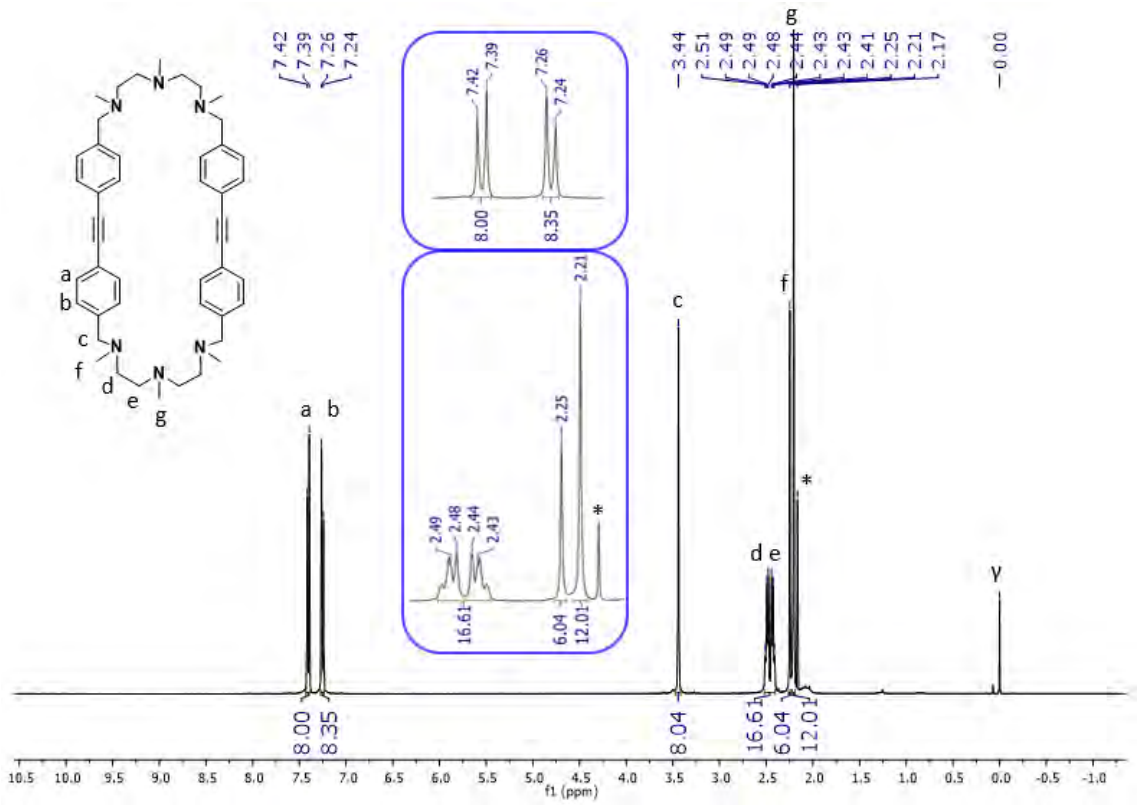

Supplementary Figure 24. ^{13}C-NMR of Me_2pTp macrocycle. Experiment performed in $CDCl_3$ at 298 K (400 MHz). (ϕ) $CHCl_3$.

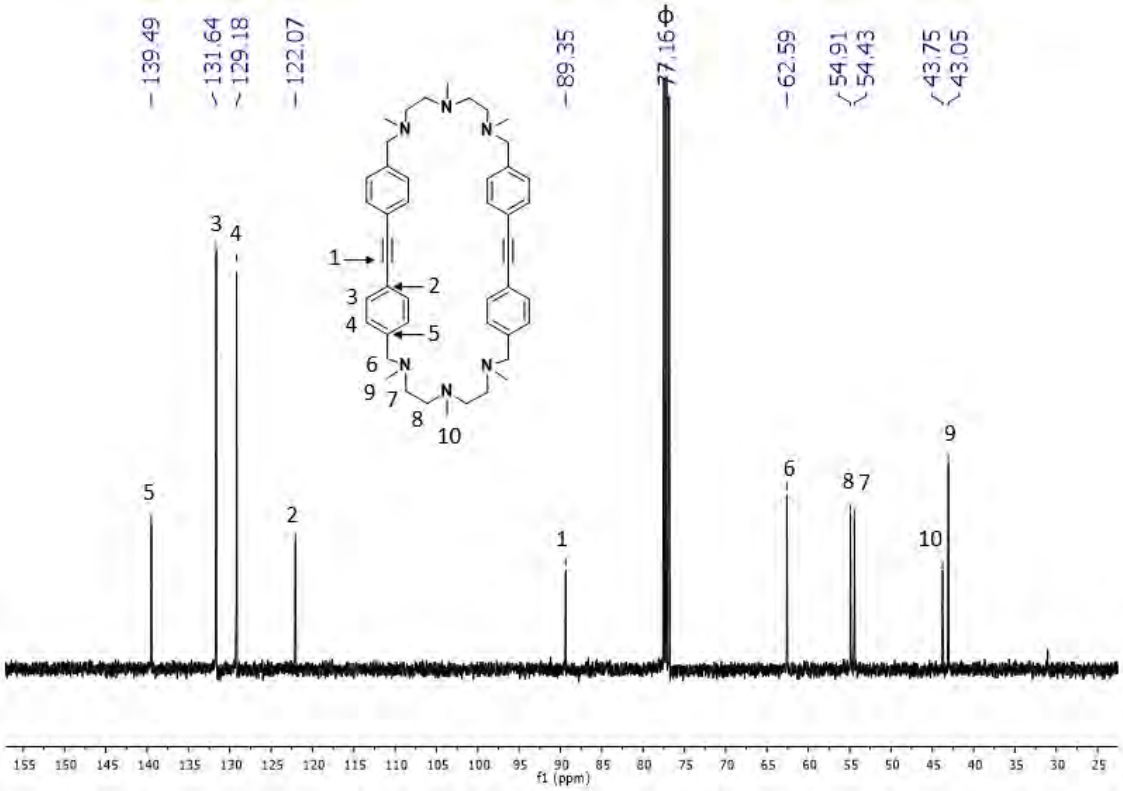

Supplementary Figure 25. HMBC of Me_2pTp macrocycle. Experiment performed in $CDCl_3$ at 298 K (400 MHz).

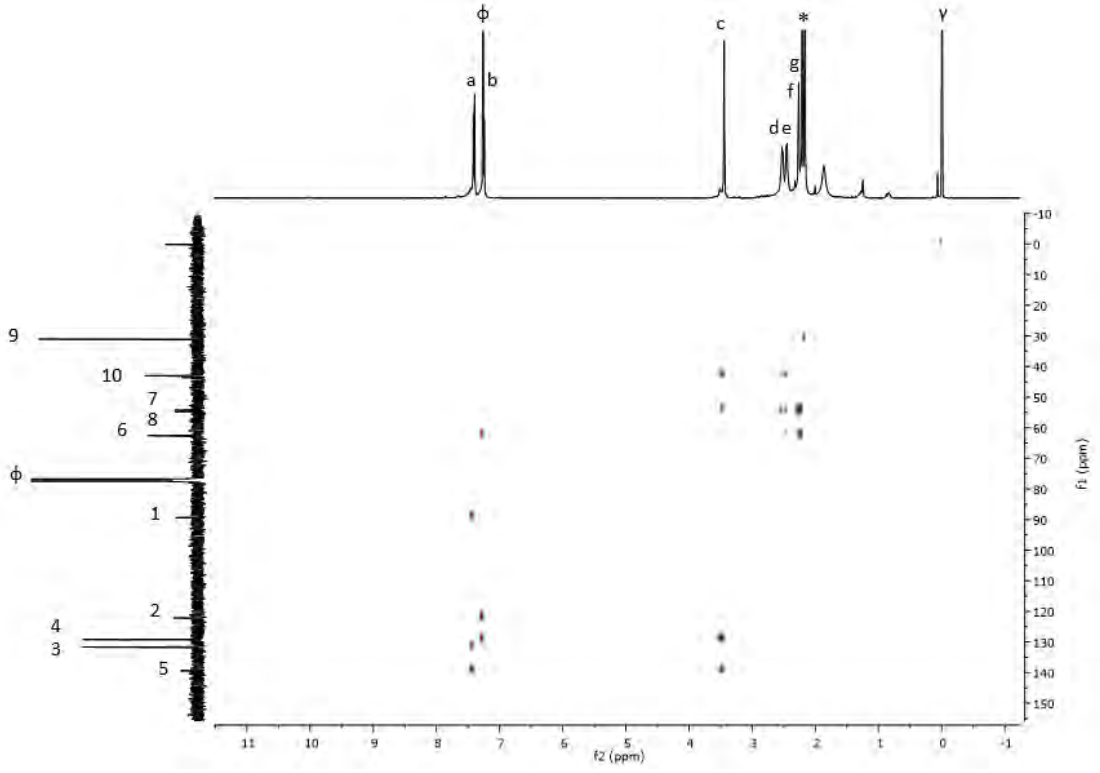

Supplementary Figure 26. HSQC of Me_2pTp macrocycle. Experiment performed in $CDCl_3$ at 298 K (400 MHz).

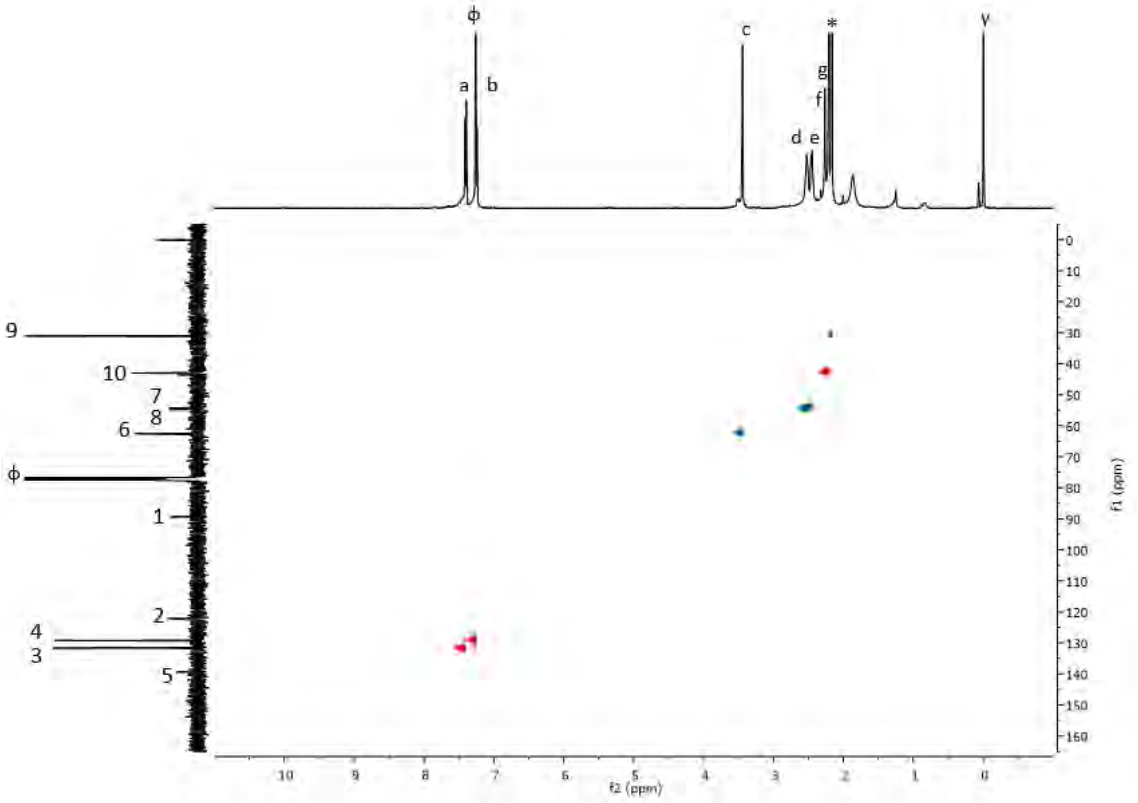

Supplementary Figure 27. COSY of Me_2pTp macrocycle. Experiment performed in $CDCl_3$ at 298 K (400 MHz).

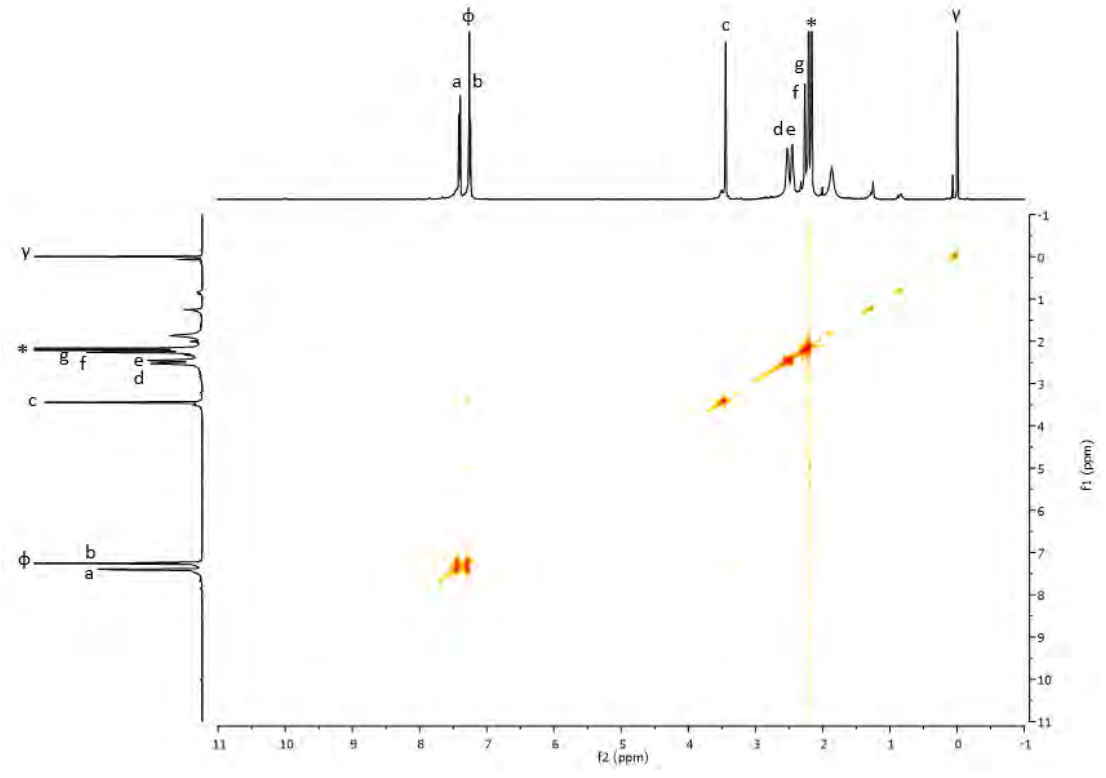

Supplementary Figure 28. TOCSY of Me_2pTp macrocycle. Experiment performed in $CDCl_3$ at 298 K (400 MHz).

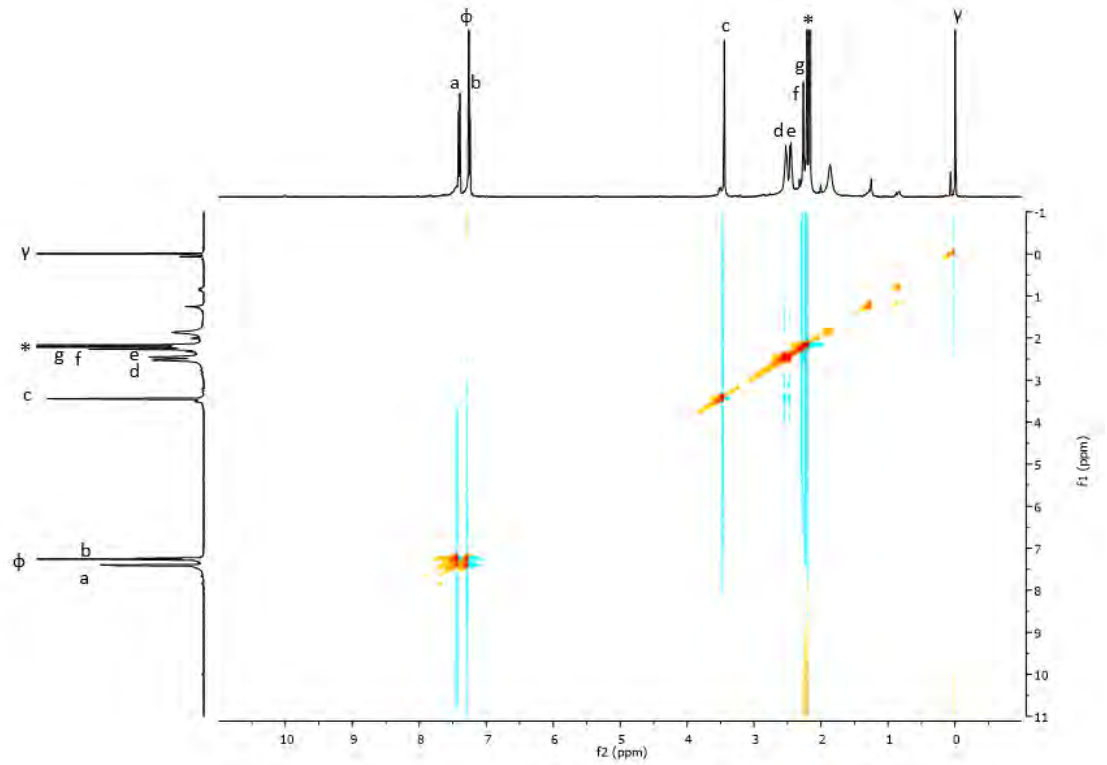

Supplementary Figure 29. NOESY of Me_2pTp macrocycle. Experiment performed in $CDCl_3$ at 298 K (400 MHz).

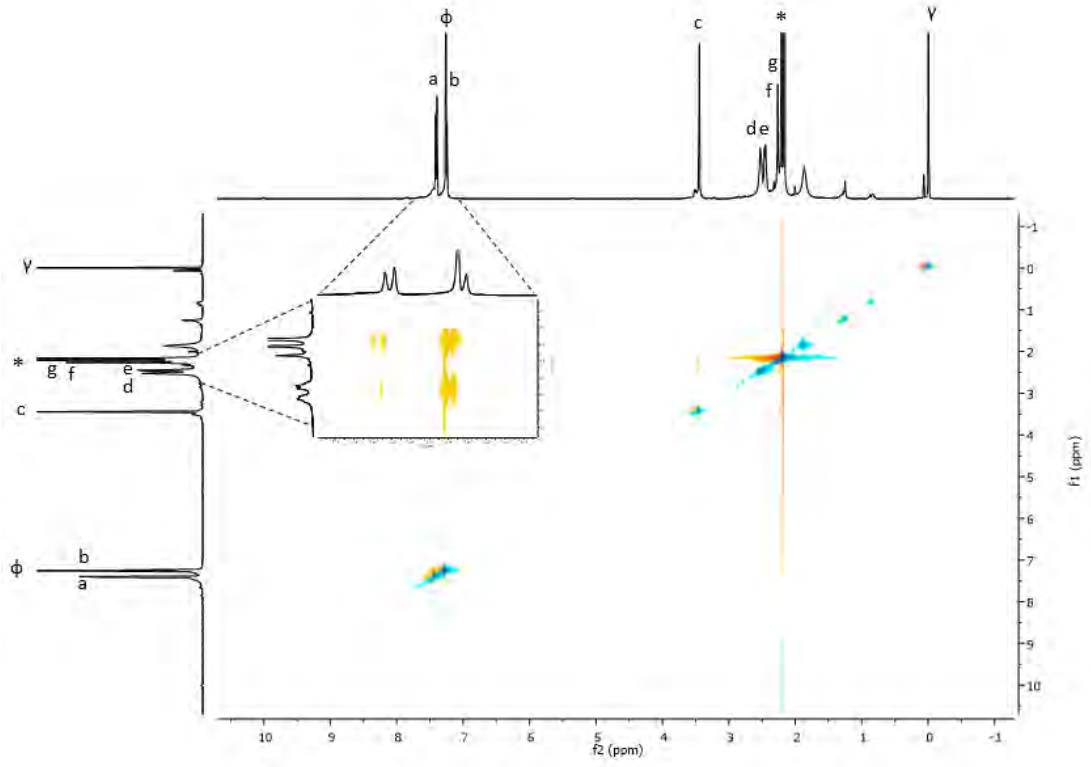

Supplementary Figure 30. HRMS spectrum of Me_2pTp macrocycle. Sample solved in chloroform and registered with a Bruker MicrOTOF-Q-II mass spectrometer.

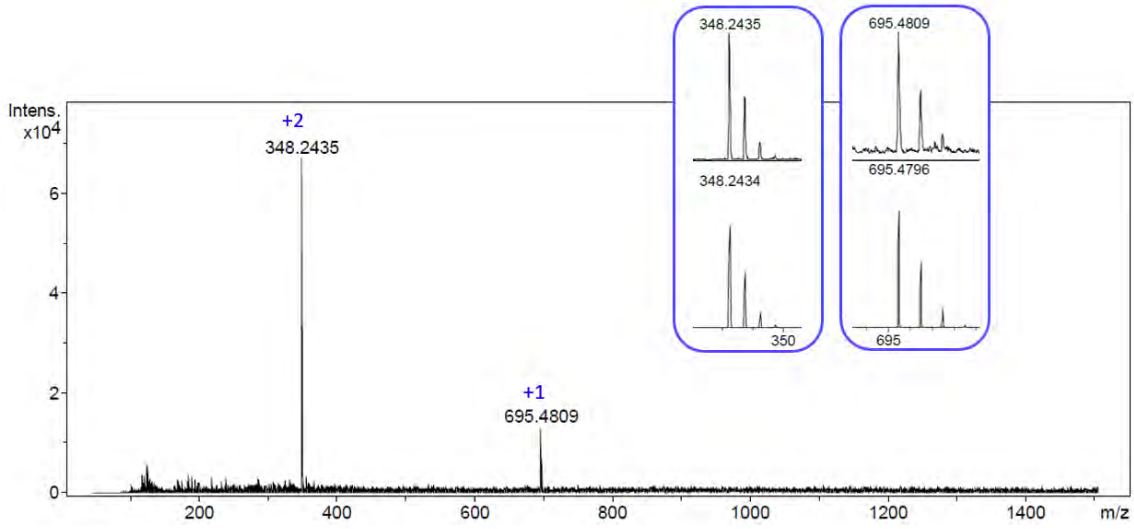

2.5. Synthesis and characterization of dinuclear Pd^{II} molecular clip, $[Pd_2(Me_2pTp)(AcO)_2](OTf)_2$

Supplementary Figure 31. Synthesis of $[Pd_2(Me_2pTp)(AcO)_2](OTf)_2$. Schematic representation for the synthesis of Pd-6 clip.

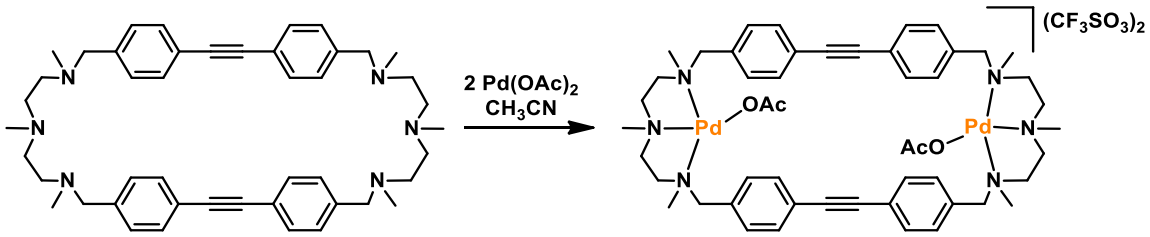

Supplementary Figure 32. ^{1}H-NMR of $[Pd_2(Me_2pTp)(AcO)_2](OTf)_2$. Experiment performed in CD_3CN at 298 K (400 MHz). (ϕ) CH_3CN, (*) diethyl ether, (#) H_2O.

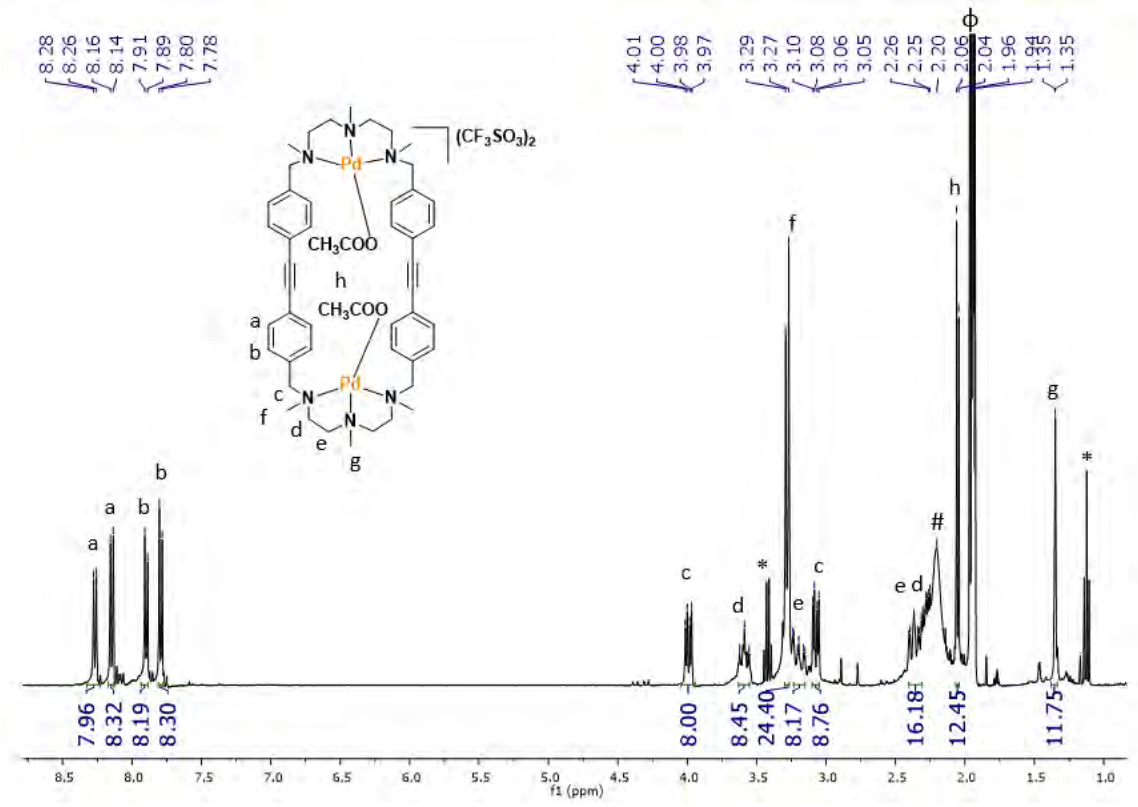

Supplementary Figure 33. ^{13}C-NMR of $[Pd_2(Me_2pTp)(AcO)_2](OTf)_2$. Experiment performed in CD_3CN at 298 K (100 MHz). (ϕ) CH_3CN.

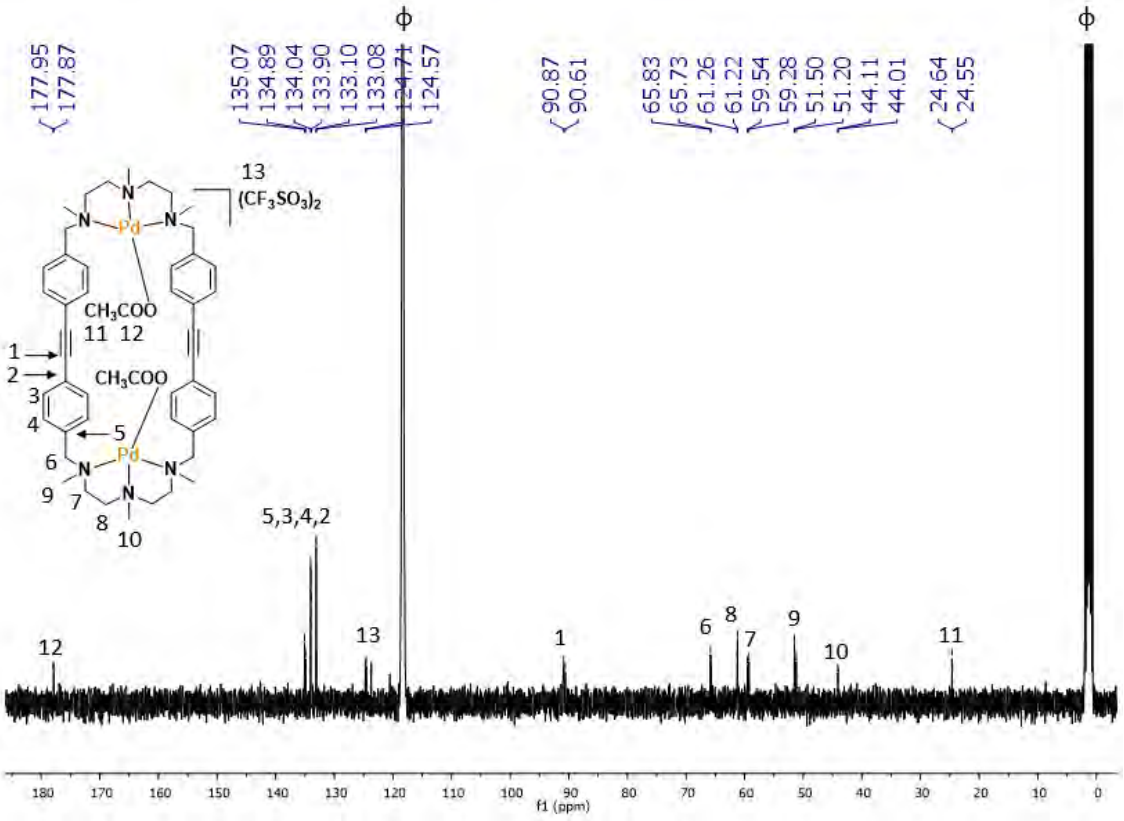

Supplementary Figure 34. HMBC of $[Pd_2(Me_2pTp)(AcO)_2](OTf)_2$. Experiment performed in CD_3CN at 298 K (400 MHz).

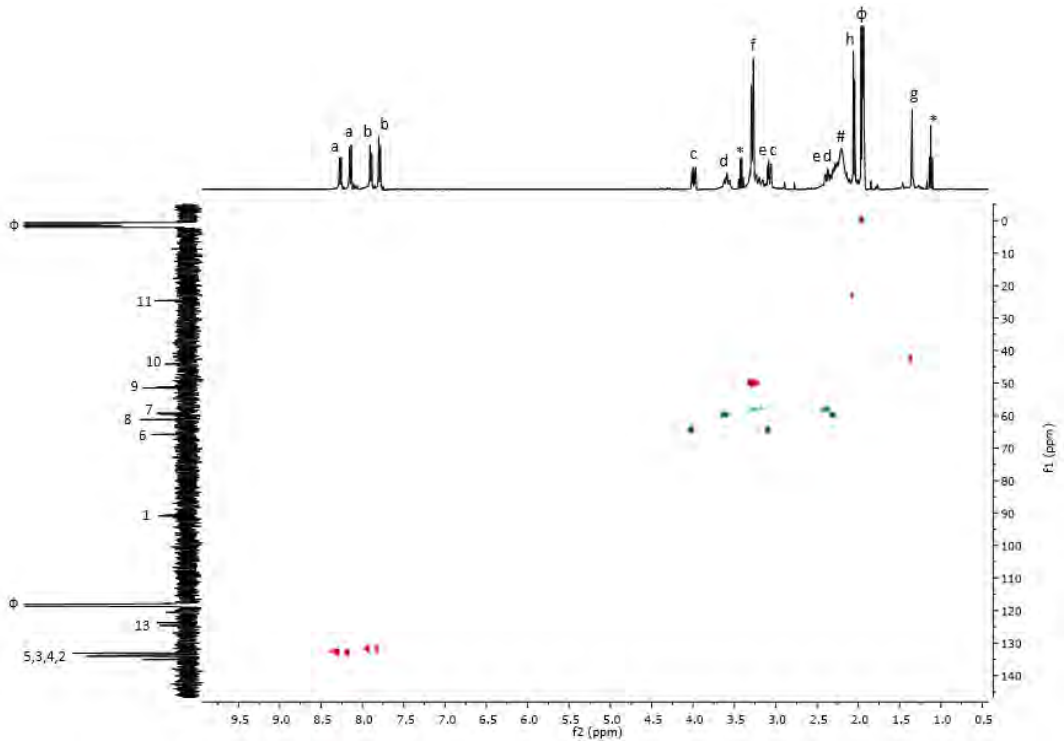

Supplementary Figure 35. HSQC of $[Pd_2(Me_2pTp)(AcO)_2](OTf)_2$. Experiment performed in CD_3CN at 298 K (400 MHz).

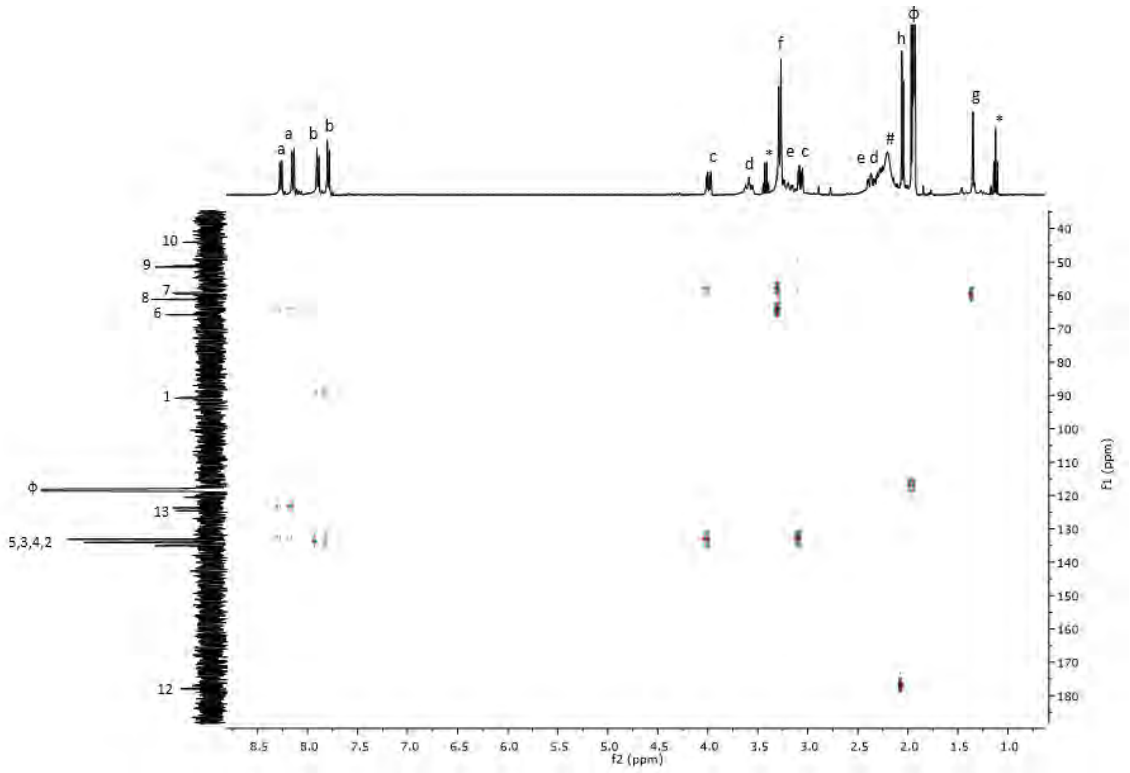

Supplementary Figure 36. COSY of $[Pd_2(Me_2pTp)(AcO)_2](OTf)_2$. Experiment performed in CD_3CN at 298 K (400 MHz).

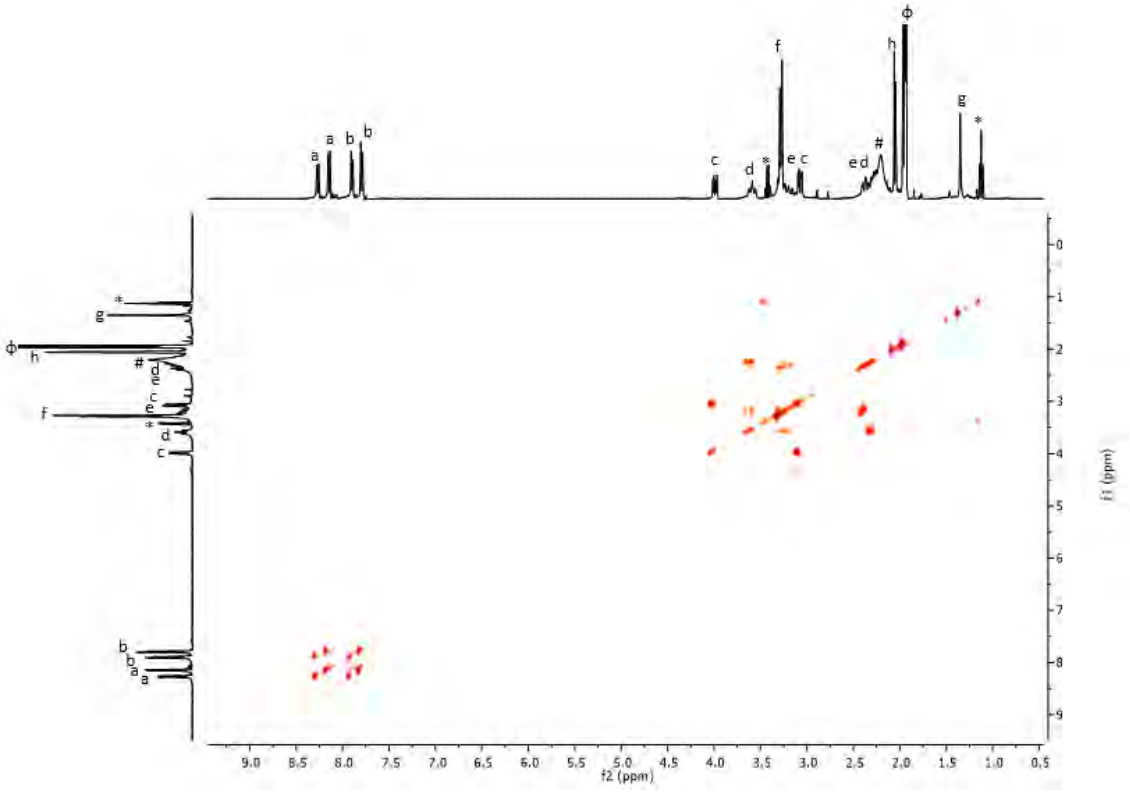

Supplementary Figure 37. TOCSY of $[Pd_2(Me_2pTp)(AcO)_2](OTf)_2$. Experiment performed in CD_3CN at 298 K (400 MHz).

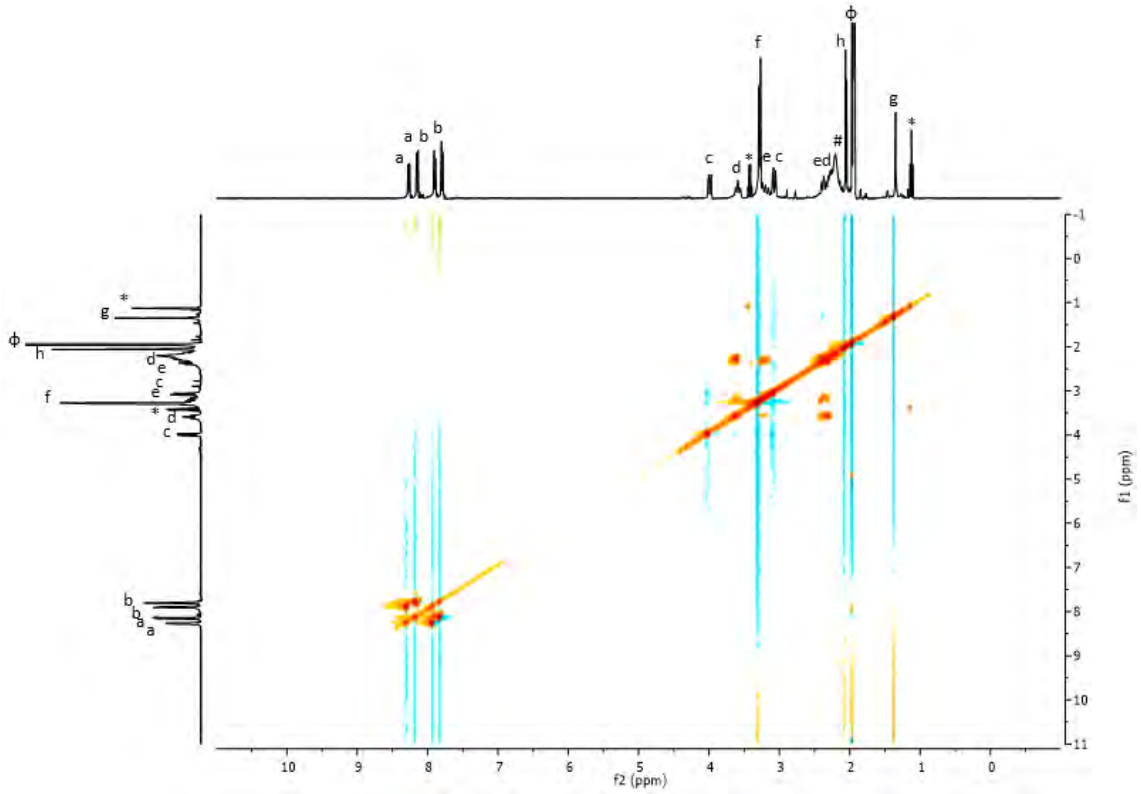

Supplementary Figure 38. NOESY of $[Pd_2(Me_2pTp)(AcO)_2](OTf)_2$. Experiment performed in CD_3CN at 298 K (400 MHz).

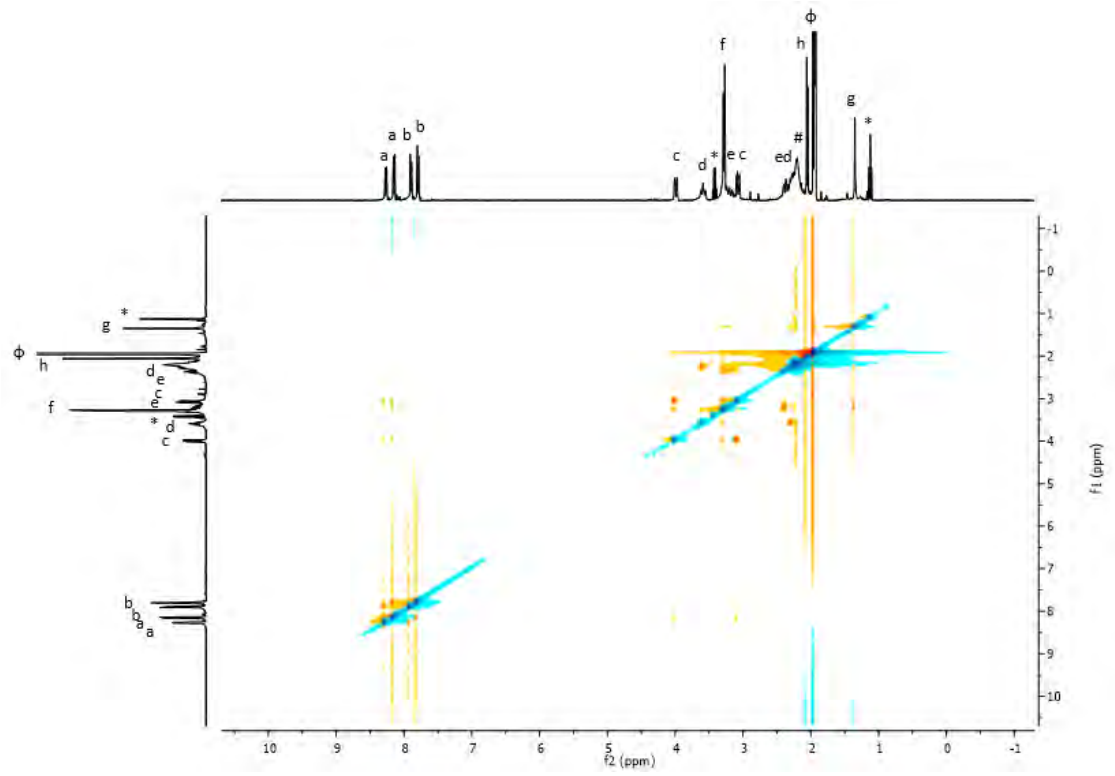

Supplementary Figure 39. HRMS spectrum of $[Pd_2(Me_2pTp)(AcO)_2](OTf)_2$. Sample solved in acetonitrile and registered with a Bruker MicrOTOF-Q-II mass spectrometer.

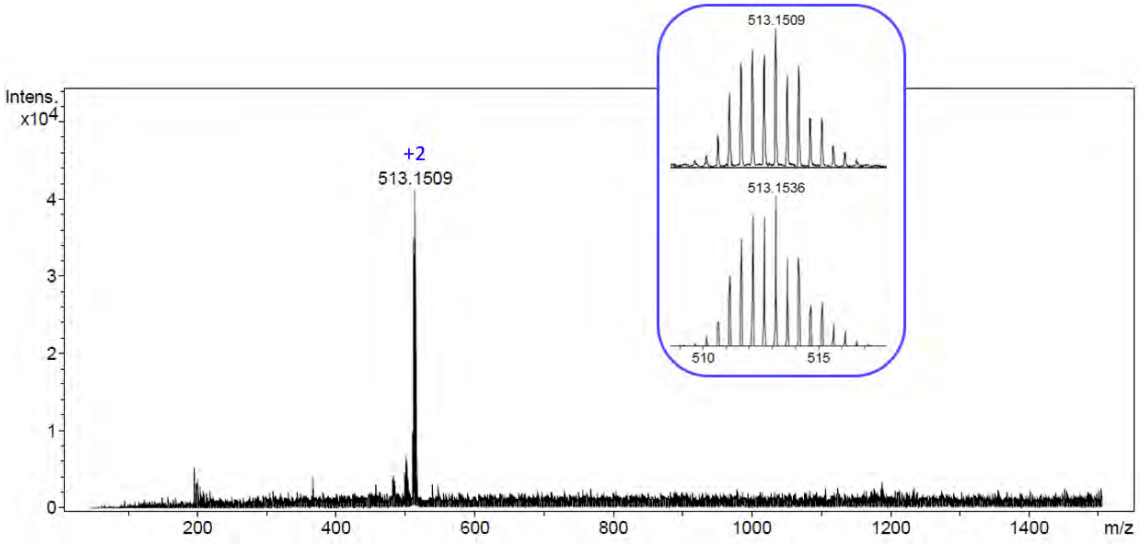

2.6. Synthesis and characterization of dinuclear Cu^{II} molecular clip $[Cu_2(Me_2pTp)(OTf)_2](OTf)_2$

Supplementary Figure 40. Synthesis of $[Cu_2(Me_2pTp)(OTf)_2](OTf)_2$. Schematic representation for the synthesis of Cu-7 clip.

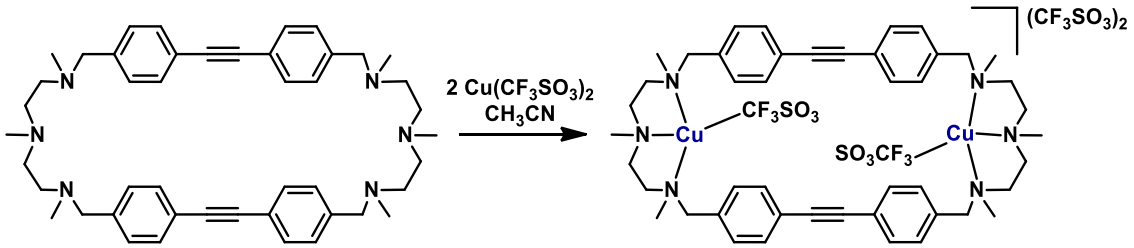

Supplementary Figure 41. HRMS spectrum of $[Cu_2(Me_2pTp)(OTf)_2](OTf)_2$. Sample solved in acetonitrile and registered with a Bruker MicrOTOF-Q-II mass spectrometer.

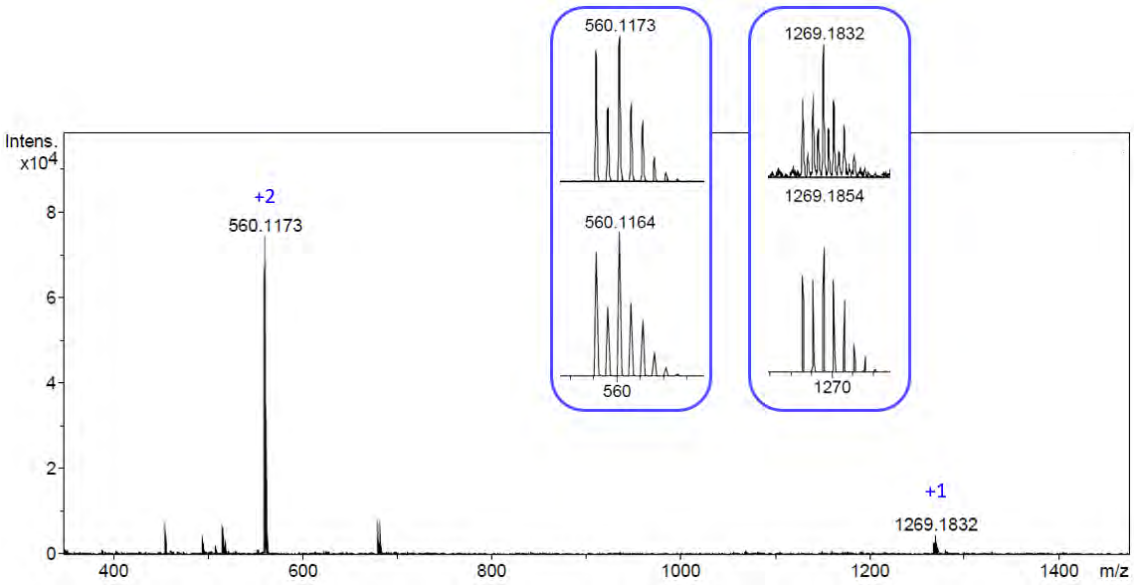

Supplementary Figure 42. Crystal structure of macrocyclic compound $[Cu_2(Me_2pTp)(OTf)_2](OTf)_2$. (**CCDC 1984937**) H atoms were omitted for clarity. Cu(II) presents a d^8 electronic configuration which enhance copper ions to adopt a tetracoordinated square-planar geometry formed by three N atoms of the macrocyclic ligand (Me_2pTp). Two CH_3CN molecules from the solvent were coordinated in a monodentate mode.

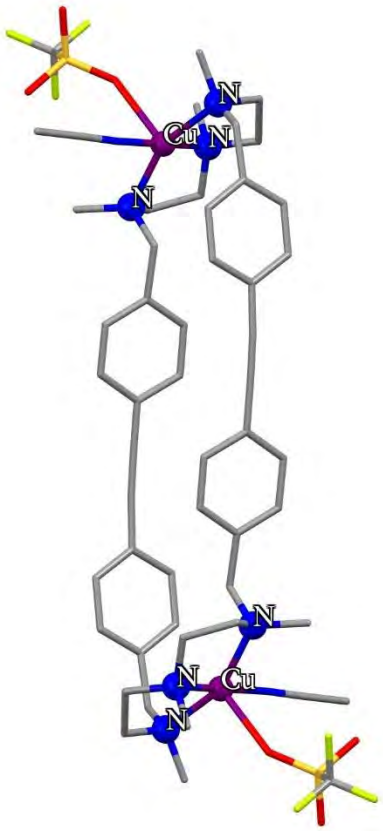

2.7.Synthesis and characterization of tetragonal prismatic nanocapsule 6·$(BArF)_8$

Supplementary Figure 43. Synthesis of **6**·$(BArF)_8$ nanocapsule and labelling of protons for NMR assignment (nanocapsule scheme from XRD data CCDC 1984575).

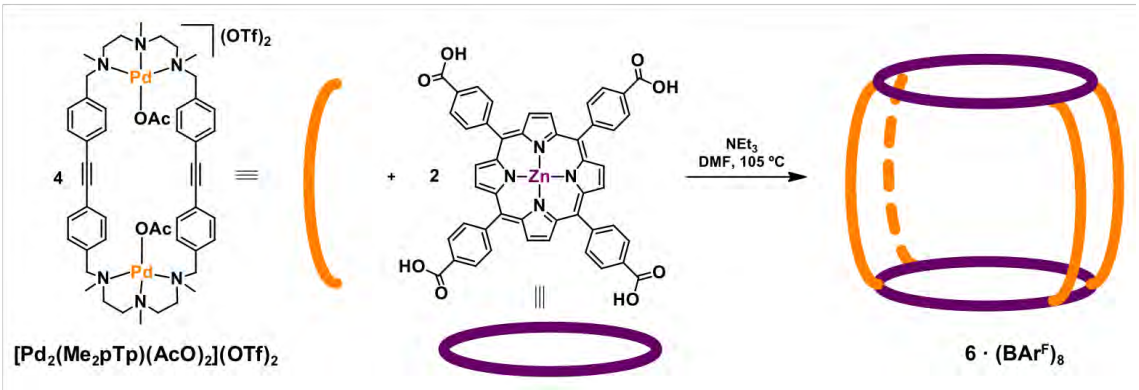

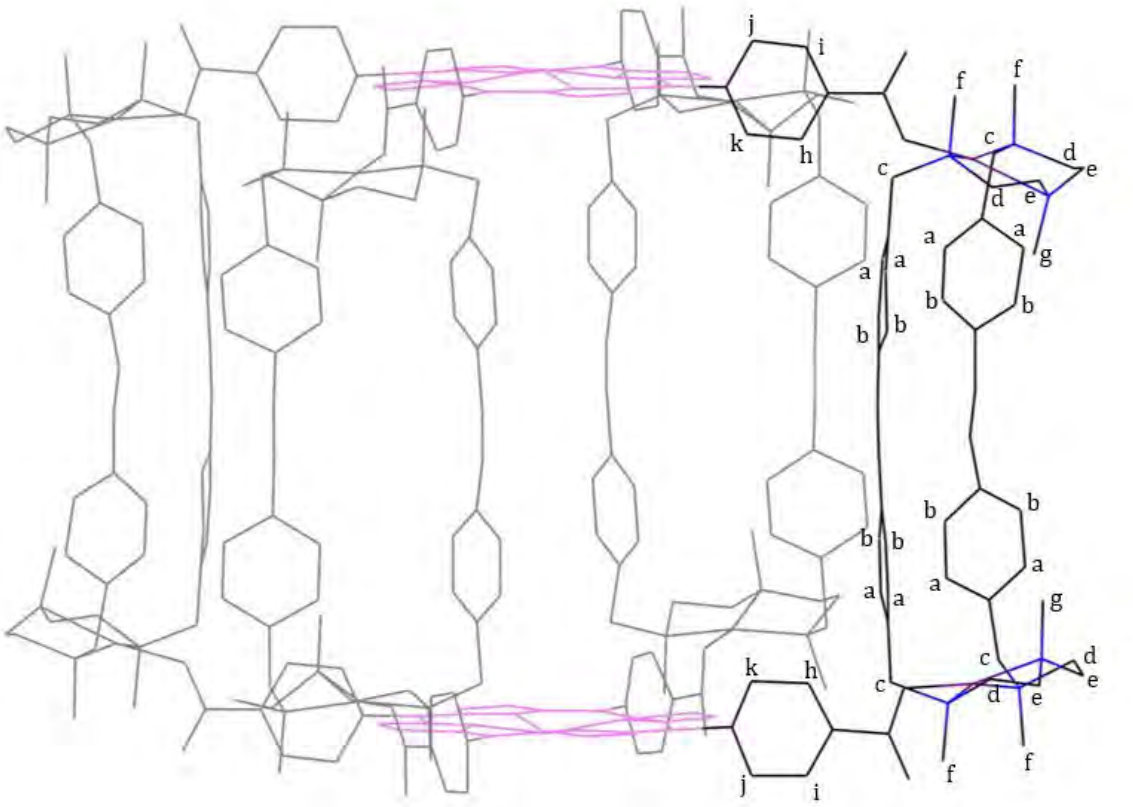

Supplementary Figure 44. ^{1}H-NMR of **6**·$(BArF)_8$ nanocapsule. Experiment performed in CD_3CN at 298 K (400 MHz). (γ) dcm, (*) diethyl ether, (μ) dmf, (#) H_2O, (ϕ) CH_3CN.

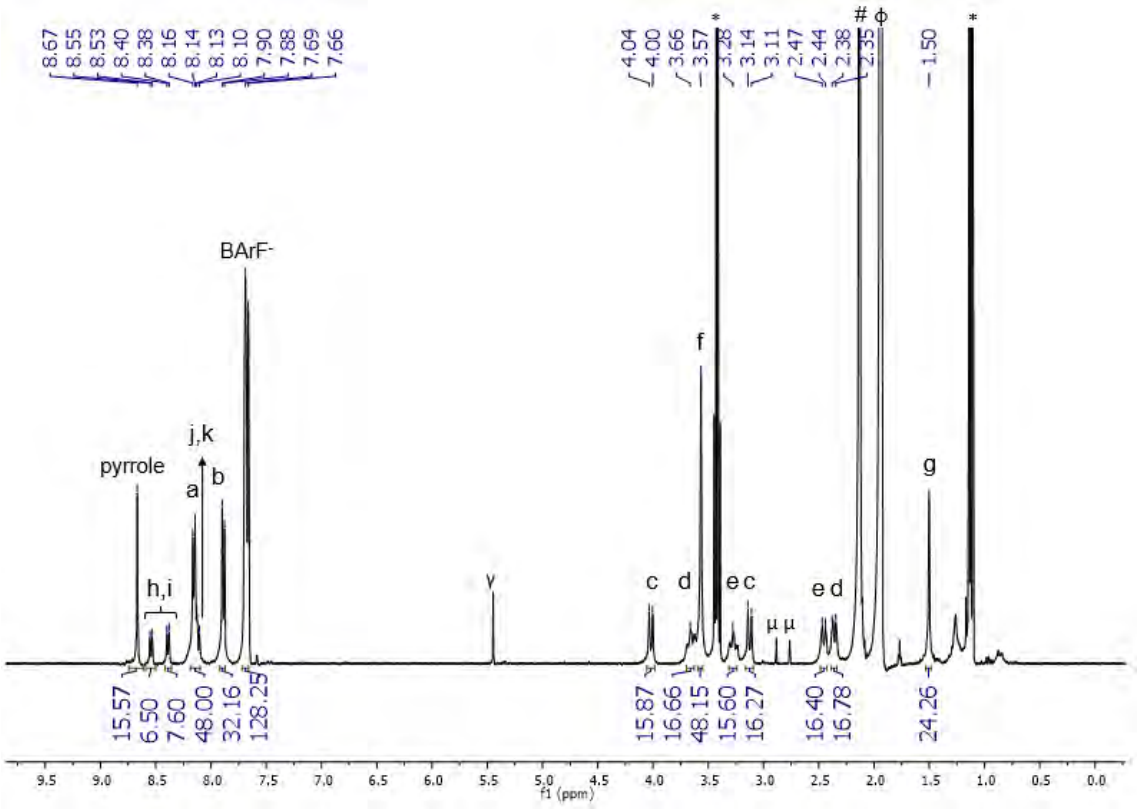

Supplementary Figure 45. HMBC of **6**·$(BArF)_8$ nanocapsule. Experiment performed in CD_3CN at 298 K (400 MHz).

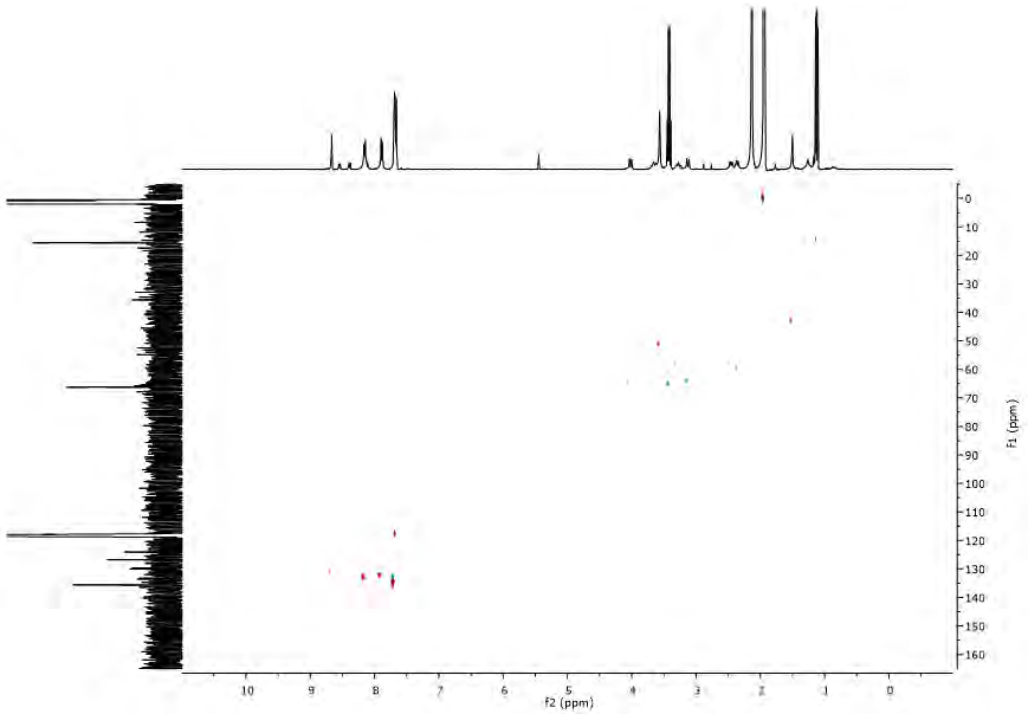

Supplementary Figure 46. HSQC of **6**·$(BArF)_8$ nanocapsule. Experiment performed in CD_3CN at 298 K (400 MHz).

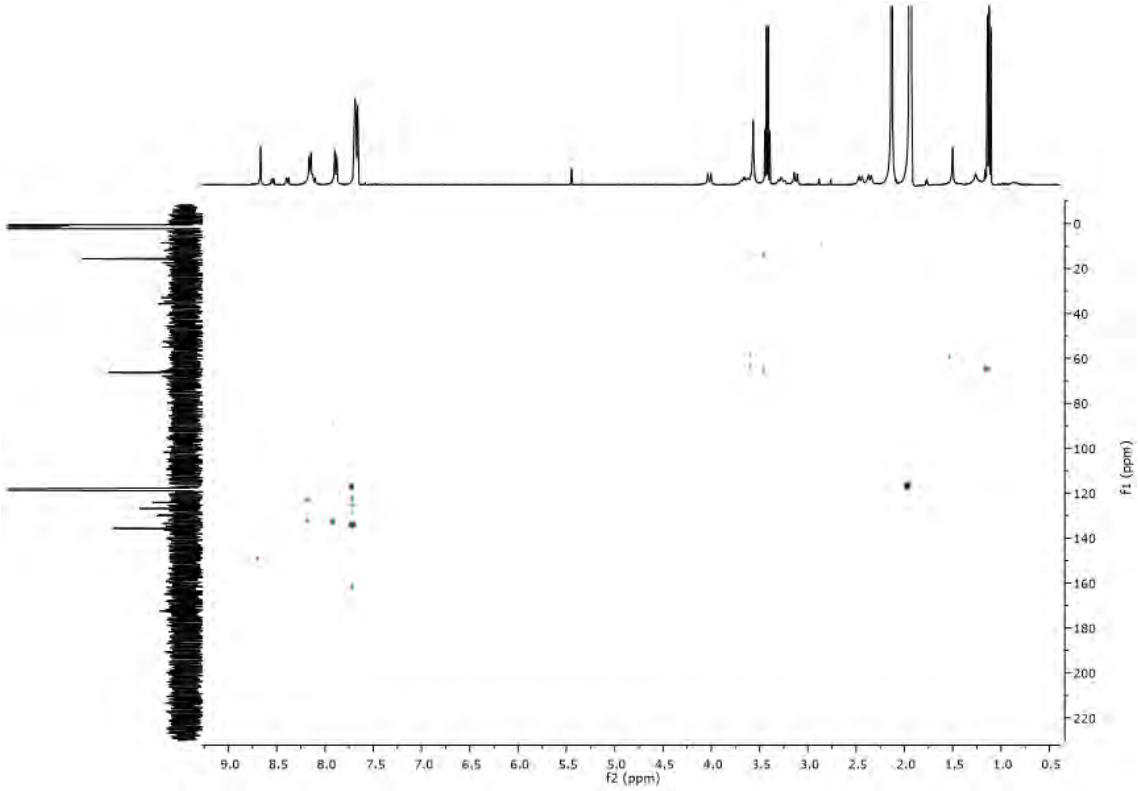

Supplementary Figure 47. COSY of **6**·$(BArF)_8$ nanocapsule. Experiment performed in CD_3CN at 298 K (400 MHz).

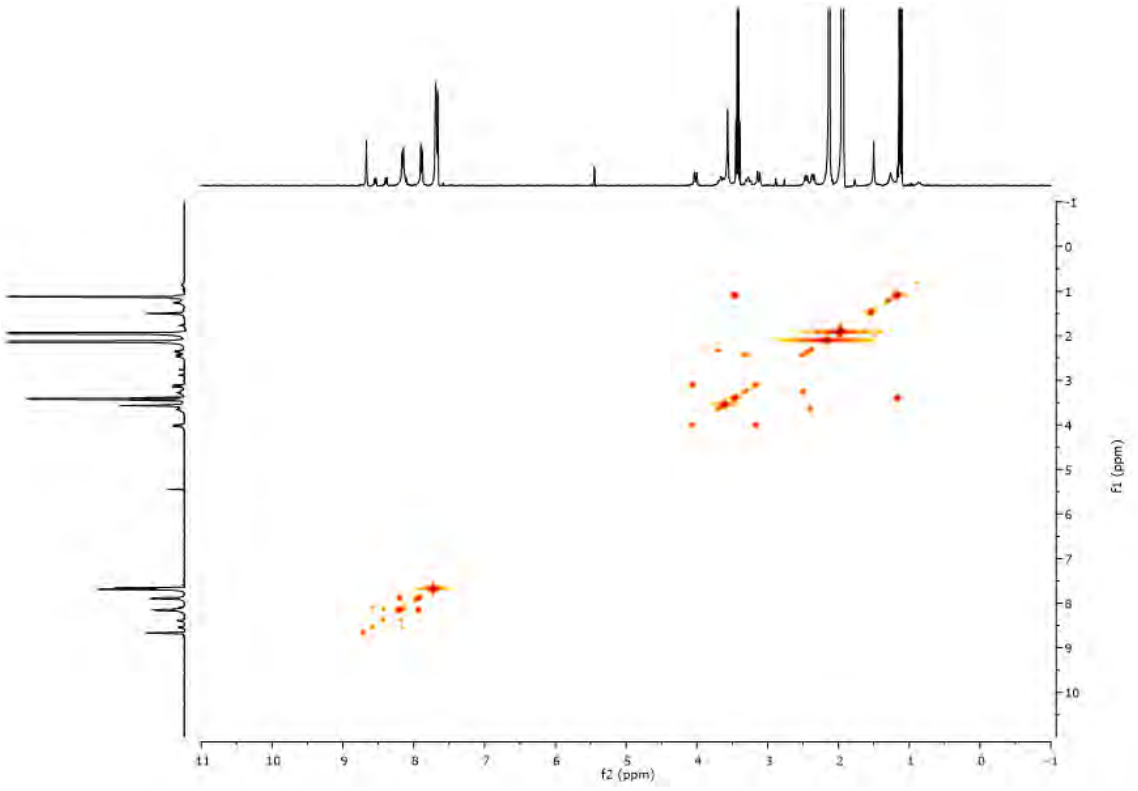

Supplementary Figure 48. TOCSY of **6**·$(BArF)_8$ nanocapsule. Experiment performed in CD_3CN at 298 K (400 MHz).

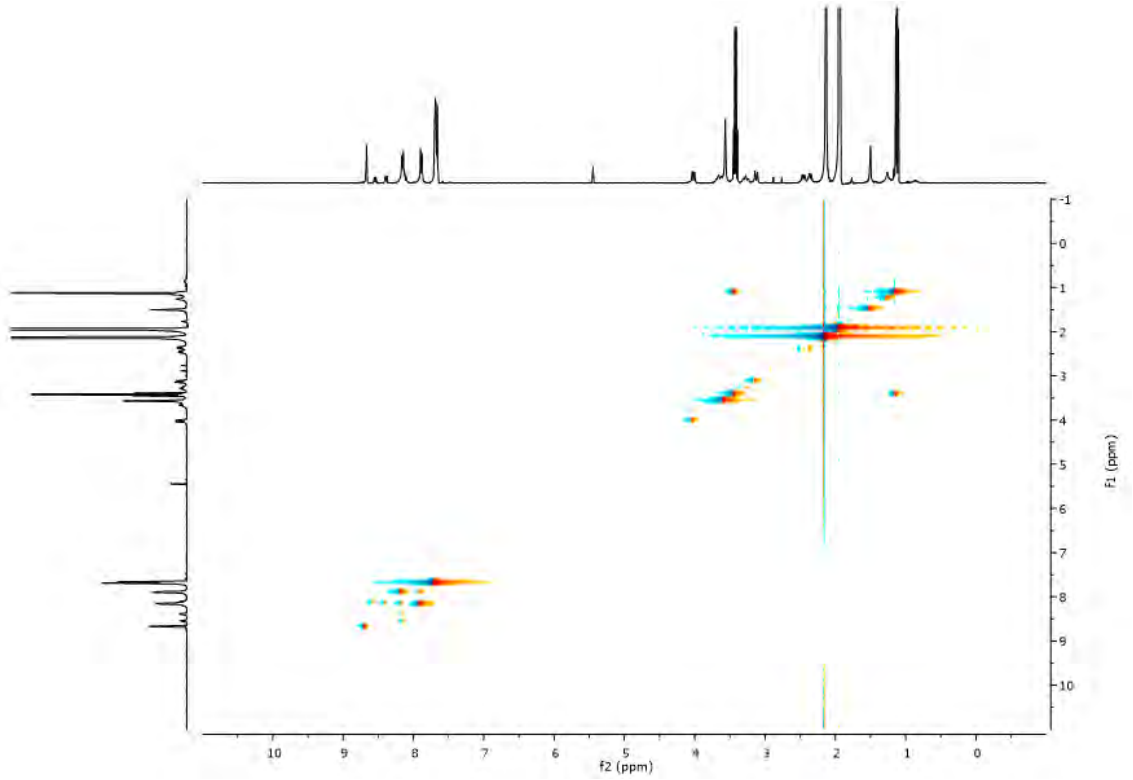

Supplementary Figure 49. NOESY of **6**·$(BArF)_8$ nanocapsule. Experiment performed in CD_3CN at 298 K (400 MHz).

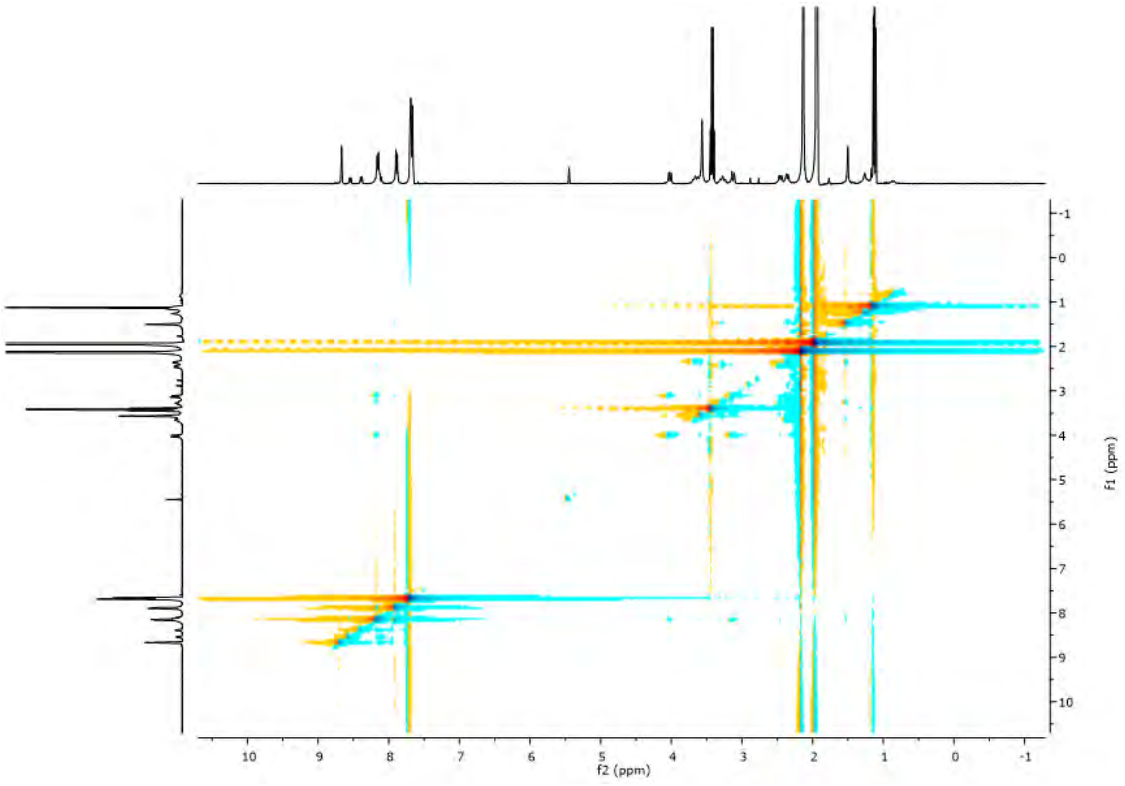

Supplementary Figure 50. HRMS spectrum of **6**·$(BArF)_8$ nanocapsule. Sample solved in acetonitrile and registered with a Bruker MicrOTOF-Q-II mass spectrometer.

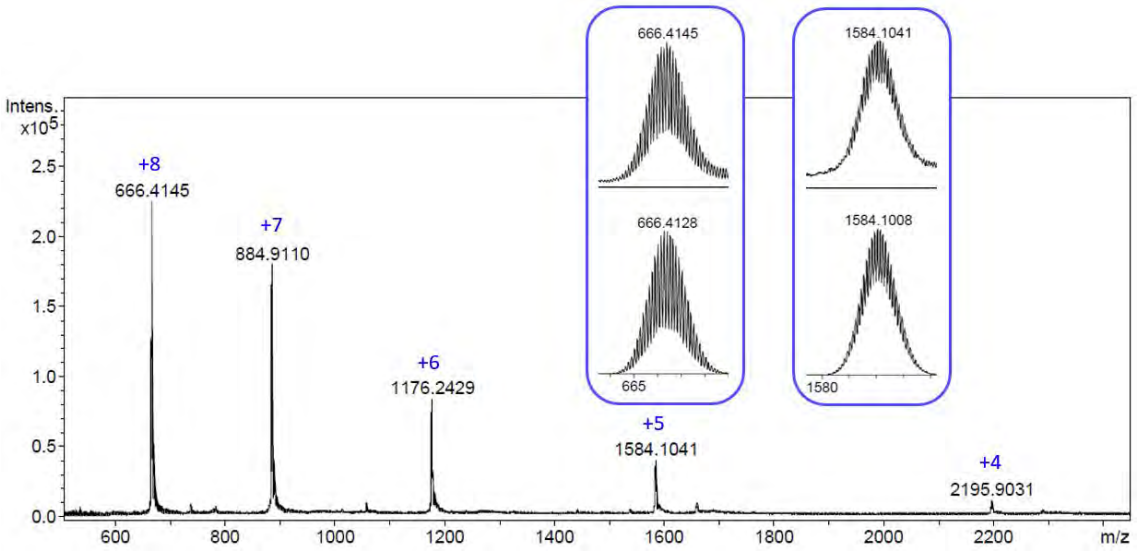

Supplementary Figure 51. DOSY NMR spectrum of **6**·$(BArF)_8$ nanocapsule (in CD_3CN).

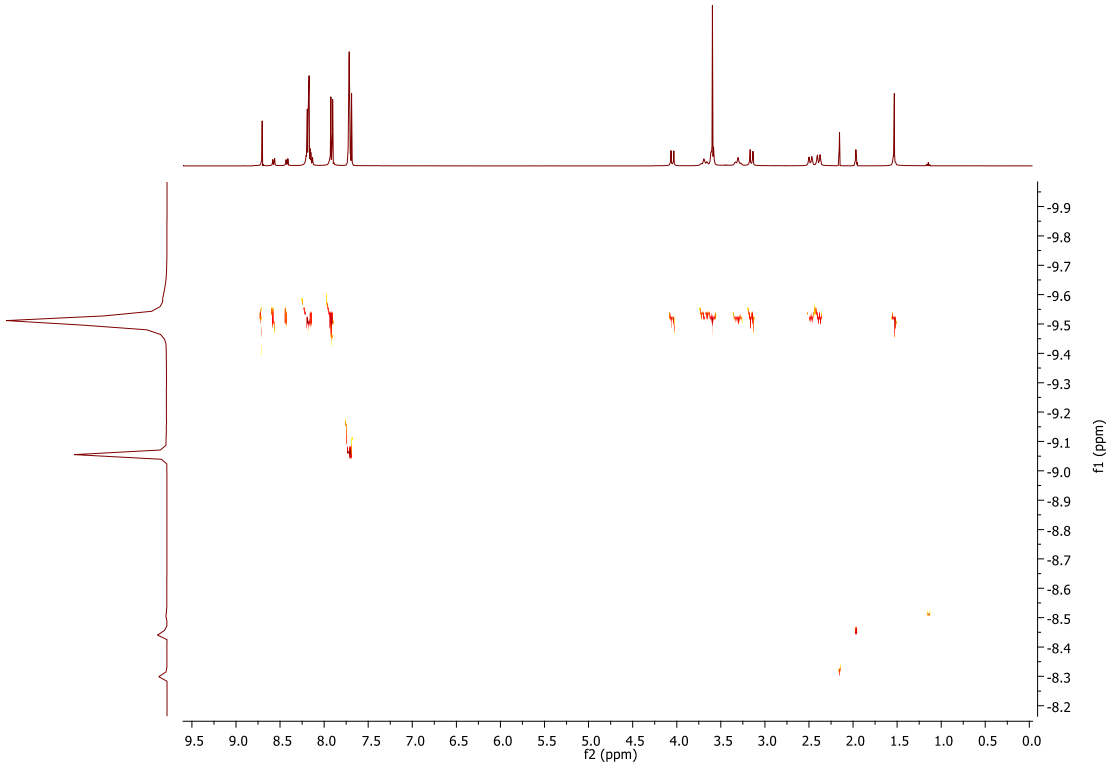

2.8.Synthesis and characterization of tetragonal prismatic nanocapsule 7·(BArF)$_8$

Supplementary Figure 52. Synthesis of **7**·(BArF)$_8$ nanocapsule.

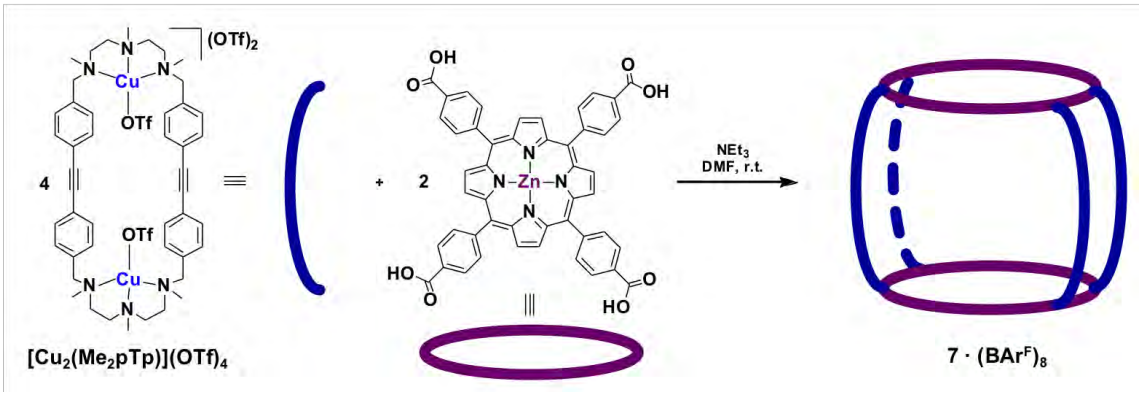

Supplementary Figure 53. HRMS spectrum of **7**·(BArF)$_8$ nanocapsule. Sample solved in acetonitrile and registered with a Bruker MicroTOF-Q-II mass spectrometer.

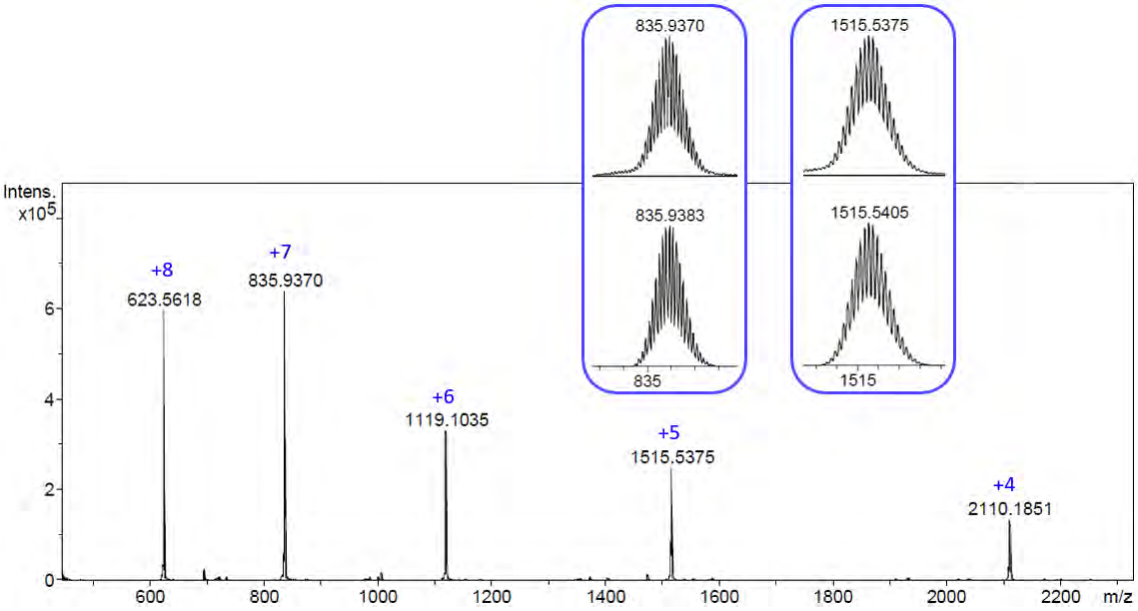

2.9.Characterization of C_{60}⊂[10]CPP⊂6·$(BArF)_8$

Supplementary Figure 54. HRMS spectrum of **C_{60}⊂[10]CPP⊂6**·$(BArF)_8$ nanocapsule. Sample solved in acetonitrile and registered with a Bruker MicroTOF-Q-II mass spectrometer.

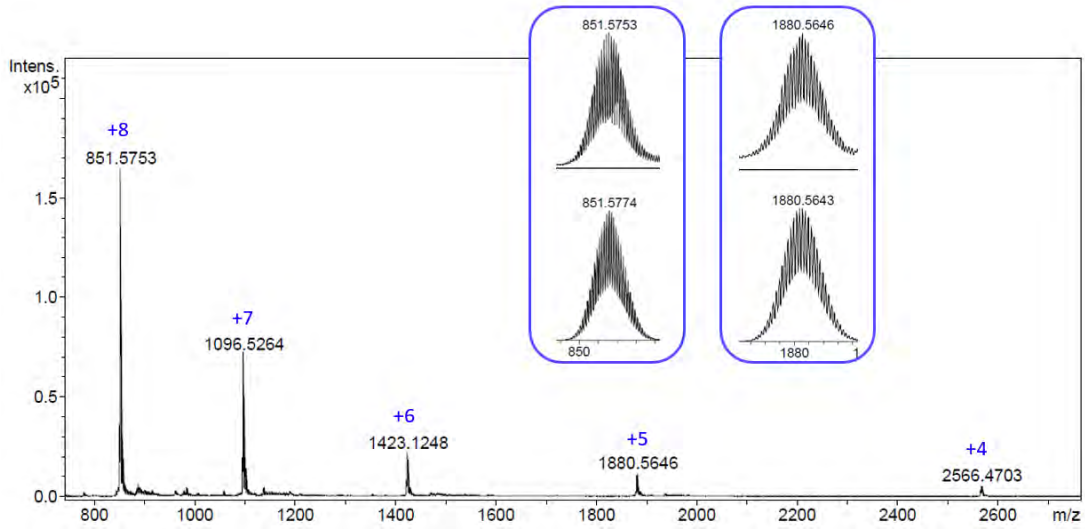

Supplementary Figure 55. ^{1}H-NMR of **C_{60}⊂[10]CPP⊂6**·$(BArF)_8$ nanocapsule. Experiment performed in CD_3CN at 298 K (400 MHz). (γ) dcm, (#) H_2O, (ϕ) CH_3CN.

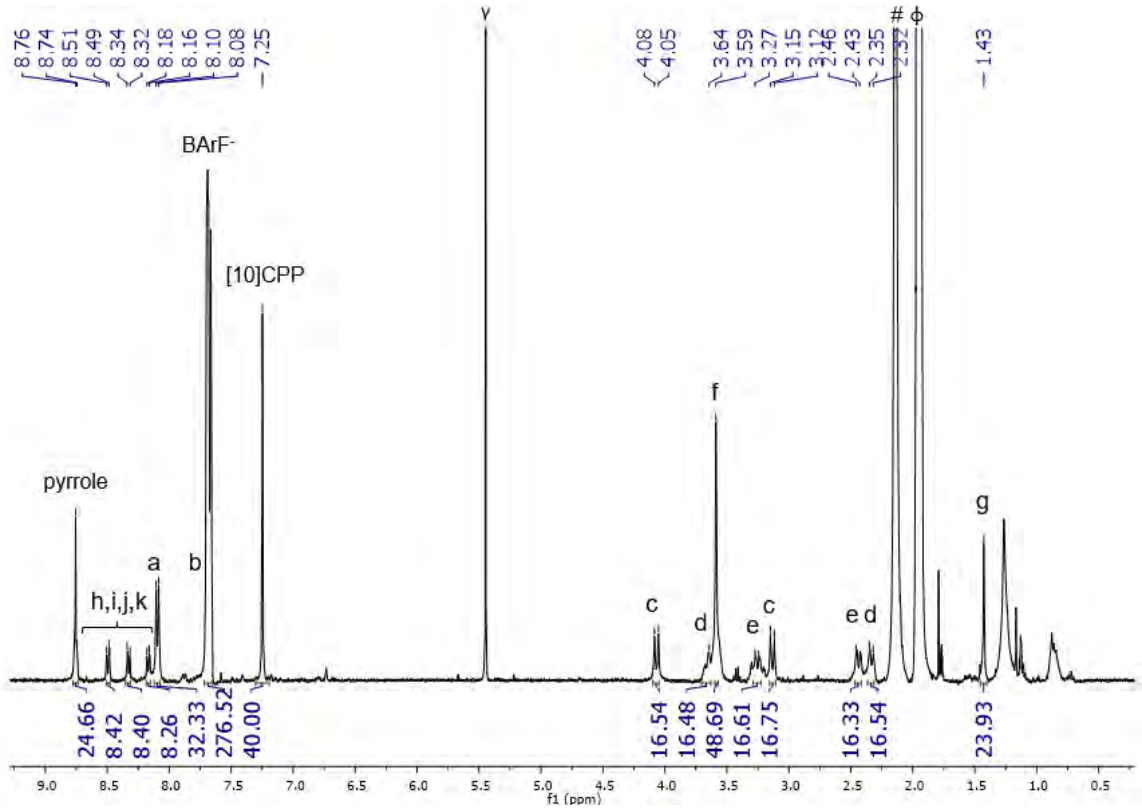

Supplementary Figure 56. ^{13}C-NMR spectrum of **C_{60}⊂[10]CPP⊂6**·$(BArF)_8$. Experiment was performed in CD_3CN at 298 K (151 MHz). Peaks between 10 and 40 ppm correspond to grease.

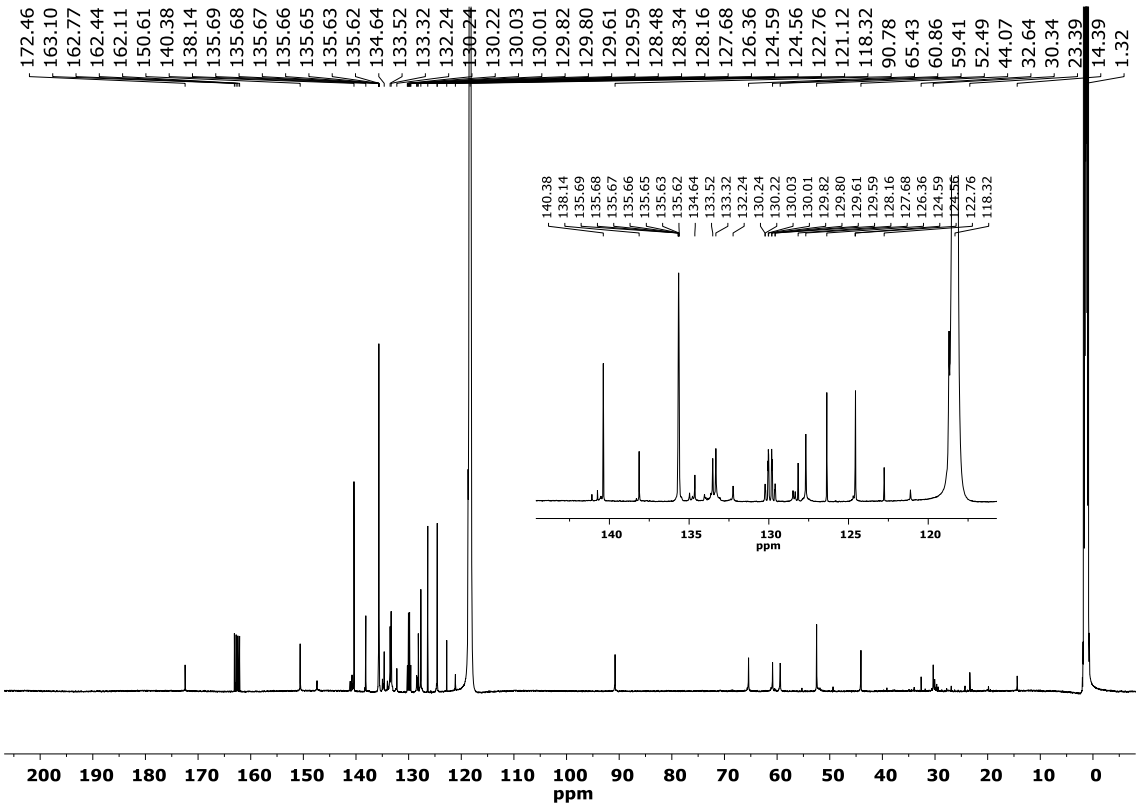

Supplementary Figure 57. COSY spectrum of **C_{60}⊂[10]CPP⊂6**·$(BArF)_8$. Experiment was performed in CD_3CN at 298 K (601 MHz).

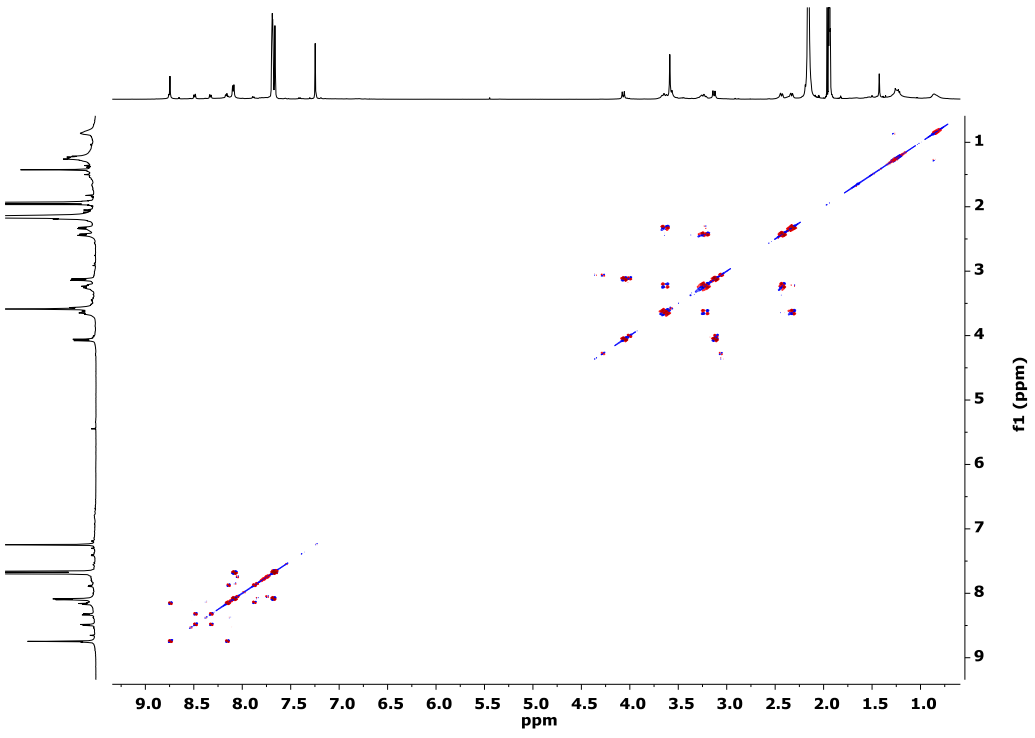

Supplementary Figure 58. HSQC spectrum of **C_{60}⊂[10]CPP⊂6**·$(BArF)_8$. Experiment was performed in CD_3CN at 298 K (601 MHz).

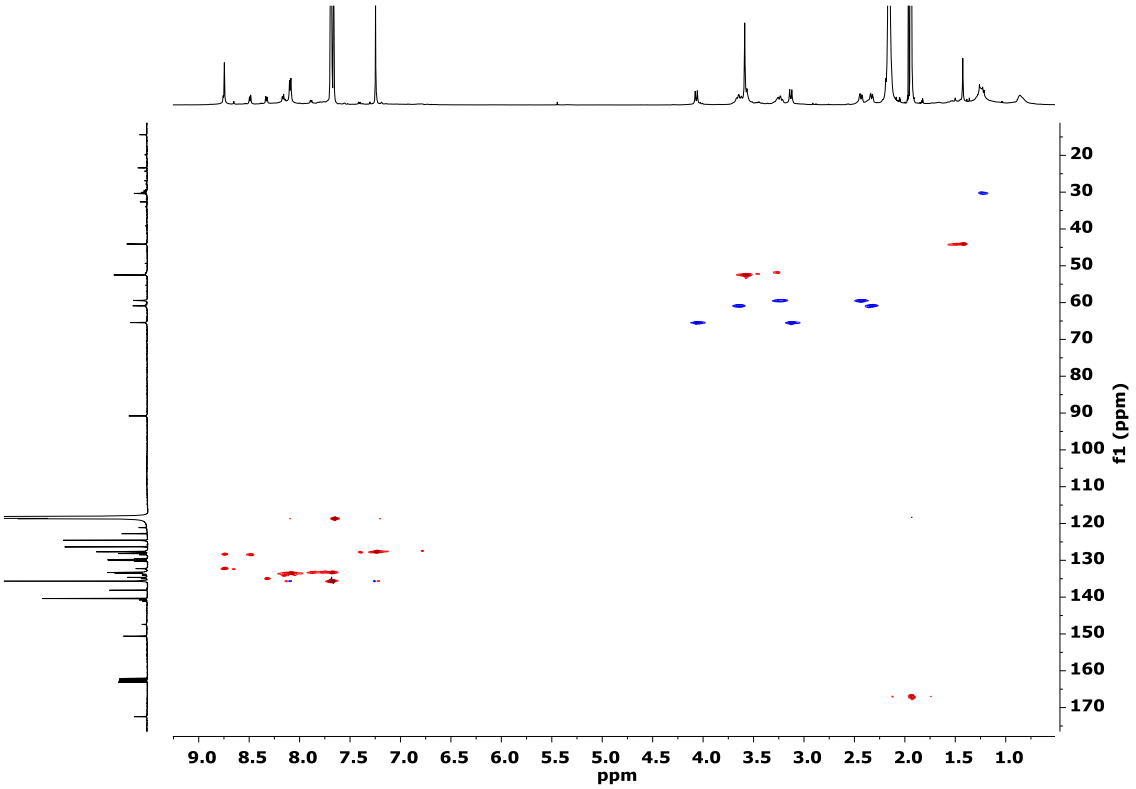

Supplementary Figure 59. HMBC spectrum of **C_{60}⊂[10]CPP⊂6**·$(BArF)_8$. Experiment was performed in CD_3CN at 298 K (601 MHz).

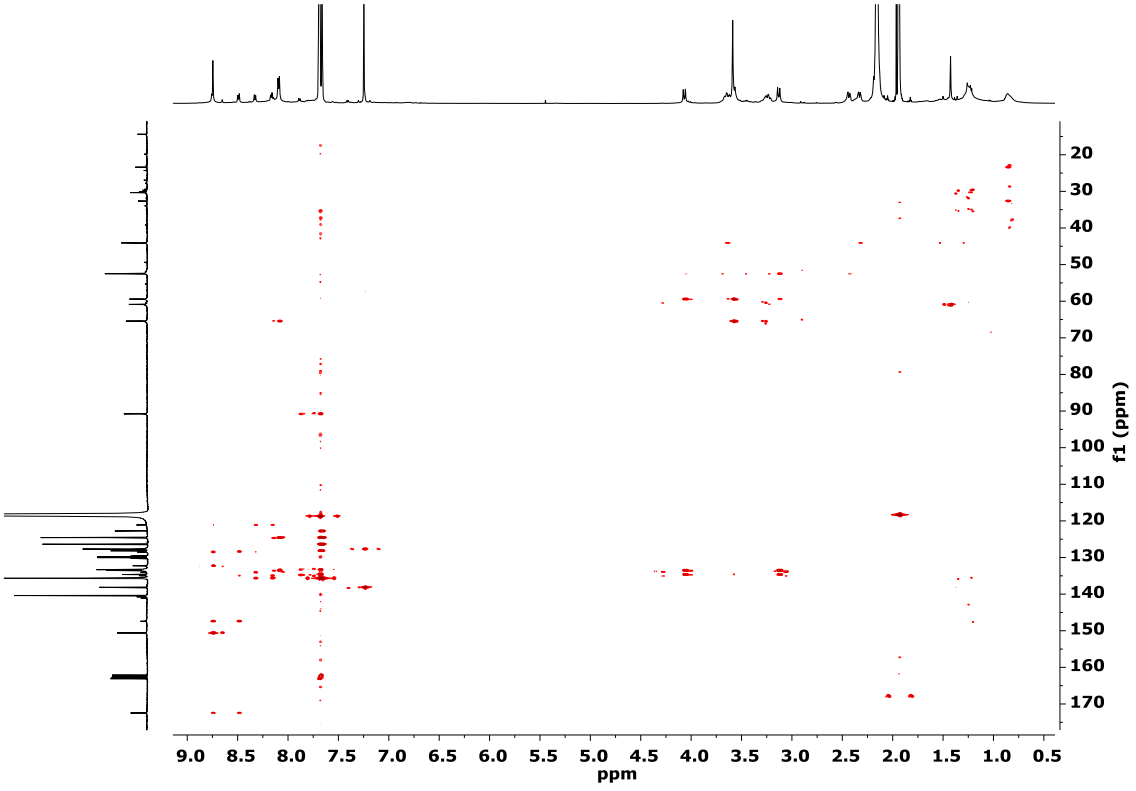

Supplementary Figure 60. Magnification of the aromatic region of the HMBC spectrum of **C_{60}⊂[10]CPP⊂6**·$(BArF)_8$ from Supplementary Figure 59.

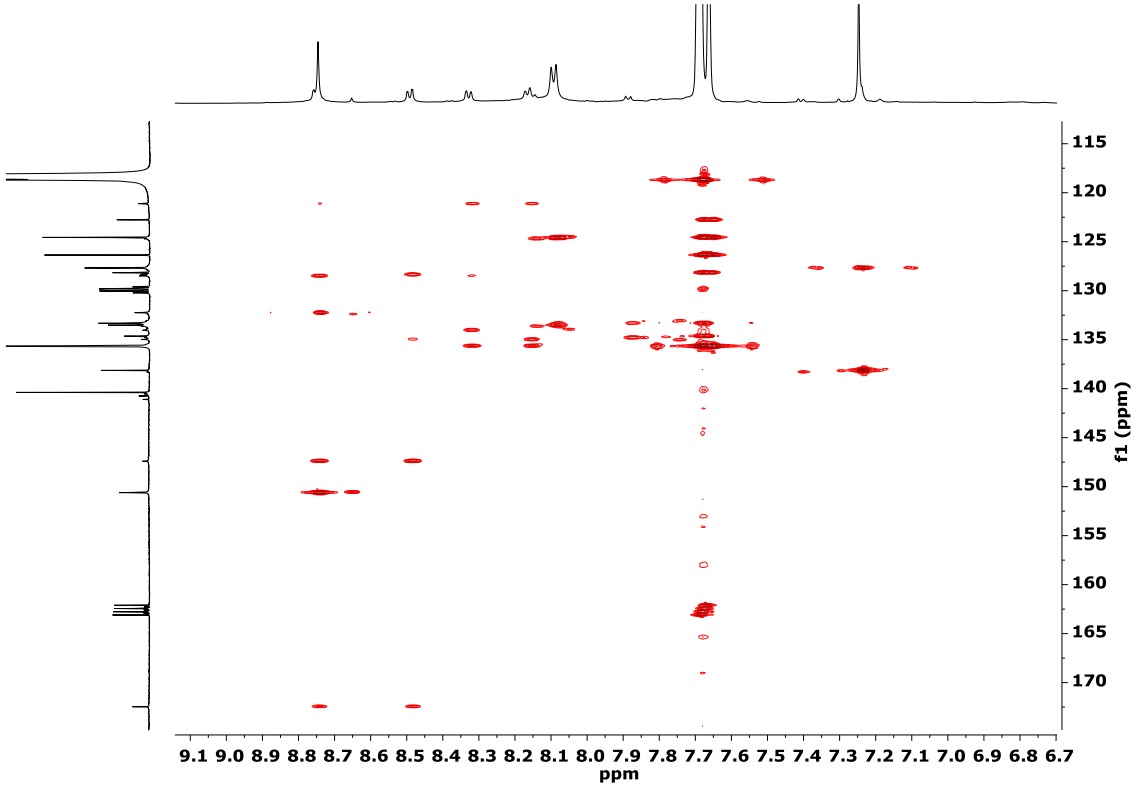

Supplementary Figure 61. NOESY of **C_{60}⊂[10]CPP⊂6**·$(BArF)_8$ nanocapsule. Experiment performed in CD_3CN at 298 K (400 MHz).

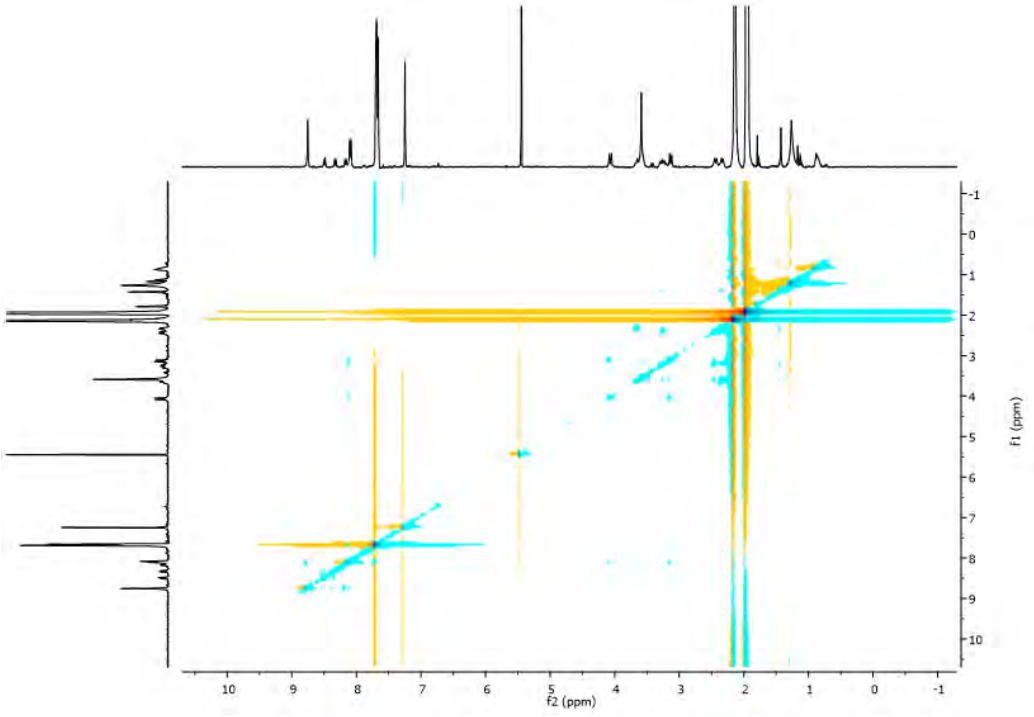

Supplementary Figure 62. DOSY NMR spectrum of **C_{60}⊂[10]CPP⊂6**·$(BArF)_8$ nanocapsule (in CD_3CN).

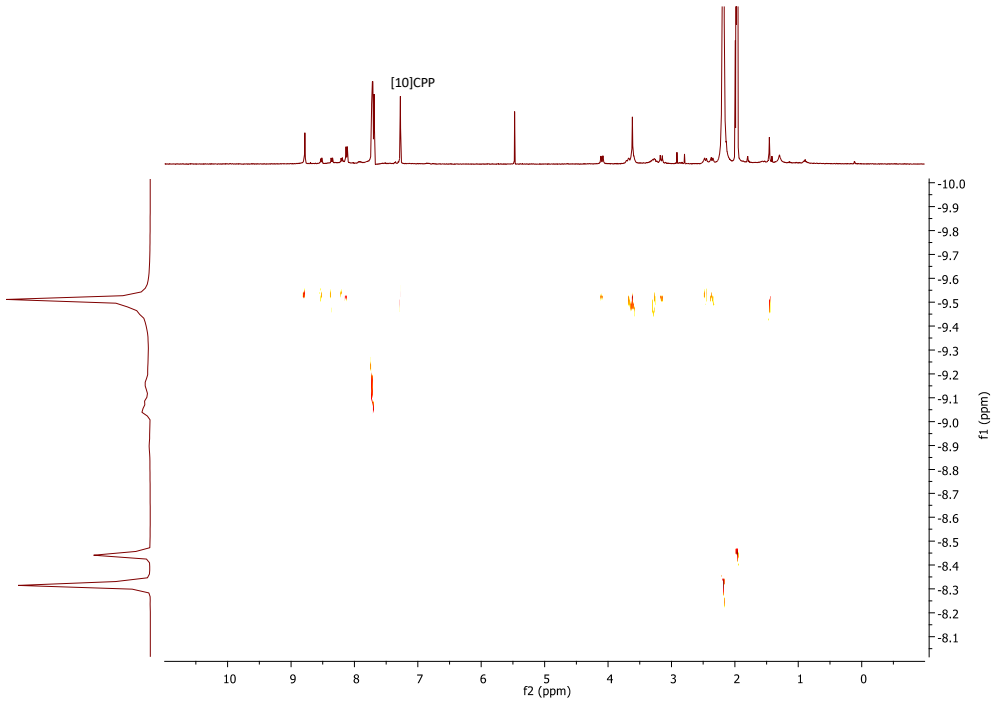

2.10. Characterization of C_{60}⊂[10]CPP⊂7·$(BArF)_8$

Supplementary Figure 63. HRMS spectrum of **C_{60}⊂[10]CPP⊂7**·$(BArF)_8$ nanocapsule. Sample solved in acetonitrile and registered with a Bruker MicroTOF-Q-II mass spectrometer.

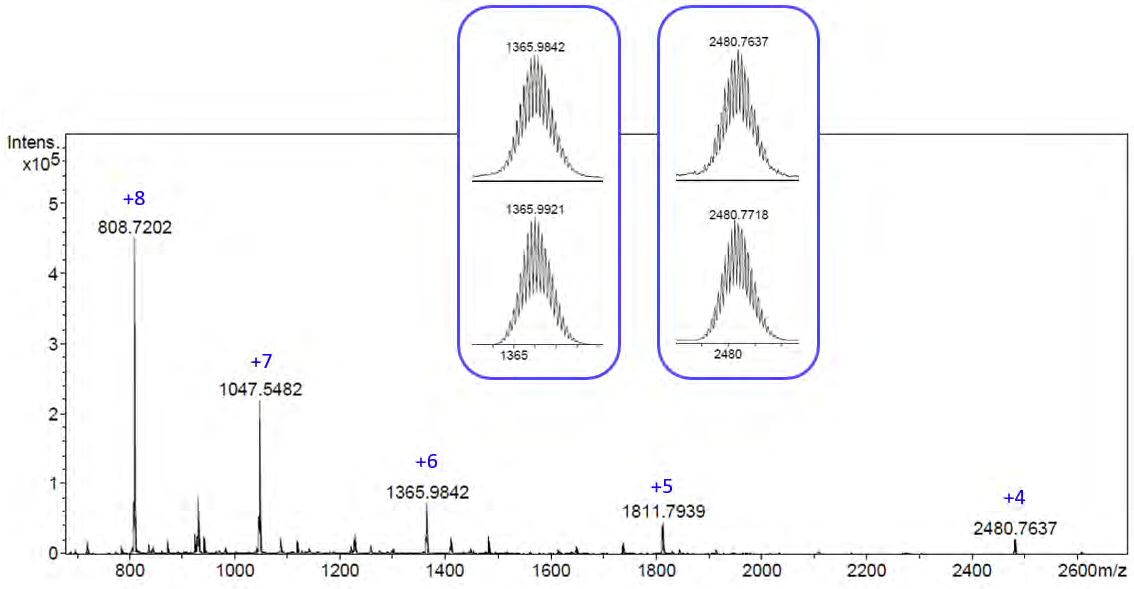

2.11. Exchange reaction of 4·(BArF)$_8$ with C$_{60}$⊂[10]CPP

Supplementary Figure 64. HRMS monitoring for the encapsulation reaction of 2.5 equiv. of **C$_{60}$⊂[10]CPP** with the smaller nanocapsule **4**·(BArF)$_8$,[9] showing the sole encapsulation of C$_{60}$ and leaving [10]CPP in solution.

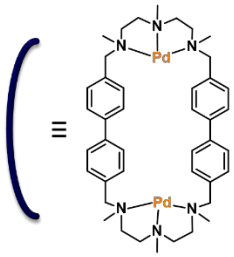

≡

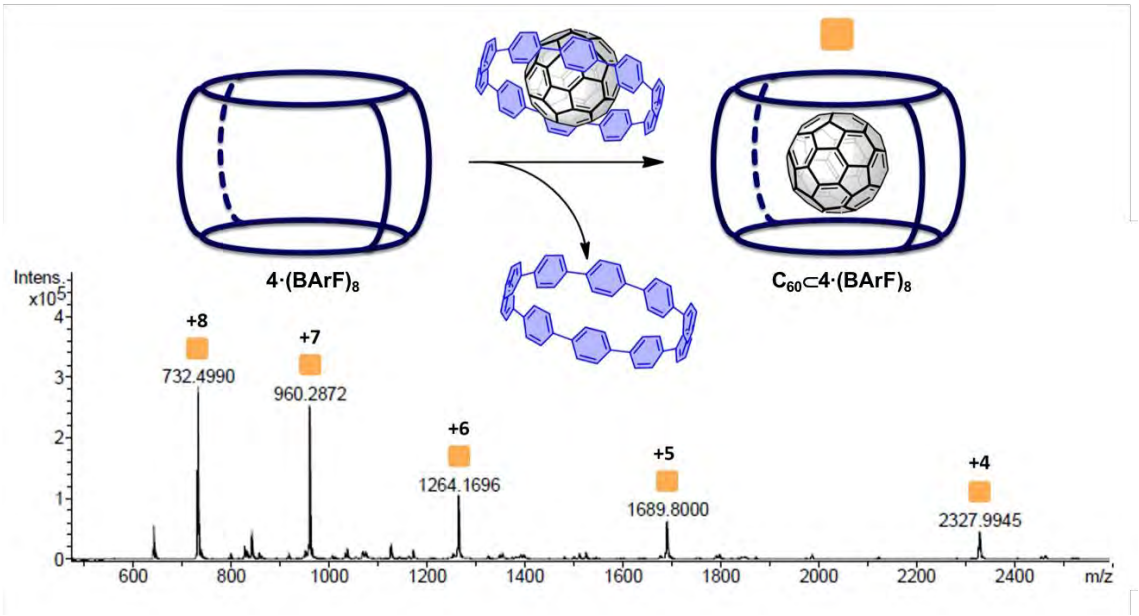

2.12. Characterization of the fullerene bis-adducts from Bingel reaction with Matryoshka system

Supplementary Figure 65. Detailed work-up flow for the quantification of fullerene bis-adducts from Bingel reaction with Matryoshka system (depicted for ***trans*-3-(1-C_{60})**).

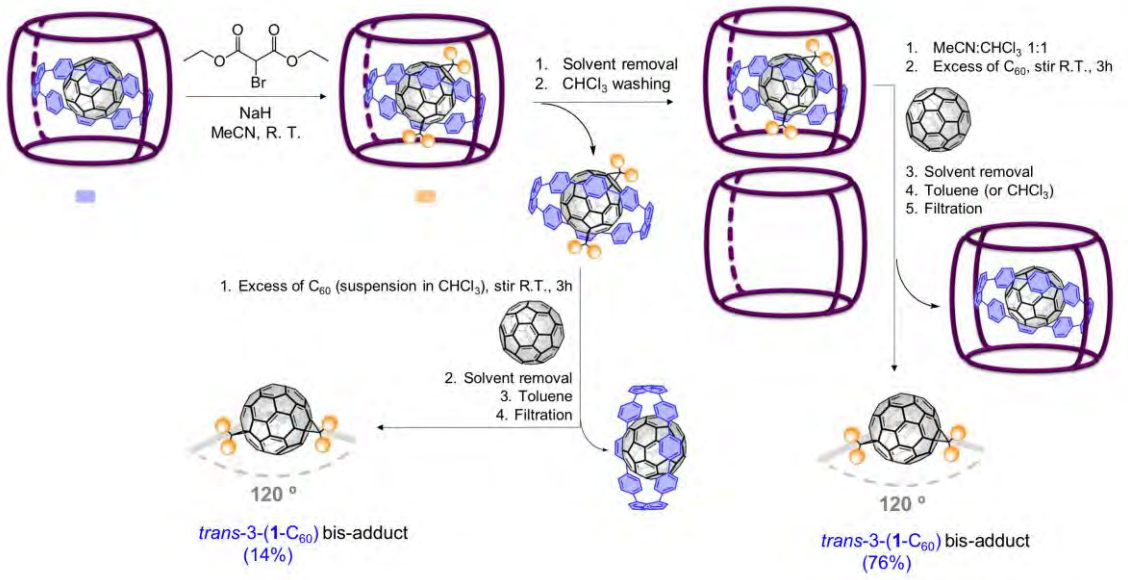

Supplementary Figure 66. a) Exposure of **C_{60}⊂[10]CPP⊂6**·$(BArF)_8$ to Bingel cyclopropanation conditions with diethyl bromomalonate leads to the chemo- and regioselective formation of the ***trans*-3** bis-adduct; exchange with pristine C_{60} liberates the product. b) HRMS monitoring of the bis-adduct formation upon addition of 5 equiv. of bromomalonate (two sequential additions of 2.5 equiv.). c) HPLC analysis of the extracted product (λ = 320 nm; * C_{60}; $ non-fullerene impurities). d) UV-vis of the product, diagnostic of a ***trans*-3**-(**1**-C_{60}) Bingel bis-adduct.

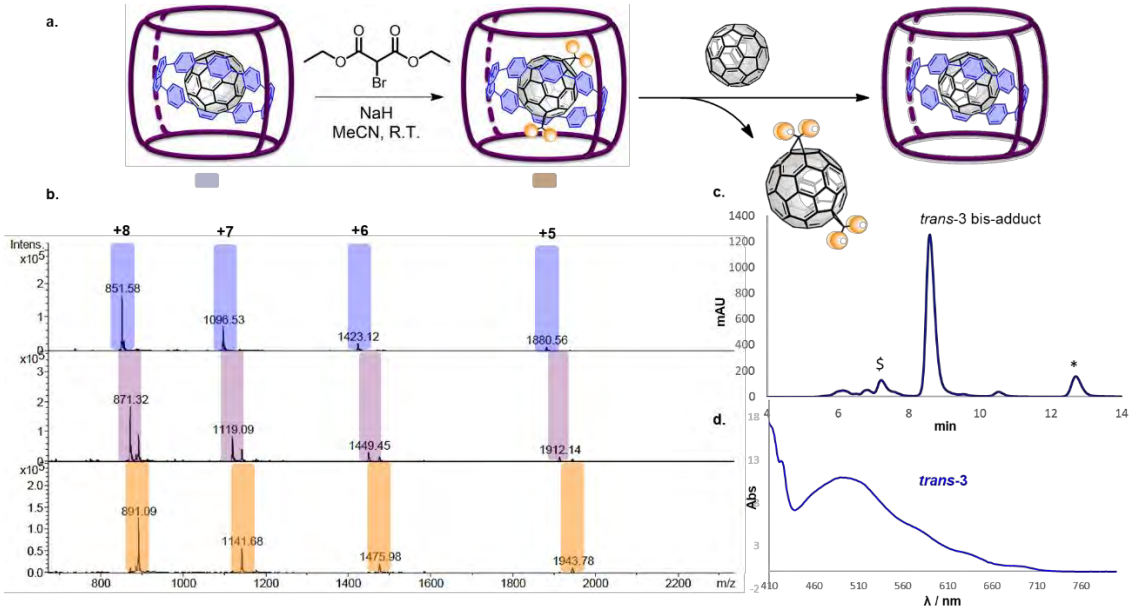

Supplementary Figure 67. HRMS spectrum of ***trans*-3**-(**1**-C_{60})⊂**[10]CPP⊂6**·$(BArF)_8$. Sample solved in acetonitrile and registered with a Bruker MicroTOF-Q-II mass spectrometer.

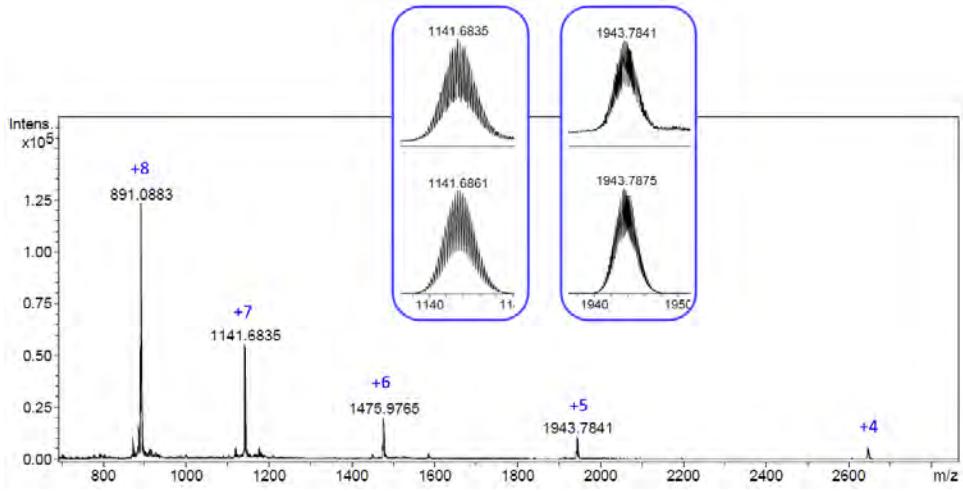

Supplementary Figure 68. a) Exposure of **C_{60}⊂[10]CPP⊂6**·$(BArF)_8$ to Bingel cyclopropanation conditions with diisopropyl bromomalonate leads to the chemo- and regioselective formation of the ***trans*-3** bis-adduct; exchange with pristine C_{60} liberates the product. b) HRMS monitoring of the bis-adduct formation upon addition of 5 equiv. of bromomalonate (two sequential additions of 2.5 equiv.). c) HPLC analysis of the extracted product (λ = 320 nm; * C_{60}; $ non-fullerene impurities). d) UV-vis of the product, diagnostic of a ***trans*-3**-(**2**-C_{60}) Bingel bis-adduct.

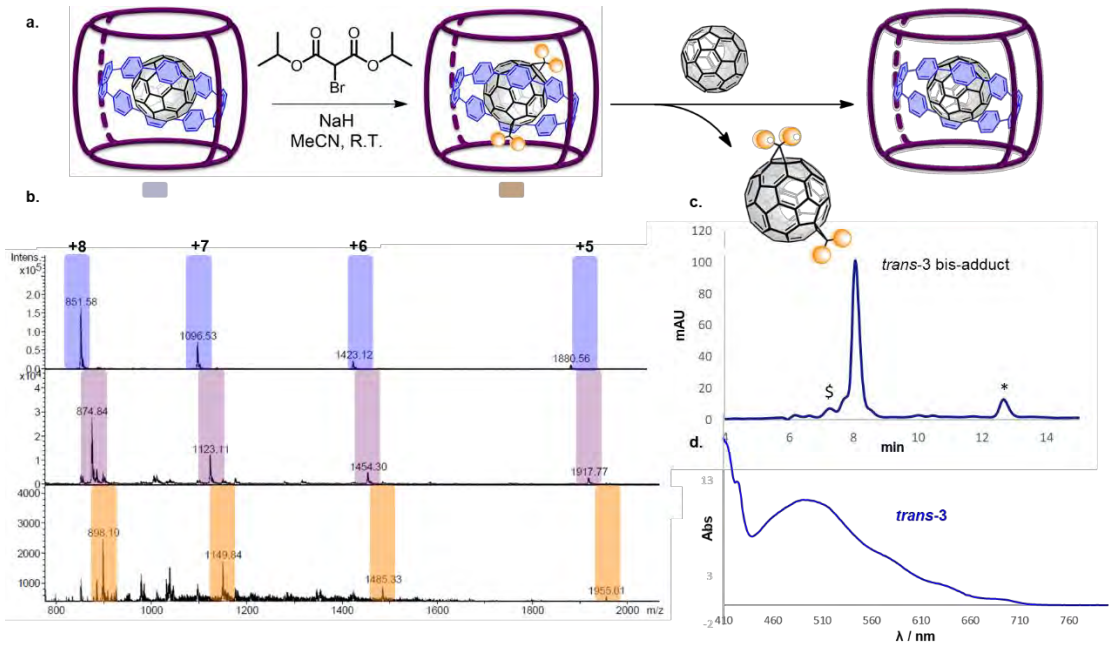

Supplementary Figure 69. a) Exposure of **C_{60}⊂[10]CPP⊂6**·$(BArF)_8$ to Bingel cyclopropanation conditions with dibenzyl bromomalonate leads to the chemo- and regioselective formation of the ***trans*-3** bis-adduct; exchange with pristine C_{60} liberates the product. b) HRMS monitoring of the bis-adduct formation upon addition of 5 equiv. of bromomalonate (two sequential additions of 2.5 equiv.). c) HPLC analysis of the extracted product (λ = 320 nm; * C_{60}; $ non-fullerene impurities). d) UV-vis of the product, diagnostic of a ***trans*-3**-(**3**-C_{60}) Bingel bis-adduct.

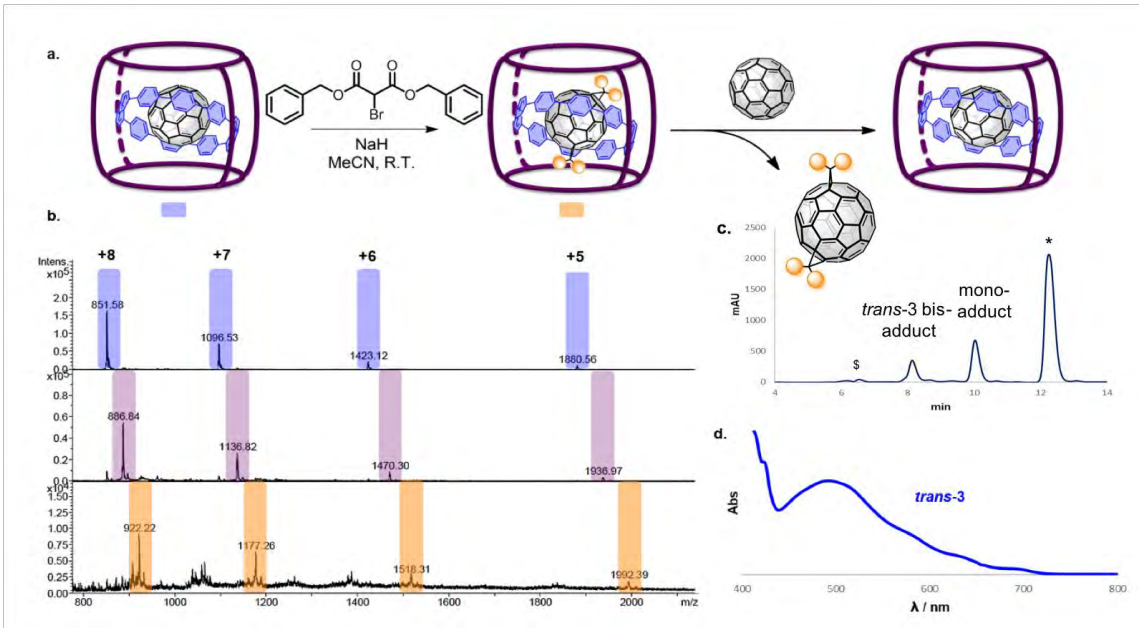

2.13. Characterization of the fullerene bis-adducts from Bingel reaction with bare C_{60}

Diethyl bromomalonate *trans*-3-(1-C_{60}) bis-adduct

Supplementary Figure 70. HPLC chromatogram showing a single peak (left) and UV-Vis absorption spectrum (right) corresponding to ***trans*-3** bis-adduct.[10] (bottom) Calibration curve for HPLC quantification.

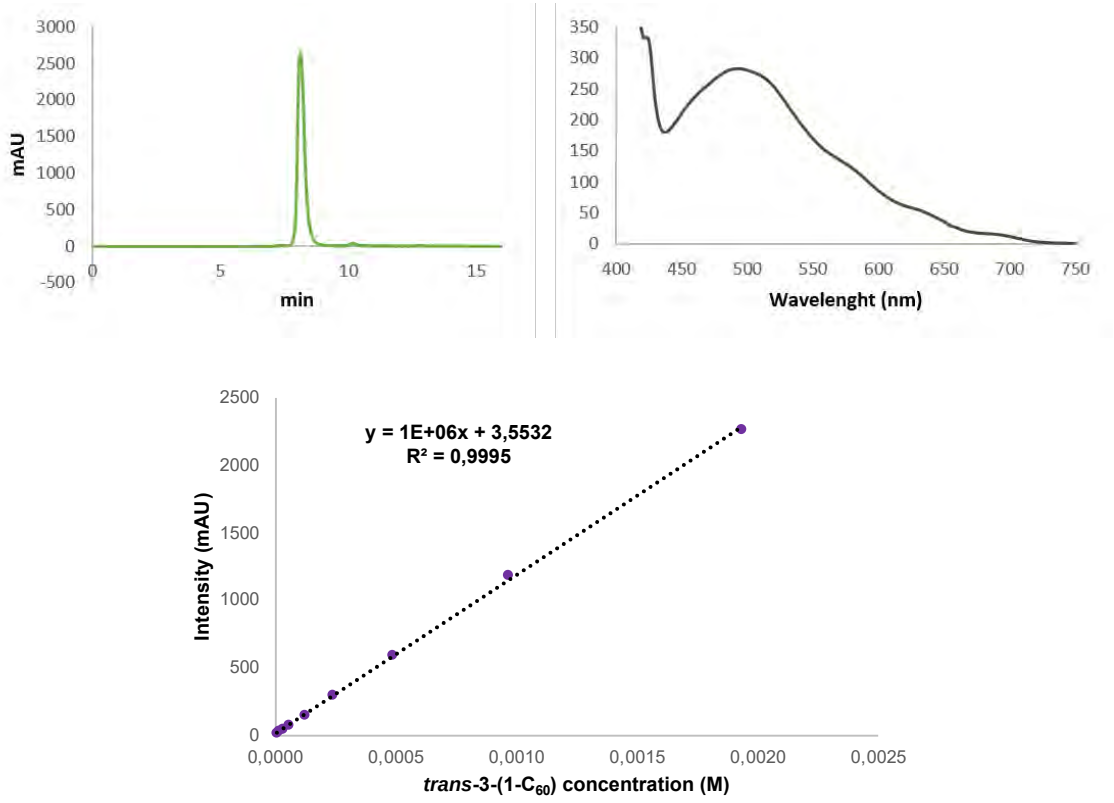

Supplementary Figure 71. ^{1}H-NMR spectrum of ***trans*-3-(1-C_{60})** (600 MHz, 298 K, $CDCl_3$). (ϕ) $CHCl_3$, (#) H_2O, (γ) TMS.

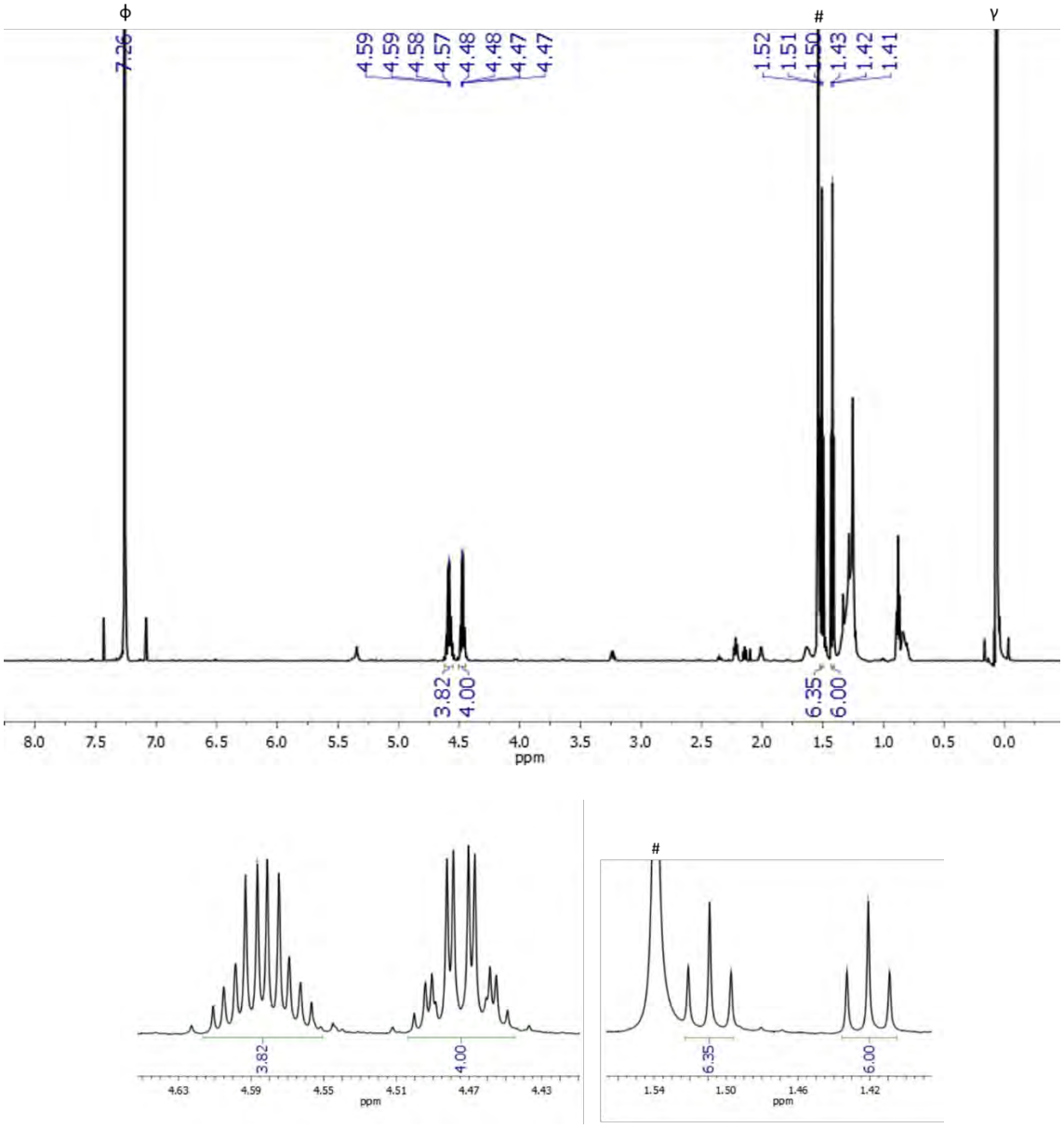

Supplementary Figure 72. ^{13}C-NMR spectrum of ***trans*-3-(1-C_{60})** (150 MHz, 298 K, $CDCl_3$).

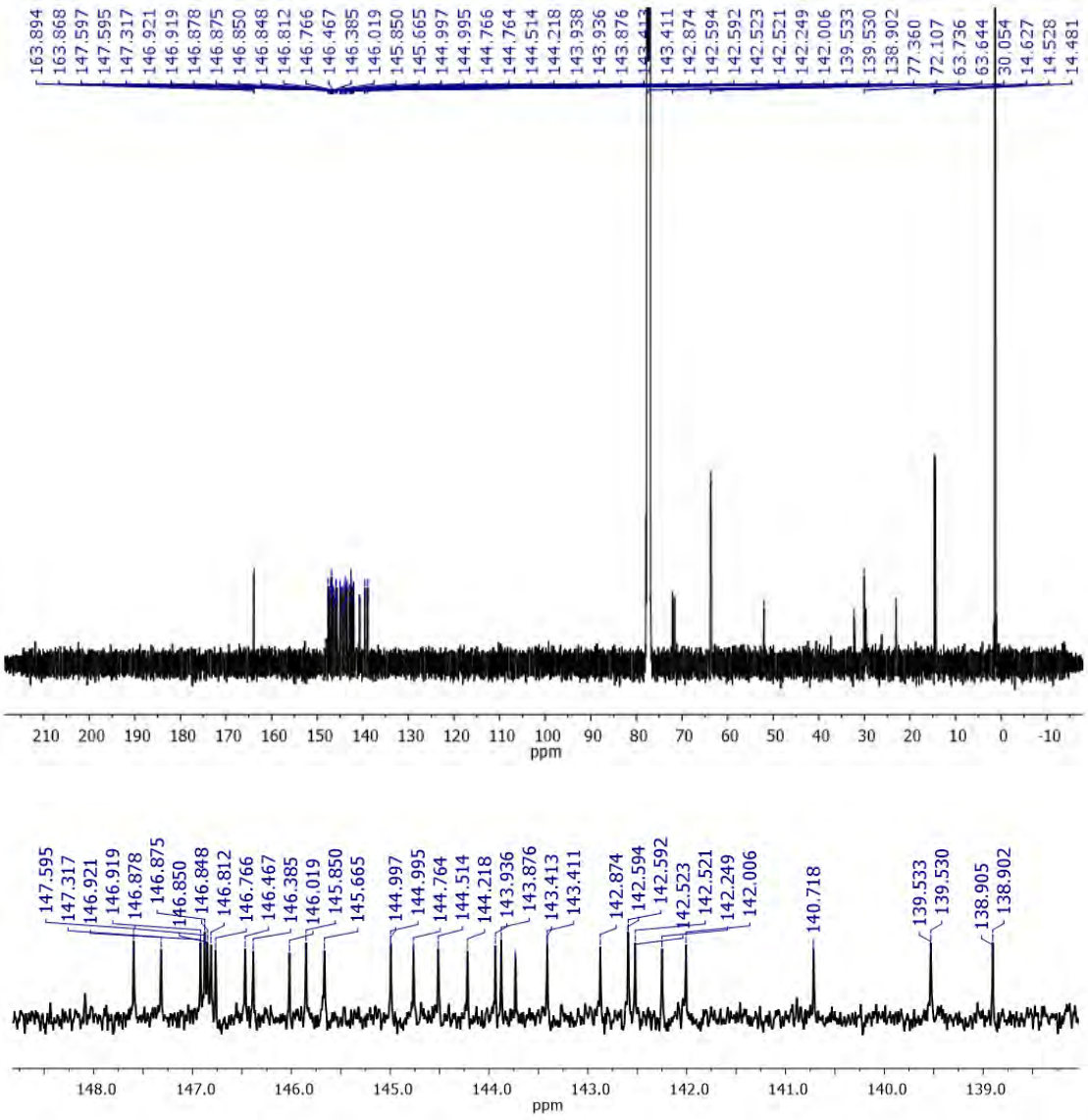

Diisopropyl bromomalonate *trans*-3-(2-C_{60}) bis-adduct

Supplementary Figure 73. HPLC chromatogram showing a single peak (left) and UV-Vis absorption spectrum (right) corresponding to ***trans*-3** bis-adduct.[10] (bottom) Calibration curve for HPLC quantification.

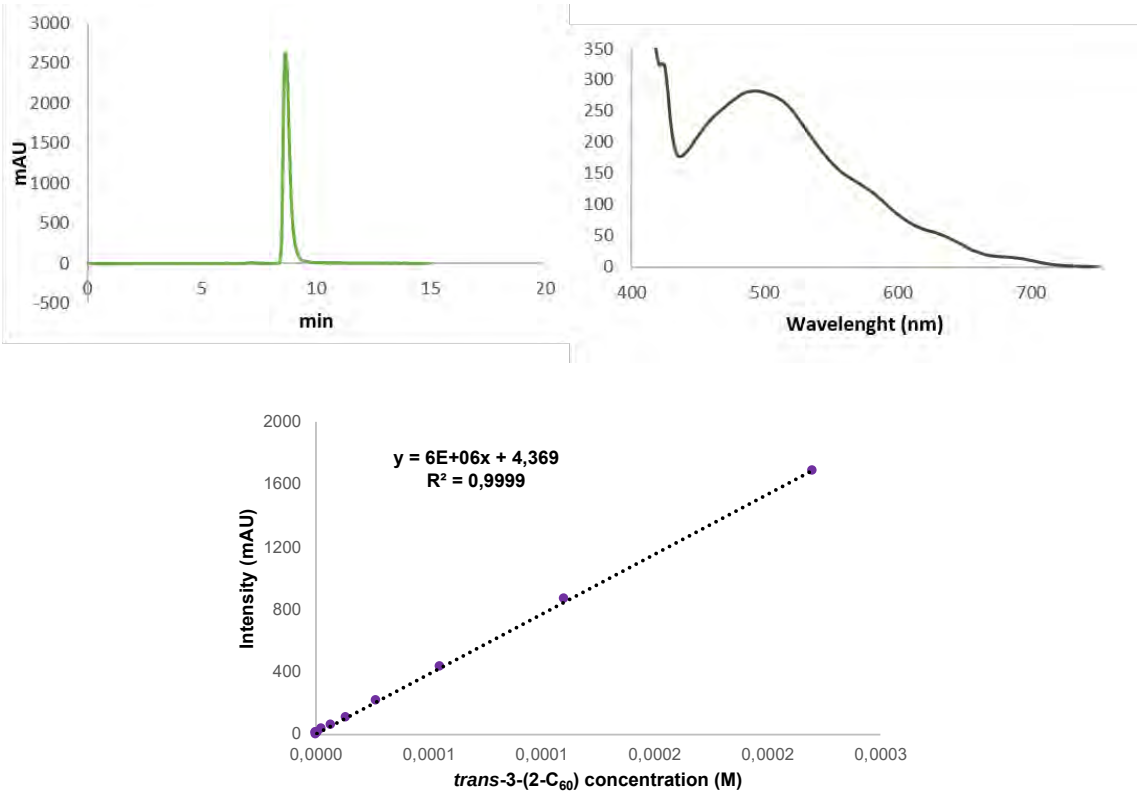

Supplementary Figure 74. ^{1}H-NMR spectrum of ***trans*-3-(2-C_{60})** (600 MHz, 298 K, $CDCl_3$). (ϕ) $CHCl_3$, (#) H_2O, (γ) TMS.

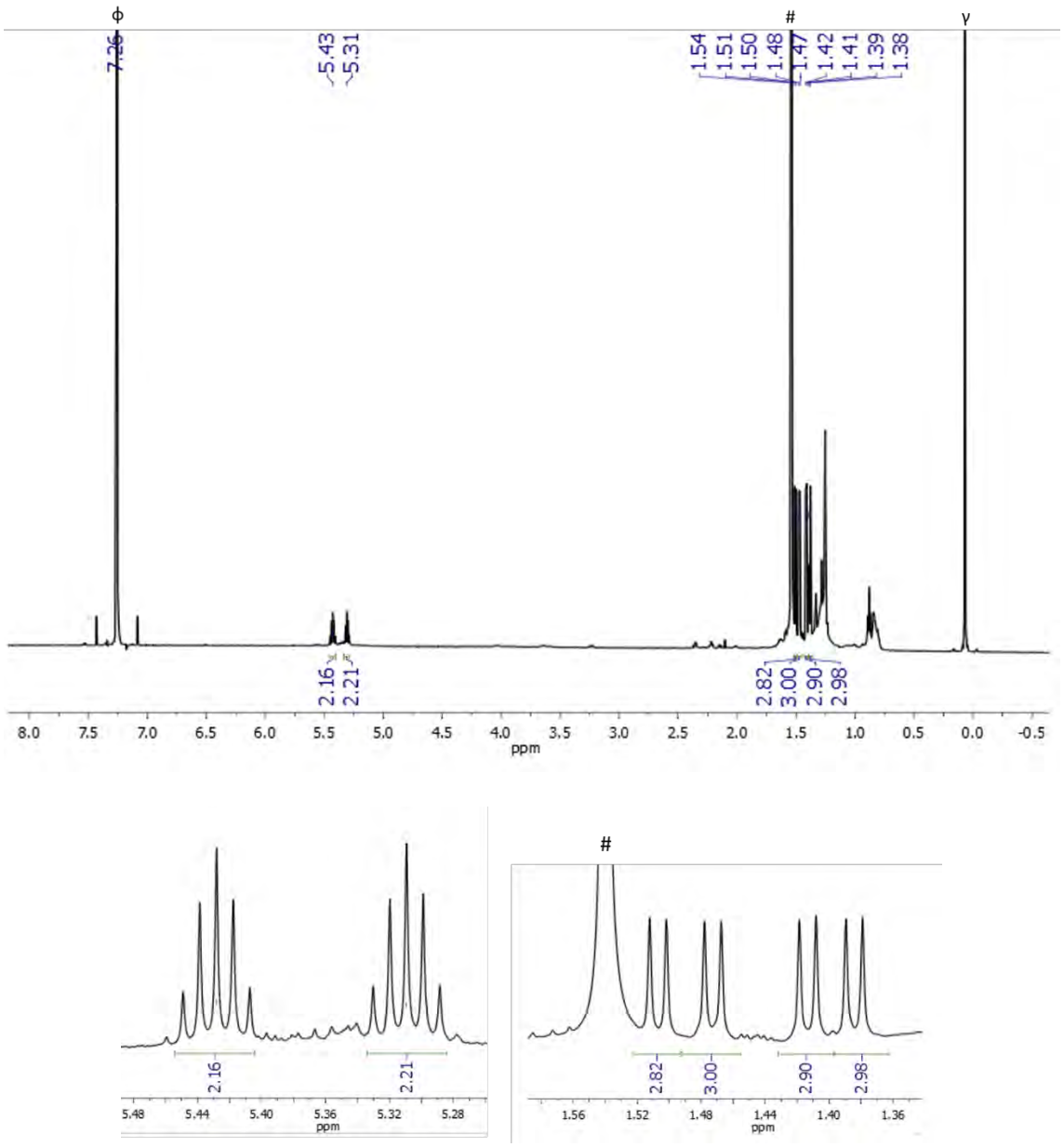

Supplementary Figure 75. ^{13}C-NMR spectrum of ***trans*-3-(2-C_{60})** (150 MHz, 298 K, $CDCl_3$).

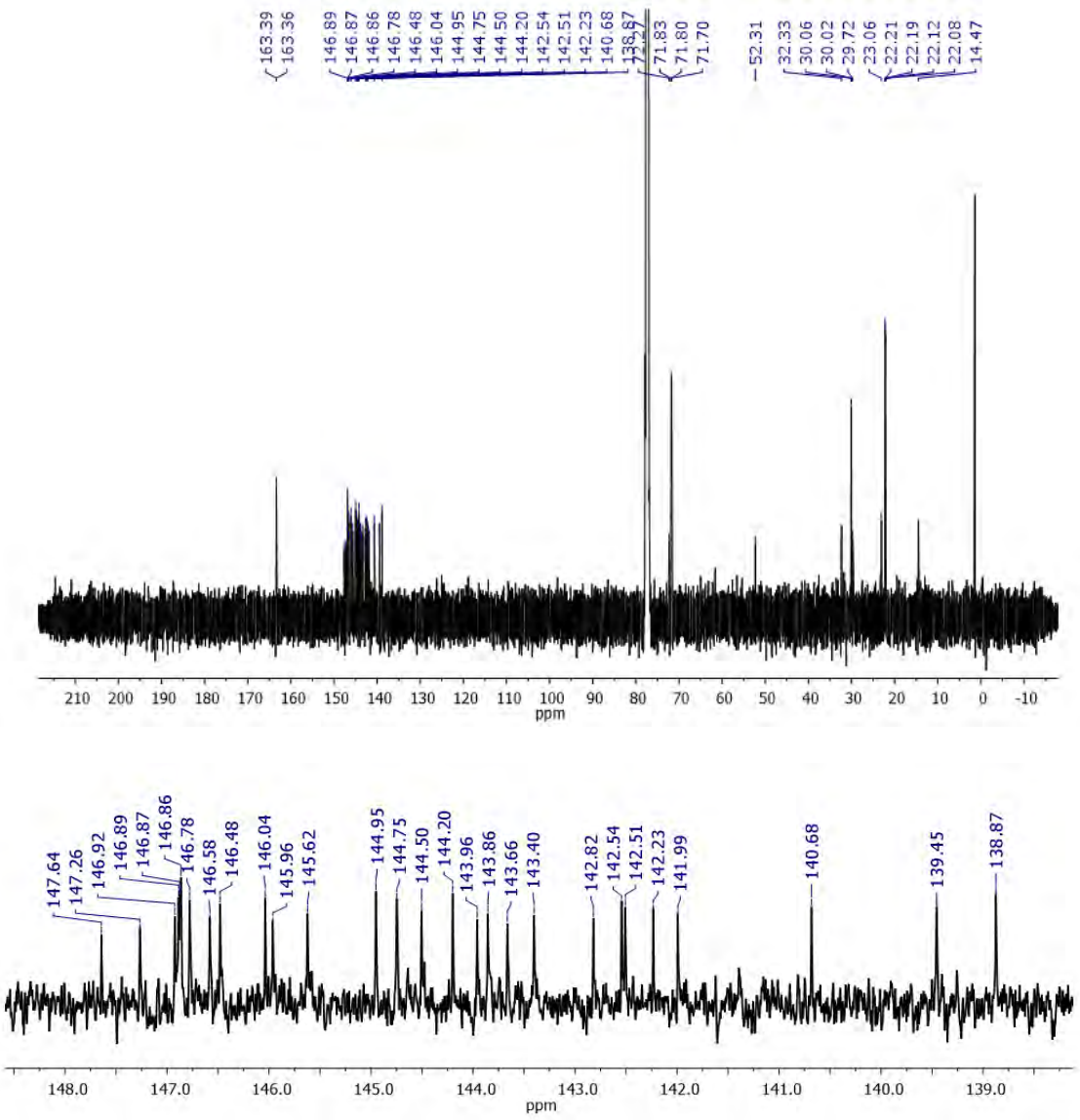

Dibenzyl bromomalonate *trans*-3-(3-C_{60}) bis-adduct

Supplementary Figure 76. (top) HPLC chromatogram showing a single peak (left) and UV-Vis absorption spectrum (right) corresponding to ***trans*-3** bis-adduct.[10] (bottom) Calibration curve for HPLC quantification.

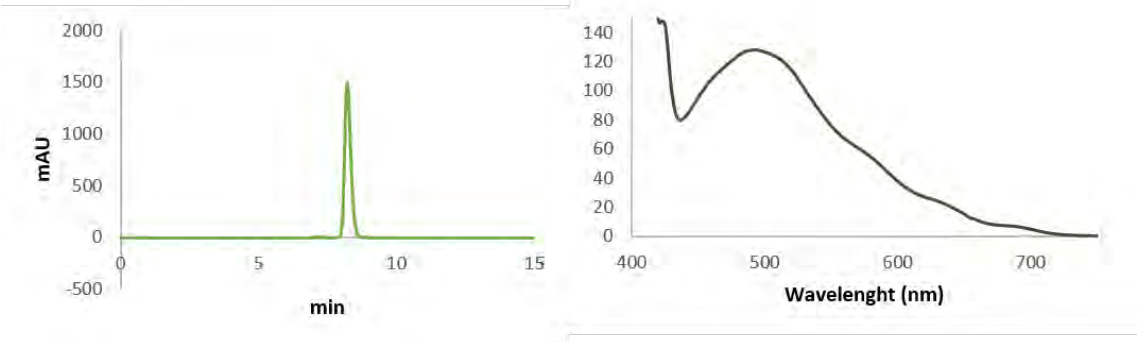

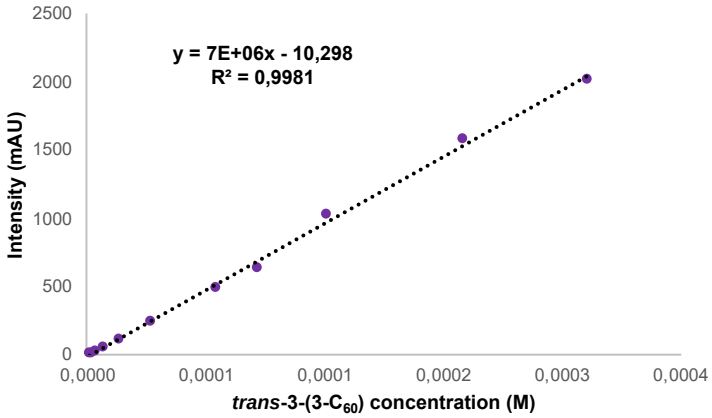

Supplementary Figure 77. ^{1}H-NMR spectrum of ***trans*-3-(3-C_{60})** (600 MHz, 298 K, $CDCl_3$). (ϕ) $CHCl_3$, (#) H_2O, (*) H grease, (γ) TMS.

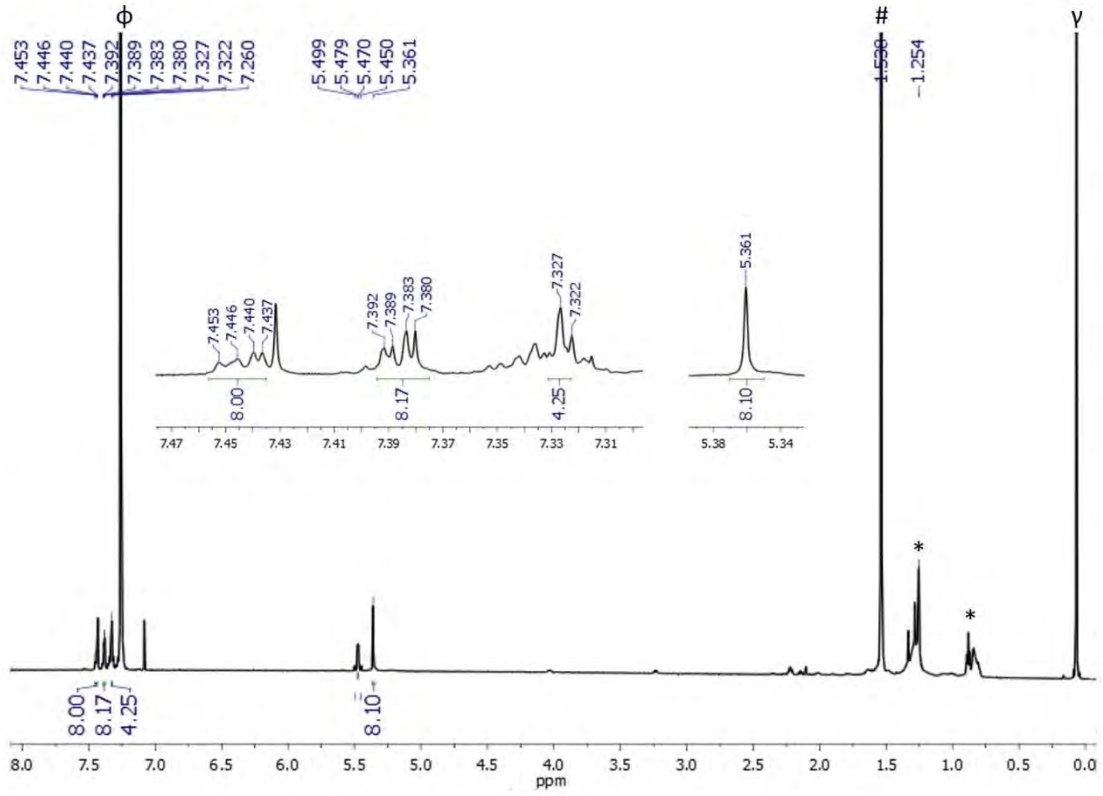

Supplementary Figure 78. ^{13}C-NMR spectrum of ***trans*-3-(3-C_{60})** (150 MHz, 298 K, $CDCl_3$).

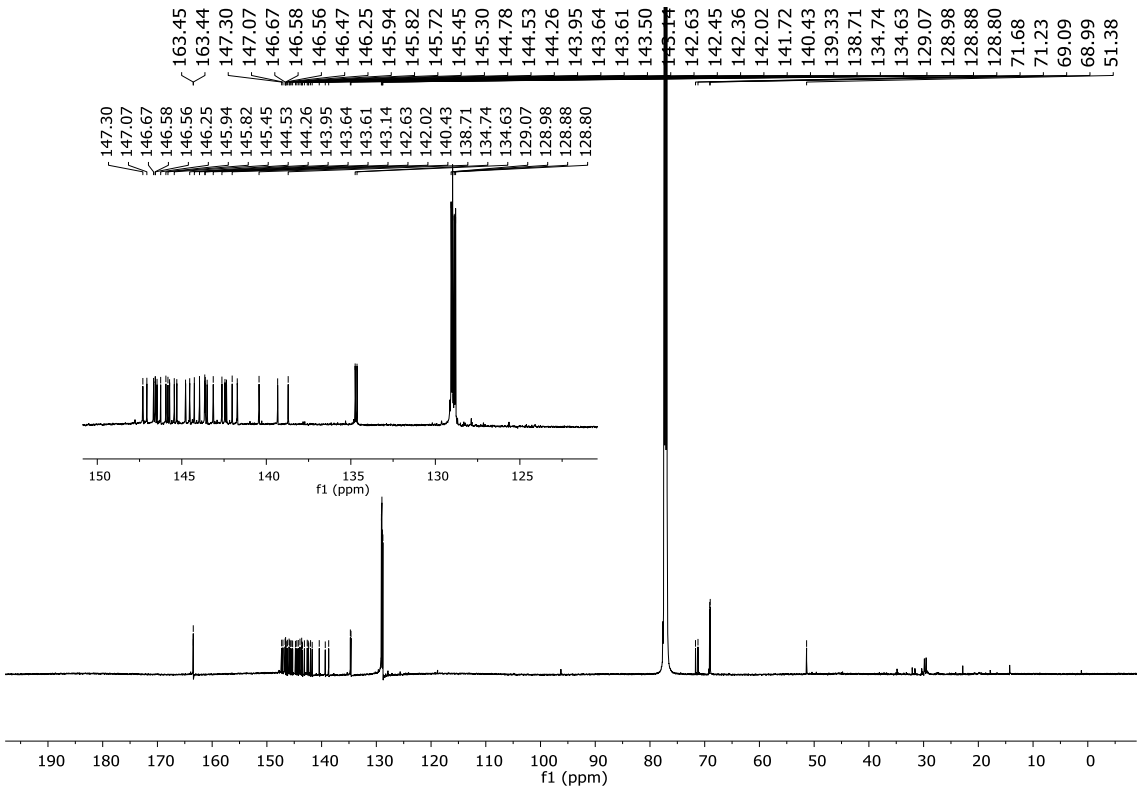

2.14. Characterization of *trans*-3-(1-C_{60})⊂[10]CPP⊂6·$(BArF)_8$

Supplementary Figure 79. ^{1}H-NMR of ***trans*-3-(1-C_{60})⊂[10]CPP**⊂(**6**·BArF)$_8$ nanocapsule. Experiment performed in CD_3CN at 298 K (400 MHz).

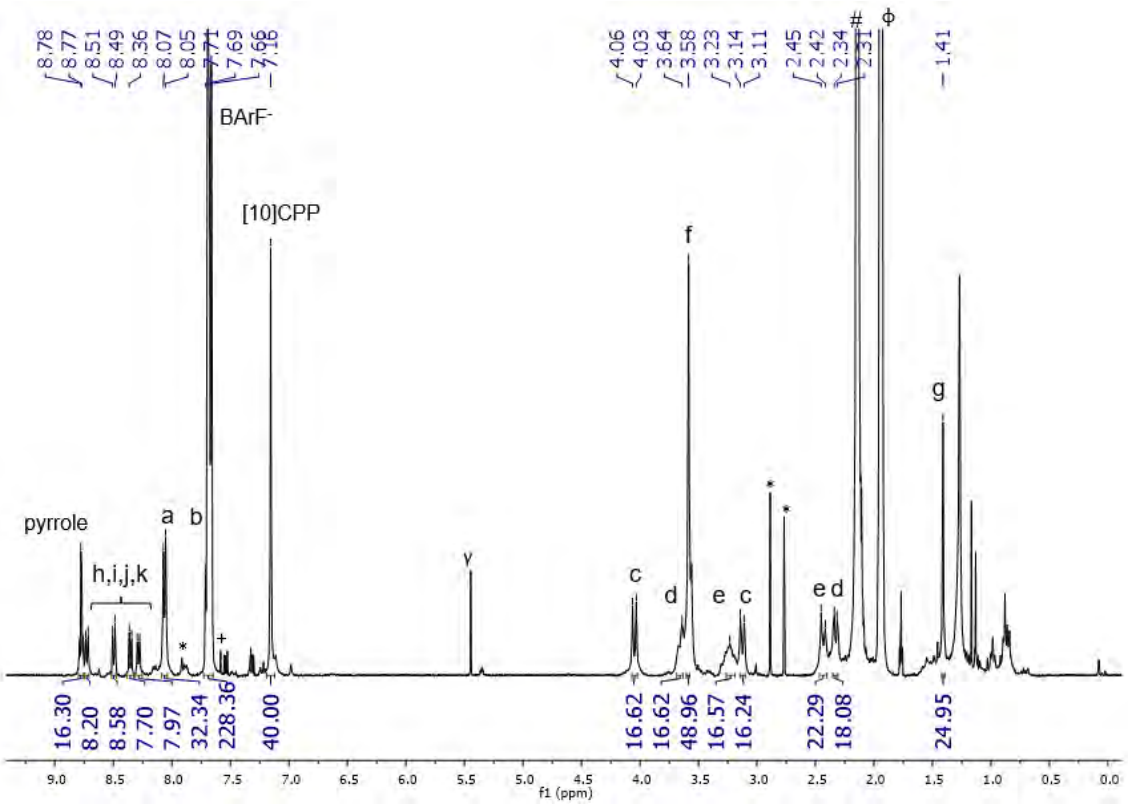

Supplementary Figure 80. HMBC of ***trans*-3-(1-C_{60})⊂[10]CPP**⊂(**6**·$BAr^F)_8$ nanocapsule. Experiment performed in CD_3CN at 298 K (400 MHz).

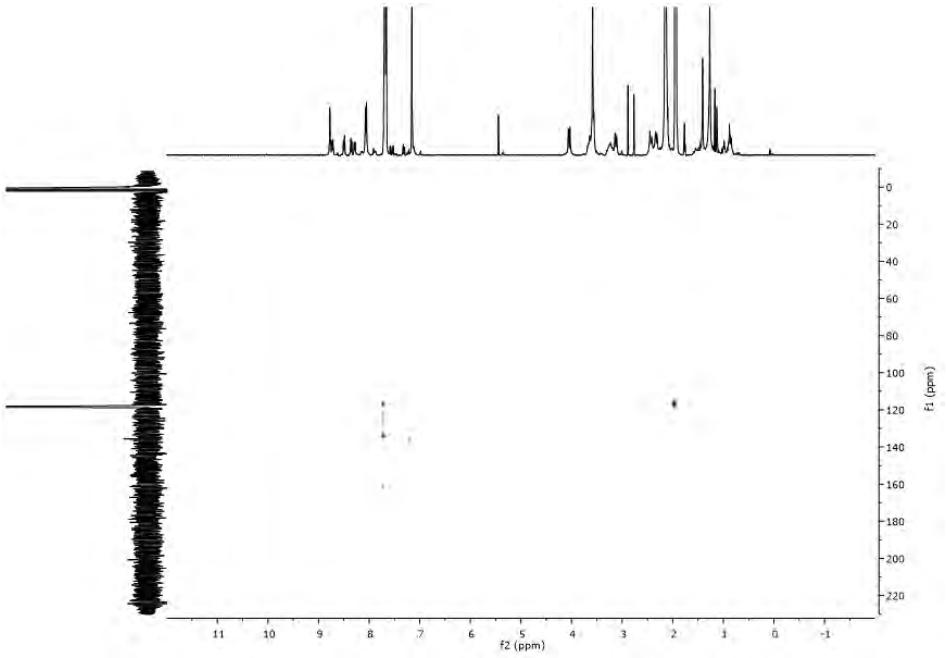

Supplementary Figure 81. HSQC of ***trans*-3-(1-C_{60})⊂[10]CPP⊂(6·BArF)$_8$** nanocapsule. Experiment performed in CD_3CN at 298 K (400 MHz).

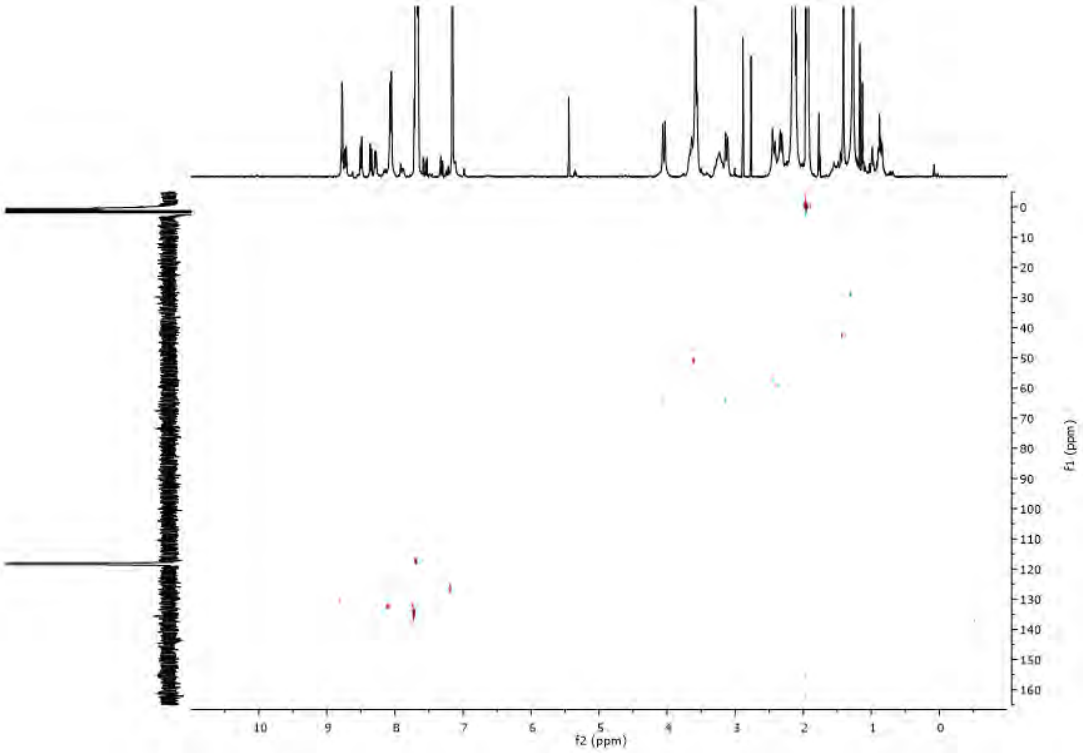

Supplementary Figure 82. COSY of ***trans*-3-(1-C_{60})⊂[10]CPP⊂(6·BArF)$_8$** nanocapsule. Experiment performed in CD_3CN at 298 K (400 MHz).

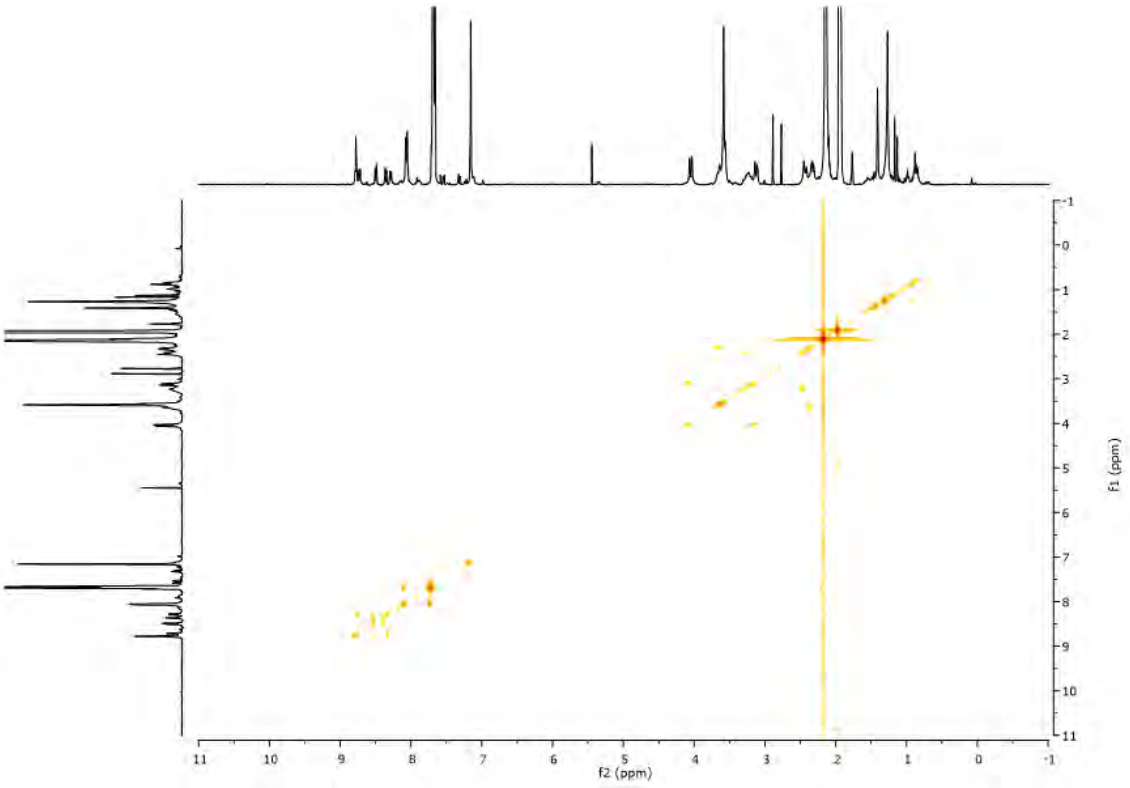

Supplementary Figure 83. TOCSY of ***trans*-3-(1-C_{60})⊂[10]CPP⊂(6·BArF)$_8$** nanocapsule. Experiment performed in CD_3CN at 298 K (400 MHz).

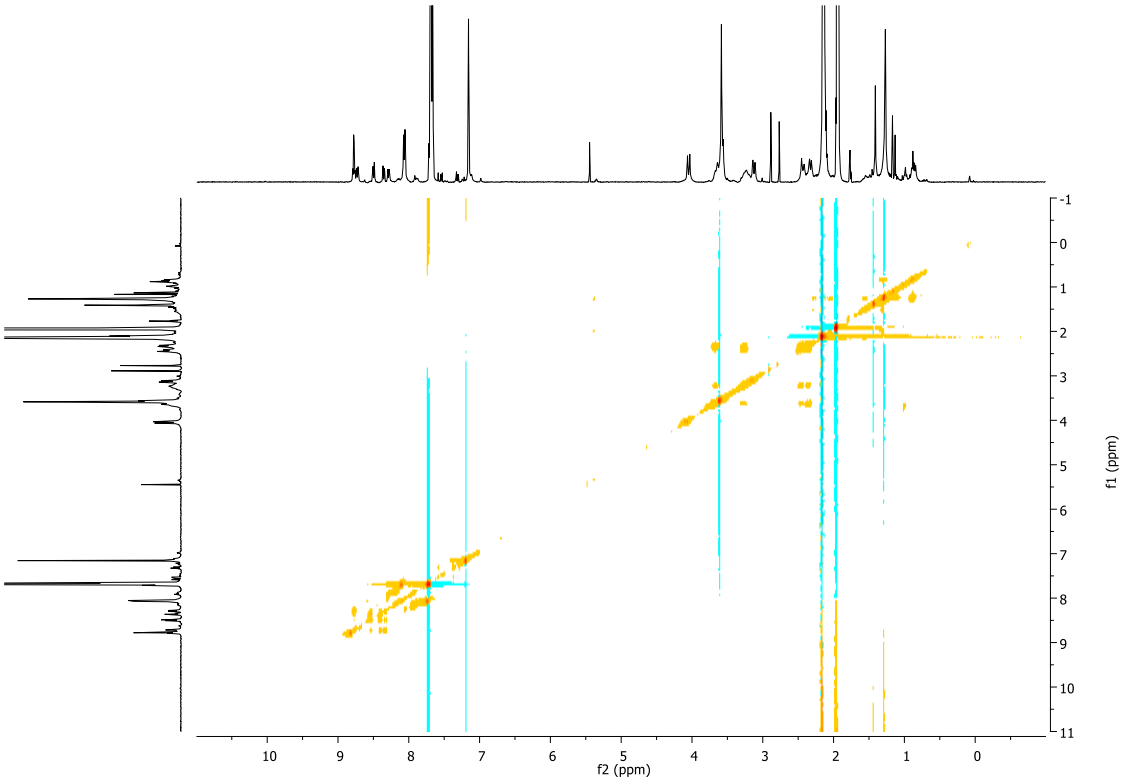

Supplementary Figure 84. NOESY of ***trans*-3-(1-C_{60})⊂[10]CPP⊂(6·BArF)$_8$** nanocapsule. Experiment performed in CD_3CN at 298 K (400 MHz).

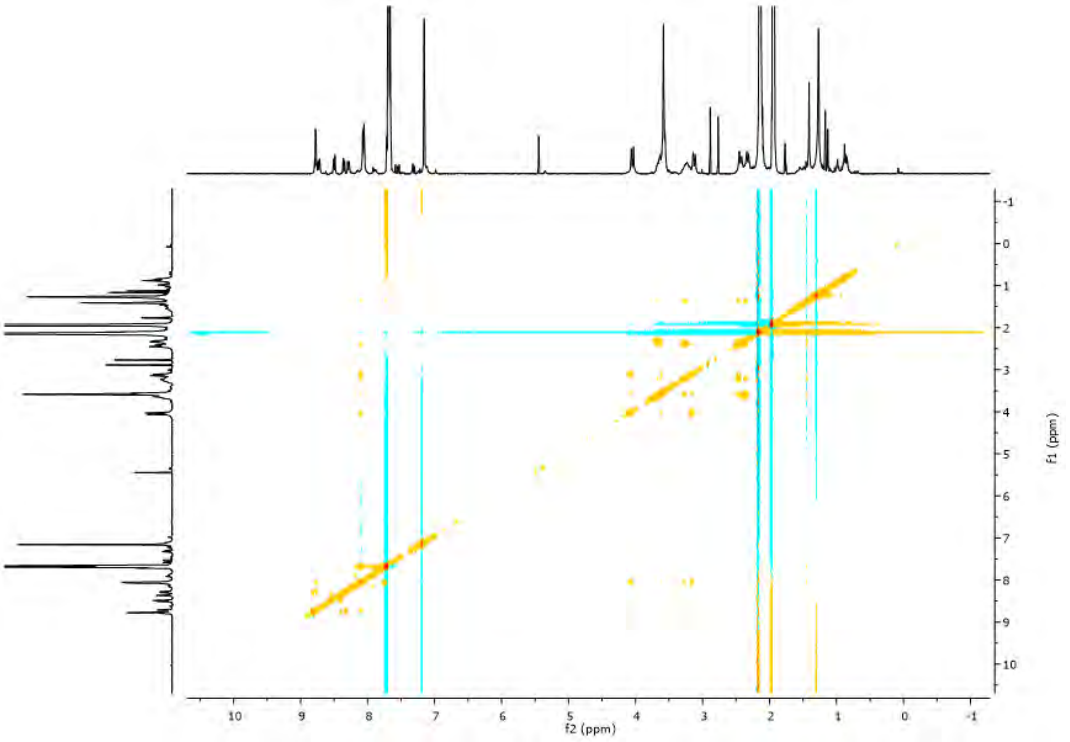

Supplementary Figure 85. DOSY NMR spectrum of ***trans*-3-(1-C_{60})@[10]CPP⊂6**·$(BArF)_8$ nanocapsule (in CD_3CN).

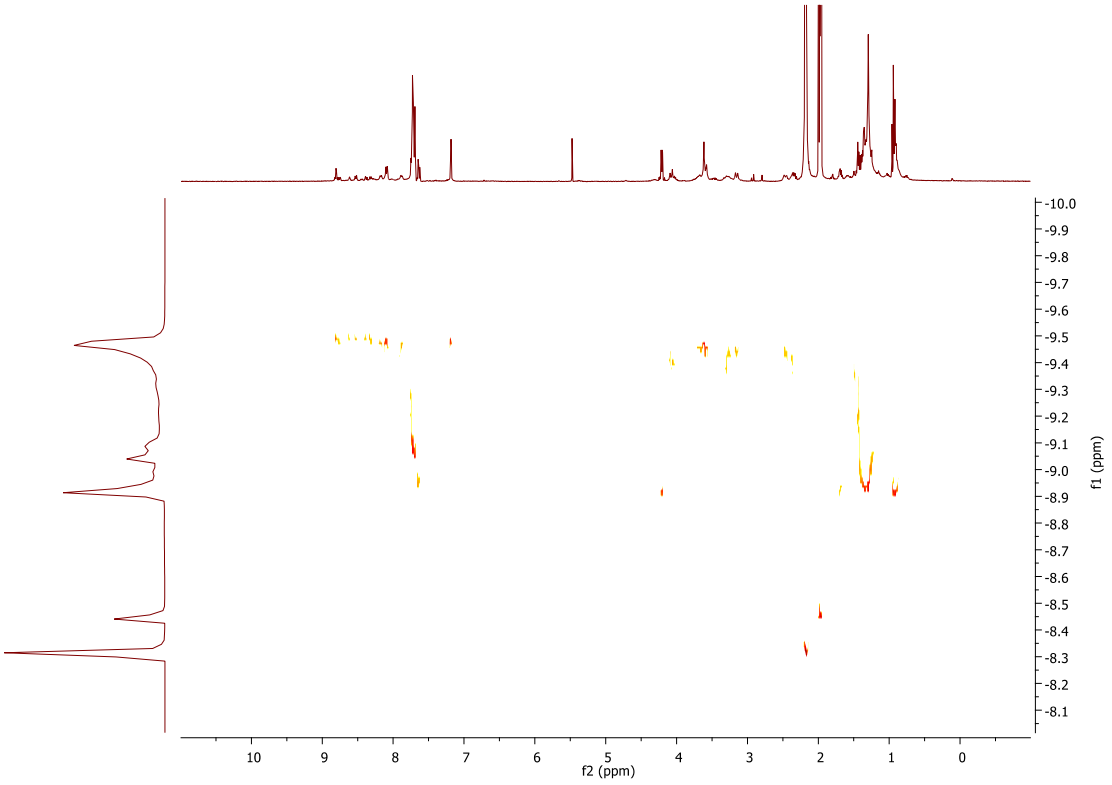

2.15. Characterization of *trans*-3-(1-C_{60})⊂[10]CPP

Supplementary Figure 86. ^{1}H-NMR of ***trans*-3-(1-C_{60})⊂[10]CPP** ($CDCl_3$, 400 MHz, 298 K). (ϕ) $CHCl_3$, (+) toluene, (*) ethyl acetate, (μ) acetone, (#) water, (γ) TMS.

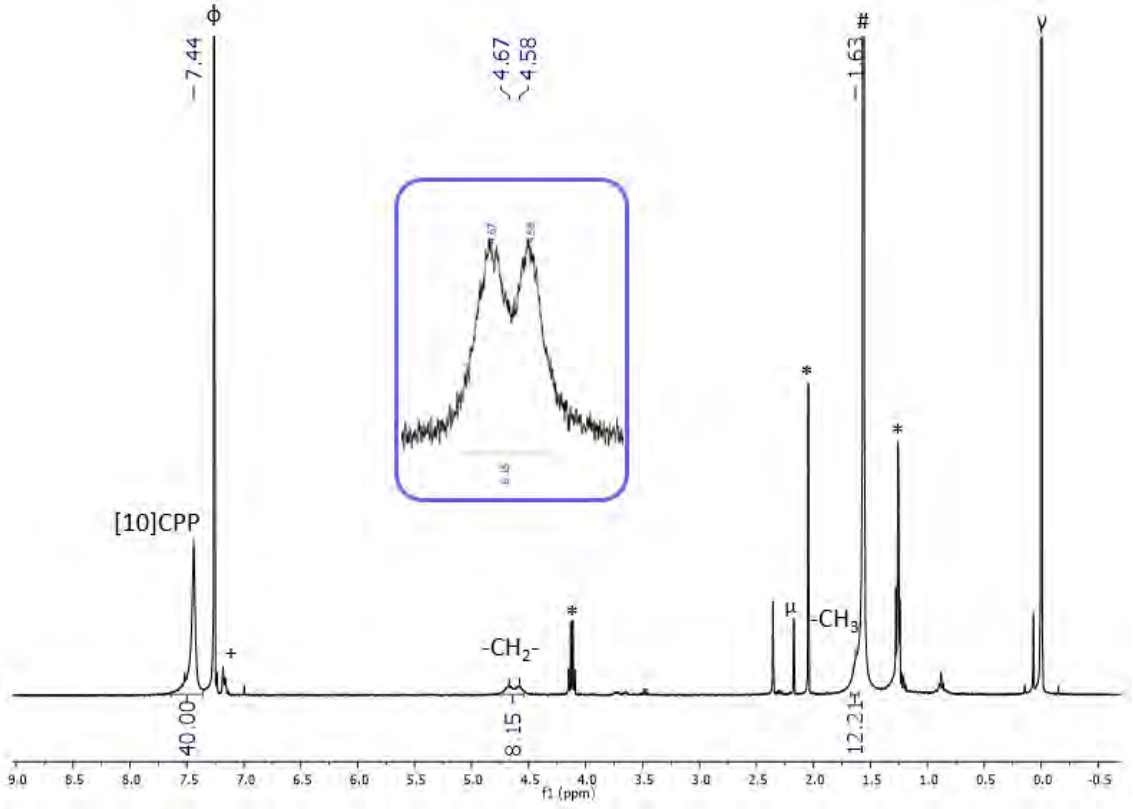

2.16. Comparative ^{1}H-NMR spectra

Supplementary Figure 87. Comparative ^{1}H-NMR spectrum (CD_3CN, 400 MHz, 298 K) of (a) **6**·$(BArF)_8$, (b) **C_{60}⊂[10]CPP⊂6**·$(BArF)_8$ and (c) ***trans*-3-(1-C_{60})⊂[10]CPP⊂6**·$(BArF)_8$.

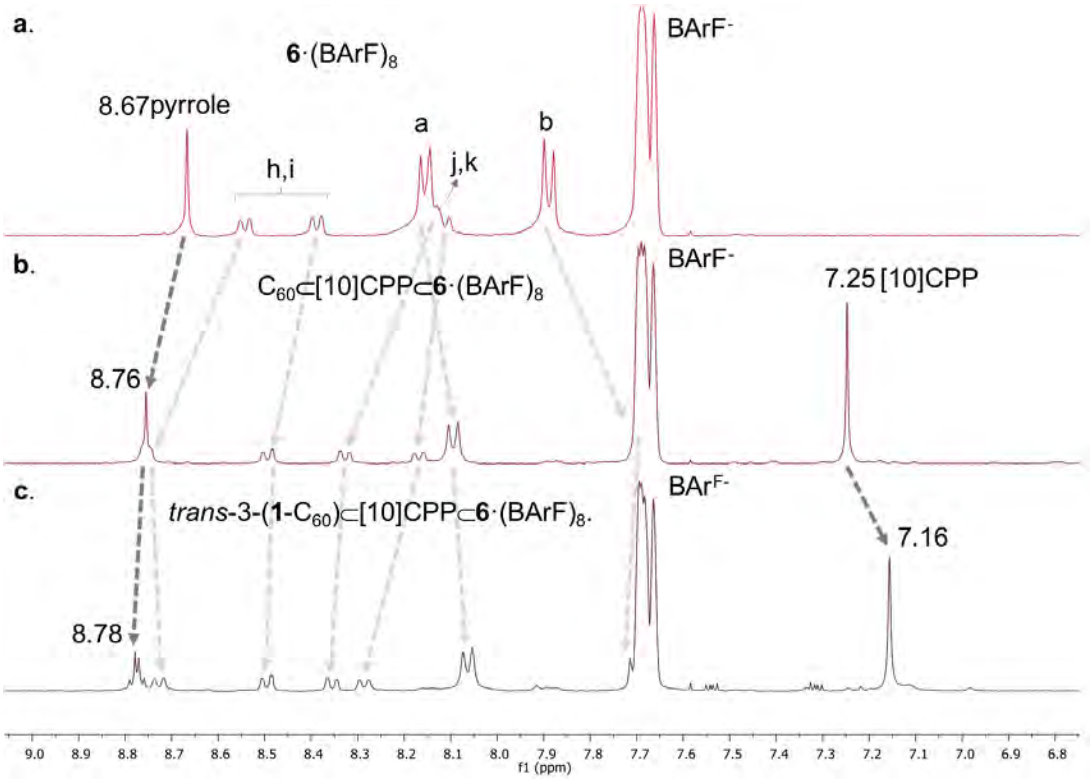

Supplementary Figure 88. Comparative ^{1}H-NMR spectrum ($CDCl_3$, 400 MHz, 298 K) of (a) [10]CPP, (b) **C_{60}⊂[10]CPP** and (c) ***trans*-3-(1-C_{60})⊂[10]CPP**.

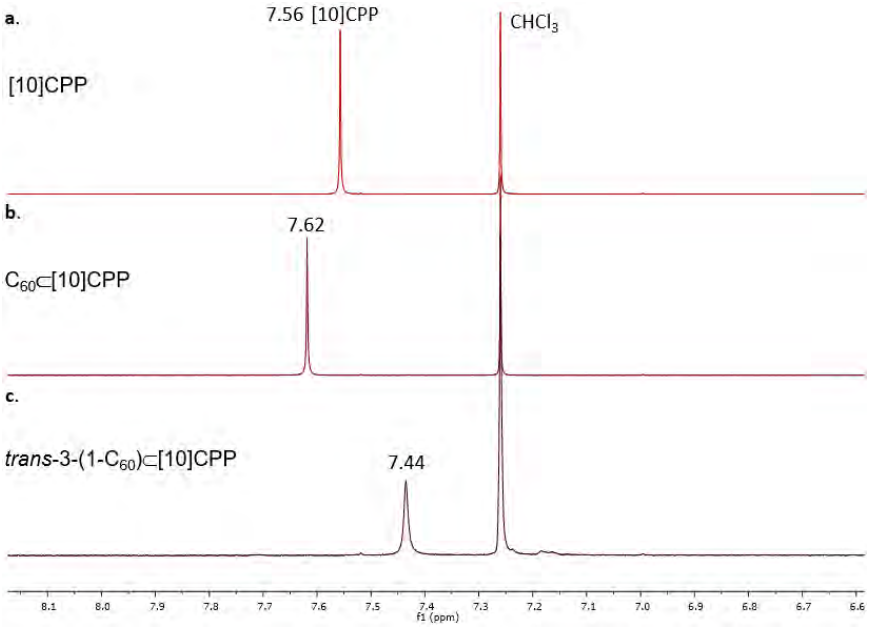

2.17. Host-guest binding studies

Experimental procedure and general remarks

All titrations were performed in PhMe/MeCN (9:1 by volume) at room temperature on a fluorescence spectrophotometer Perkin Elmer FL 6500 and a UV-Vis spectrophotometer Perkin Elmer Lambda 365. Depending on the kind of titration (fluorescence or UV-vis), a fluorescence quartz cuvette (10×10 mm or 10×4 mm) or a UV-vis cuvette (10×10 mm) with a PTFE stopper was used. The solvent was degassed by the freeze-pump-thaw method (argon) prior to use to avoid the potential formation of singlet oxygen.[11] Concentration of either host or guest species was kept constant over the course of titration. Concentrations of stock solutions were determined by quantitative ^{1}H NMR (qNMR) using dimethyl terephthalate as an internal standard (TraceCERT® NMR standard purchased from Sigma-Aldrich).

Titration data was fitted by using the online calculator Bindfit (http://supramolecular.org).[12] For data fitting according to 1:2 and 2:1 binding models, the "full model" was used, i.e. both association constants – K_1 and K_2 – were fitted independently.[12,13] All raw data, calculated fits and related data can be accessed via http://supramolecular.org (see the web links below).

Fluorescence titrations: [10]CPP + C_{60}

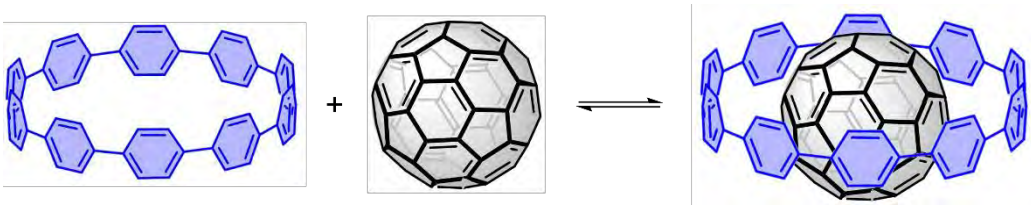

Supplementary Figure 89. Representative titration data for [10]CPP/C_{60} host-guest system. Solvent: PhMe/MeCN (9:1). (A) Changes in emission spectra of [10]CPP (2.0×10^{-7} M, λ_{exc} = 340 nm) upon addition of C_{60} (0 – 2.4×10^{-6} M). (B) Fit of the titration data according to 1:1 binding model. (C) Dependence of molar fractions of [10]CPP and C_{60}/[10]CPP on relative amount of C_{60} added. (D) Residual plots.

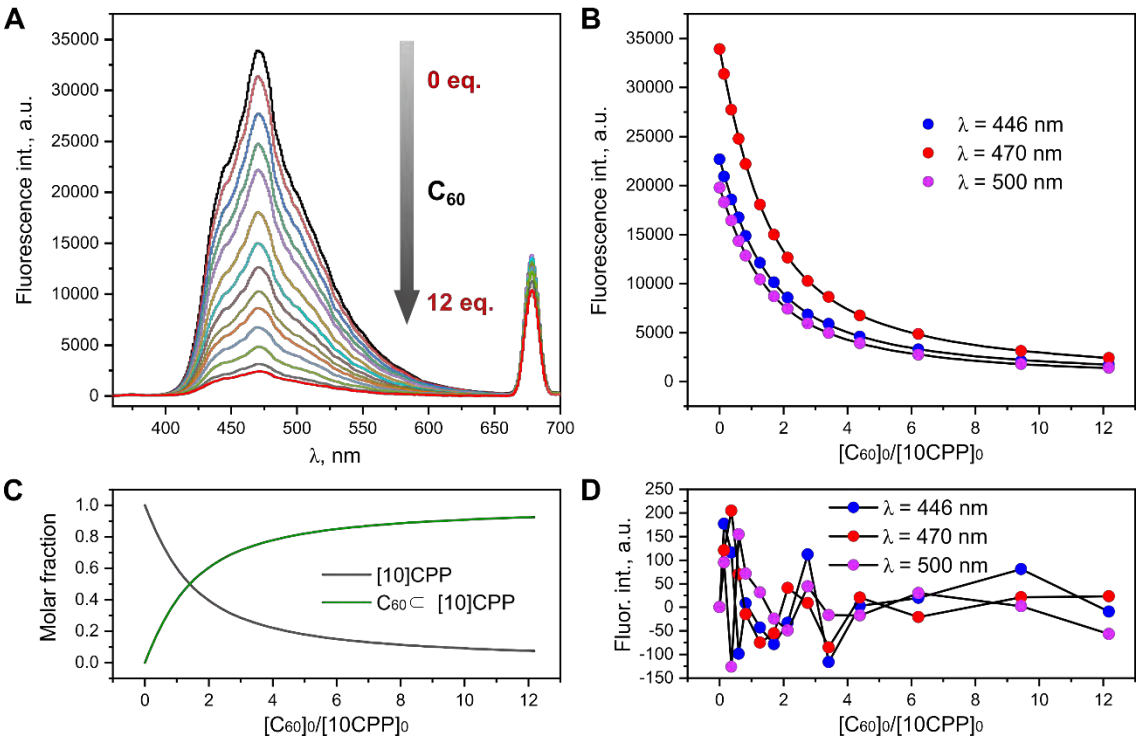

Supplementary Table 1. Comparison of different binding models used to fit the representative titration data shown in Supplementary Figure 89. Solvent: PhMe/MeCN (9:1). Fit method: Nelder-Mead. $[10CPP]_0 = 2.0\times10^{-7}$ M; $[C_{60}]_0$: 0 – 2.4×10^{-6} M.

	1:1 model	1:2 model		2:1 model	
	K, M^{-1}	K_1, M^{-1}	K_2, M^{-1}	K_1, M^{-1}	K_2, M^{-1}
	5.5×10^{6}	5.7×10^{6}	7.7×10^{4}	3.6×10^{6}	-3.5×10^{5}
Error	± 0.68%	± 0.91%	± 21%	± 5.6%	± -12%
RMS	76.0	74.6		64.7	
Covariance	7.7×10^{-5}	7.4×10^{-5}		5.7×10^{-5}	

Comment. Fitting the titration data according to 1:2 or 2:1 binding model does not improve the quality of fit, i.e. RMS and covariance are not significantly reduced in comparison to those for 1:1 model. Moreover, 2:1 binding model does not give an adequate value for K_2. Therefore, binding of C_{60} to [10]CPP in PhMe/MeCN (9:1) at room temperature can be best described by 1:1 binding model.

Supplementary Table 2. Association constants for C_{60}/[10]CPP obtained for four independent titrations by fitting the data according to 1:1 binding model. Solvent: PhMe/MeCN (9:1). Fit method: Nelder-Mead. $s/\sqrt{n}$ – standard deviation of the mean, where s – standard deviation, n – number of measurements; $t_{(0.05,\,3)} \times s/\sqrt{n}$ – 95% confidence interval, where $t_{(0.05,\,n-1)}$ – Student's t at 95% confidence level.[12]

$[10CPP]_0$, M	$[C_{60}]_{0,\,final}$, M	K, M^{-1}	Error, %	Average K, M^{-1}	$s/\sqrt{n}$, M^{-1}	$t_{(0.05,\,3)} \times s/\sqrt{n}$, M^{-1}
2.0×10^{-7}	1.5×10^{-6}	6.0×10^{6}	± 0.81	**5.7×10^{6}**	0.1×10^{6}	$\pm 0.4\times10^{6}$
2.0×10^{-7}	2.4×10^{-6}	5.5×10^{6}	± 0.68			
1.0×10^{-7}	1.7×10^{-6}	5.9×10^{6}	± 0.83			
9.9×10^{-8}	1.8×10^{-6}	5.5×10^{6}	± 2.6			

Supplementary Table 3. Links to the raw titration data, calculated fits and statistical information for the titrations.

$[10CPP]_0$, M	Web link
2.0×10^{-7}	http://app.supramolecular.org/bindfit/view/c25872d5-af76-43e9-a42e-8e690dcc990c
2.0×10^{-7}	http://app.supramolecular.org/bindfit/view/42c3452b-7e53-414a-92e3-434bcb8582cf
1.0×10^{-7}	http://app.supramolecular.org/bindfit/view/10ed8541-2dc7-4557-860d-6bc917d0c005
9.9×10^{-8}	http://app.supramolecular.org/bindfit/view/681131f7-e31b-4b00-bb69-e4bb8ac805a6

Fluorescence titrations: [10]CPP + nanocapsule 6·(BArF)$_8$

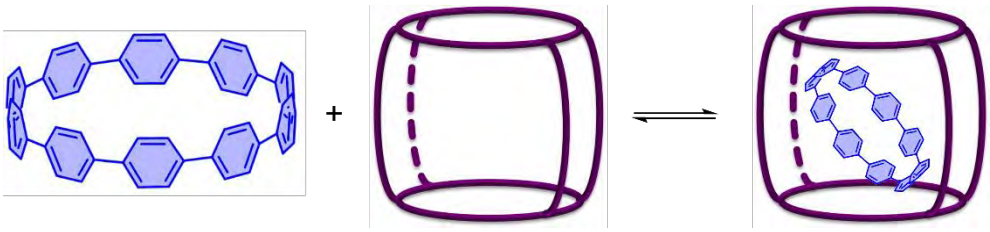

Supplementary Figure 90. Representative titration data for **6**/[10]CPP host-guest system. Solvent: PhMe/MeCN (9:1). (A) Changes in emission spectra of [10]CPP (2.0×10^{-7} M, λ_{exc} = 340 nm) upon addition of nanocapsule **6**·(BArF)$_8$ (0 – 1.6×10^{-5} M). (B) Fit of the titration data according to 1:1 binding model. (C) Dependence of molar fractions of [10]CPP and [10]CPP/**6**·(BArF)$_8$ on relative amount of **6**·(BArF)$_8$. (D) Residual plots.

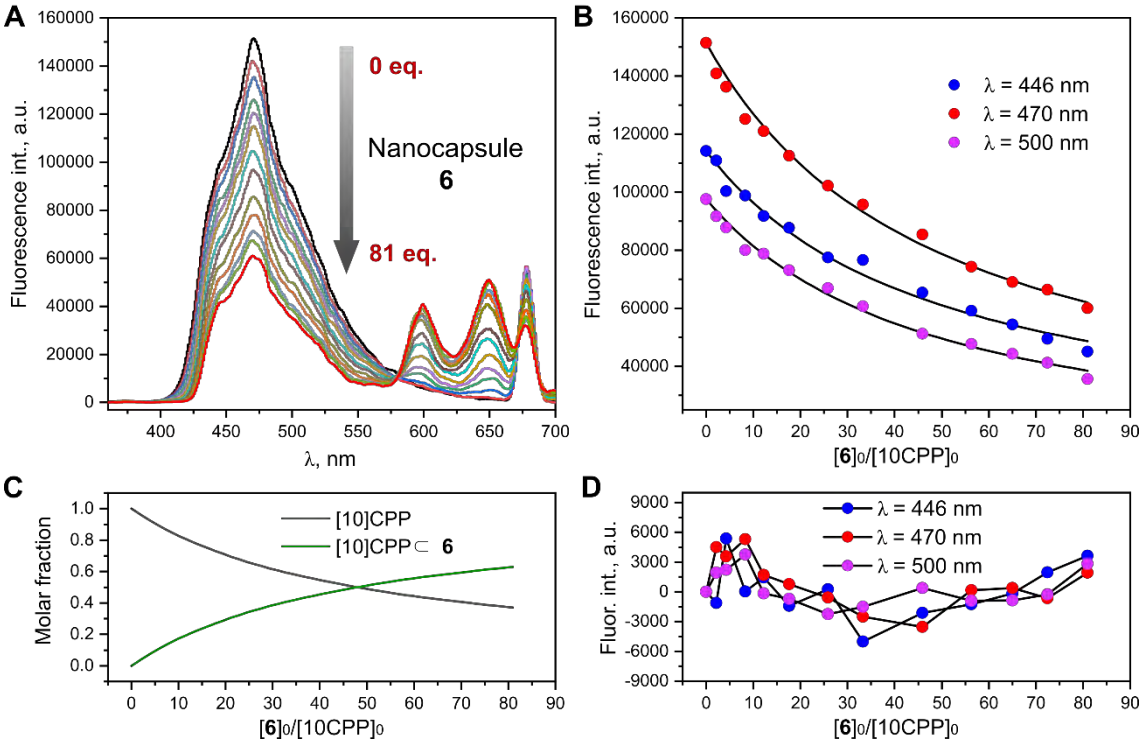

Supplementary Table 4. Comparison of different binding models used to fit the representative titration data shown in Supplementary Figure 90. Solvent: PhMe/MeCN (9:1). Fit method: Nelder-Mead. [10CPP]$_0$ = 2.0×10^{-7} M; [**6**·(BArF)$_8$]$_0$: 0 – 1.6×10^{-5} M.

	1:1 model	1:2 model		2:1 model	
	K, M^{-1}	K_1, M^{-1}	K_2, M^{-1}	K_1, M^{-1}	K_2, M^{-1}
	1.1×10^5	1.1×10^6	2.7×10^4	28	2.4×10^{11}
Error	± 3.6%	± 13%	± 2.8%	± 29%	± 1.3%
RMS	2327	1244		1267	
Covariance	8.1×10^{-3}	2.4×10^{-3}		2.5×10^{-3}	

Comments:

1) *Titration type*. This titration was performed in the unusual "Guest+Host" fashion, i.e. the host was added to a solution of the guest. The reason for this approach is the large difference in quantum yields between nanocapsule **6**·$(BArF)_8$ and [10]CPP: fluorescence of [10]CPP is much stronger than fluorescence of **6**·$(BArF)_8$, leading to spectral overlap if the emission of **6**·$(BArF)_8$ was to be observed.

2) *Binding model*: in comparison to the 1:1 model, the 1:2 and 2:1 binding models give slightly reduced RMS and covariance as well as somewhat improved residual plots. However, these models do not allow to obtain reproducible (with an adequate standard deviation) binding constants for different titration experiments and the association constants for both alternative models are not plausible based on complementary XRD evidence. Therefore, binding of [10]CPP to nanocapsule **6**·$(BArF)_8$ in PhMe/MeCN (9:1) at room temperature most likely follows the 1:1 binding model.

Supplementary Table 5. Association constants for [10]CPP/**6**·$(BArF)_8$ obtained for three independent titrations by fitting the data according to 1:1 binding model. Solvent: PhMe/MeCN (9:1). Fit method: Nelder-Mead. $s/\sqrt{n}$ – standard deviation of the mean, where s – standard deviation, n – number of measurements; $t_{(0.05,\,3)} \times s/\sqrt{n}$ – 95% confidence interval, where $t_{(0.05,\,n-1)}$ – Student's t at 95% confidence level.[12]

Entry	$[10CPP]_0$, M	$[6]_{0,\,final}$, M	K, M^{-1}	Error, %	Average K, M^{-1}	$s/\sqrt{n}$, M^{-1}	$t_{(0.05,\,2)} \times s/\sqrt{n}$, M^{-1}
1	2.0×10^{-7}	2.2×10^{-5}	1.10×10^{5}	± 2.8			
2	2.0×10^{-7}	1.6×10^{-5}	1.05×10^{5}	± 3.6	**1.1×10^{5}**	0.03×10^{5}	$\pm 0.1\times10^{5}$
3	2.0×10^{-7}	1.6×10^{-6}	1.14×10^{5}	± 3.7			

Supplementary Table 6. Links to the raw titration data, calculated fits and statistical information for the titrations with **6**/[10]CPP host-guest system.

Entry	Web link
1	http://app.supramolecular.org/bindfit/view/261ed1a6-bf1e-4db3-aa66-827a086e4585
2	http://app.supramolecular.org/bindfit/view/40053dcf-ffe8-4191-a3b3-eb40f729f5c2
3	http://app.supramolecular.org/bindfit/view/8854eafa-36e1-47e2-b7bd-8aab3bb38ab2

UV-Vis titrations: nanocapsule 6·(BArF)$_8$ + C_{60}

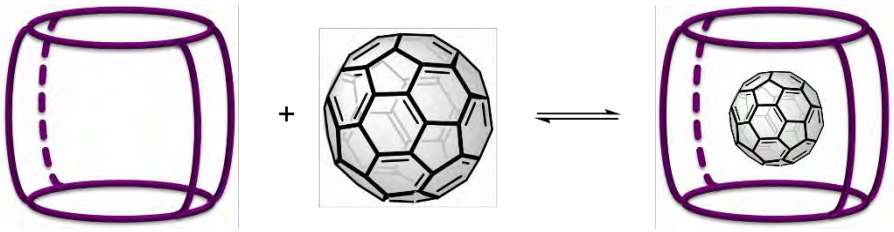

Supplementary Figure 91. Representative titration data for **6**·(BArF)$_8$/C_{60} host-guest system. Solvent: PhMe/MeCN (9:1). (A) Changes in absorption spectra of nanocapsule **6**·(BArF)$_8$ (4.1×10^{-7} M) upon addition of C_{60} (0 – 1.0×10^{-4} M). (B) Fit of the titration data according to 1:1 binding model. (C) Dependence of molar fractions of **6**·(BArF)$_8$ and C_{60}/**6**·(BArF)$_8$ on relative amount of C_{60}. (D) Residual plot.

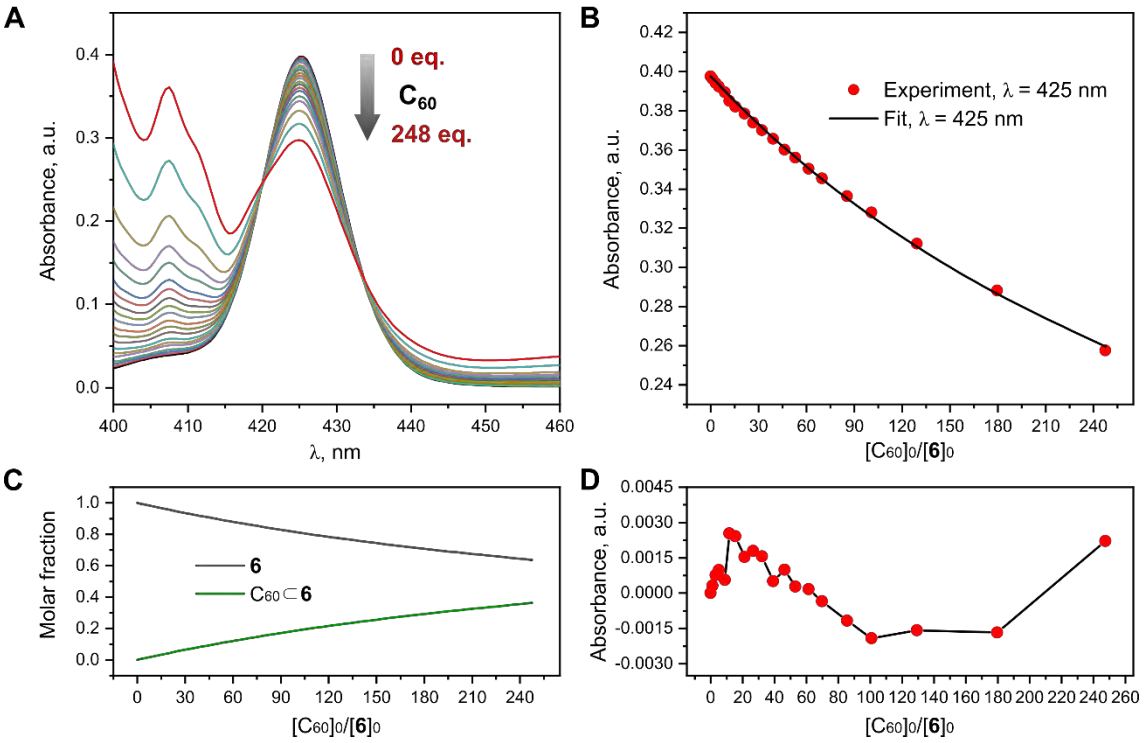

Supplementary Table 7. Comparison of different binding models used to fit the representative titration data shown in Supplementary Figure 91. Solvent: PhMe/MeCN (9:1). Fit method: Nelder-Mead. [**6**·(BArF)$_8$]$_0$ = 4.1×10^{-7} M; [C_{60}]$_0$: 0 – 1.0×10^{-4} M.

	1:1 model	1:2 model		2:1 model	
	K, M^{-1}	K_1, M^{-1}	K_2, M^{-1}	K_1, M^{-1}	K_2, M^{-1}
	5.7×10^3	8.8×10^4	2.3×10^3	8	3.1×10^9
Error	± 1.7%	± 2.9%	± 1.0%	± 9.1%	± 17%
RMS	1.4×10^{-3}	3.9×10^{-4}		7.8×10^{-4}	
Covariance	1.2×10^{-3}	1.1×10^{-4}		4.2×10^{-4}	

Comments:

1) *Spectroscopic technique.* For this equilibrium, the fluorescence titration experiment had two key limitations in comparison to UV-vis experiment. First, at low concentrations of nanocapsule **6**·$(BArF)_8$ ($<1\times10^{-7}$ M), which would give a linear dependence of the fluorescence response on the light absorbed, fluorescence of **6**·$(BArF)_8$ was very weak. This led to a high error of the measurement. Second, prolonged irradiation of the solution of **6**·$(BArF)_8$ with a laser beam (λ_{exc} = 425 nm) during fluorescence titration caused partial photobleaching of **6**·$(BArF)_8$, presumably as a result of generation of singlet oxygen by the nanocapsule.[11] Therefore, the host-guest interaction between nanocapsule **6**·$(BArF)_8$ and C_{60} was studied by means of UV-vis titration.

2) *Binding model*. In comparison to the 1:1 model, the 1:2 and 2:1 binding models give reduced RMS and covariance as well as improved residual plots. However, the 2:1 model produces highly implausible binding constants and both models do not allow to obtain reproducible (with an acceptable standard deviation) binding constants for the three different titration experiments. Therefore, binding of C_{60} to nanocapsule **6**·$(BArF)_8$ in PhMe/MeCN (9:1) at room temperature most likely follows the 1:1 binding model. It is worth noting that a 1:2 (or 1:3) model would be physically plausible (one *endo* binding event, followed by 1-2 *exo* binding events), but that the important first binding constant K_1 has a magnitude that would NOT affect any conclusions drawn in this study.

3) *Guest absorption*. Fullerene C_{60} is a "non-silent" guest, i.e. C_{60} absorbs light at the wavelength of interest (λ_{max} = 425 nm). In order to take into account the absorption of a guest, the equation for fitting titration data to 1:1 model must have an extra term $\varepsilon_G[G]_0$, where ε_G is molar absorptivity of a guest and $[G]_0$ is a total guest concentration.[14] We experimentally determined ε_G of C_{60} at λ = 425 nm (397 $M^{-1}cm^{-1}$) in the standard solvent mixture and subtracted $\varepsilon_G[G]_0$ from the observed absorption at 425 nm for each data point. This approximation allowed us to analyze (and share) the titration data with online calculator BindFit, since currently it can fit titration data for "silent" guests only. We did however fit the data with the 1:1 model for "non-silent" guests by nonlinear curve fitting in OriginPro® 2019b (iteration algorithm: Levenberg Marquardt) and the binding constants obtained in this way are identical to those obtained with BindFit.

Supplementary Table 8. Association constants for C_{60}/**6**·$(BArF)_8$ obtained for three independent titrations by fitting the titration according to 1:1 binding model. Solvent: PhMe/MeCN (9:1). Fit method: Nelder-Mead. $s/\sqrt{n}$ – standard deviation of the mean, where s – standard deviation, n – number of measurements; $t_{(0.05,\,2)} \times s/\sqrt{n}$ – 95% confidence interval, where $t_{(0.05,\,n-1)}$ – Student's t at 95% confidence level.[12]

Entry	$[6]_0$, M	$[C_{60}]_{0,\,final}$, M	K, M^{-1}	Error, %	Average K, M^{-1}	$s/\sqrt{n}$, M^{-1}	$t_{(0.05,\,2)} \times s/\sqrt{n}$, M^{-1}
1	4.1×10^{-7}	8.4×10^{-5}	5.0×10^{3}	± 2.9			
2	4.1×10^{-7}	1.0×10^{-4}	5.7×10^{3}	± 1.7	**5.4×10^{3}**	0.2×10^{3}	$\pm 0.9\times10^{3}$
3	4.1×10^{-7}	9.8×10^{-5}	5.4×10^{3}	± 1.8			

Supplementary Table 9. Links to the raw titration data, calculated fits and statistical information for the titrations with **6**·$(BArF)_8/C_{60}$ host-guest system.

Entry	Web link
1	http://app.supramolecular.org/bindfit/view/1a791f90-e0d7-4e32-9105-4966a6ca784b
2	http://app.supramolecular.org/bindfit/view/5bb3979d-caf2-46d4-bfc6-381a9c0de82a
3	http://app.supramolecular.org/bindfit/view/d6646126-dc4c-4db8-98b7-47a7afee7983

Fluorescence titrations: [10]CPP + C_{60} in the presence of nanocapsule 6·$(BArF)_8$

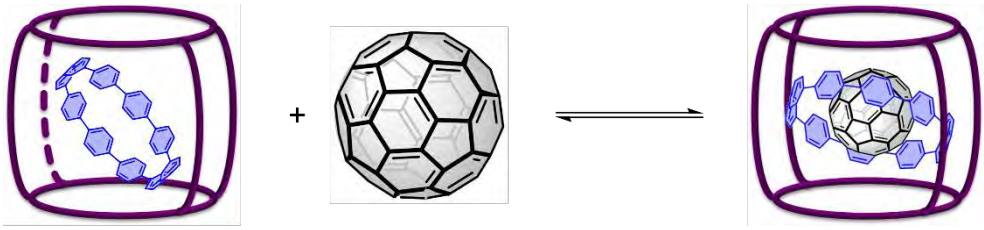

Supplementary Figure 92. Representative titration data for **6**·$(BArF)_8$ /[10]CPP/C_{60} host-guest system. Solvent: PhMe/MeCN (9:1). (A) Changes in emission spectra of [10]CPP (2.0×10^{-7} M, λ_{exc} = 340 nm) upon addition of C_{60} (0 – 1.9×10^{-6} M) in the presence of nanocapsule **6**·$(BArF)_8$ (6.1×10^{-6} M, 30 equiv. with respect to [10]CPP). (B) Fit of the titration data according to 1:1 binding model. (C) Dependence of molar fractions of [10]CPP and C_{60}/[10]CPP on relative amount of C_{60}. (D) Residual plots.

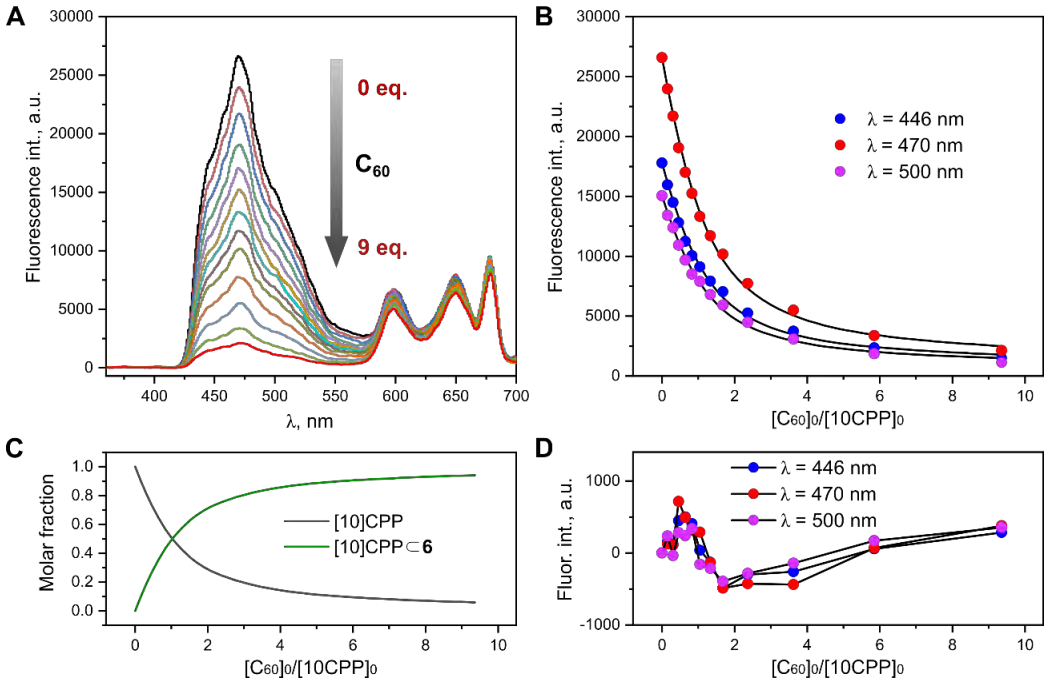

Supplementary Table 10. Comparison of different binding models used to fit the representative titration data shown in Supplementary Figure 92. Solvent: PhMe/MeCN (9:1). Fit method: Nelder-Mead. $[10CPP]_0 = 2.0\times10^{-7}$ M; $[C_{60}]_0$: 0 – 1.9×10^{-6} M; [**6**·$(BArF)_8$ $]_0 = 6.1\times10^{-6}$ M.

	1:1 model	1:2 model		2:1 model	
	K, M^{-1}	K_1, M^{-1}	K_2, M^{-1}	K_1, M^{-1}	K_2, M^{-1}
	9.5×10^6	1.9×10^7	4.0×10^5	1.3×10^7	7.8×10^6
Error	± 4.3%	± 5.9%	± 12%	± 8.6%	± 18%
RMS	307	234		122	
Covariance	2.3×10^{-3}	1.3×10^{-3}		3.8×10^{-4}	

Comments:
1) *Rationale*. Having confirmed that the C_{60}/[10]CPP is the strongest binary association event, this titration serves to answer the question whether the presence of the nanocapsule (constant concentration) significantly affects the stability of the C_{60}/[10]CPP complex).[15,16]
2) *Binding model*. Because we fit a ternary complex based on a binary model, this experiment is by nature an approximation only. It is therefore not surprising that the 1:2 model and especially the 2:1 binding model give a better quality of fit. The main purpose of the experiment is however to draw a comparison to the binary 1:1 complex C_{60}/[10]CPP, and it is remarkable that the 1:1 model allows a reasonably good fit and also a good statistical error (see below) for these ternary titrations.

Supplementary Table 11. Association constants for C_{60}/[10]CPP/**6**·$(BArF)_8$ obtained for three independent titrations by fitting the data according to 1:1 binding model. Solvent: PhMe/MeCN (9:1). Fit method: Nelder-Mead. $s/\sqrt{n}$ – standard deviation of the mean, where s – standard deviation, n – number of measurements; $t_{(0.05,\ n-1)} \times s/\sqrt{n}$ – 95% confidence interval, where $t_{(0.05,\ n-1)}$ – Student's t at 95% confidence level.[12]

Entry	$[10CPP]_0$, M	$[C_{60}]_{0,\ final}$, M	K, M^{-1}	Error, %	Average K, M^{-1}	$s/\sqrt{n}$, M^{-1}	$t_{(0.05,\ 2)} \times s/\sqrt{n}$, M^{-1}
1	2.0×10^{-7}	1.7×10^{-6}	9.3×10^{6}	± 6.5			
2	2.0×10^{-7}	1.9×10^{-6}	9.5×10^{6}	± 4.3	**9.3×10^{6}**	0.09×10^{6}	± 0.4×10^{6}
3	2.0×10^{-7}	1.9×10^{-6}	9.2×10^{6}	± 5.7			

Supplementary Table 12. Links to the raw titration data, calculated fits and statistical information for the titrations with **6**·$(BArF)_8$ /[10]CPP/C_{60} host-guest system.

Entry	Web link
1	http://app.supramolecular.org/bindfit/view/69b03125-f1f2-4a14-aa85-6914ab3a85fb
2	http://app.supramolecular.org/bindfit/view/b587fe4f-f276-4595-8a82-06c0b2f7370c
3	http://app.supramolecular.org/bindfit/view/32be7daf-e76f-41f9-8485-a87942db36e2

Fluorescence titration: [10]CPP + *trans*-3-(1-C_{60}) bis-adduct

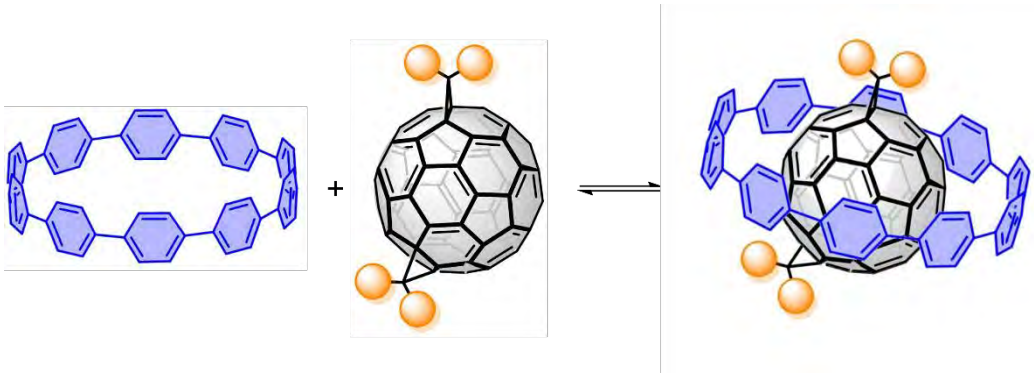

Supplementary Figure 93. Representative titration data for [10]CPP/***trans*-3-(1-C_{60})** host-guest system. Solvent: PhMe/MeCN (9:1). (A) Changes in emission spectra of [10]CPP (2.0×10^{-7} M, λ_{exc} = 340 nm) upon addition of ***trans*-3-(1-C_{60})** (0 – 9.9×10^{-6} M). (B) Fit of the titration data according to 1:1 binding model. (C) Dependence of molar fractions of [10]CPP and ***trans*-3-(1-C_{60})**/[10]CPP on relative amount of ***trans*-3-(1-C_{60})**. (D) Residual plots.

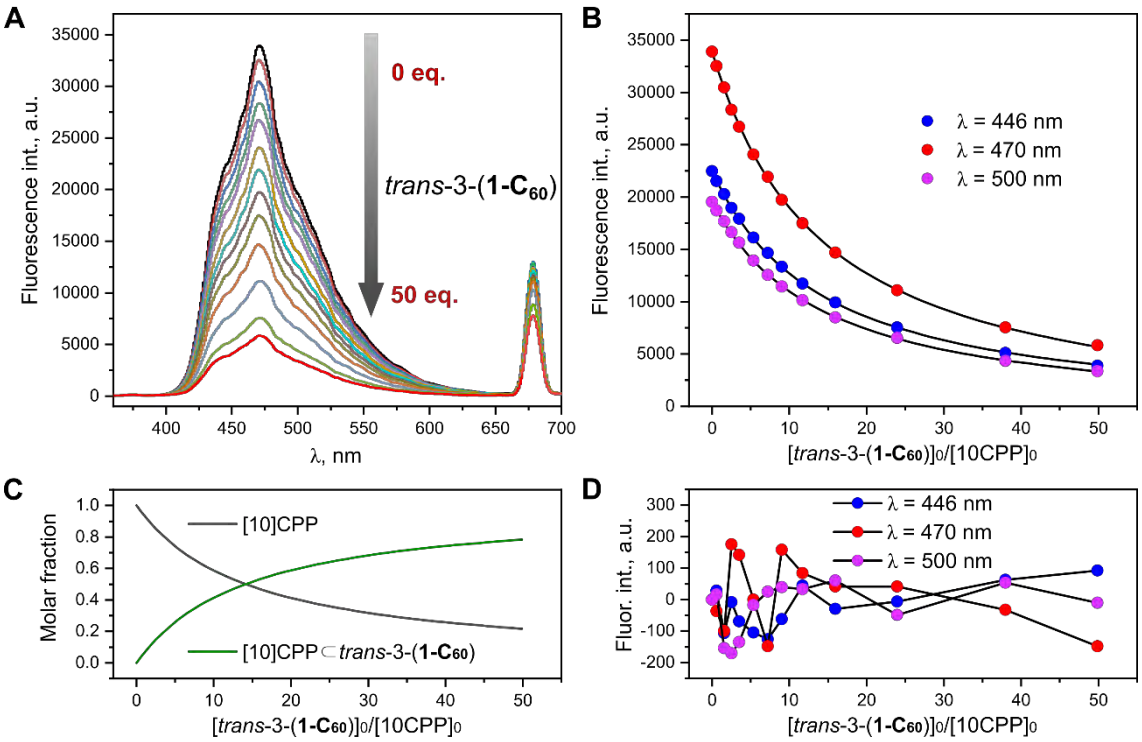

Supplementary Table 13. Comparison of different binding models used to fit the representative titration data shown in Supplementary Figure 93. Solvent: PhMe/MeCN (9:1). Fit method: Nelder-Mead. $[10CPP]_0 = 2.0\times10^{-7}$ M; $[$***trans*-3**-(**1-C$_{60}$**$)]_0$: 0 – 9.9×10^{-6} M.

	1:1 model	1:2 model		2:1 model	
	K, M^{-1}	K_1, M^{-1}	K_2, M^{-1}	K_1, M^{-1}	K_2, M^{-1}
	3.7×10^5	3.6×10^6	3.2×10^5	5.0×10^5	1.7×10^5
Error	± 0.61%	± 4.1%	± 0.95%	± 5.1%	± 18%
RMS	86.3	68.9		69.3	
Covariance	1.4×10^{-4}	8.9×10^{-5}		9.0×10^{-5}	

Comment. Fitting the titration data according to 1:2 or 2:1 binding model does not improve the quality of fit, i.e. RMS and covariance are not significantly reduced in comparison to those for 1:1 model. Therefore, binding of ***trans*-3**-(**1-C$_{60}$**) to [10]CPP in PhMe/MeCN (9:1) at room temperature can be best described by the 1:1 binding model.

Supplementary Table 14. Association constants for ***trans*-3**-(**1-C$_{60}$**)/[10]CPP obtained for three independent titrations by fitting the data according to 1:1 binding model. Solvent: PhMe/MeCN (9:1). Fit method: Nelder-Mead. $s/\sqrt{n}$ – standard deviation of the mean, where s – standard deviation, n – number of measurements; $t_{(0.05,\,3)} \times s/\sqrt{n}$ – 95% confidence interval, where $t_{(0.05,\,n-1)}$ – Student's t at 95% confidence level.[12]

$[10CPP]_0$, M	$[$*trans*-3-(1-C$_{60}$$)]_{0,\,final}$, M	K, M^{-1}	Error, %	Average K, M^{-1}	$s/\sqrt{n}$, M^{-1}	$t_{(0.05,\,2)} \times s/\sqrt{n}$, M^{-1}
2.0×10^{-7}	6.2×10^{-6}	3.4×10^5	± 0.75			
2.0×10^{-7}	8.0×10^{-6}	3.8×10^5	± 1.0	**3.6×10^5**	0.1×10^5	$\pm 0.5\times10^5$
2.0×10^{-7}	9.9×10^{-6}	3.7×10^6	± 0.61			

Supplementary Table 15. Links to the raw titration data, calculated fits and statistical information for the titrations.

$[10CPP]_0$, M	Web link
2.0×10^{-7}	http://app.supramolecular.org/bindfit/view/d2ca3801-e472-460e-82a5-080eff9a5d45
2.0×10^{-7}	http://app.supramolecular.org/bindfit/view/fbf30532-1b8b-4bba-aa8f-4e371ecee3a0
2.0×10^{-7}	http://app.supramolecular.org/bindfit/view/bccc0cda-1b70-4606-9be9-0247e793576d

2.18. X-Ray diffraction studies

Single Crystal XRD at Alba Synchrotron (Barcelona)

The crystallographic data of **C_{60}⊂[10]CPP⊂7**·$(BArF)_8$ (**CCDC 1984575**) and ***trans*-3**-(**1**-C_{60})⊂**[10]CPP⊂7**·$(BArF)_8$ (**CCDC 1984576**) were collected at the XALOC beamline of the ALBA synchrotron at 100 K using a MD2M single-axis diffractometer (Maatel, France) and a Pilatus 6 M detector (Dectris, Switzerland).[17] The data sets were collected on omega single-axis scans with 1s per frame exposures at λ = 0.82653 Å. The data were collected in single-axis rotation leading to a low theta fraction value. All crystals were found to diffract only to limited resolution (1.20 - 1.30 Å), and in addition they showed degradation due to radiation damage. This poor diffracting quality and fast degradation is attributed to the solvent loss and severe motion from the solvent and BArF molecules. In addition, the positional disorder of three-shell supramolecular arrangement influences the limited diffracting quality of the crystals, resulting in relatively large final residual values. Nevertheless, the structures were solved using SHELXT[18] and refined by full matrix least-squares based on F^2 using SHELXL97[19] and OLEX2.[20] The position of the atoms belonging to nanocages were clearly located from the electron density maps. Large electron density was also found inside the cages, allowing the assignment of several atomic positions as belonging to the C_{60} and [10]CCP molecules. Based on these coordinates, the entire molecules were introduced and refined with the use of rigid-body restrains, leading to stable refinements. Both C_{60} and [10]CCP molecules are statistically disordered over two positions inside the nanocages, with half occupancy in each case. Attempts to locate and refine solvent molecules and BArF anions were unsuccessful, and therefore a solvent mask was applied to complete the refinements.[21]

Single Crystal XRD - BRUKER SMART APEX CCD

Dark blue crystals of $[Cu_2(Me_2pTp)(OTf)_2](OTf)_2$ (**CCDC 1984937**) were grown from slow diffusion of diethyl ether in a CH_3CN solution of the compound, and used for low temperature (100(2) K) X-ray structure determination. The measurement was carried out on a *BRUKER SMART APEX CCD* diffractometer using graphite-monochromated Mo *K*□ radiation (□□= 0.71073 Å) from an X-ray tube. The measurements were made in the range 2.8247 to 27.4162° for θ. Hemi-sphere data collection was carried out with ω and φ scans. A total of 50450 reflections were collected of which 4151 [R(int) = 0.063] were unique. Programs used: data collection, Smart;[22] data reduction, Saint+;[23] absorption correction, SADABS.[24] Structure solution and refinement was done using SHELXTL.[25] The structure was

solved by direct methods and refined by full-matrix least-squares methods on F^2. The non-hydrogen atoms were refined anisotropically. The H-atoms were placed in geometrically optimized positions and forced to ride on the atom to which they are attached.

CheckCIF Alerts and ORTEP crystallographic data

CheckCIF A and B Alerts and their corresponding response:

$[Cu_2(Me_2pTp)(OTf)_2](OTf)_2$: No A or B level alerts

$C_{60}\subset$[10]CPP$\subset$7·$(BArF)_8$
Level A alerts:
THETM01_ALERT_3_A The value of sine(theta_max)/wavelength is less than 0.550
Calculated sin(theta_max)/wavelength = 0.4198
Author Response: No reflections were observed at resolution higher than 1.2A
Level B alerts:
PLAT082_ALERT_2_B High R1 Value ..... 0.17 Report
PLAT084_ALERT_3_B High wR2 Value (i.e. > 0.25) ..... 0.44 Report
Author Response: Severe disorder and limited diffracting quality resulted in high R values
PLAT220_ALERT_2_B NonSolvent Resd 1 C Ueq(max) / Ueq(min) Range 9.6 Ratio;
PLAT241_ALERT_2_B High MainMol Ueq as Compared to Neighbors of N3FA, C6, C7FA, C32, C8CA, C9EA, C2HA, C7WA, C4GA, C86, and
PLAT242_ALERT_2_B Low MainMol Ueq as Compared to Neighbors of Cu4, Cu5, O6,
Author Response: Observed differences in Ueq values are due to disorder and low resolution
PLAT341_ALERT_3_B Low Bond Precision on C-C Bonds ..... 0.02422 Ang.
Author Response: Result of the limited diffraction quality and resolution reached
PLAT731_ALERT_1_B Bond Calc 1.49(3), Rep 1.5(4) ..... 10 su-Rat
C5QA -C7GA 1.555 7.666 ..... # 190 Check
Author Response: due to limited resolution, DFIX was used for some atoms

***trans*-3-(1-C_{60})$\subset$[10]CPP$\subset$7·$(BArF)_8$**

Level A alerts:
THETM01_ALERT_3_A The value of sine(theta_max)/wavelength is less than 0.550
Calculated sin(theta_max)/wavelength = 0.3846
Author Response: No reflections were observed at resoluton higher than 1.3A
PLAT084_ALERT_3_A High wR2 Value (i.e. > 0.25) ..... 0.48 Report
O2AA O2 O6BA O3 O1AA O4 etc.
Author Response: Severe disorder and limited diffracting quality resulted in high R values

Level B alerts:
PLAT082_ALERT_2_B High R1 Value ..... 0.19 Report
Author Response: Severe disorder and limited diffracting quality resulted in high R value
PLAT241_ALERT_2_B High MainMol Ueq as Compared to Neighbors of N2, C8, C7FA, C3QA, C0JA, Check

PLAT242_ALERT_2_B Low MainMol Ueq as Compared to Neighbors of C6, C6FA, C1GA, C6BA, Check
Author Response: Observed differences in Ueq values are due to disorder and low resolution
PLAT341_ALERT_3_B Low Bond Precision on C-C Bonds ..... 0.03264 Ang.
Author Response: Result of the limited diffraction quality and resolution reached
PLAT731_ALERT_1_B Bond Calc 1.65(4), Rep 1.6(7) ..... 10 su-Rat
C5QA -C7GA 1.555 7.666 ..... # 187 Check
Author Response: due to limited resolution, DFIX was used for some atoms

Supplementary Figure 94. ORTEP representation of the asymmetric unit of $[Cu_2(Me_2pTp)(OTf)_2](OTf)_2$ (CCDC code 1984937). Thermal parameters are represented with 50% of probability.

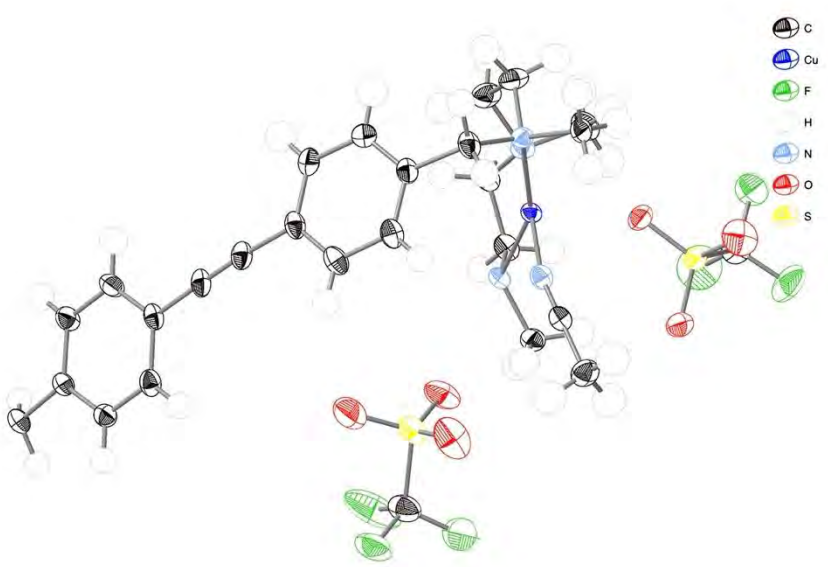

Supplementary Figure 95. ORTEP representation of the asymmetric unit of **C_{60}⊂[10]CPP⊂7**·$(BArF)_8$ (CCDC code 1984575). Thermal parameters are represented with 50% of probability.

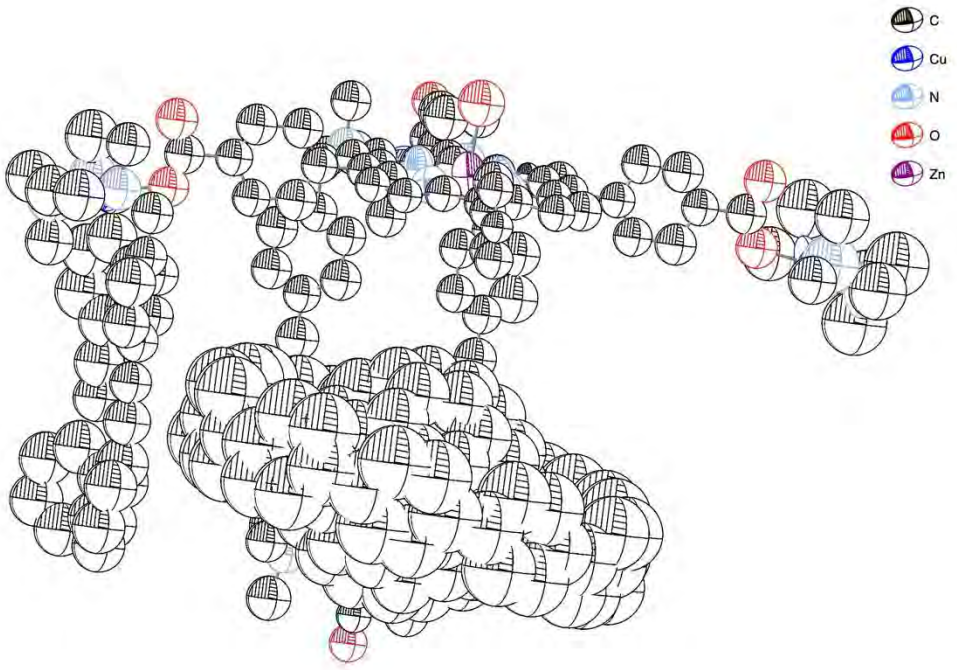

Supplementary Figure 96. ORTEP representation of the asymmetric unit of ***trans*-3**-(**1**-C_{60})⊂**[10]CPP⊂7**·$(BArF)_8$ (CCDC code 1984576). Thermal parameters are represented with 50% of probability.

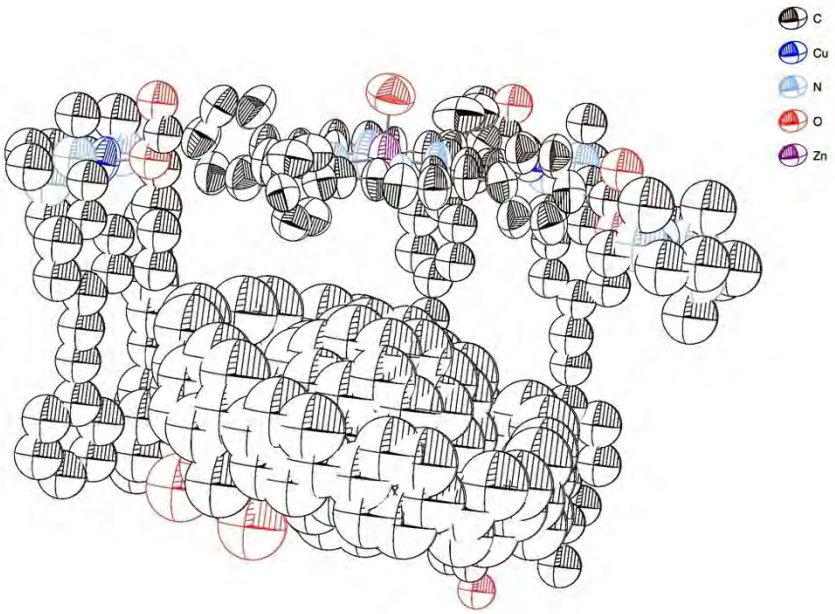

3. Supplementary Tables

Supplementary Table 16. XRD data for $[Cu_2(Me_2pTp)(OTf)_2](OTf)_2$, **$C_{60}$⊂[10]CPP⊂7**·$(BArF)_8$, ***trans*-3-(1-$C_{60}$)⊂[10]CPP⊂7**·$(BArF)_8$.

	$[Cu_2(Me_2pTp)(OTf)_2](OTf)_2$	**C_{60}⊂[10]CPP⊂7·$(BArF)_8$**	***trans*-3-(1-C_{60})⊂[10]CPP⊂7·$(BArF)_8$**
CCDC code	1984937	1984575	1984576
formula	$C_{27}H_{32}CuF_6N_4O_6S_2$	$C_{365}Cu_8F_{0.25}N_{32}O_{18}Zn_2$	$C_{405}Cu_8N_{32}O_{22}Zn_2$
fw	750.22	6143.35 [a)]	6303.43 [a)]
Crystal system	Monoclinic	Monoclinic	Monoclinic
Space group	C 1 2/c 1	*C*2/*c*	*C*2/*c*
a (Å)	27.3228(11)	45.890(9)	45.910(9)
b (Å)	16.6485(7)	45.990(9)	46.090(9)
c (Å)	16.8350(7)	39.660(8)	39.670(8)
α (deg)	90	90	90
β (deg)	125.0820(10)	90.87(3)	90.63(3)
γ (deg)	90	90	90
V (Å^3)	6266.7(5)	83692(29)	83936(29)
Z	8	4	4
Dc (Mg m^{-3})	1.590	0.488 [a)]	0.422 [a)]
T (K)	100	100	100
λ (Å)	0.71073	0.8265	0.8265
μ (mm-1)	0.914	0.422	0.422
2ϑ max (deg)	27.4162	40.60	37.07
reflns collected	50450	25293	127489
indep. reflns	4151	25293	19905
params	419	654	874
GOF on F^2	1.066	1.358	1.905
$R_{indices\ (I>2\sigma(I))}$	0.0642	0.1694	0.1920
$R_{indices\ (all\ data)}$	0.0916	0.1935	0.2109

a) Excluding solvent and BArF molecules

Supplementary Table 17. Diffusion coefficients (D) and solvodynamic radii (r_S) extracted from DOSY NMR in CD_3CN (D_{CD3CN}= $10^{-8.5}$ m^2 s^{-1}).

	D ($m^2 \cdot s^{-1}$)	**r_S (Å)**
4·$(BArF)_8$	3.1 x 10^{-10}	19.0
6·$(BArF)_8$	2.8 x 10^{-10}	22.1
C_{60}⊂[10]CPP⊂6·$(BArF)_8$	2.8 x 10^{-10}	22.1
***trans*-3**-(**1**-C_{60}) ⊂ **[10]CPP⊂6**·$(BArF)_8$	2.9 x 10^{-10}	21.1

4. Supplementary References

1 Xu, Y. *et al.* Concave–Convex π–π Template Approach Enables the Synthesis of [10]Cycloparaphenylene–Fullerene [2]Rotaxanes. *J. Am. Chem. Soc.* **140**, 13413-13420 (2018).

2 Iwamoto, T., Watanabe, Y., Sakamoto, Y., Suzuki, T. & Yamago, S. Selective and Random Syntheses of [n]Cycloparaphenylenes (n = 8–13) and Size Dependence of Their Electronic Properties. *J. Am. Chem. Soc.* **133**, 8354-8361 (2011).

3 Park, K. *et al.* Synthesis of Symmetrical and Unsymmetrical Diarylalkynes from Propiolic Acid Using Palladium-Catalyzed Decarboxylative Coupling. *J. Org. Chem.* **75**, 6244-6251 (2010).

4 Iwamoto, T., Watanabe, Y., Sadahiro, T., Haino, T. & Yamago, S. Size-Selective Encapsulation of C60 by [10]Cycloparaphenylene: Formation of the Shortest Fullerene-Peapod. *Angew. Chem. Int. Ed.* **50**, 8342-8344 (2011).

5 He, D., Du, X., Xiao, Z. & Ding, L. Methanofullerenes, C60(CH2)n (n = 1, 2, 3), as Building Blocks for High-Performance Acceptors Used in Organic Solar Cells. *Org. Lett.* **16**, 612-615 (2014).

6 Bingel, C. Cyclopropanierung von Fullerenen. *Chem. Ber.* **126**, 1957-1959 (1993).

7 Jin, B., Shen, J., Peng, R., Zheng, R. & Chu, S. Efficient cyclopropanation of [60]fullerene starting from bromo-substituted active methylene compounds without using a basic catalyst. *Tetrahedron Lett.* **55**, 5007-5010 (2014).

8 Hirsch, A., Lamparth, I. & Karfunkel, H. R. Fullerene Chemistry in Three Dimensions: Isolation of Seven Regioisomeric Bisadducts and Chiral Trisadducts of C60 and Di(ethoxycarbonyl)methylene. *Angew. Chem. Int. Ed. Eng.* **33**, 437-438 (1994).

9 García-Simón, C. *et al.* Sponge-like molecular cage for purification of fullerenes. *Nat. Commun.* **5**, 5557 (2014).

10 Djojo, F., Herzog, A., Lamparth, I., Hampel, F. & Hirsch, A. Regiochemistry of Twofold Additions to [6,6] Bonds in C60: Influence of the Addend-Independent Cage Distortion in 1,2-Monoadducts. *Chem. Eur. J.* **2**, 1537-1547 (1996).

11 Colomban, C. *et al.* Self-Assembled Cofacial Zinc–Porphyrin Supramolecular Nanocapsules as Tuneable 1O2 Photosensitizers. *Chem. Eur. J.* **24**, 4371-4381 (2018).

12 Brynn Hibbert, D. & Thordarson, P. The death of the Job plot, transparency, open science and online tools, uncertainty estimation methods and other developments in supramolecular chemistry data analysis. *Chem. Commun.* **52**, 12792-12805 (2016).

13 Thordarson, P. Determining association constants from titration experiments in supramolecular chemistry. *Chem. Soc. Rev.* **40**, 1305-1323 (2011).

14 Thordarson, P. Binding Constants and their Measurement, in *Supramolecular Chemistry* doi: 10.1002/9780470661345.smc9780470661018 (2012).

15 Cai, K. *et al.* Molecular Russian dolls. *Nat. Commun.* **9**, 5275 (2018).

16 Thordarson, P. *et al.* Allosterically Driven Multicomponent Assembly. *Angew. Chem. Int. Ed.* **43**, 4755-4759 (2004).

17 Juanhuix, J. *et al.* Developments in optics and performance at BL13-XALOC, the macromolecular crystallography beamline at the Alba Synchrotron. *J. Synchrotron Rad.* **21**, 679-689 (2014).

18 Sheldrick, G. SHELXT - Integrated space-group and crystal-structure determination. *Acta Cryst. A* **71**, 3-8 (2015).

19 Sheldrick, G. Crystal structure refinement with SHELXL. *Acta Cryst. C* **71**, 3-8 (2015).

20 Dolomanov, O. V., Bourhis, L. J., Gildea, R. J., Howard, J. A. K. & Puschmann, H. OLEX2: a complete structure solution, refinement and analysis program. *J. Appl. Cryst.* **42**, 339-341 (2009).

21 Spek, A. Structure validation in chemical crystallography. *Acta Cryst. D* **65**, 148-155 (2009).

22 Bruker Advanced X-ray Solutions. SMART: Version 5.631, 1997-2002.

23 Bruker Advanced X-ray Solutions. SAINT +, Version 6.36A, 2001.

24 Sheldrick, G. M. Empirical Absorption Correction Program, Universität Göttingen, 1996. Bruker Advanced X-ray Solutions. SADABS Version 2.10, 2001.

25 Sheldrick, G. M. Program for Crystal Structure Refinement, Universität Göttingen, 1997 Bruker Advanced X-ray Solutions. SHELXTL Version 6.14, 2000-2003. SHELXL-2013 (Sheldrick, 2013).

Annex 2. Supporting information Chapter III

Supramolecular purification of C_{84} from fullerene extract

Ernest Ubasart,[a] Cristina García-Simón,[a] Míriam Pujals,[a] Karam Asad,[b] Nikos Chronakis,[b] Teodor Parella,[c] Xavi Ribas[a,*]

TABLE OF CONTENTS

1. Supplementary Methods

1.1. Materials and Instrumentation

Reagents and solvents were purchased from commercial sources and used without further purification unless otherwise stated. NMR data were collected on a Bruker 400 MHz AVANCE spectrometer in $CDCl_3$ or CD_3CN, and calibrated relative to the residual protons of the solvent. ESI-MS measurements were performed on a Bruker MicroTOF-Q-II using $CDCl_3$ or CH_3CN as a mobile phase. HPLC analysis of fullerenes was performed on an Agilent series 1200 chromatograph equipped with a Cosmosil Buckyprep-M column, or on a LC-9130 NEXT apparatus (Japan Analytical Industry Co.Ltd.) with monitoring at 320 nm and using toluene as an eluent at a flow rate of 0.5 ml/min. MALDI-TOF measurements were performed on a Bruker Daltonics Autoflex maX using DCTB and NaTFA as matrix. UV-Vis spectra were recorded on an Agilent 8452 UV-Vis spectrophotometer using a 1 cm quartz cell and CH_3CN as a solvent. Fullerene extract (70% C_{60}, 28% C_{70} and 2% higher fullerenes) was purchased from SES Research and used as received. Azafullerene $(C_{59}N)_2$ and nanocapsules **6**·$(BArF)_8$ and **7**·$(BArF)_8$ were prepared according to reported procedures.[1-3]

1.2. Synthesis and characterization of dialdehyde (ppp)

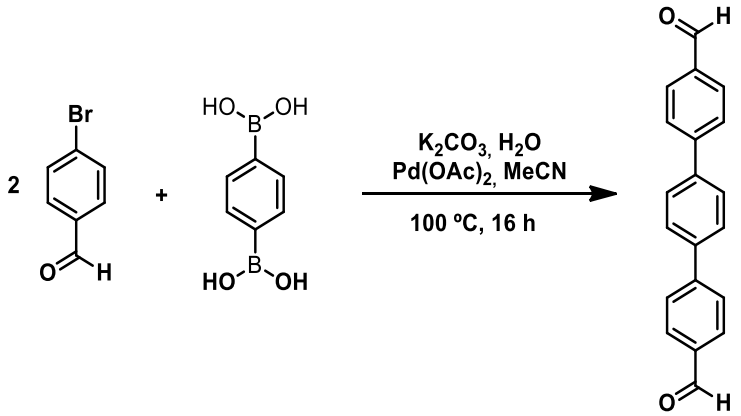

Supplementary Figure 1. Synthesis of (1,1':4',1''-terphenyl)-4,4''-dicarbaldehyde (ppp).

(1,1':4',1''-terphenyl)-4,4''-dicarbaldehyde (ppp) was synthetized following reported procedures.[4] 4-Bromobenzaldehyde (2.0 g, 1 mmol) was added in a 100 ml round-bottom flask. Benzene-1,4-diboronic acid (0.9 g, 0.6 mmol) dissolved in 16 ml of acetonitrile was then added followed by the addition of K_2CO_3 (1.8 g, 2.4 mmol) dissolved in 26 ml of milliQ water. Finally, $Pd(OAC)_2$ (0.12 g, 0.1 mmol) was added and the reaction mixture was heated

at 110 ºC for 16 h. After this time, 50 ml of water were added and the product was extracted with dichloromethane (3 x 20 ml). The organic phases were combined, dried over anhydrous $MgSO_4$ and filtered. The remaining solution was dried under vacuum and the product was obtained as a pale-yellow solid. (Yield: 80%).

^{1}H-NMR (400 MHz, $CDCl_3$) δ ppm: 10.08 (s, 2H, -CH), 7.99 (d, J=8.4 Hz, 4H, arom), 7.82 (d, J=8.2 Hz, 4H, arom), 7.77 (s, 4H, arom).

^{13}C-NMR (100 MHz, $CDCl_3$) δ ppm: 192.0 (C=O), 146.4 (C arom), 139.9 (C arom), 135.6 (C arom), 130.5 (CH arom), 128.2 (CH arom), 127.8 (CH arom).

HRMS (*m/z*): calculated 309.0889, found 309.0886 for ({diarylalkyne-ppp + Na}$^{+1}$); calculated 327.0998, found 327.0992 for ({diarylalkyne-ppp + H_2O + Na}$^{+1}$), calculated 341.1154, found 341.1148 for ({diarylalkyne-ppp + CH_3OH + Na}$^{+1}$).

1.3. Synthesis and characterization of S_2ppp

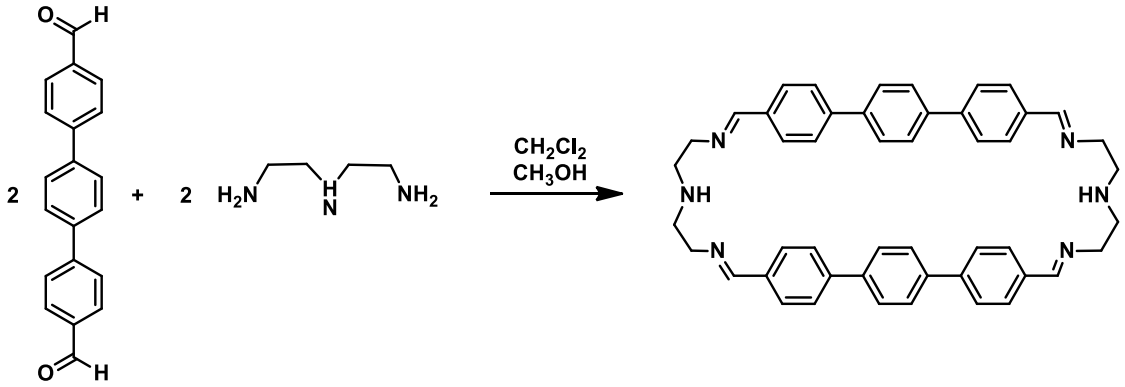

Supplementary Figure 2. Synthesis of the S_2ppp macrocycle.

(1,1':4',1''-terphenyl)-4,4''-dicarbaldehyde (0.78 g, 1 mmol) was dissolved in 250 ml of DCM and charged in a 250 ml addition funnel. Then, diethylenetriamine (294 µl, 1 mmol) was added in a 500 ml round-bottom flask containing 250 ml of MeOH. The dialdehyde solution was added dropwise into the amine solution during a period of 6 h and stirred for 16 h. After this time, a white solid was obtained.

^{1}H-NMR (400 MHz, $CDCl_3$) δ ppm: 8.35 (s, 4H, arom), 7.60 (d, J=8.3 Hz, 8H, arom), 7.49 (s, 8H, arom), 7.47 (d, J=8.3 Hz, 8H, arom), 3.84-3.82 (m, 8H, CH_2), 3.04-3.02 (m, 8H, CH_2).

^{13}C-NMR (100 MHz, $CDCl_3$) δ ppm: 162.0 (C sp^2 imine), 142.3 (C arom), 139.5 (C arom), 135.2 (C arom), 128.7 (CH arom), 127.5 (CH arom), 127.0 (CH arom), 60.1 (-CH_2-), 48.7 (-CH_2-).

HRMS (*m/z*): calculated 354.1965, found 354.1975 for ({S_2ppp + H}$^{+2}$); calculated 707.3857, found 707.3868 for ({S_2ppp + H}$^{+1}$).

1.4. Synthesis and characterization of H_2ppp

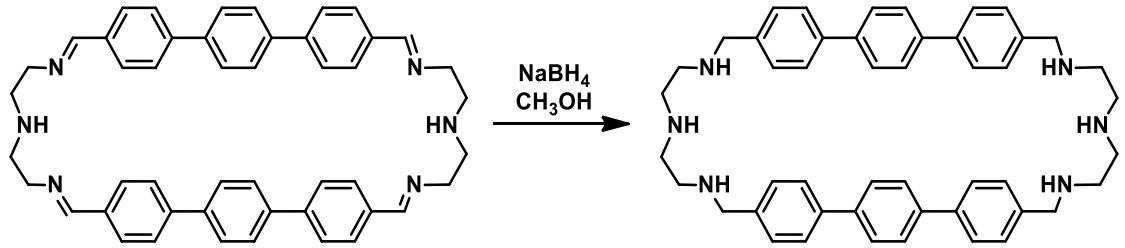

Supplementary Figure 3. Synthesis of H_2ppp.

$NaBH_4$ (0.52 g, 10 mmols) was added into a S_2ppp solution in methanol and the reaction mixture was stirred for 16 h. After this time, 20 ml of an acid solution (HCl:H_2O 1:10) were added and the crude reaction mixture was stirred for 45 minutes. Then, the solution was evaporated under reduced pressure until a constant volume and 100 ml of H_2O were added. The product was extracted with $CHCl_3$ (3 x 50 ml) and the organic phases were combined, dried over anhydrous $MgSO_4$ and filtered. The remaining solution was dried under vacuum to afford the product as a white solid. (Yield: 87%).

^{1}H-NMR (400 MHz, $CDCl_3$) δ ppm: 7.54 (s, 8H, arom), 7.51 (d, J=8.2 Hz, 8H, arom), 7.37 (d, J=8.2 Hz, 8H, arom), 3.84 (s, 8H, CH_2), 2.93-2.85 (m, 16H, CH_2).

^{13}C-NMR (100 MHz, $CDCl_3$) δ ppm: 139.8 (C arom), 139.6 (C arom), 139.2 (C arom), 128.7 (CH arom), 127.4 (CH arom), 127.0 (CH arom), 53.7 (-CH_2-), 49.1 (-CH_2-), 48.4 (-CH_2-).

HRMS (*m/z*): calculated 358.2278, found 358.2281 for ({H_2ppp + H}$^{+2}$); calculated 715.4483, found 715.4493 for ({H_2ppp + H}$^{+1}$).

1.5. Synthesis and characterization of Me_2ppp

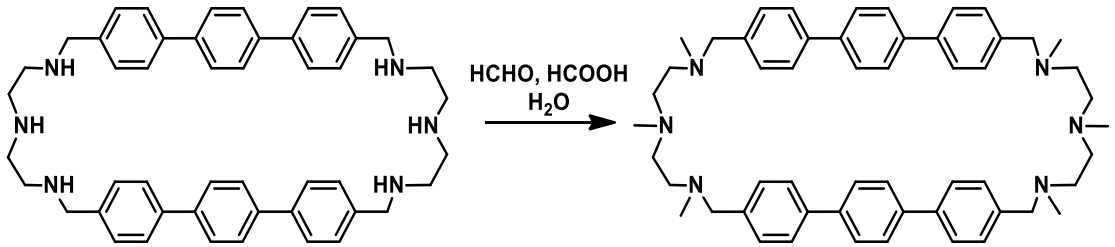

Supplementary Figure 4. Synthesis of the macrocyclic ligand, Me_2ppp.

H_2ppp (0.97 g, 1 mmol) were added to a 100 ml round-bottom flask and mixed with 12 ml of formaldehyde, 10 ml of formic acid and 20 ml of water. The resulting mixture was heated at reflux for a period of 16 h. After this time, the reaction mixture was cooled to room temperature and the solvent was removed under reduced pressure. Then, 50 ml of NaOH

1M were added and the product was extracted with $CHCl_3$ (3 x 25 ml). The organic phases were combined, dried over anhydrous $MgSO_4$ and filtered. The remaining solution was dried under vacuum and the product was purified by recrystallization with acetone. (Yield: 80%).
^{1}H-NMR (400 MHz, $CDCl_3$) δ ppm: 7.48 (s, 8H, arom), 7.46 (d, J=8.2 Hz, 8H, arom), 7.32 (d, J=8.2 Hz, 8H, arom), 3.51 (s, 8H, CH_2), 2.59-2.53 (m, 16H, CH_2), 2.31 (s, 6H, CH_3), 2.24 (s, 12H, CH_3).
^{13}C-NMR (100 MHz, $CDCl_3$) δ ppm: 139.6 (C arom), 139.3 (C arom), 138.3 (C arom), 129.7 (CH arom), 127.3 (CH arom), 126.8 (CH arom), 62.3 (-CH_2-), 54.8 (-CH_2-), 54.6 (-CH_2-), 43.8 (-CH_3), 43.1 (-CH_3).
HRMS (*m/z*): calculated 400.2747, found 400.2741 for ({Me_2ppp + H}$^{+2}$); calculated 799.5422, found 799.5421 for ({Me_2ppp + H}$^{+1}$).

1.6. Synthesis and characterization of dinuclear Pd^{II} molecular clip $[Pd_2(Me_2ppp)(AcO)_2](OTf)_2$

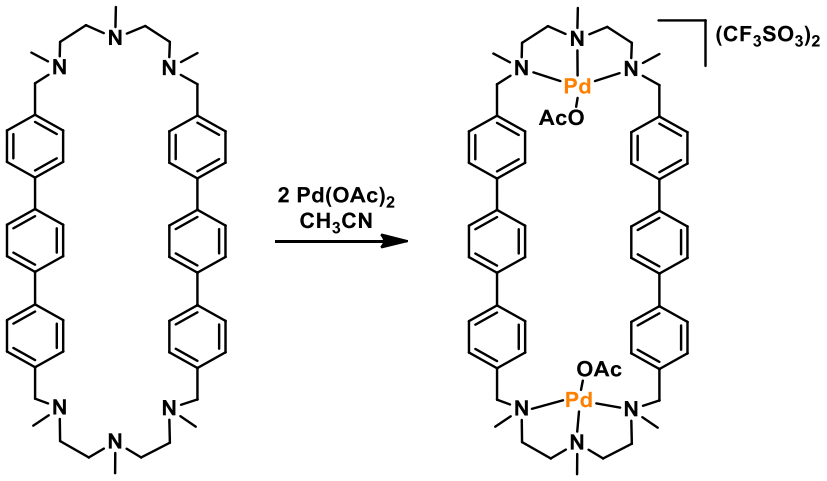

Supplementary Figure 5. Synthesis of $[Pd_2(Me_2ppp)(AcO)_2](OTf)_2$.

In a 250 ml round-bottom flask, Me_2ppp (0.172 g, 1 mmol), $Pd(AcO)_2$ (0.101 g, 2.1 mmols) and 85 ml of anhydrous CH_3CN were mixed. The mixture was heated at reflux under a nitrogen atmosphere for 16h. After this time, the reaction mixture was cooled to room temperature. Subsequently, an excess of CF_3SO_3Na salt was added (4.2 mmols) and the mixture was stirred vigorously for 8h. The mixture was concentrated to the half of the volume under reduced pressure, filtered through Celite and recrystallized by slow diffusion of diethyl ether. The product was obtained as a yellow crystalline solid. (Yield: 86%).
^{1}H-NMR (400 MHz, CD_3CN) δ ppm: 8.34 (d, J=8.2 Hz, 8H, arom), 8.25 (d, J=8.2 Hz, 8H, arom), 8.08 (d, J=8.2 Hz, arom), 7.99 (d, J=8.2 Hz, arom), 7.90 (s, 8H, arom), 7.82 (s, 8H, arom), 4.05

(dd, 8H, CH_2), 3.64-3.57 (m, 8H, CH_2), 3.32 (s, 12H, CH_3), 3.30 (s, 12H, CH_3), 3.24-3.15 (m, 8H, CH_2), 3.09 (dd, 8H, CH_2), 2.36-2.28 (m, 16H, CH_2), 2.09 (s, 6H, AcO), 2.08 (s, 6H, AcO), 1.41 (s, 6H, CH_3), 1.35 (s, 6H, CH_3).

^{13}C-NMR (100 MHz, $CDCl_3$) δ ppm: 177.8 (C=O, AcO), 177.8 (C=O, AcO), 141.5 (arom), 141.3 (arom), 140.1 (arom), 139.9 (arom), 134.2 (arom), 134.1 (arom), 133.7 (arom), 133.6 (arom), 128.5 (arom), 128.3 (arom), 128.2 (arom), 128.1 (arom), 123.6 (CF_3SO_3), 120.5 (CF_3SO_3), 65.8 (-CH_2-), 65.7 (-CH_2-), 61.2 (-CH_2-), 59.3 (-CH_2-), 59.2 (-CH_2-), 51.4 (-CH_3), 51.2 (-CH_3), 44.0 (-CH_3), 43.8 (-CH_3), 24.7 (-CH_3, AcO), 24.6 (-CH_3, AcO).

HRMS (*m/z*): calculated 565.1851, found 565.1864 for ({$Pd_2(Me_2ppp)(AcO)_2$}$^{+2}$); calculated 1279.3226, found 1279.3247 for ({$Pd_2(Me_2ppp)(AcO)_2(CF_3SO_3)_1$}$^{+1}$).

1.7. Synthesis and characterization of dinuclear Cu^{II} molecular clip $[Cu_2(Me_2ppp)(OTf)_2](OTf)_2$

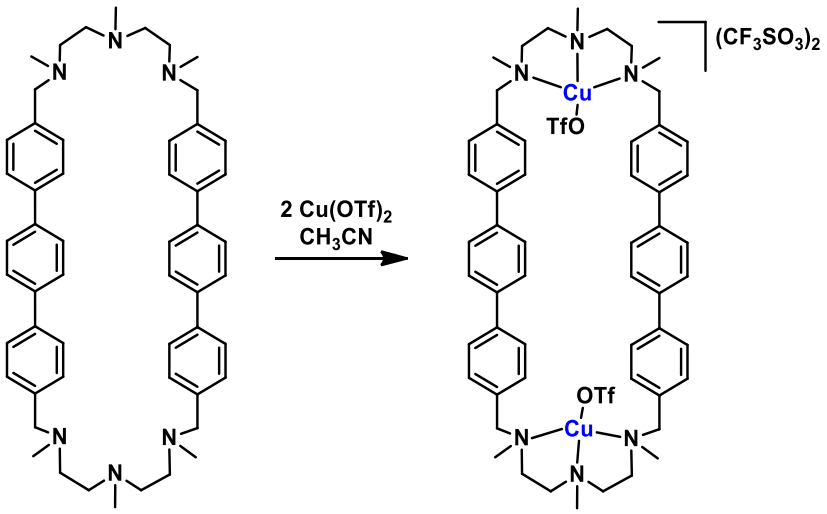

Supplementary Figure 6. Synthesis of $[Cu_2(Me_2ppp)(OTf)_2](OTf)_2$.

In a 20 ml glass vial, Me_2ppp (0.095 g, 1 mmol) and $Cu(CF_3SO_3)_2$ (0.090 g, 2 mmols) were dissolved in 8.5 ml of CH_3CN. The mixture was stirred at room temperature for 16 h. After this time, the reaction crude was filtered through Celite and recrystallized by slow diffusion of diethyl ether. The product was obtained as a blue crystalline solid. (Yield: 93%).

HRMS (*m/z*): calculated 612.1478, found 612.1465 for ({$Cu_2(Me_2ppp)(CF_3SO_3)_2$}$^{+2}$); calculated 1373.2481, found 1373.2401 for ({$Cu_2(Me_2ppp)(CF_3SO_3)_3$}$^{+1}$).

1.8. Synthesis and characterization of Pd^{II}-based tetragonal prismatic nanocapsule 8·$(BArF)_8$

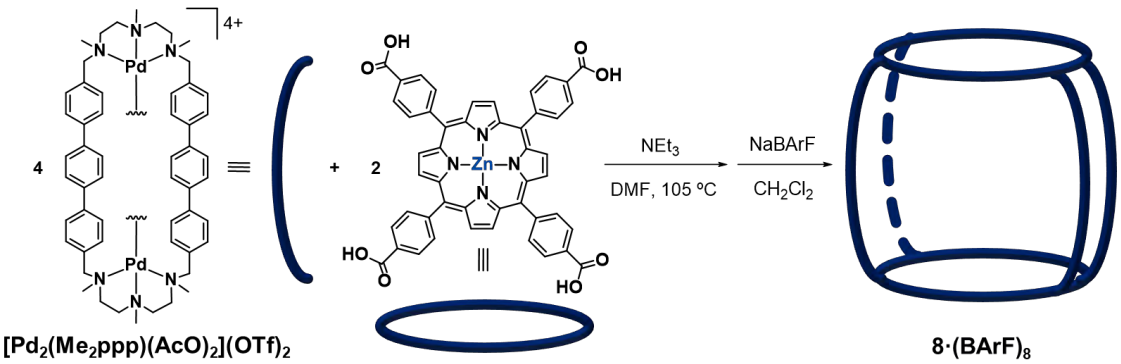

Supplementary Figure 7. Schematic representation for the synthesis of **8**·$(BArF)_8$ nanocapsule.

5,10,15,20-tetrakis(4-carboxyphenyl)porphyrin-Zn^{II} (0.09 g, 2 mmols) were added in a 50 ml round-bottom flask and dissolved in 8 ml of DMF. Then, 76 µl of triethylamine dissolved in 4 ml of DMF were added to the porphyrin solution. Finally, molecular clip $[Pd_2(Me_2ppp)(AcO)_2](CF_3SO_3)_2$ (0.23 g, 4 mmols) was dissolved in 20 ml of DMF were added to the reaction mixture and the solution was heated at 105 °C under reflux for 24 h. The reaction crude was cooled to room temperature, filtered through Celite and recrystallized by diffusion of diethyl ether. The **8**·$(CF_3SO_3)_8$ crystalline solid obtained was suspended in 12 ml of DCM, an excess of NaBArF salt was added (6 to 10 mmols) and the mixture was stirred vigorously for 16 h. The mixture was filtered through Celite and the product was obtained by precipitation by slow diffusion of diethyl ether. (Yield: 72%).

^{1}H-NMR (400 MHz, CD_3CN) δ ppm: 8.71 (s, 16H, pyrrole ring), 8.63 (d, J=8.2 Hz, 8H, arom-porph), 8.41 (d, J=8.2 Hz, 8H, arom-porph), 8.25 (d, J=8.2 Hz, 32H, arom-clip), 8.21 (d, 8H, arom-porph), 8.12 (d, 8H, arom-porph), 8.05 (d, J=8.2 Hz, 32H, arom-clip), 7.76 (s, 32H, arom-clip), 7.68-7.65 (m, 96H, $BArF^-$), 4.07 (d, J=13 Hz, 16H, -CH_2-), 3.69 (m, 16H, -CH_2-), 3.59 (s, 48H, N-CH_3), 3.15 (d, J=13 Hz, 16H, -CH_2-), 2.47 (dd, J=13.5 Hz, 16H, -CH_2-), 2.39 (dd, J=13.5 Hz, 16H, -CH_2-), 1.56 (s, 24H, N-CH_3).

^{13}C-NMR (100 MHz, $CDCl_3$) δ ppm: 161.9 (BArF), 149.6 (pyrrole ring), 134.7 (BArF), 134.0 (arom-porph), 133.0 (arom-clip), 131.5 (pyrrole ring), 127.4 (arom-porph), 127.4 (arom-clip), 125.8 (arom-porph), 123.1 (arom-clip), 117.3 (BArF), 64.5 (-CH_2-), 60.0 (-CH_2-), 58.4 (-CH_2-), 51.5 (-CH_3), 43.1 (-CH_3).

HRMS (*m/z*): calculated 718.4442, found 718.4405 for ([**8**·$(BArF)_0$]$^{+8}$); calculated 944.3744, found 944.3704 for ([**8**·$(BArF)_1$]$^{+7}$); calculated 1245.6147, found 1245.6103 for ([**8**·$(BArF)_2$]$^{+6}$); calculated 1667.5511, found 1667.5432 for ([**8**·$(BArF)_3$]$^{+5}$); calculated 2300.2057, found 2300.1789 for ([**8**·$(BArF)_4$]$^{+4}$).

1.9. Synthesis and characterization of Cu^{II}-based tetragonal prismatic nanocapsule $9\cdot(BArF)_8$

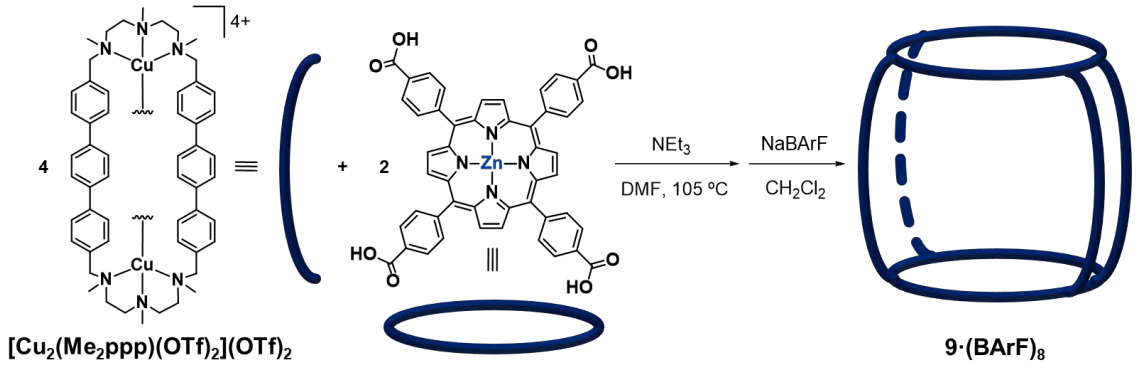

Supplementary Figure 8. Schematic representation for the synthesis of **9**·$(BArF)_8$ nanocapsule.

5,10,15,20-tetrakis(4-carboxyphenyl)porphyrin-Zn^{II} (9.2 mg, 2 mmols) was weighted in a 20 ml glass vial and dissolved in 1.0 ml of DMF. Then, 7.5 µl of triethylamine dissolved in 0.5 ml of DMF were added to the porphyrin solution. Finally, molecular clip $[Cu_2(Me_2ppp)(CF_3SO_3)_2](CF_3SO_3)_2$ (24.6 mg, 4 mmols) was dissolved in 2.5 ml of DMF were added to the mixture and the solution was stirred at room temperature for 16 h. The reaction crude was filtered through Celite and recrystallized by diethyl ether diffusion. Product **9**·$(CF_3SO_3)_8$ was obtained as a crystalline solid and suspended in 12 ml of DCM. An excess of NaBArF salt was added (6 to 10 mmols) and the mixture was stirred vigorously for 16 h. The mixture was filtered through Celite and the product was obtained by precipitation with slow diffusion of diethyl ether. (Yield: 75%).

HRMS (*m/z*): calculated 675.5940, found 675.5879 for ([**9**·$(BArF)_0]^{+8}$); calculated 895.4028, found 895.3954 for ([**9**·$(BArF)_1]^{+7}$); calculated 1188.4811, found 1188.4734 for ([**9**·$(BArF)_2]^{+6}$); calculated 1598.7908, found 1598.7825 for ([**9**·$(BArF)_3]^{+5}$); calculated 2214.5054, found 2214.4970 for ([**9**·$(BArF)_4]^{+4}$).

1.10. Extract encapsulation procedure

Encapsulation in solution. **X**·$(BArF)_8$ (**X** = 4,6,7,8,9) (15 mg, 1 mmol) was weighted and dissolved in 222 µl of acetonitrile. Then 100 mmols of fullerene extract, containing 60% C_{60}, 28% C_{70} and 2% higher fullerenes, in 2000 µl toluene were added. The mixture was stirred at room temperature for 7 days and analysed by HR-ESI-MS.

Solid state encapsulation. **X**·$(BArF)_8$ (**X** = 4,6,7,8,9) (15 mg, 1 mmol) was weighted. Then 100 mmols of fullerene extract in toluene, containing 60% C_{60}, 28% C_{70} and 2% higher fullerenes, were added. The mixture was stirred at room temperature for 12 hours and analysed by HR-ESI-MS, and then for 7 days and analysed again by HR-ESI-MS.

a. Fullerene extract + 7·$(BArF)_8$

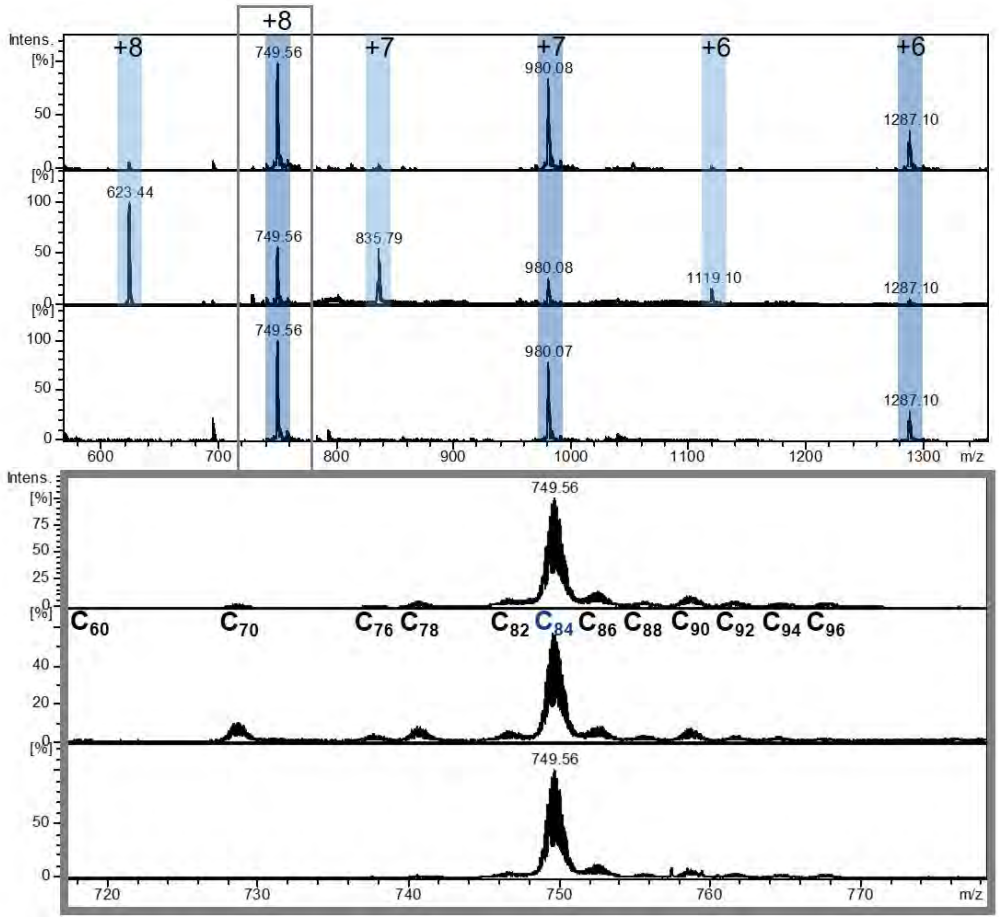

Supplementary Figure 9. HR-MS-ESI. a) **7**·$(BArF)_8$ in solution (toluene:CH_3CN 9:1), 100 eq. of fullerene extract, r.t., 7 days. b) **7**·$(BArF)_8$ in the solid state (suspension in toluene), 100 eq. of fullerene extract, r.t., 12 hours. c) **7**·$(BArF)_8$ in the solid state (suspension in toluene), 100 eq. of fullerene extract, r.t., 7 days.

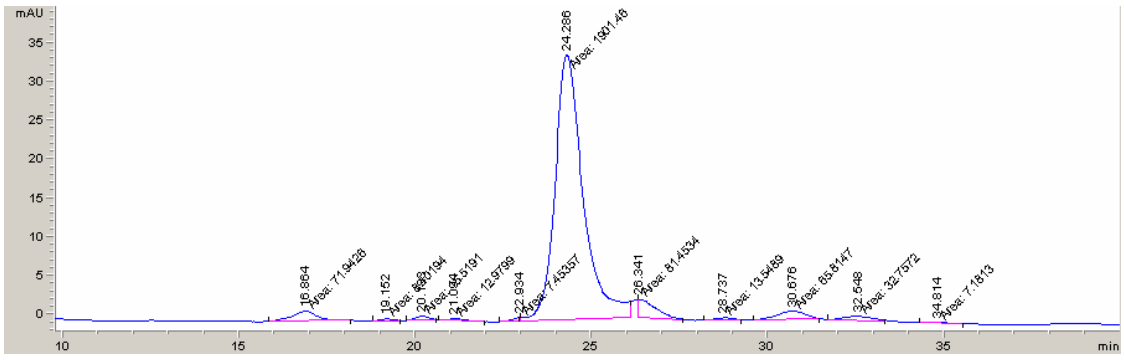

Supplementary Figure 10. HPLC after the addition of 20 eq. of TfOH to **7**·$(BArF)_8$ and solubilizing the C_{84} and other higher fullerenes in toluene.

Supplementary Table 1. HPLC data.

	TIME	AREA	HEIGHT	WIDTH	AREA%	SYMMETRY
1	16.86	71.90	1.30	0.92	3.24	1.07
2	19.15	8.40	0.29	0.49	0.37	0.72
3	20.18	15.50	0.54	0.48	0.70	1.12
4	21.09	13.00	0.30	0.72	0.59	0.56
5	22.93	7.50	0.44	0.28	0.34	0.00
6	**24.29**	**1901.50**	**34.10**	**0.93**	**85.71**	**0.71**
7	26.34	81.50	2.30	0.58	3.67	0.03
8	28.74	13.50	0.36	0.63	0.61	1.03
9	30.68	65.80	1.10	0.99	2.97	1.14
10	32.55	32.80	0.55	0.99	1.48	1.01
11	34.81	7.20	0.14	0.89	0.32	0.71

b. Fullerene extract + 6·$(BArF)_8$

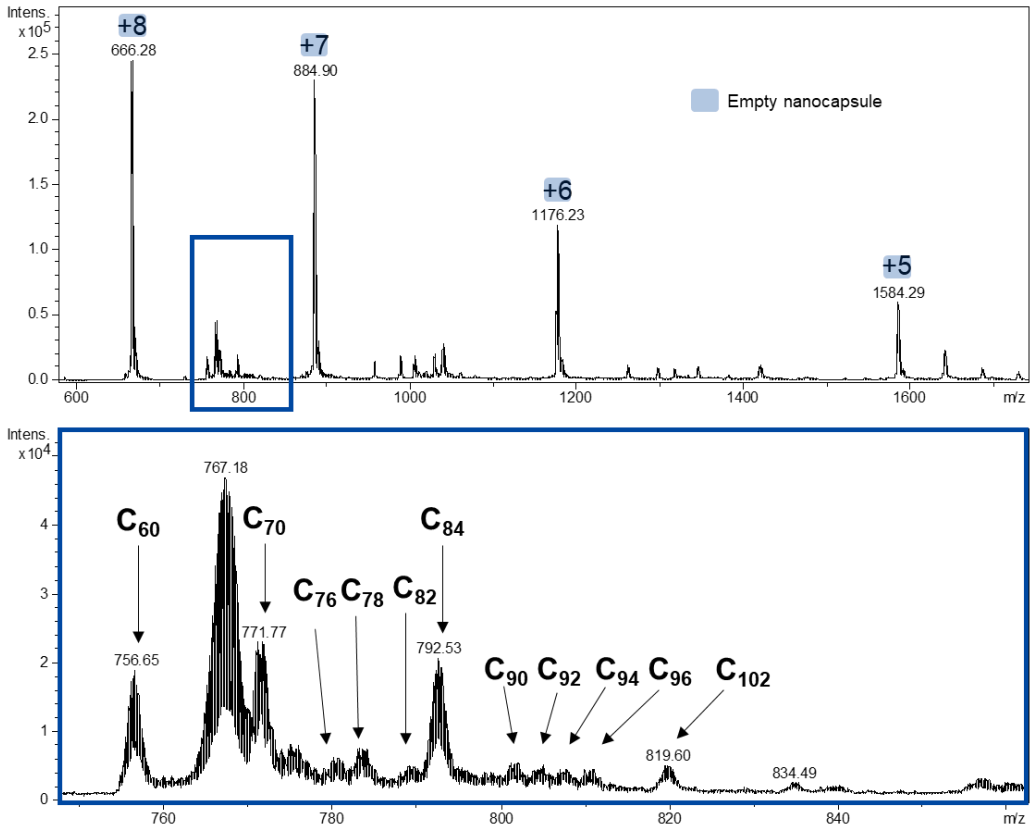

Supplementary Figure 11. HR-MS-ESI after the addition of 100 eq. of fullerene extract to **6**·$(BArF)_8$ at r.t. for 7 days in the solid state (suspension in toluene).

c. Fullerene extract + 8·$(BArF)_8$

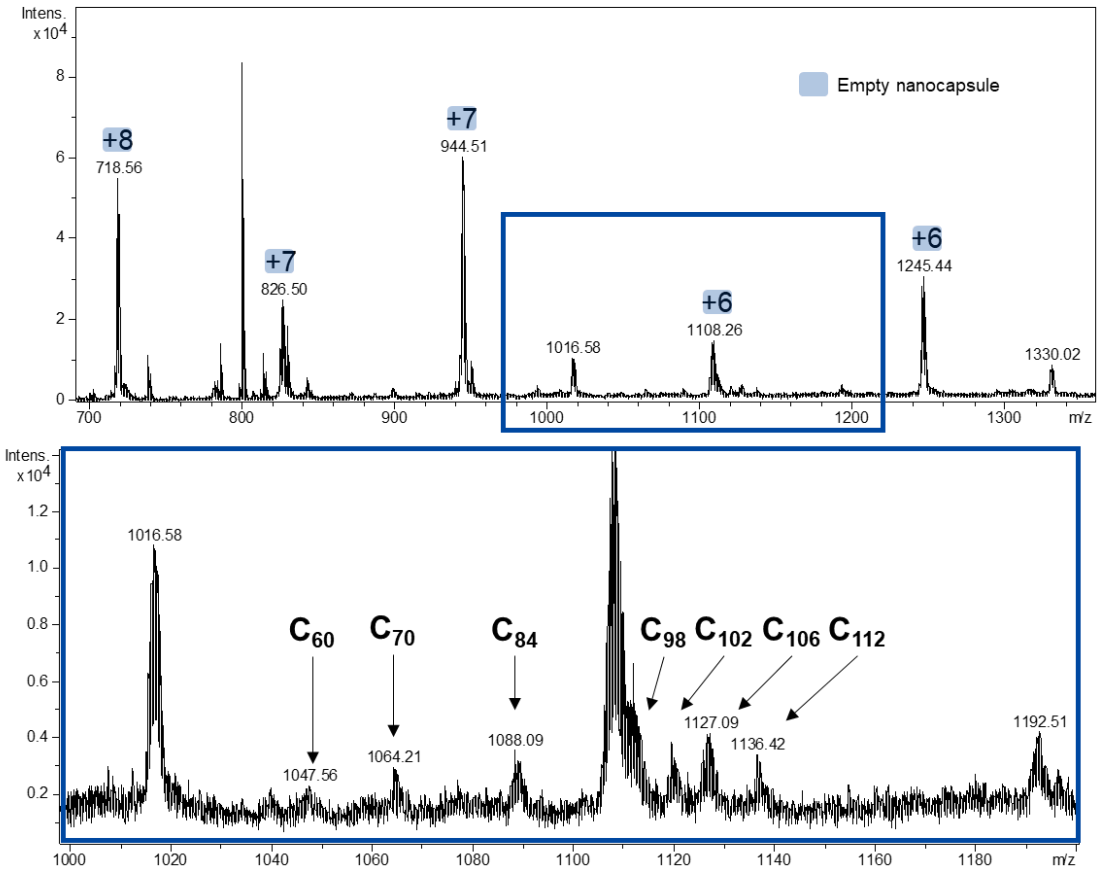

Supplementary Figure 12. HR-MS-ESI after the addition of 100 eq. of fullerene extract to **8**·$(BArF)_8$ at r.t. for 7 days in the solid state (suspension in toluene).

1.11. C_{84} isolation and characterization

a. HPLC-DAD

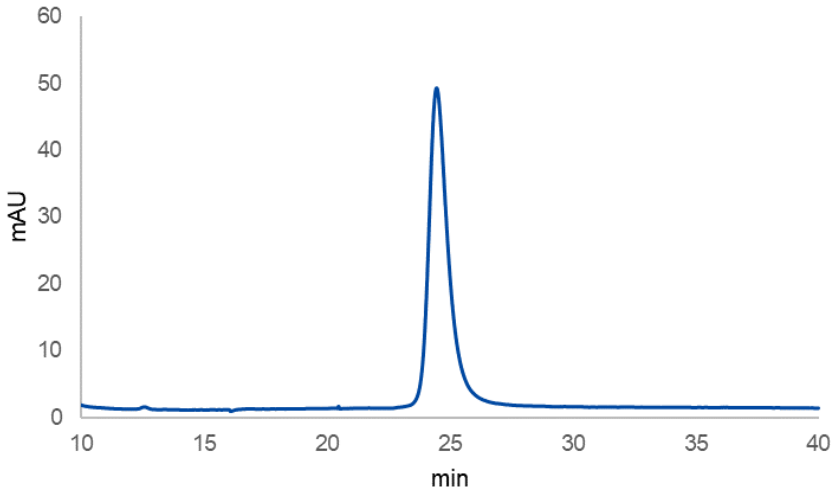

Supplementary Figure 13. HPLC-DAD chromatogram of C_{84} released from nanocapsule **7**·$(BArF)_8$ and collected.

b. UV-Vis

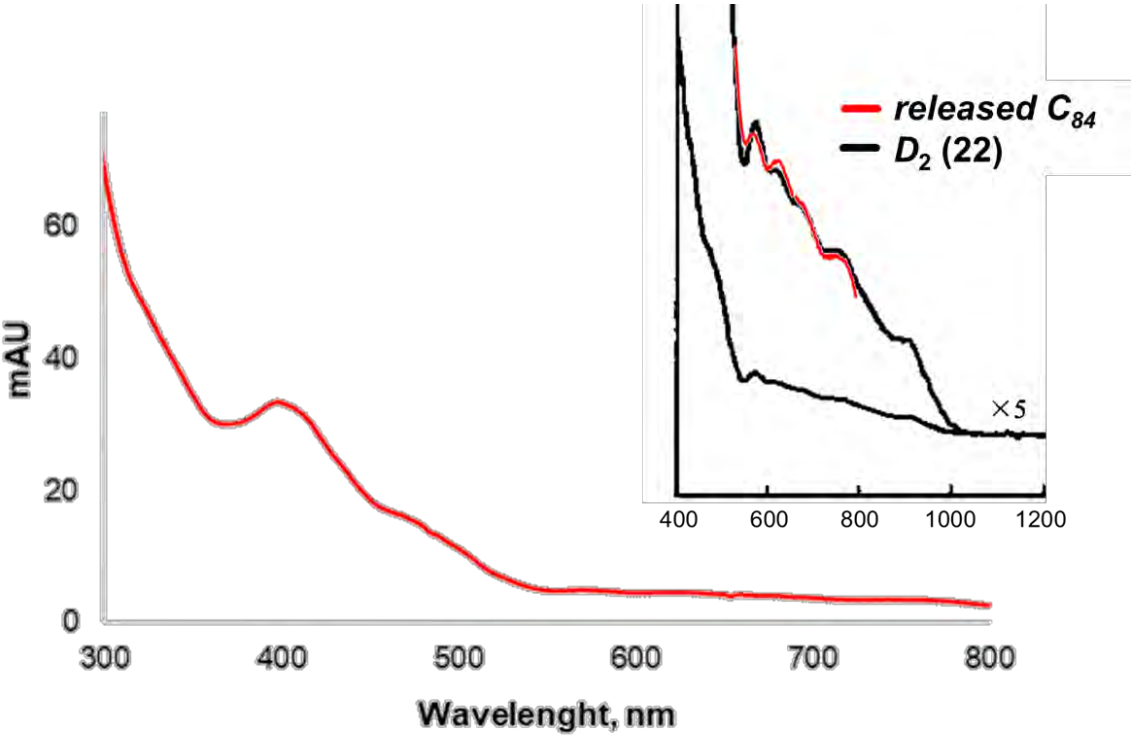

Supplementary Figure 14. (a) UV-Vis spectrum of purified C_{84} and comparison with the reported $D_2(22)$ UV-Vis spectra.

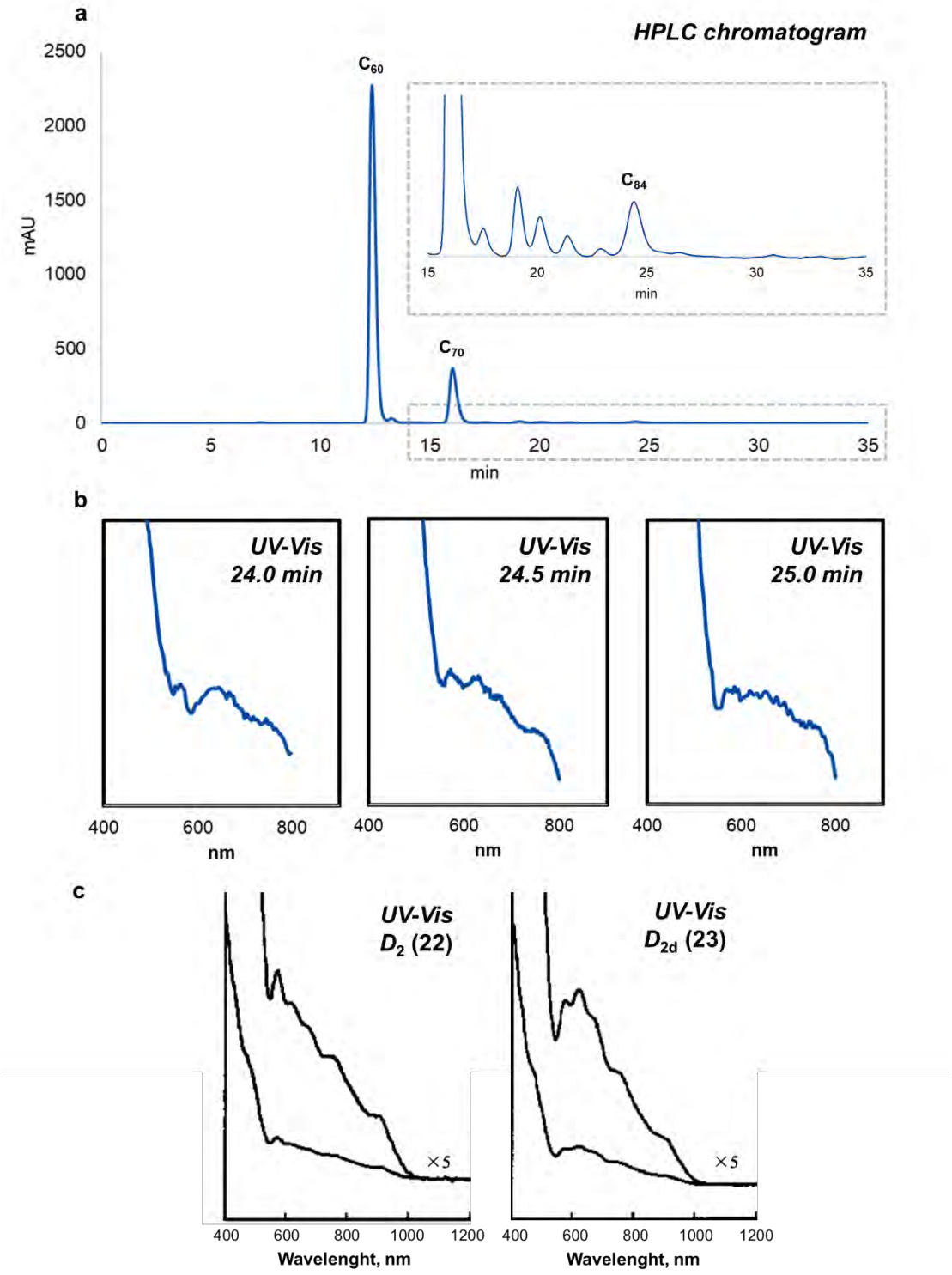

Supplementary Figure 15. (a) HPLC chromatogram of the fullerene extract. (b) UV-Vis spectrum at the head (24.0 min), middle (24.5 min) and tail (25.0 min) of C_{84} peak. (c) UV-Vis spectrum of the reported D_2 (22) and D_{2d} (23) isomers.

c. MALDI-TOF

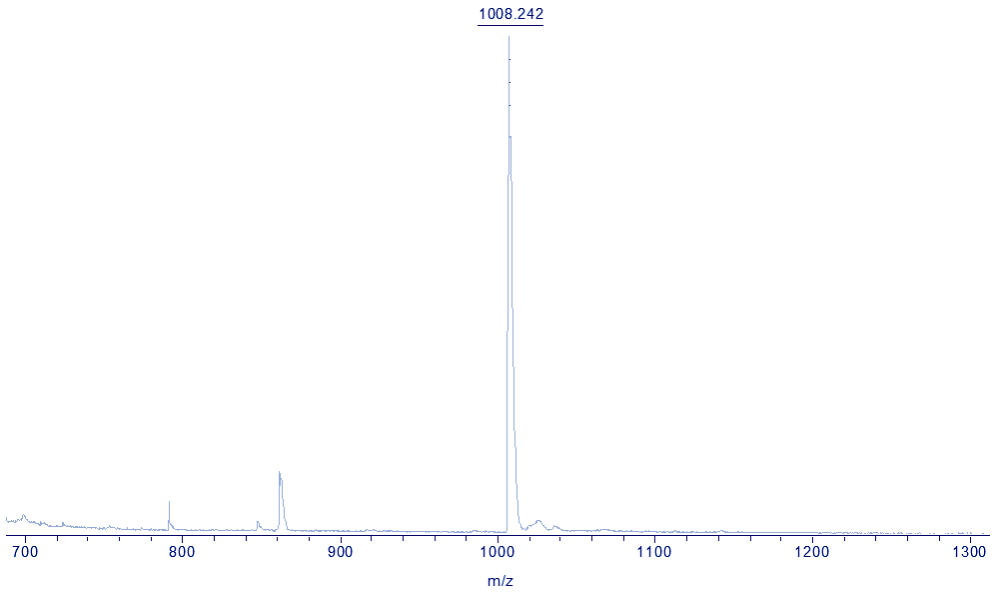

Supplementary Figure 16. MALDI-TOF spectrum of purified C_{84}.

d. ^{13}C-NMR

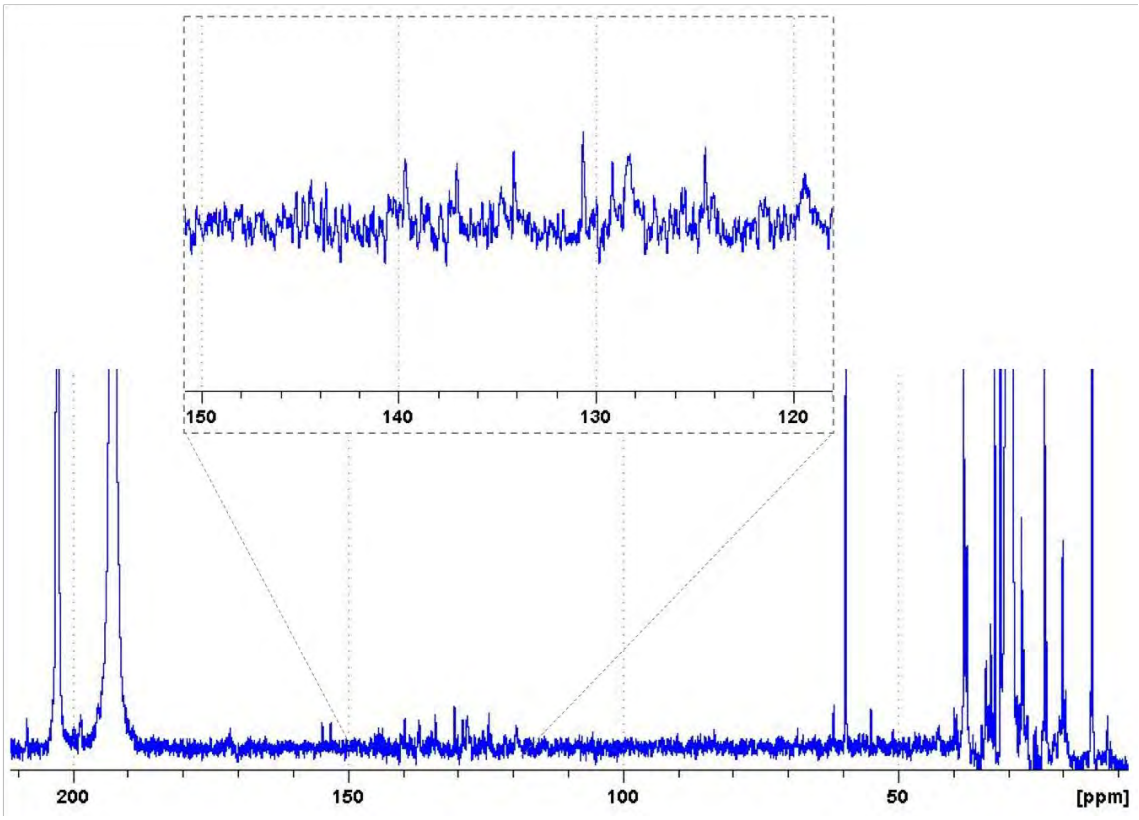

Supplementary Figure 17. ^{13}C-NMR spectrum of the purified C_{84} registered with a 500 MHz NMR (equipped with a cryoprobe) for 3 days (1.6·x 105 scans, CS_2:acetone-d6, 40 mM $Cr(acac)_3$ as relaxing agent, d1 = 2s)."

e. C_{84}⊂**7**·$(BArF)_8$

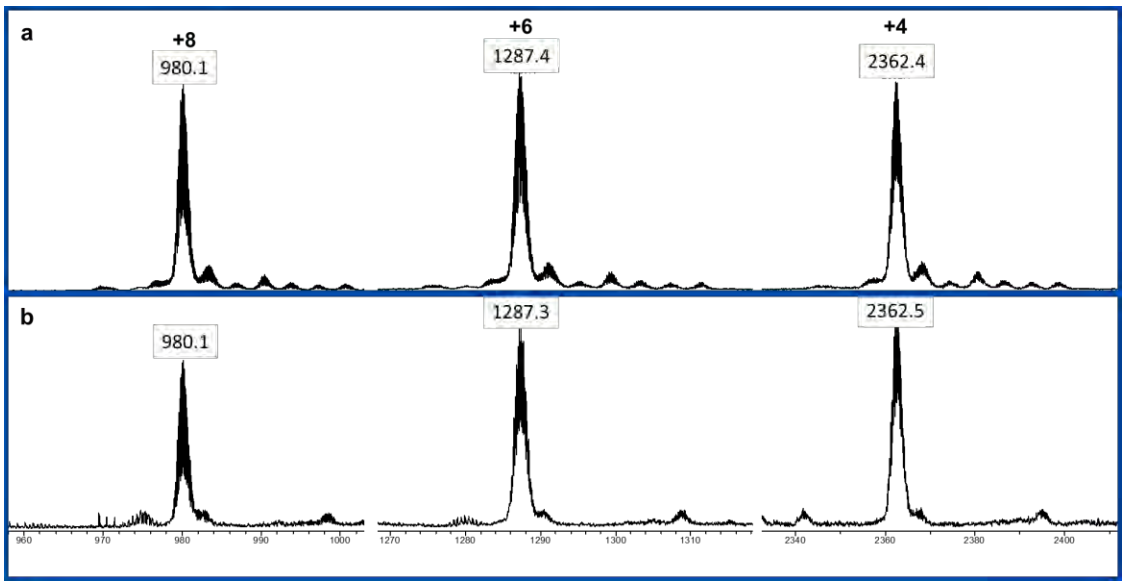

Supplementary Figure 18. HR-MS-ESI after encapsulation of fullerene extract (a) and after encapsulation of the purified C_{84} to **7**·$(BArF)_8$ (b).

1.12. C_{84} binding constant calculation

a. $C_{84}\subset$**7**·$(BArF)_8$ + **8**·$(BArF)_8$

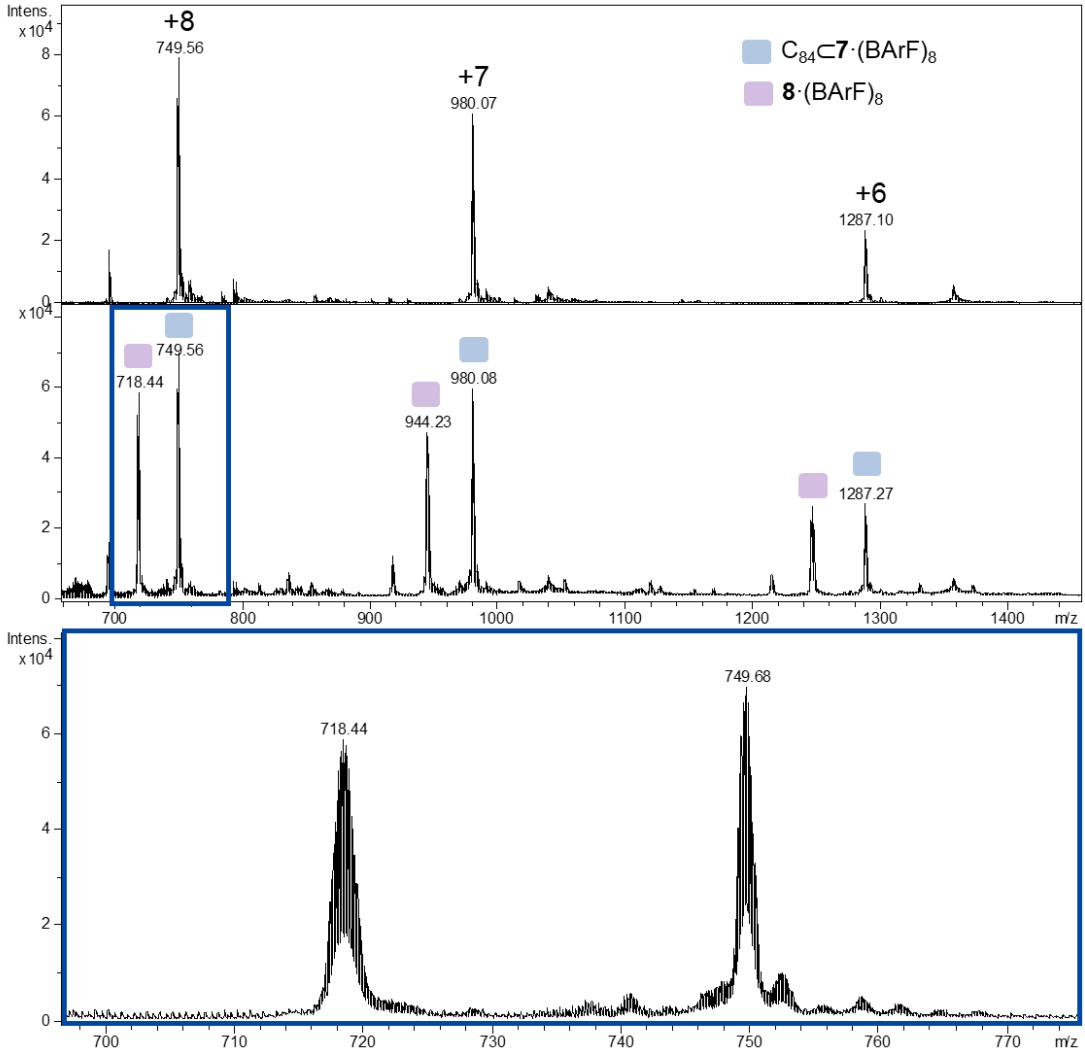

Supplementary Figure 19. HR-MS-ESI of the encapsulation of fullerene extract (C_{84} mainly) with 15 mg of **7**·$(BArF)_8$ (in the solid state) (top), HR-MS-ESI of the addition of **8**·$(BArF)_8$ into the $C_{84}\subset$**7**·$(BArF)_8$ solution (center) and zoom of the latter (bottom).

b. $(C_{59}N)_2 \subset$**7**$\cdot(BArF)_8$ + fullerene extract (100 eq., 4d, toluene)

(1) Encapsulation of $(C_{59}N)_2$ into **6**$\cdot(BArF)_8$. **(2)** Addition of fullerene extract (100 eq) in toluene and stirring at room temperature for 4 days.

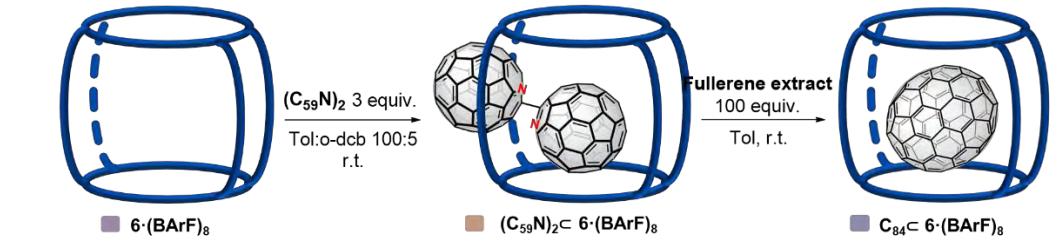

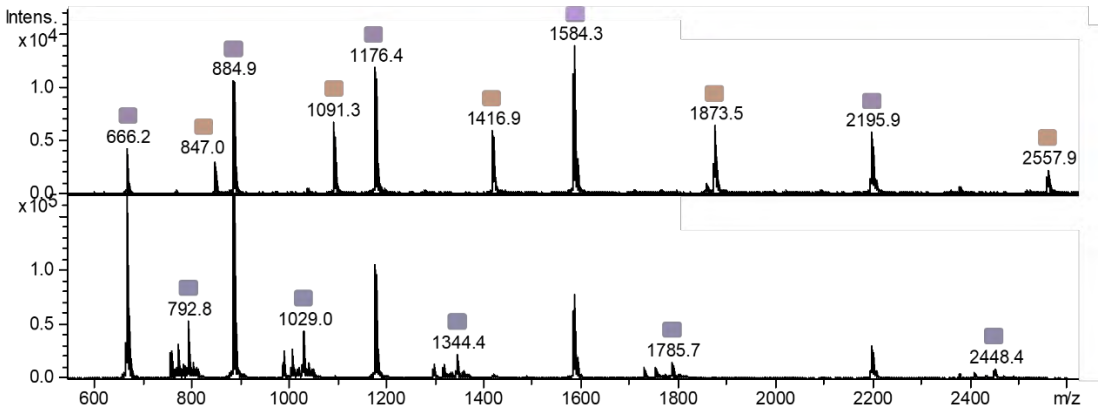

Supplementary Figure 20. HR-MS-ESI of $(C_{59}N)_2 \subset$**6**$\cdot(BArF)_8$ (top) and after exchanging with C_{84} (bottom).

1.13. UV-Vis titrations

Experimental procedure and general remarks

All titrations were performed in a mixture of PhMe/MeCN/*o*-DCB (9:1:0.09, v/v) at room temperature, on an Agilent 8452 UV-vis spectrophotometer using a 1 cm quartz cell. Concentration of either host or guest species was kept constant over the course of titration. Titration data was fitted by using the online calculator Bindfit (http://supramolecular.org).[5]

Supplementary Table 2. Comparison of different binding constants. Solvent: PhMe/MeCN/*o*-DCB (9:1:0.09).

NANOCAPSULE	K_1 (M^{-1})	K_2 (M^{-1})	K ± ERROR (M^{-1})
4 [ref [1]]	-	-	**9.4 (± 0.5) x 10^5**
6	1.2 x 10^7	8.2 x 10^6	**1.0 (± 1.1) x 10^7**
7	1.7 x 10^6	1.4 x 10^6	**1.6 (± 0.1) x 10^6**
8	5.0 x 10^7	3.6 x 10^7	**4.3 (± 1.0) x 10^7**
9	1.6 x 10^7	9.2 x 10^6	**1.3 (± 0.6) x 10^7**

a. UV-Vis titration: $(C_{59}N)_2$ + 6·$(BArF)_8$

A

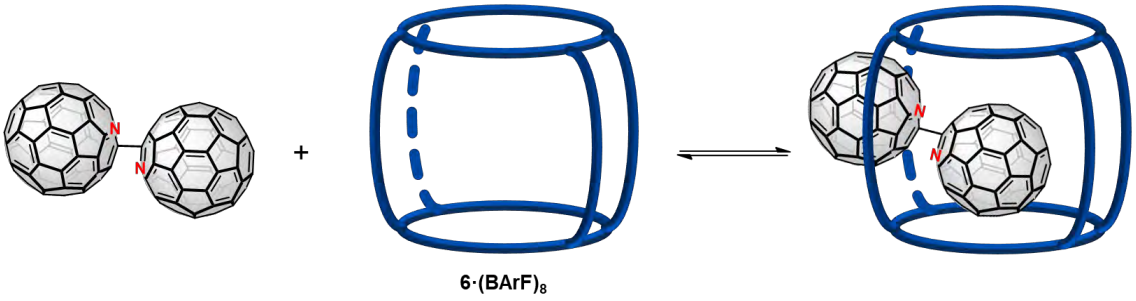

B

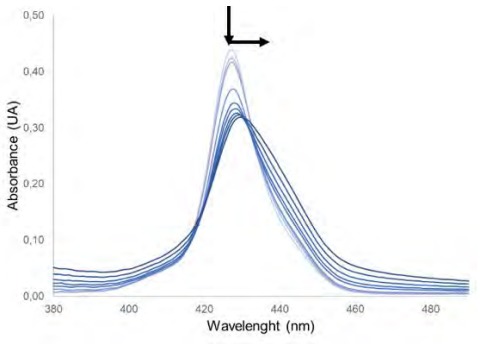

C

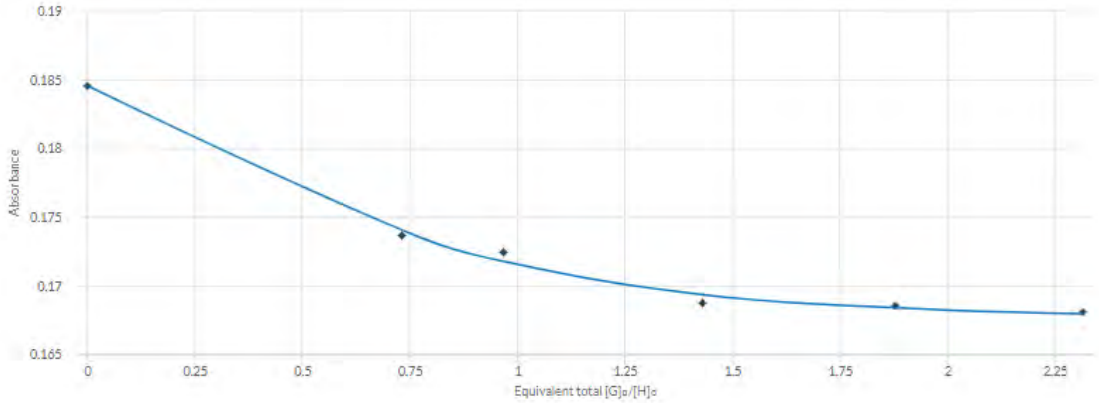

Supplementary Figure 22. Representative titration data for **6**/$(C_{59}N)_2$ host-guest system. Solvent: PhMe/MeCN/*o*-DCB (9:1:0.09). (A) Changes in absorption spectra of **6** (8.3×10^{-7} M, λ_{exc} = 420 nm) upon addition of diazafullerene $(C_{59}N)_2$ (0 – 3.4×10^{-5} M). (B) Fit of the titration data according to 1:1 binding model. See supplementary excel input files "6_T1" and "6_T2" for the detailed report from supramolecular.org page.

b. UV-Vis titration: $(C_{59}N)_2$ + 7·$(BArF)_8$

A

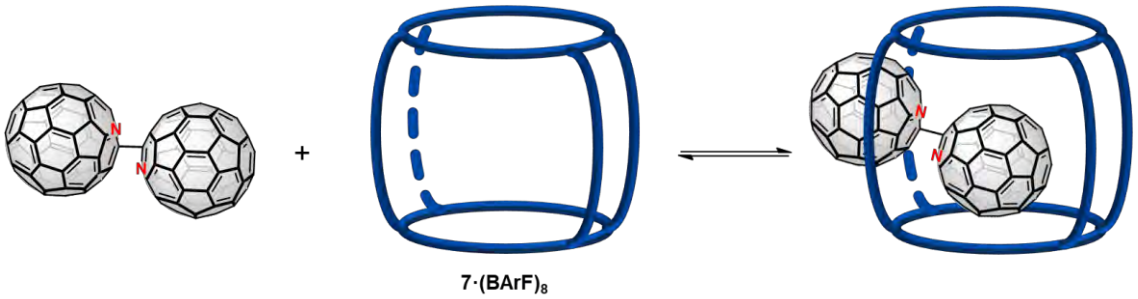

B

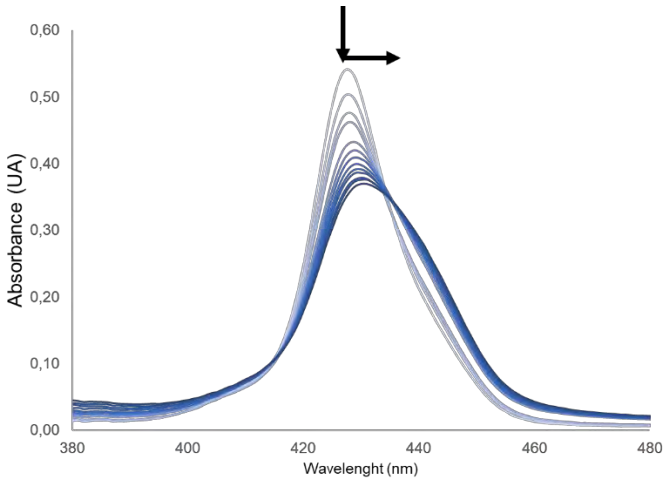

C

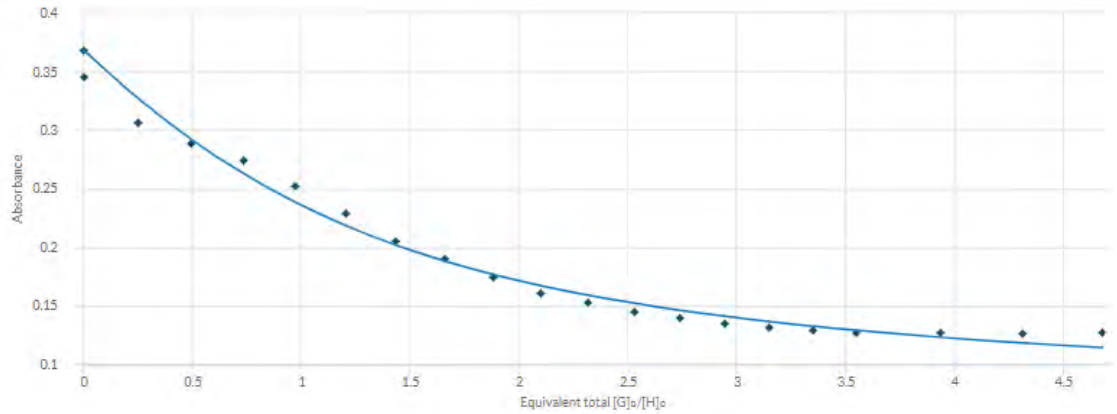

Supplementary Figure 23. Representative titration data for **7**/$(C_{59}N)_2$ host-guest system. Solvent: PhMe/MeCN/*o*-DCB (9:1:0.09). (A) Changes in absorption spectra of **7** (8.3×10^{-7} M, λ_{exc} = 420 nm) upon addition of diazafullerene $(C_{59}N)_2$ (0 – 6.4×10^{-5} M). (B) Fit of the titration data according to 1:1 binding model. See supplementary excel input files "7_T1" and "7_T2" for the detailed report from supramolecular.org page.

c. UV-Vis titration: $(C_{59}N)_2$ + 8·$(BArF)_8$

A

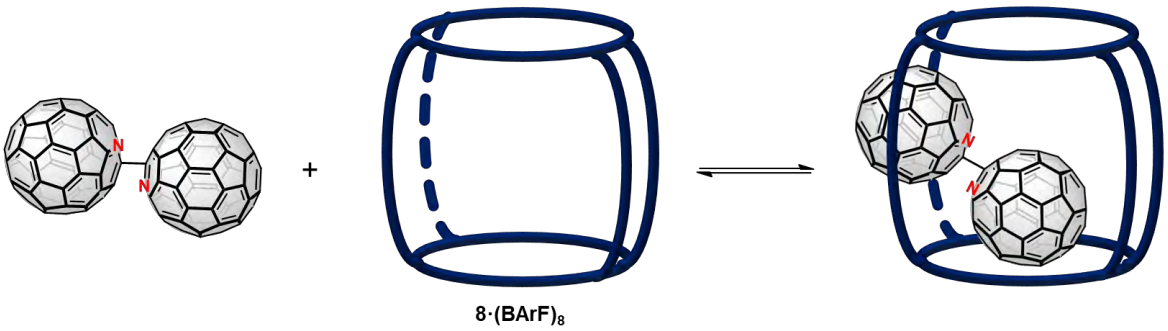

B

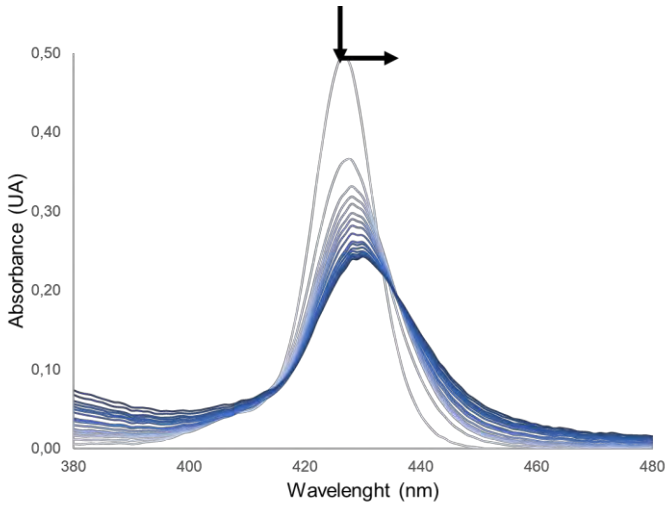

C

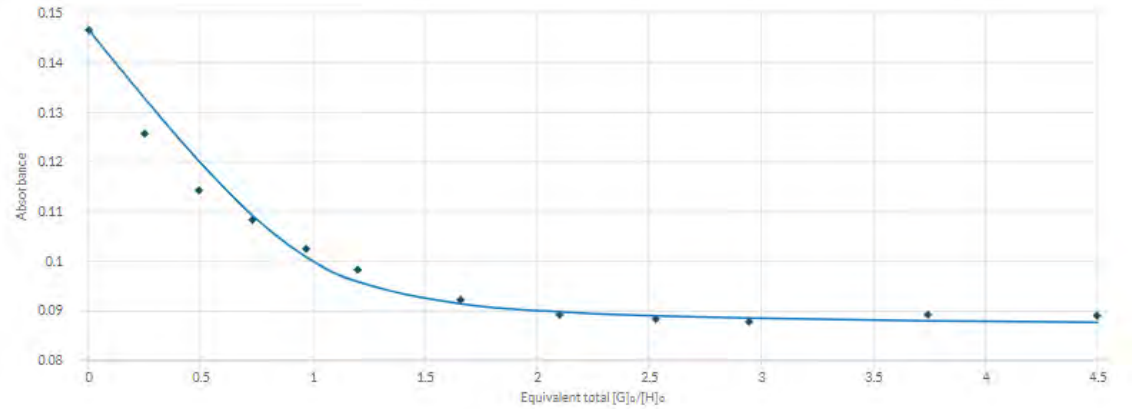

Supplementary Figure 24. Representative titration data for **8**/$(C_{59}N)_2$ host-guest system. Solvent: PhMe/MeCN/*o*-DCB (9:1:0.09). (A) Changes in absorption spectra of **8** (4.3×10^{-7} M, λ_{exc} = 420 nm) upon addition of diazafullerene $(C_{59}N)_2$ (0 – 3.7×10^{-5} M). (B) Fit of the titration data according to 1:1 binding model. See supplementary excel input files "8_T1" and "8_T2" for the detailed report from supramolecular.org page.

d. UV-Vis titration: $(C_{59}N)_2$ + 9·$(BArF)_8$

A

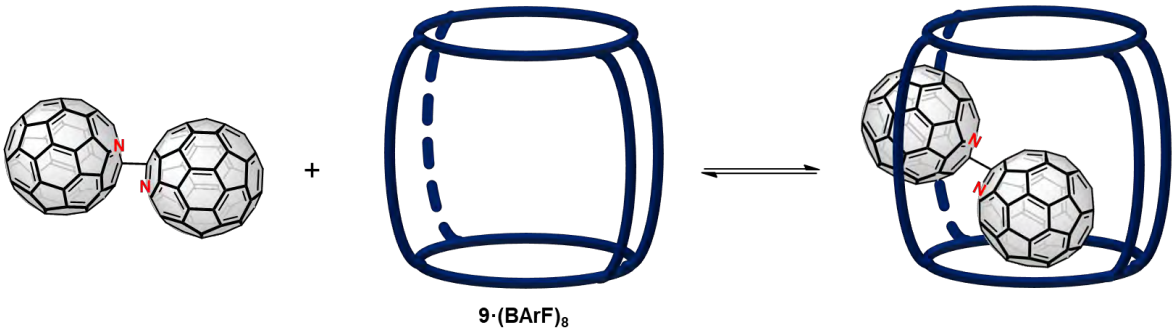

B

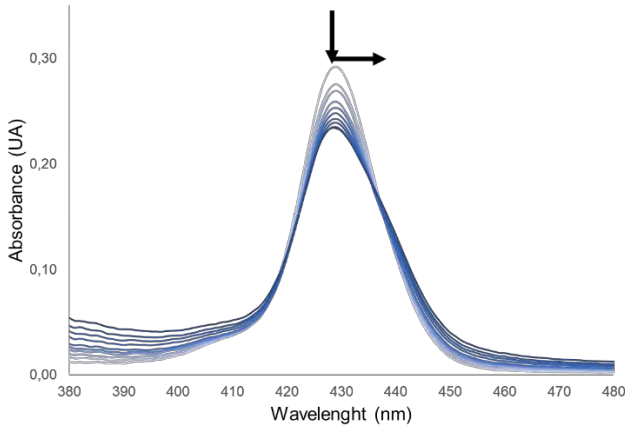

C

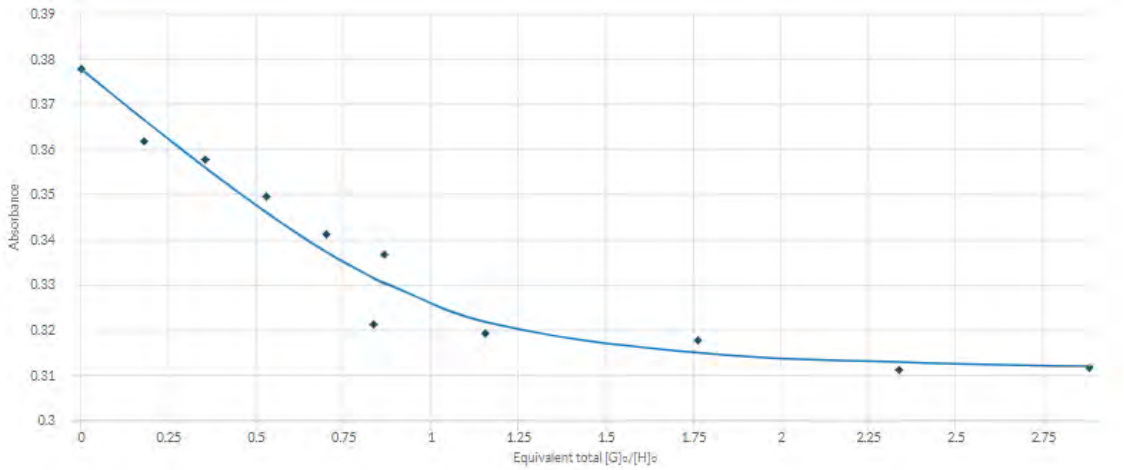

Supplementary Figure 25. Representative titration data for **9**/$(C_{59}N)_2$ host-guest system. Solvent: PhMe/MeCN/*o*-DCB (9:1:0.09). (A) Changes in absorption spectra of **9** (8.3×10^{-7} M, λ_{exc} = 420 nm) upon addition of diazafullerene $(C_{59}N)_2$ (0 – 9.2×10^{-5} M). (B) Fit of the titration data according to 1:1 binding model. See supplementary excel input files "9_T1" and "9_T2" for the detailed report from supramolecular.org page.

2. Supplementary Figures

2.1. Characterization of dialdehyde (ppp)

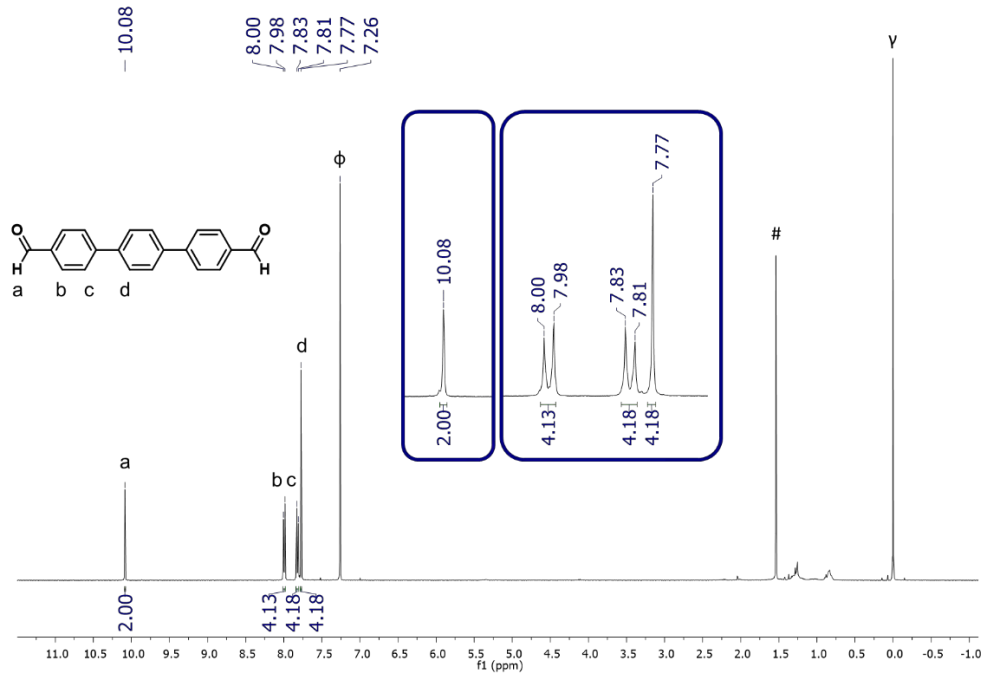

Supplementary Figure 26. ^{1}H-NMR of (1,1':4',1''-terphenyl)-4,4''-dicarbaldehyde (ppp). Experiment performed in $CDCl_3$ at 298 K (400 MHz). (ϕ) $CHCl_3$, (#) H_2O, (γ) TMS.

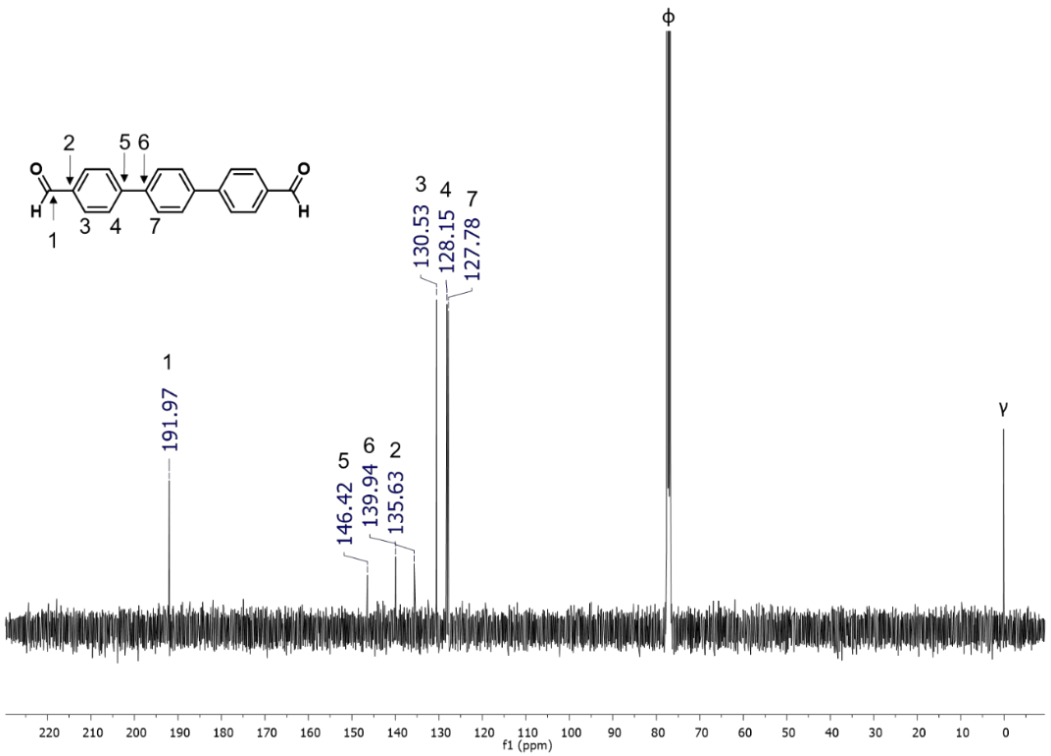

Supplementary Figure 27. ^{13}C-NMR of (1,1':4',1''-terphenyl)-4,4''-dicarbaldehyde (ppp). Experiment performed in $CDCl_3$ at 298 K (100 MHz). (ϕ) $CHCl_3$, (γ) TMS.

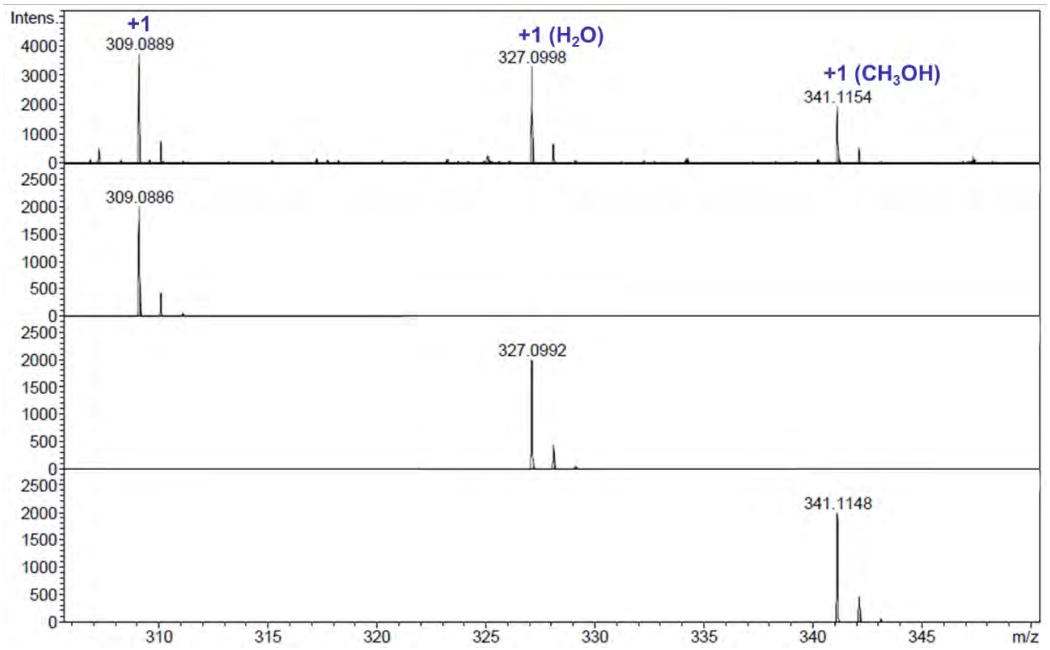

Supplementary Figure 28. HRMS spectrum of (1,1':4',1''-terphenyl)-4,4''-dicarbaldehyde (ppp). Experimental (top) and theoretical isotopic pattern for selected peaks is shown. Sample was dissolved in chloroform and the spectrum was registered on a Bruker Micro TOF-Q-II exact mass spectrometer.

2.2. Characterization of S_2ppp

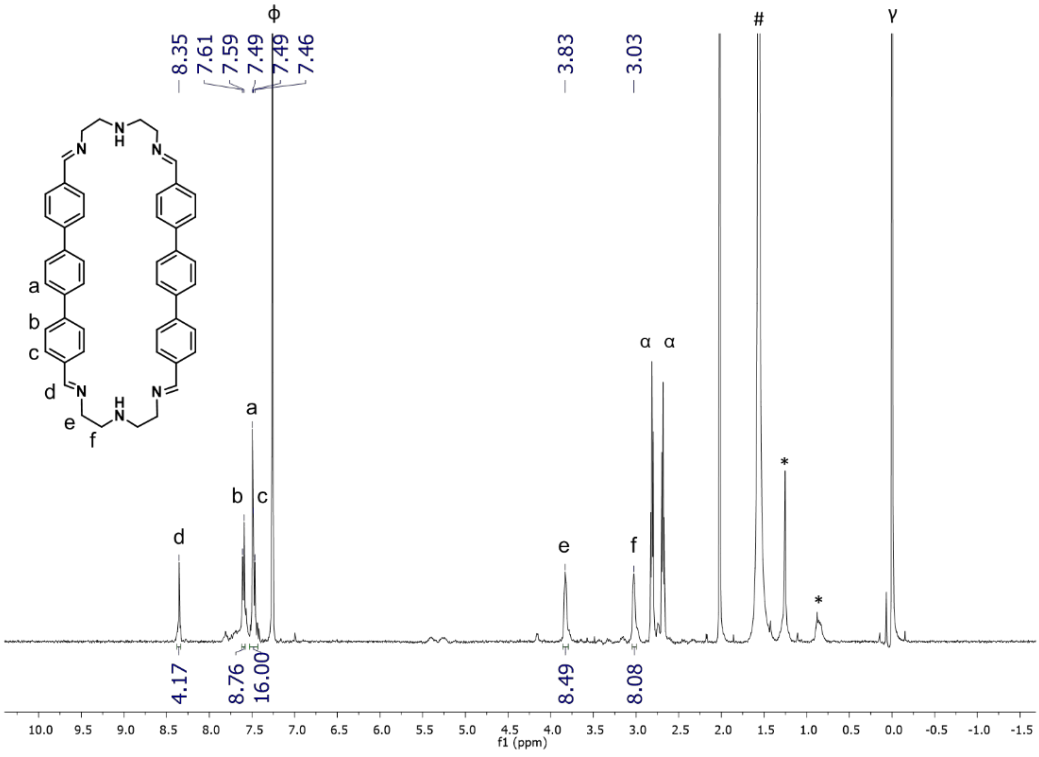

Supplementary Figure 29. ^{1}H-NMR of S_2ppp macrocycle. Experiment was performed in $CDCl_3$ at 298 K (400 MHz). (ϕ) $CHCl_3$, (*) H grease, (γ) TMS, (α) diethylentriamine.

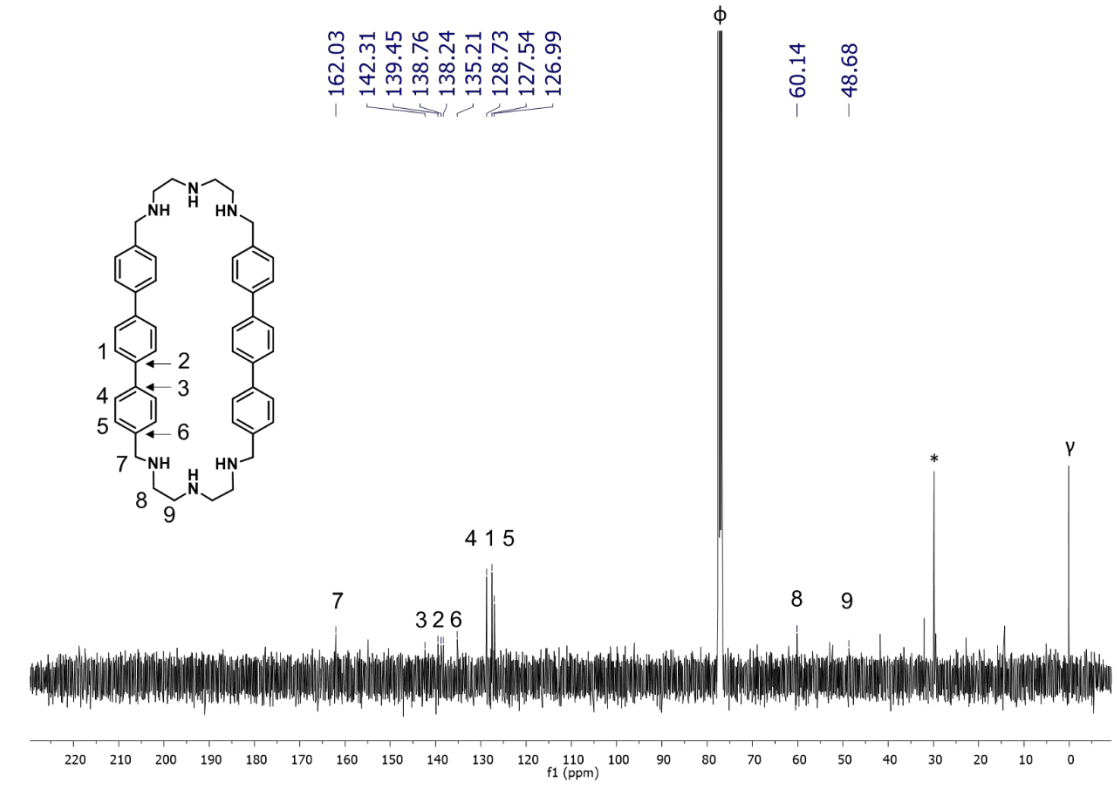

Supplementary Figure 30. ^{13}C-NMR of S_2ppp macrocycle. Experiment was performed in $CDCl_3$ at 298 K (100 MHz). (ϕ) $CHCl_3$, (γ) TMS.

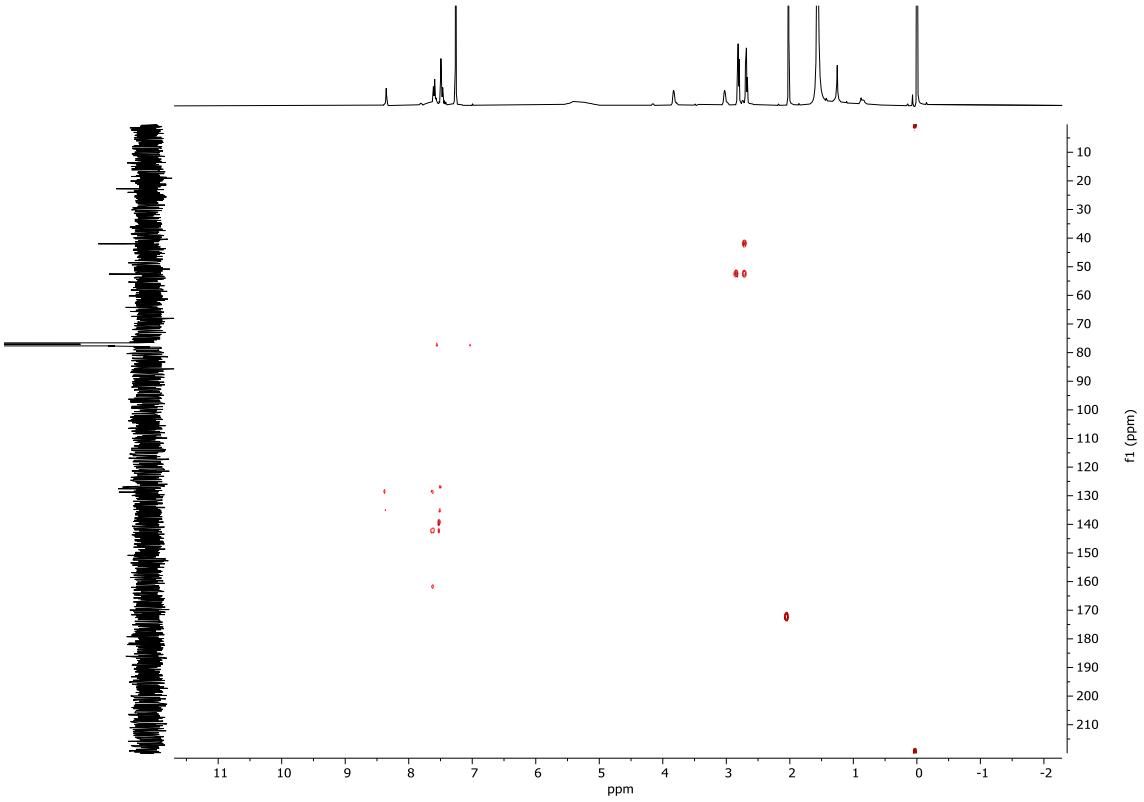

Supplementary Figure 31. HMBC of S_2ppp macrocycle. Experiment was performed in $CDCl_3$ at 298 K (400 MHz).

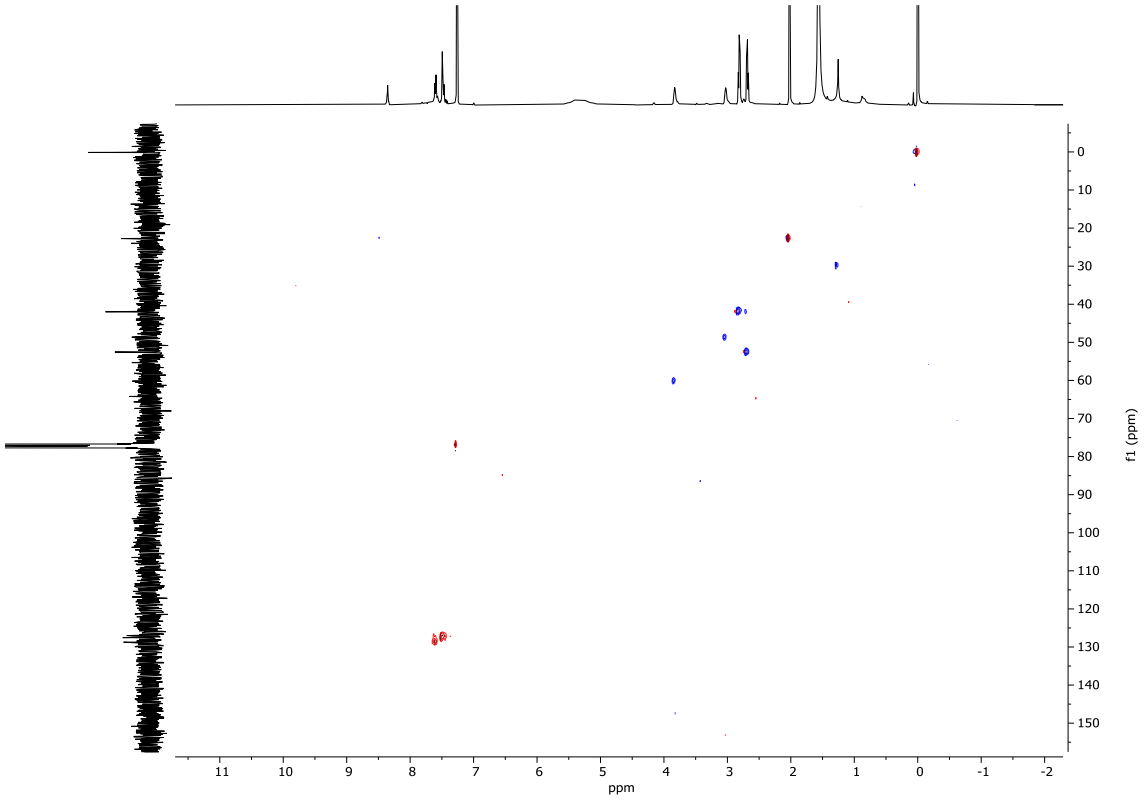

Supplementary Figure 32. HSQC of S_2ppp macrocycle. Experiment was performed in $CDCl_3$ at 298 K (400 MHz).

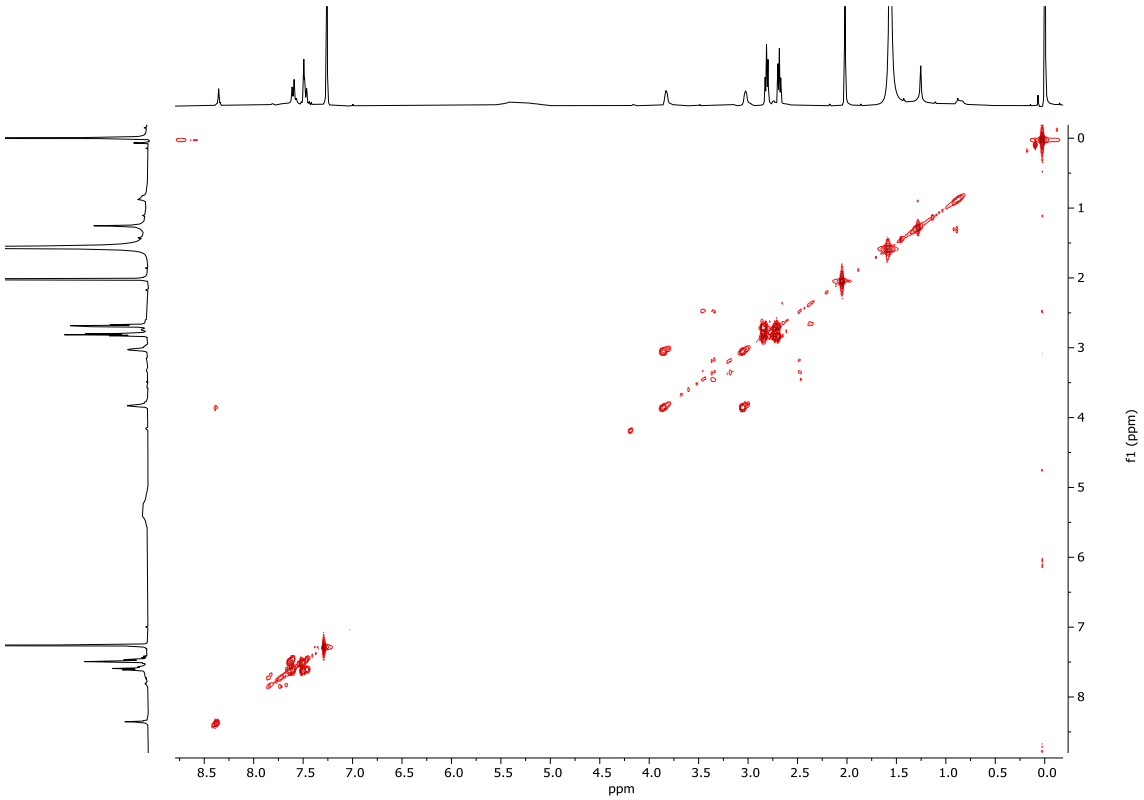

Supplementary Figure 33. COSY of S_2ppp macrocycle. Experiment was performed in $CDCl_3$ at 298 K (400 MHz).

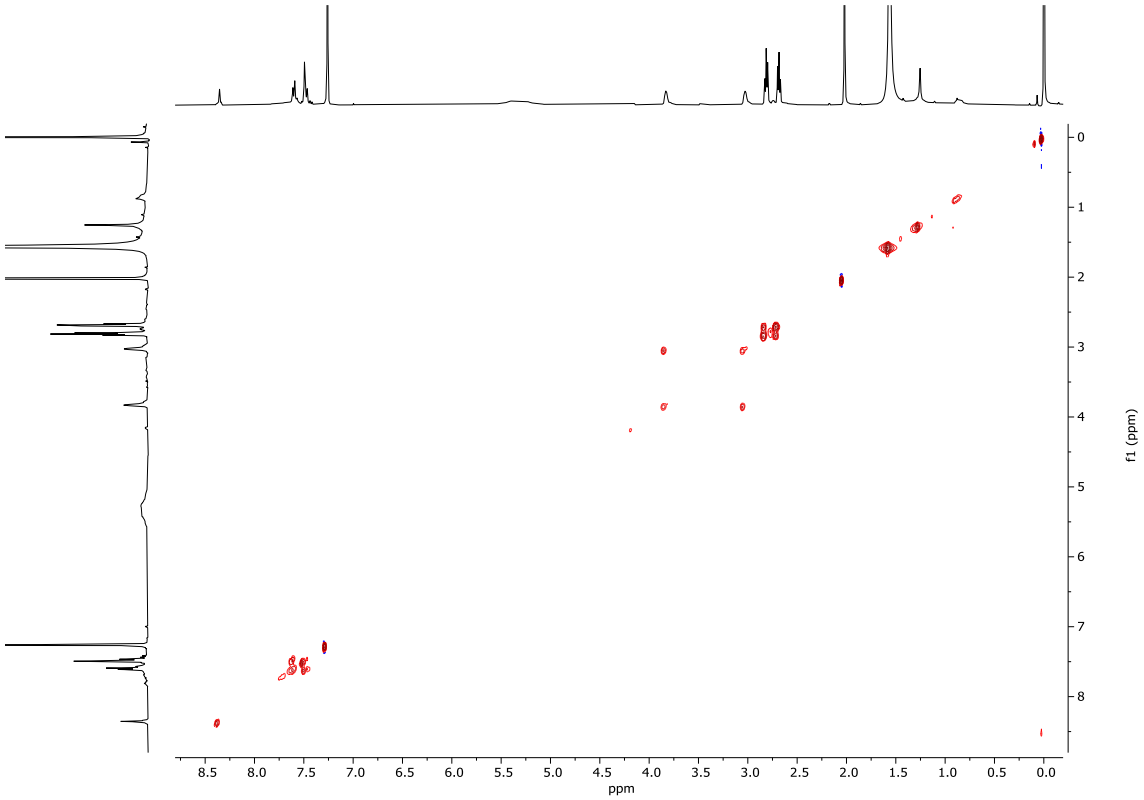

Supplementary Figure 34. TOCSY of S_2ppp macrocycle. Experiment was performed in $CDCl_3$ at 298 K (400 MHz).

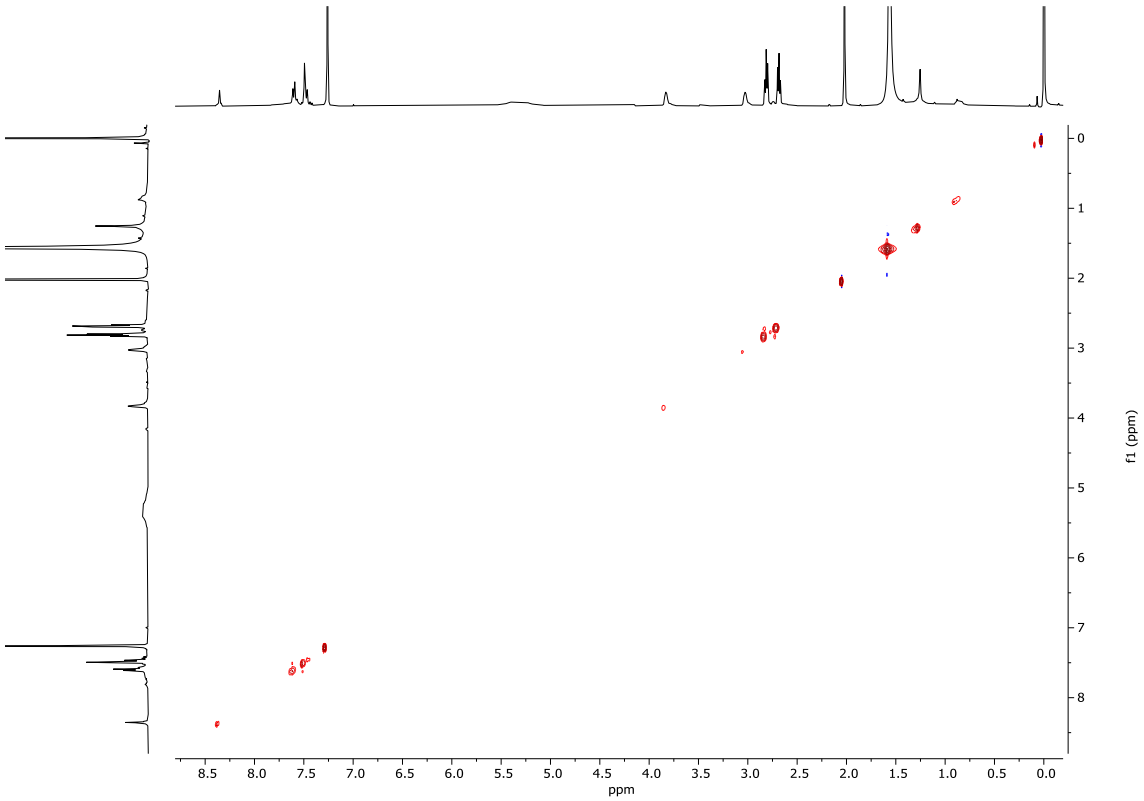

Supplementary Figure 35. NOESY of S_2ppp macrocycle. Experiment was performed in $CDCl_3$ at 298 K (400 MHz).

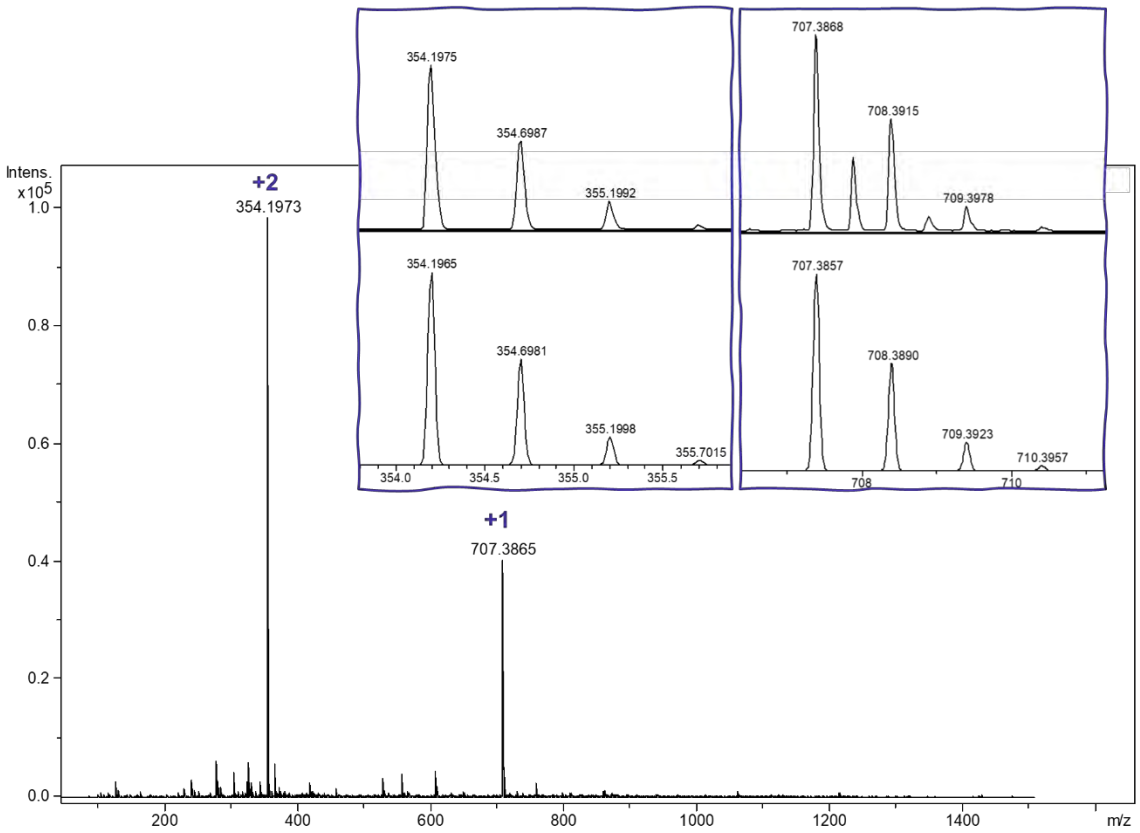

Supplementary Figure 36. HRMS spectrum of S_2ppp macrocycle. Experimental (top) and theoretical (bottom) isotopic pattern for selected peaks is shown. The sample was dissolved in chloroform and the spectrum was registered on a Bruker Micro TOF-Q-II exact mass spectrometer.

2.3. Characterization of H_2ppp

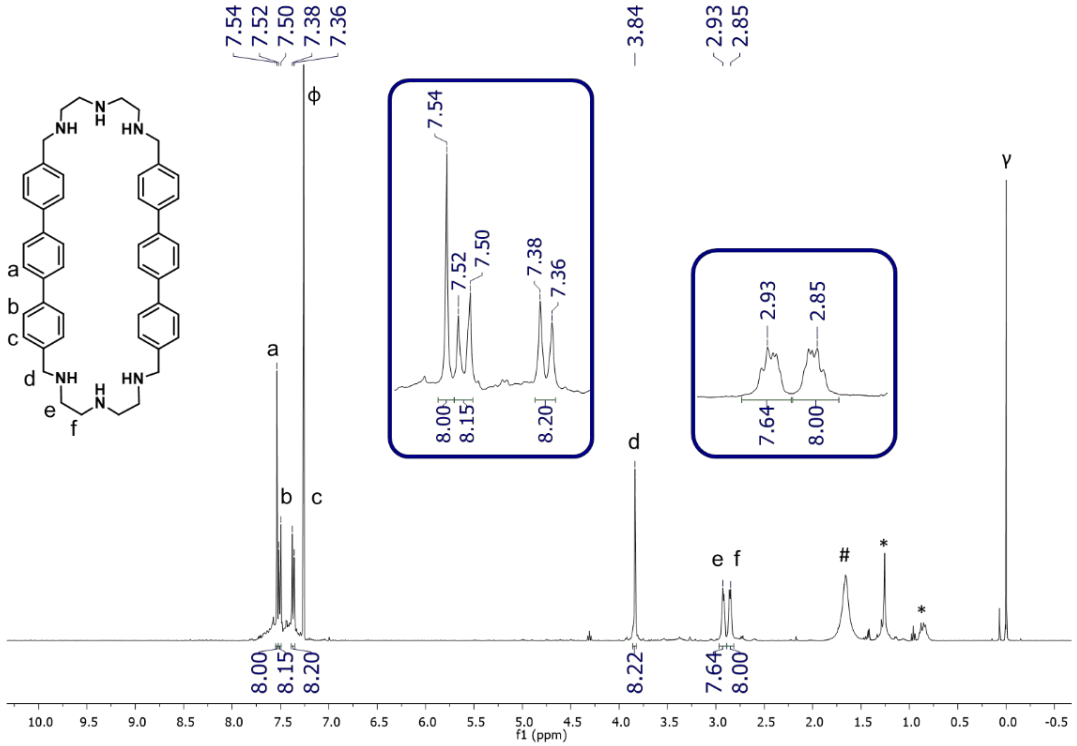

Supplementary Figure 37. ^{1}H-NMR of H_2ppp macrocycle. Experiment was performed in $CDCl_3$ at 298 K (400 MHz). (ϕ) $CHCl_3$, (*) H grease, (γ) TMS.

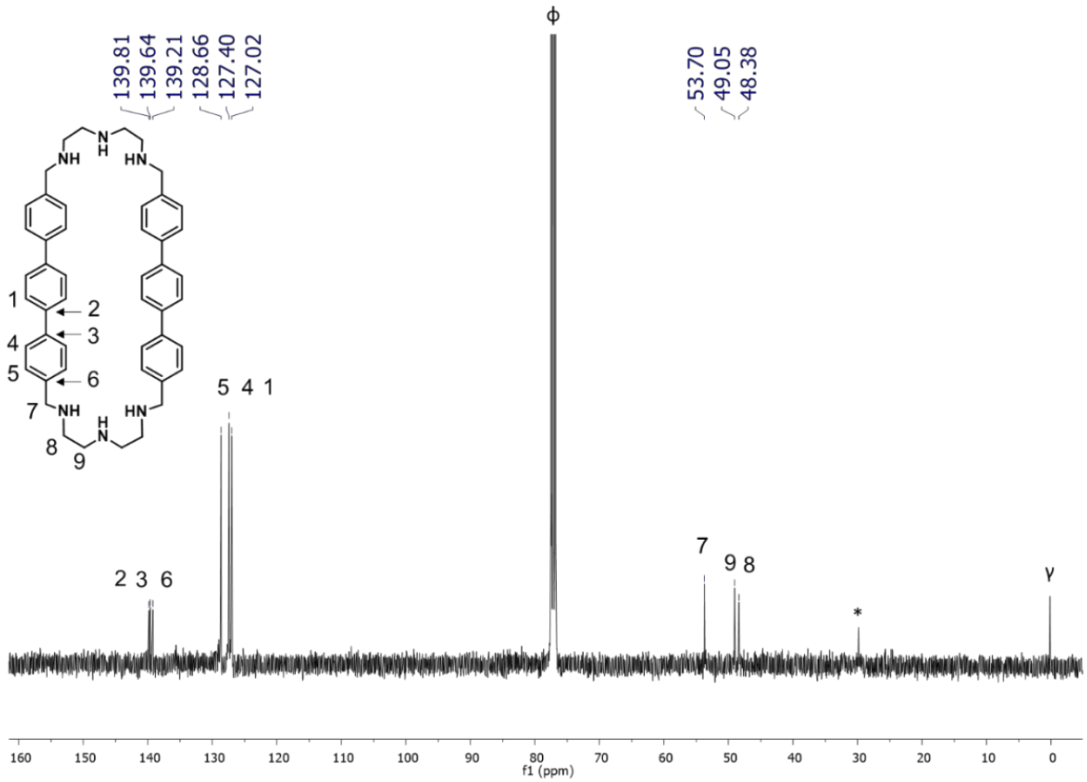

Supplementary Figure 38. ^{13}C-NMR of H_2ppp macrocycle. Experiment was performed in $CDCl_3$ at 298 K (100 MHz). (ϕ) $CHCl_3$, (*) H grease, (γ) TMS.

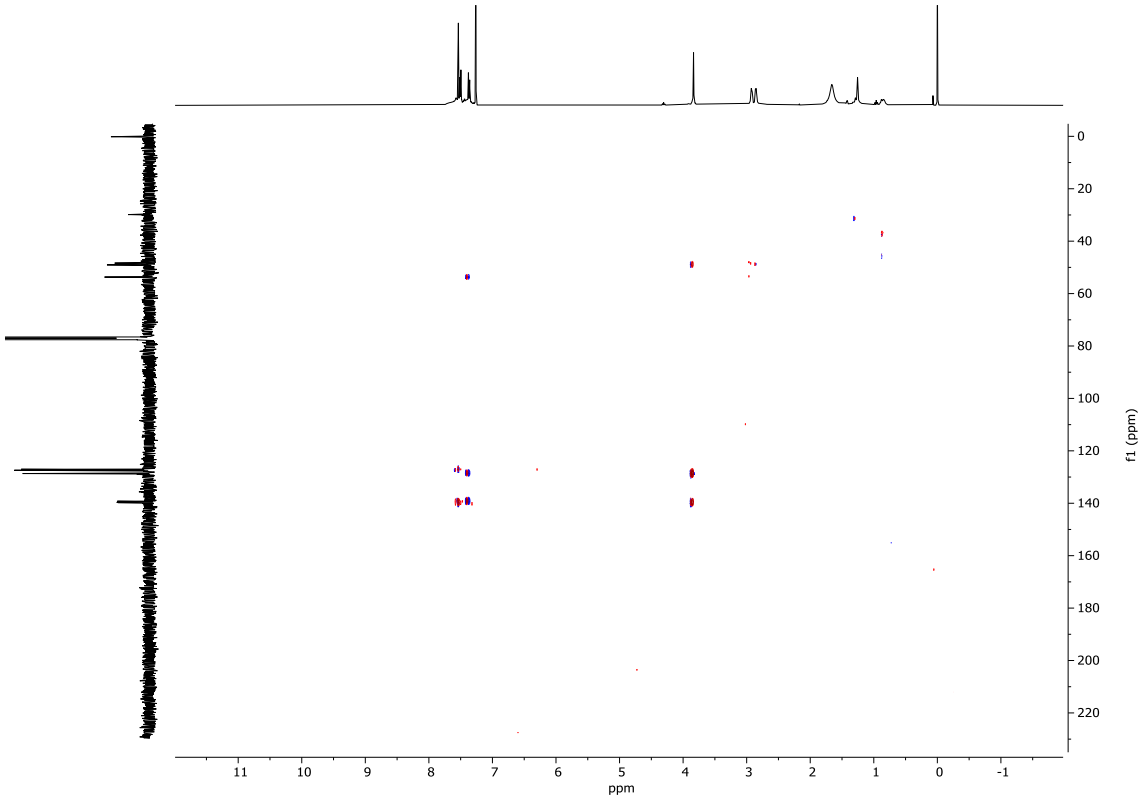

Supplementary Figure 39. HMBC of H_2ppp macrocycle. Experiment was performed in $CDCl_3$ at 298 K (400 MHz).

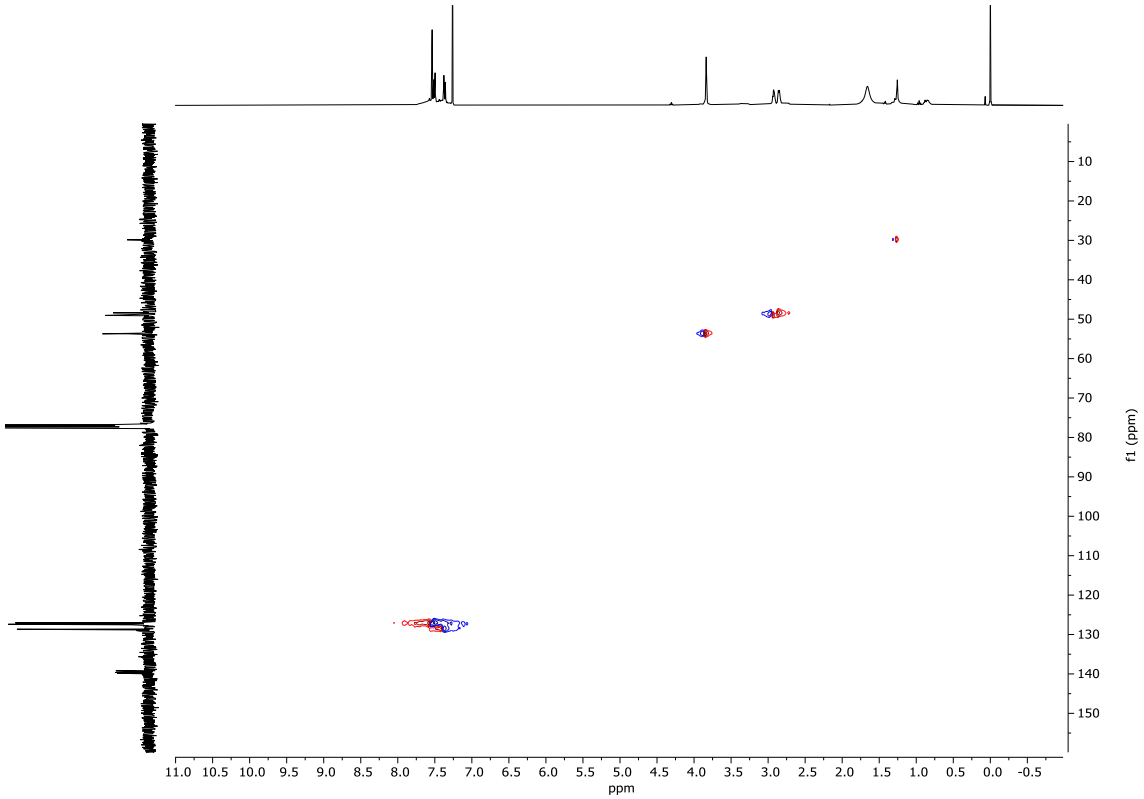

Supplementary Figure 40. HSQC of H_2ppp macrocycle. Experiment was performed in $CDCl_3$ at 298 K (400 MHz).

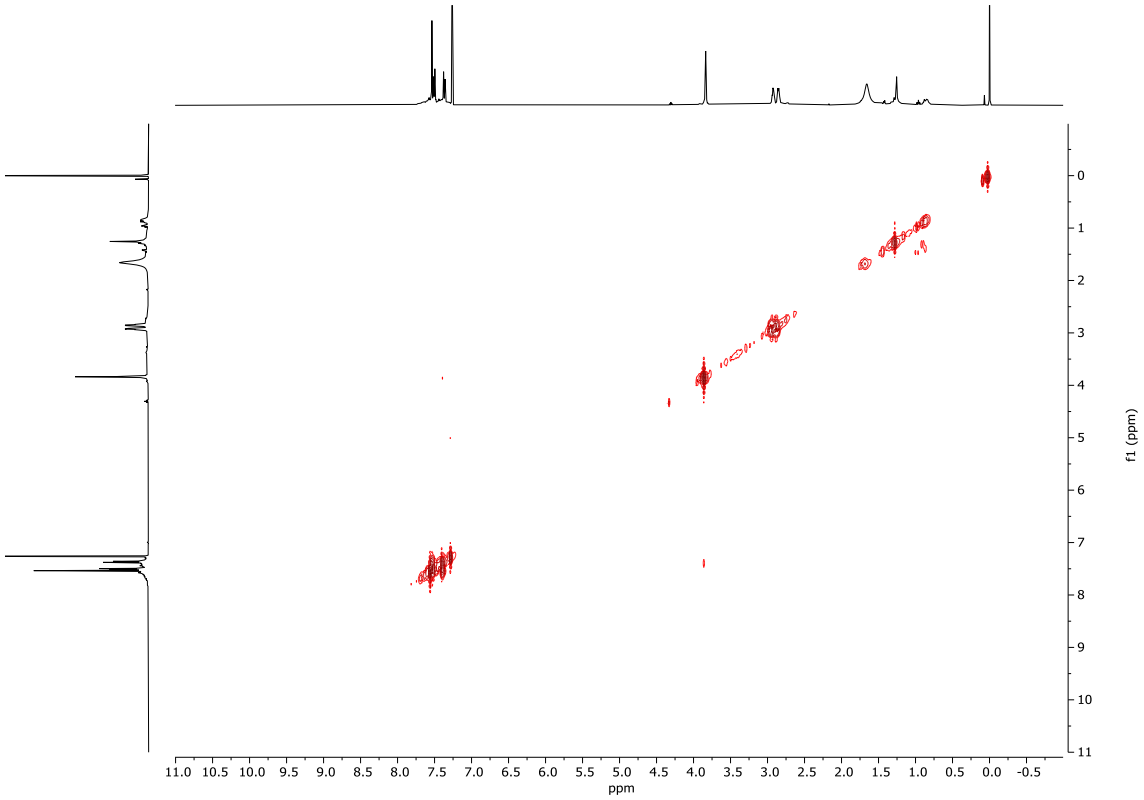

Supplementary Figure 41. COSY of H_2ppp macrocycle. Experiment was performed in $CDCl_3$ at 298 K (400 MHz).

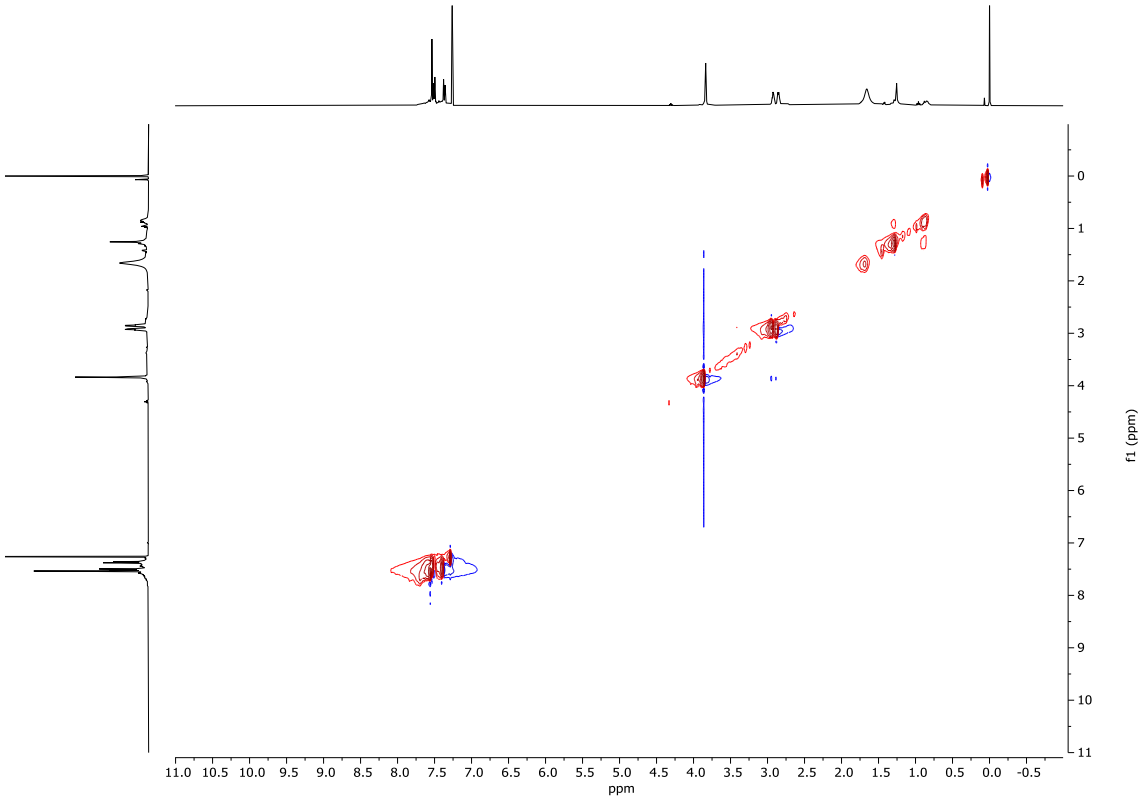

Supplementary Figure 42. TOCSY of H_2ppp macrocycle. Experiment was performed in $CDCl_3$ at 298 K (400 MHz).

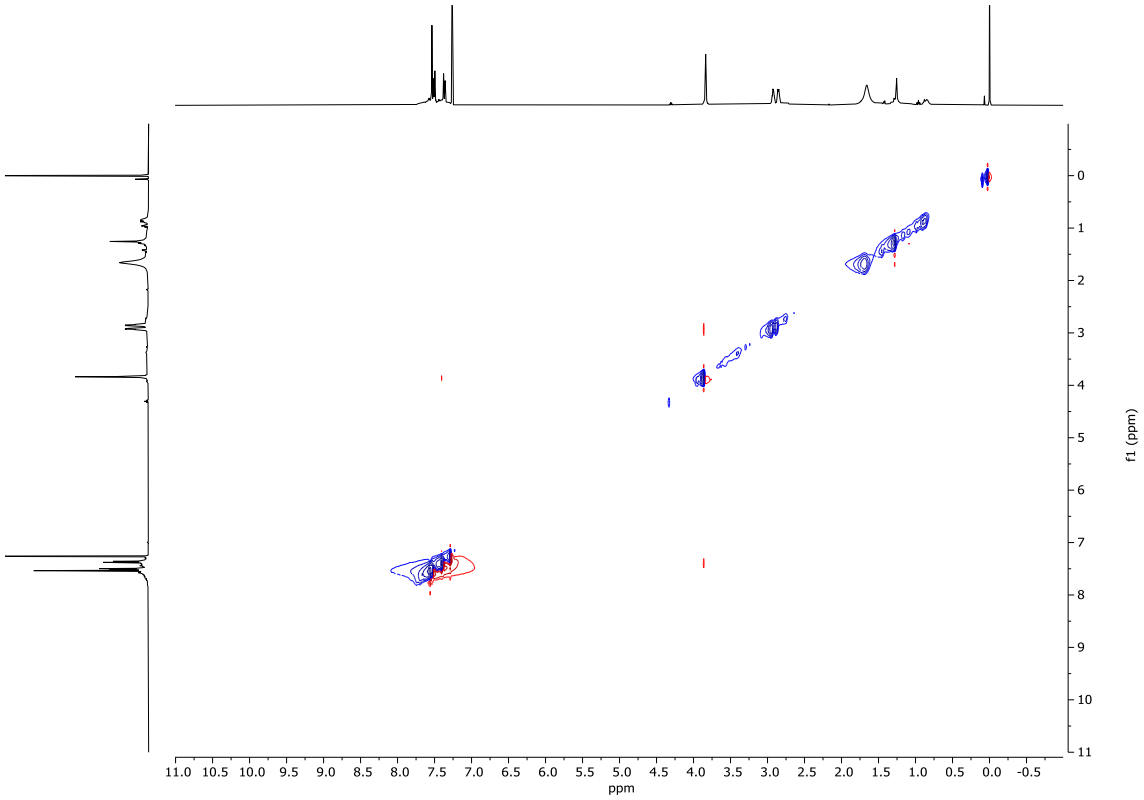

Supplementary Figure 43. NOESY of H_2ppp macrocycle. Experiment was performed in $CDCl_3$ at 298 K (400 MHz).

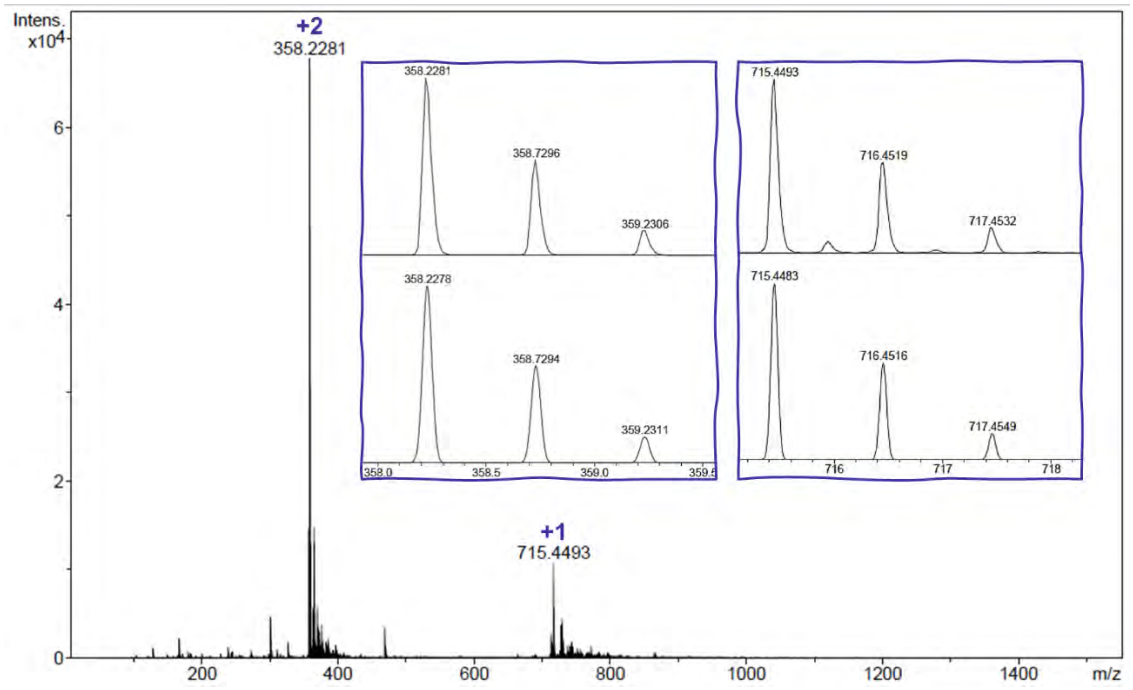

Supplementary Figure 44. HRMS spectrum of H_2ppp macrocycle. Experimental (top) and theoretical (bottom) isotopic pattern for selected peaks is shown. The sample was dissolved in chloroform and the spectrum was registered on a Bruker Micro TOF-Q-II exact mass spectrometer.

2.4. Characterization of the macrocyclic ligand Me_2ppp

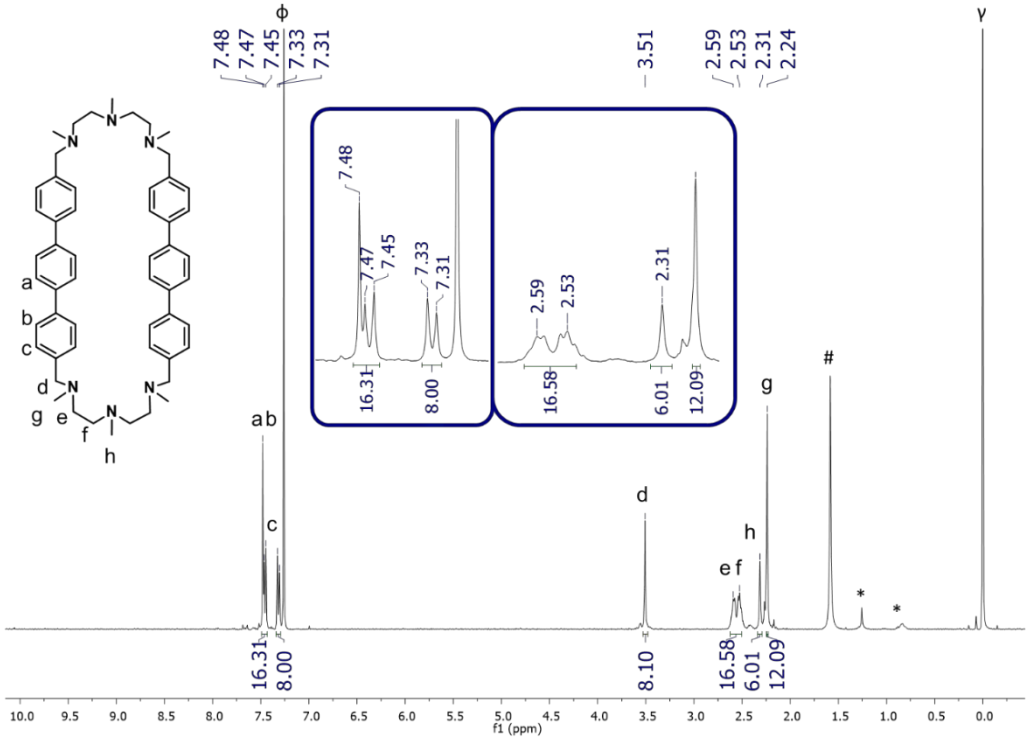

Supplementary Figure 45. ^{1}H-NMR of Me_2ppp macrocycle. Experiment was performed in $CDCl_3$ at 298 K (400 MHz). (#) H_2O, (*) H grease, (γ) TMS.

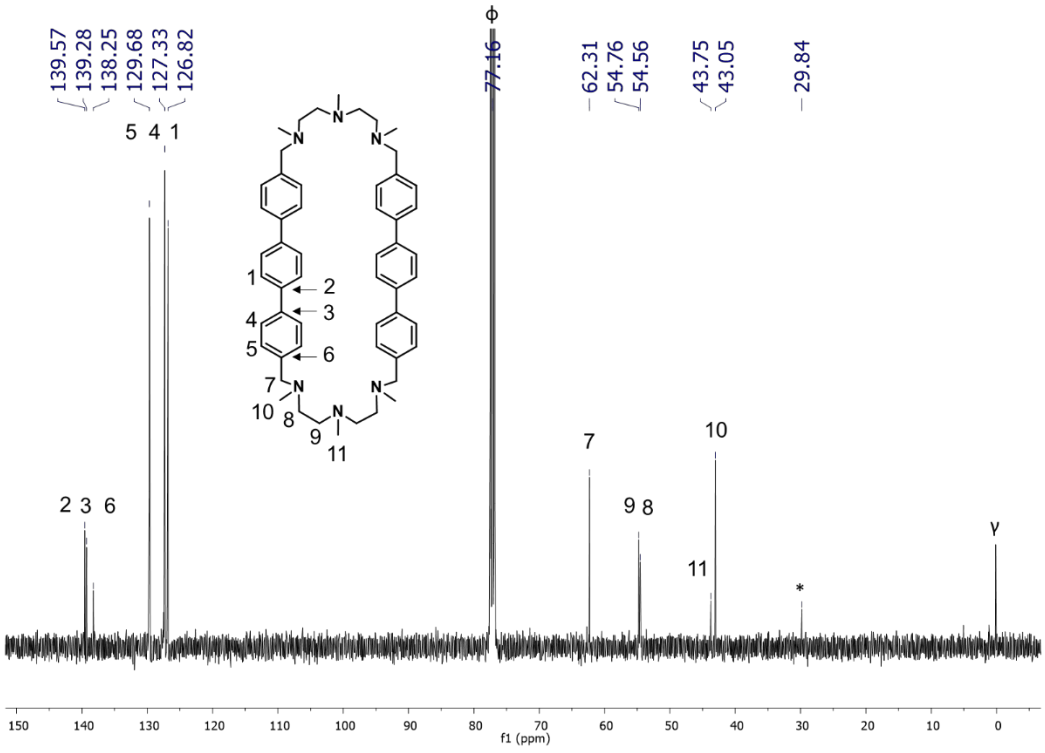

Supplementary Figure 46. ^{13}C-NMR of Me_2ppp macrocycle. Experiment was performed in $CDCl_3$ at 298 K (100 MHz). (ϕ) $CHCl_3$, (*) H grease, (γ) TMS.

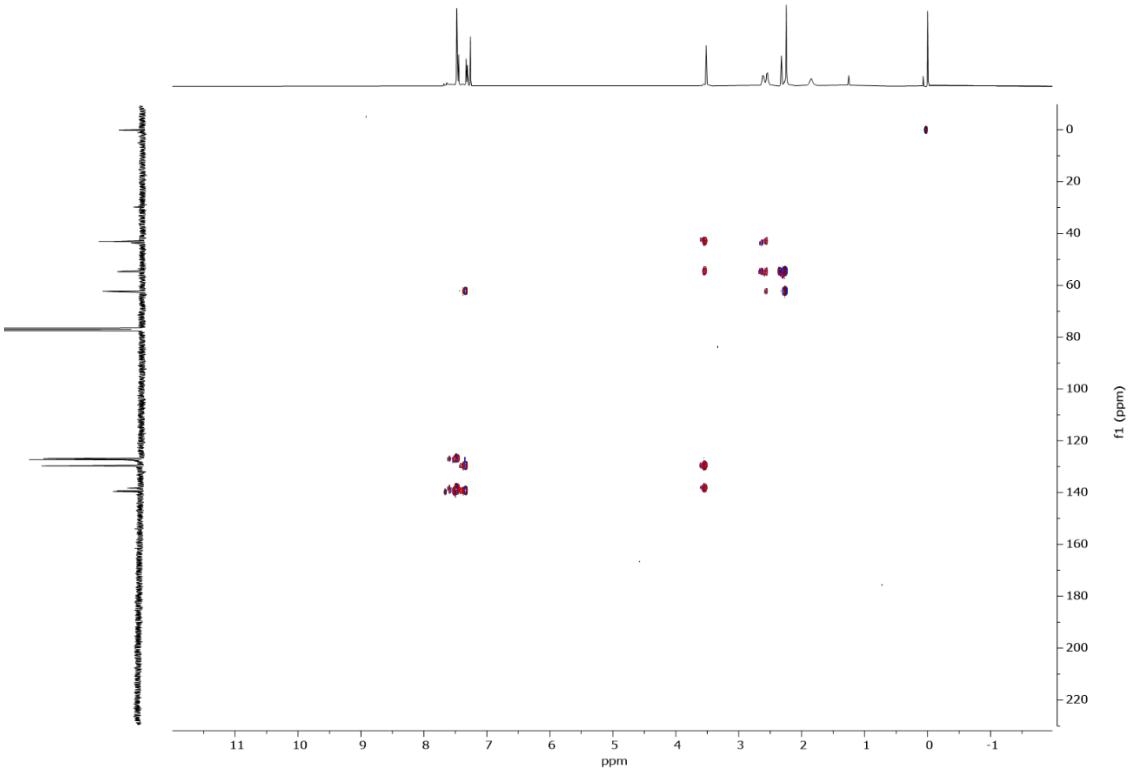

Supplementary Figure 47. HMBC of Me_2ppp macrocycle. Experiment was performed in $CDCl_3$ at 298 K (400 MHz).

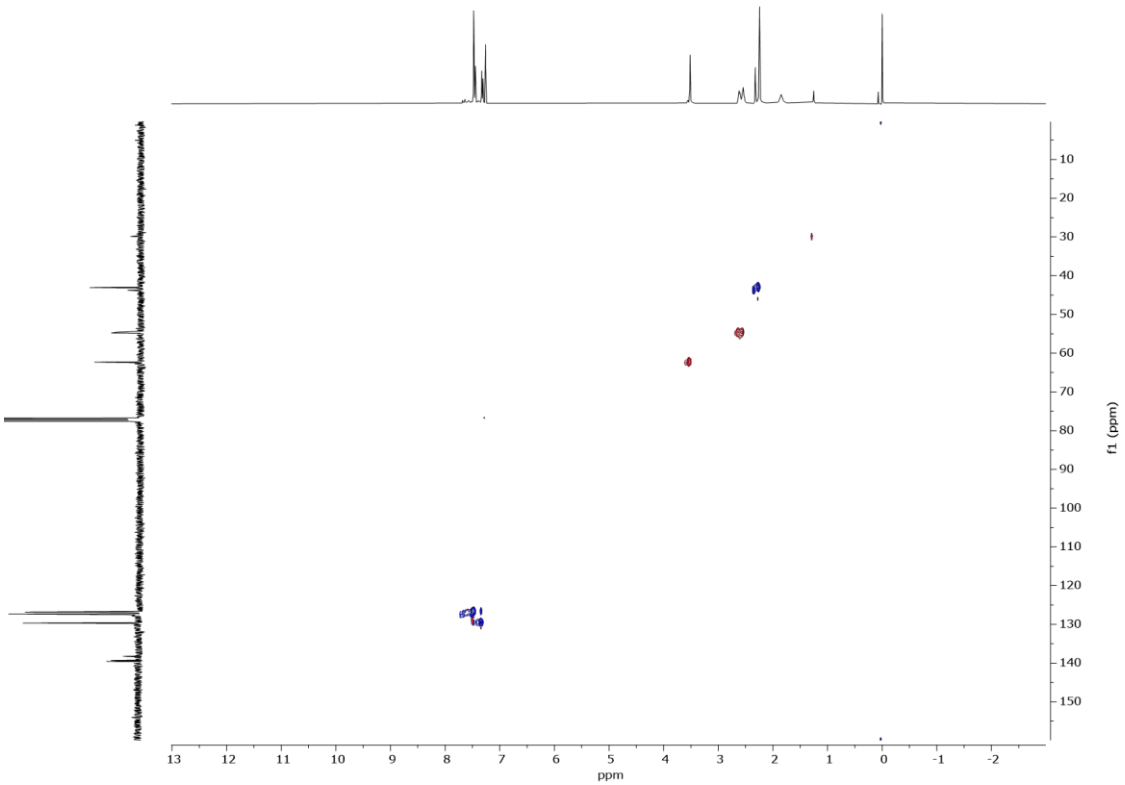

Supplementary Figure 48. HSQC of Me_2ppp macrocycle. Experiment was performed in $CDCl_3$ at 298 K (400 MHz).

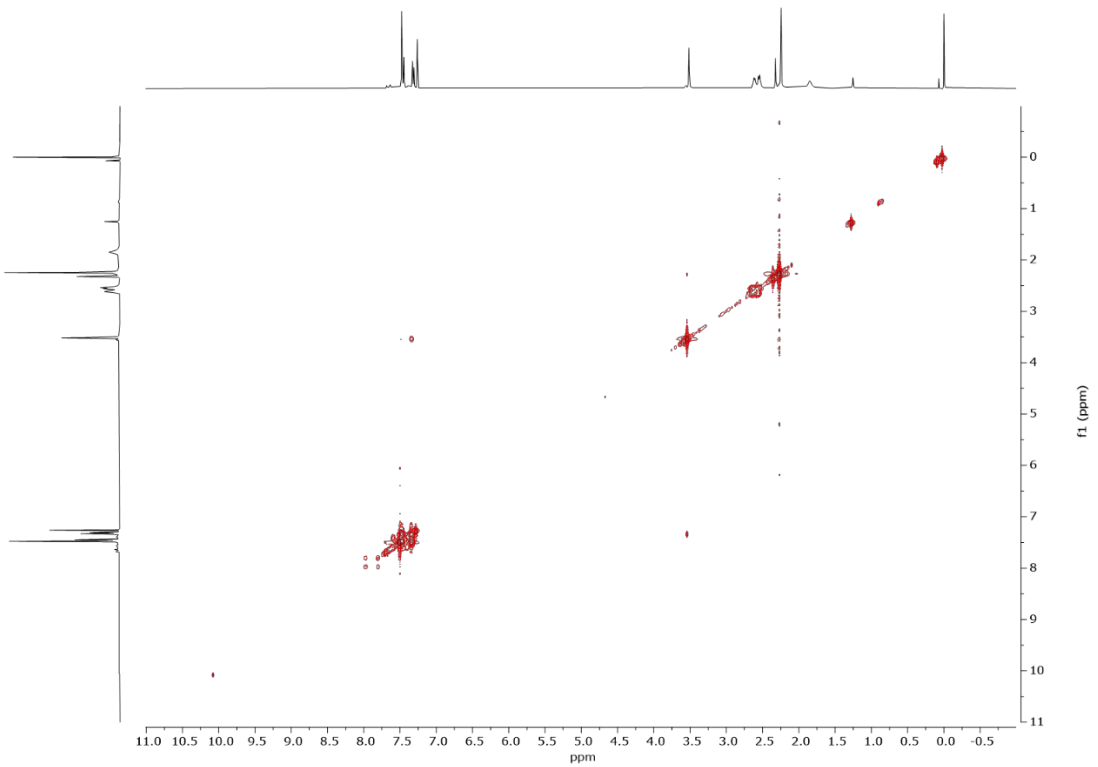

Supplementary Figure 49. COSY of Me_2ppp macrocycle. Experiment was performed in $CDCl_3$ at 298 K (400 MHz).

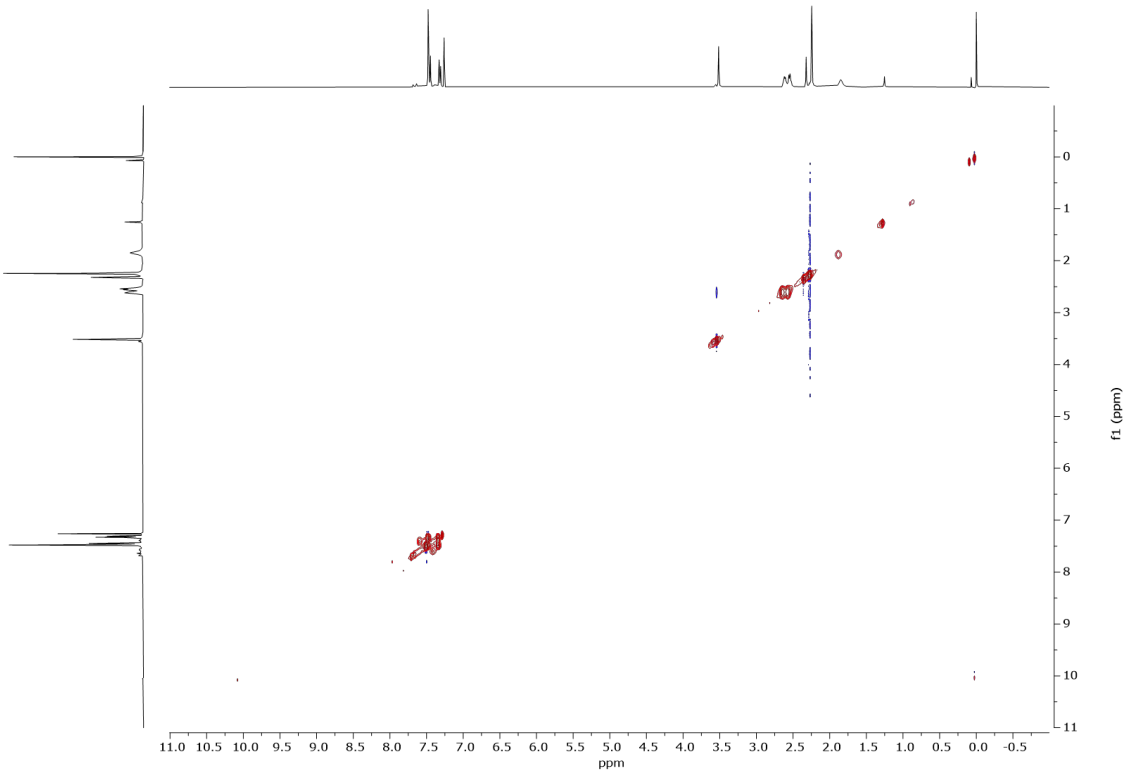

Supplementary Figure 50. TOCSY of Me_2ppp macrocycle. Experiment was performed in $CDCl_3$ at 298 K (400 MHz).

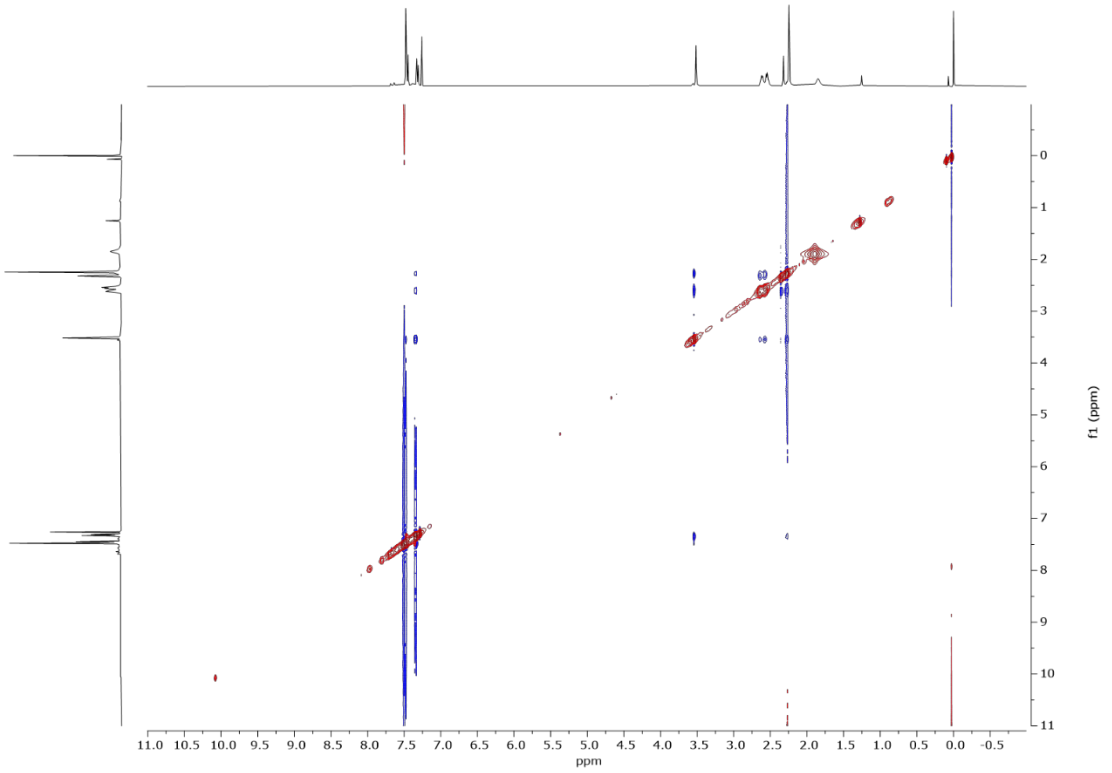

Supplementary Figure 51. NOESY of Me_2ppp macrocycle. Experiment was performed in $CDCl_3$ at 298 K (400 MHz).

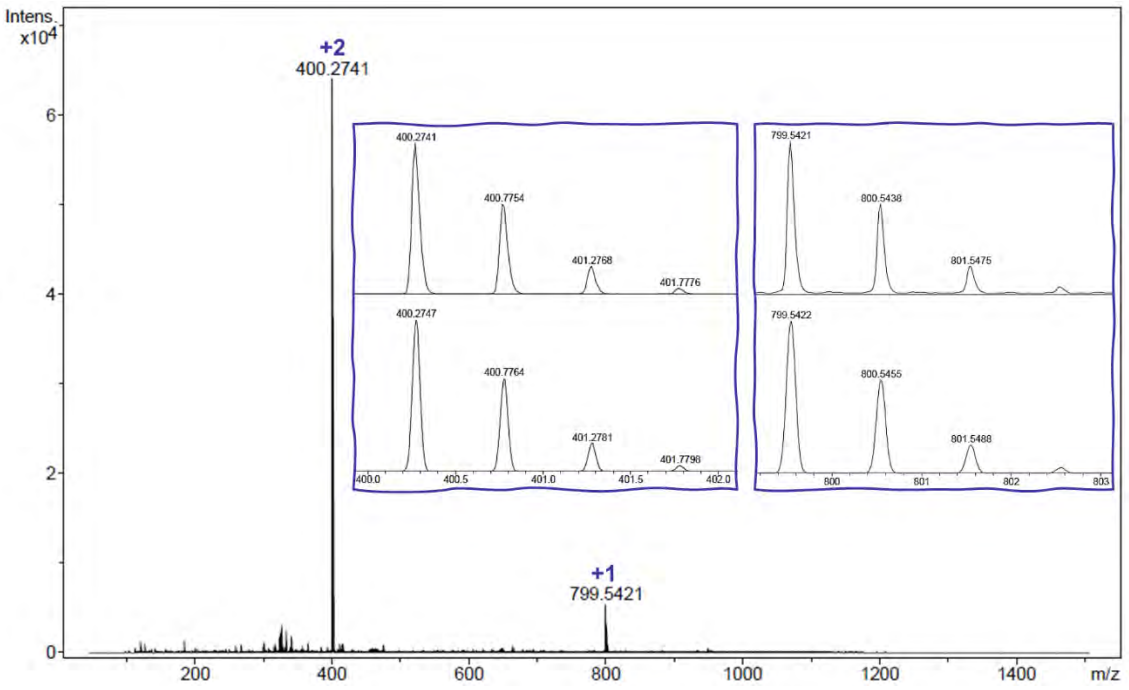

Supplementary Figure 52. HRMS spectrum of Me_2ppp macrocycle. Experimental (top) and theoretical (bottom) isotopic pattern for selected peaks is shown. The sample was dissolved in chloroform and the spectrum was registered on a Bruker Micro TOF-Q-II exact mass spectrometer.

2.5. Characterization of dinuclear Pd^{II} molecular clip [Pd_2-Me_2ppp·$(AcO)_2(OTf)_2$]

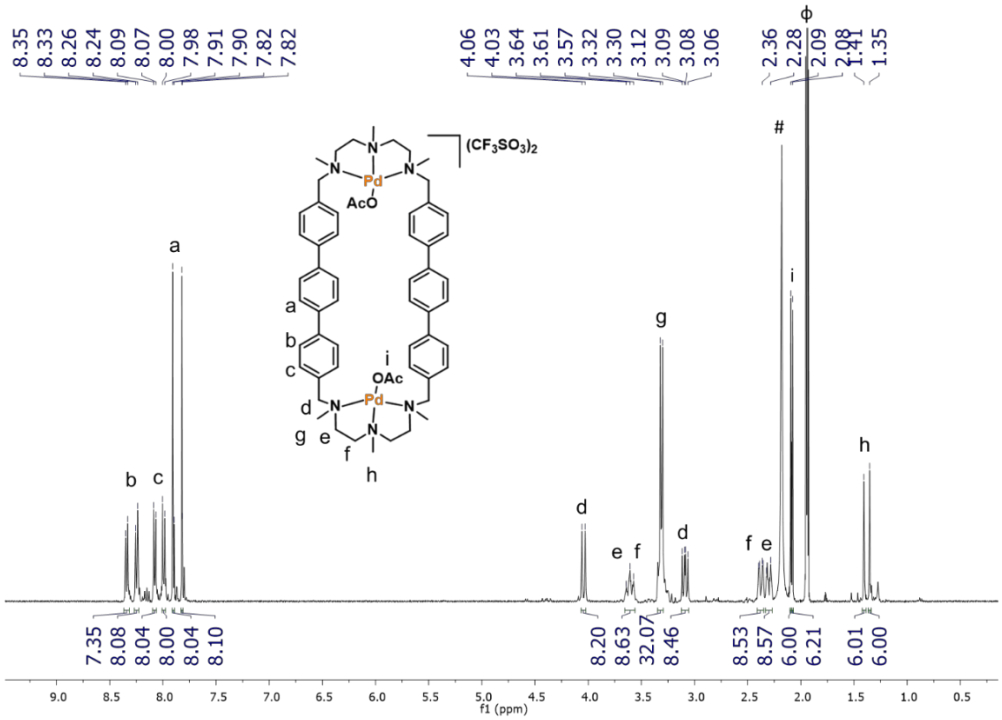

Supplementary Figure 53. ^{1}H-NMR of [Pd_2(Me_2ppp)$(AcO)_2$]$(OTf)_2$. Experiment was performed in CD_3CN at 298 K (400 MHz). (ϕ) CH_3CN, (#) H_2O.

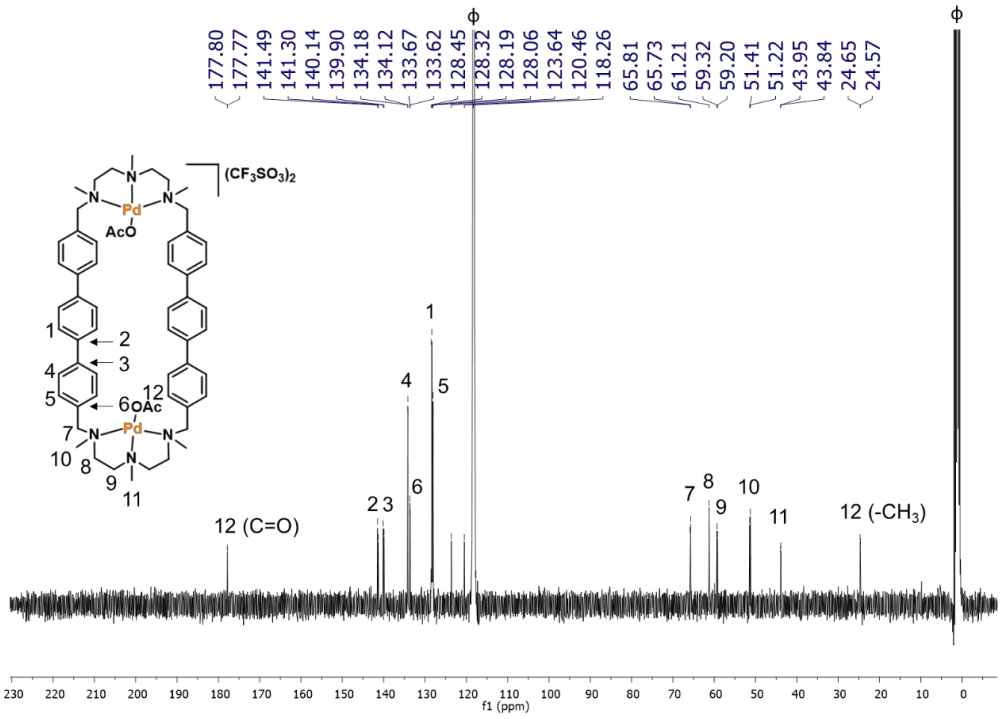

Supplementary Figure 54. ^{13}C-NMR of [Pd_2(Me_2ppp)$(AcO)_2$]$(OTf)_2$. Experiment was performed in CD_3CN at 298 K (100 MHz). (ϕ) CH_3CN.

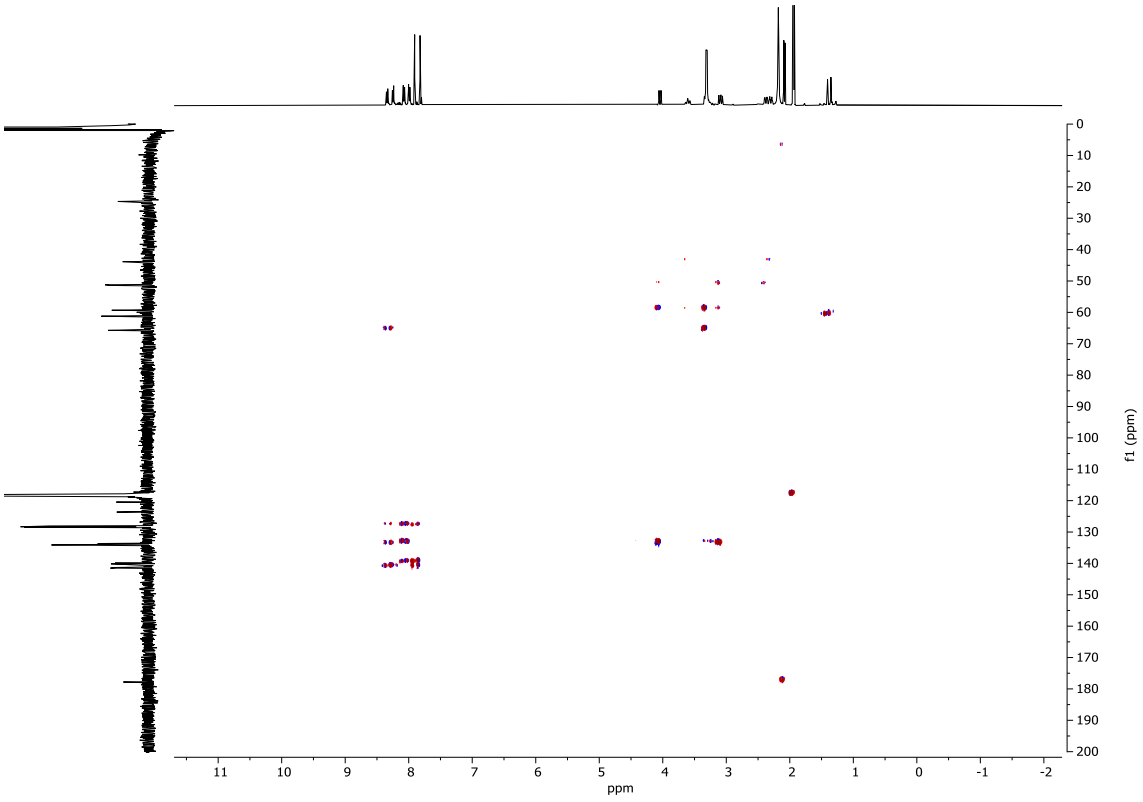

Supplementary Figure 55. HMBC of $[Pd_2(Me_2ppp)(AcO)_2](OTf)_2$. Experiment was performed in CD_3CN at 298 K (400 MHz).

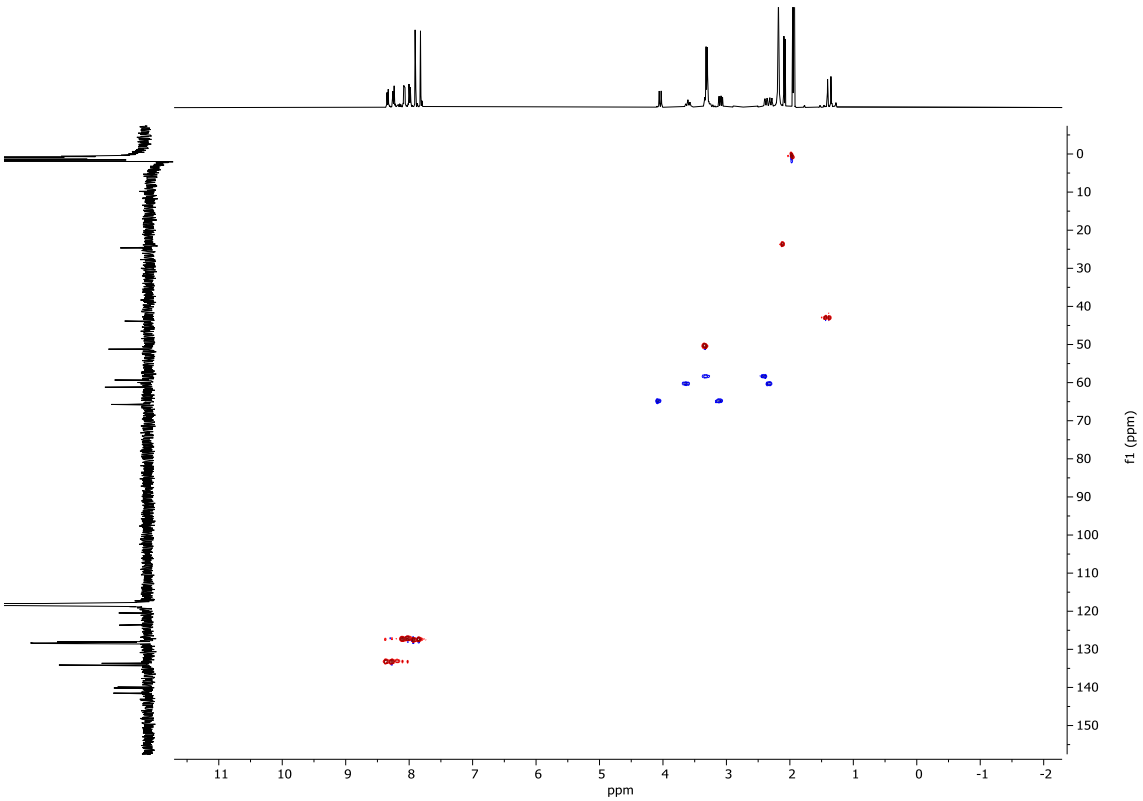

Supplementary Figure 56. HSQC of $[Pd_2(Me_2ppp)(AcO)_2](OTf)_2$. Experiment was performed in CD_3CN at 298 K (400 MHz).

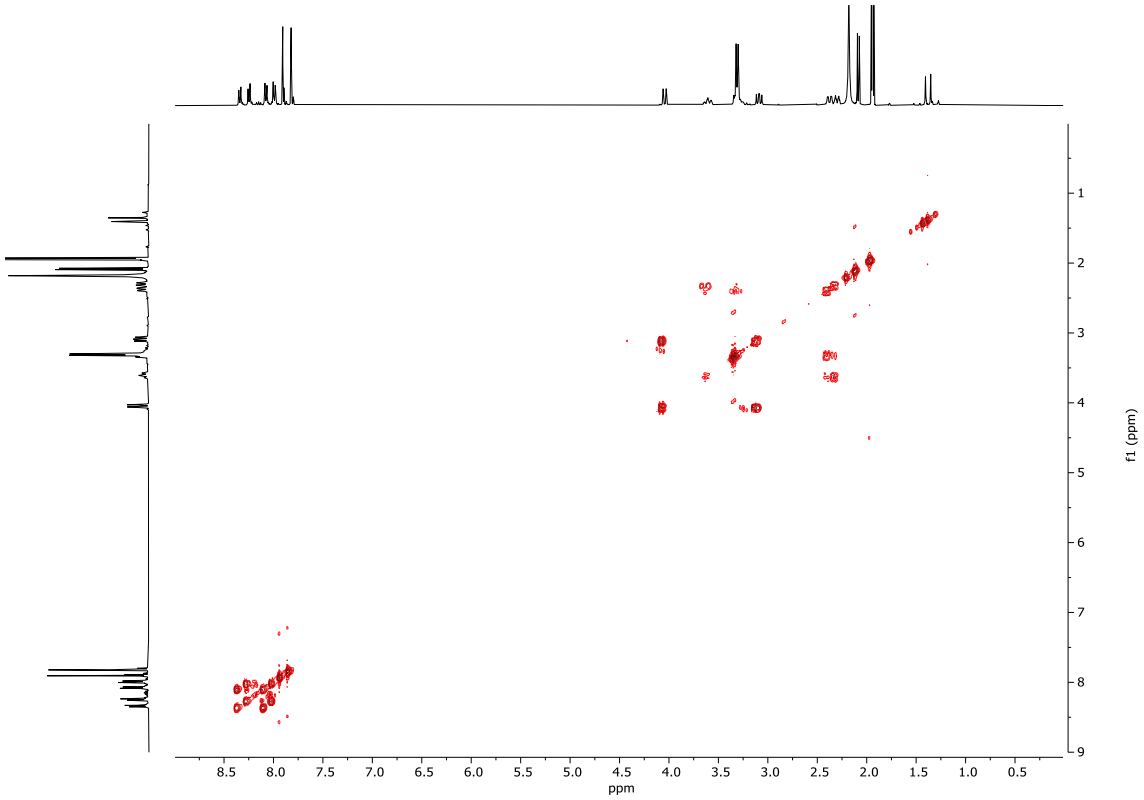

Supplementary Figure 57. COSY of $[Pd_2(Me_2ppp)(AcO)_2](OTf)_2$. Experiment was performed in CD_3CN at 298 K (400 MHz).

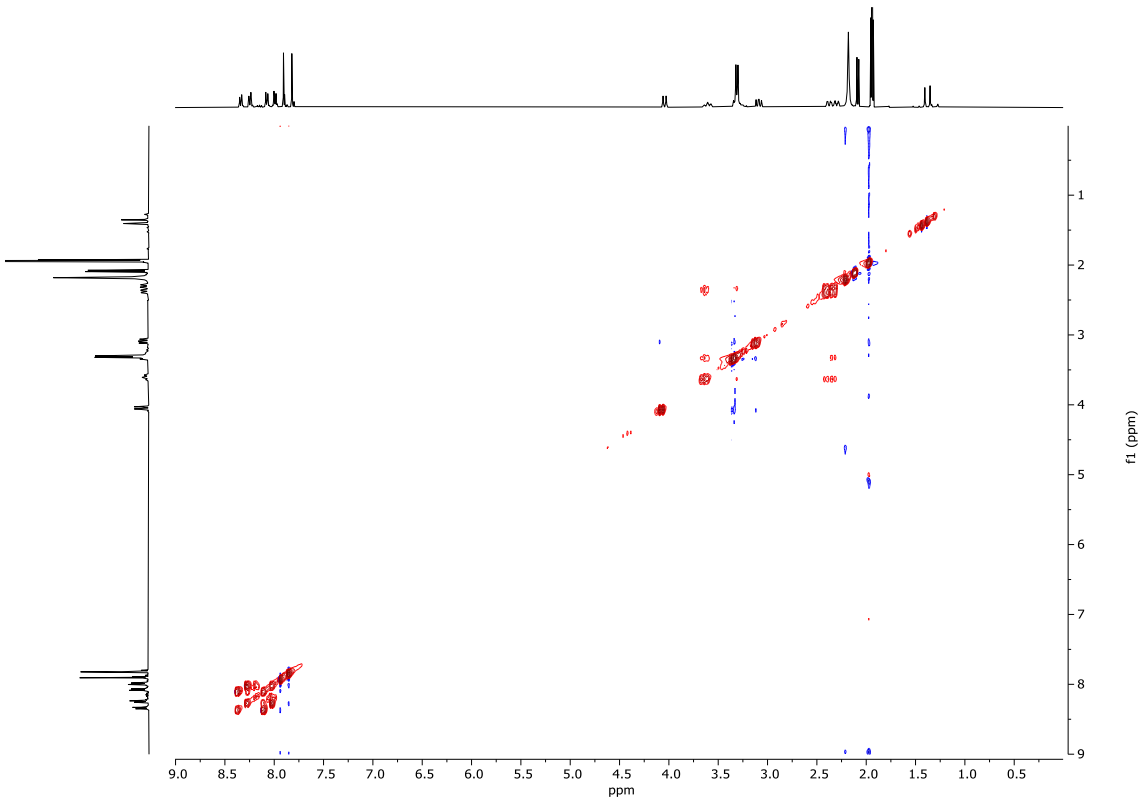

Supplementary Figure 58. TOCSY of $[Pd_2(Me_2ppp)(AcO)_2](OTf)_2$. Experiment was performed in CD_3CN at 298 K (400 MHz).

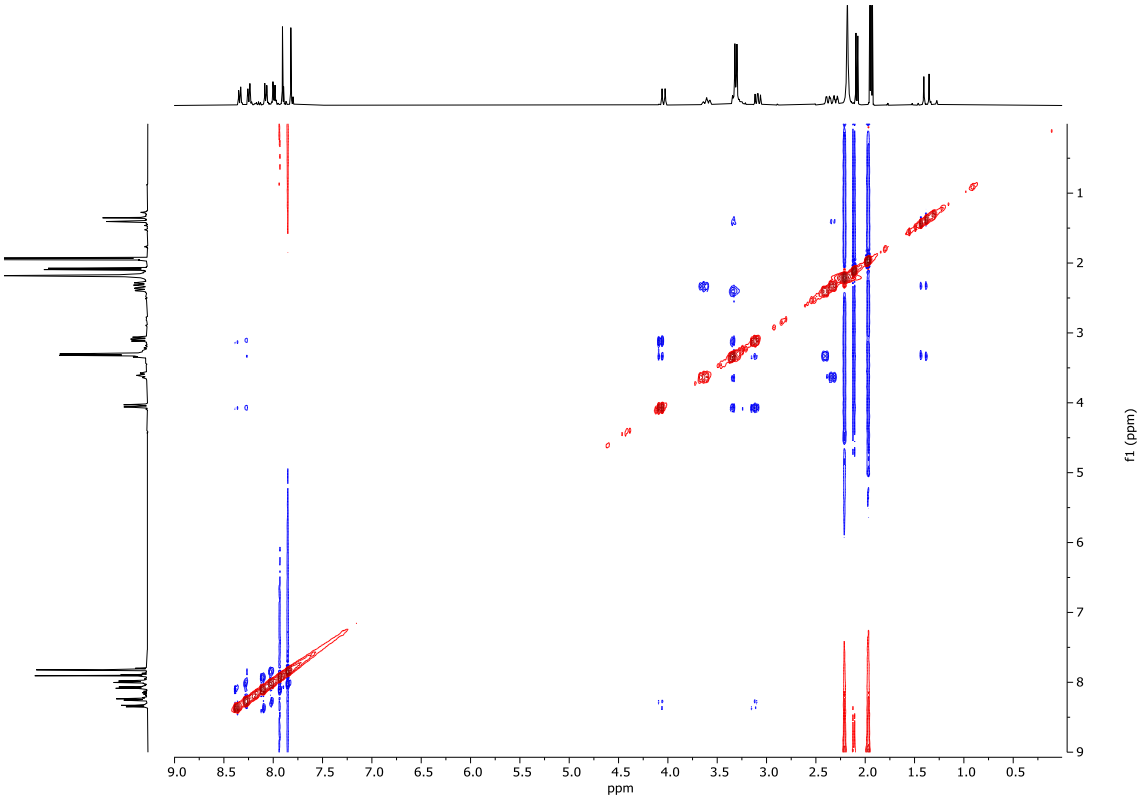

Supplementary Figure 59. NOESY of $[Pd_2(Me_2ppp)(AcO)_2](OTf)_2$. Experiment was performed in CD_3CN at 298 K (400 MHz).

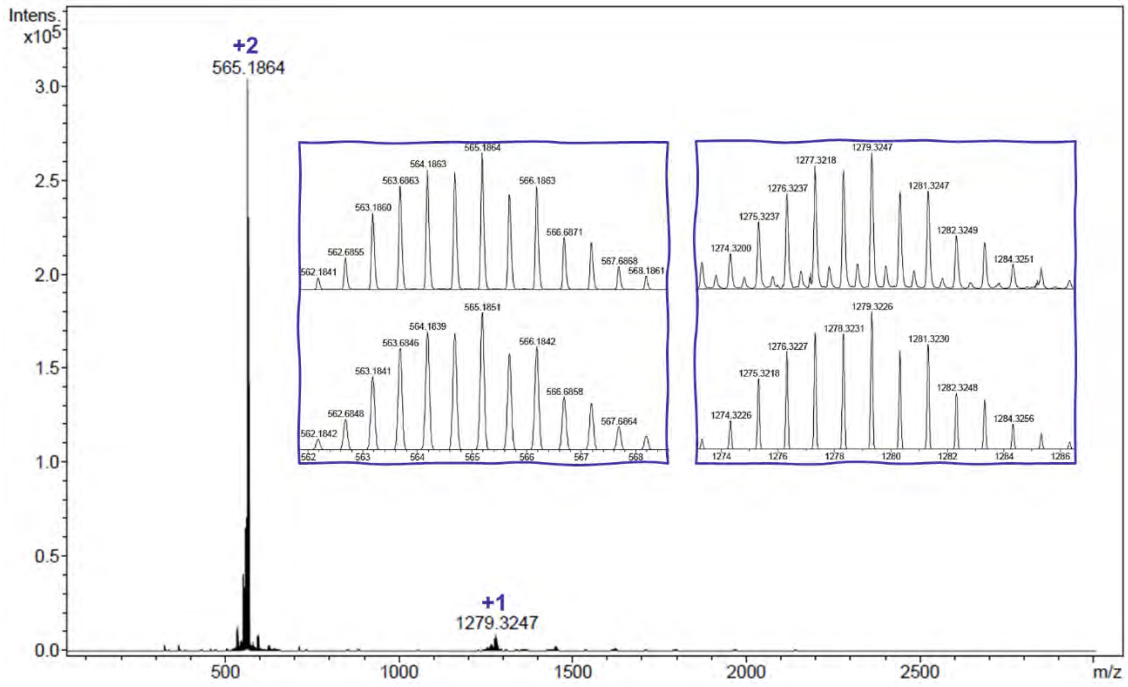

Supplementary Figure 60. HRMS spectrum of $[Pd_2(Me_2ppp)(AcO)_2](OTf)_2$. Experimental (top) and theoretical (bottom) isotopic pattern for selected peaks is shown. The sample was dissolved in acetonitrile and the spectrum was registered on a Bruker Micro TOF-Q-II exact mass spectrometer.

2.6. Characterization of dinuclear Cu^{II} molecular clip $[Cu_2(Me_2ppp)(OTf)_2](OTf)_2$

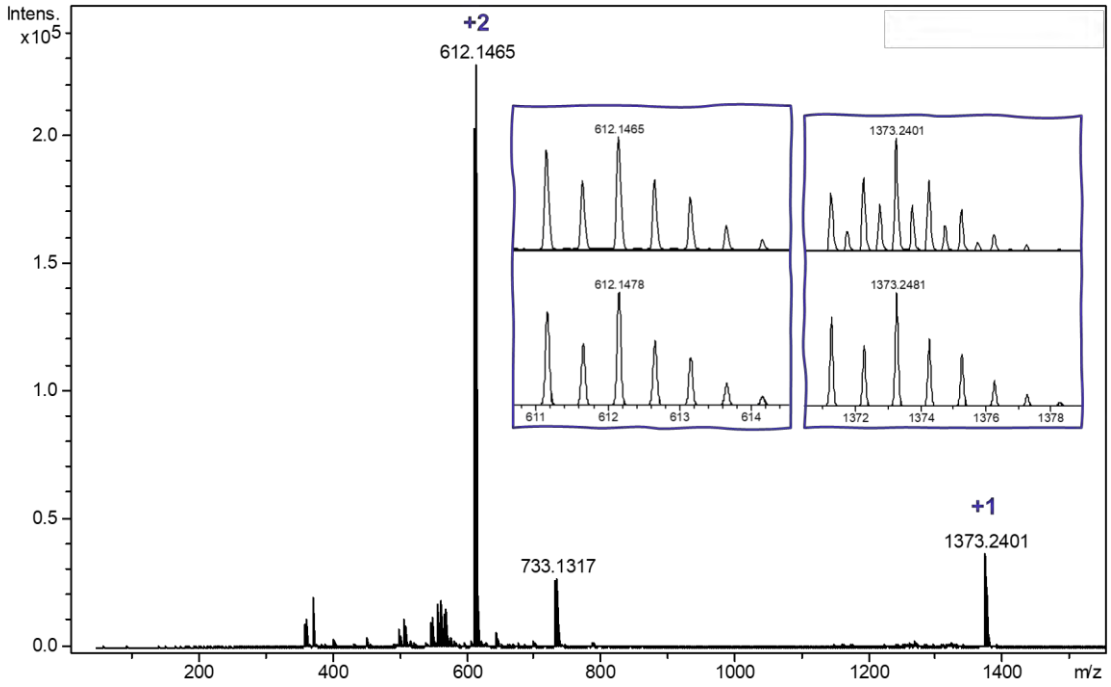

Supplementary Figure 61. HRMS spectrum of $[Cu_2(Me_2ppp)(OTf)_2](OTf)_2$. Experimental (top) and theoretical (bottom) isotopic pattern for selected peaks is shown. The sample was dissolved in acetonitrile and the spectrum was registered on a Bruker Micro TOF-Q-II exact mass spectrometer.

2.7. Characterization of tetragonal prismatic nanocapsule 8·(BArF)$_8$

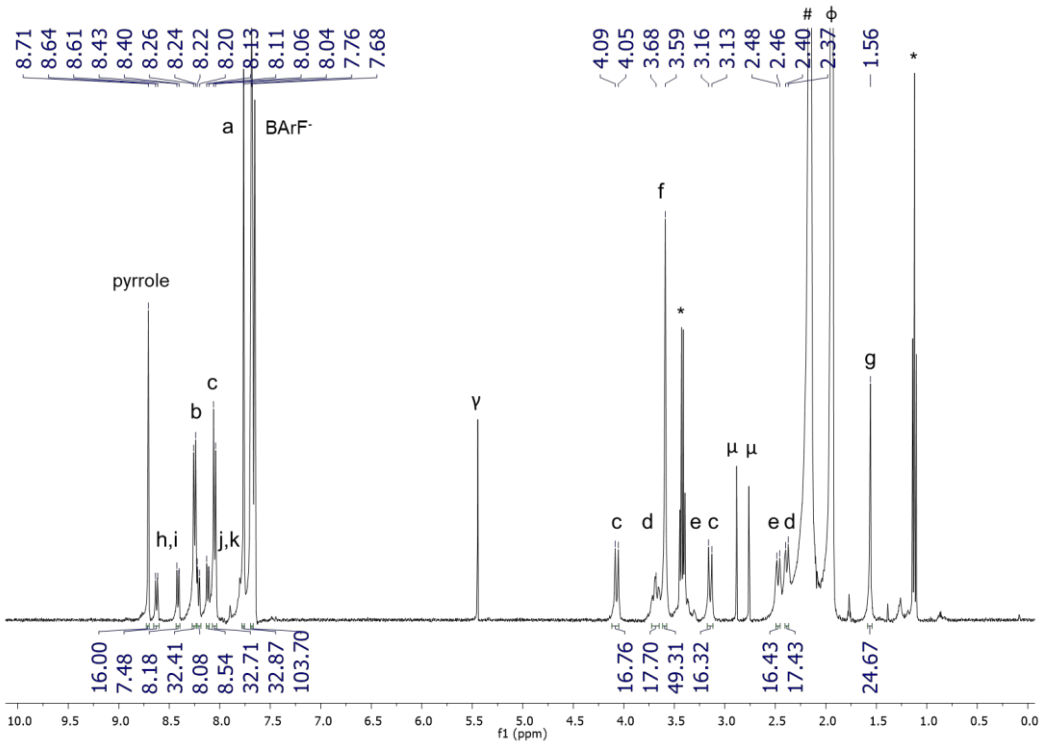

Supplementary Figure 62. ^{1}H-NMR of **8**·(BArF)$_8$ nanocapsule. Experiment was performed in CD_3CN at 298 K (400 MHz). (γ) DCM, (*) diethyl ether, (μ) dmf, (#) H_2O, (ϕ) CH_3CN.

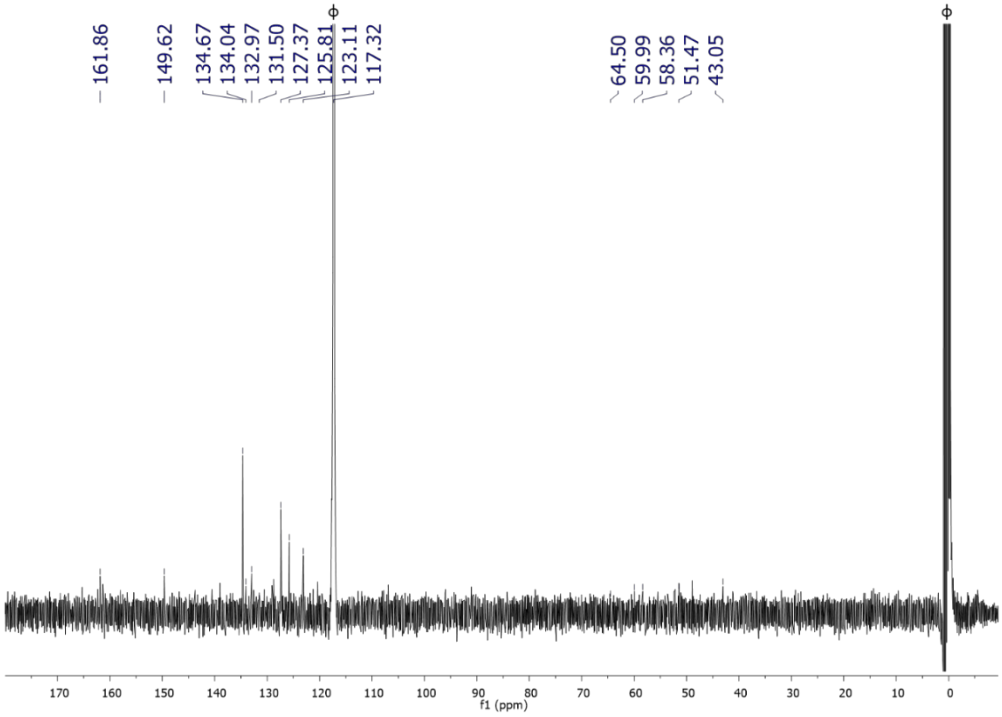

Supplementary Figure 63. ^{13}C-NMR of 8·(BArF)$_8$ nanocapsule. Experiment was performed in CD_3CN at 298 K (100 MHz). (ϕ) CH_3CN.

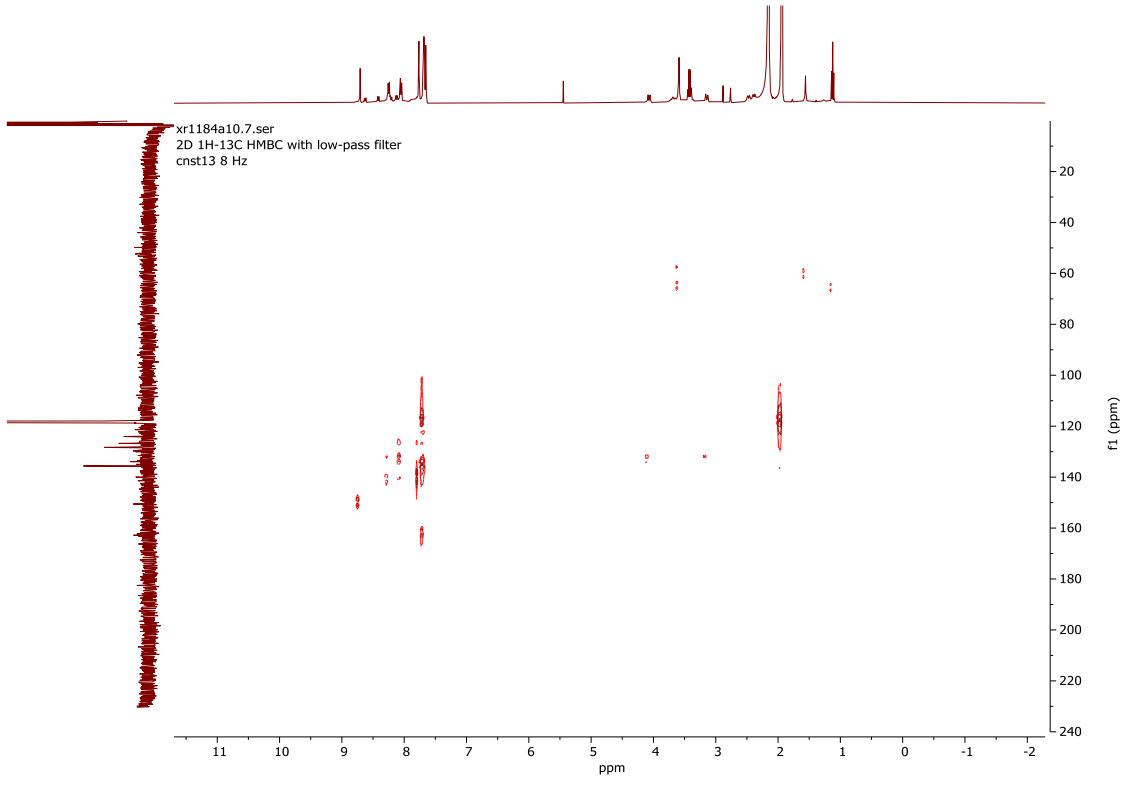

Supplementary Figure 64. HMBC of **8**·(BArF)$_8$ nanocapsule. Experiment was performed in CD_3CN at 298 K (400 MHz).

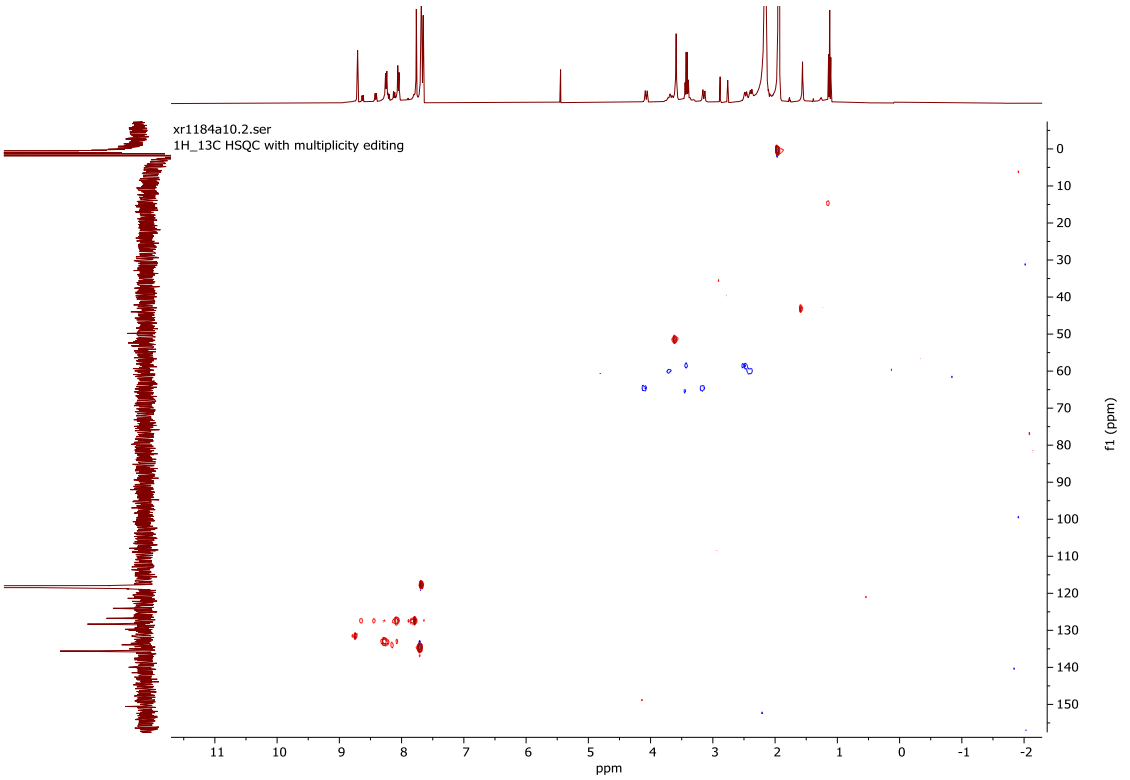

Supplementary Figure 65. HSQC of **8**·$(BArF)_8$ nanocapsule. Experiment was performed in CD_3CN at 298 K (400 MHz).

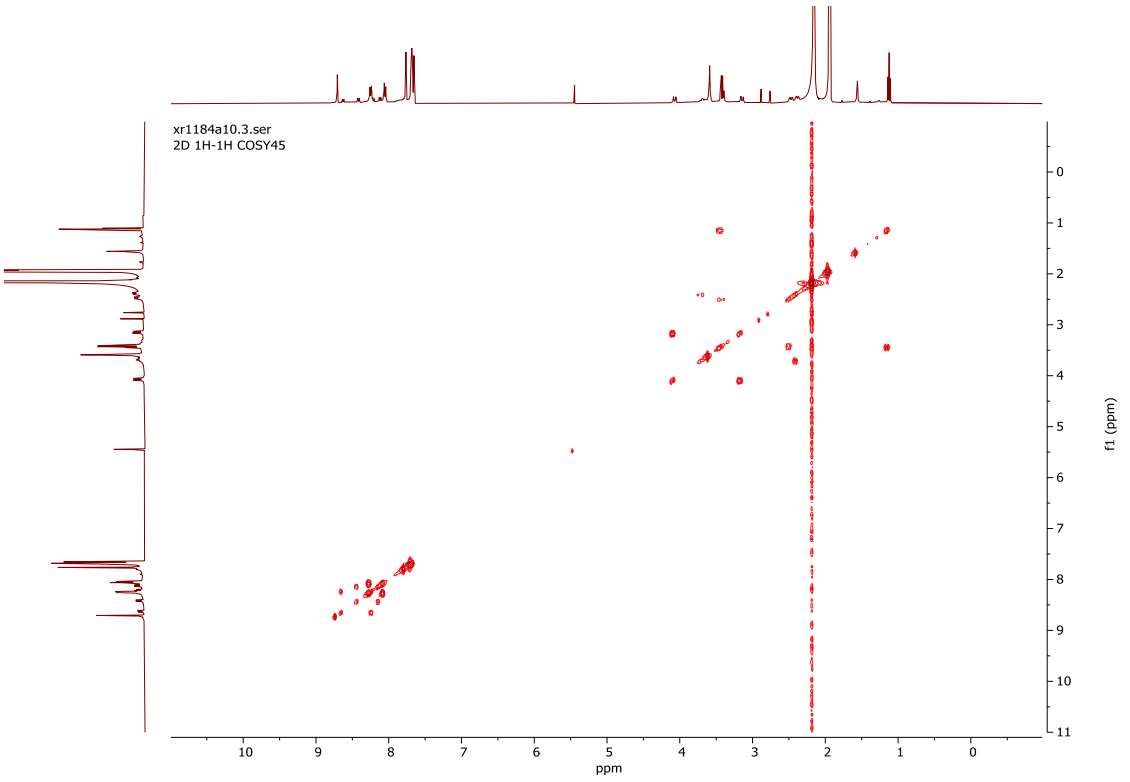

Supplementary Figure 66. COSY of **8**·$(BArF)_8$ nanocapsule. Experiment was performed in CD_3CN at 298 K (400 MHz).

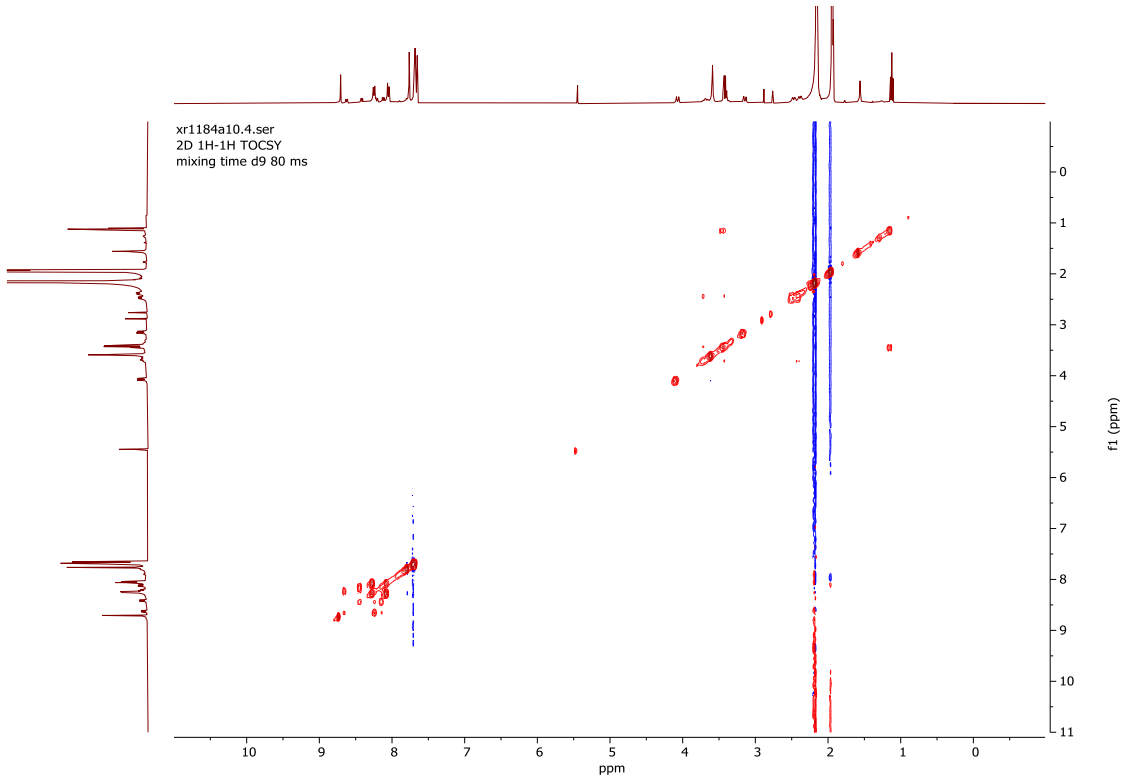

Supplementary Figure 67. TOCSY of **8**·$(BArF)_8$ nanocapsule. Experiment was performed in CD_3CN at 298 K (400 MHz).

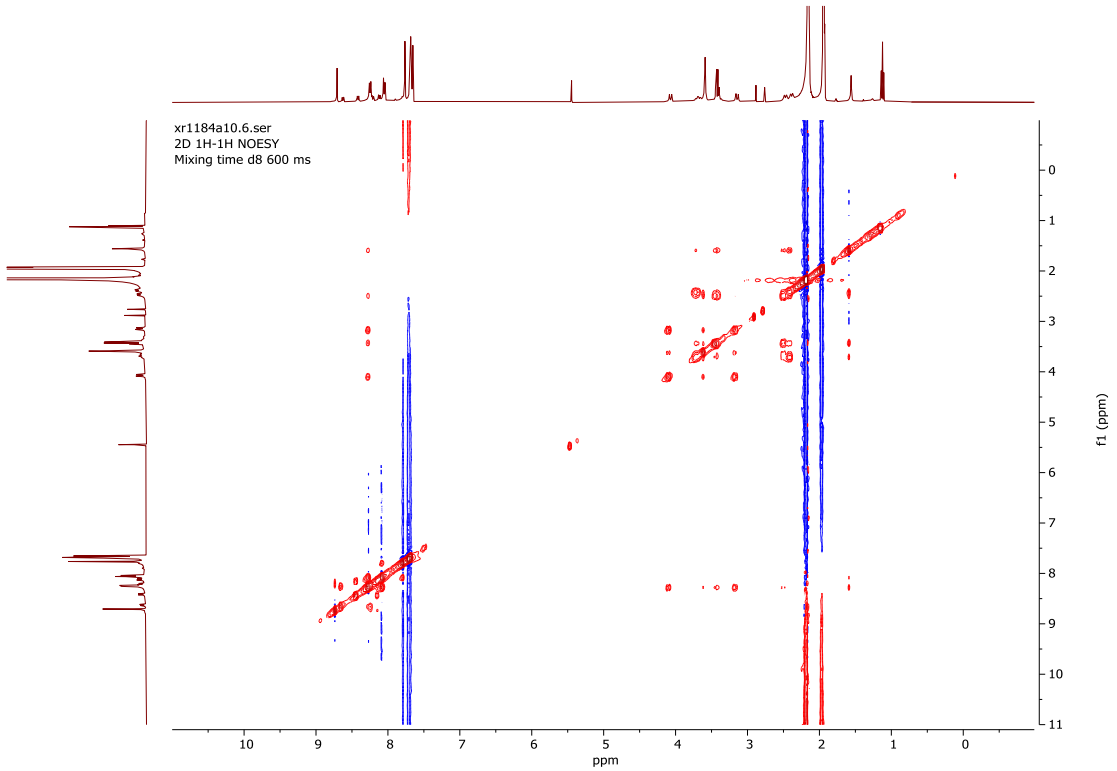

Supplementary Figure 68. NOESY of **8**·$(BArF)_8$ nanocapsule. Experiment was performed in CD_3CN at 298 K (400 MHz).

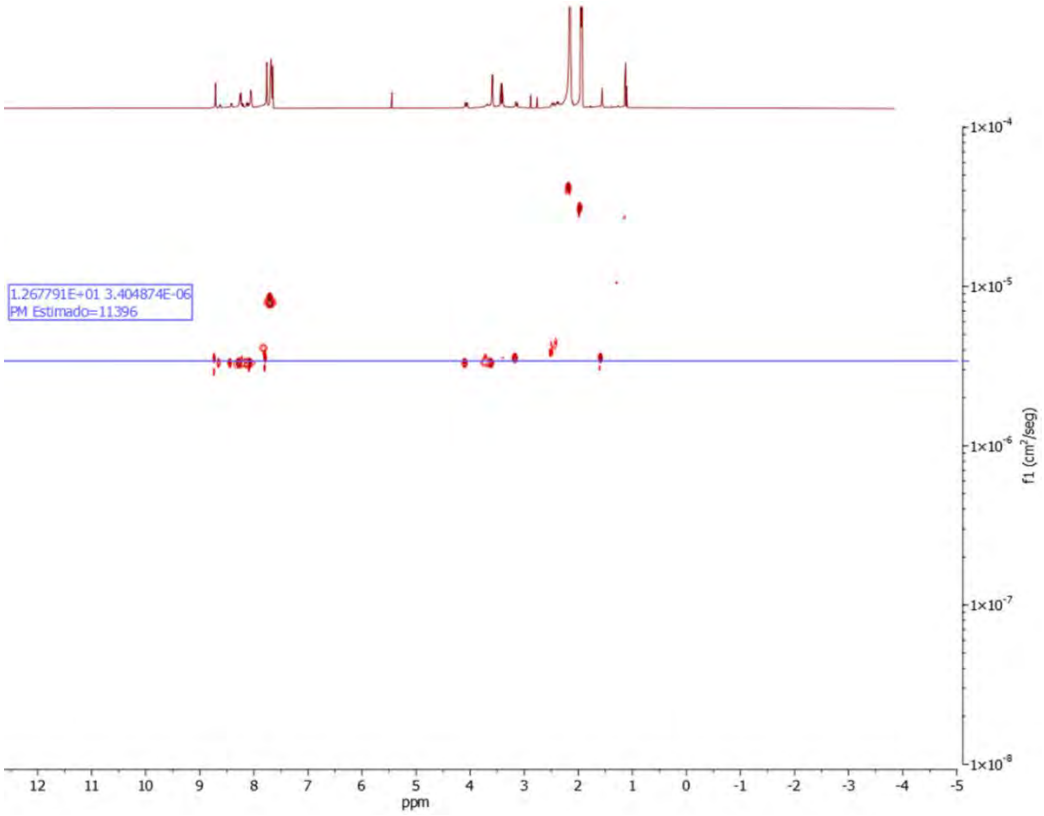

Supplementary Figure 69. DOSY of **8**·$(BArF)_8$ nanocapsule. Experiment was performed in CD_3CN at 298 K (400 MHz). (ϕ) CH_3CN.

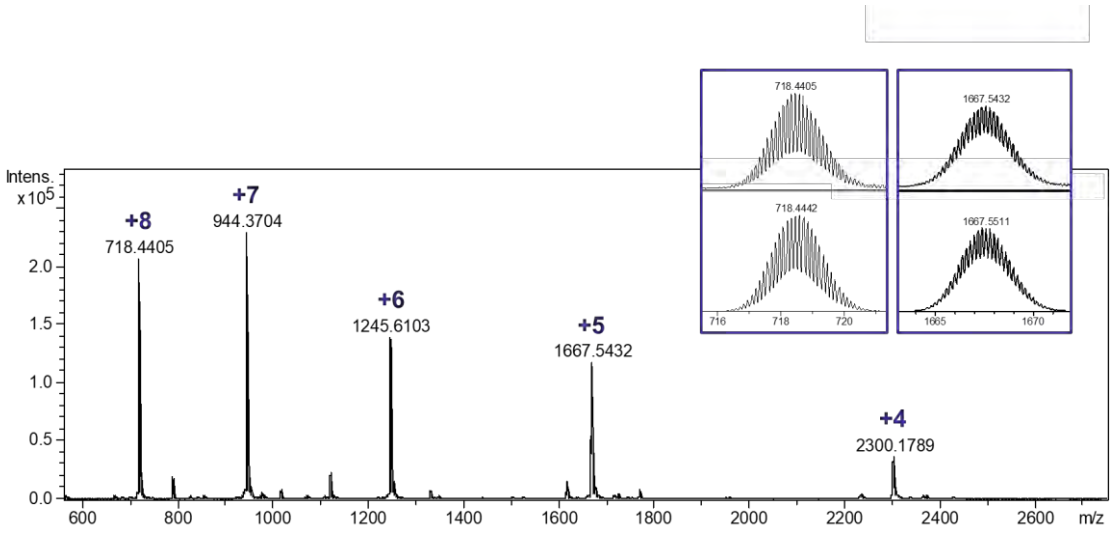

Supplementary Figure 70. HRMS spectrum of **8**·$(BArF)_8$ nanocapsule. Experimental (top) and theoretical (bottom) isotopic pattern for selected peaks is shown. The sample was dissolved in acetonitrile and the spectrum was registered on a Bruker Micro TOF-Q-II exact mass spectrometer.

2.8. Characterization of tetragonal prismatic nanocapsule 9·(BArF)$_8$

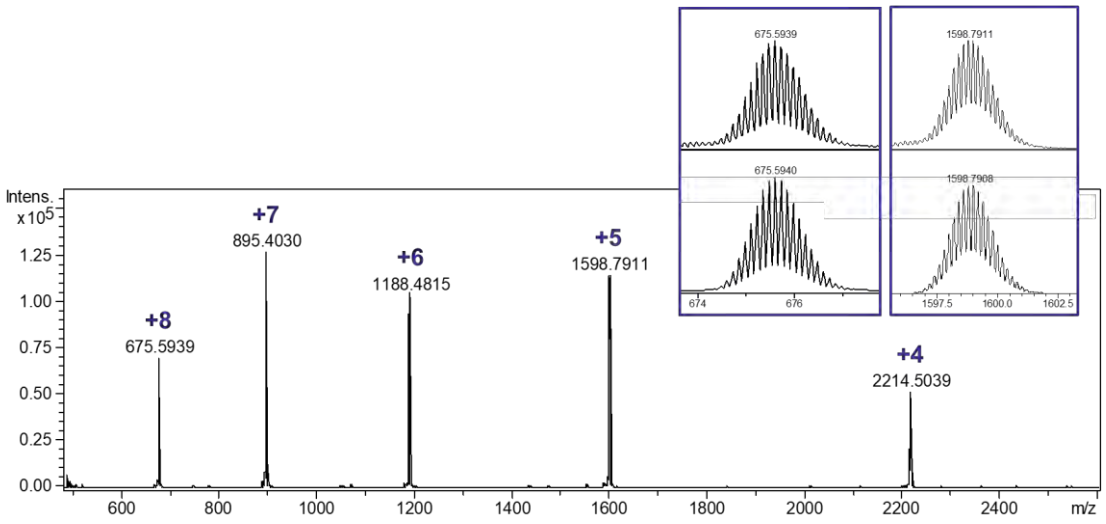

Supplementary Figure 71. HRMS spectrum of **9**·(BArF)$_8$ nanocapsule. Experimental (top) and theoretical (bottom) isotopic pattern for selected peaks is shown. The sample was dissolved in acetonitrile and the spectrum was registered on a Bruker Micro TOF-Q-II exact mass spectrometer.

3. Supplementary References

1. C. García-Simón, C. Colomban, Y. A. Çetin, A. Gimeno, M. Pujals, E. Ubasart, C. Fuertes-Espinosa, K. Asad, N. Chronakis, M. Costas, J. Jiménez-Barbero, F. Feixas and X. Ribas, *J. Am. Chem. Soc.*, 2020, **142**, 16051-16063.

2. J. C. Hummelen, B. Knight, J. Pavlovich, R. González and F. Wudl, *Science*, 1995, **269**, 1554-1556.

3. E. Ubasart, O. Borodin, C. Fuertes-Espinosa, Y. Xu, C. García-Simón, L. Gómez, J. Juanhuix, F. Gándara, I. Imaz, D. Maspoch, M. von Delius and X. Ribas, *Nat. Chem.*, 2021, **13**, 420-427.

4. O. Prakash, H. Joshi, K. N. Sharma, A. K. Sharma and A. K. Singh, *Eur. J. Inorg. Chem.*, 2015, **2015**, 520-526.

5. D. Brynn Hibbert and P. Thordarson, *Chem. Commun.*, 2016, **52**, 12792-12805.

Annex 3. Supporting information Chapter IV

Supramolecular nanocapsules as two-fold stabilizers of outer-cavity sub-nanometric Ru NPs and inner-cavity ultra-small Ru clusters

Ernest Ubasart, Irene Mustieles Marin, Juan Manuel Asensio, Gabriel Mencia, Ángela M. López-Vinasco, Cristina García-Simón, Iker del Rosal, Romuald Poteau,* Bruno Chaudret,* Xavi Ribas*

TABLE OF CONTENTS

1. Supplementary Methods

1.1.Materials and Instrumentation

Reagents and solvents were purchased from VWR Prolabo and Sigma-Aldrich. They were dried on alumina desiccant and degassed by passing Ar through for 20 min. Pyrazine was purchased from Sigma Aldrich and used without further purification. Ru(COD)(COT) was purchased from Nanomeps. ESI-MS measurements were performed on a Bruker MicroTOF-Q-II using CH_3CN as a mobile phase. The TEM samples were prepared by dropcast of the solution in a copper grid covered with an amorphous C film, and then dried under vaccum prior to measurement. The TEM images were recorded in a JEOL 1400 microscope working at 120 kV. HR-TEM images were recorded in a probe corrected JEOL ARM Cold-FEG operated at 200 keV.

The catalytic solutions were analyzed by gas chromatography (GC PerkinElmer 580) equipped with a capillary column Elite-5MS (PerkinElmer) and a FID detector and using H_2 as carrier gas. The GC is coupled to a Clarus SQ8T mass spectrometer. Conversion and yields were calculated by comparison of the peak areas of reagent, products and internal standard.

1.2.Procedure for the synthesis of nanocapsules and sub-nanometric nanoparticles

Nanocapsules **6**·$(BArF)_8$ and **8**·$(BArF)_8$ were synthesised following reported methodologies.[1, 2]

The synthesis of Ru NPs was performed in the glove box. For this, 2 mg of nanocapsule were dissolved in 2mL of THF in a Fisher-Porter bottle.[3, 4] To this solution, 324, 199, 149, 100 or 50 μL of a 0.064 M solution of Ru(COD)(COT) (1 mL THF) were added, corresponding to 130, 80, 60, 40 and 20 eq of Ru, respectively. Then 0.2 equivalents of pyrazine with respect to Ru were added, namely 170, 104, 78, 52 or 26 μL of a 0.024 M solution (10mL THF). Finally, 1 mL of THF was added to the solution. The final volume of the solutions was 3.5, 3.3, 3.2, 3.1 and 3.0 mL, respectively. The FP was taken out of the glovebox and charged with 1 bar of H_2. Prior to loading, the line was purged with 3 cycles H_2/vacuum. The solution was stirred for 2 min at room temperature and then the pressure was released. In the case of E12 the same procedure is followed by adding 324 μL of a 0.064 M solution of

Ru(COD)(COT) (which corresponds to 130 eq) and 170 μL of a 0.32 M solution of pyrazine (which corresponds to 1 eq). The total volume is 3.5 mL.

For the HRMS-ESI-QTOF analysis, 1 mL of acetonitrile was added to the solution, to solubilize the nanocapsule, followed by two drops of Hg. The mixture was stirred overnight and then filtered to remove the excess of NPs congregated with the Hg (except for E3 and E4).

1.3. Catalytic tests

The catalytic reactions were performed in a Fisher Porter which was load at the air. Different volumes of the Ru NPs solutions were added depending on the Ru equivalents employed in the formation of the NPs; they are specified in Table S1. In all the cases the catalytic loading was 0.25 mol%. To the solutions, 135 μL of styrene (1 mmol) and 227 μL of dodecane (1 mmol), as internal standard, were added. The volume of the solutions was completed to 5.5 mL with THF. In the case of the NPs synthesized employing 20 eq of Ru, 1.5 mL of the Ru NPs solution and 71 μL of styrene were employed, and the total volume of the solution was 3 mL. Then, the line was purged with 3 cycles of H_2/vaccum, the air of the Fisher-Porter was removed, and the Fisher-Porter was loaded with 3 bar of H_2. The mixture was stirred for 5 h at 50 °C. For the GC analysis, 2 drops of the solution were filtered over celite and diluted in 2 mL of THF.

Ru NPs solution	eq. Ru employed	[Ru] mother sol (mM)	V taken (mL)	mol Ru	[Ru] (mM)
E3	130	5.9	0.5	2.9E-06	0.53
E8	130	5.9	0.5	2.9E-06	0.53
E9	80	3.8	0.77	2.9E-06	0.53
E10	60	2.9	1	2.9E-06	0.53
E11	40	2.0	1.46	2.9E-06	0.53
E12	130	5.9	0.5	2.9E-06	0.53
E13*	32	1.0	1.5	1.5E-06	0.53

Table S1. Volumes and concentrations employed in the catalytic mixtures. Total volume of the solutions is 5.5 mL (THF). *Total volume 3 mL.

2. Supplementary Figures

2.1.Ru NPs characterization by TEM and HR-TEM

E1. Pd-pTp (**6**·$(BArF)_8$), 130 eq Ru, 0 eq pyrazine, THF, 10min.

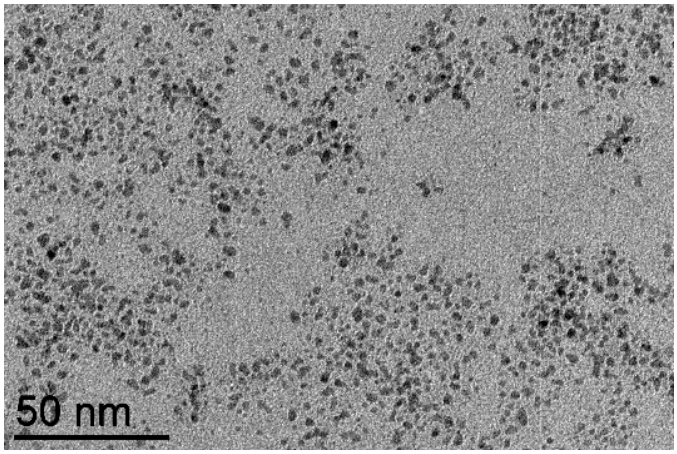

Figure S1. E1. Pd-pTp (**6**·$(BArF)_8$), 130 eq Ru, 0 eq pyrazine, THF, 10min (X120k).

E2. Pd-pTp (**6**·$(BArF)_8$), 130 eq Ru, 0.2 eq pyrazine, THF, 10min.

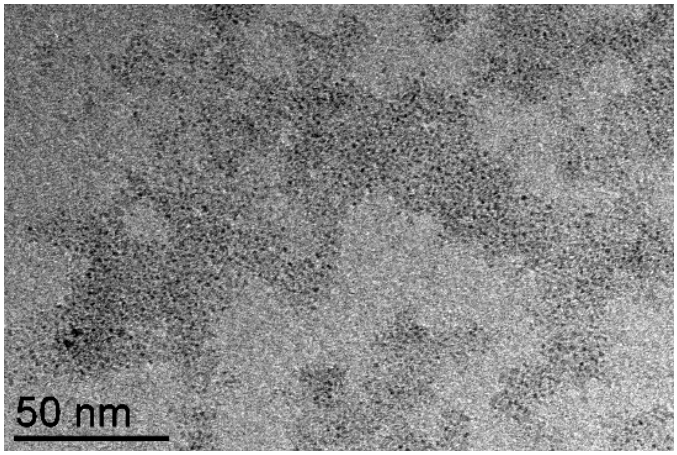

Figure S2. E2. Pd-pTp (**6**·$(BArF)_8$), 130 eq Ru, 0.2 eq pyrazine, THF, 10min (X120k).

E3. Pd-ppp (**8**·$(BArF)_8$), 130 eq Ru, 0 eq pyrazine, THF, 10min.

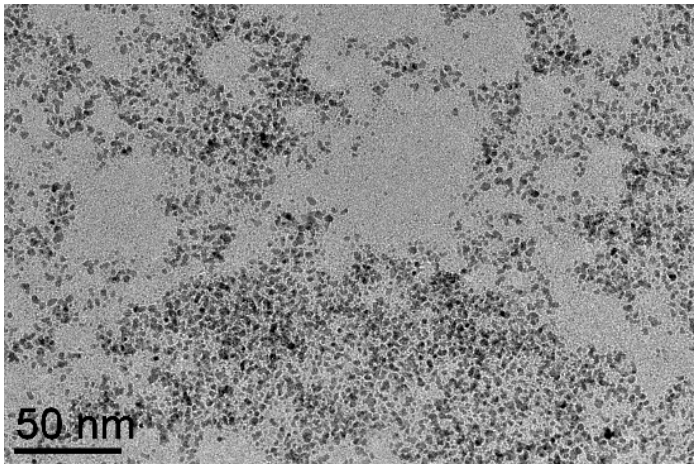

Figure S3. E3. Pd-ppp (**8**·$(BArF)_8$), 130 eq Ru, 0 eq pyrazine, THF, 10min (X120k).

E4. Pd-ppp (**8**·$(BArF)_8$), 130 eq Ru, 0.2 eq pyrazine, THF, 10min.

A

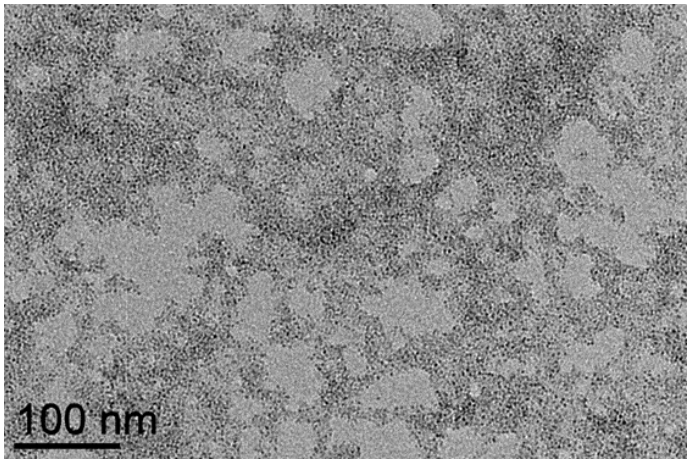

B

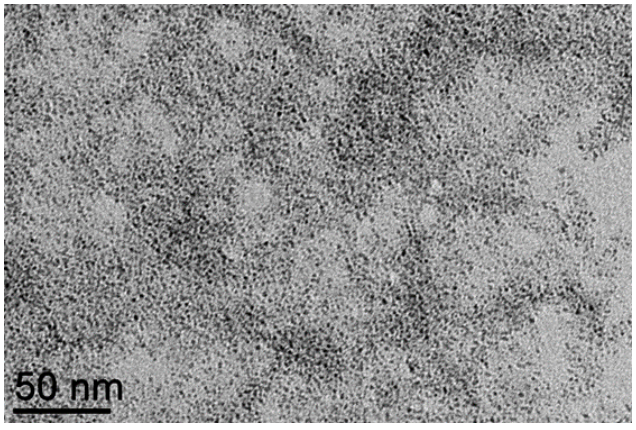

Figure S4. E4. Pd-ppp (**8**·$(BArF)_8$), 130 eq Ru, 0.2 eq pyrazine, THF, 10min. (A) X40k, (B) X80k.

E5. Pd-ppp (**8**·$(BArF)_8$), 40 eq Ru, 0.2 eq pyrazine, THF, 10min.

A

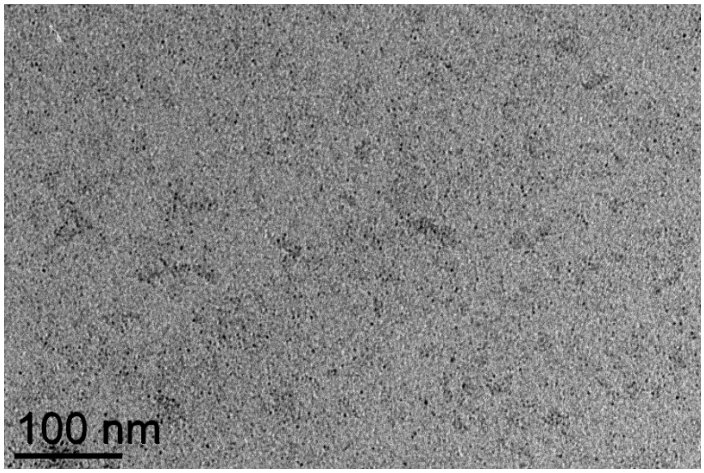

B

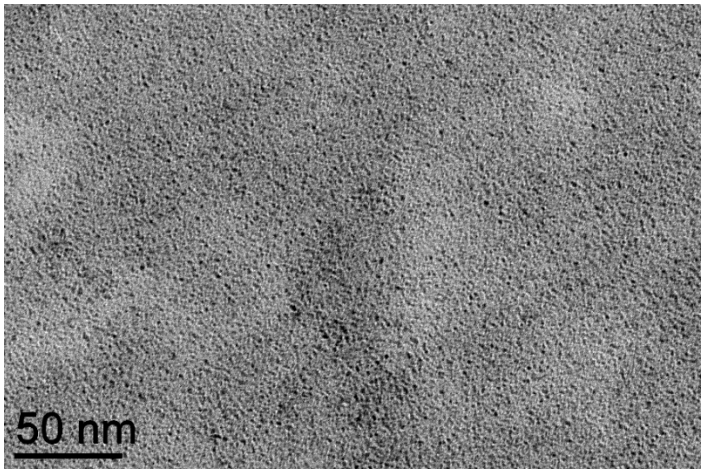

C

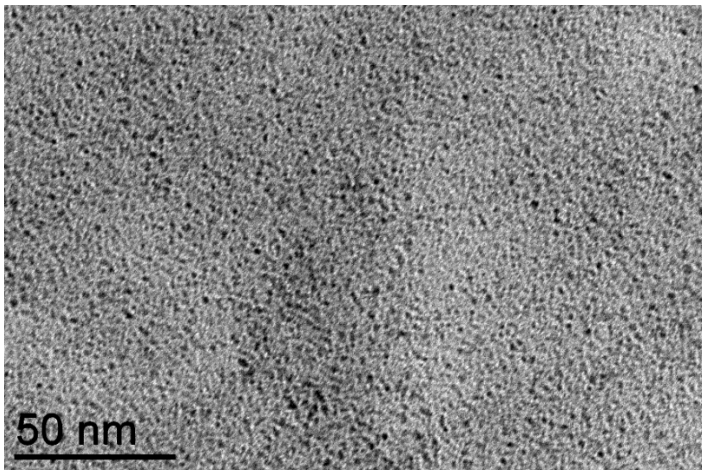

Figure S5. E5. Pd-ppp (**8**·$(BArF)_8$), 40 eq Ru, 0.2 eq pyrazine, THF, 10min. (A) X40k, (B) X80k, (C) 120k.

E6. Pd-ppp (**8**·$(BArF)_8$), 20 eq Ru, 0.2 eq pyrazine, THF, 10min.

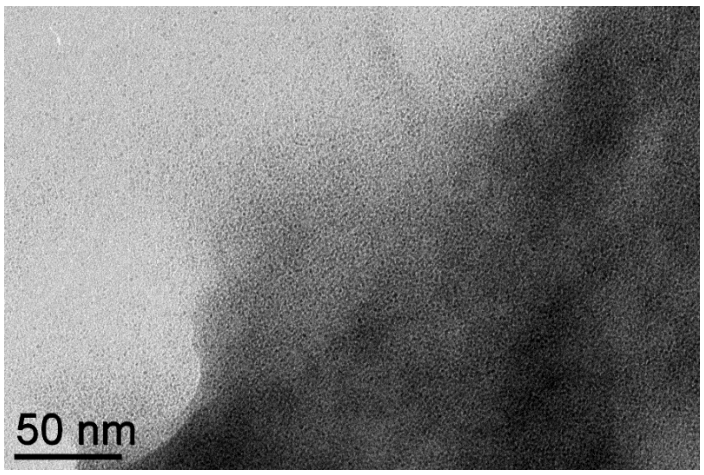

Figure S6. E6. Pd-ppp (**8**·$(BArF)_8$), 20 eq Ru, 0.2 eq pyrazine, THF, 10min (X80k).

E7. Pd-ppp (**8**·$(BArF)_8$), 200 eq Ru, 0.2 eq pyrazine, THF, 2min.

A

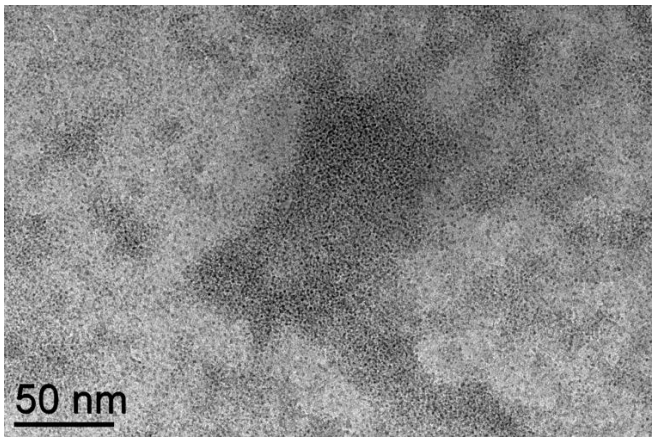

B

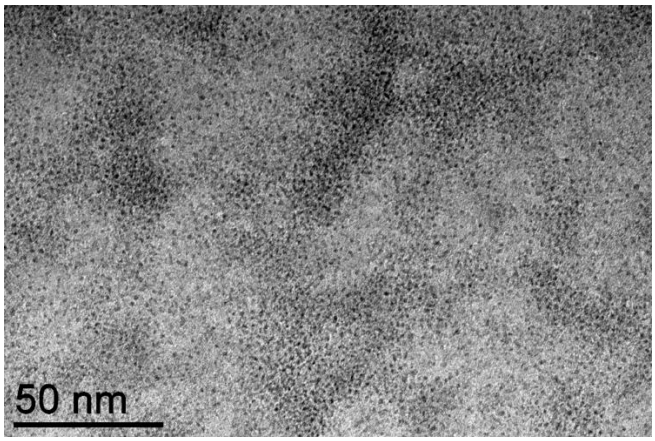

Figure S7. E7. Pd-ppp (**8**·$(BArF)_8$), 200 eq Ru, 0.2 eq pyrazine, THF, 2min. (A) X80k, (B) X120k.

E8. Pd-ppp (**8**·$(BArF)_8$), 130 eq Ru, 0.2 eq pyrazine, THF, 2min.

A

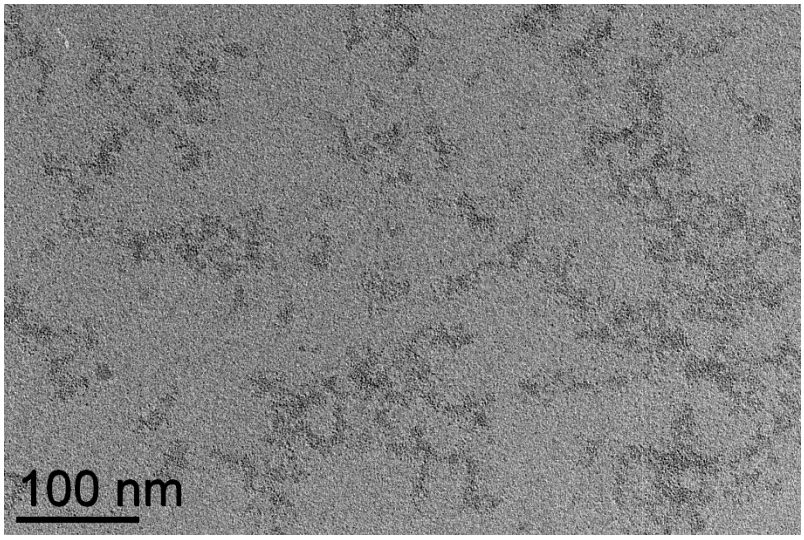

B

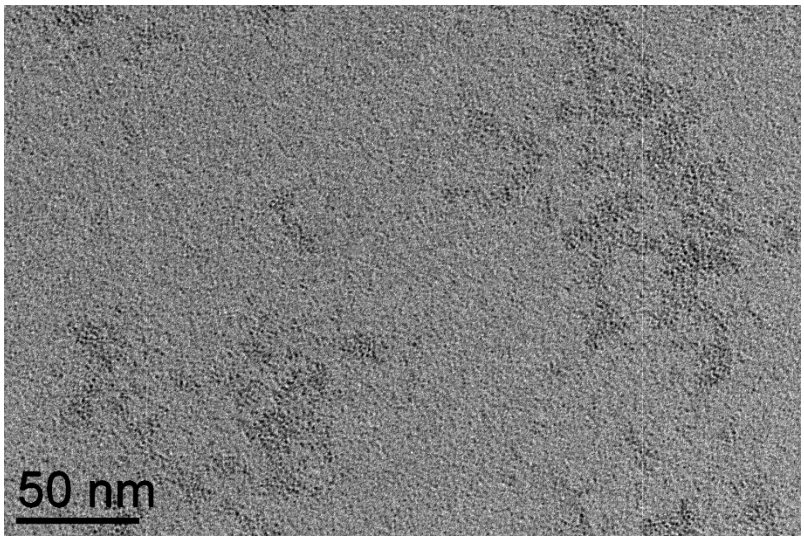

Figure S8. E8. Pd-ppp (**8**·$(BArF)_8$), 130 eq Ru, 0.2 eq pyrazine, THF, 2min. (A) X40k, (B) X80k.

E9. Pd-ppp (**8**·$(BArF)_8$), 80 eq Ru, 0.2 eq pyrazine, THF, 2min.

A

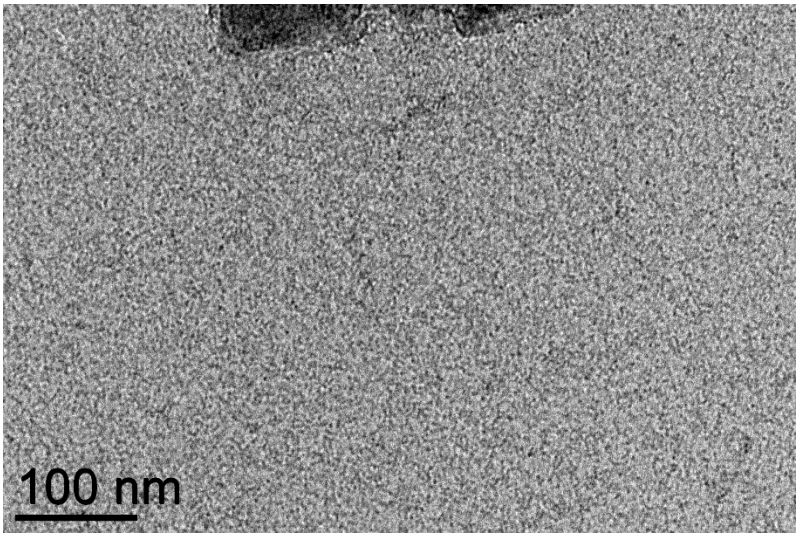

B

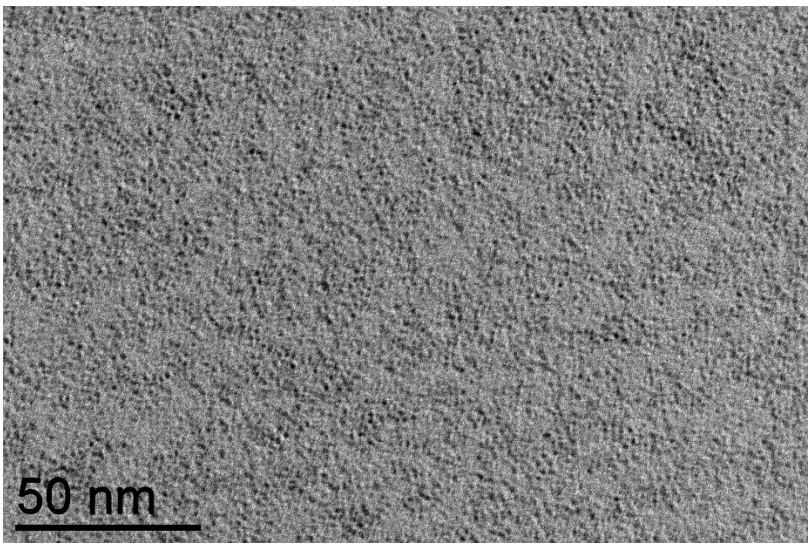

Figure S9. E9. Pd-ppp (**8**·$(BArF)_8$), 80 eq Ru, 0.2 eq pyrazine, THF, 2min. (A) X40k, (B) X120k.

E10. Pd-ppp (**8**·$(BArF)_8$), 60 eq Ru, 0.2 eq pyrazine, THF, 2min.

A

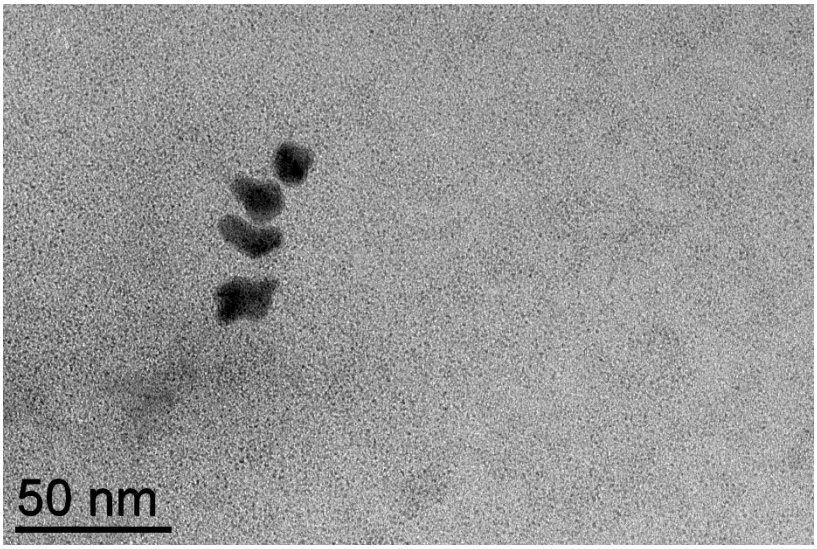

B

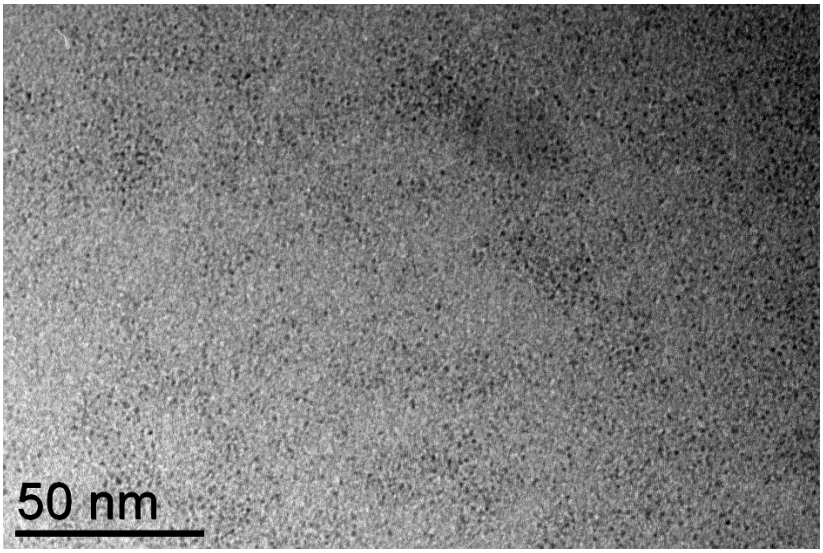

Figure S10. E10. Pd-ppp (**8**·$(BArF)_8$), 60 eq Ru, 0.2 eq pyrazine, THF, 2min. (A) X100k, (B) X120k.

E11. Pd-ppp (**8**·$(BArF)_8$), 40 eq Ru, 0.2 eq pyrazine, THF, 2min.

A

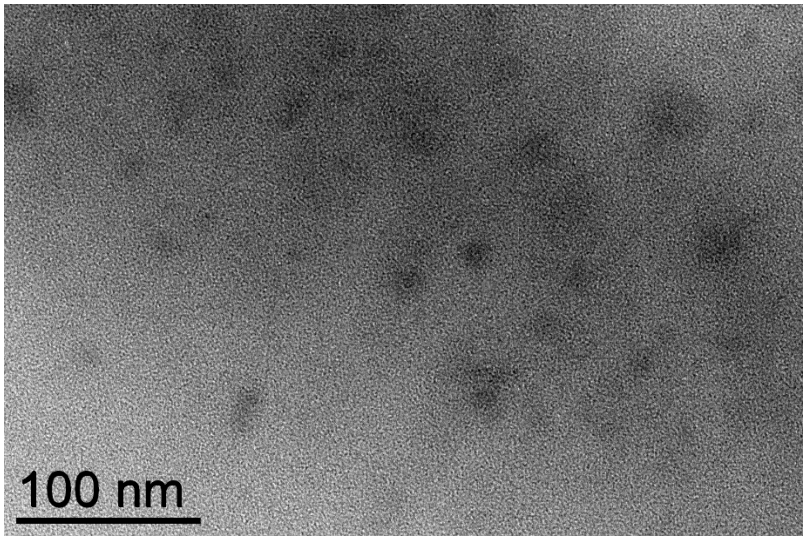

B

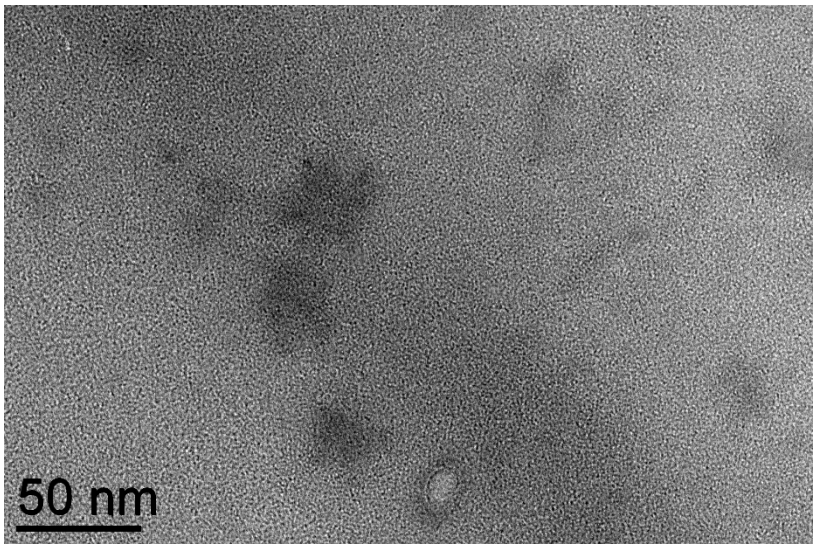

Figure S11. E11. Pd-ppp (**8**·$(BArF)_8$), 40 eq Ru, 0.2 eq pyrazine, THF, 2min. (A) X60k, (B) X80k.

E12. Pd-ppp (**8**·$(BArF)_8$), 130 eq Ru, 1 eq pyrazine, THF, 2min.

A

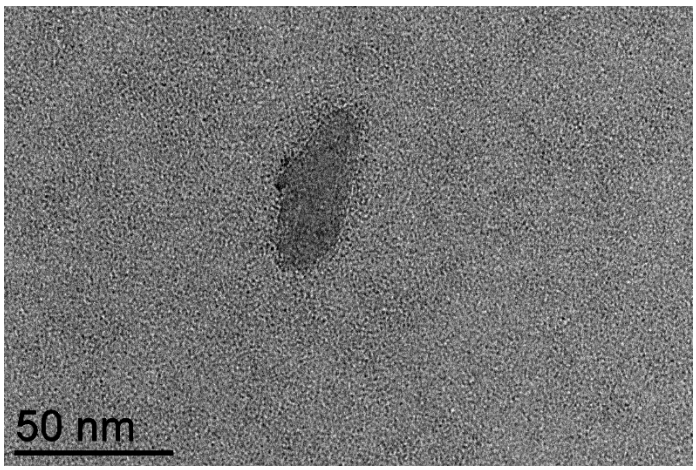

B

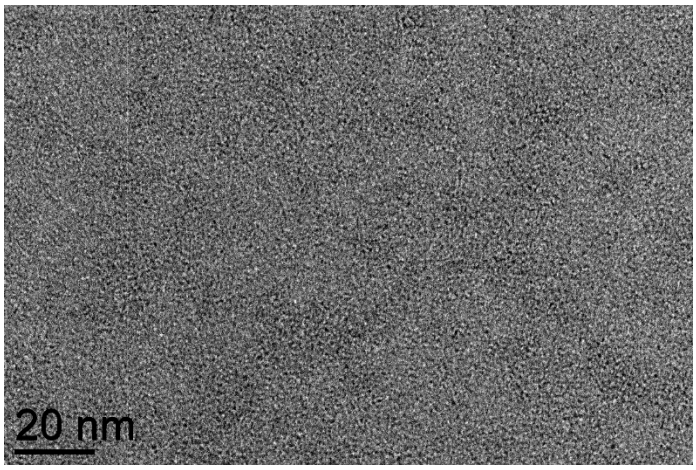

C

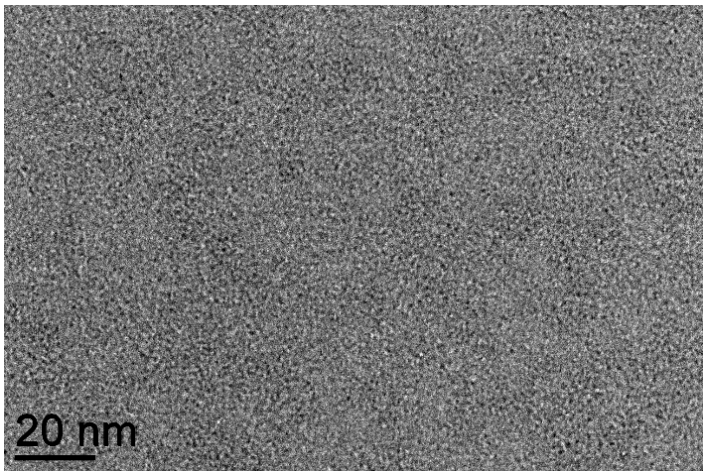

Figure S12. E12. Pd-ppp (**8**·$(BArF)_8$), 130 eq Ru, 1 eq pyrazine, THF, 2 min. (A) X120k, (B) X150k, (C) 150k.

E13. Pd clip ([$Pd_2(Me_2ppp)(AcO)_2$]$(OTf)_2$), 32 eq Ru, 0.2 eq pyrazine, THF (drops MeCN), 10min.

A

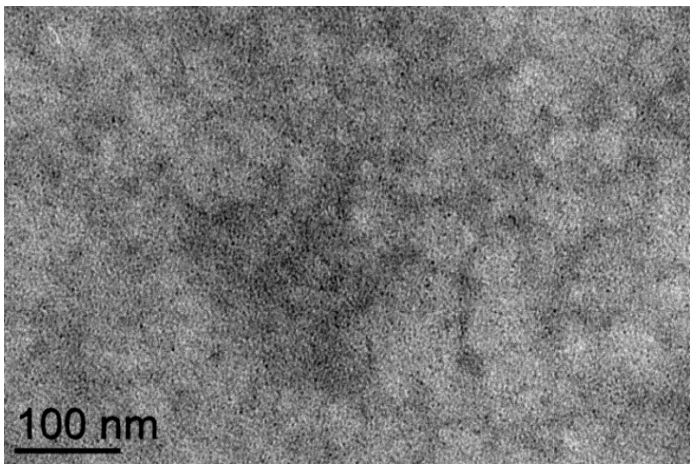

B

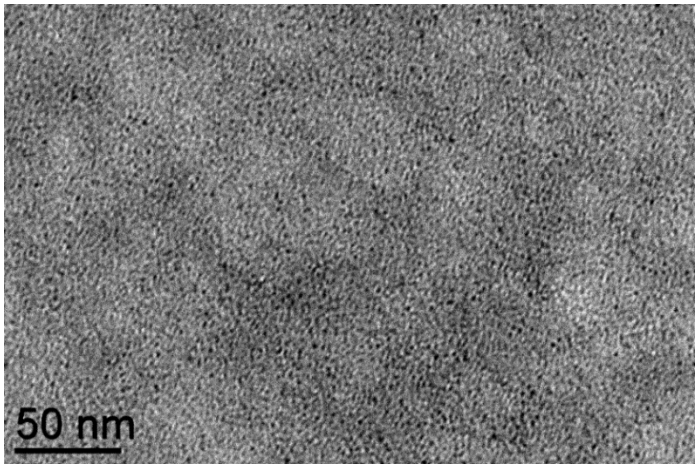

C

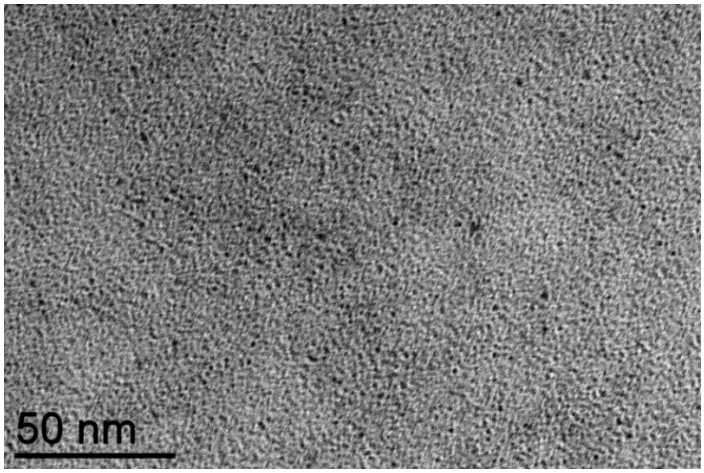

Figure S13. E13. Pd clip ([$Pd_2(Me_2ppp)(AcO)_2$]$(OTf)_2$), 32 eq Ru, 0.2 eq pyrazine, THF (drops MeCN), 10min. (A) X40k, (B) X80k, (C) X120k.

E14. Porf Zn (Zn-TCPP), 65 eq Ru, 0.2 eq pyrazine, THF (drops DMF), 10min.

A

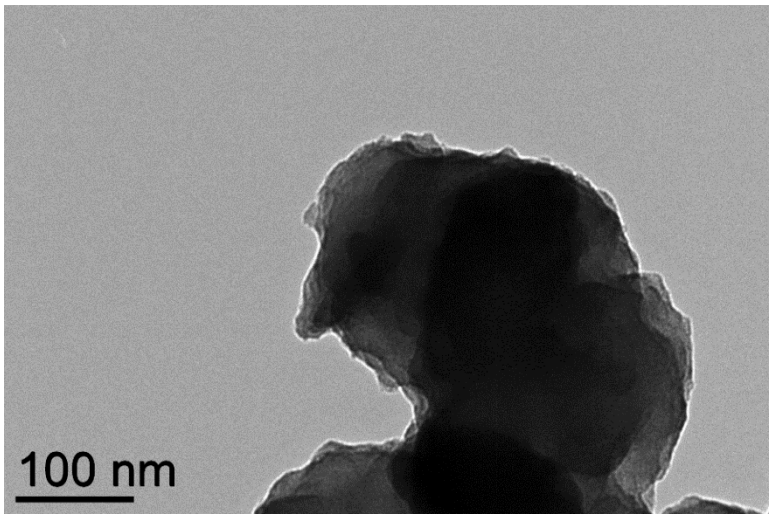

Figure S14. E14. Porf Zn (Zn-TCPP), 65 eq Ru, 0.2 eq pyrazine, THF (drops DMF), 10min. (A) X40k.

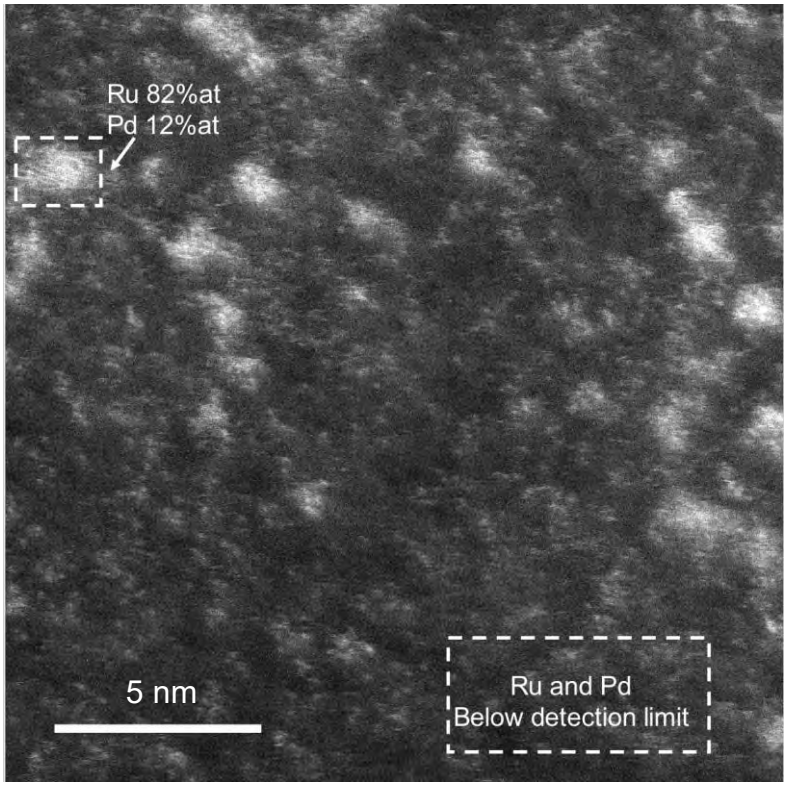

Figure S15. HR-TEM-EDX characterization corresponding to E2.

2.2.Ru NPs size distribution

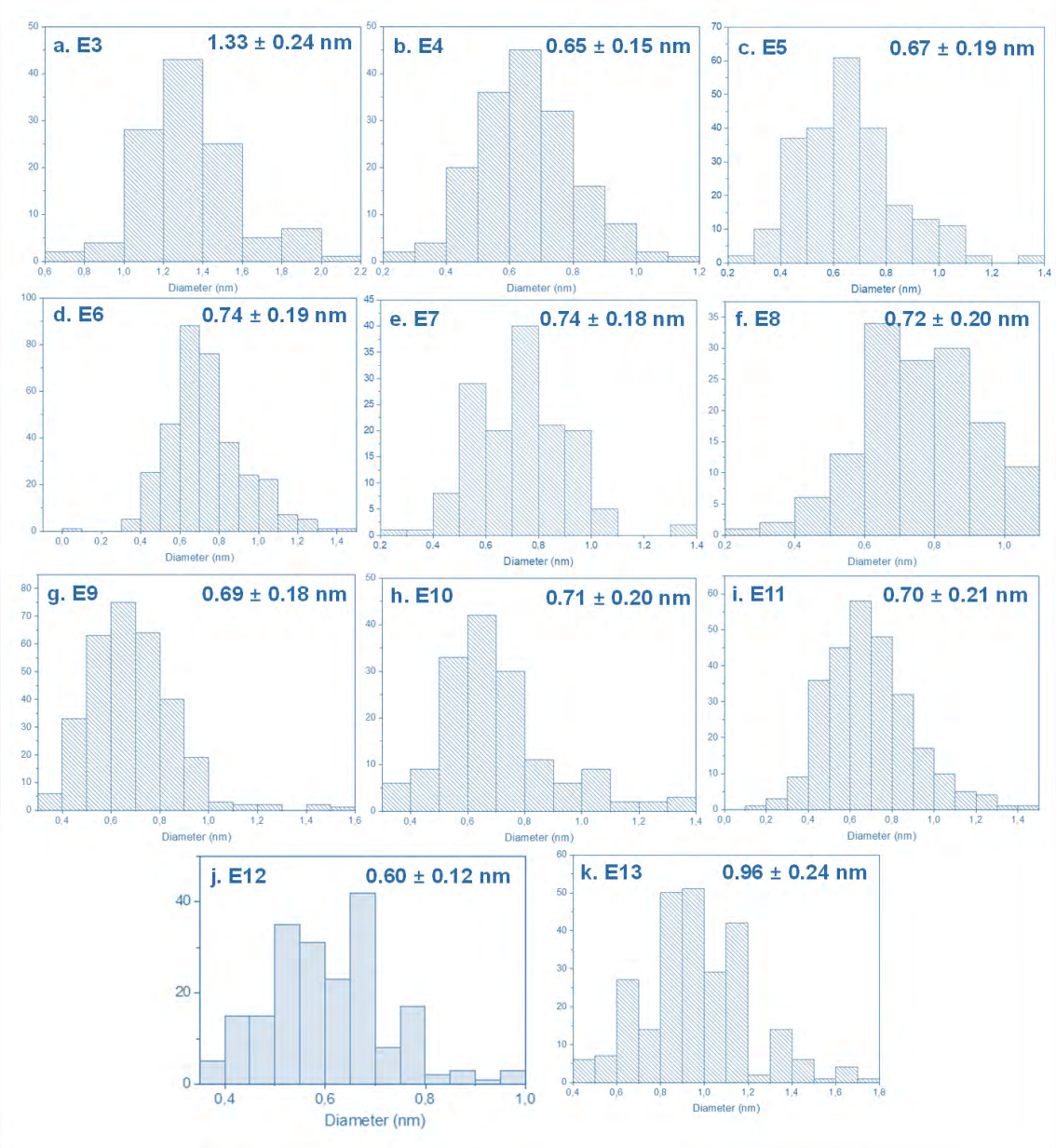

Figure S16. Ru NPs size distribution for E3 (**a**), E4 (**b**), E5 (**c**), E6 (**d**), E7 (**e**), E8 (**f**), E9 (**g**). E10 (**h**), E11 (**i**), E12 (**j**) and E13 (**k**).

2.3.Ru NPs characterization by HRMS

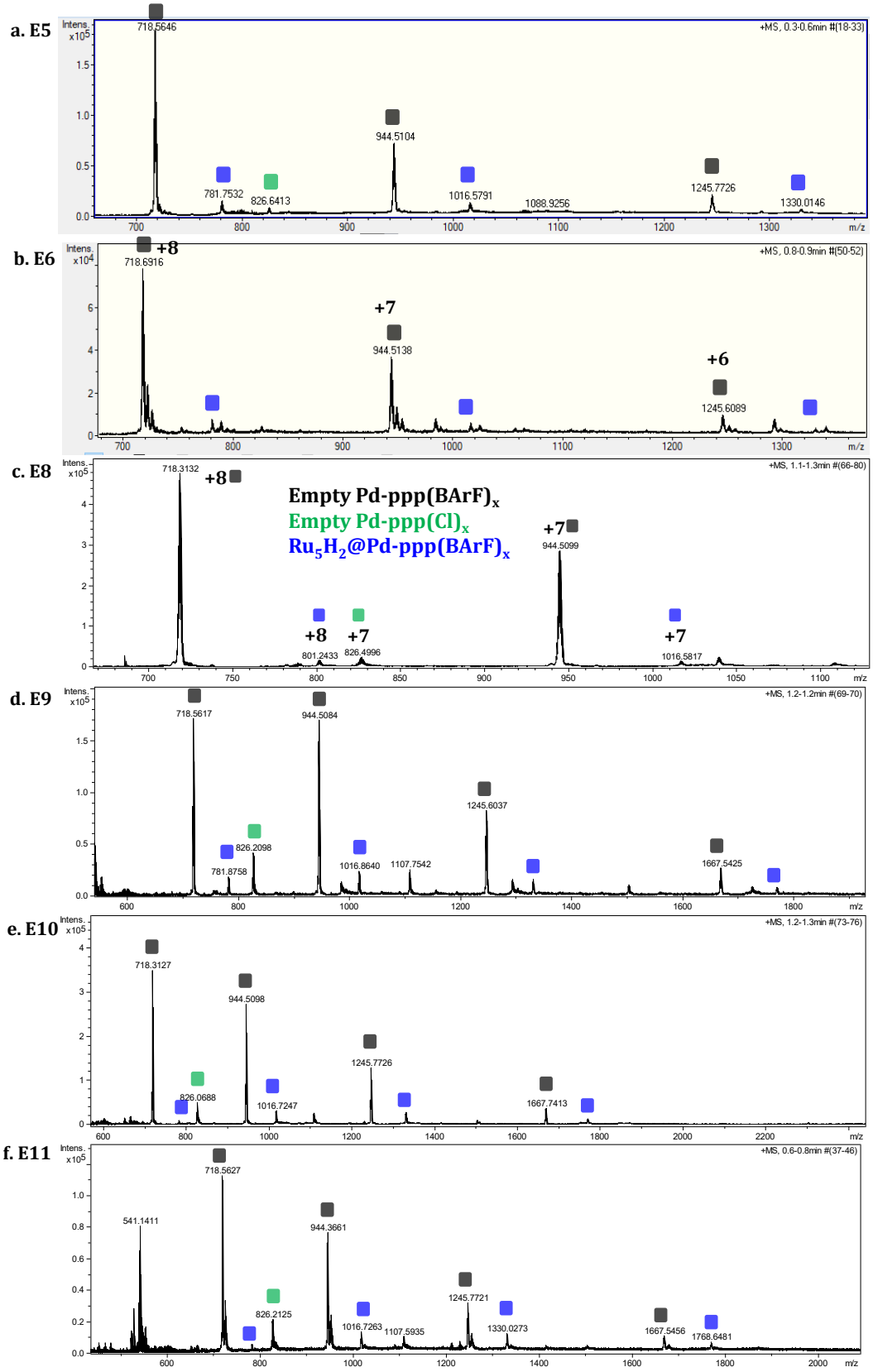

Figure S17. HR-ESI-MS of final experiment solutions. Recoveries of the nanocapsule were 95% for E6, 40% for E5, >98% for E8, 40% for E11, 76% for E9 and 82% for E10.

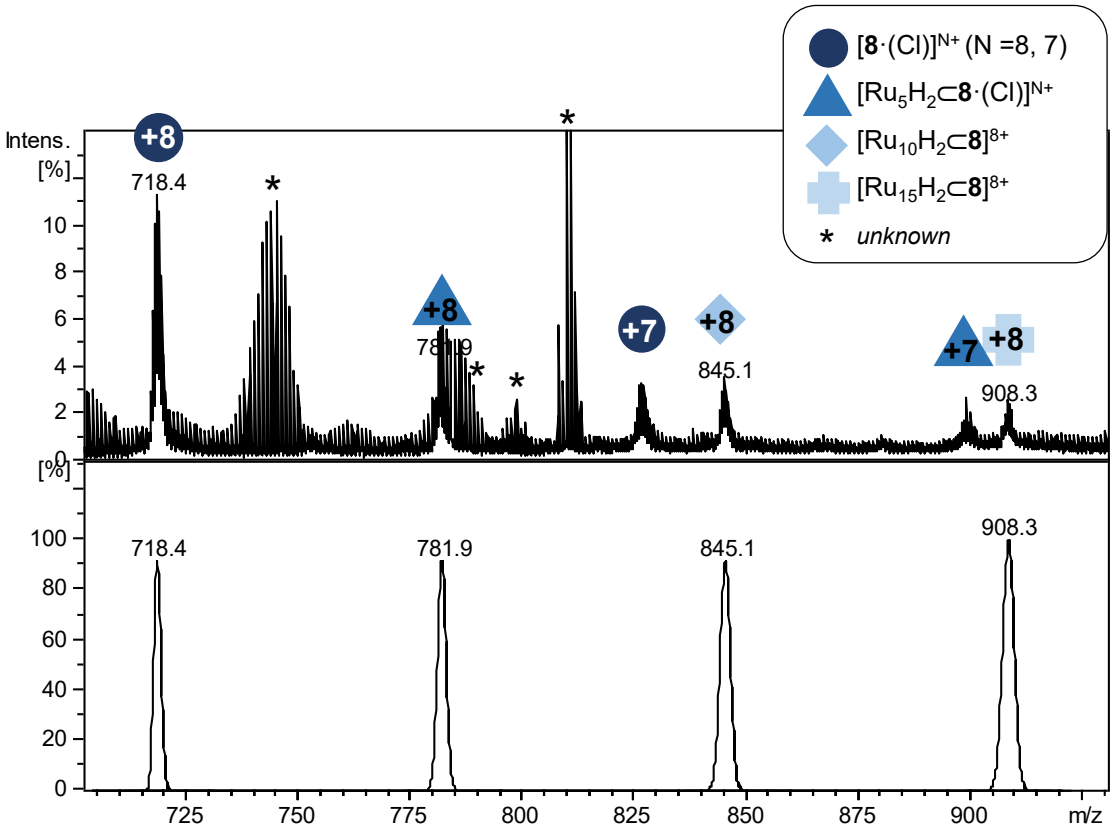

Figure S18. HR-ESI-MS of experiment E4 containing nanocapsule **8**·$(BArF)_8$ peaks filed with Ru_5H_2, $Ru_{10}H_2$ and $Ru_{15}H_2$.

2.4.X-ray diffraction of Cu-ppp clip

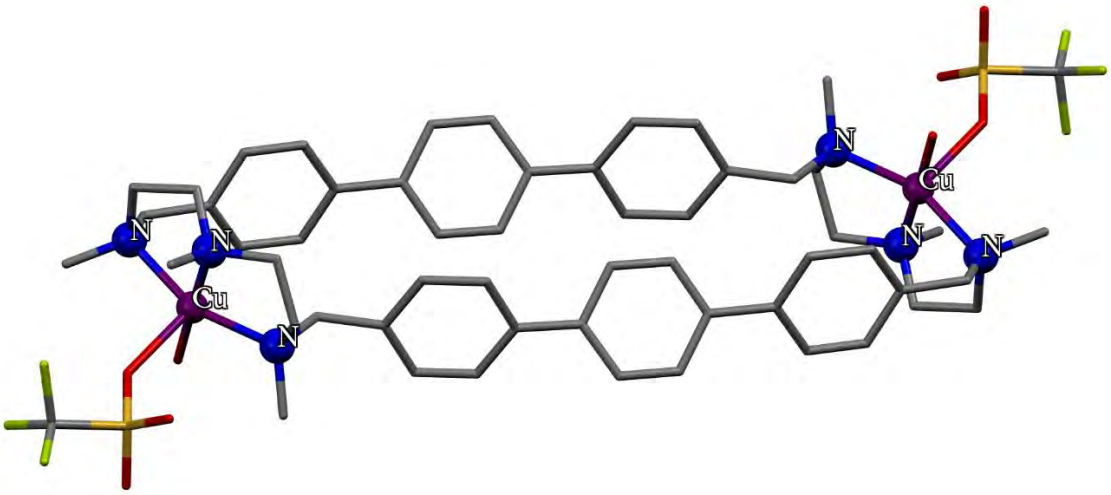

Figure S19. Crystal structure of macrocyclic compound $[Cu_2(Me_2ppp)(OTf)_2](OTf)_2$ (**CCDC 2127407**), synthesized following a reported procedure.[2] H atoms were omitted for clarity. Cu(II) presents a d^8 electronic configuration which enhance copper ions to adopt a tetracoordinated square-planar geometry formed by three N atoms of the macrocyclic ligand (Me_2ppp). Two H_2O molecules from the solvent were coordinated in a monodentate mode. Analogue structure is envisioned for the Pd clip ($[Pd_2(Me_2ppp)(AcO)_2](OTf)_2$)[2] used in this work (see experiment E12).

3. Supplementary Tables

Table S1. XRD data for $[Cu_2(Me_2ppp)(OTf)_2](OTf)_2$. (CCDC 2127407)

	$[Cu_2(Me_2ppp)(OTf)_2](OTf)_2$
CCDC code	EUL6P167_6_2on
formula	$C_{58}H_{76}Cu_2F_{12}N_6O_{17}S_4$
fw	1612.56
Crystal system	Monoclinic
Space group	C 1 2/c 1
a (Å)	31.531(5)
b (Å)	16.223(2)
c (Å)	17.453(2)
α (deg)	90
β (deg)	121.297(8)
γ (deg)	90
V (Å^3)	7629.(2)
Z	4
Dc (Mg m^{-3})	1.404
T (K)	100
λ (Å)	0.71076
μ (mm-1)	0.760
2ϑ *max (deg)*	25.01
reflns collected	46113
indep. reflns	6578
params	463
GOF on F^2	1.982
$R_{indices\ (I>2\sigma(I))}$	0.1455
$R_{indices\ (all\ data)}$	0.1923

4. DFT results and analysis of the Ru clusters and NP

4.1.Computational details

DFT calculations of metal nanoclusters. Software: Vienna ab initio simulation package, VASP;[5, 6] spin polarized DFT; exchange-correlation potential approximated by the generalized gradient approach proposed by Perdew, Burke, and Ernzerhof (PBE);[7, 8] projector augmented waves (PAW) full-potential reconstruction;[9, 10] PAW data sets for Ru treating the (*n*-1)*p*, (*n*-1)*d* and *ns* states (i.e. 14 valence electrons); kinetic energy cutoff: 500 eV; Γ-centered calculations;[11] Gaussian smearing (σ) of 0.02 eV width, energies being therefore extrapolated for σ = 0.00 eV; geometry optimization threshold: residual forces on any direction less than 0.02 eV/Å; supercell size: 26Å~26Å~29 Å^3 for all species and 28Å~32Å~22 Å^3 for $Ru_{57}H_{44}$ stabilized by the pillars model (ensures a vacuum space of at least ca. 10 Å between periodic images of the nanoclusters).

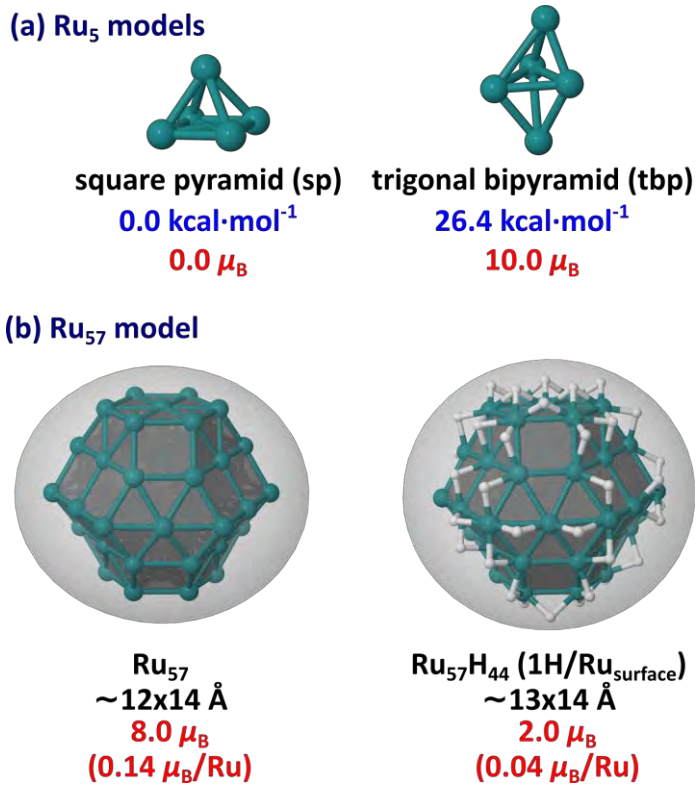

Figure S20. (a) Square pyramid (**sp**) and trigonal bipyramid (**tb**) Ru_5 models. Their relative energy (blue, in kcal/mol) and magnetic moment (red) are reported below. (b) bare Ru_{57} NP and its hydrogenated counterpart, with $1H/Ru_{surface}$. The approximate diameter of the

spheroidal shape accounts for the van der Waals radius of atoms (H: ~120 pm; Ru: ~180 pm, see also Ref.[12]); the two numbers are the a and c diameters of the ellipsoid.

Ru_5 models: the **sp** and **tb** models are reported in Figure S18a.
Ru_{57} model : The model is an hcp spheroid with a diameter of ~1nm . Its structure is reported in Figure S18b.
Adsorption energies.

$$E_{\mathrm{ads}}(\mathrm{H}) = \frac{1}{n}\left[E(n\mathrm{H}^*) - E(\mathrm{NP}) - \frac{n}{2}E(\mathrm{H_2})\right] \quad (1)$$

$$E_{\mathrm{ads}}(\mathrm{L}) = \frac{1}{n}\left[E(n\mathrm{L}^*) - E(\mathrm{NP}) - nE(\mathrm{L})\right] \quad (2)$$

i.e. in the case of hydrides it is a dissociative adsorption energy.

Ab initio thermodynamics. The method and a review of applications to surface science was published in Ref.[13]. Let us consider the adsorption process of one species, L, which is the starting point of the Langmuir–Hinshelwood mechanism in heterogeneous catalysis. It can be summarized as: M + nL → nL* (M = metal cluster or nanoparticle and * stands for "chemisorbed") and the Gibbs free energy for this reaction is calculated as:

$$\Delta G_{\mathrm{ads}}(\mathrm{L}, T, p) = \left[\Delta G^{\circ} - n\mu(\mathrm{L})\right]/A \quad (3)$$

where A is the surface area of the metal cluster or NP, μ is the chemical potential of the L ligand and ΔGº is calculated after DFT energies and vibrational contributions to energies. The free energy diagram reported in Figure 10 of the manuscript was calculated with our in-house *aithermo* software.[14] Methodological details and examples of applications done by some of us can be found in Refs.[14-18].

Second order energy differences. The second–order energy difference Δ_2E is well known to be an important stability criterion in cluster science.[19, 20] In the present case, it is defined as:

$$\Delta_2 E(n) = E(n+1) + E(n-1) - 2E(n) \quad (4)$$

where E(n) is the energy of the most stable $Ru_5H_n(\eta^6\text{-PhH})_2(\eta^6\text{-pyz})_3$ isomer.

It reflects the stability of a Ru_5H_n cluster with respect to Ru_5H_{n+1} and Ru_5H_{n-1} species, the higher $\Delta_2E(n)$ the more stable the cluster of size n. It usually exhibits an odd-even alternation.

4.2.Additional DFT results

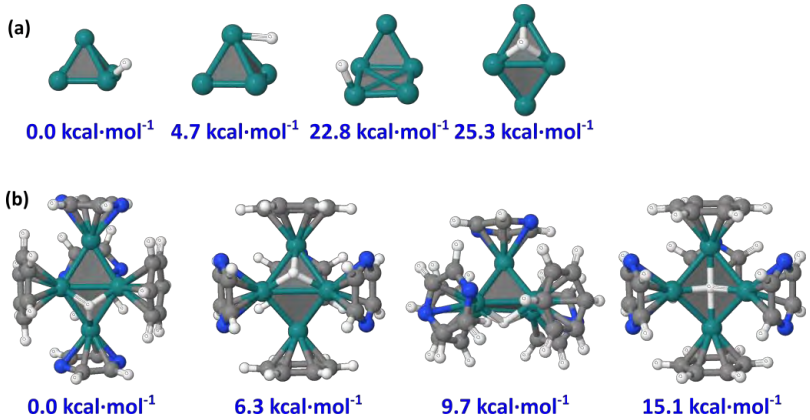

Figure S21. (a) Bare Ru_5H isomers; (b) $Ru_5H(\eta^6\text{-PhH})_2(\eta^6\text{-pyz})_3$ isomers. Relative energies in blue.

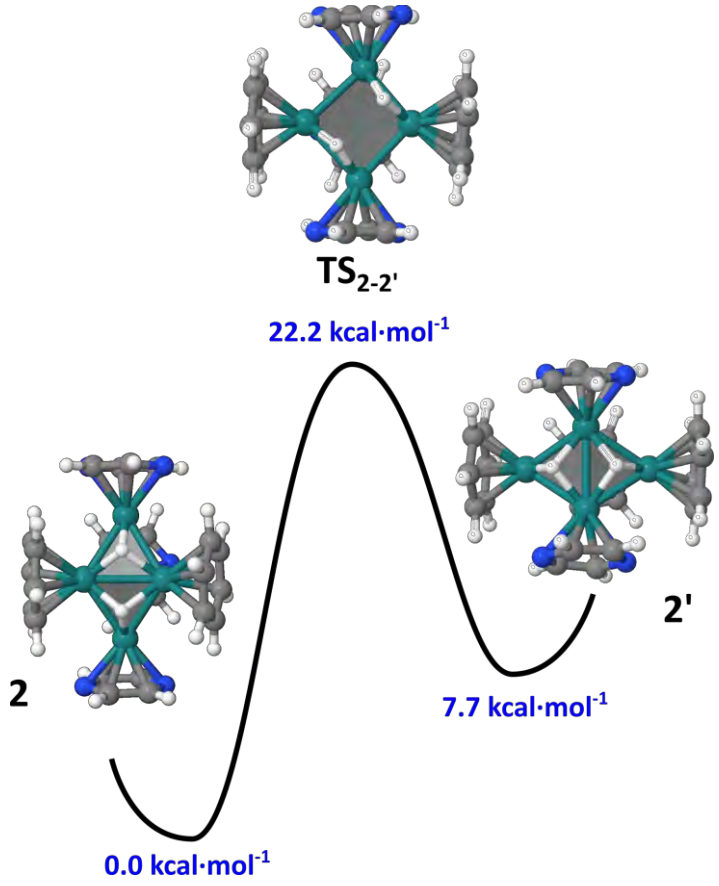

Figure S22. Isomerization pathway of the **bp**-$Ru_5H_2(\eta^6\text{-PhH})_2(\eta^6\text{-pyz})_3$ cluster, via an **sp**-$Ru_5H_2(\eta^6\text{-PhH})_2(\eta^6\text{-pyz})_3$ transition state. **2**: two equatorial pyz, one equatorial PhH and two axial pyz; **2'**: 3 equatorial pyz and two axial PhH.

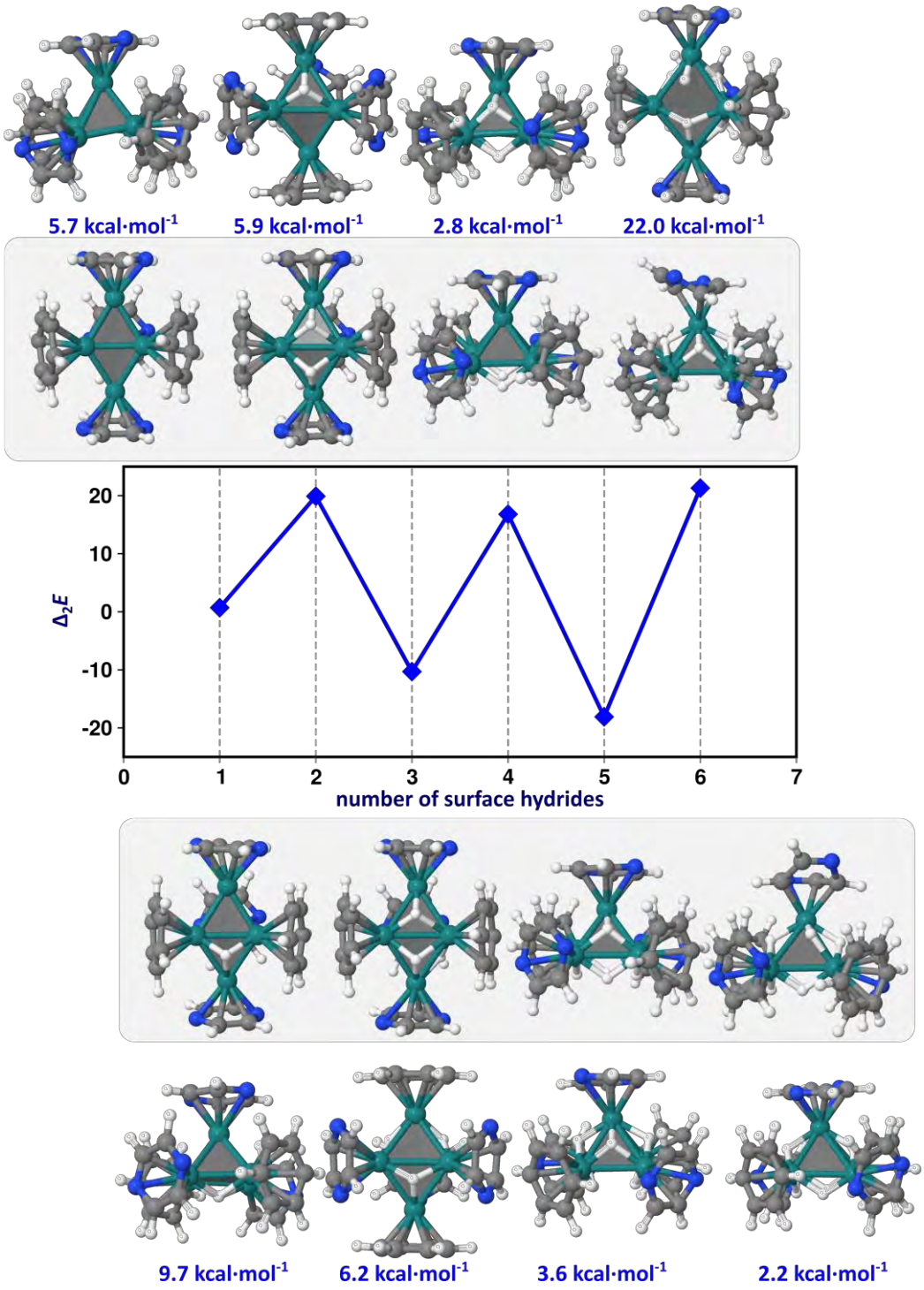

Figure S23. Second-order energy differences for the most stable $Ru_5H_n(PhH)_2(pyz)_3$ isomer, *n*=1-6 (structures on a grey background). Even-*n* closed-shell clusters are more stable than the radical odd-*n* clusters, as expected. The second low-lying isomer found in this study is also shown for each size, with its energy (in blue) relative to the lowest one.

5. Supplementary References

1. E. Ubasart, O. Borodin, C. Fuertes-Espinosa, Y. Xu, C. García-Simón, L. Gómez, J. Juanhuix, F. Gándara, I. Imaz, D. Maspoch, M. von Delius and X. Ribas, *Nat. Chem.*, 2021, **13**, 420-427.

2. E. Ubasart, C. García-Simón, M. Pujals, K. Asad, N. Chronakis, T. Parella and X. Ribas, *Org. Chem. Front.*, 2021, **8**, 4101-4105.

3. L. M. Martínez-Prieto and B. Chaudret, *Acc. Chem. Res.*, 2018, **51**, 376-384.

4. L. M. Martínez-Prieto, C. Urbaneja, P. Palma, J. Cámpora, K. Philippot and B. Chaudret, *Chem. Commun.*, 2015, **51**, 4647-4650.

5. G. Kresse and J. Furthmüller, *Phys. Rev. B*, 1996, **54**, 11169-11186.

6. G. Kresse and J. Furthmüller, *Comput. Mater. Sci.*, 1996, **6**, 15-50.

7. J. P. Perdew, K. Burke and M. Ernzerhof, *Phys. Rev. Lett.*, 1996, **77**, 3865-3868.

8. J. P. Perdew, K. Burke and M. Ernzerhof, *Phys. Rev. Lett.*, 1997, **78**, 1396-1396.

9. P. E. Blöchl, *Phys. Rev. B*, 1994, **50**, 17953-17979.

10. G. Kresse and D. Joubert, *Phys. Rev. B*, 1999, **59**, 1758-1775.

11. H. J. Monkhorst and J. D. Pack, *Phys. Rev. B*, 1976, **13**, 5188-5192.

12. S. S. Batsanov, *Inorg. Mater.*, 2001, **37**, 871-885.

13. K. Reuter, C. Stampf and M. Scheffler, in *Handbook of Materials Modeling: Methods*, ed. S. Yip, Springer Netherlands, Dordrecht, 2005, DOI: 10.1007/978-1-4020-3286-8_10, pp. 149-194.

14. L. Cusinato, I. del Rosal and R. Poteau, *Dalton Trans.*, 2017, **46**, 378-395.

15. I. del Rosal, L. Truflandier, R. Poteau and I. C. Gerber, *J. Phys. Chem. C*, 2011, **115**, 2169-2178.

16. L. Cusinato, L. M. Martínez-Prieto, B. Chaudret, I. del Rosal and R. Poteau, *Nanoscale*, 2016, **8**, 10974-10992.

17. R. González-Gómez, L. Cusinato, C. Bijani, Y. Coppel, P. Lecante, C. Amiens, I. del Rosal, K. Philippot and R. Poteau, *Nanoscale*, 2019, **11**, 9392-9409.

18. N. Rothermel, H.-H. Limbach, I. del Rosal, R. Poteau, G. Mencia, B. Chaudret, G. Buntkowsky and T. Gutmann, *Catal. Sci. Tech.*, 2021, **11**, 4509-4520.

19. W. D. Knight, K. Clemenger, W. A. de Heer, W. A. Saunders, M. Y. Chou and M. L. Cohen, *Phys. Rev. Lett.*, 1984, **52**, 2141-2143.

20. R. Poteau and F. Spiegelmann, *J. Chem. Phys.*, 1993, **98**, 6540-6557.